Preface

The 2018 GFD Program theme was *Sustainable Fluid Dynamics* with Professor Andrew Woods of the University of Cambridge serving as principal lecturer. Andy showed the audience in the cottage and on the porch how to find similarity solutions everywhere, from deep in the earth to high in the atmosphere. He expanded on his lectures with the fellows during "Andy time", and stayed on throughout the summer to participate in the traditional debates on the porch with participants old and new. Andy also contributed enthusiastically to the supervision of the fellows, particularly when there was an opportunity to squirt food dye into an experiment.

The first ten chapters of this volume document these lectures, each prepared by pairs of the summer's GFD fellows. Following the principal lecture notes are the written reports of the fellows' own research projects. This summer's fellows were:

- Neeraja Bhamidipati, University of Cambridge
- Laura Cope, University of Cambridge
- Edward Hinton, University of Cambridge
- Christopher Howland, University of Cambridge
- Andrea Lehn, Massachusetts Institute of Technology
- Sara Lenzi, University of Turin
- Thomas Le Reun, Aix-Marseille Université
- Tyler Lutz, Yale University
- Sutirtha Sengupta, University of California, Santa Cruz
- Rohit Supekar, Massachusetts Institute of Technology
- Bowen Zhao, Yale University

In 2018, the Sears Public Lecture was delivered by Professor John Dabiri of Stanford University on the topic of "Biological Propulsion in (and of?) the Ocean". Over a hundred listeners filed into Redfield for the occasion, and then enjoyed refreshments in the evening air afterwards outside the auditorium.

Neil Balmforth and Colm-cille Caulfield acted as the co-directors for the summer, and once the FIFA Men's World Cup was over, did their best to ensure the smooth running of the summer. A large number of long-term staff members ensured that the fellows never lacked for guidance, and the seminar series was filled by a steady stream of visitors, talking about topics as diverse as sneezes, squeezes and shear. Anders Jensen worked his usual magic in the Lab, dealing inventively with lava, fountains and recalcitrant plumes with typical good humour, and Janet Fields and Julie Hildebrandt smoothly ran the program as always, with all delays to (and omissions from) the Proceedings Volume being entirely Colm-cille's fault...

Table of Contents

2018 Geophysical Fluid Dynamics Participants

FELLOWS

Neeraja Bhamidipati	University of Cambridge
Laura Cope	University of Cambridge
Edward Hinton	University of Cambridge
Christopher Howland	University of Cambridge
Andrea Lehn	Massachusetts Institute of Technology
Sara Lenzi	University of Turin
Thomas Le Reun	Aix-Marseille Université
Tyler Lutz	Yale University
Sutirtha Sengupta	University of California, Santa Cruz
Rohit Supekar	Massachusetts Institute of Technology
Bowen Zhao	Yale University

STAFF AND VISITORS

Thomasina Ball	University of British Columbia
Neil Balmforth	University of British Columbia
Joseph Biello	University of California, Davis
Anthony Bonfils	Nordic Institute of Theoretical Physics
Lydia Bourouiba	Massachusetts Institute of Technology
Keaton Burns	Massachusetts Institute of Technology
Colm-cille Caulfield	University of Cambridge
Claudia Cenedese	Woods Hole Oceanographic Institution
Megan Davies Wykes	University of Cambridge
Charlie Doering	University of Michigan
Thomas Eaves	University of Dundee
Giovanni Fantuzzi	Imperial College London
Alexey Fedorov	Yale University
Glenn Flierl	Massachusetts Institute of Technology
Andrew Fowler	University of Limerick
Basile Gallet	CEA, Saclay
Pascale Garaud	University of California, Santa Cruz
David Goluskin	University of Victoria
Peter Harrington	University of California, Santa Cruz
Pedram Hassanzadeh	Rice University
Karl Helfrich	Woods Hole Oceanographic Institution
Ian Hewitt	University of Oxford
Duncan Hewitt	University of Cambridge
Andrew Hogg	University of Bristol
Herbert Huppert	University of Cambridge
Edward Johnson	University College London
Alexis Kaminski	University of California, Berkeley
Rich Kerswell	University of Cambridge

Navaneeth Kizhakke Marath	Nordic Institute of Theoretical Physics
Katarzyna Kowal	Northwestern University
Jacob Langham	University of Bristol
Detlef Lohse	University of Twente
Dan Lucas	Keele University
Shreyas Mandre	University of Warwick
D. Mark Martinez	University of British Columbia
Craig McConnochie	Woods Hole Oceanographic Institution
Colin Meyer	Dartmouth College
Woosok Moon	Nordic Institute of Theoretical Physics
Heidi Nepf	Massachusetts Institute of Technology
Matt Olson	University of Michigan
Francesco Paparella	New York University Abu Dhabi
Michael Patterson	University of Bristol
Joseph Pedlosky	Woods Hole Oceanographic Institution
Victoria Pereira	Oxford University
Satyajit Pramanik	Nordic Institute of Theoretical Physics
Matthew Scase	University of Nottingham
Andre Souza	Massachusetts Institute of Technology
Edward Spiegel	Columbia University
Bruce Sutherland	University of Alberta
Jim Thomas	University of North Carolina
Ian Tobasco	University of Michigan
Barbara Turnbull	University of Nottingham
George Veronis	Yale University
Brian von Herzen	The Climate Foundation
Gregory Wagner	Massachusetts Institute of Technology
Chen Wang	University of British Columbia
Jack Whitehead	Woods Hole Oceanographic Institution
Andrew Woods	University of Cambridge

2018 Principal Lecturers

Andrew Woods

2018 Geophysical Fluid Dynamics Summer School Participants

First Row (L-R): (Standing) Craig McConnochie, (Seated) Andrew Woods, Edward Hinton, Thomas Le Reun, Tyler Lutz, Neeraja Bhamidipati, George Veronis, Rohit Supekar, Christopher Howland, Andrea Lehn, Laura Cope, Sutirtha Sengupta, Sara Lenzi, Bowen Zhao

Second Row (L-R): Duncan Hewitt, Neil Balmforth, Colm-cille Caulfield, Thomas Eaves, Basile Gallet, Mark Martinez, Ted Johnson, Glenn Flierl, Chen Wang, Joe Pedlosky, Andre Souza, Rich Kerswell, Karl Helfrich, Kristen Fauria, Brian von Herzen

Missing from photo: Joseph Biello, Anthony Bonfils, Megan Davies-Wykes, Giovanni Fantuzzi, Andrew Fowler, Pascale Garaud, David Goluskin, Peter Harrington, Pedram Hassanzadeh, Ian Hewitt, Andrew Hogg, Herbert Huppert, Jacob Langham, Alexis Kaminski, Navaneeth Kizhakke, Marath, Katarzyna Kowal, Detlef Lohse, Dan Lucas, Shreyas Mandre, Colin Meyer, Woosok Moon, Matt Olson, Francesco Paparella, Michael Patterson, Satyajit Pramanik, Matthew Scase, Bruce Sutherland, Jim Thomas, Ian Tobasco, Barbara Turnbull, Greg LeClaire Wagner

GFD Lecture Schedule

PRINCIPAL LECTURES – Andrew Woods

Monday, June 18
Turbulent, Buoyancy-driven Flows: Plume Dynamics

Tuesday, June 19
Confined Plumes and Mixing

Wednesday, June 20
Plumes in Confined Spaces

Thursday, June 21
Ventilated Plumes, Plumes in a Tube, and Ventilation with Multiple Openings

Friday, June 22
Inertial Gravity Currents: Ash Flows and Turbidities

Monday, June 25
Modeling Ash Flows and Volcanoes

Tuesday, June 26
Volcanic Plumes and Porous Rock

Wednesday, June 27
Porous Media Gravity Currents

Thursday, June 28
More Challenges in Porous Media for CO2 Sequestration

Friday, June 29
Flow in Porous Rocks: The Influence of Temperature, Fluid-Rock Interactions and Viscous Instabilities

SEMINARS

Monday, July 2
Preconditioning Numerical Solvers for Steady State and Traveling Waves
Jacob Langham, University of Bristol

Tuesday, July 3
Layers, Localization and Relaminarization in Stratified Plane Couette Flow with Horizontal Shear
Dan Lucas, Keele University

Wednesday, July 4
HOLIDAY

Thursday, July 5
Instabilities in Particle-laden Flows
Pascale Garaud, University of California Santa Cruz

For What it's Worth: An Analyst's Hunt for Asymptotic Heat Transport in Raleigh-Bénard Convection
Charles Doering, University of Michigan

Friday, July 6
On the Optimal Design of Wall-to-Wall Heat Transport
Ian Tobasco, University of Michigan

Wall-to-Wall Optimal Transport Theory and 2D Computations
Andre Souza, Georgia Institute of Technology

Monday, July 9
Bridging the Scale Hierarchy Problem in Ocean Biogeochemical Models
Francesco Paparella, New York University Abu Dhabi

Tuesday, July 10
The Fluid and Elastodynamics of Cracking Rocks: Or How to Frack Into and Out of Trouble
Herbert Huppert, University of Cambridge

Wednesday, July 11
Rapidly Rotating Dynamos at Large Reynolds Number
Basile Galet, CEA Saclay

Thursday, July 12
The Effect of Pre-Existing Turbulence on Stratified Shear Instability
Alexis Kaminski, Oregon State University

Friday, July 13
Reduced-order Modeling of Rayleigh-Bènard Turbulence
Pedram Hassanzadeh, Rice University

Monday, July 16
A Unified Nonlinear Stochastic Time-series Analysis for Climate Science
Woosok Moon, Nordic Institute for Theoretical Physics

Tuesday, July 17
Plumes in Stratified Fluids
Bruce Sutherland, University of Alberta

Wednesday, July 18
Double Diffusive Convection
Detlef Lohse, University of Twente

Thursday, July 19
Subglacial Processes and the Flow of Ice Sheets
Katarzyna Kowal, University of Cambridge & Northwestern University

Friday, July 20
Liesegang Rings
Andrew Fowler, University of Limerick

Monday, July 23
Bounding Extreme Events on a Chaotic Attractor
David Goluskin, University of Victoria

Tuesday, July 24
Effect of Temperature on Cross Ventilation
Megan Davies Wykes, University of Cambridge

Wednesday, July 25
Plumes and Gravity Currents: Some New Ideas on Some Old Problems
Andrew Hogg, University of Bristol

Thursday, July 26
The Fluid Dynamics of Disease Transmission Laboratory
Lydia Bourouiba, Massachusetts Institute of Technology

Friday, July 27
Garbage Patches
Glenn Flierl, Massachusetts Institute of Technology

Monday, July 30
Rotationally Suppressed and Rotationally Forced Raleigh-Taylor Instability
Matthew Scase, University of Nottingham

SEARS PUBLIC LECTURE
Biological Propulsion in (and of?) the Ocean
John Dabiri, Stanford University

Tuesday, July 31
Unsupervised Clustering for Coherent Structure Identification and Lagrangian Data Assimilation
John Dabiri, Stanford University

Wednesday, August 1
How Vegetation Alters Waves and Currents, and the Feedbacks to Environmental System Function
Heidi Nepf, Massachusetts Institute of Technology

Thursday, August 2
Geothermal Heat Exchange
Ian Hewitt, University of Oxford

Friday, August 3
Flow-driven Compaction of a Fibrous Porous Medium
Thomas Eaves, University of British Columbia

Monday, August 6
Convective Plumes in a Heterogenous Porous Formation
Duncan Hewitt, University of Cambridge

Tuesday, August 7
A Modified Howard-Marcus-Welander Loop for Ocean Millennial Variability
Alexey Fedorov, Yale University

Wednesday, August 8
Particles Breaking out of Debris Flows
Barbara Turnbull, University of Nottingham

Thursday, August 9
Squeeze Dispersion and the Enhancement of Diffusion by Strain
Gregory LeClaire Wagner, Massachusetts Institute of Technology

Hot Rocks and Cool Stars
Ned Right, UCLA

Friday, August 10
An Enthalpy Method for Subglacial Frozen Fringe
Colin Meyer, University of Oregon

FELLOWS' PRESENTATIONS

Tuesday, August 21

Horizontal Shear Instabilities in the Stellar Interior
Laura Cope, University of Cambridge

How Mixed is the Ocean Mixed Layer?
Neeraja Bhamidipati, University of Cambridge

Defending Against Viscous Flows
Edward Hinton, University of Cambridge

Centrifugally forced Raleigh-Taylor Instability: Growth of Varicose Perturbations
Sutirtha Sengupta, University of California Santa Cruz

Wednesday, August 22

Viscoplastic Flow Around a Cylinder: Nuggets or No Nuggets?
Rohit Supekar, Massachusetts Institute of Technology

Spooky Mixing at a Distance: Nonlocal Eddy Fluxes from Stochastic Advection
Tyler Lutz, Yale University

Instability of Piecewise, Uniform, Quasi-geostrophic Vortex Above Topography
Bowen Zhao, Yale University

Interacting Plumes in a Rotating Environment: The Special Case of a Single Plume
Christopher Howland, University of Cambridge

Thursday, August 23

Fountains Jets, and Rotation, Oh My!
Andrea Lehn, Massachusetts Institute of Technology

Swimming with Posts
Sara Lenzi, University of Turin

Porous Convection with Internal Heating: Driving Enceladus' Hydrothermal Activity
Thomas Le Reun, Aix Marseille Université

Lecture 1
Turbulent, Buoyancy-driven Flows: Plume Dynamics

Notes by Andrea Lehn and Tyler Lutz

June 18, 2018

1 Introduction

Buoyancy-driven plumes appear in a diverse range of environmental phenomena: from hydro-thermal vents on the sea floor to the transport of microbes through a hospital ventilation system. Buoyant plumes develop when a buoyant fluid is released from a local source into an ambient environment, which may be stratified or rotating, especially in a geophysi-cal contexts. Above Reynolds number order 10^3, these plumes become turbulent, meaning the molecular properties of the fluid are unimportant. In many cases, the buoyancy of the plume may become reversed, creating a fountain.

The interaction of turbulent plumes with their environments is dominated by via mixing through the action of turbulent entrainment. The transportation of mass, energy and particulate matter via buoyant plumes underpins many environmental phenomena, a few of which are illustrated below:

- the upwelling of buoyant oil from undersea oil spills and the plumes of smoke generated if the oil catches fire at the surface;
- hydrothermal plumes at the sea floor releasing hot gas, generating a buoyant plume;
- buoyancy driven flows in buildings such as the cooling or heating of walls, or plumes of relatively hot or cold air forced from building HVAC systems; and
- eruptions of magma, basalt and ash into the atmosphere from volcanoes.

In this first lecture, the classic plume equations describing mass, momentum and buoyancy are developed using two key assumptions: a self-similar top-hat profile and a linear entrainment velocity. We begin from dimensional analysis for a simple case, assuming a linear relationship between buoyancy and the density difference. A more formal development employing an integral approach follows. A turbulent plume in an unstratified environment has a self similar shape that varies in amplitude with distance away from the source, which is shown in section 2.2. The self similar profile has the scaling predicted by dimensional analysis. Fountains are not discussed in this lecture, but a scaling for the equilibrium height of a plume in a density stratified ambient is derived. For buoyant plumes, it is important

to note that fluid mass, chemical mass (e.g. salt) and total thermal energy flux are conserved in buoyant plumes. When these quantities evolve as the plume undergoes mixing they generate buoyancy, which impacts the dynamics of the plume.

2 Plume Theory

2.1 Dimensional analysis

An important quantity in plumes is the buoyancy flux, which represents the density deficit driving the flow. The buoyancy flux is conserved in the special case where a linear relationship exists between density and buoyancy. Assuming changes in density are small and can be linearized, one can write the buoyancy flux simply. Changes in buoyancy may be due to changes in salinity or temperature

$$\Delta\rho = -\rho_0 \alpha \Delta T,$$
$$\Delta\rho = \rho_0 \beta \Delta S$$

where α, β are thermal expansion and salinity contraction coefficients, respectively, and ρ_0 is a reference density. Consider a plume with a volume flux Q_0 and a buoyancy flux $g' = g\Delta\rho/\rho_0$, where ρ_0 is the ambient density and $\Delta\rho$ is the difference between the plume fluid density and ambient density. The buoyancy flux is $B_0 = g'Q_0$. By performing dimensional analysis, we can learn how the plume evolves as a function of the buoyancy flux and vertical position from the source.

Beginning from the two defining parameters, volume flux and buoyancy we have,

$$[Q] = \frac{L^3}{T} \quad \text{and} \tag{1}$$
$$[g'] = \frac{L}{T^2}, \tag{2}$$

and thus the buoyancy flux is written as

$$[B] \equiv [g'Q] = \frac{L^4}{T^3}. \tag{3}$$

Assume the properties of the plume only vary with vertical distance away from the source. Using this information, we develop scalings for the velocity, volume flux and buoyancy of the plume in terms of vertical height away from the source, z. Performing a dimensional analysis to determine plume radius, b, velocity, u, volume flux integrated across the plume area, Q, buoyancy, g' and momentum flux M from the buoyancy flux B and vertical height,

z yields the following

$$b \sim z \qquad \left[L\right], \tag{4}$$

$$u \sim B^{\frac{1}{3}} z^{-\frac{1}{3}} \qquad \left[\frac{L}{T}\right], \tag{5}$$

$$Q \sim B^{\frac{1}{3}} z^{\frac{5}{3}} \qquad \left[\frac{L^3}{T}\right], \tag{6}$$

$$g' \sim B^{\frac{2}{3}} z^{-\frac{5}{3}} \qquad \left[\frac{L}{T^2}\right], \tag{7}$$

$$M \sim B^{\frac{2}{3}} z^{\frac{5}{3}} \qquad \left[\frac{L^4}{T^2}\right] \tag{8}$$

Empirical relationships can be determined via experiments, although in reality plume properties varies in space and time. A key finding of dimensional analysis is that as the fluid rises, its volume flux increases due to entrainment of the surrounding fluid. The growth in Q is compensated by a growth in radius and a decrease in velocity. The momentum flux grows with height as the buoyancy flux is released.

For the case of a plume rising in an unstratified ambient ($N = 0$), we do not expect the plume to have any characteristic vertical scale since it will continue rising unabated. By introducing stratification, we can estimate a scaling for the height at which the plume will reach neutral buoyancy, H. The velocity of the plume is decreasing as it rises even though the fluid is accelerating: the momentum flux is positive since fluid is being entrained into the plume from the ambient. The buoyancy flux decreases with height because the density of the ambient is changing.

In a stratified environment, we can quantify the stratification of the ambient, the Brunt-Vaiasala frequency, in terms of ambient density, ρ_a, as

$$N^2 \equiv -\frac{g}{\rho_0}\frac{d\rho_a}{dz}. \tag{9}$$

This describes the strength of stratification in the ambient. Its dimensions are,

$$[N] = \frac{1}{T}. \tag{10}$$

From dimensional analysis, we anticipate the equilibrium plume height to depend on the Brunt-Vaiasala frequency and buoyancy flux as

$$H \sim B^{\frac{1}{4}} N^{-\frac{3}{4}}, \tag{11}$$

which is validated with data as shown in Figure 1.

2.2 Conservation laws: Integral approach

This section establishes the conservation laws for fluxes of volume, momentum and buoyancy. To accommodate for the effects of turbulence, we separate the state variables into mean and perturbed components, writing, for instance $u = \hat{u} + \bar{u}$. In this notation,

$$\rho = \rho_0 \left(1 - \alpha(\bar{\Delta}T - \hat{\Delta}T)\right), \tag{12}$$

where ΔT represents the temperature anomaly—the difference in the plume's temperature relative to its starting value—and α is the volumetric thermal expansion coefficient. Note that this could equivalently be written for a salinity gradient using β and ΔS. The analysis that follows considers a plume with thermally driven buoyancy.

Summing over the full area of the field, we find for 2D plumes the volume flux:

$$\rho_0 Q = \overline{\int_0^\infty \int_0^{2\pi} (\hat{u} + \bar{u})\rho_0 \left(1 - \alpha(\bar{\Delta}T - \hat{\Delta}T)\right) r dr d\theta}, \tag{13}$$

which, in the limit of small α, goes like

$$\rho_0 Q \approx 2\pi\rho_0 \int_0^\infty \bar{u} r dr. \tag{14}$$

Proceeding likewise for the mean momentum flux yields

$$\begin{aligned} \rho_0 M &= \overline{\int_0^\infty \int_0^{2\pi} (\hat{u} + \bar{u})^2 \rho_0 \left(1 - \alpha(\bar{\Delta}T - \hat{\Delta}T)\right) r dr d\theta} \\ &\approx 2\pi\rho_0 \int_0^\infty \left((\bar{u})^2 + \overline{\hat{u}^2}\right) r dr, \end{aligned} \tag{15}$$

and similarly, for the heat flux (or buoyancy flux, more generally),

$$\begin{aligned} \rho_0 Q_H &= \overline{\int_0^\infty \int_0^{2\pi} (\hat{u} + \bar{u})(\bar{\Delta}T - \hat{\Delta}T)\rho_0 \left(1 - \alpha(\bar{\Delta}T - \hat{\Delta}T)\right) r dr d\theta} \\ &\approx 2\pi\rho_0 \int_0^\infty \left(\bar{u}\bar{\Delta}T + \overline{\hat{u}\hat{\Delta}T}\right) r dr. \end{aligned} \tag{16}$$

We can simplify these equations still further by neglecting $\hat{u}$ and $\hat{\Delta}T$. In summary, for a thermally driven flow, the simplified conservation laws may be written as

$$Q = 2\pi \int_0^\infty \bar{u} r dr, \tag{17}$$

$$M = 2\pi \int_0^\infty \bar{u}^2 r dr, \quad \text{and} \tag{18}$$

$$Q_H = 2\pi \int_0^\infty \bar{u}\bar{g}' r dr. \tag{19}$$

2.3 Classic plume equations

Now, the conservation laws are utilized in conjunction with two key assumptions to write the classic plume equations. To move forward, we consider the steady-state regime and

posit that the flow profile remains self-similar at all times—i.e. they can be mapped onto each other by an affine transformation. As our first assumption, we consider a simple"top hat profile" of radius b, noting that the flux equations for more realistic profiles will differ from those for the hat shape by no more than a multiplicative constant. The second assumption is that the entrainment into the plume is linearly proportional to the vertical plume velocity. We model the entrainment as being linear in the mean velocity $\bar{u}$ with an entrainment coefficient ϵ.

Under these assumptions the fluxes can be written as:

$$Q = u\pi b^2, \tag{20}$$

$$M = uQ = u^2\pi b^2 \text{ and} \tag{21}$$

$$Q_H = \Delta T Q = u\pi b^2 \Delta T. \tag{22}$$

Using our assumption that the entrainment scales linearly with the velocity and occurs only on the boundary between the plume and the ambient fluid (i.e., it scales linearly with the perimeter of a cross-sectional slice of flow)

$$\frac{dQ}{dz} = 2\pi\epsilon u b. \tag{23}$$

Recognizing that g' describes the change in momentum of a parcel of enplumed fluid, we write the momentum flux as

$$\frac{dM}{dz} = \pi b^2 g'_L, \tag{24}$$

where g'_L is a local g'. Recalling that $g' \equiv g\frac{\rho-\rho_a}{\rho_0}$ for the heat flux derivative we write

$$\frac{du\pi b^2 g'}{dz} = -u\pi b^2 N^2. \tag{25}$$

Thus, the set of equations, (23)-(25), represent the classic plume equations. The system is analytically solvable if and only if there is no stratification (i.e. $N = 0$), which simplifies to

$$\frac{dQ}{dz} = 2\epsilon M^{\frac{1}{2}} \tag{26}$$

$$M\frac{dM}{dz} = BQ \tag{27}$$

These equations, (26) and (27), admit a self-similar solution which scales as

$$b \sim z \quad u \sim B^{\frac{1}{3}} \quad g' \sim B^{\frac{2}{3}} z^{-\frac{5}{3}}. \tag{28}$$

This is the same scaling derived by dimensional analysis as expressed in equations (4)-(8).

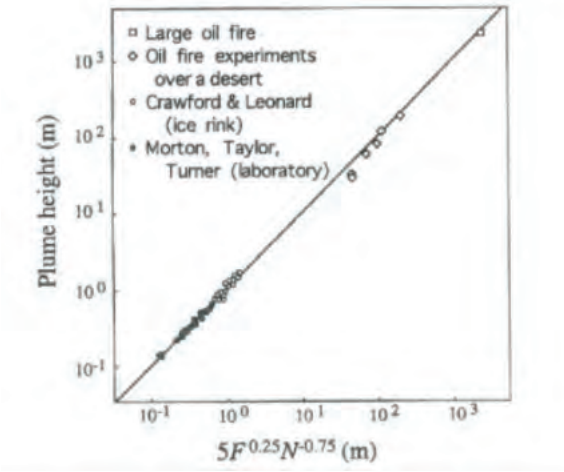

Figure 1: The maximal height attained by plumes in a stratified ambient is consistent with expectations from scaling arguments.

Lecture 2
Confined Plumes and Mixing

Notes by Neeraja Bhamidipati and Laura Cope

June 19, 2018

1 Adjustment to Self-similarity

For a steady plume, self-similarity means that the solutions are singular at the source ($g' \to \infty$ as $z \to 0$). At the nozzle, $z = 0$, $b = b_o$, $M = M_o$, and $Q = Q_o$. We define

$$z_{jet} = \left(\frac{M_o}{\pi \left(\frac{9\epsilon B}{10\pi} \right)^{2/3}} \right)^{3/4} \tag{1}$$

$$z_{mass} = \left(\frac{Q_o}{\frac{6\pi}{5\epsilon} \left(\frac{9\epsilon B}{10\pi} \right)^{1/3}} \right)^{3/5} \tag{2}$$

If the flow initially has more momentum than the self-similar plume, it is considered jet-like ($z_{jet} > z_{mass}$). The adjustment distance over which a plume with a given buoyancy flux develops momentum comparable to the momentum flux at the source is known as the jet length and is given by equation (1). On the other hand, if the plume has excess mass flux at the source ($z_{jet} > z_{mass}$), we define an adjustment length given by equation (2) which is the distance over which a plume with a given buoyancy flux develops a mass comparable to the mass at the source. In this case, the plume is considered a lazy plume and has low initial momentum at the source.

Depending on whether the plume is a jet-like plume or a lazy plume, the virtual origin, z_o, of the plume appears above or below the source respectively. The virtual origin may be expressed as

$$z_o = b_o \mathcal{F}(z_{jet}/z_o; z_{mass}/z_o) \tag{3}$$

2 Plume in a Stratified Ambient

In a stratified ambient, the buoyancy frequency, N is defined as

$$N^2 = -\frac{g}{\rho_o} \frac{\mathrm{d}\rho}{\mathrm{d}z} \tag{4}$$

The equations for a steady plume are given by

$$\frac{\mathrm{d}Q}{\mathrm{d}z} = 2\epsilon M^{1/2} \tag{5}$$

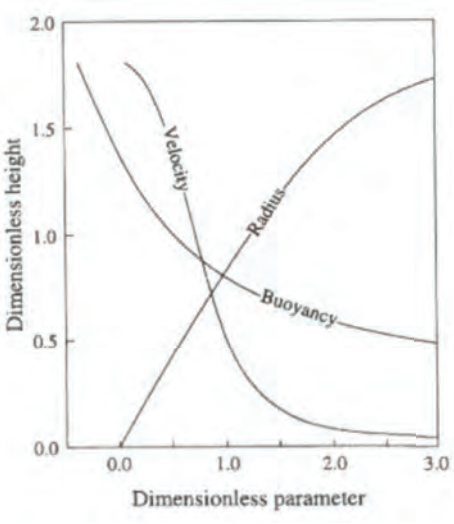

Figure 1: Variation of velocity, radius, and buoyancy profiles of a plume in a stratified ambient. (Morton et al., 1956)

$$\frac{\mathrm{d}M^2}{\mathrm{d}z} = 2BQ \tag{6}$$

$$\frac{\mathrm{d}B}{\mathrm{d}z} = -N^2 Q \tag{7}$$

In the previous chapter, we discussed the solutions to these equations where the ambient is unstratified ($N^2 = 0$) and therefore, the buoyancy flux, B, is constant. If $N^2 \neq 0$, the buoyancy flux of the plume gradually reduces with distance from the source, z, and eventually falls to zero at the neutral height. At this point, the plume still has vertical momentum and therefore continues to rise. However, it is now a negatively buoyant fountain beyond the neutral height and therefore the equations for a steady-plume no longer describe the properties of the flow. §3 discusses the properties of fountains in uniform and stratified ambients in more detail.

We rescale the parameters of the flow so that the following non-dimensional parameters are obtained

$$z = a_1 {B_o}^{1/4} N^{-3/4} \hat{z} \tag{8}$$

$$u = a_2 {B_o}^{1/4} N^{1/4} \hat{z} \tag{9}$$

$$b = a_3 B_o B^{1/4} N^{-3/4} \hat{z} \tag{10}$$

$$g' = a_4 {B_o}^{1/4} N^{5/4} \hat{z} \tag{11}$$

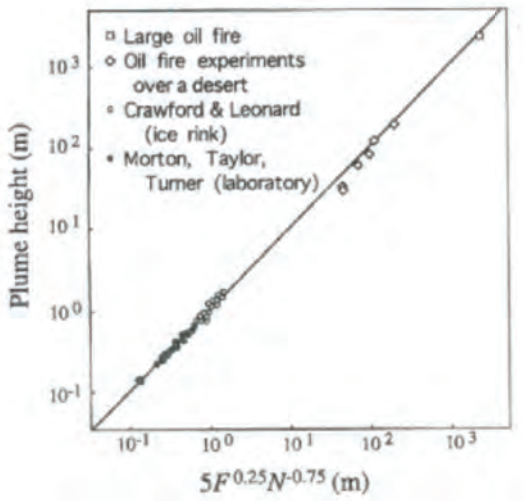

Figure 2: Height of rise compared to the scaling law for volcanic plumes with a range of values of buoyancy flux and ambient stratification.

where a_i for $i = 1, 2, 3, 4$ are constants obtained by reducing equations (5)-(7), using conditions at $z = 0$ where $Q = 0$, $M = 0$, $B = B_o$ (see Morton et al. (1956)). Figure 1 shows the numerically obtained profiles for velocity, buoyancy, and radius of a plume in a stratified ambient with a constant buoyancy frequency, N. As the velocity of the plume approaches zero, the radius diverges to enable a finite mass flux at the top height of the plume. The model for the steady-plume fails above the neutral height of the plume since beyond this height, the descending flow is entrained back into the fountain through different dynamics to that of the plume. In §3, we discuss the modeling for fountains which are negatively buoyant and driven primarily by momentum until the momentum eventually falls to zero due to the opposing buoyancy force.

Beyond the neutral height, the flow speed falls to zero and the plume reaches its maximum height. By dimensional analysis, the maximum height of rise of the plume scales as

$$H = kB_o{}^{1/4}N^{-3/4} \tag{12}$$

which corresponds to the scaling for distance given by equation (8). Although the steady-plume equations do not strictly apply beyond the neutral height, the value of k can be estimated from experimental and observational data and has a value of approximately 5. Figure 2 shows the height of rise of volcanic plumes for a range of buoyancy fluxes and stratification frequency, and illustrates the accuracy of dimensional analysis for the predictions of height of rise for these plumes.

3 Fountains

In a stratified environment, the density difference between the plume and the ambient fluid gradually reduces as the plume rises through the ambient entraining some fluid from the

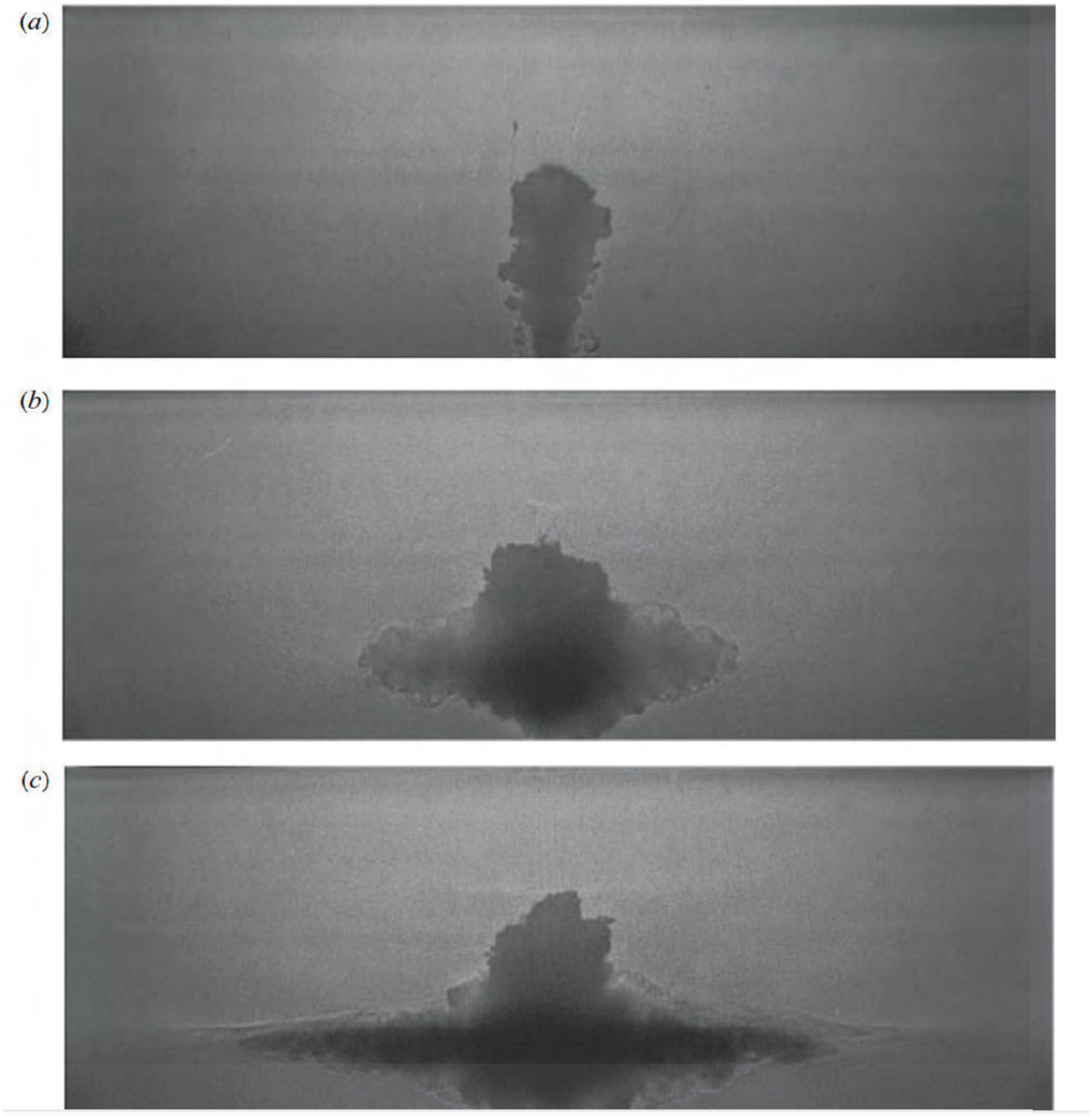

Figure 3: Development of an initially neutrally buoyant fountain rising through a stratified ambient illustrating the horizontal spreading at the intrusion height.

ambient. Eventually, the plume reaches a height at which its density equals that of the ambient, and above this neutral height, the plume is negatively buoyant. The steady-plume equations do not apply beyond this height, however, the flow continues to rise above the neutral height and behaves as a fountain which is negatively buoyant and is driven by its momentum. The momentum of the fountain eventually falls to zero at its top height, causing it to collapse, and leading to an intrusion at a certain height above the neutral height. In the region between the intrusion height and the top height of the fountain, there is mixing between the central inflow and the descending down-welling structures on the edge of the fountain.

Figure 3 shows a fountain with zero initial buoyancy rising through a stratified ambient. The fountain entrains the ambient fluid and gradually loses its momentum, and therefore collapses back and spreads laterally at the intrusion height as shown in panel (c).

From experimental observations of plumes in stratified ambient, the maximum height of rise was found to be

$$H_m = 5B^{1/4}N^{-3/4} \tag{13}$$

and the observed neutral height is given approximately by

$$H_N = 3.8B^{1/4}N^{-3/4} \tag{14}$$

However, since the flow above the neutral height is analogous to that driven by momentum ($[M] = L^4/T^2$), we expect the height of rise can alternatively be expressed as $CM^{1/4}N^{-1/2}$. The model equations are

$$\frac{dub^2}{dz} = 2\epsilon ub; \quad \frac{du^2b^2}{dz} = 2b^2g'; \quad \frac{dub^2g'}{dz} = -N^2ub^2. \tag{15}$$

Experimental evidence (see figure 4) suggests that the mean maximum height of rise of the fountains is given by

$$H_m = 3M^{1/4}N^{-1/2} \tag{16}$$

while the height of intrusion of the horizontal spreading is given by

$$H_i = 1.5M^{1/4}N^{-1/2} \tag{17}$$

The empirically obtained entrainment coefficient for fountains is $\epsilon = 0.085 - 0.09$. From the scalings for a plume, the momentum of the fountain at the neutral height scales as $M \sim BN^{-1} = kBN^{-1}$, and so

$$(H_m - H_i) = 1.5k^{1/4}B^{1/4}N^{-3/4} \tag{18}$$

We expect the intrusion height to be halfway between the neutral height (equation (14)) and the maximum height (equation (13)), so $1.5k^{1/4} = 0.6$, which implies that $k \approx 0.03$ (measurements needed).

Figure 5 shows the observed data for the intrusion height of a plume in a stratified ambient, which falls between the values of the top height and the neutral height estimated from the theoretical model for the plume.

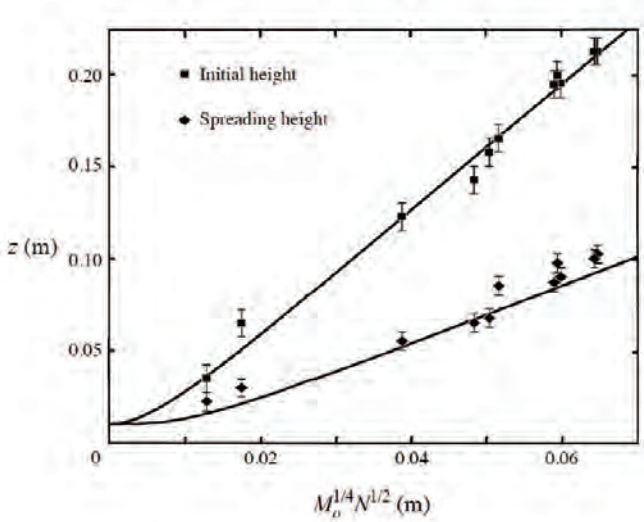

Figure 4: Experimental data for the mean maximum height of rise and the intrusion height of fountains with different values of $M_0^{1/4}N^{-1/2}$.

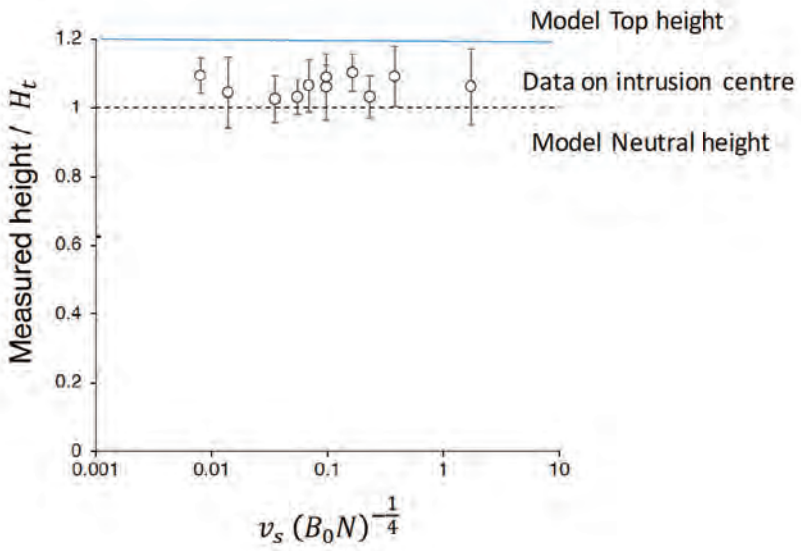

Figure 5: Experimental data of the intrusion height of a single-phase plume rising through a stratified ambient.

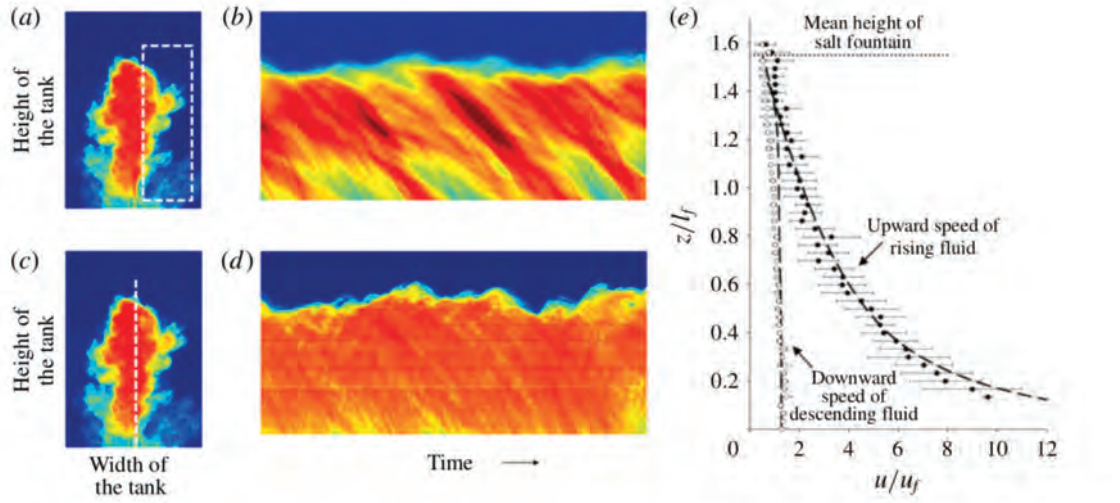

Figure 6: (a), (c) False-colour image of a photograph of a typical fountain. (b), (d) The time series of the instantaneous profile of light attenuation along the fountain centreline, as well as the horizontally averaged profile in the region near the flanks of the fountain, shown by the dashed white lines in (a) and (c) respectively. The inclined lines across which the light intensity changes in these figures illustrate the upward and downward motion of parcels of dyed fluid in the tank. In (e), solid and open circles are used to plot the average velocities using the gradient of the upward- and downward-sloping lines in these images, scaled by the characteristic fountain speed u_f. (Mingotti and Woods, 2016)

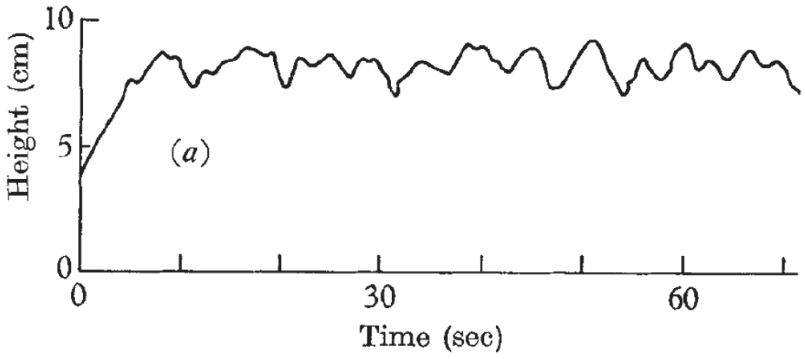

Figure 7: Fluctuation of the maximum height of the fountain above its mean.

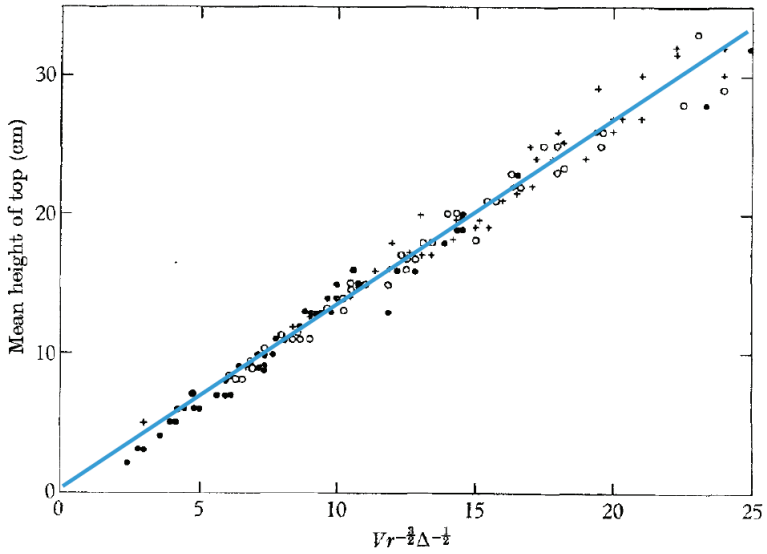

Figure 8: Variation of the mean maximum fountain height with the appropriate scaling law for the height of a fountain.

Figure 6(d) shows the presence of both an upflow and downflow at a certain distance from the centreline of the fountain represented by the white dotted line in figure 6(b). Figure 6(e) shows that the upward speed of fluid reduces rapidly with height and falls to zero eventually at the mean height of the dyed salt fountain. Figure 7 shows the fluctuation of the mean top height of the fountain, and figure 8 shows the variation of the mean top height of the fountain with the appropriate scaling law for the height of a fountain illustrating the accuracy of the scaling law. Once again, dimensional analysis is proven useful for empirically quantifying the behaviour of fountains. We shall consider a negatively buoyant ($g' < 0$) fountain rising in a uniform ambient fluid with no stratification ($N^2 = 0$). At the source, the momentum flux M_0 and buoyancy flux B_0 are respectively

$$M_0 = \pi u^2 b^2, \quad B_0 = \pi u b^2 |g'|. \tag{19}$$

If $u^2 \gg |g'|b$ ($Fr \gg 1$) at the source, then the height of rise of the fountain $H \gg b$. For large Froude numbers, the fountain entrains enough fluid to become self-similar at a certain distance from the source and forgets information about the source conditions. Since $[M] = L^4/T^2$ and $[B] = L^4/T^3$, the Froude number at the source is given by

$$\mathrm{Fr} = \frac{M_0^{3/4}}{b B_0^{1/2}} \tag{20}$$

For $Fr = O(1)$, the fountain is less developed and we get a collapse, while for $\mathrm{Fr} \gg 1$, we have a turbulent entraining fountain. In this latter regime, we expect the maximum height of rise of the fountain to be

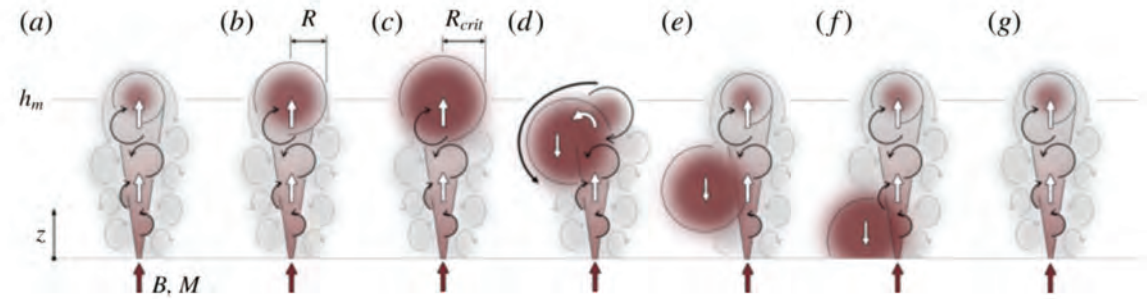

Figure 9: Cartoons illustrating the different mechanisms of collapse of a fountain. (Mingotti and Woods, 2016)

$$H = C_f \frac{M^{3/4}}{B^{1/2}}, \tag{21}$$

where $C_f = 1.7$, as determined empirically, and the frequency of oscillations about the top height is to found be $0.5B/M$. The average mass flux arriving at the top of the fountain can be estimated from measurements of radius and velocity at the mean top height of the fountain, which gives $Q \approx 1.07 M^{5/4} B^{-1/2}$

The oscillations at the top of the fountain arise from a balance between the flux of dense fluid supplied to the top of the fountain and the settling of dense fluid at the top of the fountain in the region above the mean height h_m (Figure 9). When the downward flux of fluid settling exceeds the volume flux supplied to the top of the fountain, then the discrete parcel of fluid at the top of the fountain collapses downward, and the cycle repeats. If R is the radius of one such discrete parcel of fluid, modelled as a sphere, then we expect that the radius increases according to

$$\frac{\mathrm{d}}{\mathrm{d}t}\left(\frac{4}{3}\pi R^3\right) = Q_f \tag{22}$$

where Q_f is the flux supplied to the top of the fountain. The fall speed of the discrete parcel of fluid scales as $\sqrt{g'R}$, so the downward flux is given by $Q_d = \alpha\pi R^2(\sqrt{g'R})$ where $\alpha = 0.6 \pm 0.15$ determined experimentally by Mingotti and Woods (2016). The radius of the discrete parcel grows to a maximum radius R_{crit} given by a balance of the two fluxes, and then the parcel detaches from the top of the fountain and collapses downward.

4 Applications

4.1 Deep-sea mining

There are many applications of turbulent plumes and fountains in nature. One area of application is in deep-sea mining where saline water is pumped into the surface of the ocean, and produces a descending plume which may either sink all the way past the thermocline or

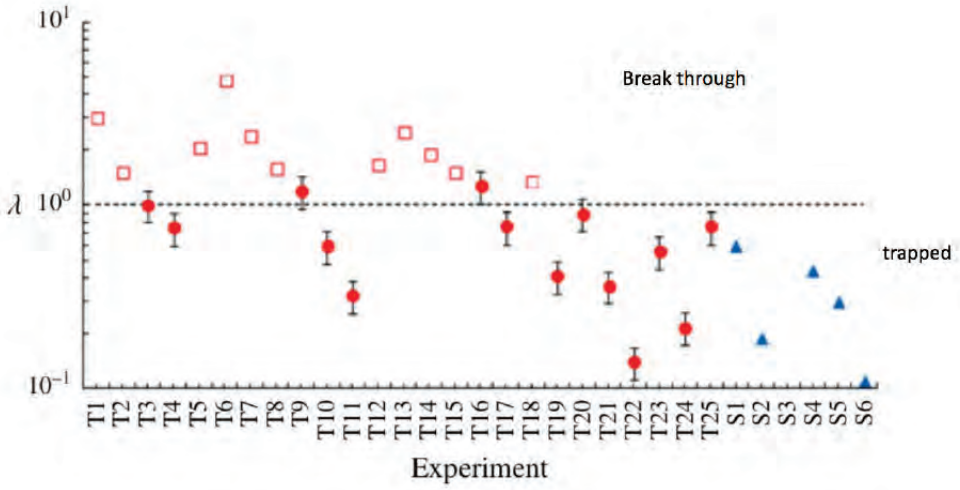

Figure 10: Experimental data illustrating the transition from trapping to breakthrough at $\lambda = 1$ for a plume at the thermocline.

might get arrested at the interface of the thermocline. From the solutions to steady plume equations, we have

$$Q \approx 0.1 B^{1/3} H^{5/3}, \quad g'_p = \frac{B}{Q} \approx 10 B^{2/3} H^{-5/3} \tag{23}$$

where g'_p is the plume buoyancy at the interface, relative to the upper layer. The constants of proportionality in the above equations are obtained empirically from measurements of the entrainment coefficient of the plume. The buoyancy of the lower layer relative to the upper layer is given by

$$g'_l = g \frac{\rho_l - \rho_u}{\rho_u} \tag{24}$$

With the above definitions for the buoyancy of the plume and the buoyancy of the lower layer, we predict that the plume penetrates the thermocline if $g'_l < g'_p$, and that it gets arrested in the thermocline if $g'_l > g'_p$. We define $\lambda = g'_l / g'_p$, which is the control parameter in determining the entrapment-breakthrough transition. Figure 10 illustrates the evidence of this result for a range of experiments.

If the plume does get arrested at the thermocline, it becomes a negatively buoyant fountain at that height. If the plume has a volume flux $Q(H)$ at this height H, from plume theory, the buoyancy flux and the momentum flux of the fountain at this height are given by

$$B_F = Q(H)(g'_l - g'_p) = B_o(\lambda - 1), M(H) = \lambda_m B_o^{2/3} H^{4/3} \tag{25}$$

We can then estimate the depth of penetration into the lower layer from fountain theory. If the Froude number of the fountain at the interface is significantly larger than one ($Fr \gg 1$), we get overshoot, and the depth of penetration is given by

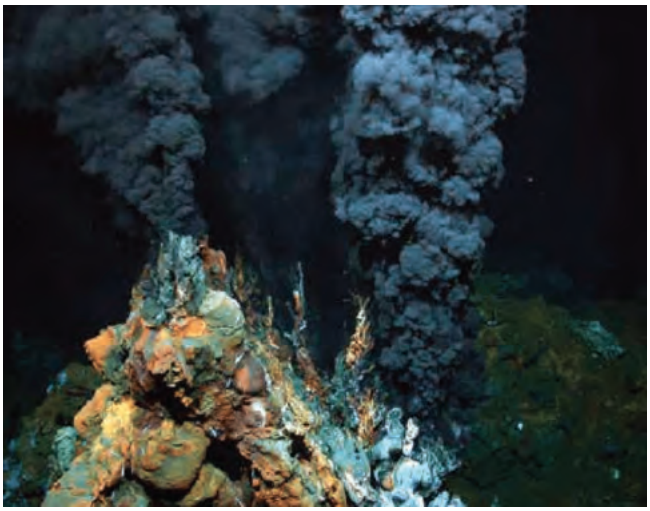

Figure 11: Photograph of a hydrothermal plume in the ocean.

$$z = 1.7\frac{\lambda_m^{3/4} M^{3/4}}{B^{1/2}(\lambda-1)^{1/2}} = \lambda_m^{3/4} H(\lambda-1)^{1/2} \tag{26}$$

4.2 Hydrothermal plumes

Hydrothermal plumes are an interesting example for plumes in which both temperature and salinity vary within the plume. Measuring source conditions in a hydrothermal plume in the depths of the ocean is not feasible because of the high source temperature conditions and pressure at these depths. The density also varies non-linearly with temperature at such high temperatures, and the aim is therefore to predict the heat flux at the source of these plumes from estimates of height of rise of these plumes. The ambient fluid can be stratified in salinity with a solutal buoyancy frequency $N_s^2 = -g\lambda_s \mathrm{d}s_a/\mathrm{d}z$, and stratified in temperature with a thermal buoyancy frequency $N_T^2 = -g\lambda_T \mathrm{d}T_a/\mathrm{d}z$. The solutal and thermal buoyancy fluxes evolve according to

$$\frac{\mathrm{d}ub^2 g_s'}{\mathrm{d}z} = -ub^2 N_s^2, \quad \frac{\mathrm{d}ub^2 g_T'}{\mathrm{d}z} = -ub^2 N_T^2 \tag{27}$$

with the total buoyancy evolving according to the sum of these two equations,

$$\frac{\mathrm{d}ub^2 g'}{\mathrm{d}z} = -ub^2 N^2 \tag{28}$$

The effective stratification frequency and buoyancy are given by,

$$N^2 = N_T^2 + N_s^2, \quad g' = g_s' + g_T' \tag{29}$$

By calculating the effective buoyancy and buoyancy frequency of the ambient fluid, we can then use the results above to estimate the rise height of a hydrothermal plume. However, the salinity and temperature of the hydrothermal plume may evolve at different

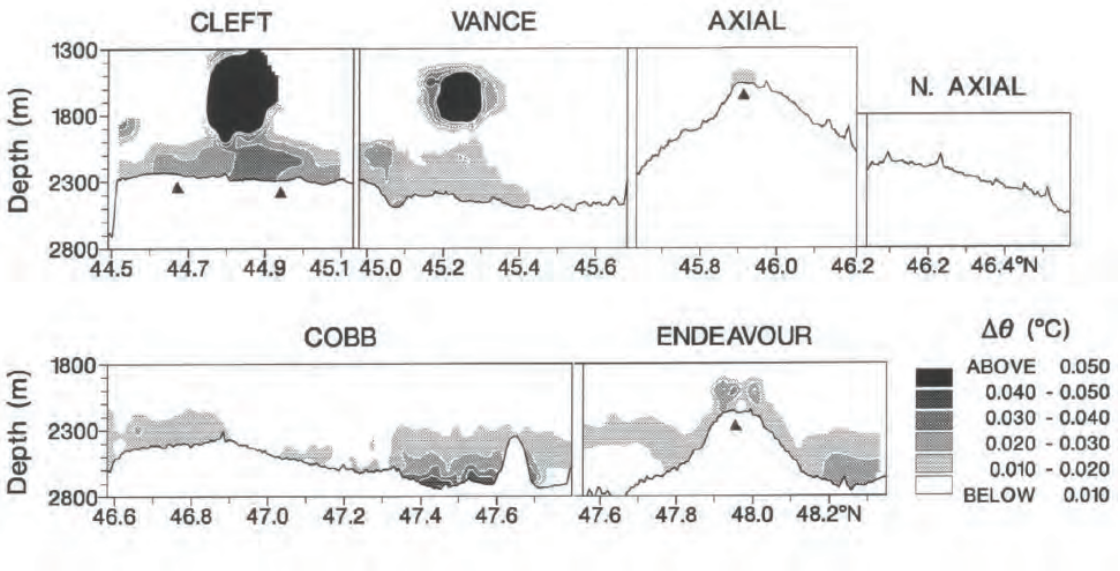

Figure 12: Summary of hydrothermal temperature anomalies observed along the crest of the Juan de Fuca Ridge, including Axial Volcano, from 1985 to 1989.

rates through mixing owing to the different values of N_T and N_s in the ambient and also owing to different source values for temperature and salinity in the plume. Indeed, in some parts of the ocean, it is possible that overall, the fluid may be stably stratified although either the temperature or the salinity may, in isolation, be unstably stratified. This can lead to very different evolutions of T and s with height in the plume. If the properties T and s are then measured at the neutral height $z = z_n$, and if the stratification of each of T_a and s_a is known, as well as the total height of rise, one can then invert the model to determine the heat flux at the sea-floor. This is done by writing down integral expressions for the heat flux and the salt flux of the form

$$Q_s(z) = Q_s(0) + \frac{\mathrm{d}s_a}{\mathrm{d}z}\int_0^z \frac{\mathrm{d}Q}{\mathrm{d}z} z \mathrm{d}z \tag{30}$$

Combining the above equation with an expression relating the total buoyancy B with $\int_0^z \frac{\mathrm{d}Q}{\mathrm{d}z} z \mathrm{d}z$ gives the expression for the heat flux at the source of the hydrothermal plume,

$$Q_T(0) = \rho C_p \left(\frac{\mathrm{d}T_a}{\mathrm{d}z} \frac{B(0)}{N^2} + Q(z)(T(z_n) - T_a(z_n)) \right) \tag{31}$$

The above approximations are valid as long as the scale over which stratification varies significantly is much larger than the scale over which the plume readjusts to self-similarity. With a volcanic plume, if we are to adopt the simple formula to estimate the height of rise of the eruption column, we need to work with the thermal energy of the plume. However, since the plume is so hot initially, the change in density does not vary linearly with mixing and so we cannot make many of the approximations used in the idealised modelling above. Nonetheless, we can estimate the height of rise by assessing the buoyancy flux of a flux of

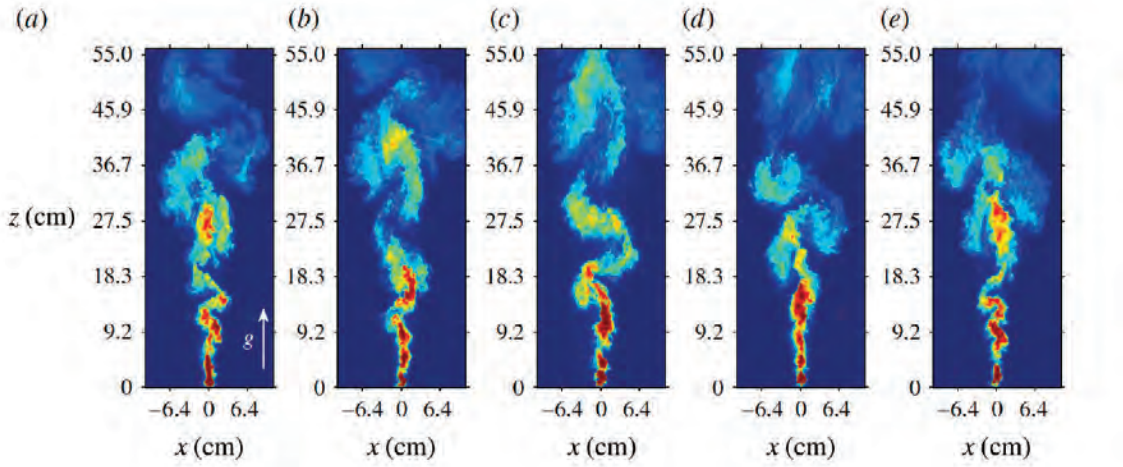

Figure 13: Series of five images illustrating the structure of a two-dimensional plume, and its evolution with time for (a) 15 s, (b) 16 s, (c) 17 s, (d) 18 s and (e) 19 s, using a false colour mapping of concentration to highlight the eddies. (Rocco and Woods, 2015)

air which is $1C$ warmer than the background temperature, and which has the same total heat flux as the volcanic plume. This will lead to an approximate estimate for the height of rise.

5 Dispersion and Mixing in Two-dimensional Plumes

The dynamics and dispersion in a two-dimensional plume is of particular interest since the eddies grow in both longitudinal and transverse directions within the plume (figure 13). In the experiment shown in figure 13, a dyed salt plume is released into a confined tank of fresh water . The tank has dimensions 70 cm x 70 cm x 1 cm so the flow can be assumed to be two-dimensional. The tank was open on the sides and base and was immersed in a larger reservoir tank, so that plume fluid could leave the tank on reaching the base, and ambient fluid could enter the sides as fluid was entrained by the plume. Figure 13 shows the eddies growing in size along the vertical direction as they entrain ambient fluid into the plume. Figure 14 shows a series of photographs which illustrates the irregular motion of eddies within the steady plume which leads to large dispersion at the leading edge of the dyed fluid.

In order to develop an understanding of the flow, we consider the time-averaged steady motion in which we assume the eddies entrain ambient fluid at a rate proportional to the mean speed of the eddies (Morton et al., 1956). If the ensemble time-averaged steady plume has vertical speed $w(x, z)$ and concentration $c(x, z)$, where x is the horizontal position in the plume relative to the centreline of the plume and z is the vertical distance from the source then we can write the volume flux, specific momentum flux and specific buoyancy flux per unit distance in the y direction as

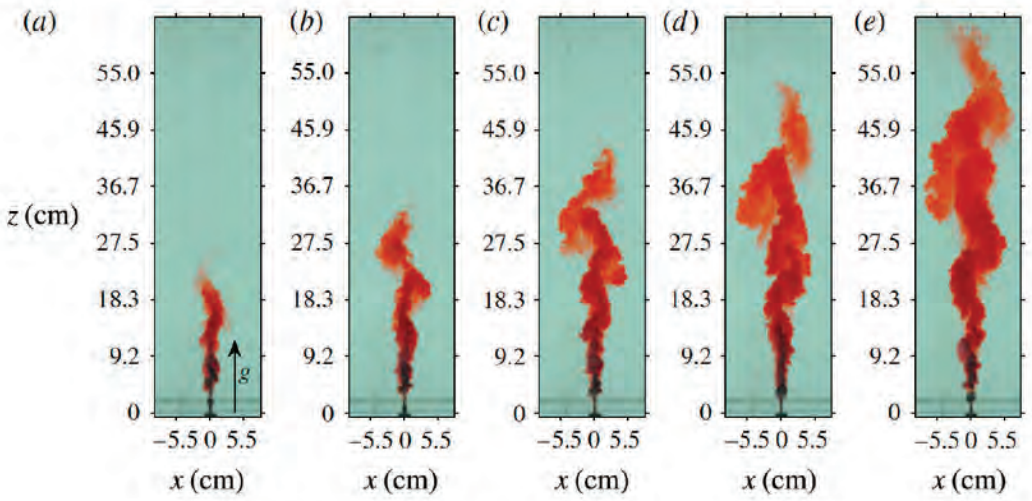

Figure 14: Photograph of an evolving two-dimensional line plume, illustrating how red dye, injected into the established steady plume, evolves with time for (a) 1.3 s, (b) 2.3 s, (c) 3.3 s, (d) 4.3 s and (e) 5.3 s. (Rocco and Woods, 2015)

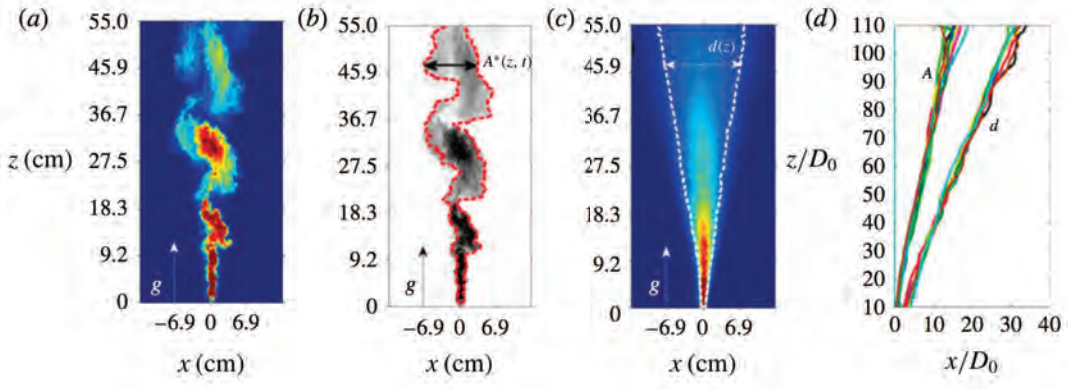

Figure 15: (a) Photograph of the instantaneous structure of a typical two-dimensional steady state plume. (b) Locations of the two bounding lines, defined as the points at which the concentration falls to a value of 1/e of the maximum concentration on each horizontal line; the distance between these lines is denoted A^*. (c) Time-averaged concentration profile within the plume. (d) Horizontal distance from the centreline at which the time-averaged concentration has a value of $1/e$ times the time-averaged centreline concentration as a function of the distance from the source (d). Also shown is a characteristic cross-plume length scale (A). At each height, this scale is determined by first measuring the horizontal distance between the two points at that height for which the concentration equals $1/e$ times the maximum concentration at that level, A^* (b), and then finding a time average of these values. (Rocco and Woods, 2015)

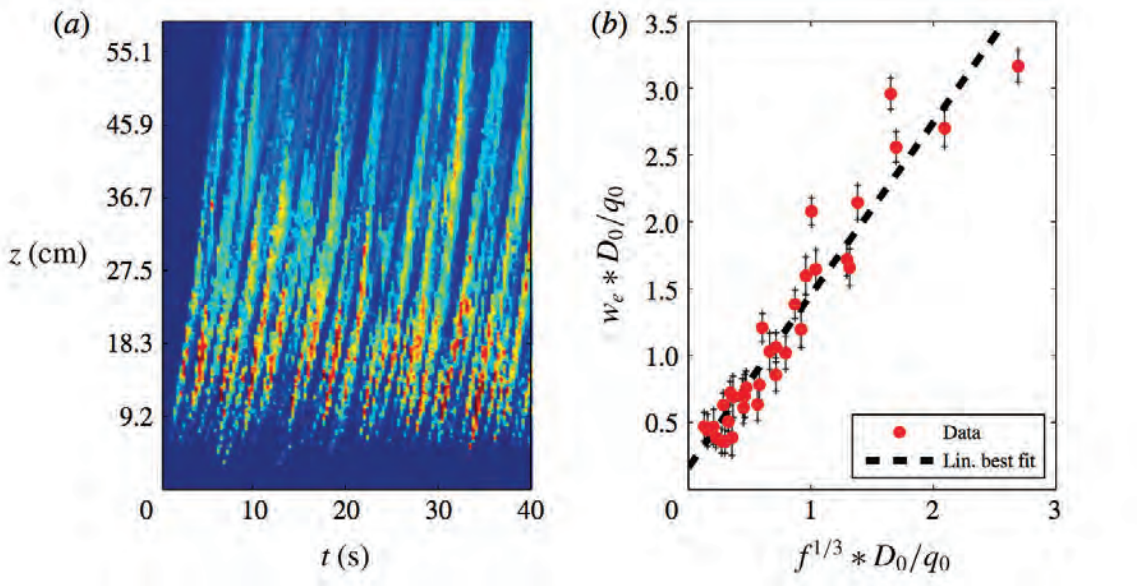

Figure 16: (a) Time series of the pixels along a vertical line at a distance $x = 3D_o$ from the centreline of the plume, shown using false colour, to illustrate the passage of the front of successive eddies. (b) Variation of the speed of the front of the plume (w_e) for a large number of different buoyancy fluxes, as determined from figures such as (a) for $x = 0$. The data collapse to the simple relation $w_1(0, z) \approx 1.30 f^{1/3}$. (Rocco and Woods, 2015)

$$q = \bar{w}\bar{b} = \int_{-\infty}^{+\infty} w \mathrm{d}x, \quad m = \bar{w}^2\bar{b} = \int_{-\infty}^{+\infty} w^2 \mathrm{d}x, \quad f = \bar{g}\bar{w}\bar{b} = \int_{-\infty}^{+\infty} w g' \mathrm{d}x \tag{32}$$

where $\bar{b}$ is the effective width of the flow, $\bar{w}$ is the horizontally averaged vertical speed, g' is the local buoyancy and $\bar{g}$ is the horizontally averaged buoyancy. The conservation of mass, momentum, and buoyancy fluxes takes the form

$$\frac{\mathrm{d}q}{\mathrm{d}z} = 2\epsilon\bar{w}, \quad m\frac{\mathrm{d}m}{\mathrm{d}z} = kqf, \quad f = const. = f_o \tag{33}$$

where f_o is the source buoyancy flux. These equations have a self-similar solution given by

$$\bar{w} = \left(\frac{kf}{2\epsilon}\right)^{1/3}, \quad b = 2\epsilon z \tag{34}$$

Note that the buoyancy flux f has dimensions L^3T^{-3}, so the eddy speed w_e scales as $f^{1/3}$ by dimensional analysis, so the vertical speed of the plume is constant and does not vary with height z. The size of the eddies scales with distance z from the source and is independent of the source buoyancy flux. Analysis of the ensemble-averaged concentration of the plume shows that the horizontal distance $d(z)$ over which the concentration reduces to a fraction $1/e$ of the centreline value varies linearly with height (figure 15(c), (d)).

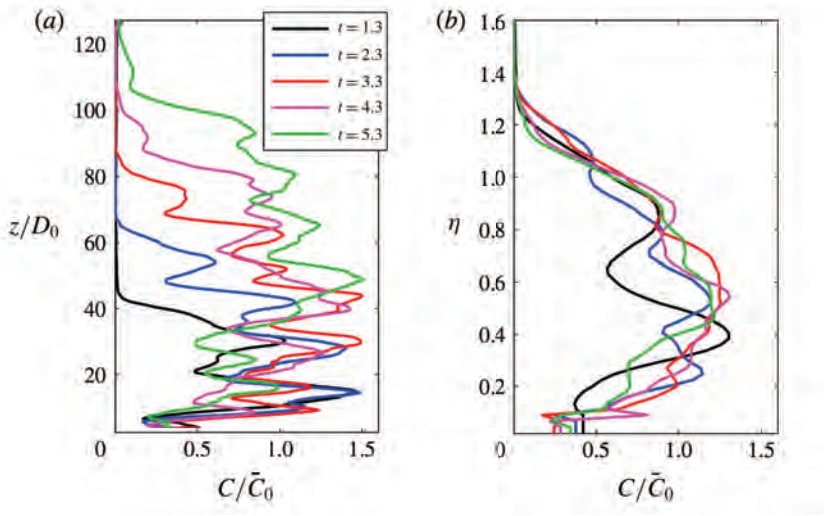

Figure 17: (a) Experimental data showing the horizontally integrated concentration of dye in the plume as a function of z at five times after the start of steady injection of red dye into the plume at t = 0. (b) Integral of the concentration at different time steps as a function of $\eta = z/(tf^{1/3})$. (Rocco and Woods, 2015)

On each horizontal line in the plume, we define $A^*(z,t)$ as the horizontal distance between the two points where the concentration of the plume has decreased to a fraction $1/e$ of the maximum concentration on that horizontal line (see figure 15(a),(b)), at a specific time instant. The time average of $A^*(z,t)$, defined as $A(z)$, for each value of the vertical distance z from the source is plotted in figure 15(d). A is estimated to be considerably smaller than d, the width of the ensemble time-averaged flow. This is since d captures the horizontal distance over which the plume oscillates, where as A is an average instantaneous measure that is smaller than the distance over which plume fluctuates over the duration of the flow.

Figure 16(a) illustrates that there is a regular series of fronts which migrate through the tank, and that as each front migrates, the colour contrast across the front decreases; these correspond to the leading edges of successive eddies, which mix and become diluted with ambient fluid. In figure 16(b), the measured speed of the front of the plume (w_e) is plotted as a function of the buoyancy flux at the source, illustrating that the data is consistent with the model predictions for a constant vertical velocity with distance from the source (Rocco and Woods, 2015).

The eddy dispersivity of the plume D is given by a function of the size z and speed w_e of the eddies, and the mixing is driven by the stretching and mixing of these eddies. We have

$$D \sim wz \sim f^{1/3}z \tag{35}$$

The horizontally averaged concentration in the plume at a distance z from the source is given by $C(z,t) = \int_{-\infty}^{+\infty} c(x,z,t)\mathrm{d}x$, which evolves according to

$$\frac{\partial C}{\partial t} + \alpha f^{1/3}\frac{\partial C}{\partial z} = \frac{\partial}{\partial z}\left(\beta z f^{1/3}\frac{\partial C}{\partial z}\right) \tag{36}$$

We define a similarity parameter $\eta = z/(tf^{1/3})$ and look for similarity solutions for equation (36). The horizontally averaged concentration is given by

$$C(z,t) = \frac{Q_c}{f^{1/3}}\mathscr{H}\left(\frac{z}{f^{1/3}t}\right) \tag{37}$$

where Q_c is the volume flux of dye released into the plume. $\mathscr{H}$ satisfies the equation

$$-\eta\frac{\mathrm{d}\mathscr{H}}{\mathrm{d}\eta} + \alpha\frac{\mathrm{d}\mathscr{H}}{\mathrm{d}\eta} = \beta\frac{\mathrm{d}}{\mathrm{d}z}\left(\eta\frac{\mathrm{d}\mathscr{H}}{\mathrm{d}\eta}\right) \tag{38}$$

For global conservation of dye in the plume, we have

$$\int_0^\infty \mathscr{H}(\eta)\mathrm{d}\eta = 1 \tag{39}$$

Solving equations (38) and (39) gives

$$\mathscr{H}(\eta) = \frac{\int_\eta^\infty \zeta^{(\alpha/\beta)-1}\exp\Big(-\frac{\zeta}{\beta}\Big)\mathrm{d}\zeta}{\int_0^\infty \zeta^{\alpha/\beta}\exp\Big(-\frac{\zeta}{\beta}\Big)\mathrm{d}\zeta} \tag{40}$$

where $\mathscr{H} \to 0$ as $\eta \to \infty$.

Now consider a finite pulse of dye of volume V_c released into the steady plume. We expect similarity solutions of the form

$$C(z,t) = \frac{V_c}{f^{1/3}t}\mathscr{G}(\eta) \tag{41}$$

where the global mass conservation of dye implies that

$$\int_0^\infty \mathscr{G}(\eta)\mathrm{d}\eta = 1 \tag{42}$$

Substituting this into equation (36) gives

$$-\frac{\mathrm{d}}{\mathrm{d}\eta}(\eta\mathscr{G}) + \alpha\frac{\mathrm{d}\mathscr{G}}{\mathrm{d}\eta} = \beta\frac{\mathrm{d}}{\mathrm{d}z}\left(\eta\frac{\mathrm{d}\mathscr{G}}{\mathrm{d}\eta}\right) \tag{43}$$

which has the solution

$$\mathscr{G}(\eta) = \frac{\eta^{\alpha/\beta}\exp\Big(-\frac{\eta}{\beta}\Big)}{\int_0^\infty \eta^{\alpha/\beta}\exp\Big(-\frac{\eta}{\beta}\Big)\mathrm{d}\eta} \tag{44}$$

The values of constants α and β can be estimated from experimental data for constant volume flux and finite release of dye into a steady plume (figure 18). The residence time

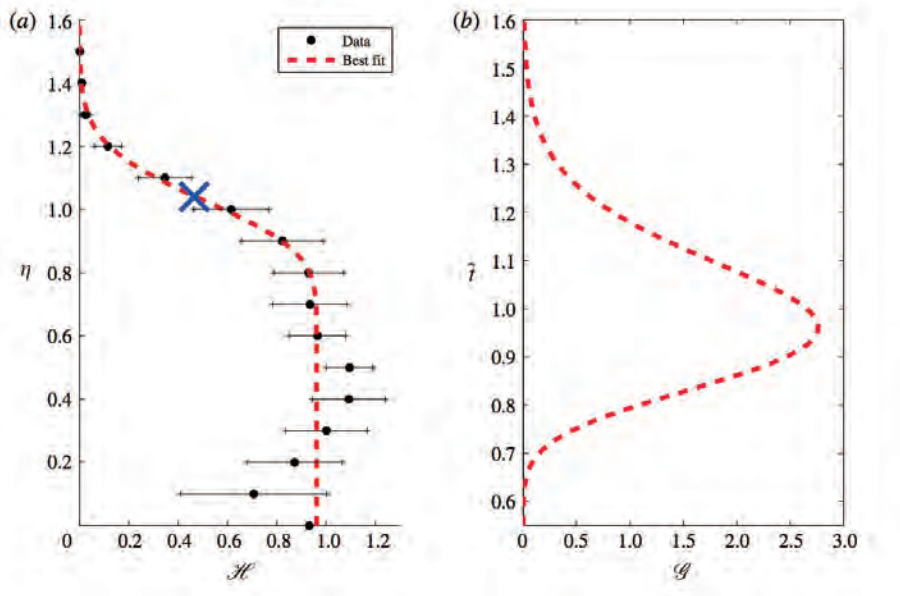

Figure 18: (a) Mean integral of the concentration obtained by averaging the mean integral concentrations of 15 experiments as a function of $z/(tf^{1/3})$; the position of the centre of mass has been identified with a blue cross. (b) Variation of the horizontally averaged concentration as a function of time, passing the point $z_0 = 1$, which results from an instantaneous release of a finite mass of tracer at $z = 0$. (Rocco and Woods, 2015)

distribution provides information about the variation with time of the horizontally averaged concentration of the tracer passing a horizontal plane above the source. Such information can be key to modelling the products of chemical reactions in the plume produced, especially when the reaction time is comparable to the travel time through the plume, so that the distribution of travel times lead to different degrees of partial reaction (Rocco and Woods, 2015).

6 2-D Momentum Jet

For two-dimensional momentum-driven jets, the conserved quantity is the momentum flux of the jet. The flow parameters for a jet scale with the momentum flux, M, and distance from the source, z, which leads to a different rate of spread of concentration in a jet compared to the rate of spread in plumes. The momentum and radius of the jet are given by

$$M = u^2 b, \quad b = \lambda z \tag{45}$$

where λ is an empirical constant that is a function of the entrainment coefficient of a jet. From equation (45), the velocity of the jet is

$$u = \frac{M^{1/2}}{(\lambda z)^{1/2}} \tag{46}$$

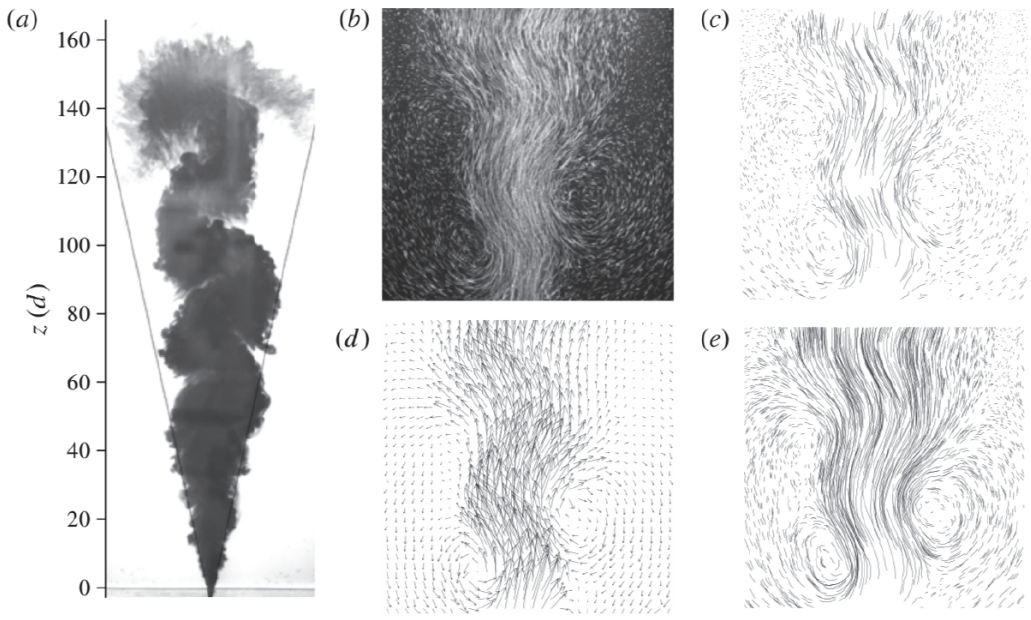

Figure 19: (a) Picture of a jet rising in a tank. The average dye edges are plotted with black lines. (b) Passive tracers shown as streaks in a typical jet. (c) Trajectories of the passive tracers shown in (b). (d) Instantaneous velocity field (arrows) of the jet shown in (b). (e) Trajectories of virtual particles seeded at the same initial locations as the particles identified in (c) and evolving as passive tracers in the time-dependent velocity field shown in (d). (Landel et al., 2012)

and the eddy diffusivity for mixing in the jet scales as

$$D \sim uz \sim M^{1/2} z^{1/2} \tag{47}$$

The horizontally averaged concentration in the jet is given by

$$C(z,t) = \int_{-\infty}^{+\infty} c(x,t)dx \tag{48}$$

Substituting the above scalings into the relation for horizontally averaged concentration yields the equation

$$\frac{\partial C}{\partial t} + \alpha \frac{M^{1/2}}{z^{1/2}} \frac{\partial C}{\partial z} = \beta \frac{\partial}{\partial z} \left(M^{1/2} z^{1/2} \frac{\partial C}{\partial z} \right) \tag{49}$$

6.1 Dispersion and mixing in two-dimensional jets

For two-dimensional steady-state jets, the self-similarity argument still applies but with different scalings appropriate for a jet. The structure of a well-established jet is shown in figure 20(a), and 20(b) shows the instantaneous positions of passive tracers in the jet. A

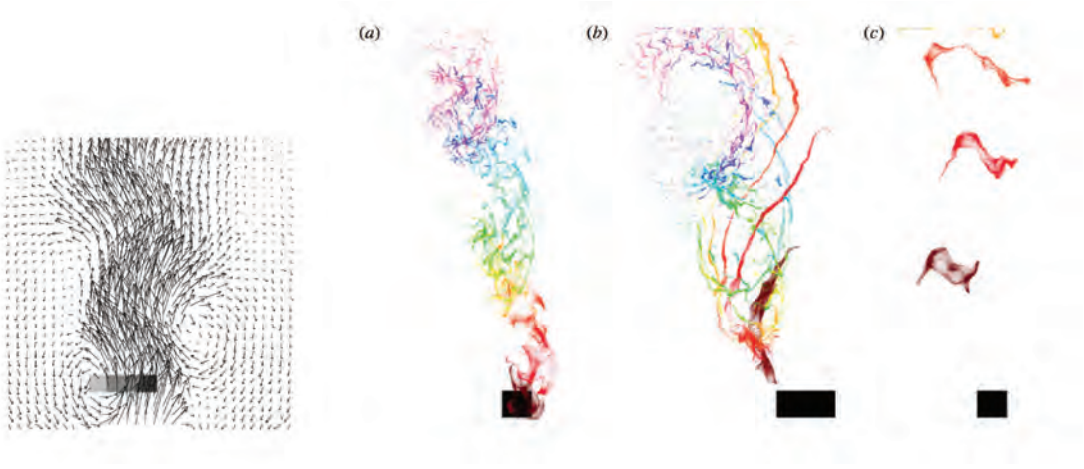

Figure 20: Evolution in time of the virtual particles seeded in the velocity field shown in the left panel as they are advected by the flow (each colour corresponds to a particular time instant): (a) cluster initially distributed at the centre of an eddy and shown in light grey in the left panel (b) cluster initially distributed at the interface between the eddy and the core and shown in grey in the left panel (c) cluster initially distributed in the core of the jet and shown in dark grey in the left panel. Each colour corresponds to a time period of 0.2 s. (Landel et al., 2012)

particle tracking algorithm can be used to identify the trajectories of the Lagrangian tracer particles in the jet at the same instant, and this is represented in figure 20(c). Figure 20(d) shows the instantaneous velocity field of the experimental jet, and figure 20(e) shows the trajectories of virtual particles advecting with the velocity field shown in figure 20(d). The good agreement between the positions of passive tracers in figure 20(b) and the positions of virtual particles in figure 20(d) shows the importance of advection for tracer dispersal within a jet.

In order to understand the interaction between the core and the eddies of a jet, virtual particle tracking technique is applied to track particles seeded into the jet at three positions within the jet - in the centre of an eddy, at the interface between an eddy and the core of the jet, and at the core of the jet. Figure 20 shows the movement of the virtual particles released with a time period of 0.2 s. The figure shows that the particles in the core of the jet are transported quickest (figure 20(c)), and the particles in the eddy go in loops and therefore travel upwards slower than the particles in the core (figure 20(a)). On the other hand, the particles at the interface between the eddy and the core (figure 20(b)) take a more complicated path and can be transported from the eddy to the core, or from the core to the eddy, as is illustrated by the presence of a loop when the particle is drawn into the eddy from the core of the jet.

Figure 22 illustrates the accuracy of theory in predicting the profiles of the horizontally averaged concentration with time and distance from the source of the jet (Landel et al., 2012).

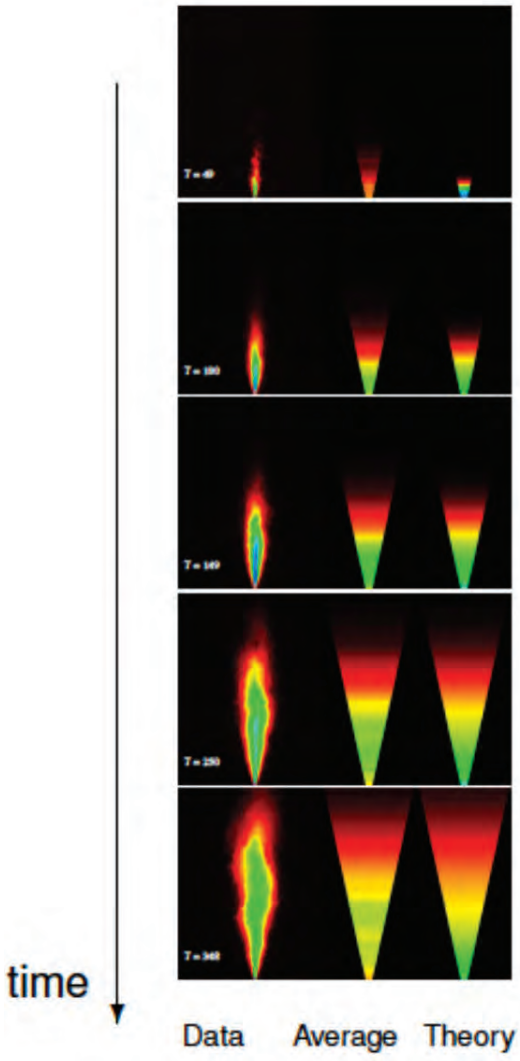

Figure 21: Comparison between the concentration profiles of horizontally averaged data and theoretical model for a jet illustrating the accuracy of theory.

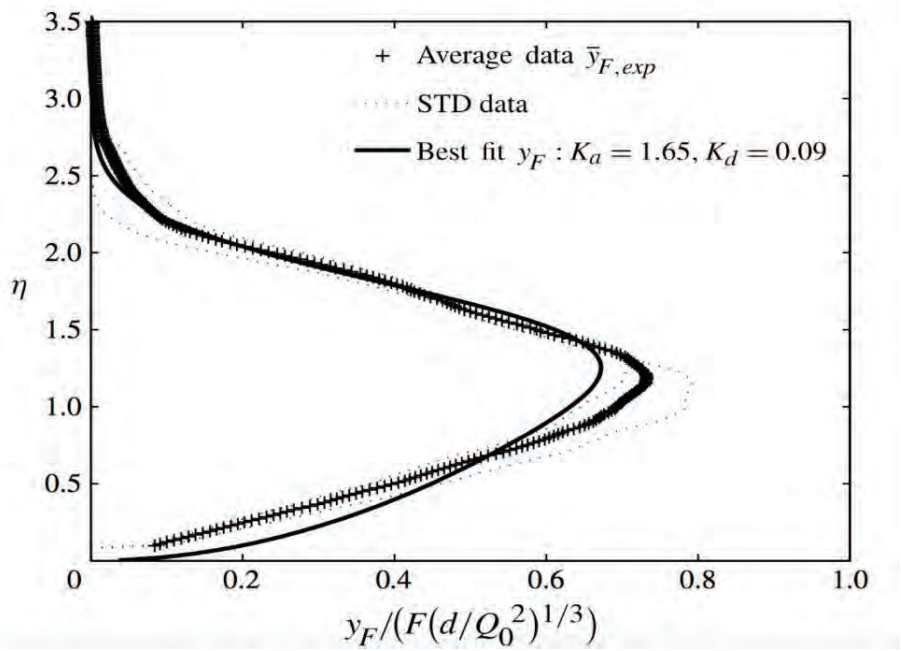

Figure 22: Comparison of the solution for the concentration of tracer in a two dimensional jet, following the supply of tracer at a constant rate for $t > 0$.

References

Landel, J. R., C. Caulfield, and A. W. Woods 2012. Streamwise dispersion and mixing in quasi-two-dimensional steady turbulent jets. *Journal of Fluid Mechanics*, 711:212–258.

Mingotti, N. and A. W. Woods 2016. On turbulent particle fountains. *Journal of Fluid Mechanics*, 793.

Morton, B., G. I. Taylor, and J. S. Turner 1956. Turbulent gravitational convection from maintained and instantaneous sources. *Proc. R. Soc. Lond. A*, 234(1196):1–23.

Rocco, S. and A. W. Woods 2015. Dispersion in two-dimensional turbulent buoyant plumes. *Journal of Fluid Mechanics*, 774.

Lecture 3
Plumes in Confined Spaces

Notes by Christopher J. Howland, Thomas Le Reun

June 20, 2018

1 Aside: Transient Effects in Plumes

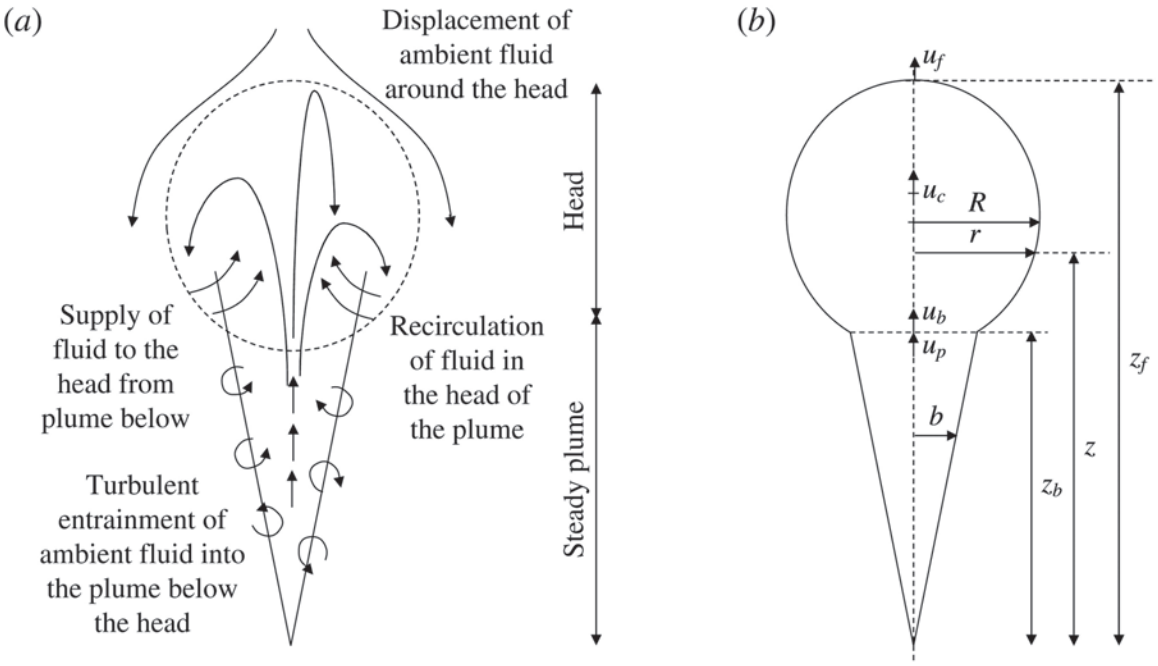

Figure 1: (a) Cartoon illustrating the motion of fluid within a starting plume and the motion of ambient fluid around the plume head. The motion of fluid within the plume head shown is in the frame of reference of the plume head. (b) Illustrating various dimensions and velocities. (Bhamidipati and Woods, 2017)

The vast majority of the problems discussed so far have assumed self-similarity of plumes and some sort of steady state. However transient effects, such as the initial growth of a plume, can be important in geophysical applications. For example, when observing a volcanic eruption, measurements of the plume become difficult once a statistically steady state is reached due to the large ash cloud that intrudes at a certain height in the atmosphere. In this case, knowing how the initial measurable growth of the plume relates to factors such as the eruption rate can be very useful.

We call such a problem where a source of buoyancy flux is switched on a 'starting plume'. The key difference between a starting plume and a steady plume is that there is now a front at the top of the plume ($z = z_f$) which mixes with the ambient fluid ahead of the plume. Experimental data from Bhamidipati and Woods (2017) shows that behind this front, in the 'head' of the plume, recirculation occurs which leads to an accumulation of approximately 60% of the total buoyancy released from the source. This recirculation also leads to the front of the plume ascending at 60% of the characteristic speed of the fluid in the steady plume that forms at later times. Figure 1 illustrates the entrainment and recirculation processes in the transient starting plume using a simple schematic. Figure 2 visualises one of the experiments from the study and shows the difference between the speed in the plume (indicated by the motion of the black dye) and the speed of the front.

Using dimensional analysis as before, treating the buoyancy flux $B \sim L^4T^{-3}$ as a conserved quantity, we expect the velocity of the front to take the form

$$u_f = \xi_f B_0^{1/3} z_f^{-1/3}. \tag{1}$$

Since $u_f = dz_f/dt$, we expect from this that $z_f^{4/3} \sim \xi_f B^{1/3} t$, and it is then possible to deduce the prefactor

$$\xi_f = \frac{z_f^{4/3} - z_0^{4/3}}{\frac{4}{3} B_0^{1/3} t}. \tag{2}$$

Bhamidipati and Woods (2017) show that this prefactor is approximately constant (and equal to 2), and the plumes collapse to a self-similar shape.

There are still many open problems relating to transient effects in plumes. It is likely, for example, that a sudden increase in the flux of an existing plume may lead to structures similar to that of a starting plume. The ensuing interaction between the new structures and the existing plume may, however, exhibit new phenomena.

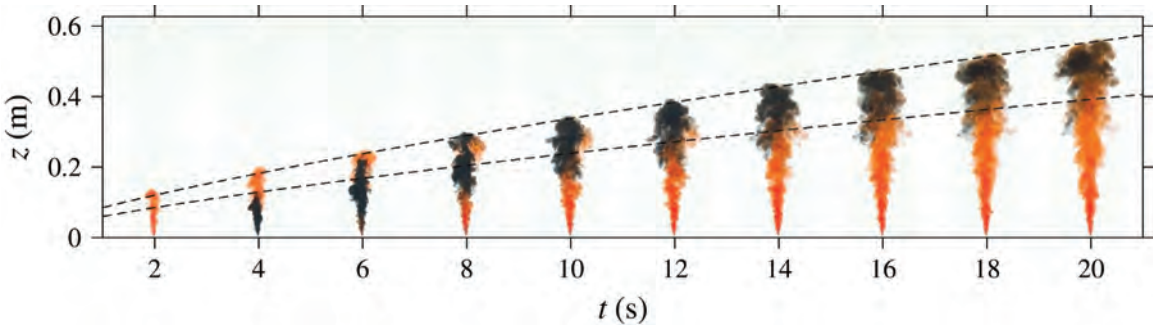

Figure 2: Propagation of a pulse of dye through the plume and accumulation of dye in the plume head. The dashed lines indicate the positions of the front (z_f) and back (z_b) of the plume head, with $z_b = 0.71 z_f$. (Bhamidipati and Woods, 2017)

2 Confined Plume with No Ventilation

2.1 Experimental configuration

In the previous sections, we have studied in detail the case of an isolated plume in unbounded environments. We consider here plumes in confined environments: although the dynamics of the plume is not spatially constrained, the constant influx of buoyant fluid and its accumulation leads to a progressive change of the ambient conditions. The problem addressed here is related to the everyday experience of unventilated rooms and halls subject to a heat source close to the ground. In particular, we would like to know the typical time elapsed before people standing on the ground start to feel uncomfortable.

We therefore consider the idealised set-up as depicted in figure 3 which has been investigated both experimentally and theoretically in the seminal study of Baines and Turner (1969). A source of buoyant fluid is located at the bottom of a closed box, and the plume develops in an environment which has initially a uniform density.

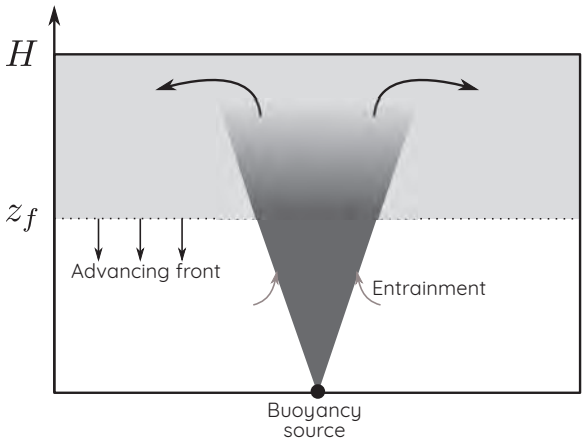

Figure 3: Schematic representation of a buoyant plume in a confined environment. This set-up was produced experimentally by Baines and Turner (1969)

2.2 Qualitative analysis of the experiment

At early times the plume rises through the uniform ambient air, before hitting the top the of the box and giving rise to a layer of warm air which is constantly fed by the plume. The density of this layer should be intermediate between the density of the plume fluid at the source and the initial cold ambient air: as the plume rises, it entrains ambient air which is then mixed with the buoyant plume as it penetrates the top layer. Due to the persistent addition of buoyancy flux at the source, the front formed between the two layers propagates downwards and the warm upper layer grows.

As discussed earlier, one important problem is to look for the typical time scale for the warm layer to fill the box. We recall from plume theory that with a typical buoyancy flux B and a typical height H (as in figure 3) the volume flux Q in the plume feeding the layer is

$$Q \sim B^{1/3} H^{5/3}. \tag{3}$$

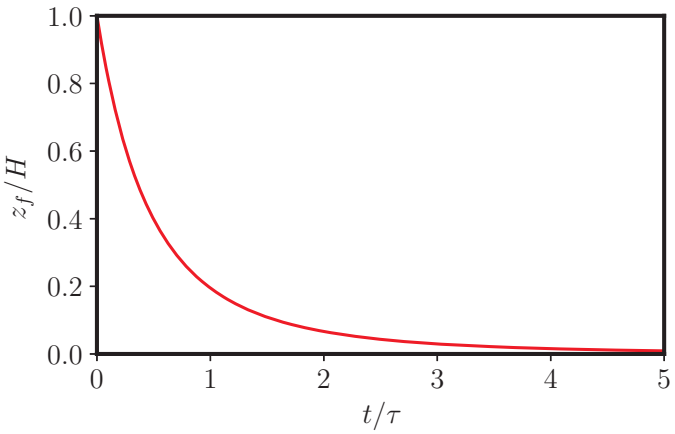

Figure 4: Plot of the time evolution of the position of the front z_f as a function of a dimensionless time t/τ for $\lambda = 1$ as described in (9).

With a box of cross-sectional area A, a typical timescale τ after which the warm upper layer fills the box is therefore

$$\tau = \frac{AH}{Q} \sim \frac{A}{B^{1/3}H^{2/3}}. \tag{4}$$

From this we can also deduce a typical front velocity

$$w_f \sim \frac{H}{\tau} = \frac{B^{1/3}H^{5/3}}{A}. \tag{5}$$

2.3 Front dynamics: a refined calculation

We wish to refine our understanding of the dynamics of the front using plume dynamics. The scaling described above already contains key ideas to describe the time evolution of the top buoyant layer. This layer is indeed fed by the plume at the height of the front z_f. As the plume is rising in ambient cold air of constant density before it penetrates the layer, the volume flux input Q_{input} inferred from plume theory is

$$Q_{\text{input}} = \lambda B^{1/3} z_f^{5/3}, \tag{6}$$

where λ is a dimensionless geometric factor. With flux conservation, the velocity of the front w_f, which is assumed to be uniform all over the box, is

$$w_f = \frac{\mathrm{d}z_f}{\mathrm{d}t} = -\frac{Q_{\text{input}}}{A - A_p(z_f)}, \tag{7}$$

where $A_p(z_f)$ is the area of the plume as it hits the top layer. For simplicity's sake, we restrict our calculation to the case where the area of the plume is small compared to the area of the box. We then get a simple differential equation for the front position z_f:

$$\frac{\mathrm{d}z_f}{\mathrm{d}t} = -\frac{\lambda}{A} B^{1/3} z_f^{5/3} \ . \tag{8}$$

It is then straightforward to infer z_f as a function of time:

$$z_f(t) \;=\; H\left(1+\frac{2\lambda}{3}\frac{t}{\tau}\right)^{-3/2} \quad . \tag{9}$$

The latter time evolution satisfies the initial condition $z_f(0) = H$ and the expected behaviour $z_f(t \to +\infty) = 0$ The function $z_f(t)$ is plotted in figure 4: we can notice that for $\lambda = \mathcal{O}(1)$, the top layer fills about 80 % of the box after a time τ.

2.4 Density inside the top layer

The last paragraph has given us hints about the dynamics of the top layer front; nevertheless we have not described properly the density inside this layer. This requires addressing the plume dynamics inside the top layer where the ambient ρ_a density is a function of height and time, and is part of the unknowns. One key assumption that allows us to make progress here is that the density gradient changes *slowly* in time.

The plume equations, taking into account slowly-varying ambient buoyancy variations and assuming that all quantities only depend on time and height z, read

$$\left\{\begin{array}{rcl} \dfrac{\partial Q}{\partial z} &=& 2\varepsilon M^{1/2} \\ \dfrac{\partial M}{\partial z} &=& 2BQ \\ \dfrac{\partial B}{\partial z} &=& \dfrac{g}{\rho_0}\dfrac{\partial \rho_a}{\partial z}Q \end{array}\right. \tag{10}$$

where ε is the entrainment rate, g is the gravity intensity, ρ_0 is a reference density and ρ_a is the unknown background density. The equations (10) must be coupled to another one describing the evolution of ρ_a as the front moves downward:

$$\frac{\partial \rho_a}{\partial t} + w_f \frac{\partial \rho_a}{\partial z} \;=\; 0 \tag{11}$$

where $w_f = Q/A$ is the velocity of the front. This last equation essentially describes advection of density as the front moves downward. The boundary and initial conditions for this problem with initial uniform background density ρ_I are:

$$\left\{\begin{array}{rcl} \rho_a(H,t) &=& \rho_p(H,t), \\ Q(0,t) &=& Q_0, \\ \rho_a(z,0) &=& \rho_I. \end{array}\right. \tag{12}$$

The full problem (10,11) has been solved analytically using asymptotic analysis and numerically in Caulfield and Woods (2002); these solutions are presented in figure 5.

We can notice that once the front has reached the bottom of the box, the plume then mixes the ambient towards buoyancy homogeneisation. This long time mixing is controlled by the ventilation flux Q_0 and takes a typical time scale $\tau_\ell = AH/Q_0$ (provided that this time scale is much larger than the filling time scale defined in (4)). A simple well-mixed model captures most of the physics of the long term density evolution. Over a time dt the

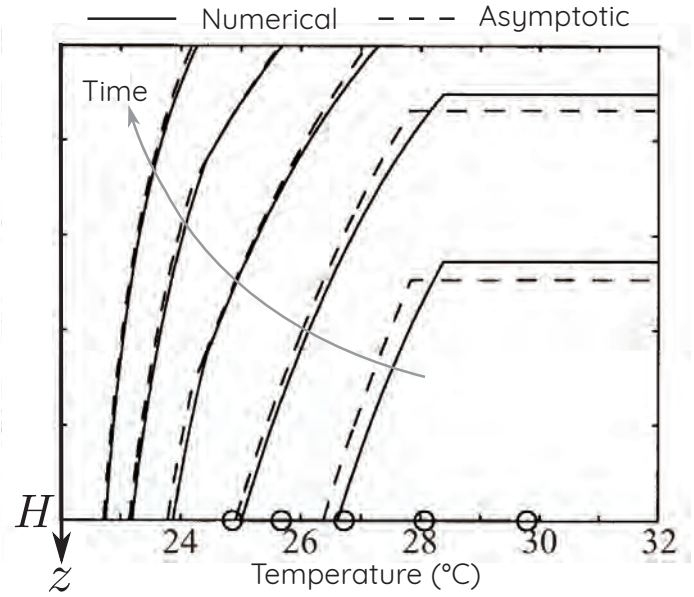

Figure 5: Numerical and asymptotic solutions of the full problem (10,11) presented in Caulfield and Woods (2002), from which this figure has been adapted.

mass inside the box varies of an amount $AH\mathrm{d}\rho_a$; the input mass is $\rho_{\mathrm{in}}Q_0\mathrm{d}t$ where ρ_{in} is the density of the incoming fluid while the output mass is $\rho_{\mathrm{a}}Q_0\mathrm{d}t$. The long term evolution of the fluid can be therefore modelled with simple first order differential equation:

$$\frac{\mathrm{d}\rho_a}{\mathrm{dt}} = \frac{1}{\tau_\ell}(\rho_{\mathrm{in}} - \rho_a) \tag{13}$$

with simple solution:

$$\rho_a = \rho_{\mathrm{in}} + (\rho_I - \rho_{\mathrm{in}})e^{-t/\tau_\ell} \tag{14}$$

which captures most of the dynamics without delving into the details of the density profile inside the box (Caulfield and Woods, 2002).

3 Confined Plume with Natural Ventilation

The last section was devoted to plumes in a confined environment with no ventilation. We review here a simple natural ventilation that can be implemented in a confined hall and propose a simple analysis of its efficiency.

3.1 Natural ventilation of a warm hall

Let us consider a room, for instance a concert hall, which is warm and well mixed. As a first idea to lower the temperature inside, an architect may think to use cold outside air and buoyancy contrast to force natural convection and air exchange with the exterior. This can be implemented as depicted in figure 6 with two stacks allowing the cold air in and the warm air out.

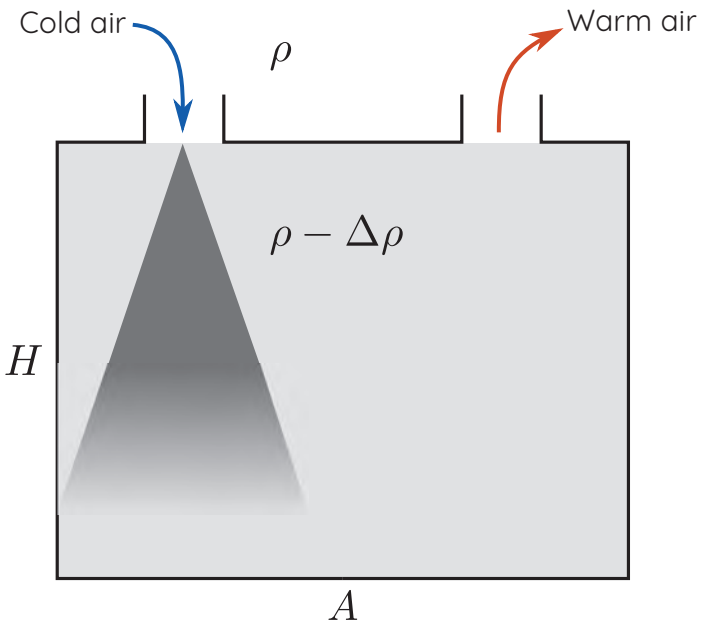

Figure 6: Schematic picture of a well-mixed warm box with two stacks ensuring natural ventilation driven by density contrast with the outside air. A is the area of the box cross-section. ρ and $\rho - \Delta\rho$ are the densities of the outside and inside air respectively.

3.2 Heuristic analysis: time evolution of the density contrast in a well-mixed hall

We aim to characterise the time evolution of the density contrast $\Delta\rho$ in the set-up depicted in figure 6 with simple heuristic arguments, as proposed in Kuesters and Woods (2011). This model is based on the assumption that the cold plume sinking in the box ensures strong mixing of density and that the ambient density is uniform throughout the box. The flow in this system is driven by the pressure difference in the stack providing outflow, which arises because of the difference in density of the air outside and inside the domain.

Let us call Q_i and Q_o the volume flux of cold air (input) and warm air (output). If the volume of the box is $\mathcal{V} = AH$, then the mass of air inside the box is

$$m_b \;=\; (\rho - \Delta\rho)\mathcal{V}. \tag{15}$$

The time variation of this mass is given by the inward and outward fluxes; over a time dt the cold air mass input is $\rho Q_i \mathrm{d}t$ and the warm air mass output is $-(\rho - \Delta\rho)Q_o \mathrm{d}t$. The values of Q_i and Q_o are given by the typical free-fall velocity v driven by the density contrast and the effective gravity $g' = g\Delta\rho/\rho$:

$$v = \sqrt{g'h} \quad \text{and} \quad Q_i = Q_o = \mathcal{S}\sqrt{g'h}\ . \tag{16}$$

where h and $\mathcal{S}$ are the height and the surface of a stack. We therefore infer the following time evolution equation for the density contrast:

$$\mathcal{V}\frac{\mathrm{d}\Delta\rho}{\mathrm{dt}} \;=\; -\,\Delta\rho\mathcal{S}\sqrt{g'(\Delta\rho)h} \tag{17}$$

which can be equivalently translated into an equation on the effective gravity g':

$$\mathcal{V}\frac{\mathrm{d}g'}{\mathrm{dt}} \;=\; -\,g'\mathcal{S}\sqrt{g'h}\;. \tag{18}$$

The solution of this last equation is then:

$$\frac{g'(t)}{g'(0)} \;=\; \left(1+\frac{t}{\tau_0}\right)^{-2} \quad,\; \tau_0 \;=\; \frac{2\mathcal{V}}{\mathcal{S}\sqrt{g'(0)h}} \tag{19}$$

where τ_0 is the typical time scale of the natural ventilation process, which is based on the typical free-fall velocity of the cold plume and on a typical length $\mathcal{V}/\mathcal{S}$. This time scale therefore merely translates the fact that all the warm air initially contained in the volume $\mathcal{V}$ has to go through the outlet of surface $\mathcal{S}$ with a typical free-fall velocity.

A more refined model including plume equations in a stratified environment, very similarly to what has been presented in the previous section, can be developed. This work has been done in Kuesters and Woods (2011), both theoretically and experimentally, and demonstrates that a stratification sets in the box. The mean buoyancy then decreases with almost constant stratification.

4 Confined Plume with Forced Ventilation

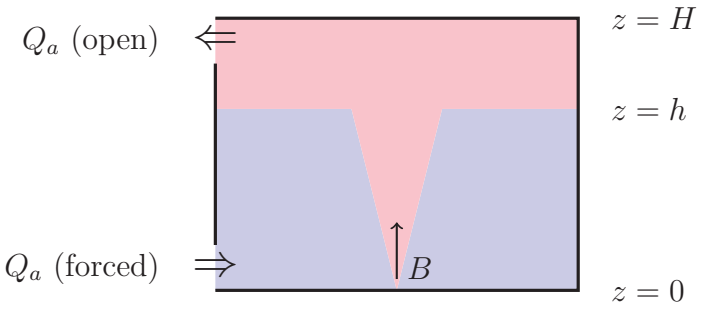

Figure 7: Schematic of a forced ventilation problem, where cool ambient air is pumped through a low inflow into a domain with a localised buoyancy source.

It is important to understand how localised heat sources can affect building ventilation by air conditioning. For example, a computer may produce a strong local source of heat which will change how well the air in a room is mixed by air conditioning.

To model this problem, we consider the setup as shown in figure 7, where a localised heat source at the bottom of a rectangular domain produces a warm plume, and the air conditioning system is modelled by a prescribed inflow (of cold air) at the bottom corner of the domain. An opening in the top corner of the domain also allows fluid outflow. In a steady state, this setup will produce a two-layer system with a warm layer above a region where the plume flows through the cool ambient. We denote the height of the interface between these two layers as h.

As shown in earlier lectures from dimensional analysis and experimental data, the volume flux of the plume at the interface will be

$$Q(h) = 0.1B^{1/3}h^{5/3}. \tag{20}$$

Since the system is assumed to be in steady state, the volume flux out of the domain must be equal to this, and volume conservation imposes that the volume flux through the inflow Q_a also takes this value:

$$Q_a = 0.1B^{1/3}h^{5/3}. \tag{21}$$

Prescribing the volume flux of the air conditioning system (Q_a) and the buoyancy flux of the heat source (B) then tells us the interface height

$$h = \left(\frac{10Q_a}{B^{1/3}}\right)^{3/5} \tag{22}$$

Comparing this interface height with the height of the domain H allows us to describe whether a room is over- or under-ventilated:

- $h > H$: the room is over-ventilated, so the air conditioning is doing more work than is necessary to cool the room;
- $h < H$: the room is under-ventilated (as shown in figure 7), so a warm layer persists in the upper part of the room.

5 Detrainment and Distributed Heat Sources

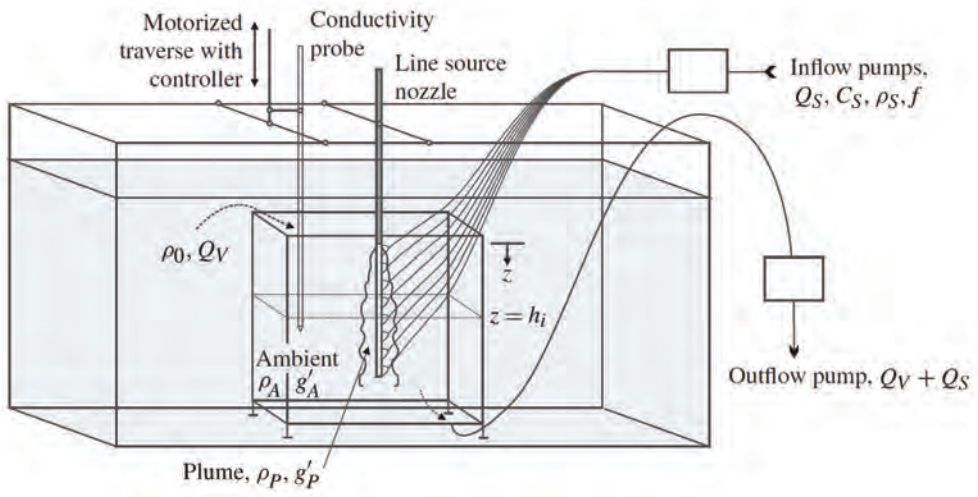

Figure 8: A sketch of the experimental apparatus used in Gladstone and Woods (2014).

In reality, not all heat sources are located at the bottom of a room. For example in large office buildings, external glass walls are increasingly common, and when these are heated

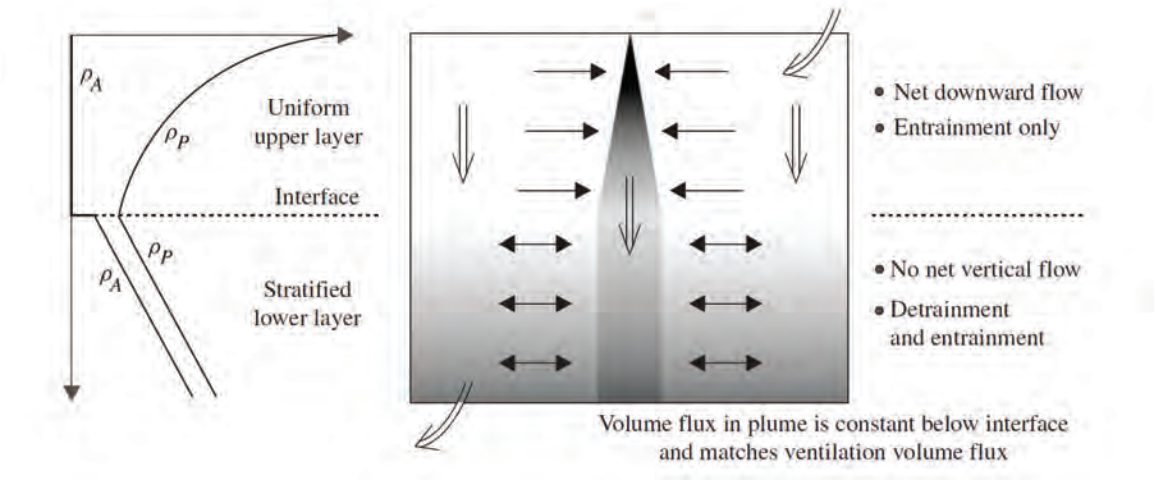

Figure 9: Schematic showing *(left)* the density profile in the plume ρ_p and the ambient ρ_a, with *(right)* the flow pattern that develops when a vertically continuous line source of buoyancy is placed in a ventilated enclosure. (Gladstone and Woods, 2014)

by the sun, a vertically distributed source of buoyancy is produced. To understand how a distributed source affects the inflow/outflow ventilation system described in the previous section, Gladstone and Woods (2014) performed the following experiment.

As shown in figure 8, a tank is immersed in a larger reservoir, with a line source in the centre of the tank supplying relatively dense fluid at a prescribed (small) volume flux Q_S at various heights. An outflow pumps fluid out of the tank at a prescribed (larger) volume flux, and since the top of the tank is open this drives a uniform flow into the tank at a volume flux Q_V. This inflow dominates the net volume flux into the tank, with Q_S contributing less than 10% of the total.

At early times, the ambient fluid in the tank is uniform and less dense than the plume fluid so the plume entrains the ambient fluid and a filling box process is observed. However at later times the system adjusts to the steady state shown in the schematic of figure 9. In the upper region of the domain a classical plume still persists, but below a transition height h_i the width of the plume does not change with height, and the ambient fluid becomes linearly stratified.

To analyse this steady state, it is useful to consider these two regions separately.

In the upper region of the domain, we can use dimensional analysis and the plume equations to make progress and determine h_i. Unlike in previous problems, there is now a distributed source of buoyancy and the conserved quantity is therefore the gradient of buoyancy flux with height which we denote by f, and not the buoyancy flux itself. By definition, f will have units

$$[f] = L^3/T^3, \tag{23}$$

which leads us to expect the following forms for velocity, plume radius and buoyancy:

$$u = C_1 f^{1/3}, \qquad b = C_2 z, \qquad g' = C_3 f^{2/3} z^{-1}. \tag{24}$$

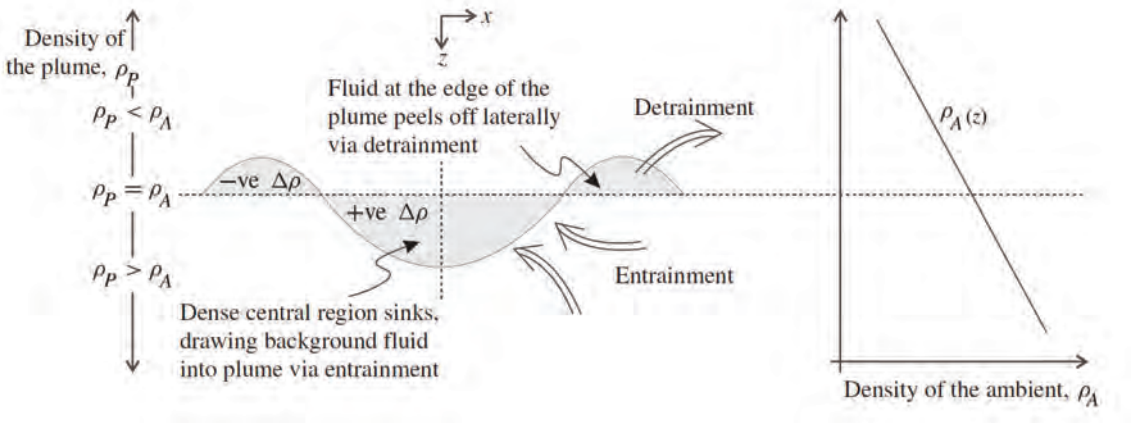

Figure 10: Illustration of the time-averaged buoyancy profile across the vertical line plume. A buoyancy surplus is created at the centre of the plume but a buoyancy deficit develops at the edge of the plume due to the stratified ambient. The buoyancy deficit leads to the intermittent detrainment of fluid from the plume, as the plume descends through the stratified ambient. (Gladstone and Woods, 2014)

The plume equations are now

$$\frac{\mathrm{d}(ub^2)}{\mathrm{d}z} = 2\epsilon ub, \qquad \frac{\mathrm{d}(u^2b^2)}{\mathrm{d}z} = g'b^2, \qquad \frac{\mathrm{d}(ub^2g')}{\mathrm{d}z} = f, \tag{25}$$

and yield the following solutions consistent with the dimensional analysis:

$$u = \left(\frac{f}{2\epsilon^2}\right)^{1/3}, \qquad b = \epsilon z, \qquad g' = \frac{2}{z}\left(\frac{f}{2\epsilon^2}\right)^{2/3}. \tag{26}$$

This provides an expression for the volume flux

$$Q = (f/2)^{1/3}\epsilon^{4/3}z^2, \tag{27}$$

from which the transition height h_i can be deduced

$$h_i = Q_i^{1/2}(f/2)^{-1/6}\epsilon^{2/3}. \tag{28}$$

Here Q_i is the volume flux of the plume at the transition height which can be found through analysis of the lower layer. We can re-define the concept of over/under-ventilation for this problem using the transition height:

- $h_i > H$: the domain is over-ventilated;
- $h_i < H$: the domain is under-ventilated and the lower layer persists below the classical plume.

Injecting a small amount of dye into the lower layer at a specific height near the plume shows that the lower layer displays interesting behaviour at odds with classical plume theory.

The dye disperses horizontally near the edge of the plume, indicating both entrainment *and* detrainment. There is no vertical motion of the dye, which indicates that the lower layer does not develop by a filling box-type process, and that the vertical volume flux is all contained in the plume in the lower layer. This means that the volume flux in (28) must be equal to the volume flux being pumped out at the bottom of the tank $Q_p = Q_V + Q_S$, and the transition height h_i can be predicted using this. One important consequence of the volume flux being constant in the lower layer is that the net entrainment must be zero in this equilibrium state. Entrainment and detrainment occur intermittently and seemingly randomly, and a potential mechanism by which this occurs is shown in figure 10.

The buoyancy gradient in the lower layer plume can be calculated since the volume flux is constant:

$$f = \frac{\mathrm{d}B}{\mathrm{d}z} = \frac{\mathrm{d}(Q_p g')}{\mathrm{d}z} = Q_p \frac{\mathrm{d}g'}{\mathrm{d}z} \quad \Rightarrow \quad \frac{\mathrm{d}g'}{\mathrm{d}z} = \frac{f}{Q_p}. \tag{29}$$

We therefore get a linear stratification in the plume which mirrors the linear stratification measured in the lower ambient as shown by figure 9. The buoyancy contrast between the plume and the ambient fluid $\Delta g' = \mathcal{F}(Q_v, f)$ is now what drives the down-flow of the plume in the lower layer. Although the combined (upper and lower) buoyancy profile of the plume appears statically unstable, the ambient stratification in the lower layer prevents this from convecting.

It is clear that in this problem of a distributed buoyancy source, the classical plume models do not apply over the whole domain. There are many open problems regarding this type of flow - in particular, there is no current model for the rate or control of detrainment. It is also unknown which other flows may exhibit a combination of entrainment and detrainment, and how to design experiments to test what controls detrainment rates.

References

Baines, W. D. and J. S. Turner, 1969. Turbulent buoyant convection from a source in a confined region. *Journal of Fluid Mechanics,* 37(1):51-80.

Bhamidipati, N. and A. W. Woods, 2017. On the dynamics of starting plumes. *Journal of Fluid Mechanics,* 833, R2.

Caulfield, C. P. and A. W. Woods, 2002. The mixing in a room by localized finite-mass-flux source of buoyancy. *Journal of Flud Mechanics,* 471.

Gladstone, C. and A. W. Woods, 2014. Detrainment from a turbulent plume produced by a vertical line source of buoyancy in a confined, ventilated space. *Journal of Fluid Mechanics*, 742:35-49.

Kuesters, A. S. and A. W. Woods, 2011. The formation and evolution of stratification during transient mixing ventilation. *Journal of Fluid Mechanics*, 670:66-84.

Lecture 4
Ventilated Plumes, Plumes in a Tube and Ventilation with Multiple Openings

Notes by Rohit Supekar, Sara Lenzi and Sutirtha Sengupta

June 21, 2018

1 Mixing by a Ventilated Plume

We continue our discussion on plumes in building environments by now considering the problem of natural ventilation in the presence of a plume that is generated by a localized heat source. An example of such an environment is a room with a heater on the floor and an opening at the ground level and at the roof. In this problem, we do not drive the mass flux of ventilation. The ventilation is driven by the buoyancy differences in the interior and exterior.

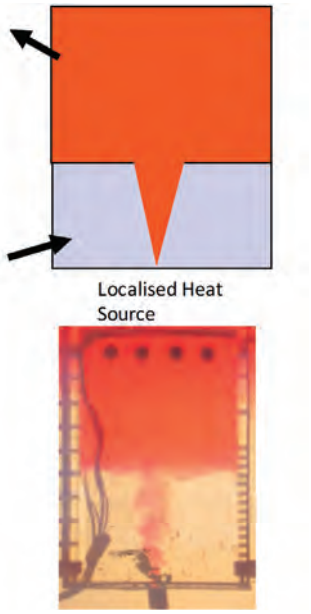

Figure 1: Top: schematic of the natural ventilation problem. Bottom: the experimental setup of the release of fresh water (red) in a salty ambient (clear). The arrows indicate the inflow and the outflow that is not forced but arises due to buoyancy differences.

Consider a box of total height H with an opening at the bottom and the top as shown in figure (1). There is inflow at the bottom and outflow at the top due to buoyancy differences. This is the modified version of the problem that we considered in the previous

lecture where the inflow was forced with the volume flux Q_a. The localized heat source provides a buoyancy flux B and creates a plume as shown. Warm fluid rises up in the plume and starts creating a buoyant layer of height $H - h$ at the top of the box. Because of the buoyancy difference, a ventilation flow begins (outflow at the top and inflow at the bottom). Eventually, the system comes to a steady state when the ventilation volume flux equals the volume flux through the plume. In other words, the plume entrains a volume flux that is equal to the inflow volume flux. The top layer becomes well mixed with reduced gravity g' which is the reduced gravity of the plume at height h.

Let us first consider the steady state. Let the area of the inlet be A_1 and the outlet be A_2. Since there is no forced volume flux for ventilation, the volume flux Q is proportional to the gravitational head given by

$$Q = cA_1(\lambda g'(H-h))^{1/2} = cA_2((1-\lambda)g'(H-h))^{1/2}. \tag{1}$$

Here, c is a loss factor and λ is a fraction that splits the gravitational head between the inlet and the outlet. From equation (1), we can solve for λ, and it is given by

$$\lambda = \frac{A_2^2}{A_1^2 + A_2^2}. \tag{2}$$

The volume flux of ventilation is thus given by

$$Q = c\frac{A_1A_2}{(A_1^2+A_2^2)^{1/2}}(g'(H-h))^{1/2} = cA^*(g'(H-h))^{1/2}, \tag{3}$$

where we replace the area factor with A^*. As we have seen earlier, the volume flux through the plume at height h is given by

$$Q_p = 0.1B^{1/3}h^{5/3}. \tag{4}$$

In steady state, $Q = Q_p$ and the buoyancy flux is conserved. Hence,

$$B = g'Q = cA^*g'(g'(H-h))^{1/2}. \tag{5}$$

Combining equations (3), (4) and (5), we can obtain an expression for the interface height as the solution of the following equation:

$$\left(\frac{h}{H}\right)^5 = 10\left(\frac{cA^*}{H^2}\right)^2\left(1-\frac{h}{H}\right). \tag{6}$$

Note that the interface height h is a function of other geometric quantities alone and is not dependent on the buoyancy flux B. This is expected since there is no forced volume flux in this case and the volume flux is decided by the buoyancy itself. Hence, the only other length scales in the problem come from the geometric factors. There is no concept of under-ventilation or over-ventilation as we saw in the case of forced ventilation. The interface is always present and is inside the room. We must also note that as the area of the openings is increased, the interface height increases due to the increased ventilation. If the area is decreased, the height of the interface decreases and the ambient fluid is localized to a very small layer at the bottom of the room. For further details of this problem, refer to reference [4].

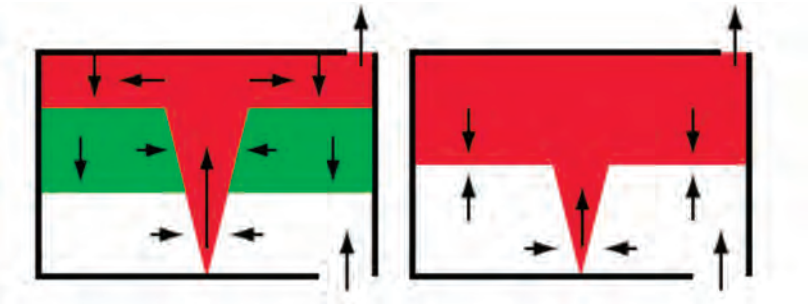

Figure 2: Schematic of the process when the buoyancy flux is increased. The original fluid in the steady state is marked by green and the more buoyant (or hotter) fluid is marked by red. Arrows indicate the flow directions.

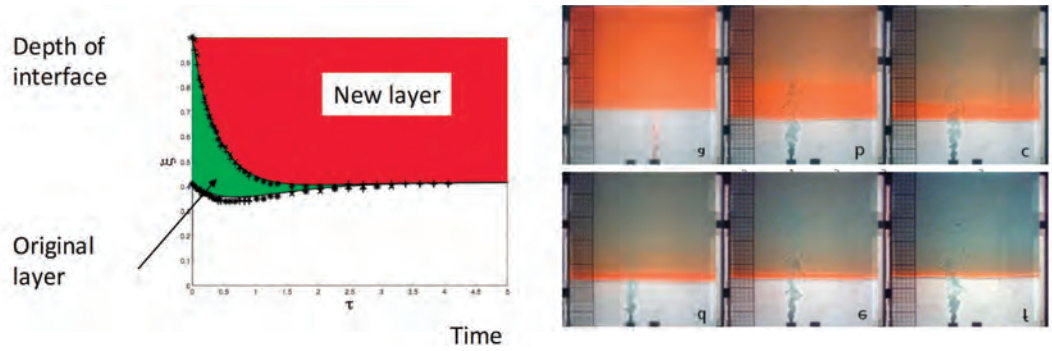

Figure 3: The experiment done by [1] and experimental results of the layer height plotted on the left. The fluid colored in blue is the more buoyant (fresher) fluid that is being released into the less buoyant (saltier) fluid that is colored in red.

1.1 Transients

1.1.1 Increasing the buoyancy flux

Let us now suppose that the steady state is perturbed by increasing the buoyancy flux (or equivalently, increasing the heating in the room). The schematic of this process is shown in figure (2).

As the buoyancy flux is increased, buoyant fluid starts rising as a plume and hits the interface. Since it is more buoyant, it keeps rising through the upper layer until the top where the fluid starts forming a new layer. This new layer is show in red in figure (2). While the more buoyant fluid is rising up, it also entrains the less buoyant fluid shown in green. The process of entrainment continues until the less buoyant fluid is completely drained out of the system leading to a new steady state with the new buoyant fluid. The new interface height is still given by equation (6), that is, it is the same as the old height. This problem was investigated by [1] and the results from their experiment are shown in figure (3).

To model this transient problem, let consider the new interface height h_n and the old

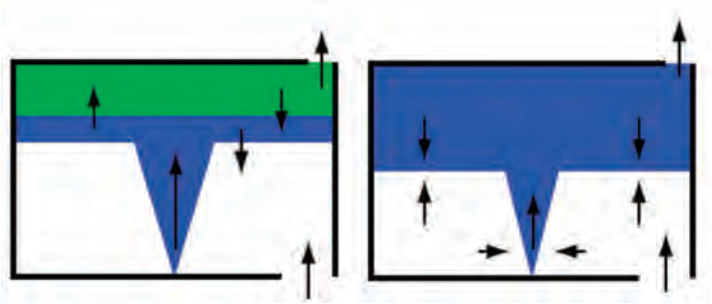

Figure 4: Schematic of the process when the buoyancy flux is decreased. The original fluid in the steady state is marked by green and the less buoyant (or cooler) fluid is marked by blue. Arrows indicate the flow directions.

interface height h_0, and write the following equations by mass conservation:

$$A\frac{dh_n}{dt} = Q_v - Q_p(h_n) \tag{7}$$

$$A\frac{dh_0}{dt} = Q_v - Q_p(h_0) \tag{8}$$

Here, A is the cross sectional area of the box and Q_v is the ventilation volume flux. The equation for buoyancy conservation is as follows:

$$A\frac{d(H-h_n)g'}{dt} = B_n + (Q_p(h_n) - Q_p(h_0))g_0' - Q_v g' \tag{9}$$

Here, g_0' is the reduced gravity of the original fluid and g' is the changing reduced gravity of the new layer that is being formed. The ventilation volume flux, that is driven by buoyancy differences is given by:

$$Q_v = A_c(g'(H-h_n) + g_0'(h_n - h_0))^{1/2}. \tag{10}$$

Here, A_c is some area factor that arises as in equation (3). The above four equations can be numerically integrated to obtain the evolution of the interface heights that are plotted in figure (3).

1.1.2 Decreasing the buoyancy flux

In the case where we decrease the buoyancy flux, less buoyant fluid starts rising as a plume and hits the interface of the original fluid. Since it less buoyant than the original fluid, it doesn't keep rising up but acts as a fountain that entrains some of the old fluid and spreads out at the interface. Subsequently, a new layer starts to build up below the original fluid which is pushed out through ventilation. This process is shown as a schematic in figure (4). The corresponding experiments in [1] of this problem are shown in figure (5).

This problem can be modeled in a similar fashion as earlier. The volume conservation

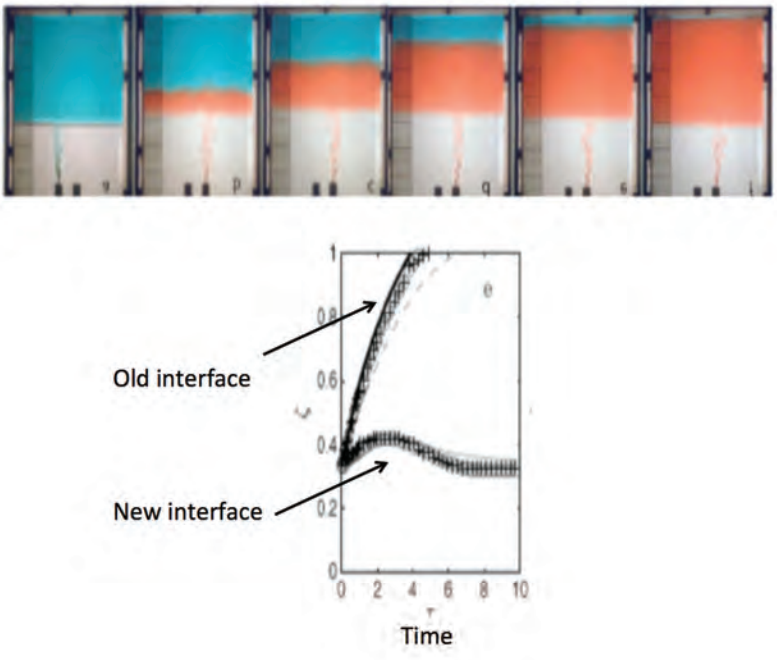

Figure 5: The experiment done by [1] and experimental results of the layer height. The fluid colored in blue is the more buoyant (fresher) and the one in red is less buoyant (saltier).

equations are as follows:

$$A\frac{dh_n}{dt} = Q_v - Q_p(h_n) \tag{11}$$

$$A\frac{(H-h_0)}{dt} = -Q_v - Q_{\text{fountain}} \tag{12}$$

Buoyancy conservation gives us

$$A\frac{d(h_0-h_n)g'}{dt} = B_n + g_0' Q_{\text{fountain}} \tag{13}$$

The ventilation volume flux is given by

$$Q_v = A_c(g'(h_0-h_n) + g'(H-h_0))^{1/2} \tag{14}$$

As earlier, the above equations can be integrated numerically to find the interface heights that are plotted in figure (5), which match very well with experimental data collected by [1].

2 Plumes in a Tube

So far in this lecture series, we have looked at plumes from a localized source of buoyancy in confined spaces, but the cross sectional area of the plume was much smaller than the

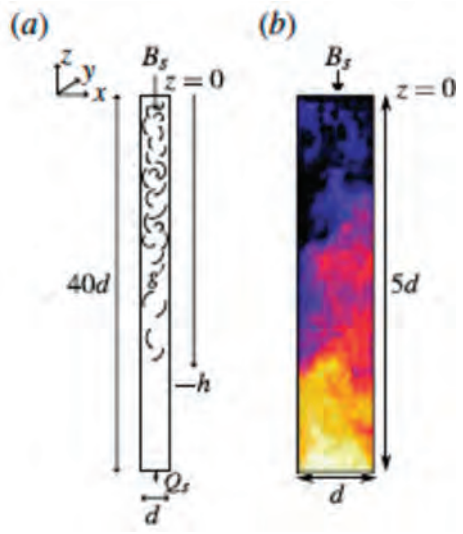

Figure 6: Left: schematic of the setup where the buoyancy source at the top creates a plume in a confined tube. Right: Colormap of the concentration of an evolving plume from the experiments by [6].

confined space. There is another class of problems where the confined space, for example a tube, is small enough so that the evolving plume hits the sides of the plume. Beyond this point, the plume is unable to evolve and the advancement of the plume depends on the mixing caused by the eddies in the tube. A schematic and an experimental realization of such a plume is shown in figure (6).

Figure (7) shows the results of the experiments performed by [6]. One striking feature of these results is that the gradient of g' is roughly constant at all times. If B is the input buoyancy flux and d is the tube diameter, from dimensional arguments we can say that

$$\frac{\Delta g_0'}{h} \sim \frac{B^{2/3}}{d^{8/3}}. \tag{15}$$

Here, $\Delta g_0'$ is net change of the reduced gravity in the tube. This is a hypothesis that is inspired from the experiments. Equating the total buoyancy change in the tube, we have that

$$d^2 \Delta g_0' h \sim Bt. \tag{16}$$

From equations (15) and (16), we find that

$$\Delta g_0' \sim B^{5/6} d^{-7/3} t^{1/2}, \tag{17}$$

$$h \sim B^{1/6} d^{1/3} t^{1/2}. \tag{18}$$

Above two equations provide scalings for the net change in the reduced gravity in the tube and the height the plume is able to penetrate as time progresses.

We will not proceed to obtain a diffusion equation for g' in the tube. The mixing is driven by the turbulent eddies that have a length scale d. Thus, $u_e \sim \sqrt{\Delta g' d}$ is the typical

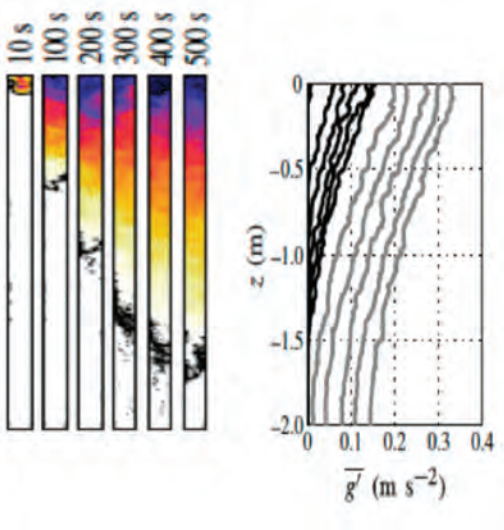

Figure 7: Experimental results by [6]. Left: Time series of the concentration in the tube when salty water is released at the top. Right: evolution of the profiles of horizontally averaged g' in the tube. The darker lines correspond to earlier times.

eddy velocity in the tube. Here, $\Delta g'$ is the difference in g' across the tube that is also given by:

$$\Delta g' \sim \frac{\partial g'}{\partial z} d. \tag{19}$$

The buoyancy flux is then given by

$$F \sim \Delta g' u_e \sim (\Delta g')^{3/2} d^{1/2} \sim d^2 \left(\frac{\partial g'}{\partial z} \right)^{3/2}. \tag{20}$$

We now add a constant λ^2 such that $F = \lambda^2 d^2 \left(\frac{\partial g'}{\partial z} \right)^{3/2}$. The conservation equation for g' can now be written as:

$$\frac{\partial g'}{\partial t} = \frac{\partial F}{\partial z} = \lambda^2 \frac{\partial}{\partial z} \left(k \frac{\partial g'}{\partial z} \right). \tag{21}$$

The above equation is a nonlinear diffusion equation where the diffusion coefficient k is given by

$$k = d^2 \left(\frac{\partial g'}{\partial z} \right)^{1/2}. \tag{22}$$

In the case where there is no background flow, equation (21) admits self-similar solutions of the following form

$$g'(z,t) = B^{5/6} d^{-7/3} t^{1/2} f(\eta), \tag{23}$$

where η is the similarity variable given by

$$\eta = \frac{z}{B^{1/6} d^{1/3} t^{1/2}}. \tag{24}$$

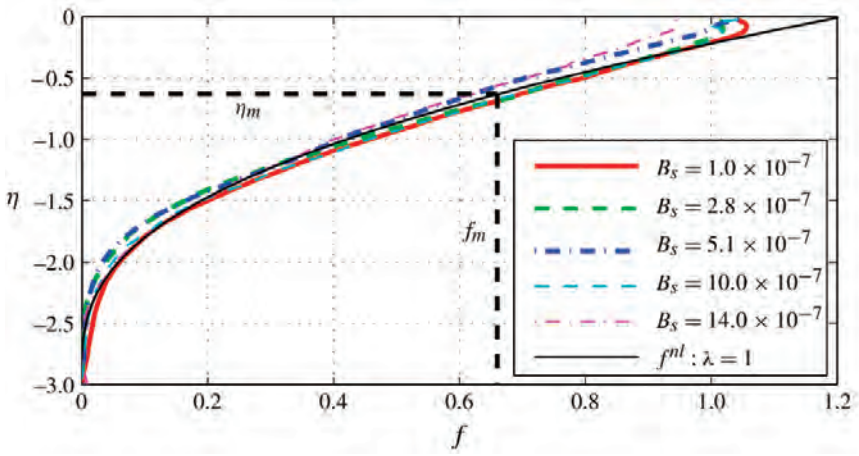

Figure 8: Rescaled data from the experiments by [6]. Here, $f = \bar{g'}/(B^{5/6}d^{-7/3}t^{1/2})$ and $\eta = z/(B^{1/6}d^{1/3}t^{1/2})$, where $\bar{g'}$ is the horintally averaged g' obtained from the experiments.

Substituting equation (23) into equation (21) gives us the following equation for the shape function $f(\eta)$:

$$f(\eta) - \eta\frac{df}{d\eta} = 2\lambda^2\frac{d}{d\eta}\left(\left(\frac{df}{d\eta}\right)^{3/2}\right). \tag{25}$$

One of the boundary conditions to solve the above equation is found by enforcing a constant buoyancy flux at the top. Thus,

$$\left.\frac{df}{d\eta}\right|_{\eta=0} = \frac{1}{\lambda^{4/3}}. \tag{26}$$

The other boundary condition is that $f \to 0$ as $\eta \to \infty$. This is valid as long as the bottom of the plume doesn't hit the bottom of the tube and the plume is still evolving. The parameter λ is found to be 1 by fitting experimental data to solutions of equation (25). The profiles of $\bar{g'}$ (horizontally averaged g') form the experiments by [6] as shown in figure (7) are rescaled as per the similarity solution and compared with the function $f(\eta)$ in figure (8). It is quite clear that the experimental data fits very well with the similarity solution.

2.1 Passive tracers

We now approach the case in which we add some *passive* tracers at the top of the domain observing their movements along the tube.
A passive tracer doesn't interact with the surrounding fluid (change in density, temperature, dynamics or others...) and for this reason it could be an optimal marker for the fluid's behavior.
In this case we add cold (salty) tracers in a hot (fresh) fluid and, as in the previews example, we observe the whole system evolves in time reaching a time-average steady state characterized by a *finite* mixing zone.
Experiments show the zone length changing at different Froude numbers ($Fr = \frac{\mathbf{v}}{\sqrt{gL}} = \frac{inertial forces}{buoyancy forces}$) see figure (9).

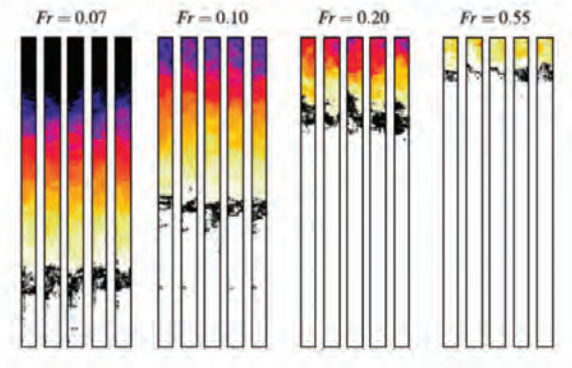

Figure 9: Different experiments : the steady state shows different lengths for the mixed zone at increasing Froude number.

We are interested now in calculating the mixing zone length using the following :

$$\frac{\partial \bar{g}'}{\partial t} + \mathbf{u}_u \frac{\partial \bar{g}'}{\partial z} = \lambda^2 d^2 \frac{\partial}{\partial z}\left(\frac{\partial \bar{g}'}{\partial z}\right)^{3/2} \tag{27}$$

$$-\lambda^2 d^2 \frac{\partial}{\partial z}\left(\frac{\partial \bar{g}'}{\partial z}\right)^{3/2}\bigg|_{z=0} = -\frac{B_s}{d^2} \tag{28}$$

$$\bar{g}'(-h_s) = \frac{\partial \bar{g}'}{\partial z}\bigg|_{z=-h_s} = 0 \tag{29}$$

where (27) is the $\bar{g}'$ conservation while the (28) and the (29) are the boundary condition for the flux at the top and zero buoyancy condition at bottom respectively.
From the previews we obtain :

$$\bar{g}'_{st} = \frac{\vec{u}_u^2}{27\lambda^4 d^4}(z + h_s)^3 \tag{30}$$

$$h_{st} = \frac{3B_s^{1/3} d^{2/3} \lambda^{4/3}}{\vec{u}_u} \tag{31}$$

which are the steady state value of the mean buoyancy profile and the length of the mixed layer.

In figure (10) experiment's and model's results are compared showing a very good accordance.

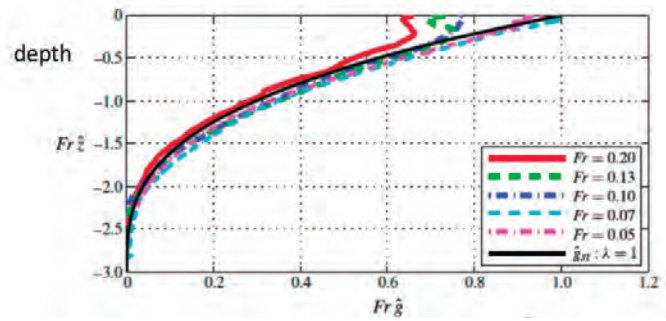

Figure 10: Rescaled profiles for g' and depth are shown, we observe a quite constant slope for the depth in function of g' with varying (increasing) Fr numbers.

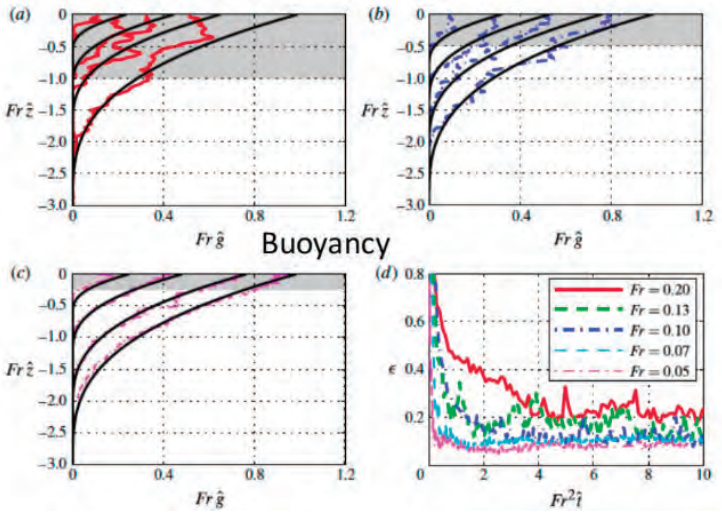

Figure 11: Rescaled profiles for g' and depth are shown, we observe a quite constant slope for the depth in function of Fr g' with varying (increasing) Fr numbers.

We point now our attention to develop a mathematical model for the passive tracer .
How does the tracer move?
Is the diffusivity controlling the passive tracer's movements in the mixed layer ?
We can describe the mean tracers concentration with the following where we used the preview results of a cubic buoyancy gradient which gives us : $\sqrt{\frac{\partial g}{\partial z}} = 1 + z$.

$$\frac{\partial \bar{c}}{\partial t} + \frac{\partial \bar{c}}{\partial z} = \frac{\partial}{\partial z}\left[kv\frac{\partial \bar{c}}{\partial v}\right] = \frac{\partial}{\partial z}\left[\frac{(z+1)}{3}\frac{\partial \bar{c}}{\partial z}\right] \tag{32}$$

In the eq.(32) the second term on the left represents the mean flux and the terms on the right are two equivalent forms for the diffusion term.

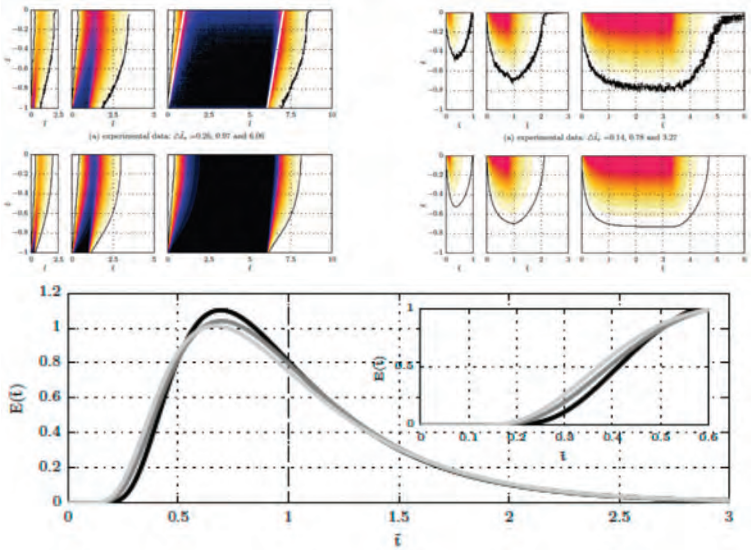

Figure 12: Experimental data : images show the time-evolution of the system (top) and temporal energy profile (bottom).

We can also consider the behavior for the symmetric problem or the case in which a passive tracer is added from the bottom.
Results show again a symmetric behavior, with the development of a finite length mixed layer and the reaching of a steady state. This behavior is shown in figure (13).

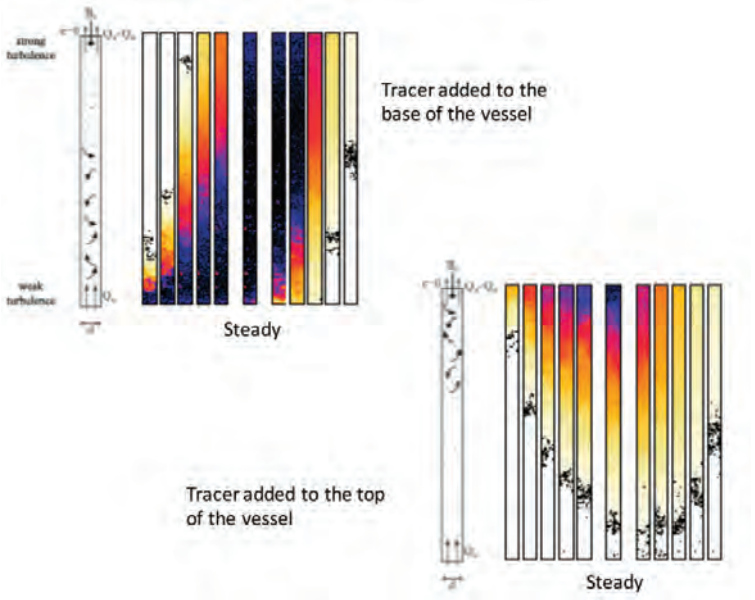

Figure 13: Symmetric problems are shown : tracers added ad bottom of the tube (top) and tracers added at top of the tube (bottom)

2.2 Tilted tube

We consider now the case of a tilted tube calling θ the angle with the vertical as shown in figure (14).

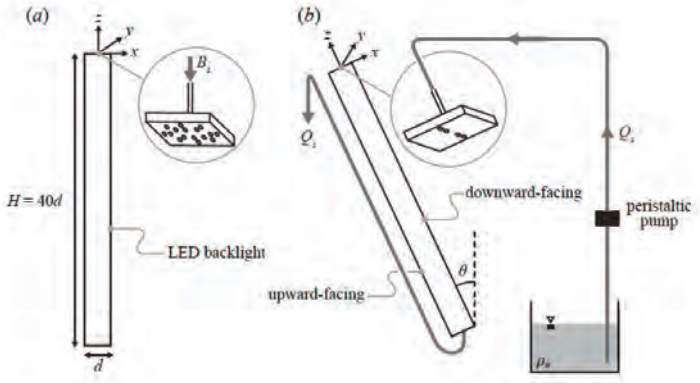

Figure 14: Tilted tube problem, being θ the tilting angle.

In this case the system is subject both to gravity and buoyancy due to density's difference. What we observe is that, in the case of a tilted tube, a mean circulation develops and this net shear enhances the net transport.
Indeed, analyzing the phenomenological behavior, we immediately observe the faster evolution of the tilted tube's dynamics respect to the non-tilted one in figure 15(a)-(b)-(c)-(e)-(f) due to the interaction of gravity with the angle of titling shows in figure 15(d).

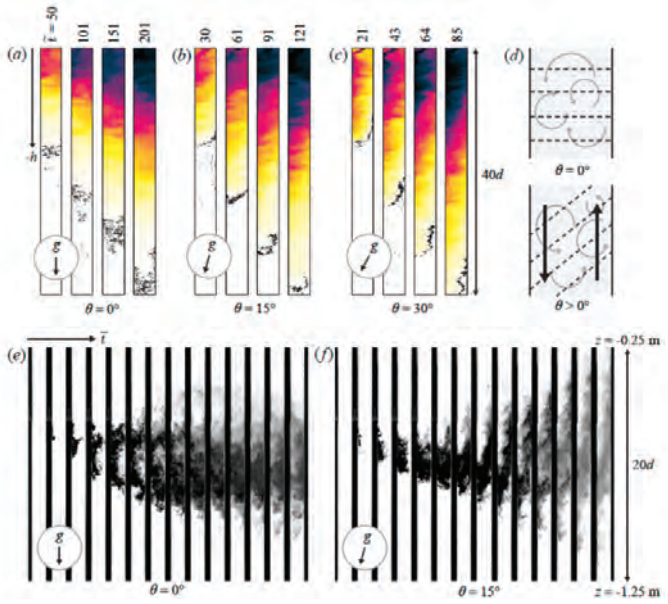

Figure 15: Tilted and non-tilted tube: simulations (top) and experiments (bottom).

In figure 15(d) the eddies-dominated environment in the case of $\theta = 0$ (top) and the mean circulation's development for the case of the tilted tube figure 15(d) (bottom) are shown.
We develop now a new mathematical model for the description of the tilted tube system using $\lambda(\theta)$ as diffusion coefficient depending on the tilting angle θ.
Using an analog form of the (27) we write for the *mean* buoyancy gradient:

$$\frac{\partial \langle \mathbf{g'} \rangle_e}{\partial t} = \lambda^2 d^2 \frac{\partial}{\partial z} \left(\frac{\partial \langle \mathbf{g'} \rangle_e}{\partial z} \right)^{3/2} \tag{33}$$

$$\langle \mathbf{g'} \rangle_e = B^{5/6} d^{-7/3} t^{1/2} f(\eta) \tag{34}$$

$$\eta = \frac{x}{B^{1/6} d^{1/3} t^{1/2}} \tag{35}$$

$$f(\eta) - \eta \frac{df}{d\eta} = 2\lambda^2 \frac{d}{d\eta} \left(\left(\frac{df}{d\eta} \right)^{3/2} \right). \tag{36}$$

$$\left. \frac{df}{d\eta} \right|_{\eta=0} = \frac{1}{\lambda^{4/3}}. \tag{37}$$

$$\int_0^1 f d\eta = 1. \tag{38}$$

where we assumed a self similar mixing state.
Comparison with experiments give some interesting results for η and λ as shown in figure (16)-(17).

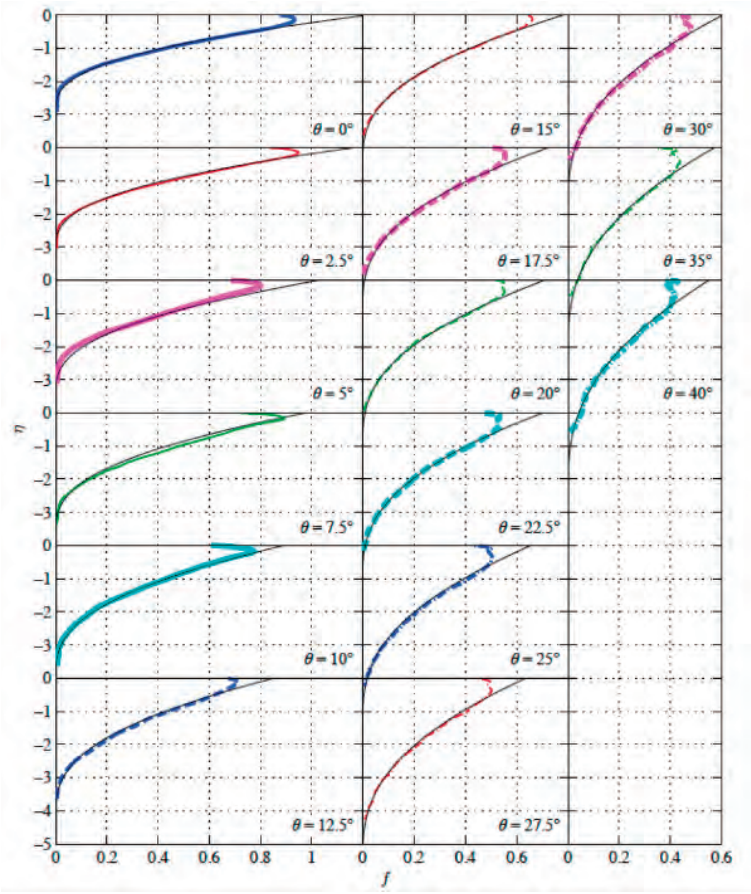

Figure 16: η values in function of f at increasing tilting angles

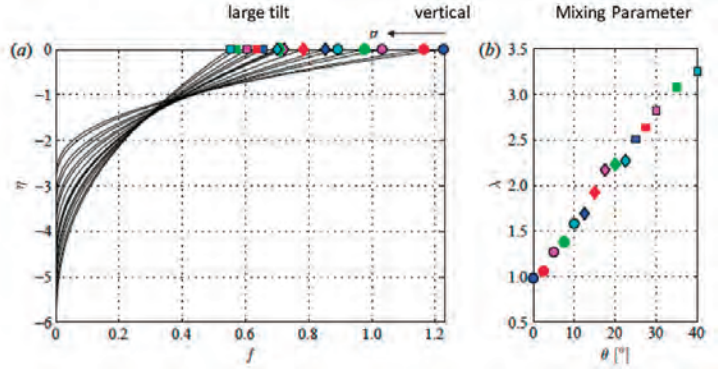

Figure 17: η in function of time (a) and λ in function of θ (b). Figure (b) shows the faster mixing (λ) at increasing tilting angle.

3 Study of Ventilation Flows through Buildings/Confined Spaces

In this section, we shall present a framework to study flows in confined spaces (e.g. auditoriums, buildings) with multiple openings/ventilations. This is exemplified through a unexpected flow case study through the ventilated Contact theater in Manchester with four such ventilation outlets that went through a flow state of where the temperature of the air through one of the openings was found to lock on to the ambient temperature for a considerable duration, as shown in Fig 18. We present here a simple model of a double ventilation enclosure with a single source of air inflow to study the different possible states and its dependence on the initial conditions of the system in consideration.

3.1 Modeling approach for ventilation with two openings

We present a simplified approach to understand ventilation flow states possible for an enclosure with multiple openings allowing for inflow/outflow of air, based on the study through flow models as well as real experiments performed and described by [2]. The model described here accounts for the simplest scenario with two ventilation openings and one inlet for a rectangular enclosure and explains the flow states depending on the geometry of this simple setup illustrated in Fig 19, which can easily be generalized to more complicated real situation to help understand these different realizable flow states that controls the ventilation and help in more efficient design of the building.

3.1.1 Case a: Inflow-outflow

The volume flux through each of the three openings in Fig 19 may be expressed as

$$\begin{aligned} Q_0 &= cA_0 \left(\frac{\triangle p}{\rho_0}\right)^{\frac{1}{2}}, \\ Q_1 &= cA_1 \left(g'(H+h_1) - \frac{\triangle p}{\rho_0}\right)^{\frac{1}{2}}, \\ Q_2 &= cA_2 \left(\frac{\triangle p}{\rho} - g'H\right)^{\frac{1}{2}}. \end{aligned} \tag{39}$$

Conservation of buoyancy flux gives

$$\begin{aligned} g'Q_1 &= B, \\ g'^2 \left(g^{'}(H+h_1) - \frac{\triangle p}{\rho_0}\right) &= \frac{B^2}{A^2}, \\ \frac{\triangle p}{\rho} &= \left(g^{'}(H+h_1) - \frac{B^2}{A_1^2 g'^2}\right). \end{aligned} \tag{40}$$

For convenience, we can rescale g' as

$$g' = \left(\frac{B^2}{A_1^2 H}\right)^{\frac{1}{3}} \hat{g}, \tag{41}$$

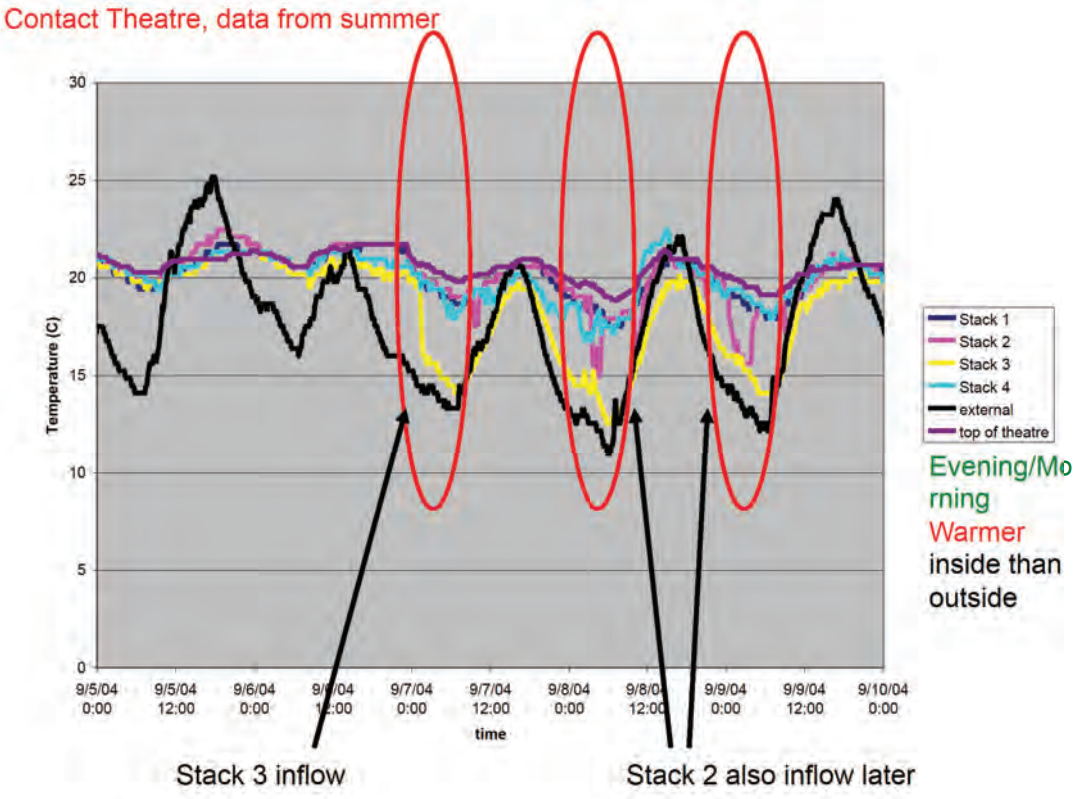

Figure 18: (Top)The Contact theater in Manchester designed for ventilation using air from outside; (Bottom) Data for the temperature inside over the summer of 2004.

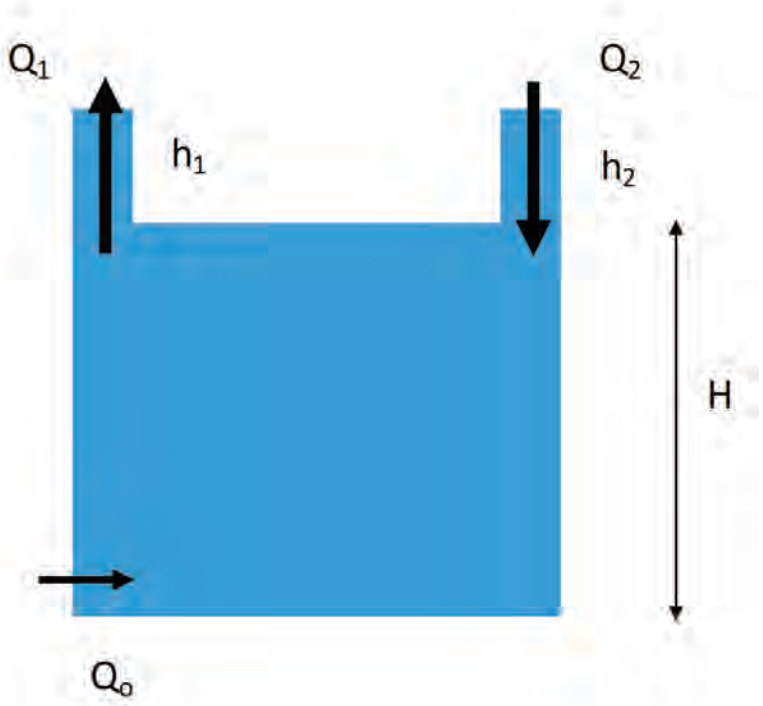

Figure 19: Flow diagram for a building model with with a inflow flux (Q_0) and opposite flows through two ventilation on top.

using which the last relation of (40) reduces to

$$\frac{\triangle p}{\rho} = \left(\frac{B^2}{A_1^2 H}\right)^{\frac{1}{3}} H\left((1+\hat{h}_1)\hat{g} - \frac{1}{g'^2}\right) \tag{42}$$

with $\hat{h}_1 = \frac{h_1}{H}$.
Volume flux conservation implies

$$\begin{aligned} Q_0 + Q_2 &= Q_1 \\ \frac{1}{\hat{g}'} &= \frac{A_0}{A_1}\left((1+\hat{h}_1)\hat{g} - \frac{1}{\hat{g}'^2}\right) + \frac{A_2}{A_1}\left(\hat{h}_1\hat{g} - \frac{1}{\hat{g}'^2}\right) \\ \frac{A_0}{A_1}\left((1+\hat{h}_1)\hat{g}^3 - 1\right)^{\frac{1}{2}} &+ \frac{A_2}{A_1}\left(\hat{h}_1\hat{g}^3 - 1\right)^{\frac{1}{2}} = 1. \end{aligned} \tag{43}$$

Limiting case ($Q_2 = 0$ and $\hat{g} = \left(\frac{1}{\hat{h}_1}\right)^{\frac{1}{3}}$) occurs when

$$A_0 = A_1 h^{\frac{1}{3}}. \tag{44}$$

3.1.2 Case b: Outflow-inflow

This is the analogous situation but with the direction of flow through the top openings reversed compared to the situation in Fig 19.

3.1.3 Case c: Outflow through both openings

For this situation as illustrated in Fig 20, the volume flux through each of the three openings is given by

$$\begin{aligned} Q_0 &= cA_0\left(\frac{\triangle p}{\rho}\right)^{\frac{1}{2}}, \\ Q_1 &= cA_1\left(g'(H+h_1) - \frac{\triangle p}{\rho}\right)^{\frac{1}{2}}, \\ Q_2 &= cA_2\left(g'(H+h_2) - \frac{\triangle p}{\rho}\right)^{\frac{1}{2}}. \end{aligned} \tag{45}$$

The buoyancy flux is given by

$$B = Q_0 g'. \tag{46}$$

Volume flux conservation in this case implies

$$\begin{aligned} Q_0 &= Q_1 + Q_2 \\ \frac{\triangle p}{\rho} &= \frac{B^2}{A_1^2 g'^2}. \end{aligned} \tag{47}$$

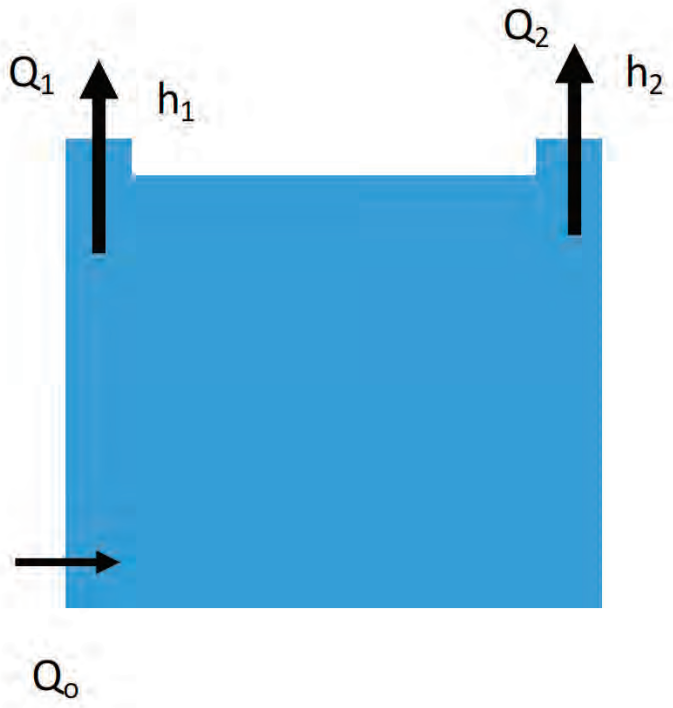

Figure 20: Flow diagram for a building model with a inflow flux (Q_0) and two outflows through ventilations on top.

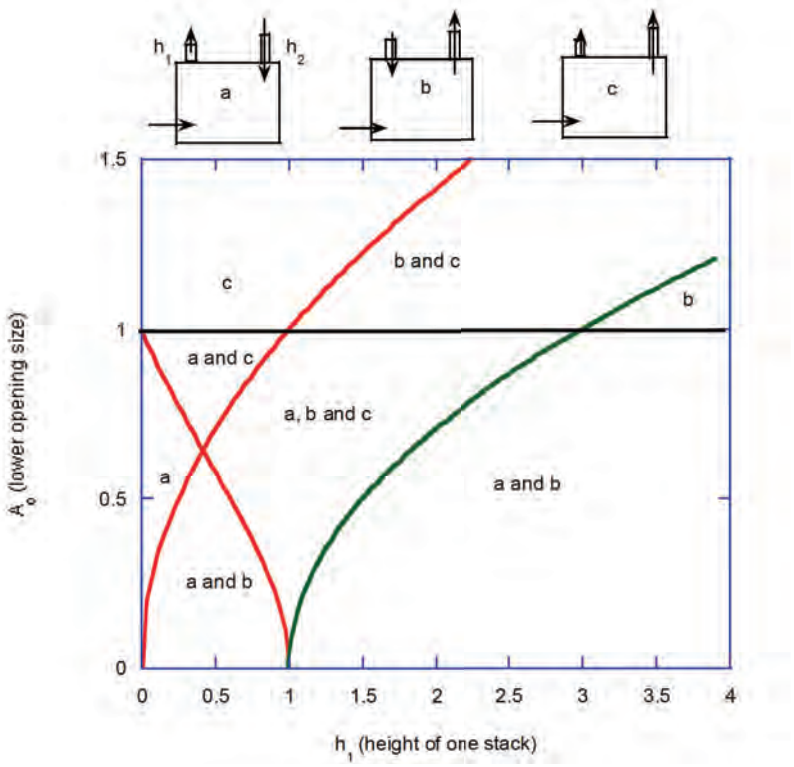

Figure 21: The different possible flow states (a,b and c) as described in Section 3.1 in the $h_1 - A_0$ parameter space depending on the initial conditions of the ventilation setting.

Rescaling as before, we obtain

$$\frac{A_0}{A_1} = \left((1+\hat{h}_1)\hat{g}^3 - 1\right)^{\frac{1}{2}} + \frac{A_2}{A_1}\left(\hat{h}_1\hat{g}^3 - 1\right)^{\frac{1}{2}}. \tag{48}$$

Hence, the limiting case in this situation occurs for

$$\hat{g}' = (1+h_1)^{-\frac{1}{3}} \tag{49}$$

which requires

$$\frac{A_0}{A_1} = \frac{A_2}{A_1}\left(\frac{1+\hat{h}_2}{1+\hat{h}_1} - 1\right)^{\frac{1}{2}} = \frac{A_2}{A_1}\left(\frac{\hat{h}_2 - \hat{h}_1}{1+\hat{h}_1}\right). \tag{50}$$

Similar results are obtained with the two openings interchanged.It is to be noted that for

3.2 Ventilation with wind-driven flow

In the preceding model of ventilation flow, we neglected the contribution of wind on driving the pressure change across the walls of the confined space, which can even dominate and thereby control ventilation dynamics. To take into account the possible effects of ventilation flows in a building which is subject to wind pressure, we can consider the case in which the

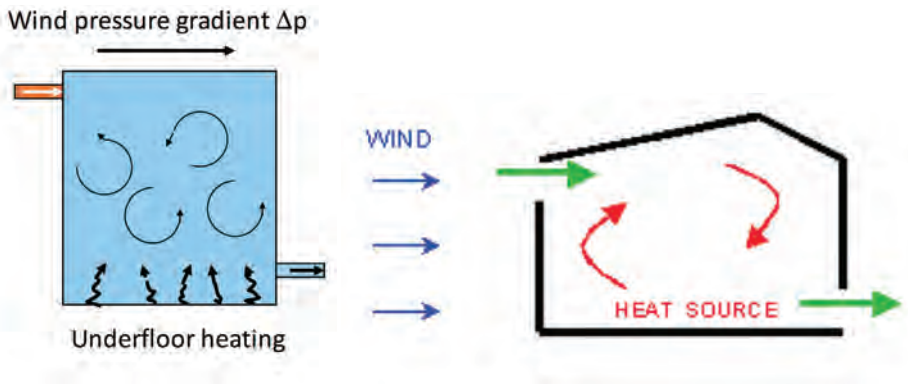

Figure 22: Flow along direction of wind

building has a high level opening upwind and a low level opening downwind with a pressure difference of $\triangle p_w$ between the two sides of the building.
For the case illustrated in 22, with the wind blowing along the direction of flow through the upper opening, the pressure at the top opening drop from $\triangle p_w$ to $\triangle p_w - \triangle p$ leading to a volume flux given by

$$Q_{top} = cA\left(\frac{\triangle p}{\rho}\right)^{\frac{1}{2}}. \tag{51}$$

At the lower opening, the pressure drop from $\triangle p_w - \triangle p - \rho g' H$ to 0 leading to a volume flux given of

$$Q_{lower} = cA\left(\frac{\triangle p_w - \triangle p}{\rho} - g' H\right)^{\frac{1}{2}}. \tag{52}$$

Matching the volume fluxes, we get

$$\triangle p = \frac{1}{2}\left(\frac{\triangle p_w}{\rho} - g' H\right). \tag{53}$$

The buoyancy flux is given by

$$B = 2^{-\frac{1}{2}} cAg'\left(\frac{\triangle p_w}{\rho} - g' H\right)^{\frac{1}{2}}. \tag{54}$$

Similarly, for flow against wind (as in Fig 23), the corresponding heating rate is given by

$$B = 2^{-\frac{1}{2}} cAg'\left(g' H - \frac{\triangle p_w}{\rho}\right)^{\frac{1}{2}}. \tag{55}$$

The above relations for B are plotted in Fig 24 (with heat flux used as a proxy for buoyancy flux on the x-axis) . The corresponding time-dependent evolution for the buoyancy within the building each case is given by

$$\begin{aligned} V\frac{dg'}{dt} &= B - 2^{-\frac{1}{2}} cAg'\left(g' H - \frac{\triangle p_w}{\rho}\right)^{\frac{1}{2}} \text{ if } g' H > \frac{\triangle p_w}{\rho} \\ V\frac{dg'}{dt} &= B - 2^{-\frac{1}{2}} cAg'\left(\frac{\triangle p_w}{\rho} - g' H\right)^{\frac{1}{2}} \text{ if } g' H > \frac{\triangle p_w}{\rho} \end{aligned} \tag{56}$$

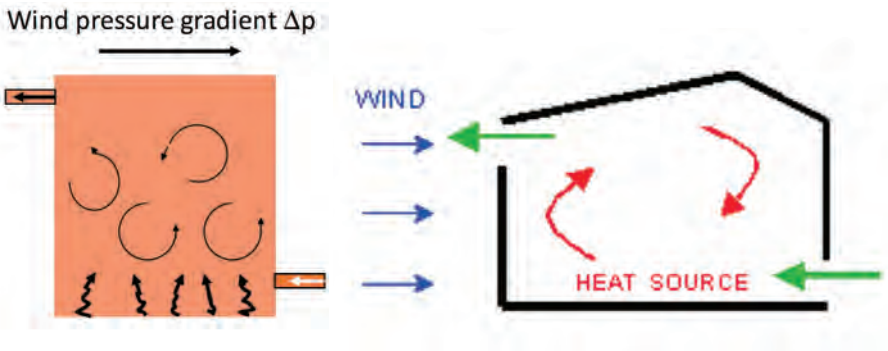

Figure 23: Flow against direction of wind

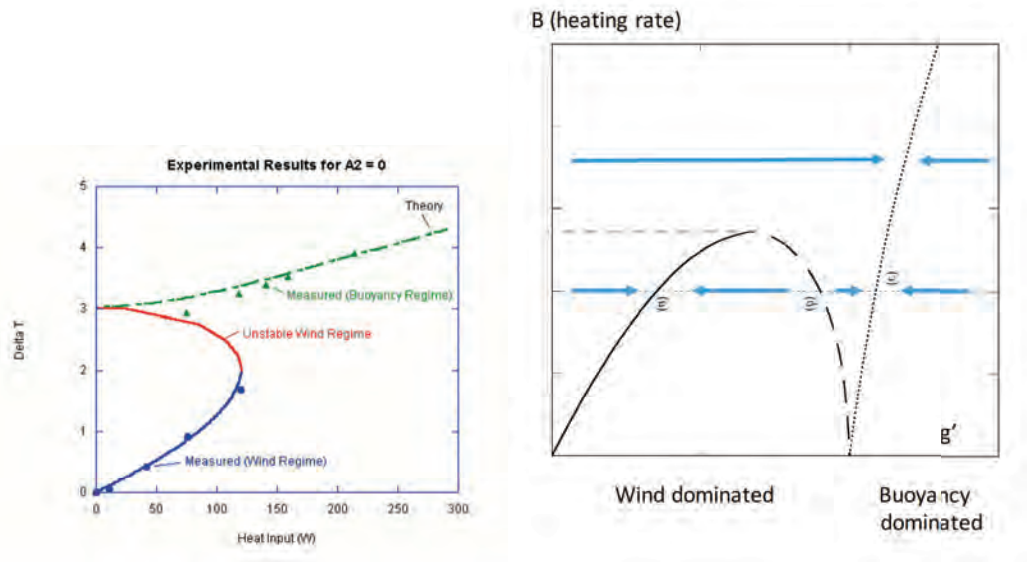

Figure 24: Illustration of the competition between buoyancy and wind, with the wind dominated and buoyancy dominated flow regimes (see 3) given by . The measured values are from a series of experiments presented in [5].

References

[1] D. J. Bower, C. P. Caulfield, S. D. Fitzgerald, and A. W. Woods, *Transient ventilation dynamics following a change in strength of a point source of heat*, Journal of Fluid Mechanics, 614 (2008), pp. 15–37.

[2] T. Chenvidyakarn and A. Woods, *Stratification and oscillations produced by pre-cooling during transient natural ventilation*, Building and Environment, 42 (2007), pp. 99 – 112.

[3] C. GLADSTONE and A. W. WOODS, *On buoyancy-driven natural ventilation of a room with a heated floor*, Journal of Fluid Mechanics, 441 (2001), p. 293314.

[4] P. F. Linden, G. F. Laneserff, and D. A. Smeed, *Emptying Filling Boxes - the Fluid-Mechanics of Natural Ventilation*, Journal of Fluid Mechanics, 212 (1990), pp. 309–335.

[5] B. LISHMAN and A. W. WOODS, *The control of naturally ventilated buildings subject to wind and buoyancy*, Journal of Fluid Mechanics, 557 (2006), p. 451471.

[6] D. D. J. A. Van Sommeren, C. P. Caulfield, and A. W. Woods, *Turbulent buoyant convection from a maintained source of buoyancy in a narrow vertical tank*, Journal of Fluid Mechanics, 701 (2012), pp. 278–303.

Lecture 5
Inertial Gravity Currents: Ash Flows and Turbidities

Notes by Neeraja Bhamidipati and Laura Cope

June 22, 2018

1 Transient Natural Ventilation of a Space with Distributed Heat Source

Transient flows in naturally ventilated spaces occur when the space adjusts from one temperature to another. We consider the problem of a space with both high-level and low-level openings for natural ventilation, where the space is heated from below by a uniformly distributed source of heat. Depending on the difference between the initial and final temperature of the room and the difference between the internal and external temperatures, three regimes of ventilation are possible (figure 1).

Regime 1 corresponds to a well-mixed interior which is a result of the interior temperature lying between the equilibrium temperature of the room and the ambient temperature. This is shown experimentally in figure 2. In this experiment, the space was heated using a uniformly distributed heat source at the bottom of the tank, and the interior fluid was dyed red. The interior fluid is assumed to be supplied with a buoyancy flux B and this leads to the generation of buoyancy g' of the fluid inside the space. This buoyancy produces a pressure difference between a vertical line inside and outside the space of magnitude $\rho_o g' H$, such that at the base of the space the pressure inside the space is lower than that outside, by an amount Δp, while the pressure at the top of the space is greater than that outside by an amount $\rho_o g' H - \Delta p$. The pressure change across each of the openings drives a flow through that opening, given by the relation $Q = cA_o(\Delta\rho/p)^{1/2}$ where A_o is the area of the opening, as described earlier. Since the flow into the base of the space matches the flow out of the top of the space, it follows that if the openings have areas A_T and A_B and loss coefficients c_T and c_B at the top and base of the space, then the condition that the flow through the two openings Q_1 and Q_2 are the same leads to the relation for the flow given by

$$Q = Q_1 + Q_2 = \frac{c_T A_T c_B A_B (g' H)^{1/2}}{(c_T^2 A_T^2 + c_B^2 A_B^2)} \tag{1}$$

and we can define an effective area A_v and loss coefficient c for the combined openings so that $Q = cA_v(g'H)^{1/2}$. If the system is in steady state, then the buoyancy flux supplied through the base of the space, B, matches the buoyancy flux which is vented from the space, $g'Q$, and so

$$B = cA_v H^{1/2} g'^{3/2} \tag{2}$$

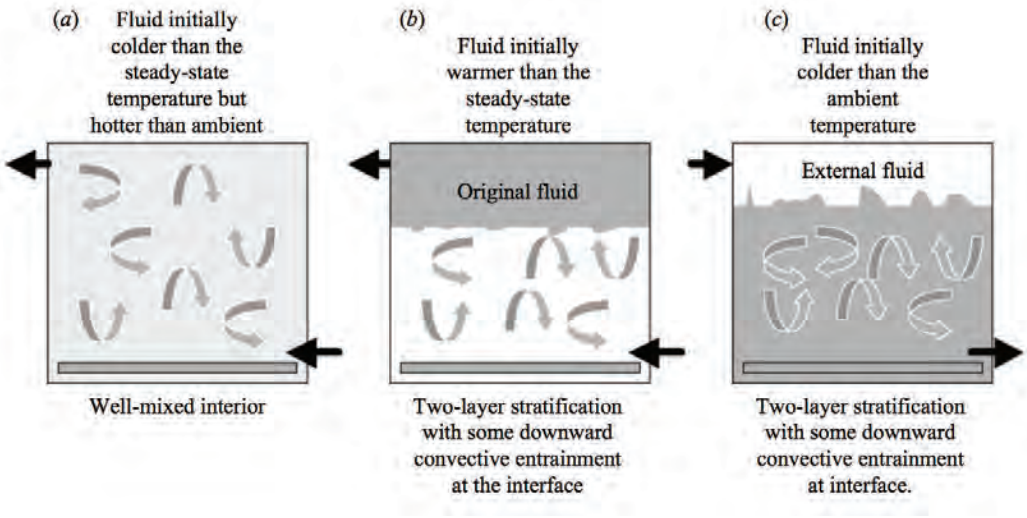

Figure 1: Schematic diagram of a room with heating at the base and vents at the top and bottom for ventilation. The three regimes correspond to (a) well-mixed upflow ventilation, (b) stratified upflow ventilation, and (c) stratified downflow ventilation. (Fitzgerald and Woods, 2007)

which leads to the prediction that in equilibrium the buoyancy is given by

$$g'_e = \left(\frac{B}{cA_v H^{1/2}} \right)^{2/3} \tag{3}$$

The data from the thermocouples in the tank (see figure 2) show that the temperature in the tank is roughly uniform, and the small fluctuations correspond to the temperature difference arising due to turbulent plumes going past the thermocouples which convect heat within the tank (figure 2(a)). The tank remains well-mixed due to the mixing caused by convection. Figure 2(c) shows a good agreement of model with experimental data.

If the buoyancy flux is changed then the system ceases to be in equilibrium. An increase in buoyancy flux to value $B(1+\lambda)$ will tend to increase the buoyancy of the overlying fluid, and so we expect that the system remains well mixed as it adjusts to the new equilibrium. The rate of change of buoyancy will then be given by the time dependent conservation of buoyancy

$$V\frac{\mathrm{d}g'}{\mathrm{d}t} = -g'Q + B(1+\lambda) \tag{4}$$

where V is the volume of the space, and $-g'Q$ is the loss of buoyancy associated with the outflow. By scaling the buoyancy with respect to the original equilibrium value, g'_e, so that $\hat{g} = g'/g'_e$, and the time with respect to the time scale Vg'_e/B, so that $s = tB/Vg'_e$, then equation (4) takes on the dimensionless form

$$\frac{\mathrm{d}\hat{g}}{\mathrm{d}s} = 1 + \lambda - (\hat{g})^{3/2} \tag{5}$$

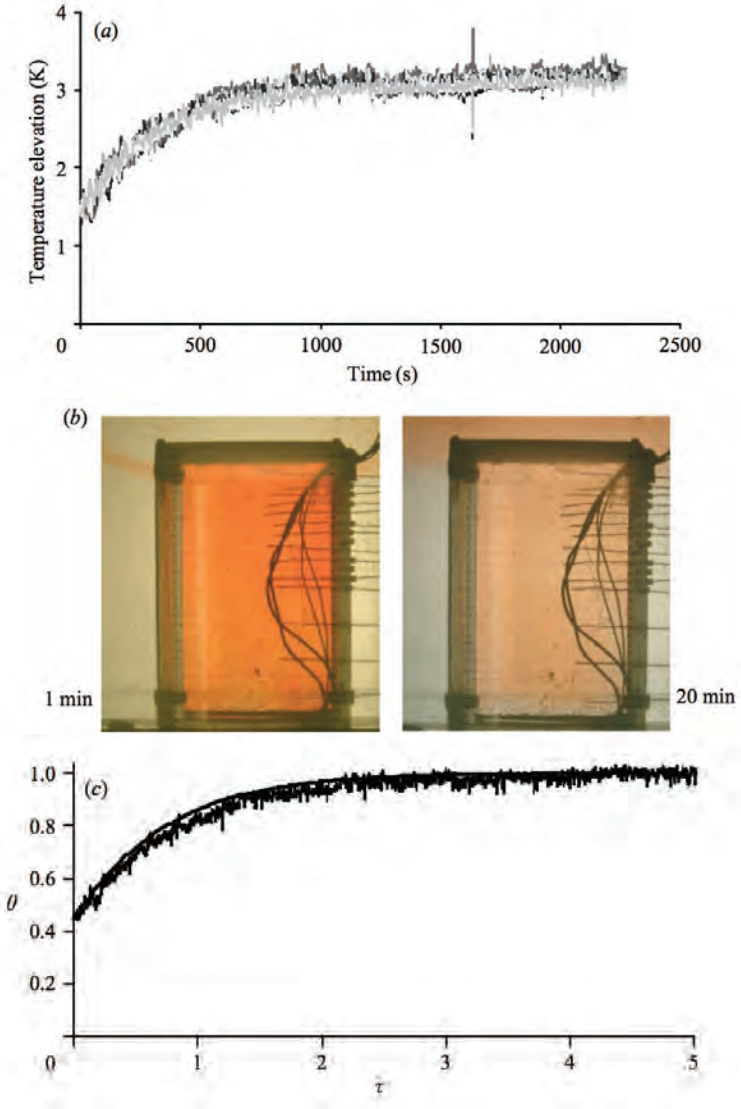

Figure 2: (a) Measured temperatures as a function of time in the tank heated by a distributed source. Different symbols represent signals from each of the thermocouples. (b) Photographs taken 1 and 20 minutess after commencement of ventilation showing that the room remained well-mixed throughout the duration of the experiment. (c) Dimensionless temperature of the interior derived from experimental data (thin noisy line) compared with the theoretical prediction (solid line). (Fitzgerald and Woods, 2007)

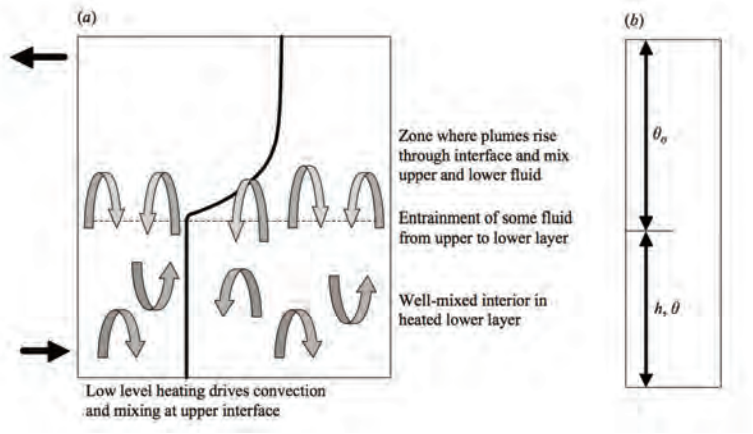

Figure 3: (a) Schematic of the process of mixing and penetrative convection at the interface between the lower heated layer and the hot upper layer, as observed in the experiments. (b) Illustration of the definition of the temperature and depth variables in the model. (Fitzgerald and Woods, 2007)

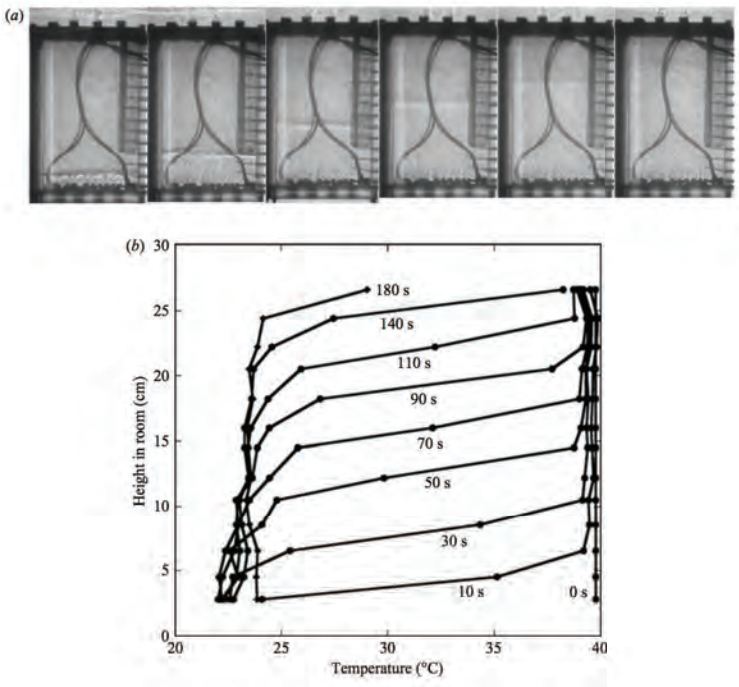

Figure 4: (a) Photographs taken at a series of times after commencement of the experiment, indicating that the upper layer of fluid originally in place is displaced vertically upwards during the transient evolution of the room, creating a two-layer stratification. (b) The vertical temperature profile in the experimental tank at a series of times. A clear thermal front is seen to rise through the room. (Fitzgerald and Woods, 2007)

This illustrates how the buoyancy gradually adjusts to the new equilibrium value

$$\hat{g} = (1+\lambda)^{2/3} \tag{6}$$

In contrast to the above relatively simple case, if the buoyancy flux at the plate is decreased to value $B(1\lambda) > 0$ then the buoyancy in the space will decrease to a smaller value. This decrease in the buoyancy leads to a smaller equilibrium ventilation flow rate. On reducing the buoyancy flux, the ventilation rate will initially be higher than the new equilibrium value, and so as new fluid enters the base of the space, its buoyancy will remain smaller than the original fluid in the space. It will therefore form a new layer and as the flow continues, this new lower layer will deepen, while the original fluid will vent from the space. To model this situation, we introduce a new lower layer, of depth h_n and buoyancy g'_n and we follow the evolution of this layer in time. The new layer deepens at a rate proportional to the ventilation flow

$$A\frac{\mathrm{d}h_n}{\mathrm{d}t} = cA_v(g'_n h_n + g'_e(H-h_n))^{1/2} \tag{7}$$

while the buoyancy of this layer evolves according to the buoyancy flux from the base of the space

$$A\frac{\mathrm{d}g'_n h_n}{\mathrm{d}t} = B(1-\lambda) \tag{8}$$

Meanwhile the upper layer of the original fluid gradually vents from the space while its buoyancy remains approximately constant. At early times, equations (7) and (8) imply that $g' \sim g'_e(1-\lambda)$ showing that the buoyancy of the new lower layer is less than the original layer, and hence the system is stably stratified. Similarly, this model suggests that $\lambda < 1$ corresponding to a decrease in the buoyancy, and therefore the lower layer would be hotter than the upper layer, leading to overturn and mixing.

Regime 2 corresponds to this case where the interior is initially warmer than the equilibrium temperature. The inflowing air from below forms a well-mixed lower layer which is colder than the temperature of the space, leading to a two-layer stratification of the space (figure 3(a)). The upflow of the cold air in the lower layer displaces the warm air upwards and out of the space. The temperature in the lower layer gradually tends to equilibrium temperature. In an experiment, the interface between the two layers can be tracked using a shadowgraph. The photographs in figure 4(a) show a well-defined front rising through the tank, and figure 4(b) shows the temperature profile within the tank. The thermal profiles show a layer of finite depth ($O(5\,\mathrm{cm})$) where the temperature gradually varies between the hot and cold layers. This is due to the mixing at the interface by the plumes rising up through the tank and entrainment from the upper layer to the lower layer.

In order to accurately model this regime, it is important to consider the effects of penetrative convection occuring at the interface between the two layers. The entrainment of the fluid from the upper layer into the lower layer leads to a slightly warmer lower layer and also causes the interface height to grow faster in time. The energy to add this potential energy comes from the kinetic energy of the convective plumes rising up through the lower layer from the heat source at the bottom of the space. This energy is a function of the

buoyancy flux per unit area, Q, of the source and the height of the lower layer, h_i. The height of the lower layer grows according to

$$\rho C_p(T_u - T_l)\frac{\mathrm{d}h_i}{\mathrm{d}t} = kQ \tag{9}$$

where T_u and T_l are the temperatures of the upper and lower layers, and C_p is the specific heat capacity of air. k is the rate of entrainment of buoyant fluid from the upper layer into the lower layer.

Regime 3 occurs when the room is initially cooler than the exterior, then on opening the vents, the original air is displaced downwards and a layer of warm ambient air deepens from above. As this lower layer drains and becomes gradually thinner, it is eventually heated to the ambient temperature by the heat source below. Meanwhile, the convective plumes rising from the heat source at the base of the room, and through the lower layer of cold air are typically able to entrain some of the overlying layer of warm air, in a somewhat analogous fashion to the penetrative convection described for Regime 3. Eventually, as the lower layer approaches the same temperature as the exterior, the air within the room becomes well-mixed. The height of the lower layer, in this scenario, reduces because of ventilation from the top and into the room, but as the buoyancy of the lower layer increases towards that of the upper layer and overturn occurs, the flow direction reverses and the system adjusts to regime 1 above.

2 Gravity Currents

Figure 5: A dense ash flow on Mount St. Helens.

Turbulent gravity currents are produced when a finite volume of dense fluid is rapidly released from a source above a horizontal boundary into an environment of lower density. The dense fluid propagates horizontally under gravity along the lower boundary of the flow domain by displacing the original fluid. Gravity currents are important in many geophysical and environmental flows, with applications in the spread of dense gas following release from

Figure 6: Pyroclastic density current on 8 January 2010 at Soufriere Hills Volcano, Montserrat.

a vessel and volcanic ash flows, and also in understanding the dynamics of cold fronts, (see figures 5 and 6). In the context of the above flows, the propagation speed and the density structure of the flow as it spreads from the source are of considerable interest.

During short lived volcanic eruptions, dilute turbulent pyroclastic density currents are often observed to spread laterally from a collapsing fountain. These flows entrain and heat air while also sedimenting particles. Both processes lead to a reduction in the bulk density and since these flows often become vertically stratified, the upper part of the flow may then exhibit a reversal in buoyancy and lift off. In order to assess the mass of air required to reduce the buoyancy of the flow and generate lift off, we need to understand the mixing into these currents.

The time for a volcanic explosion to generate a small cloud of ash particles, which rises several hundred metres above the vent followed by column collapse and generation of a dilute pyroclastic density current, will be between 1 and 10 seconds. For thermal equilibrium, the thermal diffusion time should be smaller than the timescale of the initial collapse, requiring ash particles of radius smaller than about 1 mm. We assume that the density of the ash and air mixture is given by the relation

$$\rho = \left(\frac{n}{\rho_g} + \frac{1-n}{\rho_s} \right)^{-1}, \tag{10}$$

where n is the gas mass fraction in the flow, ρ_s is the density of the ash, and ρ_g is the density of the gas in the flow ($\rho_g = P/RT$). Assuming that we reach thermal equilibrium during the initial mixing phase, conservation of thermal energy requires that

$$n\rho_g C_{pg}(T - T_a) + (1-n)\rho_s C_{ps}(T - T_a) = (1-n)\rho_s C_{ps}(T_o - T_a). \tag{11}$$

As the mass of air mixed into the flow increases, the density of the mixture decreases; this is illustrated schematically in figure 7. Buoyancy is generated once sufficient air has

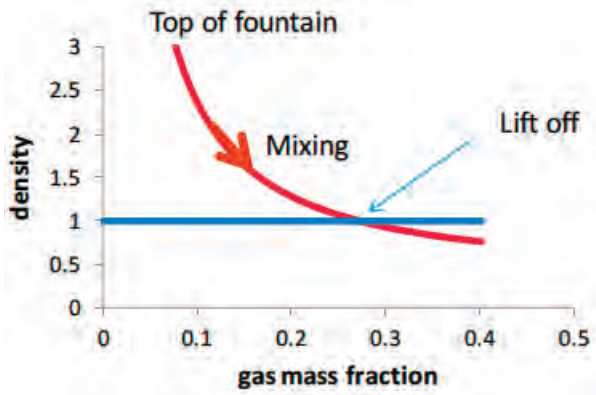

Figure 7: Schematic showing the density of a dilute pyroclastic density current propagating in valley. When the density of the mixture becomes equal to that of the surrounding air, the flow becomes buoyant.

been mixed in, causing lift-off.

Theoretical and experimental studies of gravity currents have revealed that their evolution can be described by two distinct phases. We shall look at each in turn, by considering the release of a finite volume of fluid of uniform density from behind a lock gate.

2.1 Adjustment from a homogeneous to a stratified flow

In the initial adjustment phase of the flow, we find that the leading part of the head of the gravity current is composed of original lock gate fluid and has a nearly constant depth, so that it advances with a constant speed. During this phase, a circulation develops as fluid at the front of the current mixes with some of the ambient fluid displaced by the current. The mixed fluid rises over the head, and supplies a dilute wake behind the flow.

2.1.1 Evolution of the reduced gravity, depth and position of the current

Figure 8 illustrates the time evolution of a gravity current where false-colour images correspond to the concentration of the fluid in the tank at 10 times after release of the lock gate. The current initially adjusts after removing the lock gate and as it advances through a region up to 7 times the original lock gate length, it has a nearly constant density head region, followed by a growing tail, in which the density decreases with distance behind the front and with height above the base of the current. As the current continues to lay down a dilute tail, the region of near constant density at the front of the flow becomes progressively smaller, and eventually dissipates as it advances beyond the point 7 lock gates. As the flow continues, the buoyancy everywhere in the flow becomes progressively smaller with time, with the buoyancy increasing from the lock gate towards the head.

To help visualise the changes in the flow as it advances along the tank, in figure 9 we present a false-colour image of the vertically averaged current concentration as a function of position and time. This image illustrates how the speed of the head is constant up to a distance of 7 lock gates, and, in this near lock gate region, the fluid directly behind

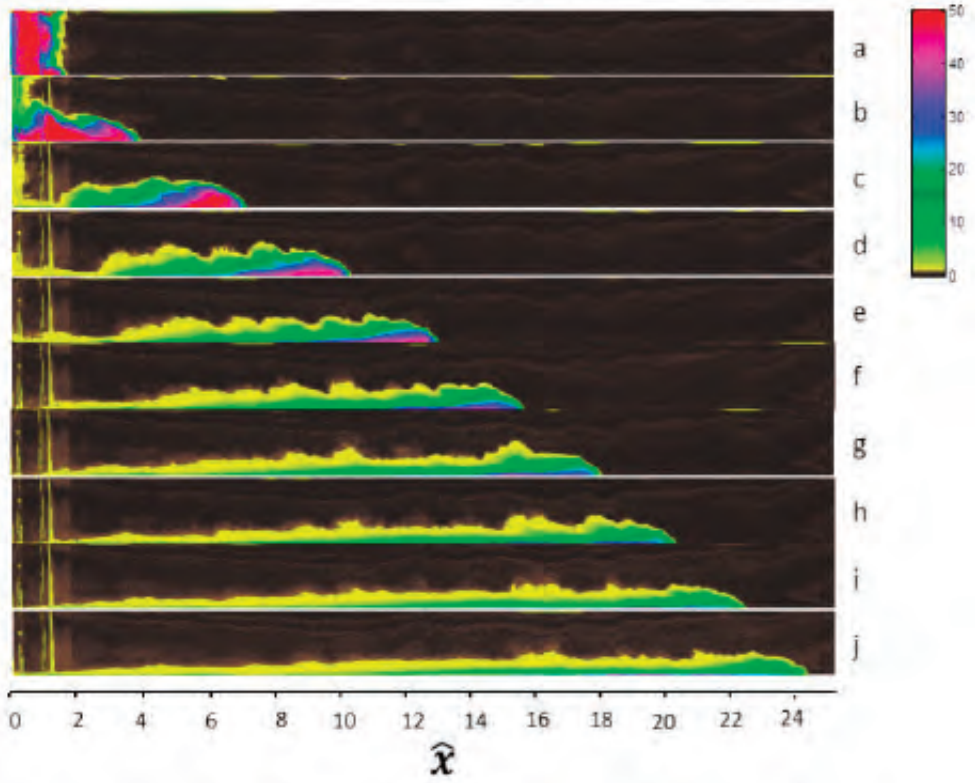

Figure 8: Photographs of a saline gravity current illustrating the evolution of the salinity. Images are taken at equal dimensionless time intervals in each case. The x-axis scale shows the position in the current as a function of the number of lock lengths beyond the lock gate. The colour scale denotes concentration of salt. (Sher and Woods, 2015)

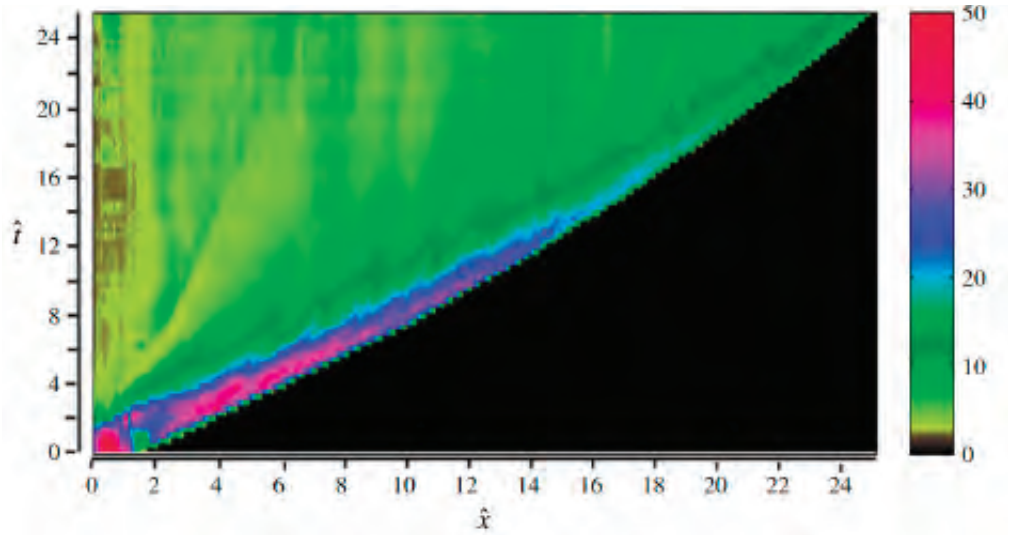

Figure 9: Evolution of the depth-averaged concentration of the current as a function of position and time. The horizontal axis represents position ahead of the lock and the vertical axis is time. The colours represent the depth-averaged salt concentration of the gravity current. The figure illustrates how the concentration varies with position and with time in the current and shows that the head of the flow becomes progressively more dilute, with the initial buoyancy in the flow being dispersed from the lock gate up to the head of the flow. (Sher and Woods, 2015)

the front of the current has reduced gravity equal to that of the fluid behind the lock gate. However, downstream of this point, the speed and the reduced gravity of the head gradually decrease with distance. The figure also shows how an ever-growing tail develops in which the concentration gradually increases from the lock gate towards the head of the current. Finally, the figure shows how, at a given position in the tank, behind the head, the concentration gradually decreases with time.

Figure 10 shows the position of the front of a variety of gravity currents as a function of time. The data collapse to a universal curve, labelled front, independent of aspect ratio, buoyancy and current volume. To illustrate how the size of the region of fluid behind the head whose reduced gravity equals that of the fluid behind the lock gate evolves in time, the position of the rear of this region has been plotted. Whilst these measurements exhibit some scatter, they also collapse onto a line.

2.1.2 Mixing at the head of the current

In order to build up understanding of how the mixing occurs, it is possible to conduct a series of experiments in which we inject and then track a small volume of dye in both (i) the current and (ii) the ambient fluid.

Figure 11 illustrates a gravity current of originally clear fluid advancing into a yellow ambient fluid. In this experiment, a pulse of blue dye was injected into the current, at the position 2.4 lock lengths when the front of the current was at position 2.6 lock lengths.

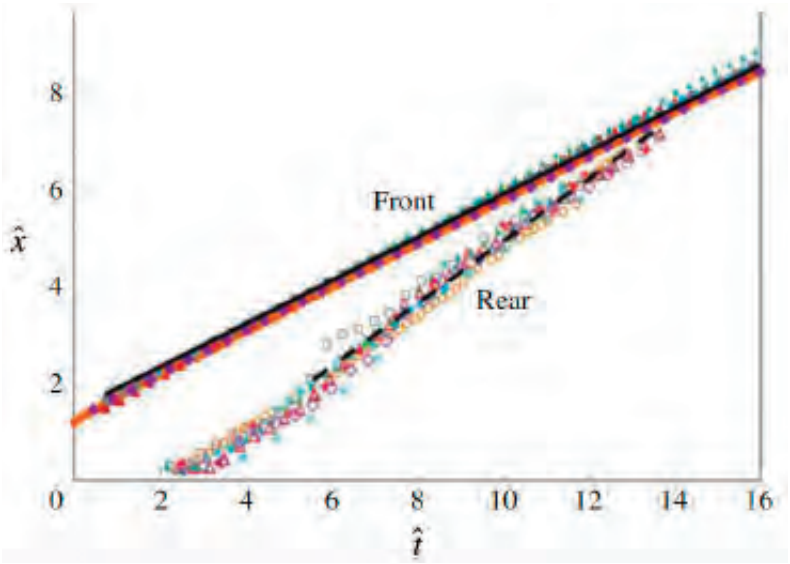

Figure 10: Diagram illustrating the position of the front and rear of the head of the current (whose reduced gravity equals that of the fluid behind the lock gate), as a function of time. (Sher and Woods, 2015)

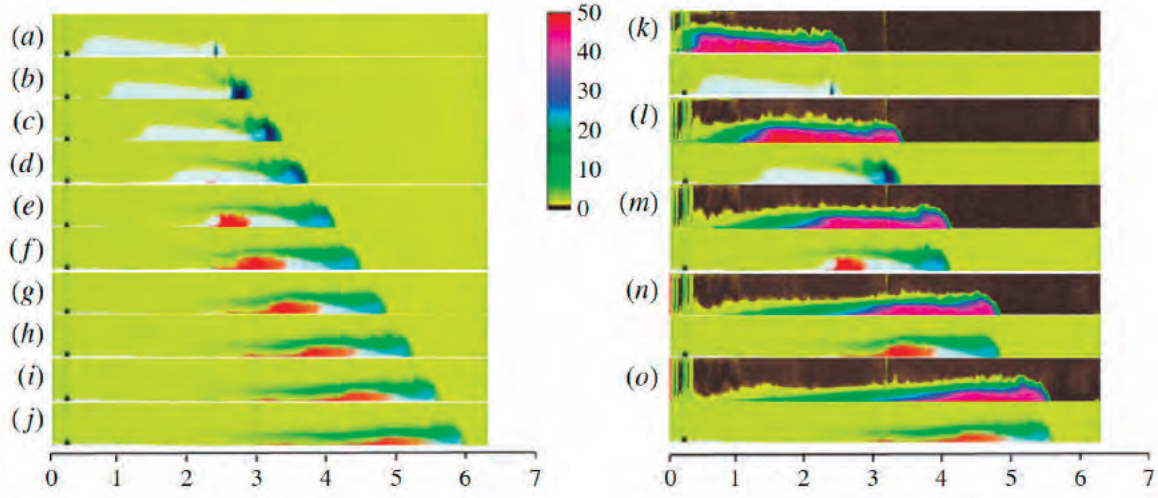

Figure 11: (aj) Series of photographs illustrating the migration of a point release of blue dye and red dye into a clear gravity current propagating through a yellow environment. (ko) Series of false-colour images of the concentration measured in an experiment with identical initial conditions, at five different times. (Sher and Woods, 2015)

Later a pulse of red dye was injected at the point 2.3 lock lengths when the front was at position 3.7 lock lengths. Panels (aj), taken at equal dimensionless time intervals, illustrate how the blue and the red dye pulses migrate with time. In panels (ko), we illustrate the density structure in an equivalent current, at five times, as obtained from a second identical experiment. As the flow continues along the flume, the blue dyed fluid catches up with the nose of the current. The front region of the current becomes blue and feeds a rising stream of dyed fluid which passes up over the top of the continuing gravity current. This forms a streak of blue fluid which propagates backwards relative to the nose of the continuing current. As the current advances the intensity of the blue dye decreases. Also, the red dye, which is initially injected in fluid further upstream in the current, progressively catches up with the front of the current.

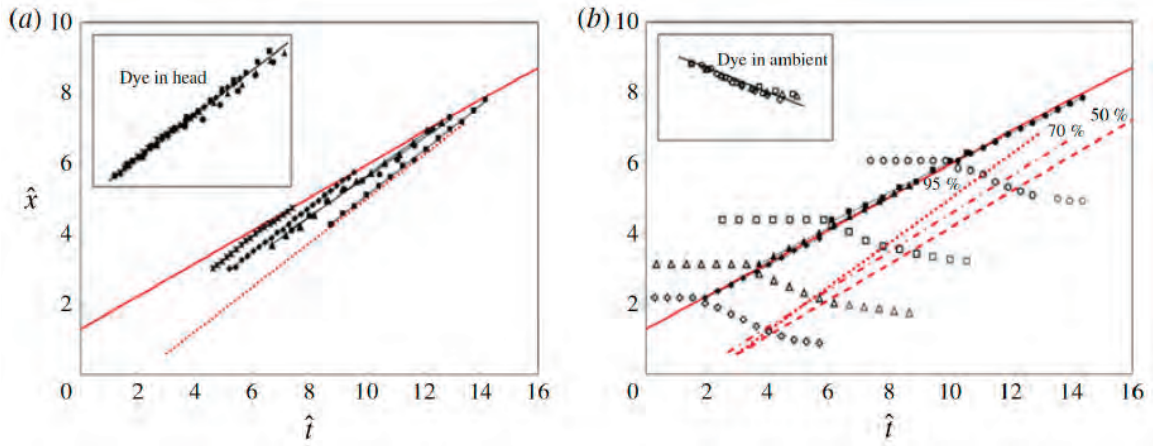

Figure 12: Characteristic diagram in which (a) the trajectory of the leading edge of a series of parcels of dye injected within several of the experimental currents are followed. In this panel, the solid and dotted red lines correspond, respectively, to the front and back of the head of the gravity current. (b) The trajectories followed by a series of parcels of dye which are injected into the ambient fluid ahead of the current. The dye begins to move backwards as the front of the current arrives, and it continues to move backwards until the rear of the head passes by. The dye then slows down substantially, as the stratified tail of the current passes by. (Sher and Woods, 2015)

In figure 12(a), the trajectories of the leading edge of a series of dye pulses injected into the currents which formed during different experiments have been plotted. It is seen that, to a reasonable approximation, the dye streaks from the different experiments advance with a uniform speed, approximately 1.35 ± 0.05 times the speed of the front of the current.

We now look at the motion of the ambient fluid as the gravity current passes by, since this provides a complementary perspective on the mixing in the head region of the flow. In figure 13 we illustrate the evolution of three regions of dyed ambient fluid originally located ahead of the current. As the undyed gravity current reaches each of the patches of dyed ambient fluid, it is seen that the ambient fluid rises over the current and mixes with some of the fluid at the front of the current. Panels (ac) show the mixing of the blue dye. Owing to the stratification in the wake, there is a weak shear flow which develops, and causes the

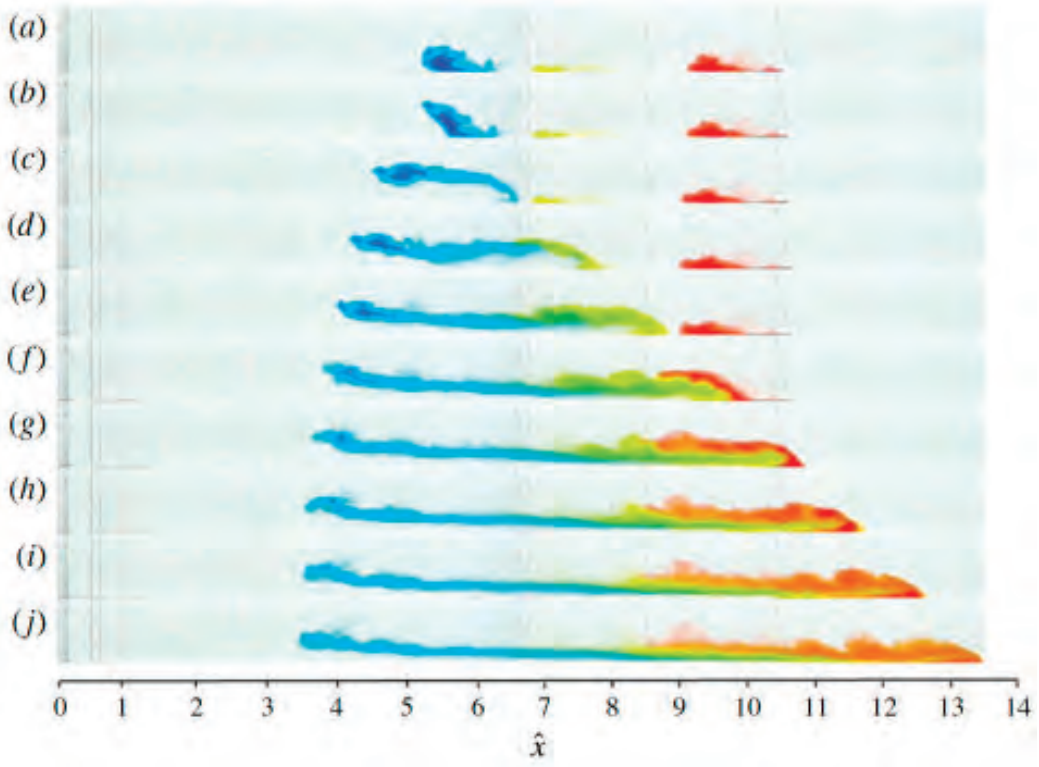

Figure 13: Illustration of the motion of three parcels of dye initially injected upstream of the gravity current. The fluid in the gravity current initially has no dye. (Sher and Woods, 2015)

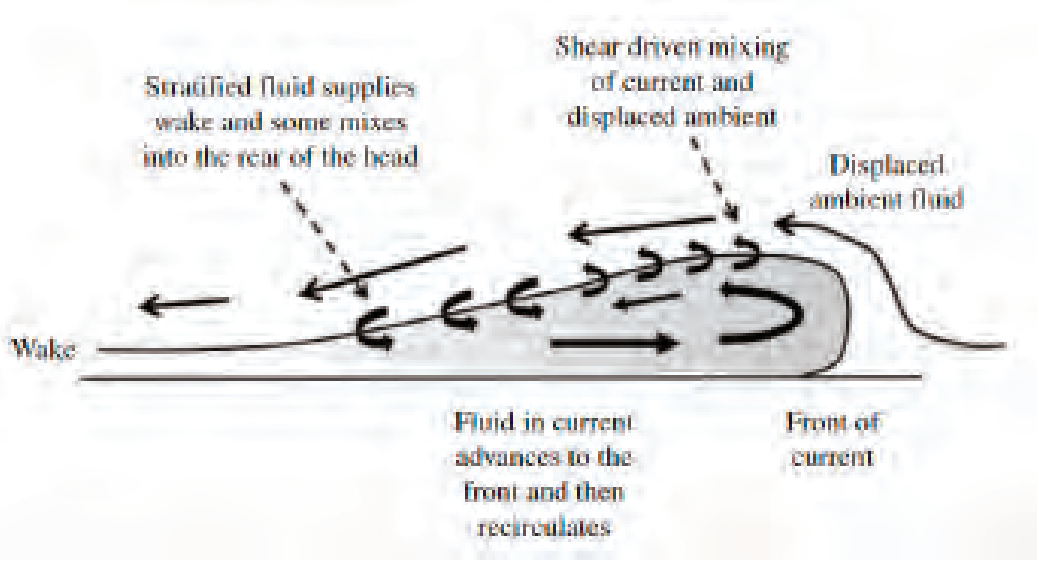

Figure 14: Illustration of the motion of three parcels of dye initially injected upstream of the gravity current. The fluid in the gravity current initially has no dye. (Sher and Woods, 2015)

blue dyed region to shear out in the wake. Very little blue fluid appears to enter the head region. Panels (d,e) show the evolution of a patch of yellow dye. After rising over the top of the current, some of this yellow dyed fluid is mixed back into the head, which appears to include an anticlockwise vortex, and the remainder of the yellow fluid is dispersed into the wake. Panels (eg) illustrate the mixing associated with a red patch of dye. This mixes in a similar manner to the yellow dye, leading to further dilution of the head and growth of the wake immediately behind the head.

For comparison with the motion of the fluid originally in the current (figure 12(a)), in figure 12(b) we show the trajectory of a series of parcels of dye injected into the ambient fluid initially ahead of the current. The leading edge of this dye appears to move backwards as the head passes. In the main figure, for comparison, we also show the position of the front of the current (solid red line) and the rear. Figure 14 summarises the flow patterns discussed during this initial mixing regime.

2.1.3 Entrainment coefficient during the mixing of the original lock fluid

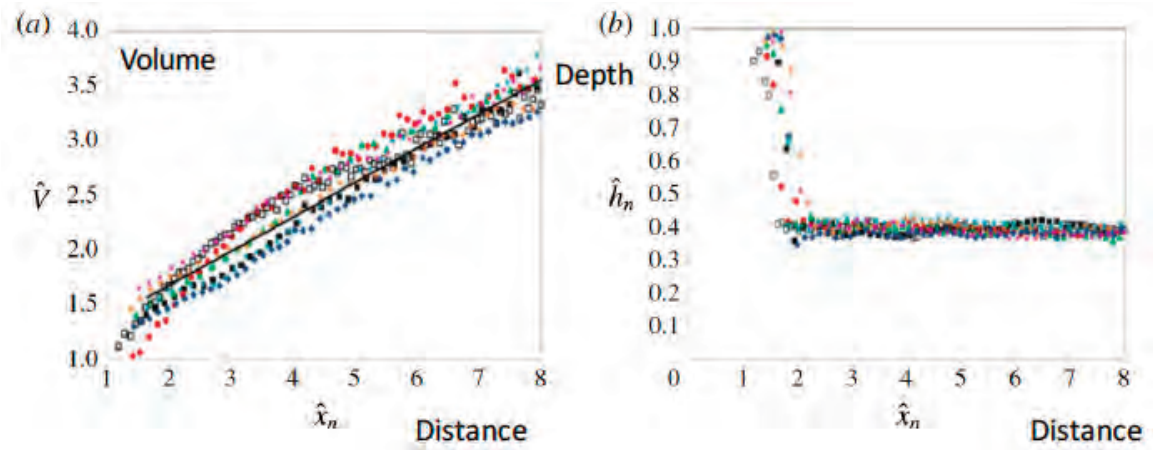

Figure 15: Variation of (a) the volume and (b) the height of the current head as a function of distance travelled. As the flow advances, there is a near linear increase in volume while the depth of the flow approaches a near constant value. (Sher and Woods, 2015)

How much mixing occurs in the head region during this initial phase of the flow? Measurements from experiments of the instantaneous volume of the gravity current and the depth just behind the front as a function of the distance travelled by the nose of the current are plotted in figure 15. While the depth remains constant in time, we see that the volume increases linearly with time, or distance travelled. Considering entrainment into the head of the current,

$$\frac{dV}{dx} = \alpha h \tag{12}$$

where it can be inferred that $\alpha = 0.65 \pm 0.1$. Once all of the original lock fluid has been mixed through the head, does a self-similar regime develop in the second phase?

2.2 The long-time self-similar regime

2.2.1 Experimental measurements

Having studied a gravity current during the initial mixing phase until the point at which it becomes fully stratified, we now consider its evolution during the second phase. From dimensional arguments, the position of the flow front should follow the scaling relation

$$x_n(t) \sim B^{1/3}(t - t_0)^{2/3} \tag{13}$$

where t_0 is an adjustment zone used to accommodate any difference in the rate of dilution of the flow during the initial mixing phase. Figure 16(a) plots the ratio $x_n(t)/[B^{1/3}(t+t_0)^{2/3}]$ against time for a series of experiments, where we see that after an initial transient period, this ratio approaches the constant value of 1.6. For these same experients, figure 16(c) shows the depth of the head of the current against time. The mean depth appears to be approximately constant with time, and we observe that $h_n(t) \sim 0.4H$ where H is the initial depth of fluid behind the lock gate.

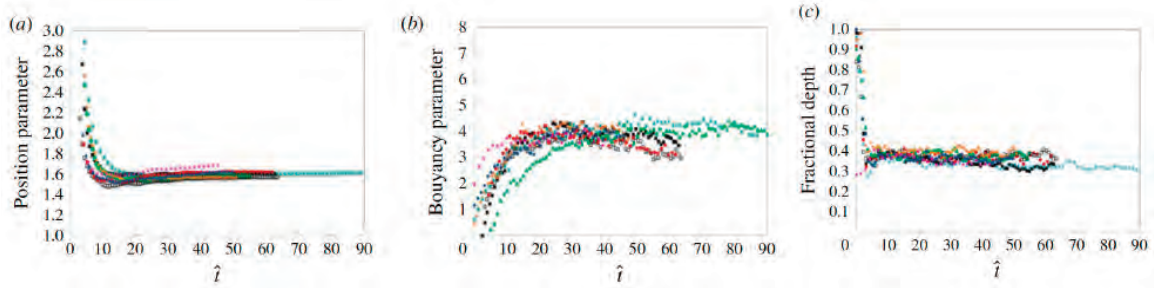

Figure 16: Data from experiments showing the time evolution of (a) the position of the nose of the current $x_n(t)/[B^{1/3}(t+t_0)^{2/3}]$, (b) $\overline{g}'_n H(t+t_0)^{2/3}B^{-2/3}$ and (c) the depth of the current behind the flow. (Sher and Woods, 2015)

If we assume that the depth of fluid in the head of the current remains approximately constant in time, then by conservation of buoyancy we would expect the reduced gravity to decrease in proportion to the horizontal extent of the flow. We expect the vertically averaged reduced gravity at the head of the flow to follow a relation of the form

$$\overline{g}'_n \sim \frac{B^{2/3}}{H(t+t_0)^{2/3}}. \tag{14}$$

Figure 16(b) plots $\overline{g}'_n H(t+t_0)^{2/3}B^{-2/3}$ against time; this approaches the value of 4 for long times.

Averaged values of the three quantities plotted in figures 16(a-c) across multiple experiments (and different times) are plotted in figure 17. In addition, averaged values of the Froude number Fr, defined by $dx_n/dt = Fr(\overline{g}'_n h_n)^{1/2}$, are plotted for the same experiments. We see that $Fr \to 0.95$.

Figure 18 shows data from a series of experiments. In figure 18(a), the vertical integral of the reduced gravity, normalised by the length of the current, is plotted while in figure

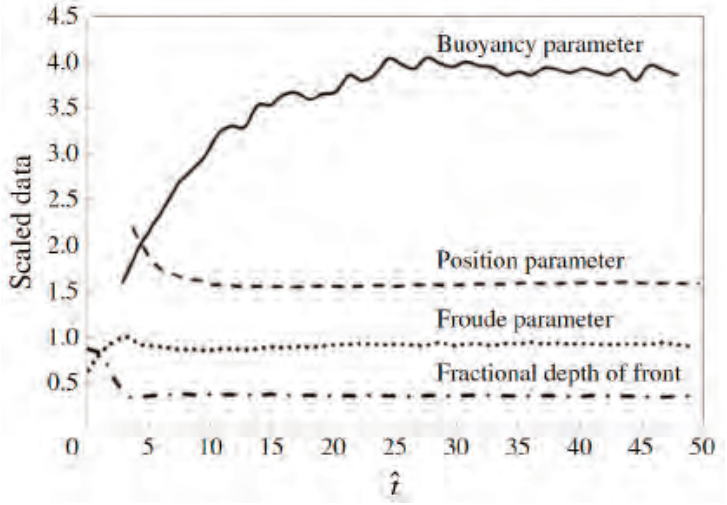

Figure 17: Averages of the data from the experiments plotted in figure 16 along with the Froude number Fr. (Sher and Woods, 2015)

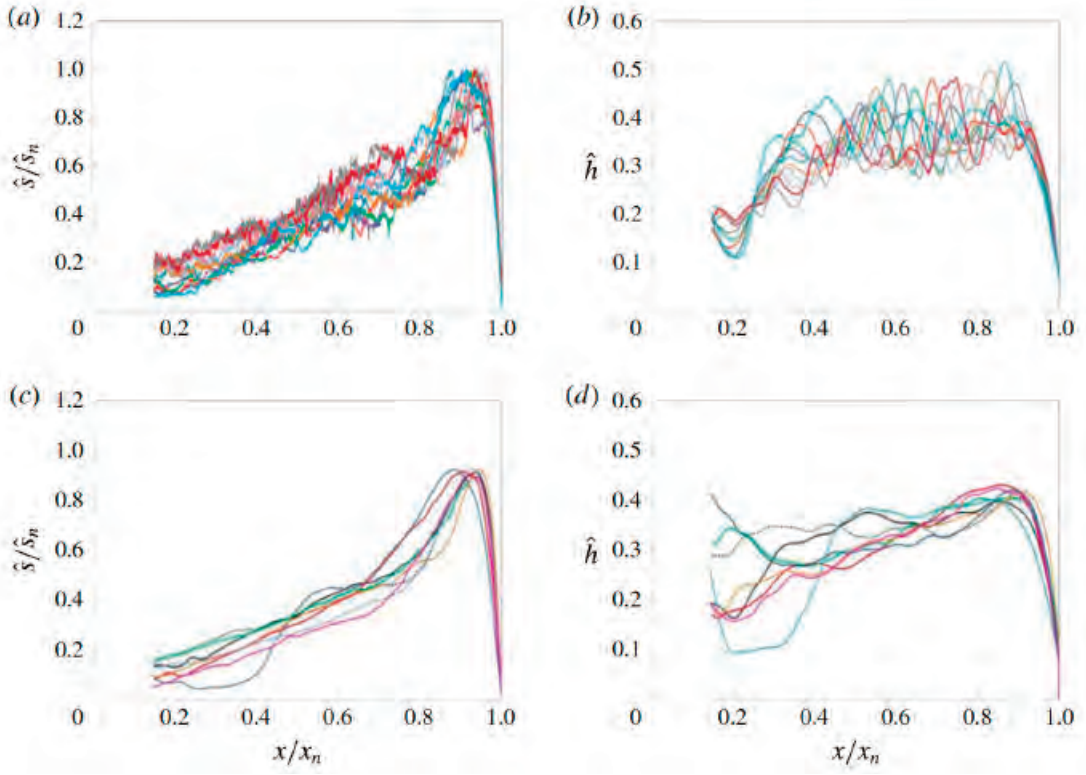

Figure 18: Variation of (a) the reduced gravity and (b) the depth of the current, normalised by the length of the current, for a series of experiments. (c) and (d) show the respective time-averaged structures. (Sher and Woods, 2015)

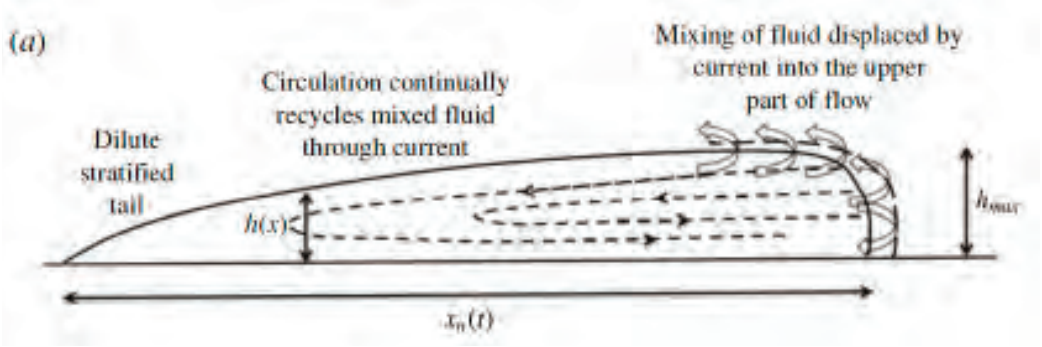

Figure 19: Schematic of the along-current flow and circulation. In this regime, self-similar solutions arise with the reduced gravity being carried further forwards. (Sher and Woods, 2015)

18(b), we can see the variation of the depth of the current, again normalised by the length of the current. These have been time-averaged in figures 18(c) and 18(d), respectively.

The data shown in figure 18 suggest that further downstream, as the influence of the initial conditions becomes less important and the current becomes fully stratified, then the depth and vertical integral of the buoyancy adjust to a particular profile along the length of the flow. A circulation develops, with the denser fluid in the current being supplied to the front of the current from the lower part of the flow where the speed is a maximum. This fluid, along with ambient fluid ahead of the current, rises over the top of the head, mixes and feeds the rear of the head and the tail of the flow with fluid of intermediate density (see figure 19). Since the reduced gravity of the fluid in the lower part of the flow exceeds that higher in the flow, we expect the vertical integral of the flux of reduced gravity to exceed the product of the vertically averaged velocity and the vertical integral of the reduced gravity at any point in the flow. As a result, surfaces of constant buoyancy travel faster than the mean flow speed and this may lead to the salinity being a maximum at the front of the current. Furthermore, the scalings for the evolution of the speed and buoyancy at the head of the current, combined with the details of the stratification in the flow, suggest that the flow is self-similar, with the mixing being a key part of the evolution. This motivates a simple, depth-averaged model for the gravity current in this second phase of the flow.

2.2.2 Structure of the current

Let us consider a finite mass of buoyancy, B, released from the origin, $x = 0$. We will assume that the mixing occurs in the head of the flow. The horizontal momentum equation is given by

$$\rho\frac{\partial u}{\partial t} + \rho(u \cdot \nabla)u = -\frac{\partial p}{\partial x}, \tag{15}$$

the equation for the conservation of buoyancy is given by

$$\frac{\partial g'}{\partial t} + \mathbf{u} \cdot \nabla g' = 0 \tag{16}$$

and the flow is assumed to be incompressible, $\nabla.\mathbf{u} = 0$. Integrating $\nabla.\mathbf{u} = 0$ across the depth h of the flow and using the fact that

$$\frac{\partial h}{\partial t} + u(h)\frac{\partial h}{\partial x} = vh \tag{17}$$

we find that

$$\frac{\partial h}{\partial t} + \frac{\partial h\overline{u}}{\partial x} = 0. \tag{18}$$

We will assume that the vertical pressure gradient is hydrostatic:

$$p(x, y, t) = p_0 + \int_y^h \rho_0 g' dy. \tag{19}$$

Integrating equation 15 across the depth of flow h, and using hydrostatic balance leads to the result

$$\int_0^h \rho\frac{\partial u}{\partial t}dy + \int_0^h \rho\left(u\frac{\partial u}{\partial x} + v\frac{\partial u}{\partial y}\right)dy = -\int_0^h \frac{\partial}{\partial x}\left[\int_y^h \rho g' dy\right]dy - h\frac{\partial p_0}{\partial x} \tag{20}$$

Combining this with $\nabla \cdot \mathbf{u} = 0$ and equation 17, we can express this equation in the form

$$\frac{\partial(h\overline{u})}{\partial t} + \beta\frac{\partial(h\overline{u}^2)}{\partial x} = -\gamma\frac{\partial(h^2\overline{g}')}{\partial x} - \frac{h}{\rho_0}\frac{\partial p_0}{\partial x} \tag{21}$$

Integrating equation 16 across the depth of the flow and combining this with $\nabla.\mathbf{u} = 0$ and equation 17, we find that

$$\frac{\partial(h\overline{g}')}{\partial t} + \alpha\frac{\partial(h\overline{g}'\overline{u})}{\partial x} = 0, \tag{22}$$

where, for constant coefficients α, β and γ,

$$h\overline{u} = \int_0^h u dy \quad ; \quad h\overline{g}' = \int_0^h g' dy \quad ; \quad \beta h\overline{u}^2 = \int_0^h u^2 dy \tag{23}$$

$$\alpha h\overline{g}'\overline{u} = \int_0^h ug' dy \quad ; \quad \gamma h^2\overline{g}' = \int_0^h \int_y^h g' dy. \tag{24}$$

We will seek solutions of the equations 18, 21 and 22 once the current has adjusted to a self-similar form. As an approximation, we consider the mixing to occur at the front of the flow. We shall solve these equations subject to appropriate boundary conditions at the head of the flow and the constraint that a finite mass of buoyancy, B, is released from the origin. The volume of the current is given by

$$V = \int_0^{x_n} h(x, t)dx. \tag{25}$$

Differentiating equation 25 by time and combining with equation 18 gives

$$\frac{dV}{dt} = \left(\frac{dx_n}{dt} - u_n\right)h_n. \tag{26}$$

We will define the entrainment coefficient E as the fraction of the ambient fluid displaced by the flow that is mixed into the flow. Then

$$\frac{dV}{dt} = Eh_n\frac{dx_n}{dt} \quad \text{and so} \quad u_n = (1-E)\frac{dx_n}{dt}. \tag{27}$$

We will assume that E is constant in the self-similar flow regime, to be determined experimentally. By conservation of buoyancy, we require that

$$B = \int_0^{x_n} \overline{g}'(x,t)h(x,t)dx. \tag{28}$$

For a self-similar flow, we expect that the speed at the nose of the flow is given in terms of the Froude number Fr, where

$$\frac{dx_n}{dt} = Fr(\overline{g}'_n h_n)^{1/2} \tag{29}$$

We will now seek self-similar solutions for this model. Our solutions shall take the form (ansatz):

$$h(x,t) = H\mathcal{H}(\eta) \quad ; \quad \overline{g}'(x,t) = \frac{B^{2/3}}{t^{2/3}H}\mathcal{G}(\eta) \quad ; \quad \overline{u}(x,t) = \frac{B^{1/3}}{t^{1/3}}\mathcal{U}(\eta) \tag{30}$$

where $\mathcal{H}$, $\mathcal{G}$ and $\mathcal{U}$ are shape functions, $\eta = x/x_n(t)$ and $x_n(t) = B^{1/3}t^{2/3}$. Substituting this ansatz into equations 18 and 22 reveals the pair of ordinary differential equations:

$$\left(-\frac{2\eta}{3} + \mathcal{U}\right)\frac{d\mathcal{H}}{d\eta} = -\mathcal{H}\frac{d\mathcal{U}}{d\eta} \tag{31}$$

$$-\frac{2\eta}{3}\frac{d}{d\eta}(\mathcal{G}\mathcal{H}) + \alpha\frac{d\mathcal{G}\mathcal{H}\mathcal{U}}{d\eta} = 0. \tag{32}$$

We expect that the pressure $p(x,t)$ will follow a scaling of the form $p(x,t) = \rho_0 B^{2/3}t^{-2/3}\mathcal{F}(\eta)$ where ρ_0 is a reference density. Substituting into equation 21 gives

$$-\frac{\lambda}{3}\mathcal{U}\mathcal{H} - \frac{2\lambda\eta}{3}\frac{d\mathcal{H}\mathcal{U}}{d\eta} + \beta\frac{d\mathcal{H}\mathcal{U}^2}{d\eta} = -\frac{d\mathcal{H}^2\mathcal{G}}{d\eta} + \mathcal{H}\frac{d\mathcal{F}}{d\eta}. \tag{33}$$

Motivated by the profiles in figure 18, we will seek a solution of the form

$$\mathcal{U} = \frac{4\lambda\eta}{9\alpha} \tag{34}$$

It follows that

$$\mathcal{H} = \mathcal{H}_0\eta^{2/(3\alpha-2)} \quad and \quad \mathcal{G} = \mathcal{G}_0\eta^{6((\alpha-1)/(3\alpha-2))} \tag{35}$$

where $\mathcal{H}_0$ and $\mathcal{G}_0$ are constants. We see that, when $\alpha > 0$, the depth and reduced gravity increase towards the front of the flow.

2.2.3 Mixing during the self-similar regime

In figures 20(a,b), the normalised experimental data from figures 18(c,d) is compared with predictions from the theoretical model. Although the general trend in the experimental data is similar to the model prediction, there appears to be a systematic difference between the data and the model in the tail of the flow in figure 20(a). This difference suggests that some of the buoyancy released from behind the lock gate becomes detached from the front of the gravity-driven flow, particularly from the rear of the current.

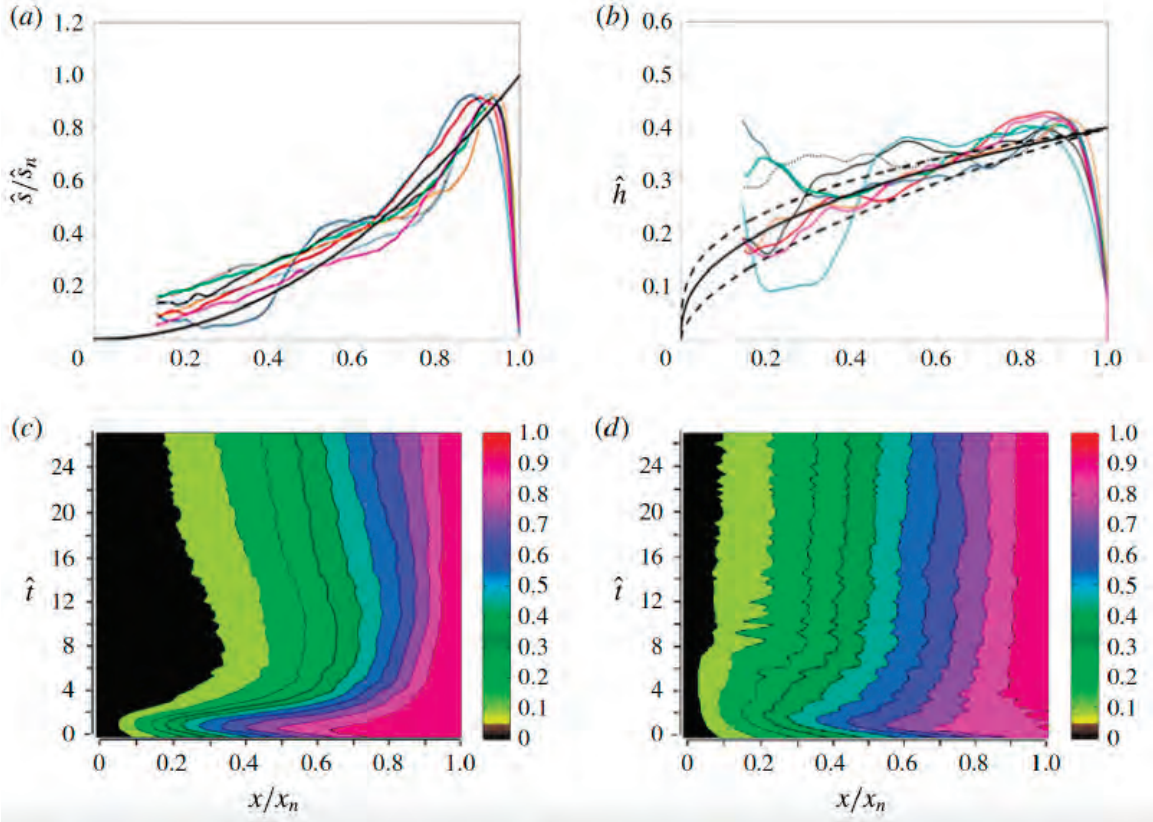

Figure 20: Variation of (a) the vertical integral of the salt concentration, normalised by the vertical integral of the salt concentration at the nose as a function of position in the current. For comparison, the model solution is also shown with the thick black curve. (b) Time average of the depth of the current as a function of the position within the current, again compared to the theoretical model prediction. (c) A colour image in which the fraction of the total buoyancy of the current in the region of the current between the rear of the lock gate and each point in the current, is plotted as a function of the dimensionless position in the current and dimensionless time. (d) A colour image of the fraction of the total volume of the current in the region of the current between the rear of the lock gate and each position in the current, as a function of the dimensionless position and dimensionless time. (Sher and Woods, 2015)

In order to demonstrate this slow loss of buoyancy from the rear of the current, figure

20(c) presents a colour image in which the fraction of the total buoyancy of the current in the region of the current between the rear of the lock gate and each point in the current, as a function of the dimensionless position in the current (x-axis) and dimensionless time (y-axis). It is seen that, gradually, the dimensionless position of each contour representing a constant fraction of the buoyancy migrates backwards in the current. This redistribution of the buoyancy is consistent with a slow loss of buoyancy from the rear of the current.

For comparison, figure 20(d) shows a colour image of the fraction of the total volume of the current in the region of the current between the rear of the lock gate and each position in the current, as a function of the dimensionless position (x-axis) and dimensionless time (y-axis). The image shows that to good approximation the volume contours are independent of the dimensionless position of the current. This suggests that even though there is a slow loss of buoyancy from the dense lower part of the flow, the current shape remains approximately the same as the current advances. Together, these figures show that strictly the flow is not self-similar owing to the slow redistribution of buoyancy from the front to the rear of the flow. However, this redistribution of buoyancy is a slow process and so the self-similar depth-averaged model seems to provide a reasonable approximate description of the overall dynamics of the gravity current following the initial transition of the flow.

2.3 Mixing in continuous gravity currents

As gravity currents evolve, a considerable mass of ambient fluid is mixed into the flow, primarily through the head and near to the source of the flux of fluid. Mixing can be analysed experimentally, and this is what we shall discuss here. We shall consider the motion of two-dimensional gravity currents produced by a constant source of buoyancy. For these flows, the source Froude number is given by

$$\mathrm{Fr} = \frac{u_0}{(g_0' h_0)^{1/2}} \tag{36}$$

An example of such an advancing gravity current is shown in figure 21. The series of false-colour images represent the evolution of the density in the flow, with the colour scale representing the mass of salt in the fluid per unit mass of fluid. Just downstream of the source, the current deepens and the upper part of the current becomes diluted by mixing with ambient fluid. Further downstream, the current has a relatively dense lower region which appears to reach the head of the flow, where a second region of mixing can be seen in the upper part of the head of the flow. This also appears to contribute to a region of relatively dilute fluid which forms on the upper surface of the flow.

In order to explore the mixing processes in more detail, figure 22 presents four panels of images for currents with Fr=2.7 (a,b) and Fr=0.4 (c,d), in which (a,c) the source fluid was initially dyed yellow, and then green, and (b,d) the ambient fluid initially ahead of the current included parcels of fluid dyed red, green and yellow. Figures 22(a,b), where there is a high Froude number input, indicate that once the source fluid is dyed green, the fluid advances through the lower part of the current and rapidly catches up the with the head. This fluid mixes with the ambient fluid originally ahead of the flow, to form an upper mixed layer which gradually lags behind the head of the flow since it travels forward more slowly than the continuing head. The strong vertical stratification in the flow is produced by a

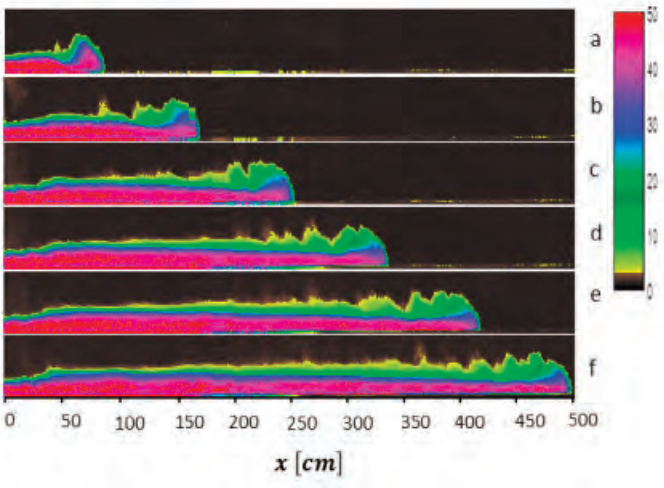

Figure 21: Series of images illustrating the evolution of the concentration field in the current as it advances along the flume. The images are shown in false colour to illustrate the dilution of the flow relative to the original source fluid. (Sher and Woods, 2017)

combination of mixing near the inflow and the head of the flow, where there appears to be a second phase of mixing. As a result, the fluid in the current undergoes a net circulation relative to the head as the current advances along the flume (see figure 23).

The process is similar when there is a low Froude number input(figures 22(c,d)), however the green dye catches the nose much more slowly and there is greater entrainment and mixing in the nose.

One of the key properties of a gravity current is the speed of the head of the current, dx_n/dt. This can be computed from figure 24(a), which plots results from different experiments with different source Froude numbers Fr_0. It can be seen that there is a weak dependence on the source Froude number. Figure 24(c) plots estimates of the Froude number at the front of the current Fr_n as a function of the source Froude number, where we see that $Fr_n \approx 1.1$.

Once the saline water enters the base of the tank, a local zone of flow adjustment and mixing develops. Examples of the inflow adjustment are shown in figure 25 for cases of high source Froude number (top) and low source Froude number (bottom). When the source Froude number is high, the current deepens over a fixed distance with a significant amount of turbulent mixing apparent on the upper surface of the flow. Further downstream, the depth then evolves more gradually. In contrast, for low source Froude numbers, the current initially accelerates and thins out, but then it appears to deepen and mix across its upper surface as in the case of the larger source Froude number. Again, it reaches a near constant depth after a fixed distance, after which it evolves much more slowly downstream. The figures on the left in figure 25 show the corresponding normalised velocity profile (dashed lines) and concentration (solid line) as a function of the normalised height. For higher Froude numbers (top), the concentration and velocity vary continuously over the full depth of the current whereas for smaller Froude numbers, the current has a relatively uniform concentration and velocity with height up to the point at which there is a transition to the

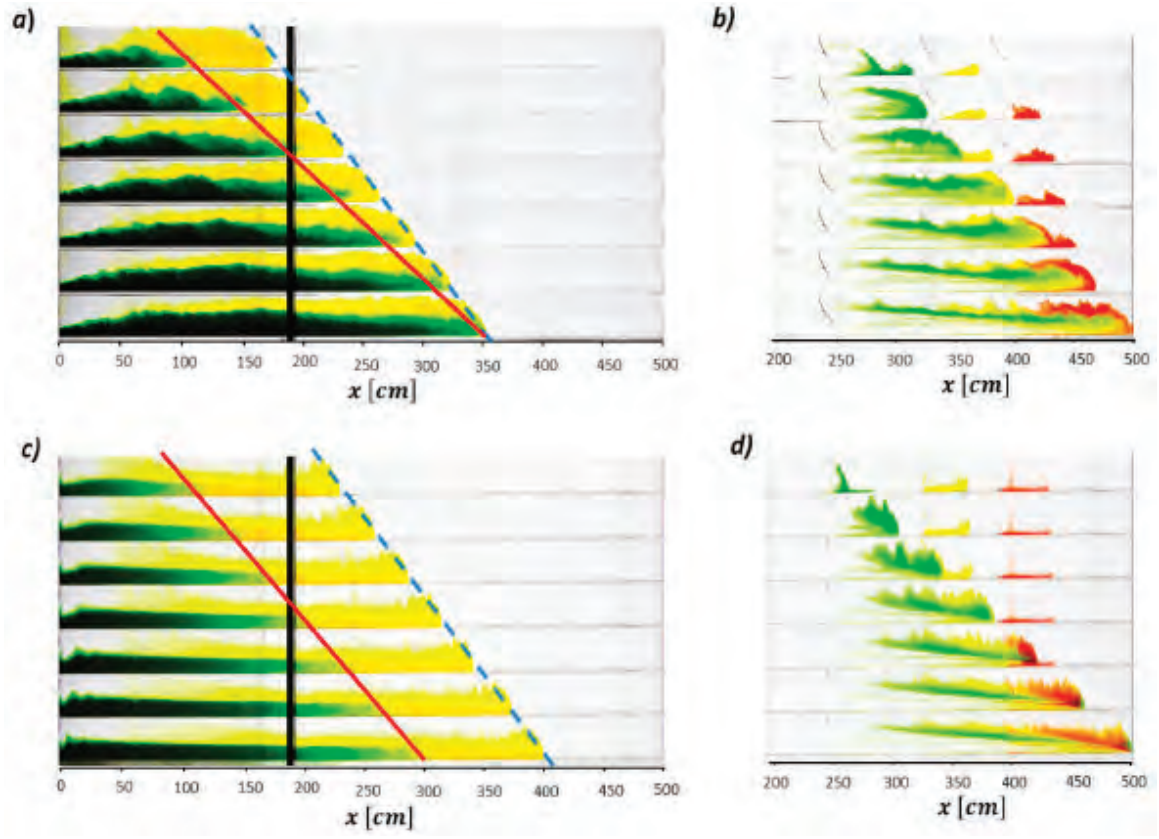

Figure 22: (a) Series of images illustrating the path followed by the source fluid as a function of time visualised by changing the colour of the source fluid from yellow to green 5s after the start of the experiment. The sloping red line illustrates the advance of the green dye front with time while the sloping dotted blue line indicates the advance of the head. (b) Series of images illustrating the evolution of regions of green, yellow and red dye originally located in the ambient fluid downstream of the current, in the case with $Fr_0 = 2.7$. (c) Series of images as in panel (a) but now with $Fr_0 = 0.4$. (d) Series of images illustrating the evolution of regions of green, yellow and red dye originally located in the ambient fluid downstream of the current, with $Fr_0 = 0.4$. (Sher and Woods, 2017)

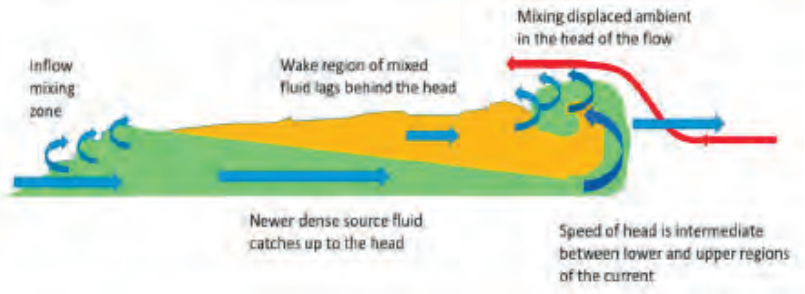

Figure 23: Schematic of the flow processes in a steady gravity current. (Sher and Woods, 2017)

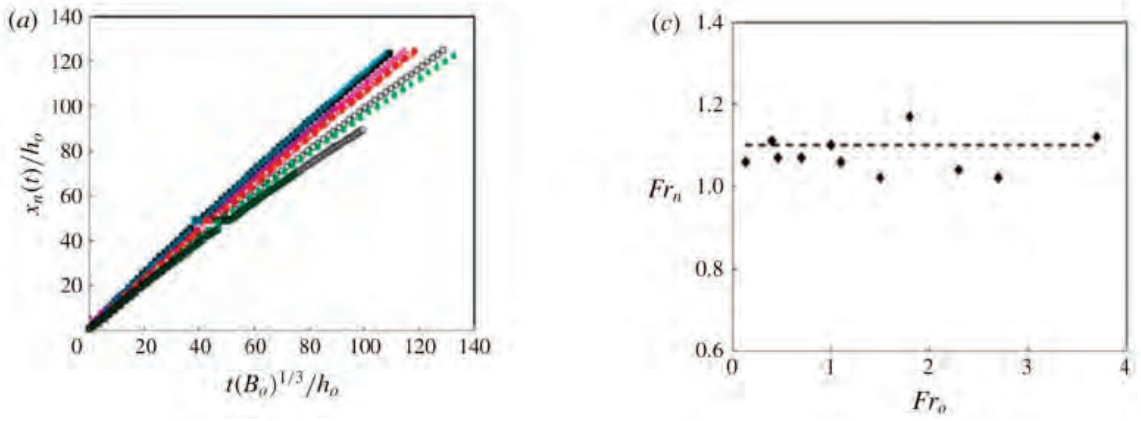

Figure 24: Position of the dimensionless head of the current as a function of dimensionless time for several experiments. (c) Variation of the Froude number of the head as a function of the source Froude number. (Sher and Woods, 2017)

overlying ambient fluid.

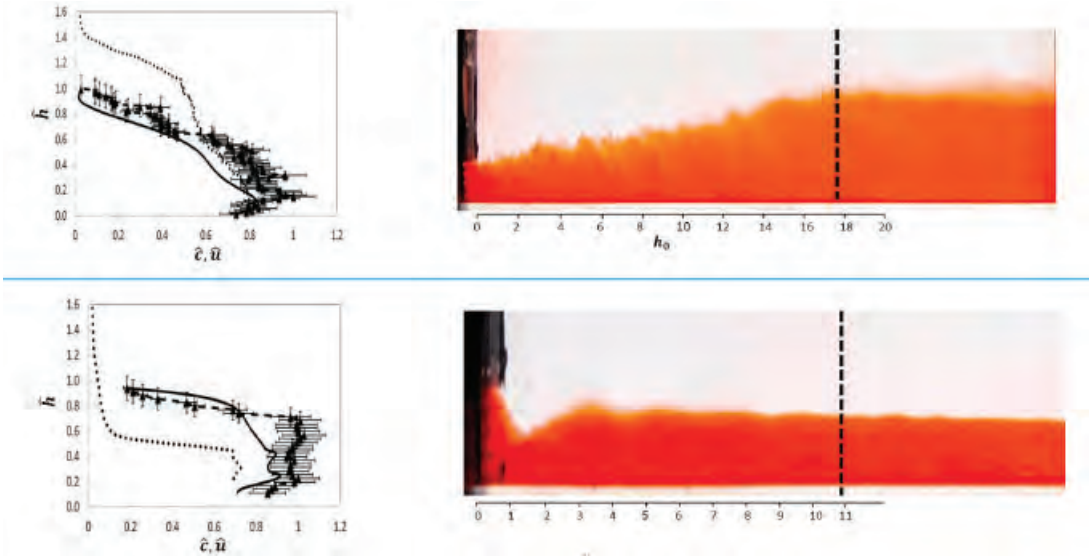

Figure 25: (Left) Variation of the vertical profile of salt concentration normalised by source salt concentration as measured just downstream of the inflow mixing zone (solid line) and just behind the head of the flow (dotted line) and the horizontal speed, normalised by the maximum horizontal speed just downstream of the inflow mixing zone (trianges, dashed line) as a function of the normalised height. Top case represents a high source Froude number while bottom case represents a low source Froude number. (right) Photographs of the current just downstream of the source for (top) high source Froude number and (bottom) low source Froude number. (Sher and Woods, 2017)

It can be seen that the upper part of the flow has a vertical gradient in velocity and

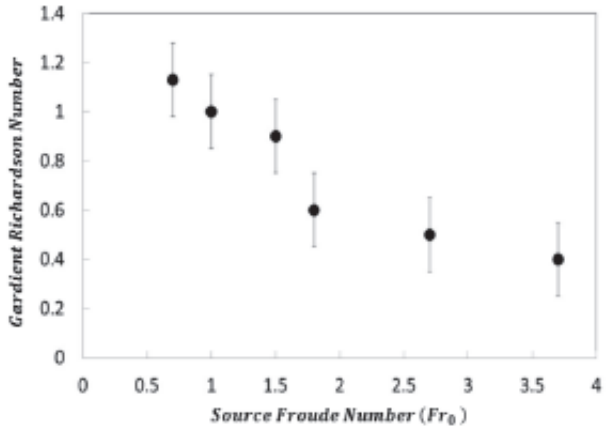

Figure 26: Estimate of the gradient Richardson number in the current just downstream of the inflow mixing zone as a function of the source Froude number. (Sher and Woods, 2017)

buoyancy, below the ambient fluid. The stability of such a region depends on the gradient Richardson number, defined by $Ri_g = dg'/dz/(du/dz)^2$ with the flow being stable for $Ri_g > 0.25$. Figure 26 plots the gradient Richardson number against the source Froude number. We note that smaller source Froude numbers are associated with larger gradient Richardson numbers limiting mixing in the main part of the flow.

Figure 27(right) plots estimates of the flux of ambient fluid, per unit width, that is mixed into the current. Plotted against the Froude number, solid triangles represent the total fractional mixing in the current, solid circles represent the fractional mixing in the inflow region (e_{in}) and open circles represent the fractional mixing in the remainder of the current. We can see that for low Froude numbers, there is relatively little mixing in the inflow mixing zone. There is a shifting balance between mixing near the source for large source Froude numbers and mixing downstream for smaller source Froude numbers.

If we follow the classical parameterisation for the rate of entrainment of ambient fluid into the upper surface of the flow and take it to be of the form $\alpha(Fr(x,t))u(x,t)$ per unit area, where Fr is a local Froude number for the flow, then we would expect the total volume of the current per unit width to increase according to the relation

$$\frac{dV}{dt} = Q_0 + e_{in}Q_0 + \int_{L_0}^{L(t)-L_n} \alpha(Fr(x,t))u dx + e_h Q_0 \tag{37}$$

where e_h is the fraction of the mixing that occurs at the head of the flow and is L_0 is the length of the mixing zone near the inflow. The middle term on the right-hand side then represents the entrainment along the upper boundary of the main part of the current away from the inflow adjustment zone and the head. If this entrainment was significant in experiments, then we would expect a gradual increase in the rate of change of volume with time. This rate of increase of the total volume of the current is plotted in figure 27(left) where the volume per unit width is displayed as a function of time. To good approximation, the volume per unit width increases linearly with time as the current advances downstream. It is inferred that, for the length scale of the currents explored here, any mixing on the upper

surface of the flow is small compared with the sum of the mixing at the source and the nose of the flow.

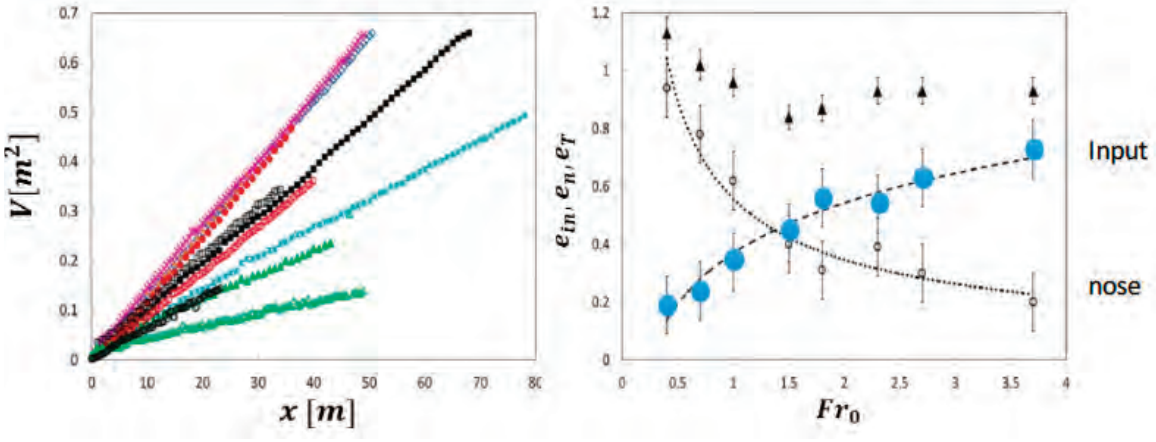

Figure 27: (a) Variation of the total fractional mixing in the current (solid triangles), the fractional mixing in the inflow region, e_{in} (solid circles) and the fractional mixing in the remainder of the current, e_n (open circles) as a function of the source Froude number. (b) Total volume of the current per unit width as a function of time. (Sher and Woods, 2017)

The fraction of the fluid displaced by the head of the gravity current that is mixed into the current, E, can be expressed as

$$Eh_n \frac{dx_n}{dt} = e_n Q_0, \tag{38}$$

where e_n is rate of entrainment of fluid downstream of the near-source mixing zone as a fraction of the source volume flux. The variation of E with Fr_0 is shown in figure 28. Currents for which $Fr_0 < 1$ involve relatively little mixing near the inflow but have a much larger entrainment at the head of the flow.

It could be anticipated that the currents take on a long-time asymptotic self-similar structure in which the distribution of density and volume along the current is primarily a function of the position relative to the nose, $\eta = x/x_n(t)$. Further, we might anticipate that this structure depends on the source Froude number given the different partitioning of the mixing between the inflow and the head and the different vertical structure of the flow. Figure 29 shows the evolution with dimensionless time of contours of (ac) the fraction of the total volume and (df) the fraction of the total buoyancy of the current in the region $0 < \xi < \eta$. Measurements are shown for three gravity currents, with input Froude numbers of 0.4 (a,d), 1.5 (b,e) and 2.7 (c,f). For each of the currents in figure 8, in (gi), we illustrate the concentration field throughout the current at one instant in time. For low Froude numbers, there is less mixing in the inflow adjustment region. A relatively dense region of fluid at the base of the flow then advances towards the head of the flow. Here, it rises and mixes with the displaced ambient fluid, forming the upper wake region of relatively low density which extends backwards from the nose of the current. In contrast, with higher inlet Froude numbers, there is much more mixing of ambient fluid in the near-source mixing

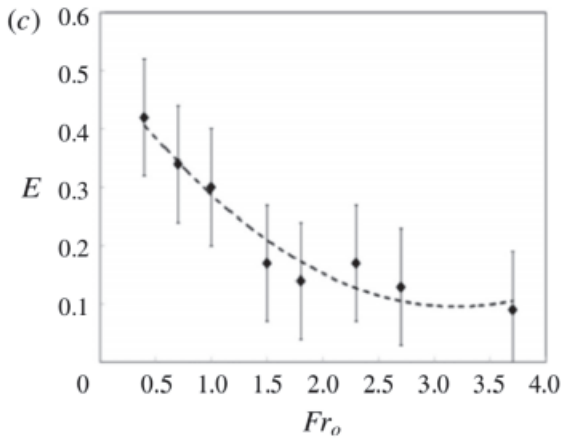

Figure 28: Variation of the nose entrainment parameter E representing the fraction of the fluid initially ahead of the current which is entrained by the current as it is displaced over the head of the current. (Sher and Woods, 2017)

zone. This leads to a much more continuous vertical stratification and there is less mixing of the displaced ambient fluid into the head of the flow.

2.4 Analytic solutions for entraining stratified gravity currents

For an entraining gravity current, the momentum flux and buoyancy flux are conserved, whereas the mass flux increases owing to entrainment. Entrainment at the interface between the gravity current and the ambient forms a mixing layer at the interface, which may suppress further entrainment. As the mixing increases, the depth of the interfacial layer gradually increases. Assuming that the pressure in the current is hydrostatic above a layer of height h, the conservation equations are given by

$$\frac{\partial}{\partial x}\left(\int_0^h u\mathrm{d}y\right) = \epsilon u(x,h), \quad \frac{\partial}{\partial x}\left(\int_0^h u^2 + \left(\int_y^h g'\mathrm{d}y^*\right)\mathrm{d}y\right) = 0, \quad \frac{\partial}{\partial x}\left(\int_0^h ug'\mathrm{d}y\right) = 0 \tag{39}$$

where $u(x,y)$ and $g'(x,y)$ are the velocity and buoyancy profiles within the current, and ϵ is the entrainment parameter. The shape factors S_1, S_2, S_3, S_4 are defined in terms of the particular structure of the velocity and buoyancy profiles. In accord with the numerical experiments of steady gravity currents by Kneller et al. (2016) (figure 30), the upstream profile is assumed to be uniform in velocity and buoyancy, similar to a plug flow, whereas downstream, the flow is stratified and the depths of the velocity and buoyancy profiles are assumed to be the same (Figure 31). The profiles of velocity and buoyancy are given by

$$u(x_d,y) = \begin{cases} u_d & \text{if } 0 \le y \le \phi h_d, \\ u_d\left(\frac{h_d - y}{h_d(1-\phi)}\right) & \text{if } \phi h_d \le y \le h_d, \end{cases} \tag{40}$$

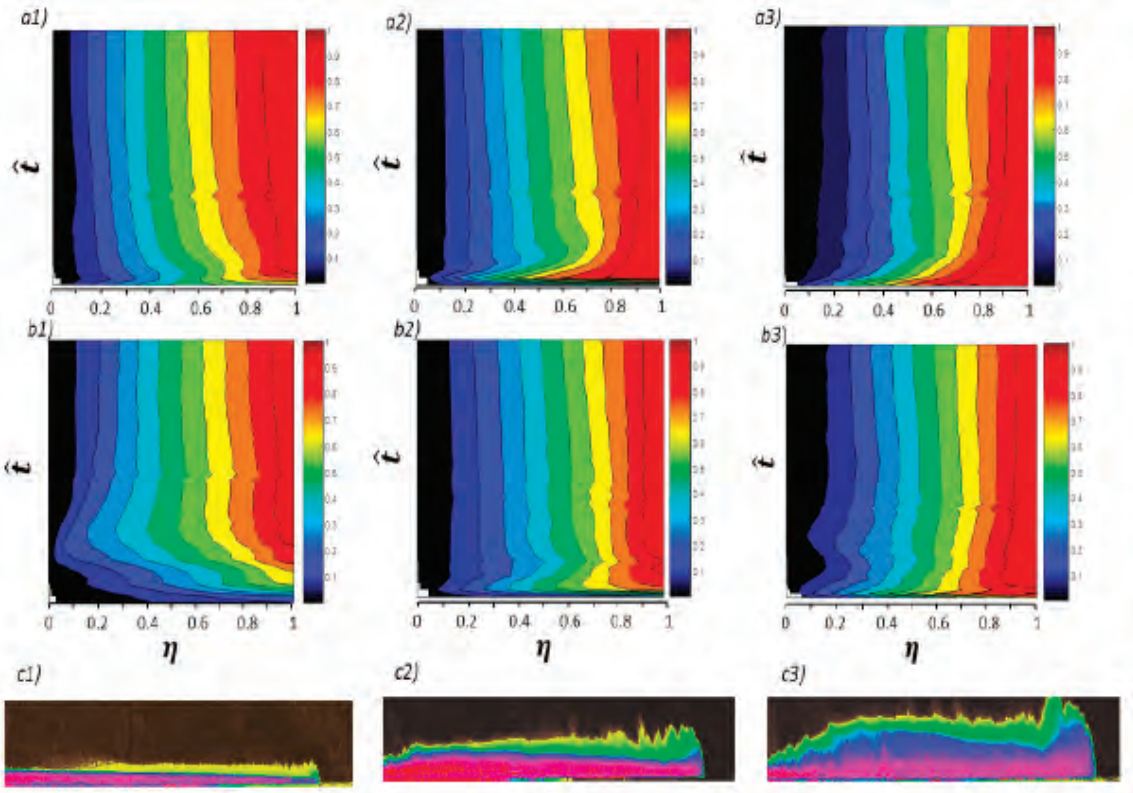

Figure 29: The evolution with dimensionless time of contours of (a-c) the fraction of the total volume and (d-f) the fraction of the total buoyancy of the current as a function of η. (g-i) Concentration field throughout the current at one instant in time. Measurements are shown for three gravity currents corresponding to (a,d,g) $Fr_0 = 0.4$, (b,e,h) $Fr_0 = 1.5$ and (c,f,i) $Fr_0 = 2.7$. (Sher and Woods, 2017)

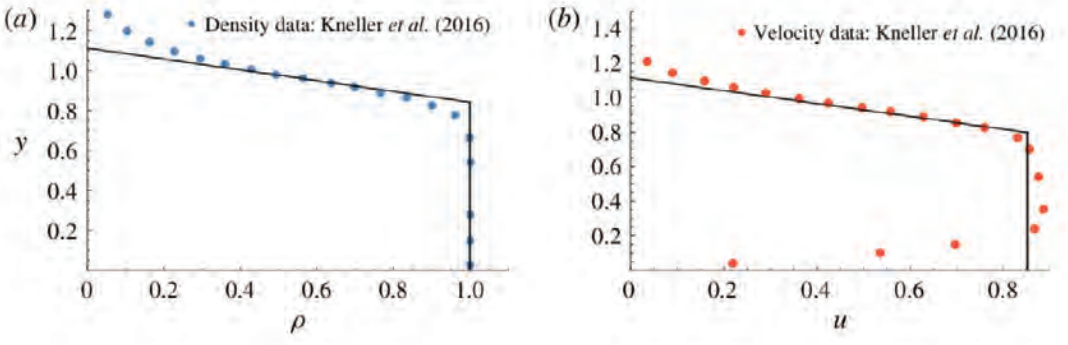

Figure 30: (a), (b) The variation of density and velocity profiles with height in a gravity current. The solid line corresponds to the theoretical model and the points correspond to data from numerical experiments done by Kneller et al. (2016). The numerical experiments consisted of bottom drag which led to a boundary layer at $y = 0$ as shown in (b).

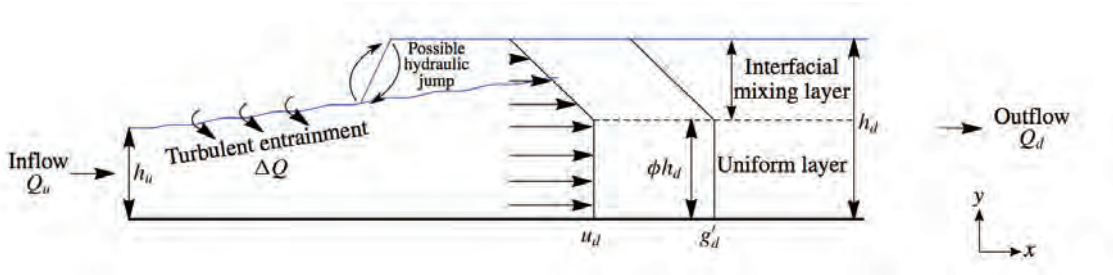

Figure 31: A schematic of the model gravity current. A uniform upstream profile at $x = 0$ evolves to a hybrid uniform-linear downstream profile via turbulent entrainment through the interface and/or possibly through a hydraulic jump. The uniform flow fraction of the velocity and density profiles is given by $\phi \in [0, 1]$. The upstream volume flux is denoted Q_u and the downstream volume flux is denoted Q_d. (Horsley and Woods, 2018)

$$g'(x_d, y) = \begin{cases} g'_d & \text{if } 0 \le y \le \phi h_d, \\ g'_d\left(\frac{h_d - y}{h_d(1-\phi)}\right) & \text{if } \phi h_d \le y \le h_d, \end{cases} \tag{41}$$

The fluid is assumed to transition between the upstream and downstream state via turbulent entrainment and mixing through the interface, or through a hydraulic jump, or a combination of both. The following averaged quantities are defined

$$S_1 \bar{u} h = \int_0^h u \mathrm{d}y, \quad S_2 \bar{u}^2 h + S_3 \bar{g}' h^2 = \int_0^h u^2 + \left(\int_y^h g' \mathrm{d}y^* \right) \mathrm{d}y, \quad S_4 \bar{u} \bar{g}' h = \int_0^h u g' \mathrm{d}y \tag{42}$$

where $\bar{u}(x)$ and $\bar{g}'(x)$ are the depth averaged velocity and buoyancy profiles, and $h(x)$ is the depth of the current. From the depth-averaged quantities (equations (42)) and the conservation laws (equations (39)) we find that the transition from a uniform source at $x = 0$ to the flow at a downstream location $x = x_d$ can be written in terms of the shape factors at $x = x_d$ in the form

$$S_1 u_d h_d - u_u h_u = \int_0^{x_d} \epsilon u(x, h) \mathrm{d}x, \quad u_u^2 + \frac{g'_u h_u^2}{2} = S_2 u_d^2 h_d + S_3 g'_d h_d^2, \quad u_u g'_u h_u = S_4 u_d g'_d h_d \tag{43}$$

where $u_u = \bar{u}(0)$, $u_d = \bar{u}(x_d)$, $g'_u = \bar{g}'(0)$, $g'_d = \bar{g}'(x_d)$, $h_u = h(0)$, $h_d = h(x_d)$ denote the upstream and downstream velocities, buoyancies, and heights of the flow, respectively.

Substituting the ideal downstream profiles (equations (40, 41)) into the conservation equations (42) leads to the following constraints on u_d, h_d as functions of ϕ and the upstream flow u_u, g'_u and h_u.

$$u_u g'_u h_u = \frac{1}{3} u_d g'_u h_d (1 + 2\phi), \quad u_u^2 h_u + \frac{1}{2} g'_u h_u^2 = \frac{1}{3} u_d^2 h_d (1 + 2\phi) + \frac{1}{6} g'_u h_d^2 (1 + \phi + \phi^2) \tag{44}$$

The downstream gradient Richardson number is defined based on the upper linearly stratified portion of the flow as

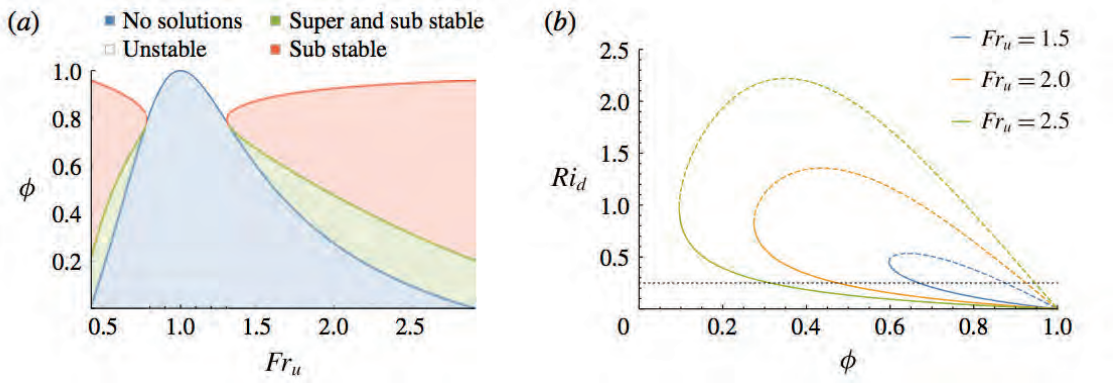

Figure 32: These figures refer to the case with a lower uniform region overlain by an interfacial linearly stratified mixing region. (a) A regime diagram illustrating the nature of solutions for an upstream Froude number Fr_u and downstream uniform flow fraction ϕ. Blue shaded areas are regions of no solution due to violation of conservation laws. Green shaded areas are where $Ri_d > 1/4$ and the downstream flow is stable for both supercritical and subcritical solutions. Red shaded areas are stable for subcritical solutions and unstable for supercritical solutions. White areas are where $Ri_d < 1/4$ and the downstream flow is unstable for all solutions. (b) The variation of downstream gradient Richardson number with uniform flow fraction ϕ. Supercritical solutions are shown as solid lines and subcritical solutions as dashed lines. The two solution branches converge when $\phi = \phi_{min}$ at $Ri_d(\phi_{min})$. The turning point of the subcritical branch gives a maximal downstream gradient Richardson number $Ri_{d_{max}}$ for each upstream Froude number Fr_u. Portions of both branches below the black dotted line $Ri_d = 1/4$ are unstable. (Horsley and Woods, 2018)

$$Ri_d = \frac{g'_d h_d (1-\phi)}{u_d^2} \tag{45}$$

and the upstream Froude number is given by

$$Fr_u = \frac{u_u}{\sqrt{g'_u h_u}} \tag{46}$$

Note that the equations for the conservation of buoyancy and momentum lead to an equation which is cubic in nature with three real roots. One of these roots is unphysical since it requires $h_d < 0$. However, the two remaining roots may be interpreted physically. One root, denoted supercritical, can be thought of as evolving continuously away from the upstream uniform flow by turbulent entrainment. The entrainment gradually erodes the interface, creating a deepening interfacial mixing layer. The other root, denoted subcritical, can be interpreted as the case in which the fluid undergoes a discontinuous hydraulic jump to a conjugate flow state where the local Froude number is less than 1. This could possibly occur after a period of supercritical interfacial entrainment. The case for which both supercritical and subcritical branches are stable is shaded green in figure 32(a). The red shaded area indicates where only the subcritical solution branch is stable and the supercritical unstable. We note that transition to a uniform flow downstream ($\phi = 1$) is always unstable

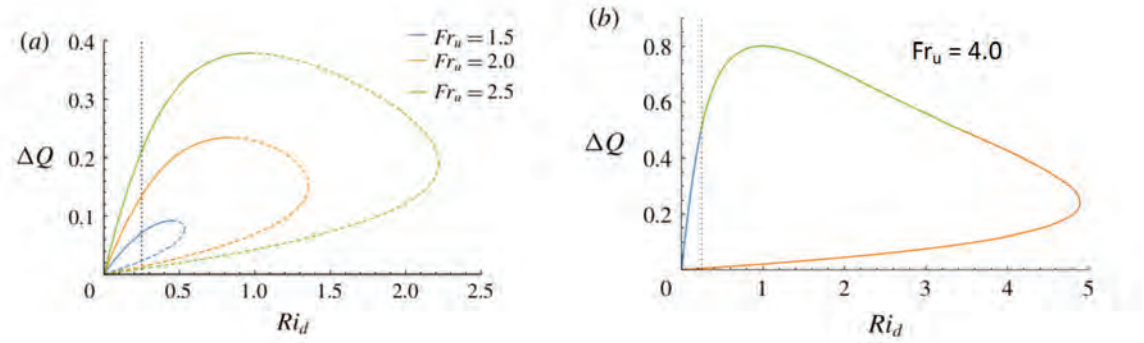

Figure 33: (a) $Fr_u < 2.291$. This figure represents the case with a lower uniform region overlain by an interfacial linearly stratified mixing region. Dimensionless entrainment flux ΔQ as a function of the downstream gradient Richardson number for a fixed upstream Froude number Fr_u. Supercritical branch solutions are shown as solid lines and subcritical as dashed lines. Maximal entrainment occurs at the convergence of the two branches ϕ_{min}. (b) $Fr_u > 2.291$. This refers to the case when the flow is fully modified and is linearly stratified throughout. The downstream entrainment flux ΔQ as a function of downstream gradient Richardson number Ri_d for a fixed upstream inflow Froude number $Fr_u = 4$. The orange curve illustrates solutions from the subcritical interfacial mixing layer model, the blue curve illustrates solutions from the supercritical interfacial mixing layer model, and the green curve illustrates solutions from the fully modified layer model. Note that in both figures, solutions to the left of the line $Ri_d = 1/4$ are unstable.

in that the gradient Richardson number tends to zero as the mixed layer thickness tends to zero, with a non-zero jump in density and velocity across the layer.

Figure 32(b) illustrates the variation of the downstream gradient Richardson number Ri_d as a function of the fractional depth of the well-mixed lower region of the flow ϕ for a series of upstream Froude numbers Fr_u. The supercritical branch, denoted with solid lines, converges to the subcritical solution branch, denoted with dashed lines, at the value $Ri_d(Fr_u, \phi_{min})$. The dotted black line indicates $Ri_d = 1/4$, below which all downstream flows are unstable.

Rewriting equations (44) in terms of the dimensionless parameter, the upstream Froude number Fr_u from equation (46) leads to an understanding that there exists a minimal ϕ for each upstream Froude number Fr_u, and this minimum decreases as Fr_u increases. If the upstream Froude number is too small, the momentum of the flow may not be sufficient to mix the current with large volumes of the ambient fluid, and this limits the possible range of ϕ values downstream. Figure 33(a) shows the variation of the dimensionless entrainment flux ΔQ as a function of the downstream gradient Richardson number for three fixed values of the upstream Froude number $F\,r_u$, all less than 2.291, which is the critical value of the Froude number. For $F\,r_u < 2.291$, the flow is never fully mixed, and for $F\,r_u > 2.291$, the flow may become fully mixed. In the latter case (figure 33(b)), very substantial dilution is possible, which is consistent with experimental values. For upstream Froude numbers in excess of 2.921, the stratified zone may extend to the lower boundary of the domain, so that

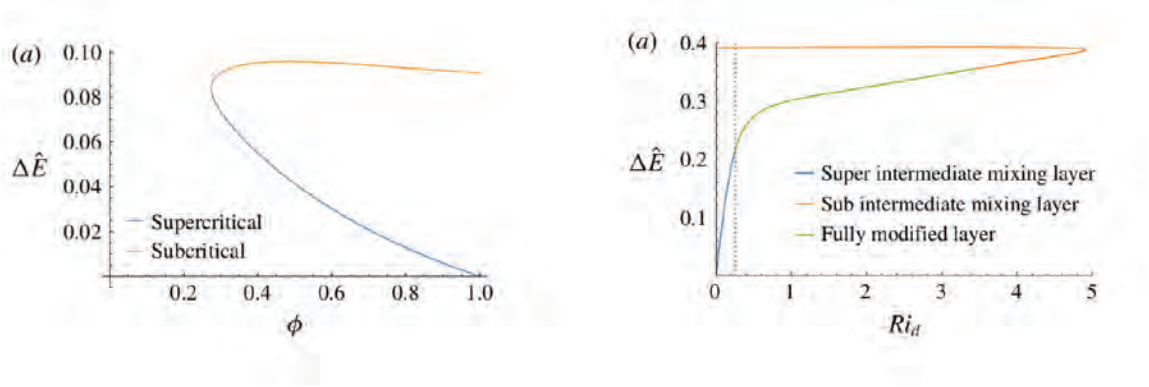

Figure 34: (Left) This refers to the case with a lower uniform region overlain by an interfacial linearly stratified mixing region. The variation of dimensionless energy dissipation ΔE with the downstream uniform flow fraction ϕ for a fixed upstream Froude number $Fr_u = 2$. The blue line corresponds to the supercritical branch, which continuously moves away from the $\phi = 1$ solution where no transition occurs. The orange line corresponds to the subcritical branch, which has finite dissipation at $\phi = 1$ corresponding to a hydraulic jump with no entrainment. This discontinuous transition can then dissipate more energy as a shear layer is created by the entrainment of fluid up to a maximum value $\Delta E = 0.096$. (Right) This refers to the case when the flow is fully modified and is linearly stratified throughout. The variation of dimensionless energy dissipation ΔE with downstream gradient Richardson number Ri_d for a fixed upstream Froude number $Fr_u = 4$. The orange curve illustrates solutions from the subcritical interfacial mixing layer model, the blue curve illustrates solutions from the supercritical interfacial mixing layer model, and the green curve illustrates solutions from the fully modified layer model. Solutions to the left of the black dotted line $Ri_d = 1/4$ are unstable.

there is no uniform region of flow.

A clear way to illustrate the difference between the two solution branches is to consider the energy dissipation $\Delta E(Fr_u, \phi)$ across the transition. The steady energy flux lost per unit distance through the transition is given by

$$\frac{\partial}{\partial x}\left(\int_0^h u\left(\frac{u^2}{2} + g'y\right)\mathrm{d}y + \int_0^h u\left(\int_y^h g'\mathrm{d}y^*\right)\mathrm{d}y\right) = \frac{\partial(\Delta E)}{\partial x} \tag{47}$$

Figures 34(a,b) show the variation of energy dissipation ΔE with the downstream uniform flow fraction ϕ and with downstream gradient Richardson number Ri_d for a fixed value of the upstream Froude number.

References

Fitzgerald, S. D. and A. W. Woods 2007. Transient natural ventilation of a room with a distributed heat source. *J. Fluid Mech.*, 591:21–42.

Horsley, M. C. and A. W. Woods 2018. A note on analytic solutions for entraining stratified gravity currents. *J. Fluid Mech.*, 836:260–276.

Kneller, B., M. M. Nasr-Azadani, S. Radhakrishnan, and E. Meiburg 2016. Long-range sediment transport in the world's oceans by stably stratified turbidity currents. *Journal of Geophys. Res.: Oceans*, 121(12):8608–8620.

Sher, D. and A. W. Woods 2015. Gravity currents: entrainment, stratification and self-similarity. *J. Fluid Mech.*, 784:130–162.

Sher, D. and A. W. Woods 2017. Mixing in continuous gravity currents. *J. Fluid Mech.*, 818:R4.

Lecture 6
Modeling Ash Flows and Volcanoes

Notes by Sutirtha Sengupta, Sara Lenzi and Andrea Lehn

June 25, 2018

1 Volcanoes

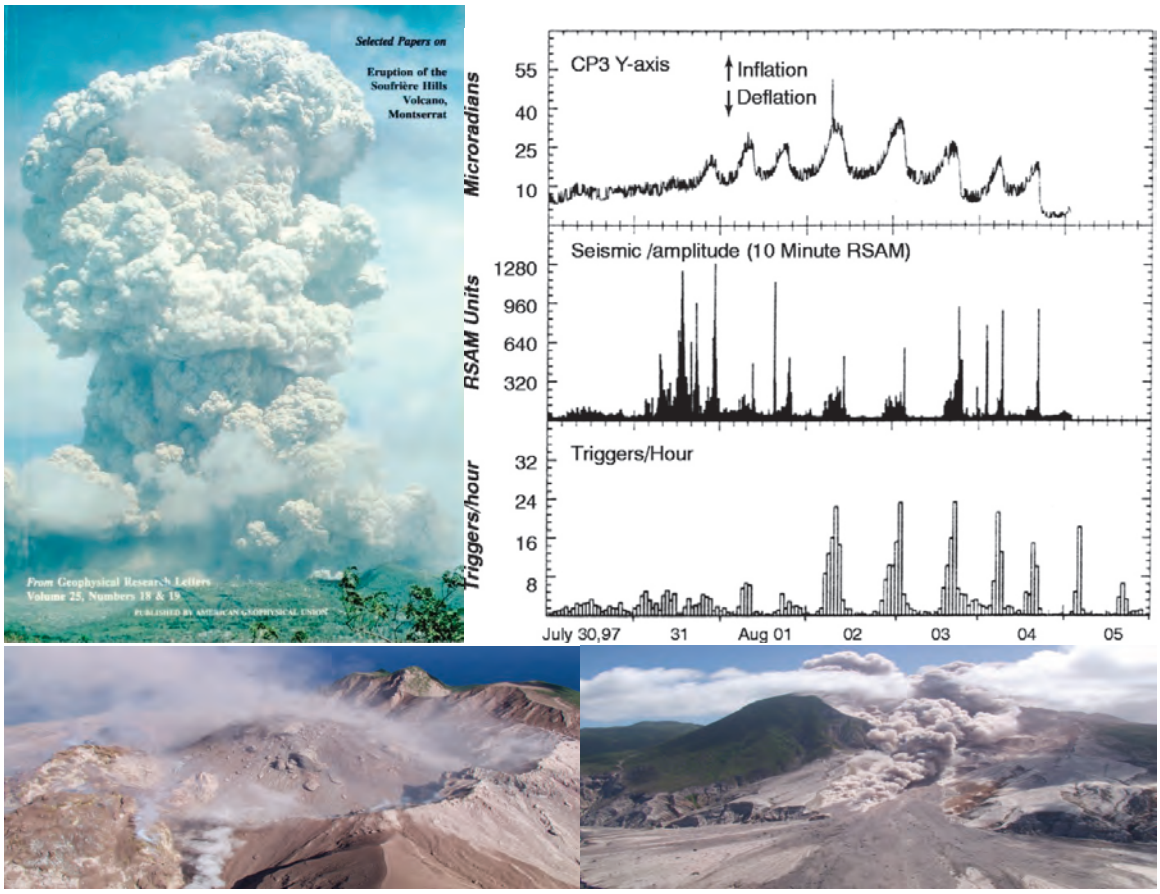

Figure 1: Pictures from the Monserrat eruption showing the explosive ash plumes, unstable lava domes and associated seismic activity as a function of time since first eruption on July 30, 1997.

2 Ash Flows

Volcanic eruptions are often accompanied by flows in which material is lofting upwards just behind the head of the flow, as shown in Fig 2. We can attempt to understand the dynamics of such ash flows both through laboratory experiments and simplified models of pyroclastic flows that will be the topic of the preliminary sections of this lecture, followed by preliminary modeling approaches to understand the basic mechanism driving these giant eruptions.

Figure 2: Left: Flow fronts such as those formed during the eruptions at Mt Unzen. Right: Pyroclastic density current on 8 January 2010 at Soufriere Hills Volcano, Montserrat (reproduced from [1], Fig 5.5b)

2.1 Experiments

2.2 What controls eruption?

The bulk density of the mixture is given by

$$\rho_m = \left[\frac{n}{\rho_g} + \frac{1-n}{\rho_s}\right]^{-1}, \tag{1}$$

where n is the gas mass fraction, ρ_g the gas density, and ρ_s the solid density. We assume a gas mass fraction given by

$$\begin{aligned} n &= n_s - s p^{\frac{1}{2}} \text{ if } p < \frac{n_s^2}{s} \\ &= 0 \text{ otherwise,} \end{aligned} \tag{2}$$

and the gas pressure given by the ideal gas law:

$$\rho_g = \frac{p}{RT}. \tag{3}$$

The magma compressibility is given by

$$\beta_m = \frac{1}{\rho_m}\frac{\partial \rho_m}{\partial P}. \tag{4}$$

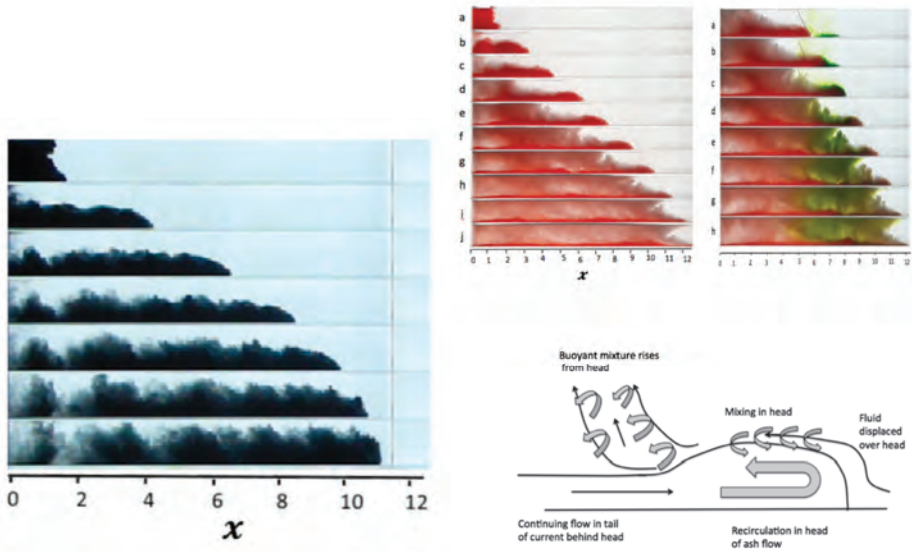

Figure 3: Left: Evolution of an initially dense salt and salt powder gravity current propagating through a flume filled with lemonade; Right: (top) Illustration of the time-dependent mixing of ambient fluid (green) into the head of the flow (red) and the subsequent lift off of mixed buoyant fluid from the rear of the head. (bottom). Schematic diagram illustrating the process of mixing and lift off.[2]

In the magma chamber, the elastic crust leads to the relation

$$dV = V\beta_c dp. \tag{5}$$

Mass changes when pressure changes according to

$$\begin{aligned} V &= \rho_m V \\ dM &= (\beta_m + \beta_c) M dp. \end{aligned} \tag{6}$$

If $\beta_m \gg \beta_c$, the eruption is controlled by magma compressibility.

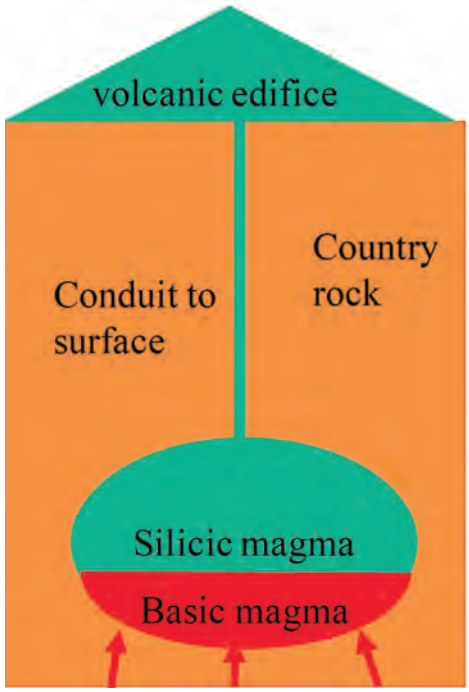

Figure 4: Basic model of a volcanic magma chamber

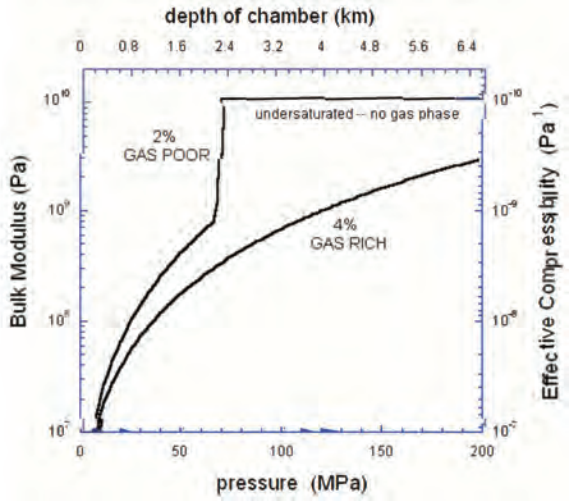

Figure 5: Plot showing the variation of magma compressibility (or the bulk modulus) with depth of the magma chamber (proxy for pressure)

3 Modeling Eruptions

Two main different kinds of simplified magma could be taken in account to describe the eruptions behavior:

- Gas-poor magma, with very rapid increasing of pressure and when the chamber is recharged with magma.
- Gas-rich magma, with more gradual increase in pressure as new magma recharges the chamber.

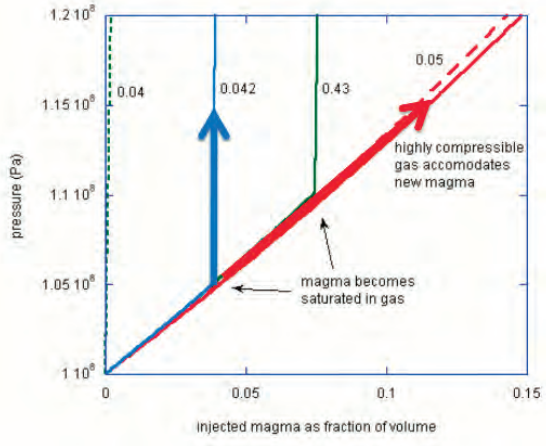

Figure 6: S

We start now to develop a simplified model for a magma chamber using some equations for heat exchange eq.(7), crystals eq.(8) and bubbles eq.(9) contents.

$$M_b c_p dT_b = -F dt \tag{7}$$

$$x_b = \frac{(T - T_b)}{200} \tag{8}$$

$$n_b = n_0 - sP^{1/2}(1 - x_b) \tag{9}$$

Where the subscript b relates to the basaltic magma, c_p is the specific heat at constant pressure and F is the heat flux from the magma chamber. The second equation means that the crystal content depends on temperature and the third equation is also known as the Henry's Law where n_b is the mass fraction of exsolved gas.

The principal driver for eruptions is the heat exchange and cooling of the magma. Eruptions take place when cooling of saturated basalt leads to formation of crystals, saturation

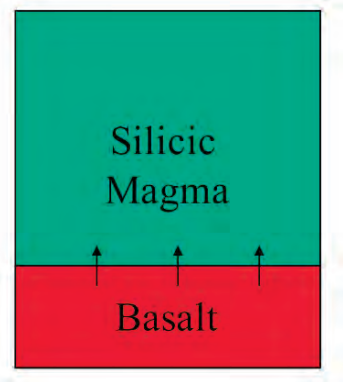

Figure 7: Scheme of magma chamber.

of the magma with gas and exsolution of gas. This leads to an increasing the pressure of the overall magma.
We also consider the following :

$$dP = -\beta_c \frac{dV_b}{V} \tag{10}$$

$$M_b = \rho_b V_b \rightarrow dV_b = -V_b \frac{d\rho_b}{\rho_b} \tag{11}$$

$$\rho_b = \left(\frac{n_b R T_b}{P} + \frac{(1-n_b)}{\rho_{bm}} \right)^{-1} \tag{12}$$

where eq.(10) is the pressure evolution and β_c is the crust compressibility, eq.(11) is mass conservation just before the eruption and eq.(12) is the bubbles mixture evolution.
Combining these equations we obtain a relation between the pressure change and the temperature change of the magma (cooling):

$$\left[\frac{V}{\beta} + \frac{V_b}{\rho_b} \frac{d\rho_b}{dP} \right] dP = \left[\frac{V_b}{\rho_b} \frac{d\rho_b}{dT_b} \right] dT_b \tag{13}$$

A more realistic case is that of fig.(7) in which we consider the interaction between basalt (subscript b) and silicic magma (subscript s) using the same conservation laws as follows :
The heat exchange relation:

$$M_b c_p dT_b = -M_s c_p dT_s \tag{14}$$

the crystal content of the basalt:

$$x_b = \frac{(T - T_b)}{200} \tag{15}$$

the gas mass fraction of the basalt:

$$n_b = n_0 - sP^{1/2}(1 - x_b) \tag{16}$$

the pressure of the chamber in terms of the volume of basalt and silicic magma, and the compressibility of the crust:

$$dP = -\beta_c \frac{dV_b + dV_s}{V} \tag{17}$$

the mass of the basalt:

$$M_b = \rho_b V_b \rightarrow dV_b = -V_b \frac{d\rho_b}{\rho_b} \tag{18}$$

the density of the basalt:

$$\rho_b = \left(\frac{n_b R T_b}{P} + \frac{(1 - n_b)}{\rho_{bm}} \right)^{-1} \tag{19}$$

Combining these equations leads to the overall relation between pressure and temperature of the basalt:

$$\left[\frac{V}{\beta} + \frac{V_b}{\rho_b} \frac{d\rho_b}{dP} + \frac{V_s}{\rho_s} \frac{d\rho_s}{dP} \right] dP = \left[\frac{V_b}{\rho_b} \frac{d\rho_b}{dT_b} - M_b \frac{V_s}{M_s \rho_s} \frac{d\rho_s}{dP} \right] dT_b \tag{20}$$

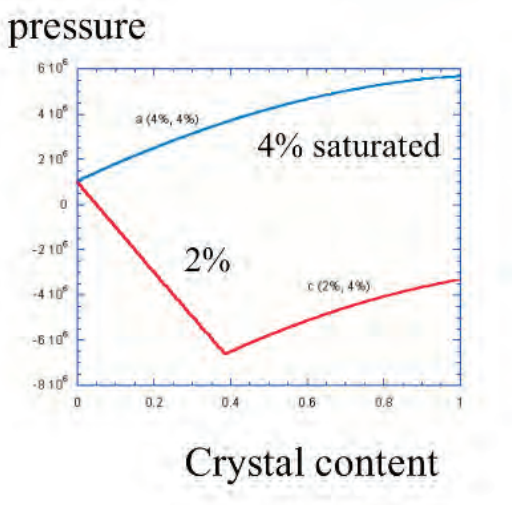

Figure 8: Different behavior for wet new magma (blue) and dry new magma (red):

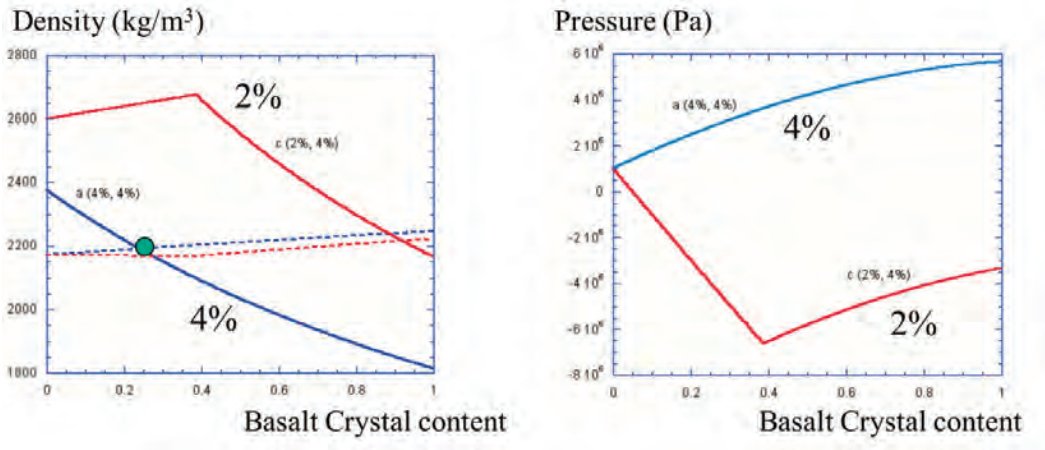

Figure 9: Density and pressure for saturated magma (blue) and initially unsaturated magma (red) to basalt crystal content. Density is higher in saturated magma case (left) but pressure increases for more hydrated magma. Eventually the unsaturated magma becomes saturated and that magma then follows a similar trend as the blue saturated magma

We analyze now how an eruption can be triggered by mixing.
If the two magmas become of comparable density, there will be an overturn event, and the magmas may mix. The basalt then cools, crystallises and generates more bubbles, starting a pressure increase. The maximum pressure increase is shown by the vertical black arrow in Fig(10b).

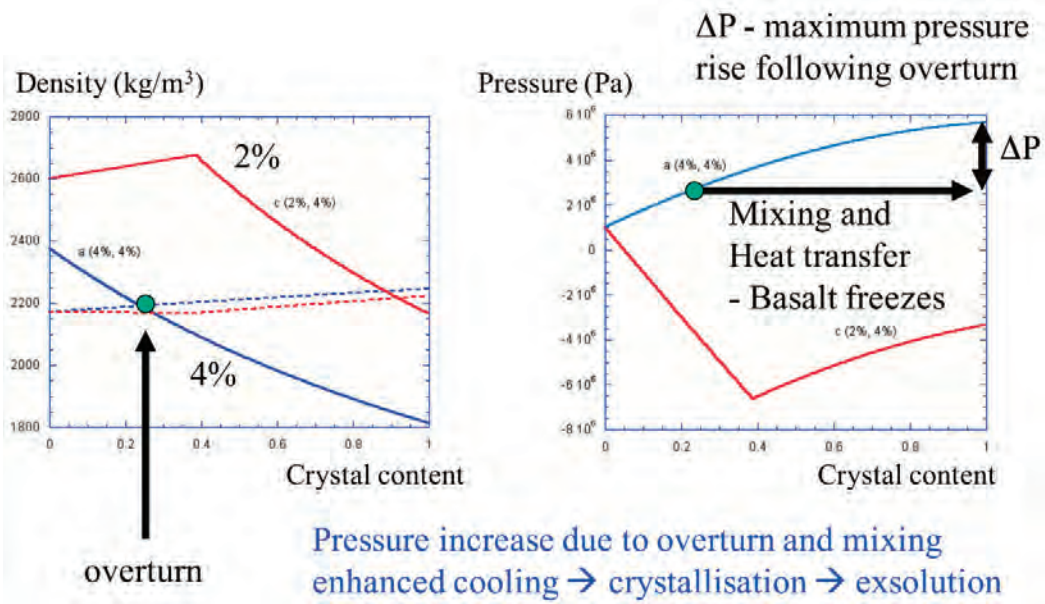

Figure 10: Evolution of density and pressure in terms of crystal content due to overturn and mixing.

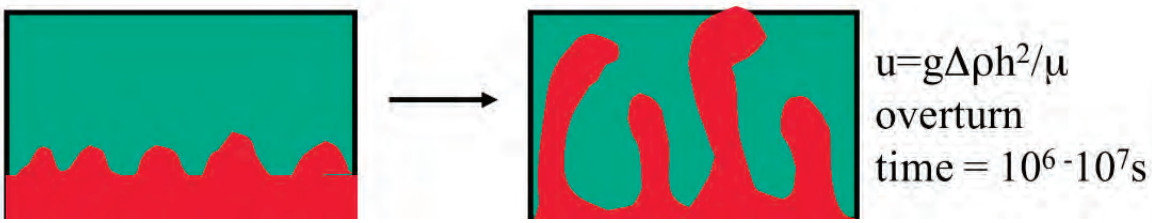

Figure 11: Overturn giving rise to Rayleigh-Taylor instabilities.

Laboratory experiments to reproduce this behavior have been developed as shown in Fig.(12)

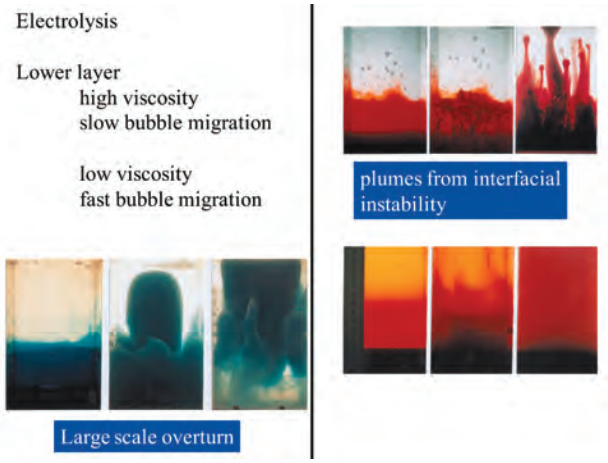

Figure 12: Laboratory experiments showing the Rayleigh-Taylor instabilities rise.

The cooling of the magma can be quantified in terms of a turbulent Rayleigh number as below.

$$\begin{aligned} \left[\rho C_p + \rho L \frac{dX}{dT}\frac{dT}{dt}\right] &= -F \\ u_{diff} &\sim \frac{k}{H} \\ u_{conv} &\sim \frac{g\alpha\Delta T H^2}{\nu} \\ Ra = \frac{u_{conv}}{u_{diff}} &= \frac{g\alpha\Delta T H^3}{\nu\kappa} \end{aligned} \tag{21}$$

where the Rayleigh number indicates the strength of convection.
If $Ra \gg 1$ the convection dominates and the heat flux is expected to be depth independent:

$$F \sim \lambda \frac{\rho C_p \kappa \Delta T}{H} Ra^{1/3} \tag{22}$$

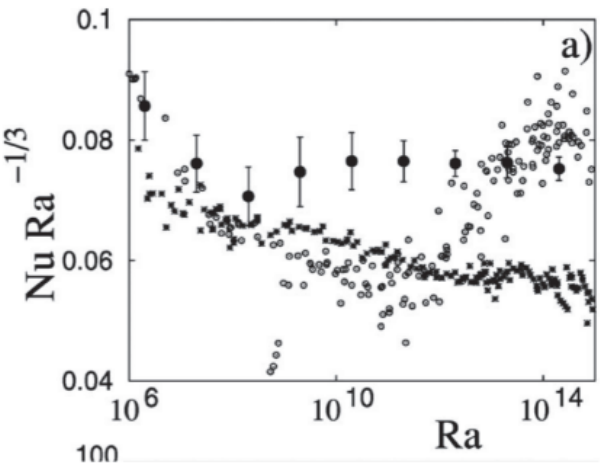

Figure 13: Behavior of heat flux for high Ra numbers.

where the cooling and the buoyant time are :

$$\begin{aligned} \tau_c &= \left(\frac{\kappa\nu}{g\alpha H^3 \Delta T}\right)^{-1/3} \frac{HL}{\lambda\kappa C_p}\frac{dX}{dT} \\ \tau_{buoy} &= \frac{H}{v_s} \end{aligned} \tag{23}$$

and it's possible to define two different regimes:
if $\tau_c \gg \tau_b$ plumes dominate
if $\tau_c \ll \tau_b$ overturn dominate

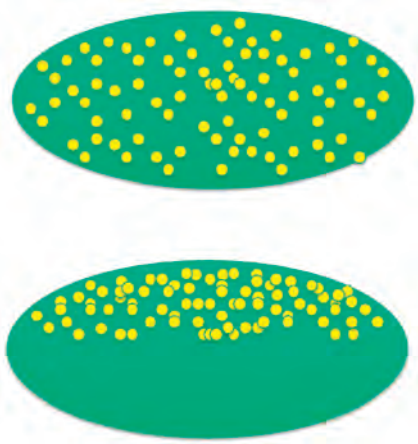

Figure 14: Ascent of bubbles in a magma chamber leads to large increase of pressure, making eruption more likely.

4 Bubble Ascent and Eruptions

Bubble ascent of gases in magma can lead to pressurization of the volcanic system. A diagram showing bubble rise is presented in Figure 14. Using the ideal gas law and assuming an elastic crust, the pressure increase with bubble rise can be calculated. Mass is conserved in the magma-bubble system. The subscript b represents gaseous parameters and m represents magma.

The system of equations is as follows

$$p = \rho RT \qquad \text{ideal gas law} \tag{24}$$

$$\frac{dV}{V} = \beta_c dp \qquad \text{elastic crust, } \beta_c \text{ is crust compressibility} \tag{25}$$

$$p(z) = p(H) + \rho_m g(z - H) \tag{26}$$

$$\rho_b(H) = \rho_b(z)\left(\frac{p(H) + \rho_b g(z - H)}{p(H)}\right) \tag{27}$$

$$d(\rho_b V_b) = -d(\rho_m V_m) \qquad \text{conservation of mass} \tag{28}$$

By solving these equations and accounting for the ascent of bubbles through the magmas we find that a 100 m ascent of bubbles generates an increase in pressure of 9-10 M Pa, leading to eruption.

5 Eruption Duration

The eruption of magma from a single chamber may be modeled using a simple linear arrangement using a friction factor, f, to capture frictional losses as the plug of magma rises in the conduit to the surface vent. For a single chamber, there is an exponentially waning eruption rate with time, $V_e(t)$. A schematic for a single chamber eruption is shown in Figure

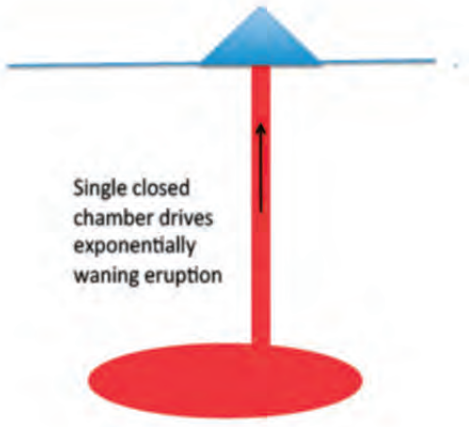

Figure 15: The volume of erupted fluid from a single chamber can be modeled using a single exponential decay function.

15.

$$\Delta V = \beta_m V_0 \Delta P \tag{29}$$

$$\frac{d(\Delta V)}{dt} = -f\Delta p \tag{30}$$

$$V_e(t) = \beta_m \Delta P_0 \left(1 - \exp^{-\frac{ft}{\beta_m V_0}}\right) \tag{31}$$

Eruptions that involve multiple chambers of magma may involve the draining of the chambers in succession, and this leads to multiple exponential functions to model the evolution of the eruption. For example, multiple chambers erupted within the Icelandic Volcano Eyjafjallajökull: deeper chambers erupted in response to the decompression caused by eruptions from higher chambers. A diagram detailing the eruption cascade of Eyjafjallajökull is shown in Figure 16. A schematic of a multi-chamber eruption is shown in Figure 17.

6 Crystal Yield Stress

During eruptions the formation of a volcanic plug regulates the rate of eruption. In a crystal pack the yield stress develops when the crystals are all in contact. A critical stress is necessary to create movement of the very viscous plug that forms, which has a viscosity to the order of 1 Pa·s. Cracking of the crystalline layer can produce paths for bubbles to de-gas, decreasing the pressure of the system. See Figure 18.

7 Eruptions: Ash Clouds vs. Pyroclastic Flows

Tall columns of ash can be generated if eruption speeds are sufficiently fast, forming what is called a Plinian eruption column. Buoyant plumes of hot ash from erupting volcanoes

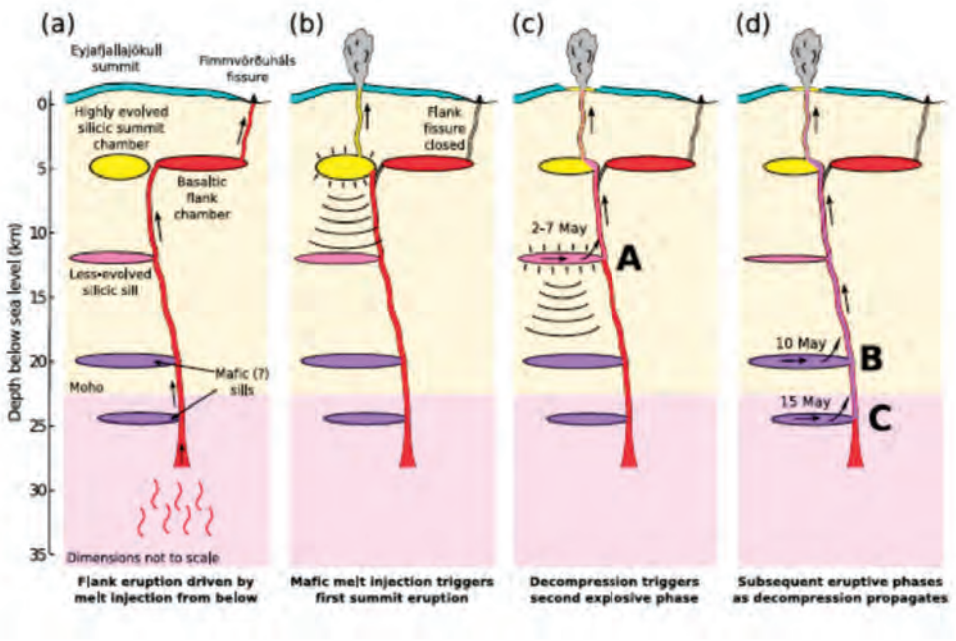

Figure 16: Ongoing eruption at Eyjafjallajökull: subsequent eruption phases began in deeper magma chambers as the decompression from prior eruptions propagated deeper into the Earth.

can rise over 40 km into the atmosphere. The flux supplying these columns is in the range of $10^6 - 10^9$ kg/s. The temperature is very hot at 1000-1200 °C. The particulate ash or pumice carried by the plume can be as small as microns, ranging from $10^{-6} - 10^{-2}$ m in size. The height of rise of eruption columns, such as those shown in Figure 19, depends on the eruption rate, atmospheric stratification, the thermal energy difference between the plume and the surrounding air and the water composition of the atmosphere.

For the case of a small exit velocity or large mass flux, the erupted material will fall back to the ground and spread laterally, forming a pyroclastic flow. Fountains that have collapsed and are traveling laterally can sometimes become buoyant after mixing with the cooler ambient air. The ash particles can rise up into the atmosphere many kilometers away from the source. This occurred in the 1980 eruption of Mount St. Helens after the ash flow traveled about 15 kilometers from the source before lifting off the ground. Ash clouds then intrude laterally into the atmosphere once thermal equilibrium between the particles and environment is achieved. Large, lateral clouds of ash are swept down wind and can rain down on surrounding areas for weeks or months after initial eruption.

7.1 Simplified approach: Estimating intensity of eruption

The height of the plume comes from the classical plume model. Ambient stratification, N, relative to adiabat provides scaling for height of column rise, H, as

$$H = 5B^{1/4}N^{-3/4}. \tag{32}$$

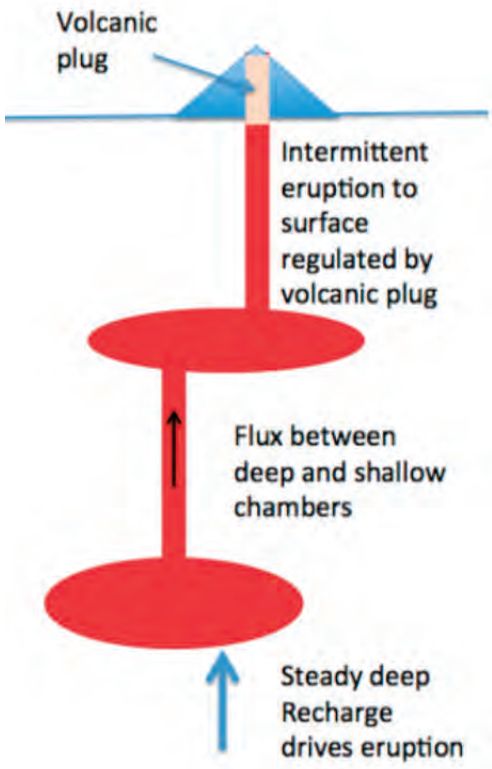

Figure 17: Viscous volcanic plug forms at vent during eruption. Deep recharge drives the ongoing eruption.

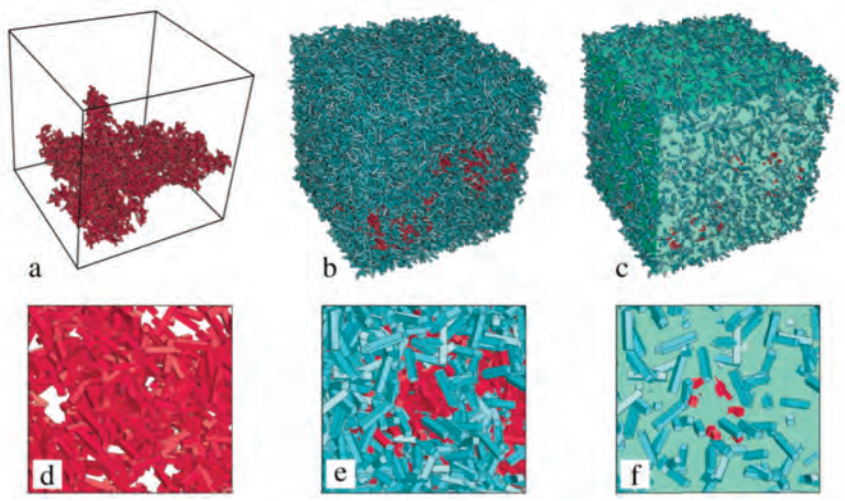

Figure 18: The formation of a crystal pack via simulation: the yield stress develops when the crystals are all in good contact, as shown in panels a and d.

Figure 19: Eruption columns of hot ash rise high up into the atmosphere.

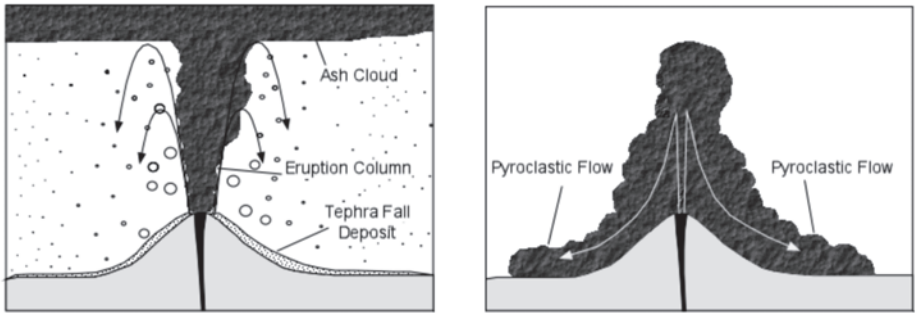

Figure 20: Left: a plume rises high up into the atmosphere and sediments fall out as the column rises. Right: a pyroclastic flow occurs when a fountain occurs at the vent.

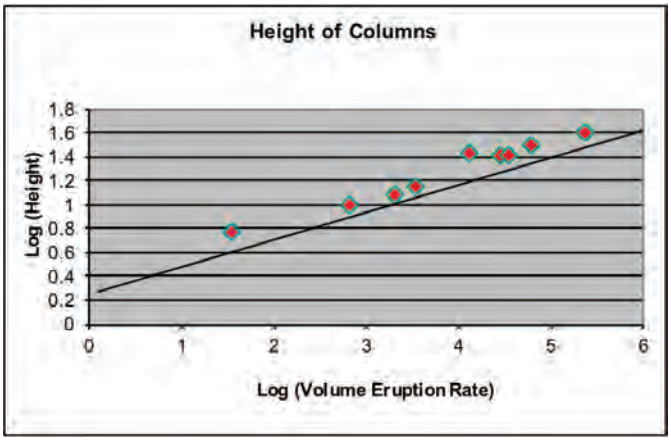

Figure 21: Column height versus eruption rate.

Buoyancy flux is not conserved generally since density doesn't vary linearly with temperature. Thermal and potential energy is conserved. Therefore, the effective buoyancy flux is given as

$$B = g(\alpha \Delta T)V_{eff} = \frac{Q_H g}{(\rho C_p)_a T_0}, \tag{33}$$

where $(\rho C_p)_a$ is the thermal capacity of the atmosphere. Data fits the model well even though the model does not capture the variation in stratification experienced as plumes rise in the atmosphere, as shown in Figure 21.

Explicitly accounting for heat exchange and particle content, whether a plume or ground flow forms can be predicted. Thermal equilibrium occurs over a fast time scale, about 100 s. Moisture is key only in small plumes, and larger particles fallout of the rising cloud. Mass conservation is,

$$\frac{dQ}{dz} = 2\pi \epsilon u \rho_a b, \tag{34}$$

where ϵ is the entrainment coefficient, u is the velocity, and b is the radius. Conservation of momentum is,

$$\frac{dM}{dz} = g(\rho - \rho_a)b^2. \tag{35}$$

Heat flux balance with temperature θ is given by the steady flow energy equation,

$$\frac{d[Q(u^2/2) + gz + C_p\theta)}{dz} = 2\pi \epsilon u b(gz + C_p \theta_a). \tag{36}$$

Density of the mixture is,

$$\rho = \left[\frac{nRT}{p} + \frac{1-n}{\rho_m}\right]. \tag{37}$$

The gas and air budget is,

$$\frac{dnQ}{dz} = 2\pi \epsilon u \rho_z b. \tag{38}$$

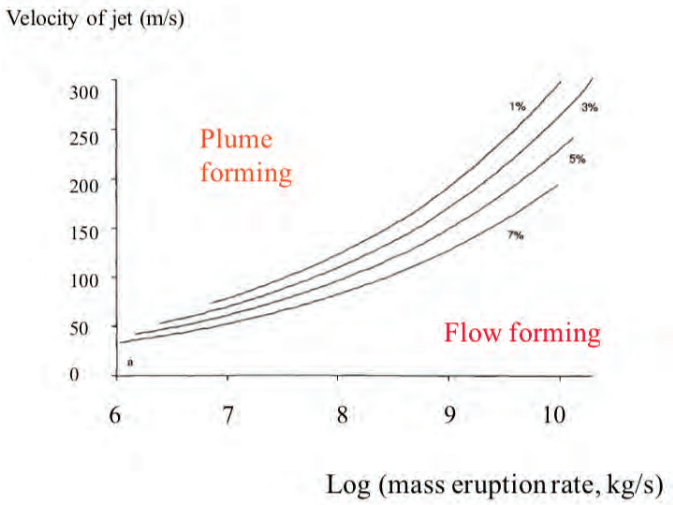

Figure 22: Higher eruption velocities form plumes while lower velocities tend to form ash flows.

Finally, the mass and momentum fluxes are familiarly written as,

$$Q = \rho u b^2 \tag{39}$$

$$M = \rho u^2 b^2. \tag{40}$$

A fast initial speed creates a buoyant plume that rises, but a slower plume becomes an ash flow, as shown in Figure 22. This is because the erupting mixture is initially a dense particle-laden flow, but as the mixture entrains air, the density decreases. If the mixture entrains sufficient air it will become buoyant prior to the momentum falling to zero. Otherwise the material will collapse to the ground and form an ash flow.

The height of the plume as a function of density and velocity can also be predicted. See Figure 23. Once the thermal energy from the cloud has been exhausted, the cloud stops rising and spreads laterally. At the top height adiabatic expansion occurs in the cold atmosphere. This is what happened with the Mount St. Helens eruption of 1980: a large ash cloud reached a top height and spread laterally, raining out particles over the Northwestern United States, as shown in in Figure 24.

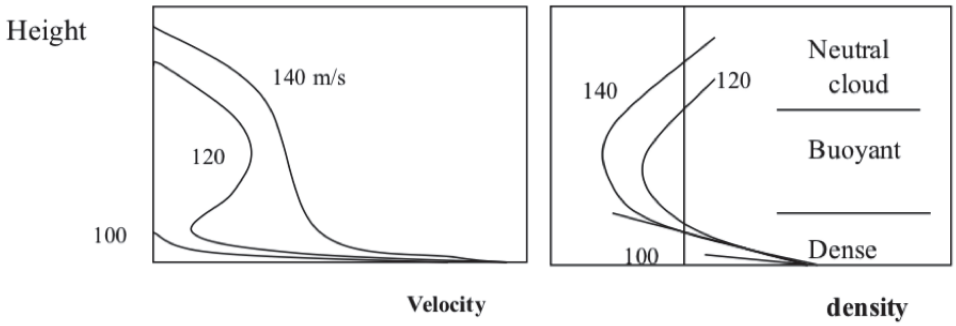

Figure 23: Height related to plume density and velocity.

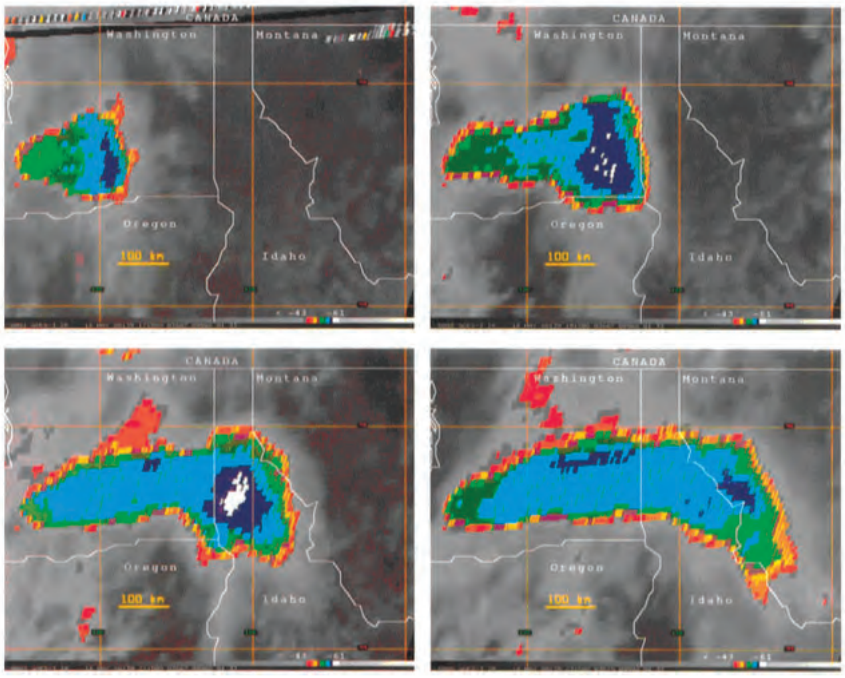

Figure 24: A neutrally buoyant cloud of ash from the Mount St.Helens eruption in 1980 travels across the Northwestern USA, distributing ash over the landscape as particles fall out.

References

[1] P. D. Cole, P. J. Smith, A. J. Stinton, H. M. Odbert, M. L. Bernstein, J. C. Komorowski, and R. Stewart, *Chapter 5 vulcanian explosions at soufrière hills volcano, montserrat between 2008 and 2010*, Geological Society, London, Memoirs, 39 (2014), pp. 93–111.

[2] D. Sher and A. W. Woods, *Experiments on mixing in pyroclastic density currents generated from short-lived volcanic explosions*, Earth and Planetary Science Letters, 467 (2017), pp. 138 – 148.

Lecture 7
Volcanic Plumes and Porous Rock

Notes by Edward Hinton and Bowen Zhao

June 26, 2018

1 Volcanic Plumes

Volcano eruptions could inject ash well above the troposphere; for example, some eruptions could reach as high as 35km, about three times the height of a commercial airplane's flight. The aim is to understand how these materials reach such a height. Sometimes large eruptions rise continually higher into the atmosphere, spreading out and forming ash clouds (Fig.1 left), while other times the material coming out from volcano rises but subsequently collapses to form a catastrophic flow (Fig.1 right).

Figure 1: Example of volcano eruption.

We begin with the case in which material rises as a dense fountain composed of particles and relatively buoyant fluid. In the lab we can take a tank full of salt water and inject a fresh water-particle mixture where the mixture is more dense than salt water. The mixture comes out as a fountain but as it rises up particles moving with its fall speed may start separating from the fluid. There are two characteristic speeds in these experiments: one is the fall speed of particles while the other one is the rise speed of the fountain.

Depending on the particle size (fall speed), the fluid could undergo full collapse or partial collapse. In situations where we have tiny particles, the particle fall speed is extremely small while the fountain speed is higher so the flow behaves as a single-phase fluid. In other situations, the initial particle fall speed is greater than the fountain speed. As we talked about, the fountain is driven by its initial momentum and would gradually slow down to the characteristic fountain speed. If the characteristic fountain speed is less than the particle fall speed, particles would start separating from the fluid before reaching the total height.

After the separation, particles would necessarily start to fall out at some height whereas the fluids, now being fresher than the ambient salt water and hence buoyant, would continue rising up. The separation thus reverses the buoyancy of the flow and the flow subsequently rises up.

We can conduct a series of experiments where we gradually increase the concentration of water in the salt (and hence the density), or equivalently increase the number of particles in the fresh-water-particle mixture but keep the mixture denser than the salt water. Starting from a case where the flow fully collapses, at some point we would reach the situation where only a certain fraction of the particle falling out is sufficient to make the rest of the flow buoyant. In this case, some of particles would fall out while the rest of the mixture would become buoyant and carry on rising. If we measure the fraction of particles that rise above some specific height in this series of experiments, we see full collapse below some critical salt content while above this critical salt content, a greater and greater fraction of the particles rise in the fountain. The key feature of this multiphase flow is that some particles rise and others drop out.

But this is not the whole story; one thing that is missing in the previous simple setup is entrainment: the effect of entrainment in an ash flow. In volcanic eruptions, the rising flow is very, very hot; the air entrained into the flow would be heated up, which would generate additional buoyancy and change the whole dynamics. In above experiments, we fixed the buoyancy of the injected freshwater. To conduct an analogous experiment considering entrainment, we would need to use the lemonade or sprite approach that we talked about for the ash flow: when mixing takes place, we can see bubbles generated and then we can examine how the fraction of rising particles changes.

In a real volcanic system, one also needs to worry about the size distribution of particles as well. Just to illustrate some of the complexity of the real system, we now look at a fountain with two sizes of particles; again inject the mixture of freshwater and smaller and larger particles into the salt water. We can tune the density of salt water to reach a situation where large particles falling out completely compensates the negative buoyancy and the rest of the mixture become neutrally buoyant. If we decrease the salt water density such that losing large particles is not enough and hence both large particles and small particles would collapse.

Next let's do some dimensional analysis to look at some details of the volcano system. The key question we want to address is how high volcanic eruptions can arise. Denote the ambient atmospheric stratification relative to the adiabat (i.e. the well mixed plume) as N. If the atmosphere stratification is neutrally buoyant relative to the adiabat then the plume can rise up without any penalty. Dimensional analysis then predicts that the height of rise (H) is proportional to the buoyancy flux (B) and inversely proportional to the ambient stratification N as $H = 5B^{1/4}N^{-3/4}$. As the volcanic plume (rocks and ashes) is very dense and hot at eruption and certainly not buoyant, it is not trivial to obtain the buoyancy flux B. However we notice that the heat flux is conserved. In fact, the heat flux is what allows the plume to rise high: as the ash transfers heat to the entrained air, the plume density is reduced enough to be able to rise up. So we can estimate the effective buoyancy flux in terms of heat flux. Recall that $B = g(\alpha\Delta T)V_{eff}$, where V_{eff} is the plume volume. For air with small temperature variations, we can show that its thermal expansion coefficient α is

just $\frac{1}{T}$:

$$\rho = \frac{P}{RT} = \frac{P}{R(T_0 + \Delta T)} = \frac{P}{RT_0}(1 - \frac{\Delta T}{T_0}) = \rho_0(1 - \alpha\Delta T)). \tag{1}$$

Therefore without worrying about details of the source, the effective buoyancy flux $B = g\alpha\frac{Q_H}{(\rho C_p)_a} = \frac{gQ_H}{(\rho C_p)_a T_0}$, where $(\rho C_p)_a$ denotes the density and heat capacity for air. The heat flux of the volcano eruption is just product of the volume flux, the specific heat capacity, the density and the actual temperature. So we can relate rise height and eruption rate. If we plot the measured historical volcano eruption height versus the volume flux on a log-log plot, we would find the slope to be roughly 1/4 (Fig.2). There is no account of stratification and many approximations are involved to get the eruption rate and so on yet the model seems to capture the general picture quite well.

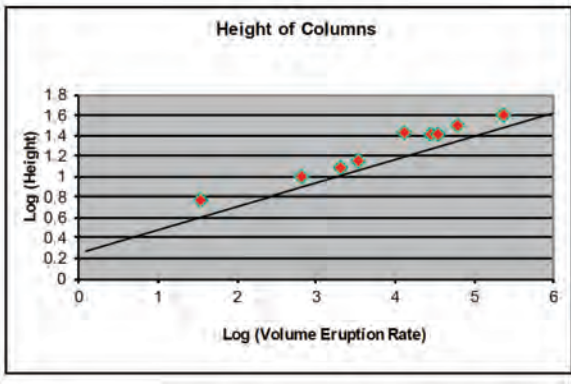

Figure 2: Historical volcano eruption height versus eruption rate.

If we want to a little more details, we can try to develop a plume model for volcano eruptions. First, we will relax the assumption of the entrainment coefficient being constant but still assume the flow property evolves sufficiently slowly so it would keep the self-similar structure although the self-similar structure will evolve with height. Then we have the following set of equations:

$$\begin{aligned}
\frac{d}{dz}Q &= 2\pi\epsilon u\rho_a b \quad \text{(mass conservation)} \\
\frac{d}{dz}M &= g(\rho - \rho_a)b^2 \quad \text{(momentum conservation)} \\
\frac{d}{dz}Q(\frac{u^2}{2} + gz + C_p\theta) &= 2\pi\epsilon ub(gz + C_p\theta_a) \quad \text{(energy\ heat flux balance)} \\
\rho &= [\frac{nRT}{P} + \frac{1-n}{\rho_m}]^{-1} \quad \text{(density of mixture)} \\
\frac{d}{dz}nQ &= 2\pi\epsilon u\rho_a b \quad \text{(gas and air budget)}
\end{aligned} \tag{2}$$

where $Q = \rho ub^2$ and $M = \rho u^2 b^2$ as before. Note that we used volume conservation before but it's better to use actual mass conservation for a plume rising to above 30km. The

plume mass change is due to entrainment of air (ρ_a). The momentum also changes due to the buoyancy force. The energy would also change due to the energy associated with entrained air. Also note that the particle flux is constant but the gas flux is increasing due to the entrainment of air. It might be worthy to point out that the increase rate of total mass and of gas fraction mass is the same, both due to entrainment of air (the RHS of first and last equation are the same).

There are some key assumptions made in the above set of equation. First, thermal equilibrium is assumed. Since the plume rise time is ∼100s while the heat transfer time for typical volcano particles (<1mm) is $\lesssim$1s, this assumption is valid. Second, we ignored moisture and associated latent heat release in the atmosphere. For big eruptions reaching 30-40 km, their heat budget far exceed the latent heat of moist convection so we can ignore the moisture to leading order. However, for small eruptions that only reach a few km such as those on Hawaii, clouds and moist convection can be triggered by the volcanic heat flux so we do need to worry about latent heat. Third, we ignored particles falling out. As we have seen in above experiments, big particles may fall out near the bottom and not all particles will rise up. Lastly, we did not consider aggregation.

Some aspects of the solution is shown in Fig. 3. As we can see, holding everything else fixed, the velocity change with height is different for different initial speed. Flow with a very high initial speed (say 140 m/s) would experience a monotonic decrease in velocity as it rises. There is a very rapid deceleration initially, then the flow decelerate much more slowly while later the flow decelerate very rapidly again. The density of the flow is also changing: very dense initially, become buoyant later while finally become denser than the ambient again (note relative density with respect to the air is shown). What happens is that the volcano plume just came out is very dense and hence decelerate rapidly; as the plume rise, it entrains a lot of air and decreases its density and becomes buoyant. The slow deceleration part in the velocity profile corresponds to the buoyant plume, whose velocity decays as $v \propto \frac{1}{z^{1/3}}$ as we showed. The buoyant plume finally reaches its neutral height with respect to the ambient stratification and starts to decelerate until stops. If the flow has a much smaller initial speed (say 100 m/s), the flow would decelerate as it becomes less and less dense until finally stops. In this case, the flow behaves like a fountain throughout the whole process and then collapses to form a ash flow. In between these two cases, the flow (say 120 m/s) would decelerate till almost zero velocity and then accelerates as it becomes buoyant due to entrainment of air; finally it decelerates due to the ambient stratification. We can summarize with the plot of speed versus flux (Fig. 3 bottom right). For a given flux, we can predict that there exists a critical speed such that below the critical speed we get an ash flow while above it we get an eruption plumes. Looking at the graph the other way around, for a given speed increasing the flux makes the flow more tend to collapse and form an ash flow. This is because entrainment only happens at the surface; it is more difficult for the flow with larger fluxes to entrain enough air before the fountain runs out of its momentum and hence more possible to collapse. Thus there seems to exist a paradox: bigger eruption actually tends to collapse although you might expect the opposite.

We can also employ the model to explain observations about volcano eruptions. People have been looking at the satellite images of plumes to derive plume top temperature. Assuming the plume temperature same as its ambient, people then work out the plume top height and predict the position of ashes in the atmosphere. However, sometimes they

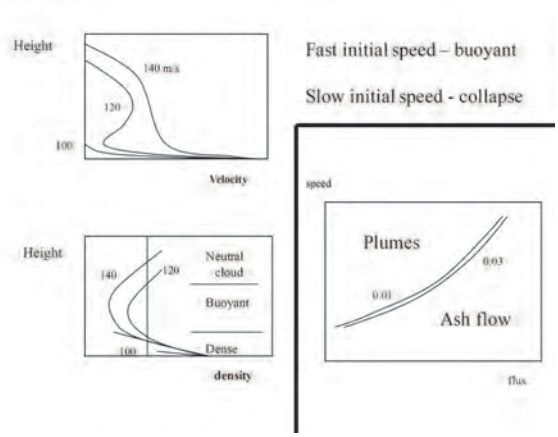

Figure 3: Solutions for the plume model. (Left top) Velocity of volcanic plumes with height for different initial speeds and (left bottom) their normalized densities with respect to the ambient. (Right) The initial speed of plumes versus the mass flux. Numbers in the left column denote initial speed while numbers in the right column denote the gas mass in the magma.

would yield two different height predictions while other times they observed plume temperature colder than anywhere in the atmosphere. For example, Fig. 4 shows the satellite image of Mt St Helens eruptions, where the plume top temperature is colder than anywhere in the atmosphere. The plume model can however resolve this puzzle. According to the model, the plume temperature decreases as it entrains air and reaches its neutral buoyancy (density) height at some point. To compensate for the heavy particles in the flow, the flow temperature is actually a little higher than the atmosphere temperature at its neutral density height. Then the flow would overshoot and cools almost adiabatically; meanwhile the atmosphere temperature stops decreasing at the Tropopause and starts increasing in the stratosphere (Fig. 4 left bottom). The plume top temperature thus is decided by the overshoot distance and can fall below the ambient temperature. As the ash clouds start spreading into its ambient, its temperature would become more and more similar to the ambient temperature, at which point the ambient temperature could be used to predict the plume height.

2 Flow in Porous Rocks

The type of questions we will address here include oil recovery challenges, carbon sequestration, geothermal power production and Mixing. To put the oil recovery problem into context, it is helpful to remind us that we currently face tremendous energy challenges. Fig. 5 shows that oil and natural gas have supplied more than half of the global energy consumption and will continue so for the next several decades. However, it is more and more difficult to get the oil and natural gas out of the ground at least in part because we don't understand well the fluid mechanics governing the flow underground.

The challenges of oil recovery arise from facts that oil is viscous relative to water, that

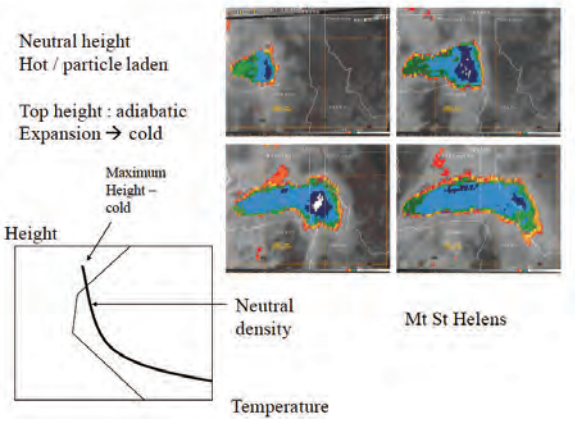

Figure 4: Satellite observation of temperature for Mt St Helens eruption.

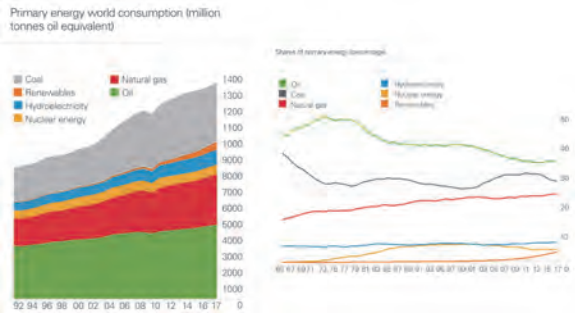

Figure 5: Historic energy consumption by energy source types.

oil is trapped by capillary forces and that rock is faulted and layered (compartments) and also that shale baffles in deposit. It is however difficult to get data; we only have low-resolution (20-30m) data inverted from seismic reflection measurements and sparse samples from drilled wells (of order 0.1-1.0 km apart and ∼150 mm in diameter).

Based on these data, people have to estimate how much oil exists and how much oil can be recovered from an oil filed (see Fig. 7 bottom right for a typical oil field). Next, they have to develop an extraction Strategy. The work flow thus include gathering data to generate pictures of the field, which is largely uncertain, building model of flow based on force and mass balance and testing scenarios with different well-placement and flow rates etc.

As oil is about three times as compressible as water, they can just drill a well and suck out the oil; 8-9% oil can be generated in place simply from decompressing the oil. To get more oil, people would inject water at one well and extract oil at second well after some time (Fig. 6). Fig. 6 (bottom) shows the flow rate measured at a production well, which reveals that at some point water would come out along with oil.

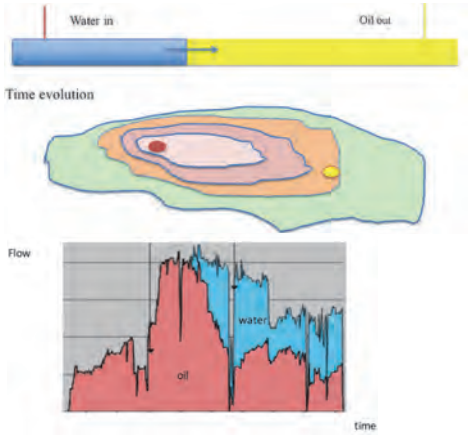

Figure 6: Oil extraction schematic.

The industry works on porous media have enormous supercomputers to simulate things in great details (Fig. 7 top right), then what we can contribute by doing GFD-type, simple analysis on subsurface flows in porous media? The problem is that they have tremendous data gap especially away from the well (Fig. 7 left). This is where understanding of fluid mechanics can play a role: we can parameterize the structures and look at the sensitivity of predictions to these structures.

Considering the complexity of rock structures and multiple scales involved in the problem, we would need a composite model: a continuum model for a single layer and a series of continuum layers on large scales, maybe also some faults cutting through the layers. In the porous media flow, it is more convenient to work with the flux velocity u ("Darcy velocity") than the actual fluid velocity v:

$$u = \frac{1}{A}\int v\phi dA, \tag{3}$$

where ϕ denotes porosity. Note that tracers or temperature in the porous media would move with the fluid velocity v instead of flux (volume) velocity u (more on this later). Flow

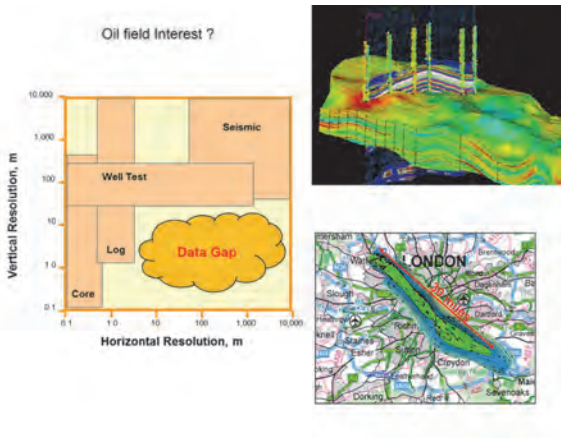

Figure 7: Oil extraction schematic.

in the porous media is governed by "Darcy's Law":

$$u = -\frac{k}{\mu}\nabla P, \tag{4}$$

where k is the permeability. This is just a low Reynolds number limit of Navier-Stokes equation. The typical Reynolds number $\frac{u\delta}{\nu}$ in the porous rocks is about $10^{-8} - 10^{-11}$: the speed u is about $10^{-7} - 10^{-8}$ m/s, grain size δ is about $10^{-3} - 10^{-4}$ m, viscosity ν is about $10^{-1} - 10^{-2}$ m^2/s. The permeability k in real rocks is actually a tensor as it depends on both the direction of pressure gradient and the orientation of grains (anisotropic medium):

$$\boldsymbol{K} = \begin{bmatrix} K_{11} & K_{12} & K_{13} \\ K_{21} & K_{22} & K_{23} \\ K_{31} & K_{32} & K_{33} \end{bmatrix}; \mu u = -\boldsymbol{K} \cdot \nabla P. \tag{5}$$

However in the industry permeability is usually simplified to be a constant, $k = \frac{\phi^3 d^2}{180(1-\phi)^2}$.

Now let's look at a simple example to get a flavor of the challenge. Suppose we have two rocks of same size but different permeability (k_1, k_2). The two rocks are placed either in series or in parallel (Fig. 8). The flow in both scenarios can be worked out easily. Flow in series:

$$\begin{aligned} u &= \frac{k_1}{\mu L}(P_a - P_b) = \frac{k_2}{\mu L}(P_c - P_b) \\ u &= \frac{2k_1 k_2}{k_1 + k_2}\frac{P_a - P_c}{2\mu L}. \end{aligned} \tag{6}$$

Flow in parallel: pressure is continuous across layers

$$u = \frac{k_1 + k_2}{2}\frac{P_a - P_c}{2\mu L}. \tag{7}$$

Define permeability ratio $\alpha = \frac{k_2}{k_1}$, the effective permeability is thus $k_1\frac{2\alpha}{1+\alpha}$ and $k_1\frac{1+\alpha}{2}$ for flow in the series and flow in parallel, respectively. The results are compared in Fig. 8

(bottom). It is seen that flows in parallel are generally larger than flows in series. However in reality water comes out as well. In the case of "parallel", initially oil would come out quickly in the high permeability rock however water would soon come out in this rock too (Fig. 9 top two panels). So the total production rate would be large initially but decrease later (Fig. 9 middle blue line). While in the case of "series", oil would come out slowly but remain the same rate for a longer time (Fig. 9 bottom). Now if we further include the consideration of an economic model for value that decays exponentially with time, we can see that the case of parallel generate more values than the case of series (Fig. 10). But if we change the discount rate or the size of the field we may get one or the other case being more valuable: it is not clear a priori which one is better.

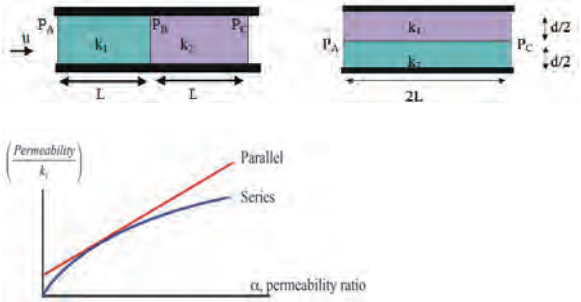

Figure 8: Simple flow in series versus in parallel.

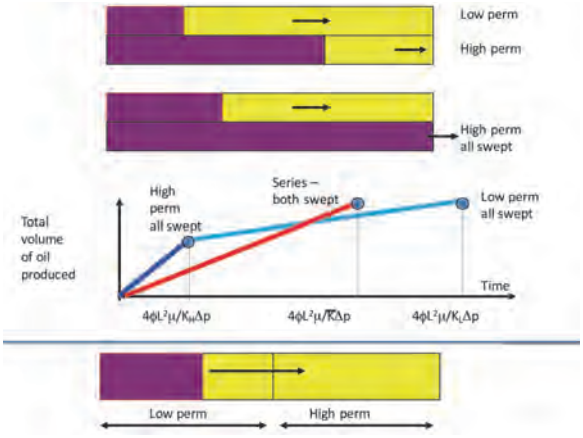

Figure 9: Flows in series versus in parallel.

Next, we can generalize this model to include multiple layers in parallel. Suppose we apply a pressure gradient across all these layers (each layer i with a depth h_i and permeability

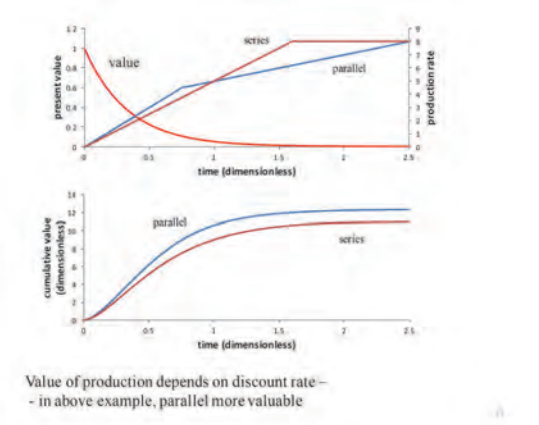

Figure 10: Flows in series versus in parallel.

k_i), then the total flow is given by

$$Q(total) = \frac{\sum h_i k_i}{\mu} \frac{dp}{dx} = \overline{u} \sum h_i. \tag{8}$$

The mean travel time, i.e. the time of flight for the center of mass is $\overline{\tau} = \frac{\phi L}{\overline{u}}$. Flow in layer i is given by

$$u_i h_i = \frac{k_i h_i}{\sum k_i h_i} Q, \tag{9}$$

and the time of flight for layer i is given by

$$\tau_i = \overline{\tau} \frac{h_i}{\sum h_i} \frac{\sum h_i k_i}{h_i k_i}. \tag{10}$$

To get an idea of the situation, let's assign random depths and permeabilities to 20 layers (Fig. 11). After we pump in some water, different fluxes of oil would come out of each layer, depending on the thickness and the permeability. As time goes on, each of these layers would progressively run out of oil. So we get less and less oil while more and more water (Fig. 11 bottom right). The low permeability layer would retain their oil for longer while the water shooting through high permeability layer would bypass the oil.

However, we do not know the depths and permeabilities of layers in reality. To handle on the uncertainty, let's randomly distribute permeabilities to five layers of equal thickness. We would pump one volume water (one volume of the reservoir size) and look at the time by when water arrives at the well (i.e. water breakthrough time). As we can see from Fig. 12, with a factor of 10 variation in permeabilities in each layer, we get a huge envelop of possible predictions. Note that a factor of 10 is a relatively small variation as $k \propto d^2$ (a factor of 3 variation in grain size would lead to a factor of 10 variation in k). This calculation illustrates the source of uncertainty in this simple example; with more complexity, we would expect more uncertainty.

Next, let's consider the effect of leakage through an impermeable layer or seal rock (such as a layer of clay) as shown in Fig. 13. Suppose we have a layer of seal rock with depth b

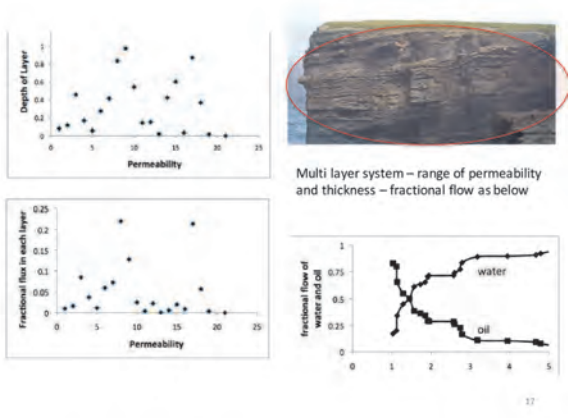

Figure 11: Flows in multiple layers in parallel.

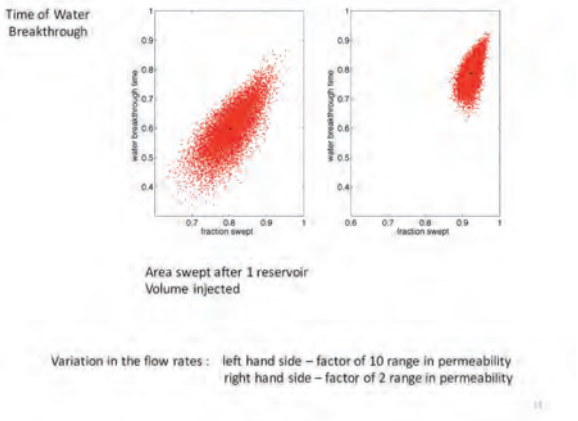

Figure 12: Water breakthrough time.

and permeablity k_b separating a permeable upper layer (h_u, k_u) and a permeable lower layer (h_l, k_l). If these layers are thin and long (i.e. $L \gg h \gg b$), we would expect a dominantly parallel flow which slightly leaks through the seal rock layer. We have "Darcy's Law" for both the upper layer and lower layer; however, the two pressure gradient might be different because of a lack of pressure communication. The pressure difference in the upper and lower layer would necessarily drive a cross-flow, also governed by "Darcy's Law". The governing equations are thus

$$\begin{aligned} u_u &= -\frac{k_u}{\mu}\frac{\partial p}{\partial x} \\ u_l &= -\frac{k_l}{\mu}\frac{\partial p}{\partial x} \\ \frac{\partial h_u u_u}{\partial x} &= -\frac{k_b}{\mu b}(p_u - p_l) \\ \frac{\partial h_l u_l}{\partial x} &= \frac{k_b}{\mu b}(p_u - p_l), \end{aligned} \tag{11}$$

where the last two equations are continuity or mass conservation equation applied to the upper layer and the lower layer, respectively. After some algebra, we get

$$\frac{\partial^4 p_u}{\partial x^4} - \frac{k_b}{b}\left(\frac{1}{h_u k_u} + \frac{1}{h_l k_l}\right)\frac{\partial^2 p_u}{\partial x^2} = 0. \tag{12}$$

It therefore follows that the leakage flux is function of a dimensionless number $\Gamma = \frac{k_b L^2}{\overline{bhk}}$, where $\frac{1}{\overline{hk}} = \frac{1}{h_u k_u} + \frac{1}{h_l k_l}$. For seal to be effective, we want $\Gamma \ll 1$ or $\frac{k_b}{k} \ll \frac{hb}{L^2}$. As shown in Fig. 13, for typical values of oil fields, Γ would vary over from 1 to 100, which implies either very effective or very ineffective seal effect.

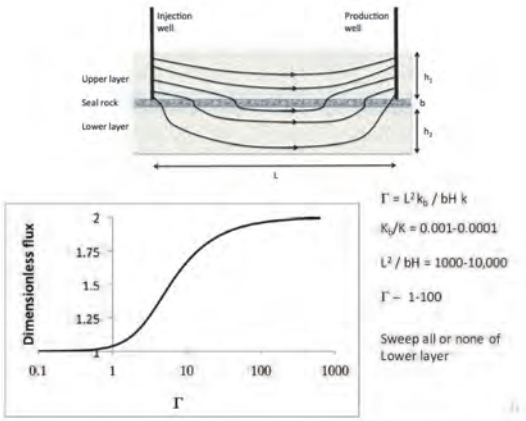

Figure 13: Seal rock.

The next complexity we want to address is that strata often align in different directions, which makes it nontrivial to calculate the effective permeability. Let's consider a simple example where the layer makes a θ angle to the pressure gradient force (Fig. 14), such that we have two characteristic permeability along the layer (k_1) and cross the layer (k_2). The

horizontal flow u is composed of a projection from along the layer direction $\frac{k_1}{\mu} P_x \cos^2\theta$ and a projection from cross the layer direction $\frac{k_2}{\mu} P_x \sin^2\theta$. Similar for the vertical flow. However, there cannot exist vertical flow due to the seal lock (assumed perfect seal for simplicity). That is, there must exist a vertical pressure gradient P_y, whose induced vertical flow exactly cancels the vertical flow from horizontal pressure gradient P_x. The set of governing equation are as follows:

$$\begin{aligned} u(P_x) &= \frac{1}{\mu}(k_1 P_x \cos^2\theta + k_2 P_x \sin^2\theta) \\ v(P_x) &= \frac{1}{\mu}(k_1 P_x \cos\theta \sin\theta - k_2 P_x \sin\theta \cos\theta) \\ u(P_y) &= \frac{1}{\mu}(k_1 P_y \sin^2\theta + k_2 P_y \cos^2\theta) \\ v(P_y) &= \frac{1}{\mu}(k_1 P_y \sin\theta \cos\theta - k_2 P_y \cos\theta \sin\theta) \\ v(P_x) + v(P_y) &= 0. \end{aligned} \tag{13}$$

After some algebra, we get

$$\begin{aligned} u &= \frac{P_x}{\mu}\left(\frac{k_1 k_2}{k_1 \sin^2\theta + k_2 \cos^2\theta}\right), \\ k_e f f &= \frac{k_1 k_2}{k_1 \sin^2\theta + k_2 \cos^2\theta}. \end{aligned} \tag{14}$$

The effective permeability $k_e f f$ is the average of k_1 and k_2 with geometric weighting. Fig. 14 (bottom) shows the ratio of $\frac{k_e f f}{k_1}$ as a function of angel θ.

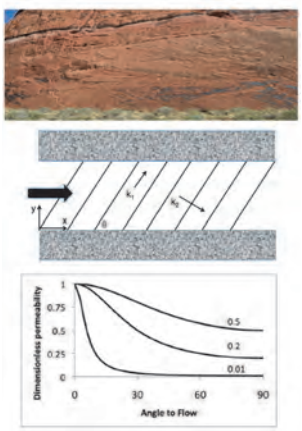

Figure 14: Seal rock.

These simple calculations are aimed to illustrate on the complexity of flows in porous rocks in the real fields.

Lecture 8
Porous Media Gravity Currents

Notes by Rohit Supekar and Tyler Lutz

June 27, 2018

1 Introduction

Sub-surface porous rocks are very heterogeneous. This is evident from the pictures of cliffs in figure (1). Notice the different strata along which the rocks are aligned. These layers typically have different values for their permeability and are separated by seals that have very low permeability. Sometimes, the seals can also have fractures across them that allow the leakage of a fluid. This heterogeneity in the structure becomes important in practical problems of oil extraction and Carbon sequestration. Carbon sequestration is the process of pumping CO_2 underground for its storage and reduction in the earth's atmosphere. The way CO_2 spreads in the porous rocks depends highly on the details of the heterogeneity. If the gas is being pumped into an aquifer, the CO_2 gas spreads laterally in the layers between seals and acts a gravity current. This is why the fundamental study of gravity currents in porous media is of importance to the practical problem of Carbon sequestration.

Figure 1: Photographs of vertical cross-sections of cliffs showing the different layers in which the rocks are arranged.

2 Gravity Currents in Porous Media

Consider a porous medium of permeability k containing an ambient fluid of density ρ_2. A fluid of density $\rho_1 > \rho_2$ spreads as a gravity current. We want to analyze the dynamics of this spreading gravity current. This configuration is shown as a schematic in figure (2).

As we have seen earlier, the momentum equations for flow in a porous medium are given by Darcy's law:

$$\boldsymbol{u} = -\frac{k}{\mu}(\nabla p + \rho g \widehat{\boldsymbol{z}}). \tag{1}$$

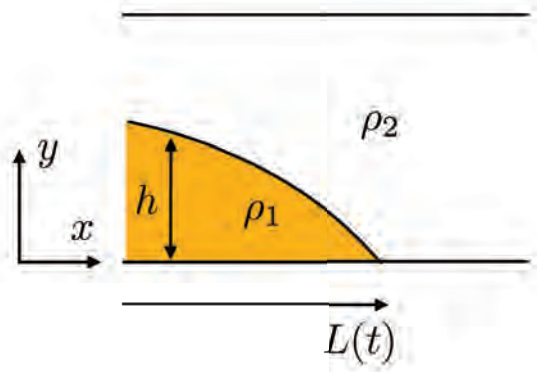

Figure 2: A schematic of a gravity current propagating in a porous medium. Here, the top and the bottom layers are assumed to be impermeable.

The continuity equation is given by

$$\nabla \cdot \boldsymbol{u} = 0. \tag{2}$$

For a long and thin gravity current, $H/L \ll 1$ which implies from the above equation that $v \ll u$. We can thus assume a hydrostatic pressure gradient in the vertical direction. The pressure is thus given by

$$P = P_H + \int_z^h \rho_1 g dz + \int_h^H \rho_2 g dz. \tag{3}$$

Substituting the above equation in the momentum equation, we obtain

$$u = -\frac{k}{\mu}(\rho_1 - \rho_2) g \frac{\partial h}{\partial x}. \tag{4}$$

Globally, we can write the following equation for conservation of mass

$$Q(t) = \int_0^{L(t)} dx \int_0^{h(x,t)} \phi dz, \tag{5}$$

where $Q(t)$ describes the change of the total volume in the gravity current which may also be assumed to be a constant in the case of a fixed volume release and ϕ describes the porosity of the medium.

The local equation for conservation of mass is as follows:

$$\phi \frac{\partial h}{\partial t} = -\frac{\partial}{\partial x}\left(\int_0^h u(x,z;t) dz\right). \tag{6}$$

Replacing u by the expression obtained from Darcy's law, we have

$$\frac{\partial h}{\partial t} = \left(\frac{k \Delta \rho g}{\mu \phi}\right) \frac{\partial}{\partial x}\left(h \frac{\partial h}{\partial x}\right). \tag{7}$$

Since there is no particular length scale in the problem, we can seek a similarity solution. We assume that the flow rate is changing according to the power law $Q(t) = Q_0 t^\gamma$ and try a solution of the form:

$$h(x,t) = \mathcal{H}(t/\tau)^\alpha f\left(\frac{x}{(t/\tau)^\beta \mathcal{H}}\right), \tag{8}$$

where the velocity scale is $S = \frac{kg\Delta\rho}{\mu\phi}$, the time scale is $\tau = \left(\frac{S^2}{Q_0}\right)^{\frac{1}{\gamma-2}}$ and the length scale is $\mathcal{H} = \left(\frac{Q_0}{S^\gamma}\right)^{\frac{1}{2-\gamma}}$. Substituting the above equation into equation (7), we obtain the following shape function that describes the shape of the gravity current:

$$3\frac{d}{d\eta}\left(f\frac{df}{d\eta}\right) = (2\gamma-1)f - (\gamma+1)\eta\frac{df}{d\eta}. \tag{9}$$

Here, $\eta = \frac{x}{(t/\tau)^\beta \mathcal{H}}$, $\alpha = \frac{2\gamma-1}{3}$ and $\beta = \frac{\gamma+1}{3}$. The boundary conditions are given by $f(\lambda) = 0$ and $\int_0^\lambda f(\eta)d\eta = 1$, where $\lambda = \frac{L}{\mathcal{H}}$ marks the leading nose of the gravity current.

We now consider the special case of a finite volume release. In this case, the parameters become: $\gamma = 0, \alpha = -1/3, \beta = 1/3$ and the shape function becomes

$$2\frac{d}{d\eta}\left[f\frac{df}{d\eta}\right] = -f - \eta\frac{df}{d\eta}. \tag{10}$$

The above equation has a simple solution given by

$$f(\eta) = (\eta_0^2 - \eta^2)/6, \tag{11}$$

where, to satisfy the boundary conditions, $\eta_0 = (9/\phi)^{1/3}$. In the dimensional coordinates, the height of the gravity current takes the following form:

$$h = \frac{H(t/\tau)^{-1/3}}{6}\left(\eta_0^2 - \frac{x^2}{H^2(t/\tau)^{2/3}}\right) \tag{12}$$

The current length is given by

$$L(t) = \eta_0 H\left(\frac{t}{\tau}\right)^{1/3} \tag{13}$$

Essentially, the height profile of the gravity current evolves through a series of parabolas, which is represented in figure (3). For further details about this problem, the reader is encouraged to read reference [1].

Porous media flows can be modeled in the laboratory with the use of a Hele-Shaw cell which is an apparatus that is made of glass slabs that are separated from each other with a very small gap. The flow along the gap of the Hele-Shaw cell is then directly proportional to the pressure gradient in the cell (due to viscous effects) and thus serves as a proxy for the porous media phenomena. Using such a Hele-Shaw cell, the results of a finite volume release of a gravity current are shown in figure (4). The similarity solution compares well with the experiments when the aspect ratio of the initial lock is 1:1.

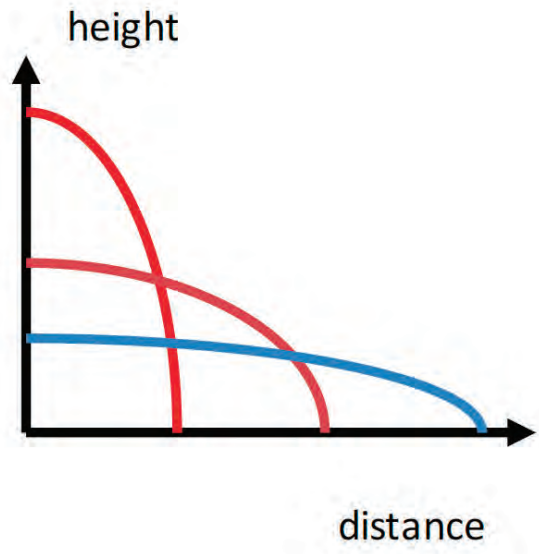

Figure 3: Evolution of the gravity current height as time progresses (from red to blue).

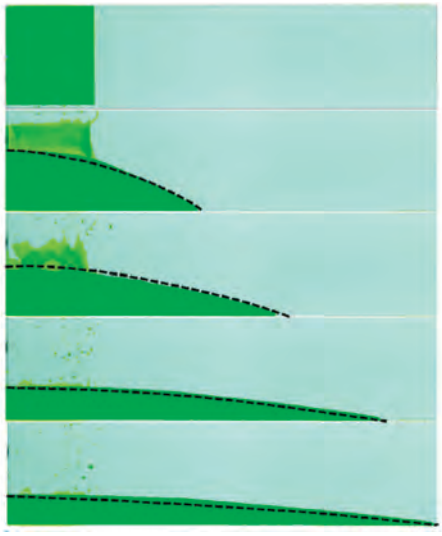

Figure 4: Evolution of a gravity current in a Hele-Shaw cell. The dotted lines indicate the theoretical height profiles.

2.1 Leakage

We will now consider the problem of porous media gravity current where the bottom surface has some leakage. This is relevant when the seals separating rock layers are partially permeable. The local equation for conservation of mass now becomes

$$\frac{\partial h}{\partial t} = S\frac{\partial}{\partial x}\left(h\frac{\partial h}{\partial x}\right) - \Lambda h. \tag{14}$$

Here, $\Lambda = \frac{k_b S}{kb}$, where k_b is the permeability of the background, k is the permeability of the lower layer, b is the width into the page and S is velocity scale we have encountered earlier. Λ parameter takes the leakage into account. The total volume in the current is given by

$$V = \phi \int_0^{L(t)} h(x,t)dx. \tag{15}$$

and due to the leakage, we have

$$\frac{dV}{dt} = Q(t) - \Lambda V. \tag{16}$$

Integrating, we get

$$V(t) = \exp(-\Lambda t)\left[V(0) + \int_0^t Q(t')\exp(\Lambda t')dt'\right]. \tag{17}$$

We now introduce a rescaled time τ given by $\tau = \frac{(1-\exp(-\Lambda t))}{\Lambda}$. The height profile of the gravity current is obtained as

$$h(x,t) = \frac{V(0)^{2/3}}{6S^{1/3}\tau^{1/3}}\exp(-\Lambda t)\left(9^{2/3} - \frac{x^2}{V(0)^{2/3}S^{2/3}\tau^{2/3}}\right), \tag{18}$$

and the length of the gravity current is given by

$$L(t) = \left[\frac{9V(0)kb}{k_b}(1-\exp(-\Lambda t))\right]^{1/3}. \tag{19}$$

As is clear from the above equation, the length asymptotically approaches a finite value, which happens due to the leakage in this problem. Comparison of this theoretical prediction with the experimental data is presented in figure (5). The slight deviation at long times occurs when the gravity current becomes too thin and viscous effects start getting important.

2.2 Two-layer gravity currents

The displacement of one fluid by a second through a porous layer is an important process in many natural and industrial flows through porous layers. It is of special interest for the oil industry in which polymer-rich water or gas may be injected into an oil field to enhance oil recovery.

We consider a problem of two immiscible fluids with different values for their density and viscosity. The schematic of this problem is shown in figure (6), which is taken from

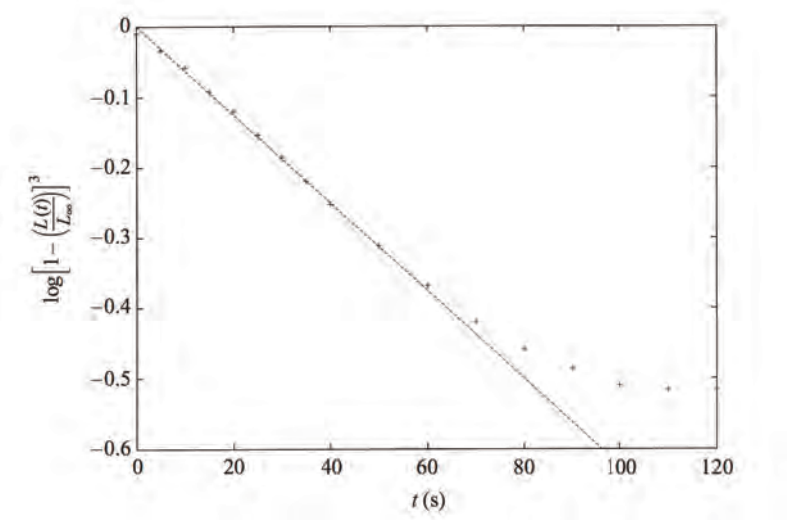

Figure 5: Experimental results by [2]. The markers indicate the experimental results and the solid line indicates the theoretical prediction.

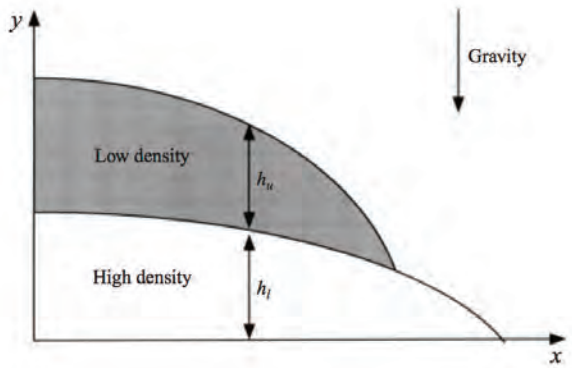

Figure 6: Schematic of the problem taken from [4].

the paper by [4]. Various scenarios of the flow are possible depending on the initial volume ratios and the viscosity ratio of the fluids. One possible scenario is shown in figure (7).

To model these two-layer flows, we proceed as before, but now we write separate equations for each layer. They are given by:

$$\frac{\partial h_u}{\partial t} = \left[\frac{k\Delta\rho_u g}{\mu_u}\right] \frac{\partial}{\partial x}\left(h_u\left(\frac{\partial h_u}{\partial x} + \frac{\partial h_l}{\partial x}\right)\right) \tag{20}$$

$$\frac{\partial h_l}{\partial t} = \left[\frac{k\Delta\rho_u g}{\mu_l}\right] \frac{\partial}{\partial x}\left(h_l\left(\frac{\partial h_u}{\partial x} + \frac{\Delta\rho_l}{\Delta\rho_u}\frac{\partial h_l}{\partial x}\right)\right) \tag{21}$$

where the subscripts u and l refer to the upper and lower layers, respectively. These coupled equations can be solved with the appropriate boundary conditions to obtain a regime chart that is shown in figure (8). The solutions of height profiles in this case are given by parabolas that are piecewise continuous.

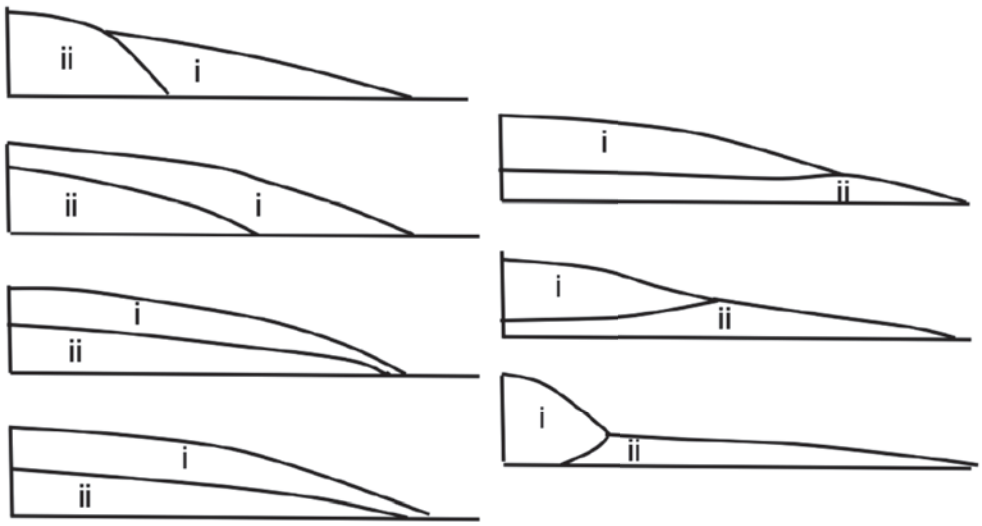

Figure 7: One particular scenario that is possible in two layer gravity current flows in porous media. The fluid ii starts behind the fluid i but then ends up squeezing under it and fluid i is left behind.

For more details about this problem, the reader is encouraged to refer to [4].

2.3 Capillary retention

So far in our analysis of different problems, we have assumed that the fluid completely drains the pores when it propagates through a porous medium. However, in reality, that might not be the case due to capillary effects. Some fluid might remain trapped in the pores as a fluid is draining out of the porous medium.

To study the effects of capillary retention on gravity current propagation, consider the schematic in figure (10). We would like to model the propagation of a buoyant fluid along a lateral boundary as shown where the fluid is partially retained in the pores. If h is the height of the current, retention is important when $\partial h/\partial t < 0$. Hence, we need a modified equation in the regions where the condition is true. If the current is spreading in both the directions laterally, there will exist a point x_m where $\partial h/\partial t = 0$. Let x_m^+ and x_m^- be the locations an infinitesimal distance after and before x_m. For the region without retention, we have

$$\frac{\partial h}{\partial t} = \frac{\partial}{\partial x}\left[h\frac{\partial h}{\partial x}\right] \quad \text{if } \frac{\partial h}{\partial t} > 0, \tag{22}$$

and for the region with capillary retention, we have

$$(1-s)\frac{\partial h}{\partial t} = \frac{\partial}{\partial x}\left[h\frac{\partial h}{\partial x}\right] \quad \text{if } \frac{\partial h}{\partial t} < 0. \tag{23}$$

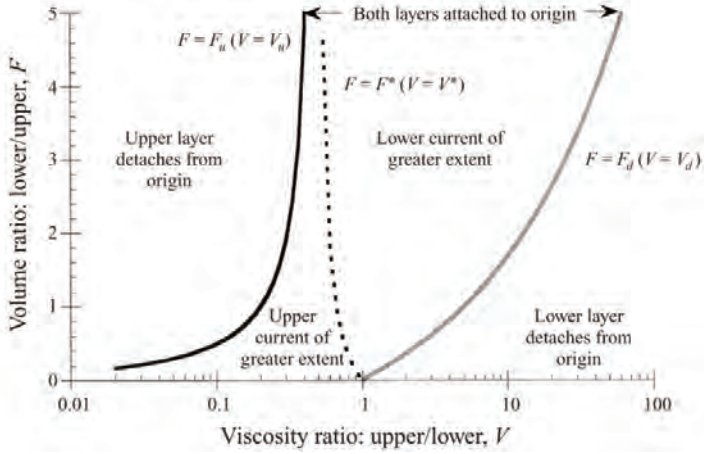

Figure 8: Regime chart of the different scenarios that are possible based on the volume ratio and viscosity ratio of the two fluids.

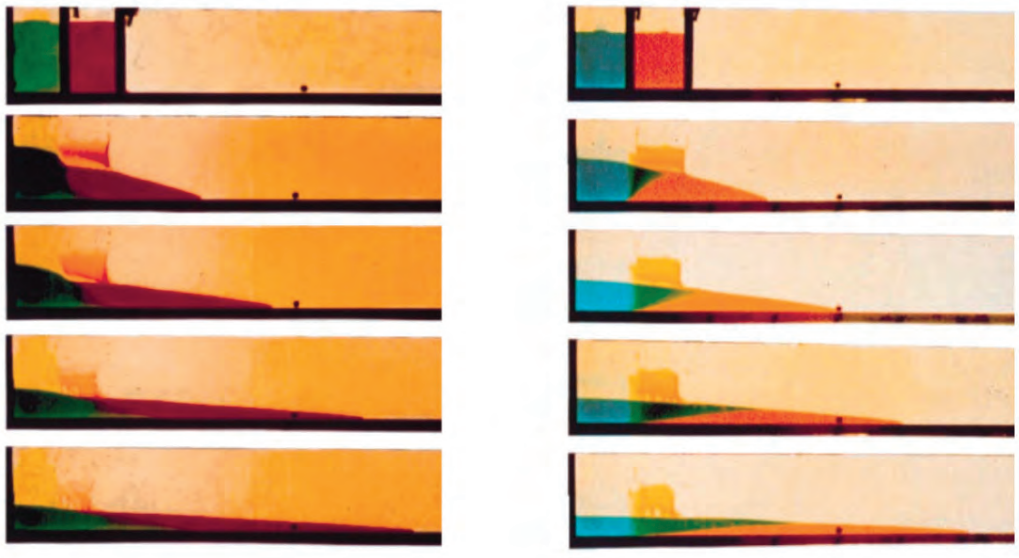

Figure 9: Experiments of two layer gravity currents in a Hele-Shaw cell by [4]. Two different scenarios are indicated in the left and the right.

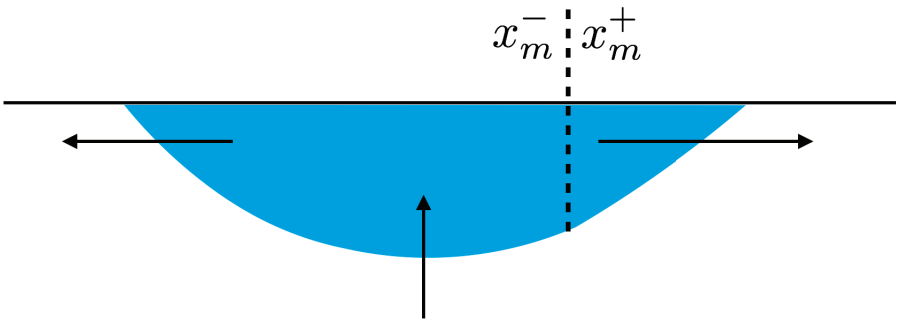

Figure 10: Schematic of gravity current propagation. The blue fluid is buoyant and spreads laterally along the upper boundary. The arrows indicate the direction of motion on the interface locally. x_m indicates the position where $\partial h/\partial t = 0$.

Here, s is the retention factor. Across x_m, the following jump conditions are implemented:

$$\left[Sh\frac{\partial h}{\partial x}\right]_{x_m^-}^{x_m^+} = 0, \tag{24}$$

$$[h]_{x_m^-}^{x_m^+} = 0. \tag{25}$$

For the above above set of equations, the total volume of the current decreases as

$$V(t) = V_0 \left(\frac{t}{\tau}\right)^{-\gamma}. \tag{26}$$

Here, γ comes out as an eigenvalue for a given value of s (similarity solutions of the 2nd kind). The variation of γ as a function of s is show in figure (11). The height of the gravity current comes as a similarity solution of the following form:

$$h = V_0^{1/2} \left(\frac{t}{\tau}\right)^{\alpha} f\left(\frac{x}{V_0^{1/2}\left(\frac{t}{\tau}\right)^{\beta}}\right), \tag{27}$$

where α and β are some constants.

2.3.1 Upslope capillary retention

Consider the schematic in figure (12) where the impermeable wall is at angle θ to the horizontal. As the fluid is less buoyant, it propagates upwards along the wall. Due to capillary retention, a part of the fluid is left behind (which is shaded in gray). We would like to develop a model for this physical phenomena.

We start by writing the mass conservation equations as earlier. For the leading edge (containing points a' and b') which is not retaining any fluid, we have the following equation:

$$\frac{\partial h}{\partial t} + S\sin\theta\frac{\partial h}{\partial x} = S\cos\theta\frac{\partial}{\partial x}\left(h\frac{\partial h}{\partial x}\right). \tag{28}$$

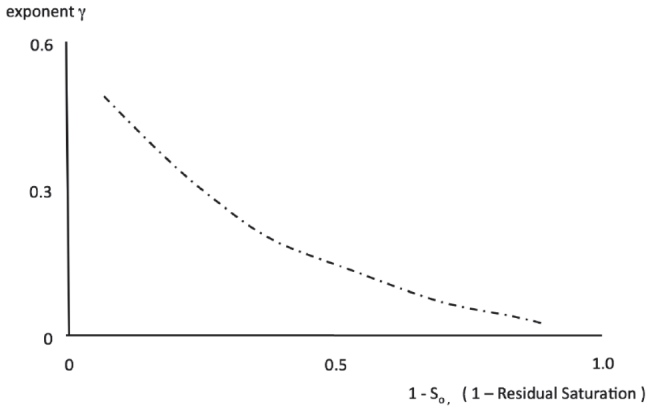

Figure 11: Variation of γ as a function of s.

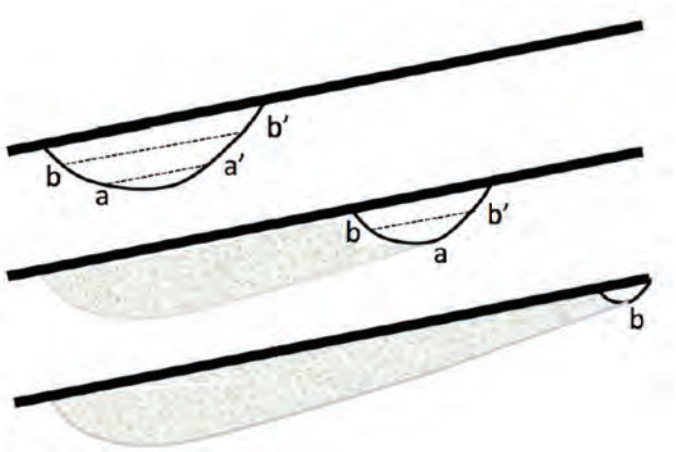

Figure 12: Schematic of the upslope propagation of a buoyant gravity current. The shaded region marks the retained fluid.

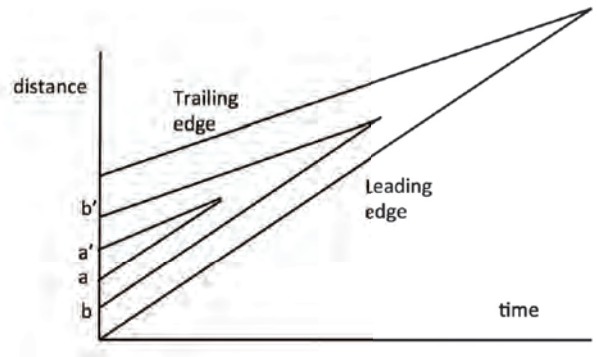

Figure 13: Diagram indicating the propagation of characteristics starting at initial locations and eventually meeting each other. The width along the y axis decreases as time progresses indicating that the gravity current width continues decreases and becomes zero at finite time due to capillary retention.

For the trailing edge (contain points a, b), which retains the fluid, we have the retention equation given by:

$$(1-s)\frac{\partial h}{\partial t} + S\sin\theta\frac{\partial h}{\partial x} = S\cos\theta\frac{\partial}{\partial x}\left(h\frac{\partial h}{\partial x}\right). \tag{29}$$

The above equations are hyperbolic with the characteristics given by

$$x(h,t;x^+) = x^+ + S\sin\theta t, \tag{30}$$

$$x(h,t;x^-) = x^- + \frac{S\sin\theta}{1-s}t. \tag{31}$$

As the trailing characteristic propagates at a faster speed, it eventually meets the leading edge characteristic at finite time. This is to say that the points a and b catch up to points a' and b' eventually. This can be shown in the diagram in figure (13). Thus, the time at which the gravity current stops propagating can be found. This happens when all of the fluid in the gravity current has been retained in the porous medium.

For more information on the effects of capillary retention in porous media gravity currents, the reader is encouraged to refer to [3].

3 Gravity Currents Through a Regular Matrix of Barriers

Porous media in geological settings generally exhibit alternating strata of different permeability. As a simple model for such media, we consider gravity-driven flow through a layered array of boundaries that are impermeable except at a discrete set of regularly spaced gaps.

3.1 Flux partitioning across a single barrier

To approach the general case of a 2-dimensional array of barriers, we would like to compare the relative fluxes of a fluid around either side of a single baffle as a function of the source height and horizontal position relative to the barrier.

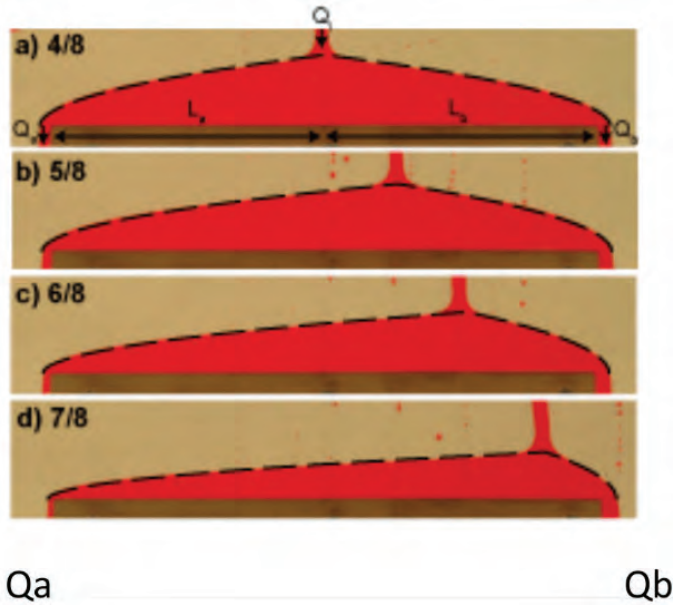

Figure 14: Flow partitioning to either side of a barrier depends on the horizontal position of the inflow relative to the centre point of the barrier.

The flow across one side of the barrier goes as:

$$Q_a = -\frac{k\Delta\rho g}{\mu} h \frac{dh}{dx}, \tag{32}$$

subject to the initial conditions

$$h(x = 0) \equiv h_s \tag{33}$$

and

$$h(x = L_a) \equiv 0. \tag{34}$$

Integrating both sides along the horizontal dimension yields:

$$Q_a L_a = \frac{k\Delta\rho g h_s^2}{2\mu}, \tag{35}$$

telling us that the amount of flow past side a of the barrier is inversely proportional to the length of that side of the barrier.

We can define a flux partitioning coefficient

$$f_a = \frac{Q_a}{Q_a + Q_b}, \tag{36}$$

which, repeating the above argument for the side b, gives us:

$$f_a = \frac{L_b}{L_a + L_b}. \tag{37}$$

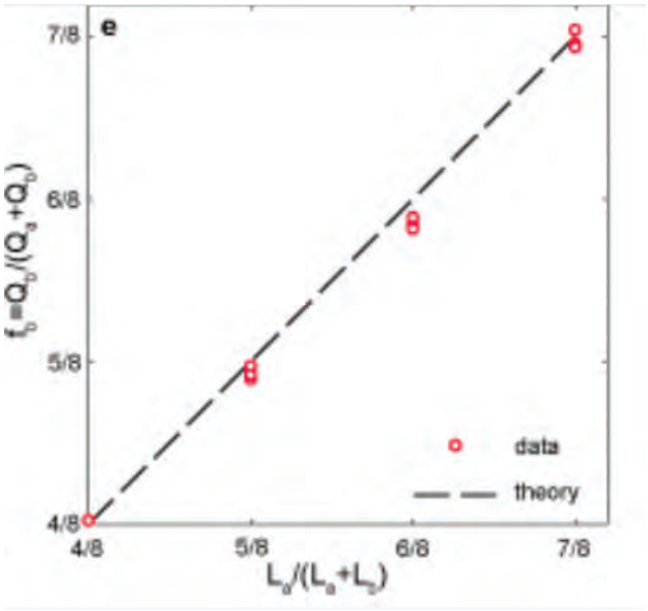

Figure 15: Our expectations for flux partitioning linear in the relative horizontal position of the inlet along the boundary are consistent with empirical data.

3.2 Barrier array

Consider an matrix of baffles consisting of evenly spaced baffles arranged in rows out of phase with each other by an amount set by f_a.

The flow through the k^{th} baffle in the n^{th} row follows a simple binomial distribution determined by f_a, namely:

$$Q_{nk} = \binom{n-1}{k-1} f_b^{k-1}(1-f_b)^{n-k}Q. \tag{38}$$

In the limit of an infinitely dense array of baffles, this approaches a Gaußian:

$$q(x,y) = \frac{Q\sqrt{h}}{L\sqrt{2\pi y f_b(1-f_b)}} e^{\frac{-hx^2}{2yL^2 f_b(1-f_b)}}. \tag{39}$$

The spatial dispersion is set by the standard deviation, namely

$$x = \sqrt{\frac{2yL^2 f_b(1-f_b)}{h}}. \tag{40}$$

Once a steady state flow has been established, we can inject tracer and watch its motion through the baffles to determine flow lines. The flow velocity components $(u,v) = (\partial_y\psi, -\partial_x\psi)$ are set by the streamfunction:

$$\psi \frac{Q\sqrt{d}}{L\left(2\pi f(1-f)\right)^{\frac{1}{2}}} \int_{\infty}^{\frac{x}{y^{\frac{1}{2}}}} \exp \frac{-s^2 d}{2\pi L^2 f(1-f)} ds. \tag{41}$$

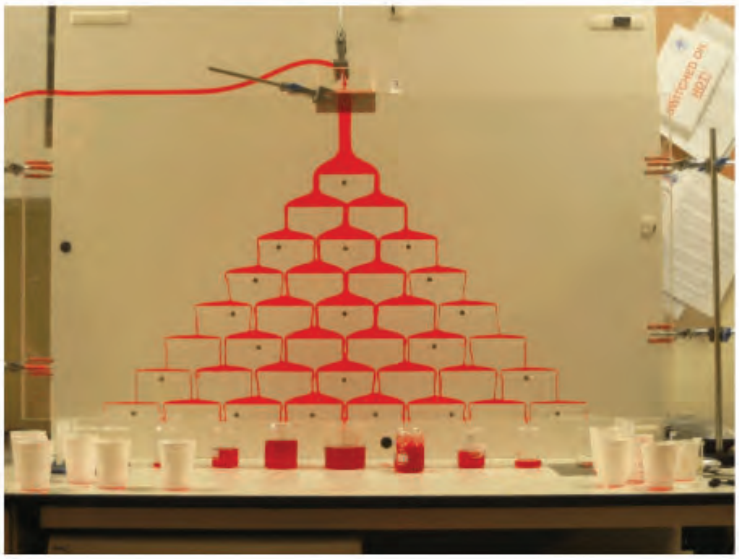

Figure 16: A layered array of baffles horizontally distributes point source flow into what, in the limit of dense baffles, approximates a Gaußian flow profile

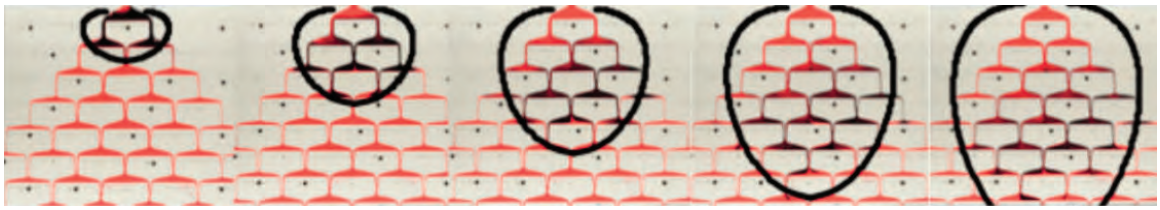

Figure 17: Tracer spreads out both vertically and horizontally with velocities determined by the streamfunction ψ

Figure 18: Plumes propagating through an angled array of barriers exhibit a preferred horizontal direction.

3.3 Angled baffles

By rotating the rows of baffles relative to the horizontal—equivalently allowing gravity to have a horizontal component—we modify the flux equation to:

$$Q_a = -\frac{k\Delta\rho g}{\mu}\left(h\frac{dh}{dx}\cos\theta \pm h\sin\theta\right). \tag{42}$$

As the angle increases, the flow up and over the inclined side of the baffle eventually reduces to zero. Denoting as Q_c the critical flux at which the flow pinches off for a given angle, we find:

$$\frac{Q_c}{Lu_b\sin\theta\tan\theta}\log\left(1-\frac{L_a}{L}\frac{Lu_b\sin\theta\tan\theta}{Q_c}\right) = -1 \tag{43}$$

Fluxes below this critical value divert completely to one side of a baffle; angled baffles far from the centre line of the flow—regions where low fluxes are observed—thus tend to merely direct flow rather than spread it out horizontally as in the $\theta = 0$ case. Tilting the baffles relative to the horizontal thus results in more tightly collimated plumes.

4 CO_2 Trapped in Anticlines

Of equal importance to the question of fluid motion through porous media is the issue of understanding how fluid is stored *in* a porous setting.

Geological sequestration of CO_2 in subterranean features called anticlines—inverted basins defined on three sides by a warped layer of impermeable rock—has been suggested

as a potential option for sustainable, long-term management of excess carbon.

The structure of the anticlines themselves, however, raises interesting questions about the durability of trapped CO_2 pockets. Background hydrogeological flows between the impermeable layers surrounding the anticline threaten to wash the CO_2 out of its trap, while dissolution of carbon into the surrounding fluid may offer it means of resurfacing through the back door.

We could like to understand how much CO_2 can be trapped in layer and how background flow affects this maximum capacity. We'd also like to generally understand the processes leading to CO_2 migration over long time scales, including the risk of catastrophic release due to earthquakes.

4.1 Background flow

Ignoring diffusion for the moment, we find the velocity of the background flow to be proportional to the change in the distance between the bottom of the trapped CO_2 and the top of the underlying impermeable layer:

$$u_w = -\frac{k}{\mu}\Delta\rho\frac{d(c-d)}{dx}, \tag{44}$$

telling us that the background flux is

$$Q = u_w(H-c), \tag{45}$$

With H the spacing between impermeable layers and c the depth of the trapped CO_2.

Defining the ratio of relative magnitudes of the forced flow to the background flow as

$$\Gamma = \frac{\mu Q}{kg\Delta\rho H} \tag{46}$$

allows us to arrange these equations and solve for the spatial profile of the CO_2, namely

$$\frac{d(c)}{dx} = \frac{d(d)}{dx} - \frac{\Gamma}{H-c}. \tag{47}$$

We find, unsurprisingly, that larger background flows lead to smaller reservoirs of trapped CO_2.

Consider now adding in the effects of diffusion.

The maximum dissolution rate is $Q(C_{sat} - C_{aq})$ set both by the background flux and the concentration difference between saturated and background water. Plugging in typical values for these quantities, we find that the CO_2 reservoir will fully dissolve on the order of 10^4 to 10^6 years, which is a rather long time indeed by human standards.

4.2 Convective flow

CO_2 saturated brine is heavier than the background water and may thus migrate upstream into the background flow. This backflow will be particularly pronounced if the anticline is at an angle to the horizontal.

The descending brine fights against the pressure gradient in the background flow by way of its own buoyancy force. The flux of descending brine will thus go as

$$Q_d = \frac{k}{\mu}(\frac{dp}{dx} + \Delta\rho g \sin\theta)h_1 \tag{48}$$

As before, the sum of ascending and descending fluxes is set gy geometry

$$Q_d + Q_a = -\frac{k}{\mu}\frac{dp}{dx}(H - h_1)\sin\theta). \tag{49}$$

This allows us to write the maximum descending flux as

$$Q_d^{max} = \frac{\Gamma}{4}(1 - \frac{1}{\Gamma})^2 Q_a, \tag{50}$$

where we've modified Γ to account for the angle θ the parallel impermeable layers make to the horizontal:

$$\Gamma = \frac{\mu Q}{kg\Delta\rho\sin\theta H}. \tag{51}$$

For low background fluxes, the counterflow can significantly exceed the background flux, while for higher backgrounds the descending flux goes to zero, resulting in unidirectional flow set by the background flux alone.

The time scale for diffusion across the layer is $\frac{H^2}{D}$, where D is the diffusion constant. Plugging in typical numbers puts this at 10^4 to 10^6 years for the counterflow to dissipate. We'd like to understand this dissipation process better.

4.3 Convective and diffusive flow

We consider a wedge of brine propagating up the flow channel against the background flow. We find the timescale for the intrusion growth to be

$$\tau_I = \sqrt{2}\frac{u_b}{u_f^2}H, \tag{52}$$

where $u_b = \frac{k\Delta}{\mu}$ and $u_b = Q/H$. We also have a diffusive time scale set by

$$\tau_D = \frac{H^2}{D} \tag{53}$$

Comparing these two time scales, we reason that $\tau_D \gg \tau_I$ leads to the development of an intrusion of parabolic profile. For $\tau_I \gg \tau_D$, however, the picture is modified significantly as we enter the diffusion-dominated regime.

We expect shear transport to balance diffusion across the layer; using this Ansatz, we can write down a nonlinear relation for buoyancy transport by balancing the depth-averaged mean buoyancy (i.e. CO_2 concentration) with the shear dispersion.

References

[1] H. E. Huppert and A. W. Woods, *Gravity driven flows in porous layers*, J. Fluid Mech., 292 (1995), p. 55 69.

[2] D. Pritchard, A. W. Woods, and A. Hogg, *On the slow draining of a gravity current moving through a layered permeable medium*, Journal of Fluid Mechanics, 444 (2001), pp. 23–47.

[3] A. W. Woods, *Flow in Porous Rocks: Energy and Environmental Applications*, Cambridge University Press, 2014.

[4] A. W. Woods and R. Mason, *The dynamics of two-layer gravity-driven flows in permeable rock*, Journal of Fluid Mechanics, 421 (2000), pp. 83–114.

Lecture 9
More Challenges in Porous Media for CO_2 Sequestration

Notes by Christopher J. Howland, Thomas Le Reun

June 28, 2018

1 Exchange Flows through Fractures in Seal Rock

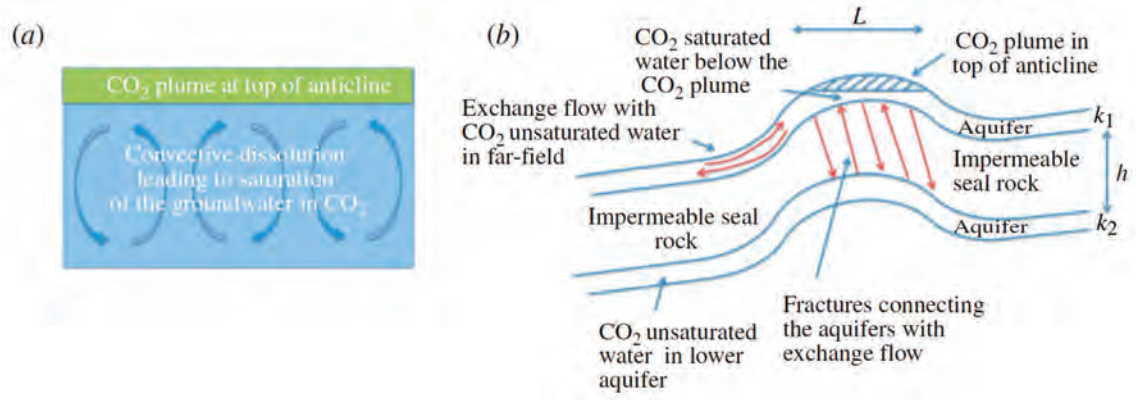

Figure 1: (a) An illustration of the convective mechanism by which CO_2 saturation occurs in an aquifer with a CO_2 trap. (b) A schematic of the large-scale flow domain with two aquifers separated by a seal rock. Possible exchange flows within and between the aquifers are highlighted. (Woods et al., 2015)

Recall the problem mentioned in the previous lecture, where CO_2 that has been pumped into deep rock accumulates at the top of an anticline. As discussed before and shown in figure 1a, convective dissolution in the aquifer leads to saturation of CO_2 in the groundwater, limiting the diffusion rate of the CO_2. In the previous section we showed how an exchange flow can develop with the far-field of the aquifer where the groundwater is unsaturated, with the potential to change this diffusion rate. Another potential mechanism by which the diffusion rate limit can be overcome is through fractures in the impermeable seal rock below the aquifer. Figure 1b shows that if these fractures connect the CO_2-saturated aquifer to another aquifer, then an exchange flow can develop between the CO_2-rich upper water and the unsaturated lower water.

Woods et al. (2015) performed the following experiments to investigate this phenomenon. In the first experiment, two vertical porous tubes that model fractures in a seal rock connect an upper reservoir of height H_u to a lower reservoir of height H_l as shown in figure 2a. The upper reservoir is initially filled with saline water to model the CO_2-saturated water of the upper aquifer, which is more dense than the unsaturated groundwater in the lower aquifer.

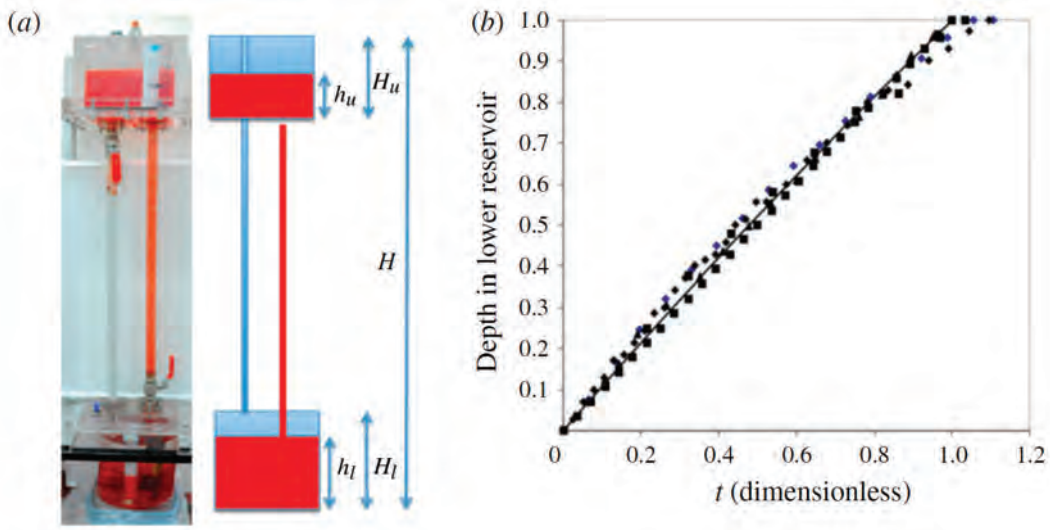

Figure 2: (a) Photograph and schematic of the experimental setup for a two-tube exchange flow. The saline water is coloured red, and the fresh water is lighter in colour. (b) Experimental results showing the depth of the saline layer in the lower reservoir as a function of dimensionless time. Data from experiments with various salinity values is displayed here. (Woods et al., 2015)

The lower reservoir is initially filled with fresh water, and when valves in the tubes are opened, an exchange flow develops with salty water flowing down one tube and fresh water flowing up the other.

Assuming the resistance to the flow is higher in the fractures than in the aquifers, we can take the pressure in each aquifer to be approximately uniform (p_l in the lower layer, p_u in the upper). We denote the density of the fresh water ρ and the density of the saline water $\rho + \Delta\rho$. Upflow is driven by a pressure difference $\Delta p = p_l - (p_u + \rho g h)$ between the lower layer and the upper layer plus the hydrostatic pressure of the light fluid in the tube. The downflow of the denser fluid is driven by the hydrostatic pressure difference $\Delta\rho g h$ minus the pressure difference Δp. If the system is in steady state, then the pressure difference must be

$$\Delta p = \frac{\Delta\rho g h}{2}, \tag{1}$$

and the upwards and downwards volume fluxes must be

$$Q_u = Q_d = \frac{kA\Delta\rho g}{2\mu}, \tag{2}$$

where A is the cross-sectional area of each tube, k is the permeability of the tubes and μ is the viscosity of the fluid.

Woods et al. (2015) also performed an experiment with five vertical pipes, representing a greater number of fractures connecting the aquifers. This experiment showed that a number of different states are possible for the exchange flow. In this case, the number of fractures which have upflow is variable and has a significant impact on total volume flux values.

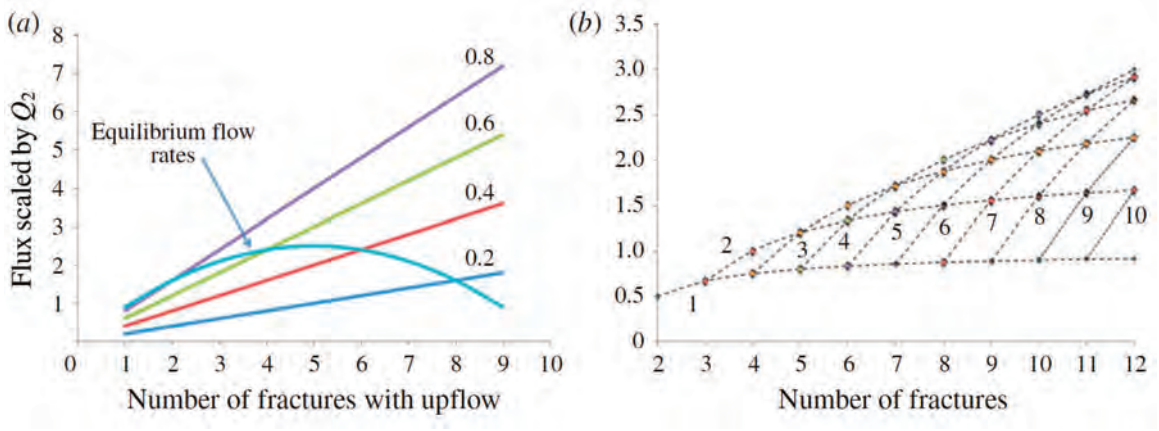

Figure 3: (a) Model predictions of the exchange flow scaled by $Q_2 = k\Delta\rho g d/\mu$ for various values of the pressure difference scaled by $\Delta\rho g h$. The curved line denotes the equilibrium solution of no net flow. (b) Model predictions of total upflow scaled by Q_2 in the case of no net flux. The symbols denote possible equilibrium solutions. (Woods et al., 2015)

The simple model used to calculate the volume fluxes above can easily be extended to explain the appearance of these multiple states, and also to capture the effect of fractures with different widths and permeabilities. We model the two aquifers as being connected by m parallel fractures with permeability k_i and aperture width d_i. Assume that n of the fractures have downflow, with the rest flowing upwards. By the same arguments as before, the volume flux due to the downflow of dense water will be

$$Q_d = \frac{\Delta\rho g h - \Delta p}{\mu h} \sum_{i=1}^{n} k_i d_i, \tag{3}$$

and the volume flux due to the upflow of light water will be

$$Q_u = \frac{\Delta p}{\mu h} \sum_{i=n+1} m k_i d_i. \tag{4}$$

For a given number of fractures m there are now multiple solutions for equilibrium ($Q_d = Q_u$) that are dependent on the number of fractures with downflow n. These are shown as the nodes on figure 3b, where the aperture and permeability of each fracture take the same values for simplicity. As the fractures are assumed to be long, these equilibrium solutions are in some sense 'stable' since a small addition of fluid to the end of a fracture is not enough to overcome the existing pressure difference in the fracture and reverse the flow. The development of the exchange flow is therefore strongly dependent on the initial conditions of the system. Along with the uncertainty in the geometry of real fractures, this means that predicting the spread of CO_2 in a layered anticline is very difficult and error-prone. Natural flows may also be complicated further by a net pressure/flow through the fractures leading to non-equilibrium solutions.

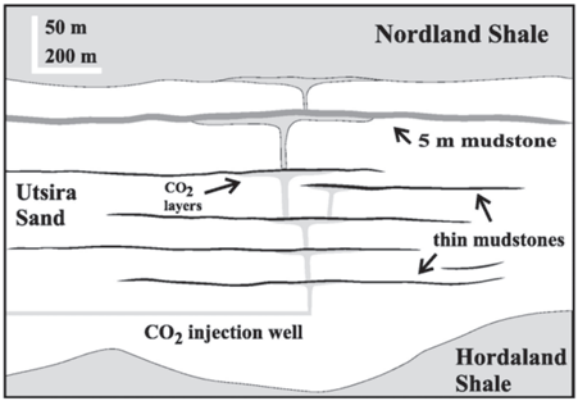

Figure 4: Cartoon of the geological context of CO_2 sequestration in the Sleipner aquifer. This figure is reproduced from Bickle et al. (2007).

2 Gravity Currents in Confined Porous Layers

2.1 CO_2 sequestration at Sleipner

With regards to the consistent increase of CO_2 emissions, the underground sequestration of the greenhouse gas is regarded as a potential solution to prevent its further accumulation in the atmosphere. Schematically, this corresponds to intruding supercritical CO_2 into aquifers, which are porous rock layers permeated with brine. This solution has been tested at Sleipner in the North Sea, with consistent injection of supercritical CO_2 at a 1 MT/yr since 1996 (Bickle et al., 2007). The schematic of the geological context of CO_2 can be found in figure 4.

Seismic data inversion allowed Bickle et al. (2007) to determine the existence of several disinctive layers separated by nine horizontal thin mudstone impermeable layers. Moreover, successive seismic profiles taken before and after the injection started have provided researchers with the ability to track the time evolution of CO_2 intrusion into those layers, as shown in figure 5 (Bickle et al., 2007). They could therefore infer that although the the injection is localised at one point, the CO_2 expands through the different layers above the injection. Such a process can be schematically visualised in figure 4. The CO_2 expansion through each of these layers has been inferred from the seismic reflection tracking: in each layer, the detectable area of CO_2 grows linearly with varying rates across the different layers.

The aim of this section is to build a simple model of the CO_2 expansion at Sleipner, which consists of several confined porous gravity currents. Inversion from the model to the seismic data could for instance help determine the porosity of the rock, and determine if the expansion is controlled by gravity and density contrast alone, or by the injection at the bottom of the site.

2.2 A confined porous gravity current

We seek to model the effects of gravity on continuous axisymmetric injection of CO_2 at flux Q into a porous layer permeated with brine, which is assumed to be less dense than CO_2.

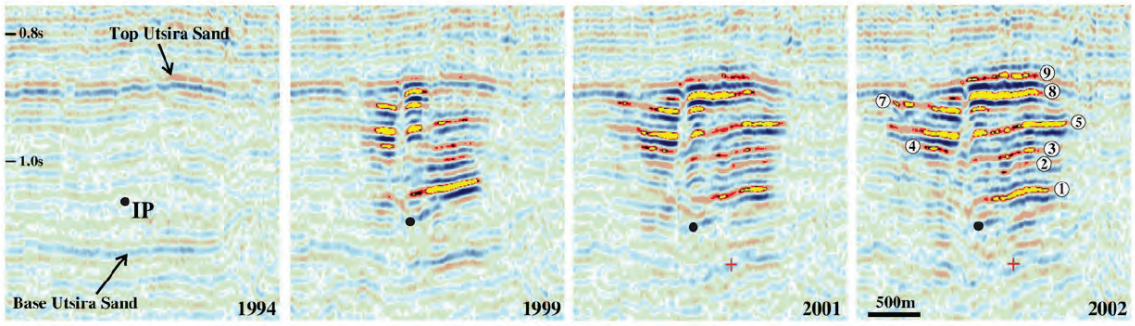

Figure 5: Successive seismic reflection profiles taken prior and after the injection started in 1995. The brightest areas are associated with the presence of CO_2. The point IP represents the injection point. Figure reproduced from Bickle et al. (2007).

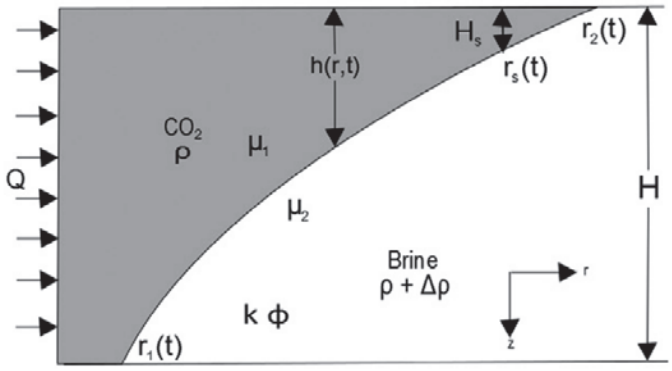

Figure 6: Schematic to model a porous gravity current of CO_2 into a confined layer of sand and brine. Figure reproduced from Dudfield and Woods (2013).

As indicated in figure 6, the two fluids have different densities μ_1 and μ_2. The horizontal velocity u_i in the fluid i (either μ_1 for CO_2 or μ_2 for the brine) obeys Darcy's law:

$$u_i = -\frac{k}{\mu_i}\frac{\partial p}{\partial r}, \tag{5}$$

where k is the sand permeability and p is the pressure field. The latter can be described by hydrostatic balance as in Nordbotten and Celia (2006):

$$p(r,z,t) = \begin{cases} p_0(r,t) + \rho g z \quad \text{for} \quad z \leqslant h, \\ p_0(r,t) + \rho g h(r,t) + (\rho + \Delta\rho) g (z - h(r,t)) \quad \text{for} \quad z > h, \end{cases} \tag{6}$$

where g is the gravity intensity. We can also define the CO_2 and brine radial fluxes as

$$\begin{cases} Q_1(r,t) &= 2\pi r h \displaystyle\int_0^{h(r,t)} u_1 \mathrm{d}z \ , \\ Q_2(r,t) &= 2\pi r (H-h) \displaystyle\int_{h(r,t)}^{H} u_2 \mathrm{d}z \ , \end{cases} \tag{7}$$

which can be made explicit with the Darcy law (5) and the hydrostatic pressure (6):

$$\begin{cases} Q_1(r,t) &= \dfrac{2\pi k}{\mu_1} r h \dfrac{\partial p_0}{\partial r} \ , \\ Q_2(r,t) &= \dfrac{2\pi k}{\mu_2} r (H-h) \left[\dfrac{\partial p_0}{\partial r} - \Delta\rho \dfrac{\partial h}{\partial r} \right] \ . \end{cases} \tag{8}$$

The time dependence of h is related to the radial variations of the flux with two continuity equations:

$$\begin{cases} \dfrac{\partial h}{\partial t} &= \dfrac{-1}{2\pi r \phi} \dfrac{\partial Q_1}{\partial r} \\ , \dfrac{\partial (H-h)}{\partial t} &= \dfrac{-1}{2\pi r \phi} \dfrac{\partial Q_2}{\partial r} \ , \end{cases} \tag{9}$$

where ϕ is the porosity of the sand. The sum of these two continuity equations yields

$$Q_1 + Q_2 = \overline{\mathrm{cst}} = Q \ . \tag{10}$$

After some algebra, which can be found for instance in Nordbotten and Celia (2006), the equation for the height h reads

$$r\frac{\partial h}{\partial t} + \frac{\partial}{\partial r}\left(\frac{h}{h + \nu(H-h)}\right) = \nu\Gamma \frac{\partial}{\partial r}\left(\frac{rh(H-h)}{h+\nu(H-h)}\frac{\partial h}{\partial r}\right) \tag{11}$$

with:

$$\nu = \frac{\mu_1}{\mu_2} \quad \text{and} \quad \Gamma = \frac{2\phi k \Delta\rho g H^2}{\mu_1 Q} \ . \tag{12}$$

We can look for a similarity solution to the equation (11); after some algebra, a self-similar function h must be such that:

$$h \ = \ HF(\eta) \quad \text{with} \quad \eta \ = \ r\left(\frac{2\pi\phi H}{Qt}\right)^{1/2} \tag{13}$$

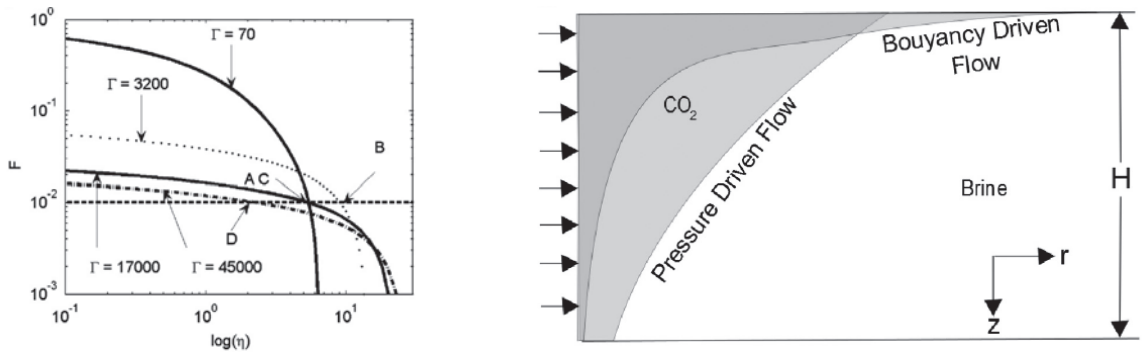

Figure 7: **Left:** solutions of equation 14) for several values of Γ. **Right:** schematic representation of gravity current profile in the two asymptotic limits of gravity and pressure driven intrusion. These two figures are reproduced from Dudfield and Woods (2013).

and F satisfies the following equation:

$$\frac{-\eta^2}{2}F' + \frac{\nu F'}{F+\nu(1-F)} = \nu\Gamma\frac{\mathrm{d}}{\mathrm{d}\eta}\left(\frac{\eta F(1-F)}{F+\nu(1-F)}F'\right) \tag{14}$$

which can be solved numerically. Note that although the viscosity ratio ν is a physical constant, Γ is a control parameter since it depends on the flux Q and the confinement of the layer H. Two asymptotic limits can be worked out:

- $\Gamma = 0$ which corresponds to the large injection flux and to a pressure driven regime;
- $\Gamma \ll 1$ which is associated with a gravity driven regime.

The different shape of F when Γ is varied can be found in figure 7.

2.3 Use of the idealised model to describe Sleipner dynamics

The aim of this paragraph is to present how the shape of the curve F may help to work out a model for Sleipner intrusions. The key point is that the seismic reflection profile has a minimum resolution under which the spatial variability of aquifer properties cannot be resolved. This means that the tip of the gravity current is unresolved: the outer boundaries of the intrusions seen from seismic profile in fact approximately correspond to the same height h of CO_2.

As it can be noticed from figure 7, it may be difficult *a priori* to discriminate between the two regimes —pressure and gravity driven— as the two mainly differ by an extended tip in the case of the gravity driven intrusion. Furthermore, it can be shown from inversion of the function F that depending on the detection threshold F_s, given one detected front η_s, inversion may give two different values of the parameter Γ —see figure 8. This non-uniqueness may alter the inversion of temporal variation of seismic data.

With all these complications, the next step is to include more layers, starting for simplicity with two. Knowing the total injection flux Q and the time evolution of the radius at detection threshold for the two layers, the aim is to constrain the value of the flux in each

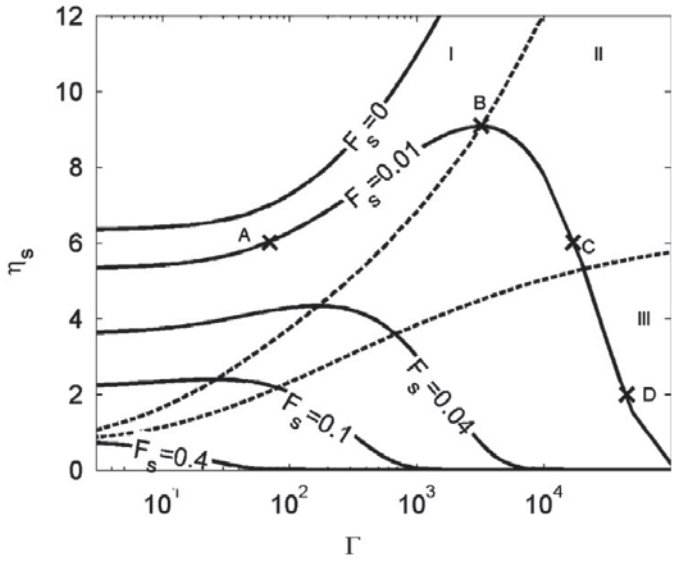

Figure 8: Line plotting of the locations of points with constant $F(\eta;\Gamma)$ as a function of Γ and the rescaled position of the front η_s. The plane is divided in three regions: if a point is located along a curve in area II, there exists a point with the same η_s in area I.

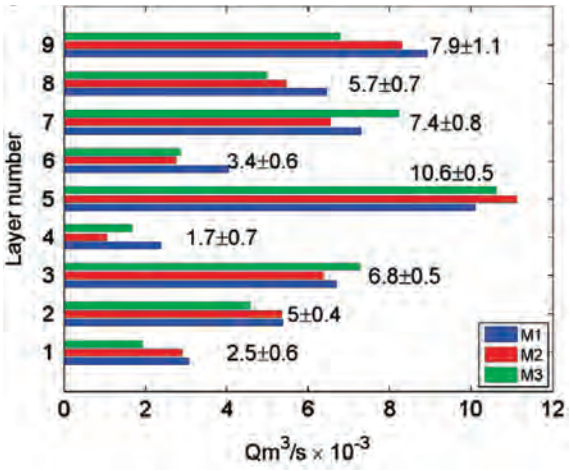

Figure 9: Values of the flux in each of the nine Sleipner layers inferred from inversion via three different models. **Right:** values of the total volume of CO_2

layer Q_1 and Q_2, along with the permeability of each layer k_1 and k_2. Such an inversion is possible only via the inclusion of further assumption or models relating the layers to one another. For instance, Dudfield and Woods (2013) compare three independent models:

- the permeability of the two layers are assumed to be the same;
- the pressure drop between two layers is given by hydrostatic balance taking the density of CO_2 (referred as CO_2-static);
- the pressure drop between two layers is given by hydrostatic balance taking the density of water.

An example of the extension of the inversion method to Sleipner's nine layers is shown in figure 9 and shows the flux is well constrained with an error bar of approximately 10%. Such a narrow band is due to the integral nature of the flux which does not suffer from large variations as the length of the tip varies from one model to another. This is however not the case of permeabilities which are far less well constrained – see Dudfield and Woods (2013) for further details. Without an improvement in the resolution of seismic profiles or a measurement of pressure across the layers, such an inversion remains therefore particularly difficult to perform. This illustrates how little is known from flows in aquifer despite repeated seismic measurements.

3 Gravity Currents in Layers: Tracer Confusion

As well as seismic surveys performed to gather information on underground structure, tracer tests can be done to determine how CO_2 spreads through porous rock underground. In this section, we will show why simple gravity current models may produce errors when inferring fluxes from these tracer tests in layered rocks that are often targeted as good regions for carbon storage. The internal structure of such rocks can be visualised on cliffs such as those at Loop Head in County Clare in the west of Ireland.

Simple gravity current models that we have considered before take the form

$$u = -\frac{k\Delta\rho g}{\mu}\frac{\partial h}{\partial x}, \tag{15}$$

for the spreading velocity in the current and neglect any variations with height. We now consider the problem of a gravity current being produced in a system of permeable layers separated by impermeable horizontal boundaries (following section 10.5 of Woods (2014)). Assuming the source pressure is constant, an overpressure Δp_0 will be produced in the top-most layer of the system. If the height of the layered system is H, the pressure horizontally near the source will be vertically distributed as

$$\Delta p = \Delta\rho g(H - y) + \Delta p_0. \tag{16}$$

The experimental results in figure 10 show that in all except the top layer, a region exists where the current fully floods the layer. We can model this fully flooded zone as moving with a Darcy velocity related to the pressure:

$$\frac{\mathrm{d}L(y,t)}{\mathrm{d}t} = \frac{k[\Delta\rho g(H - y) + \Delta p_0]}{\mu L}. \tag{17}$$

Ahead of this region, the vertical pressure gradient is expected to be hydrostatic and we get a local equation in each layer for the migration of the flow

$$\phi\frac{\partial h_n}{\partial t} = \frac{k\rho g}{\mu}\frac{\partial}{\partial x}\left(h_n\frac{\partial h_n}{\partial x}\right), \tag{18}$$

where h_n is the local height of the fluid in the n-th layer. In this nose region, it is possible to find a similarity solution of the form

$$h = h(x/(Dt)^{1/2}), \tag{19}$$

where $D = k\Delta\rho g\Delta h/\mu$ and Δh is the height of a layer.

Comparing the spreading of a gravity current in this multilayered system with that produced in a homogeneous reservoir by an equal level of pressure injection, it is found that a difference in flux of 6.2% is observed. This non-negligible change is due to the highly varying speeds of the fully flooded regions in the different layers of the system as determined by (17). The different speeds in each layer also have important implications for tracer tests. If a finite amount of tracer is injected into the system at the source of the gravity current, then the tracer will arrive at an observation well downstream in a series of discrete pulses from each layer. This skews the time series measurement of tracer concentration and needs to be taken into account when using such data to infer spreading rates and fluxes of the gravity current. Ensuring estimates of these quantities are accurate is important when trying to assess potential breakthrough times when CO_2 may escape a trap.

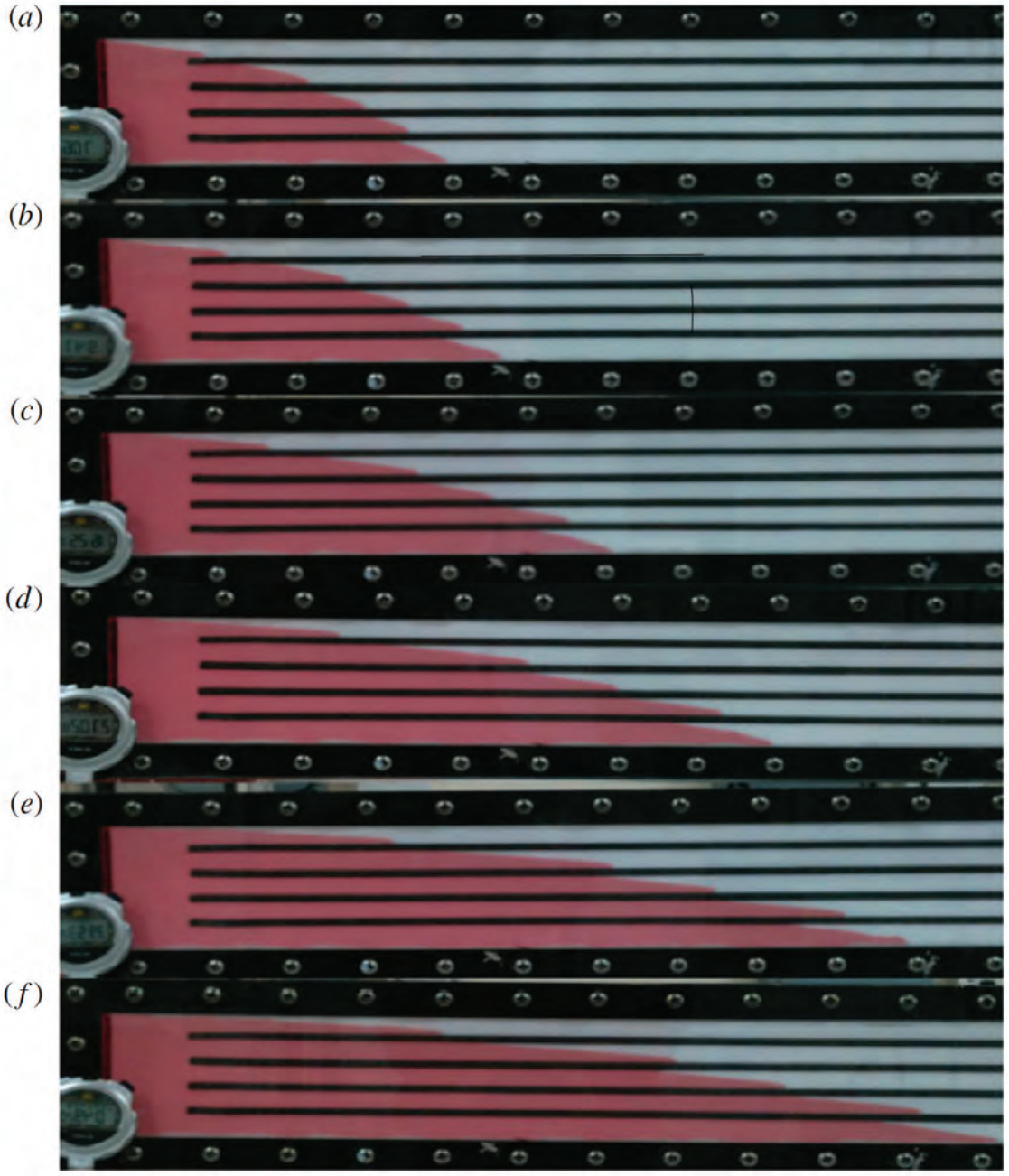

Figure 10: Photographs of the gradual spreading of a gravity current in a five-layer Hele–Shaw cell, in which there is a source reservoir of constant depth. For scale, the vertical height of the darker zone of fluid between the upper and lower boundaries of the cell, at the left-hand end of the cell, is 10cm. (Farcas and Woods, 2015)

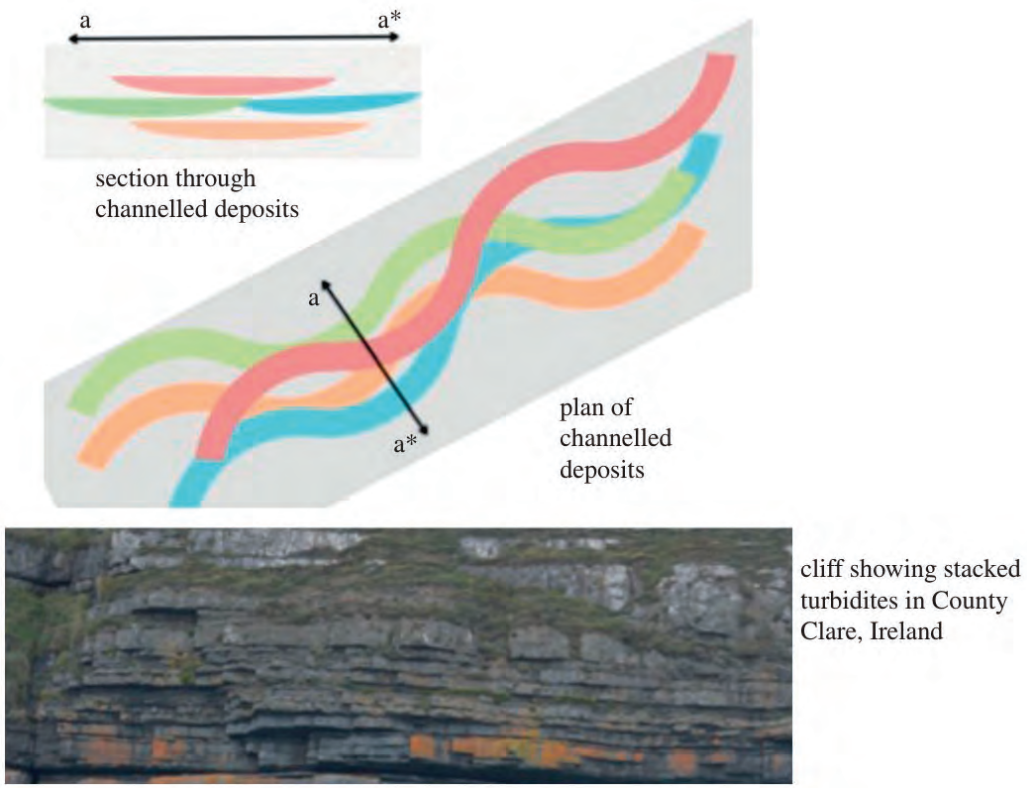

Figure 11: Schematic of typical sediment deposits in continental shelf context. These deposits are often associated to underwater current with topography, the resulting layers are therefore channelled. This is the case for instance in the Ross formation in Ireland which is pictured here. This figure is reproduced from Woods and Mingotti (2016).

4 Porous Gravity Current in Depth-varying Channels

4.1 Geological context and experimental modelling

Sediment deposit on continental margins or shelves are often associated with underwater currents, be it turbidites or channels. They result in sedimentary layers with varying height and of short lateral extent, reflecting the shape of the channel or the current, as depicted in figure 11. In this section, we are interested in how this varying topography may alter the intrusion of fluid gravity currents inside such sedimental layers.

The idealised experimental analogue consists of a confined gravity current in a Hele-Shaw cell with varying depth – see figure 12. Unlike section 2, the flow is vertically confined such that gravity only imposes the the influx Q at the entrance of the Hele-Shaw cell. Note that the viscosity ratio between the intruding and the preceding fluid must by larger than one unless a Saffman-Taylor finger develops, leading to completely different dynamics.

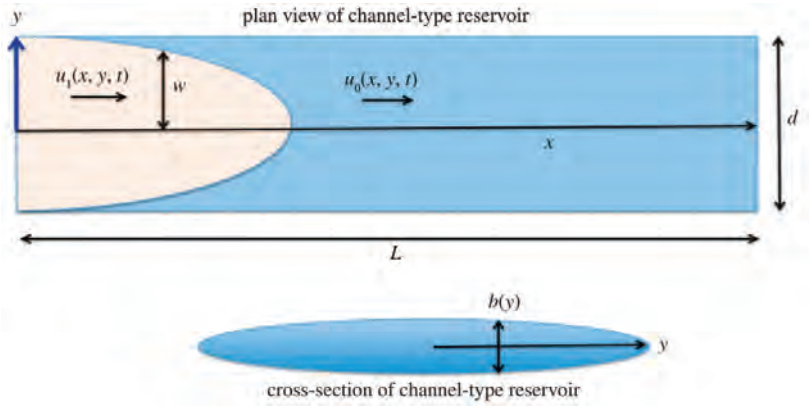

Figure 12: Schematic view of the Hele-Shaw cell with varying depth used in the experiments of Woods and Mingotti (2016). The experimental setup is such that $b \ll d \ll L$. Typically, $b \sim 3$ mm, d 15 cm and $L = 180$ cm. Figure reproduced from Woods and Mingotti (2016).

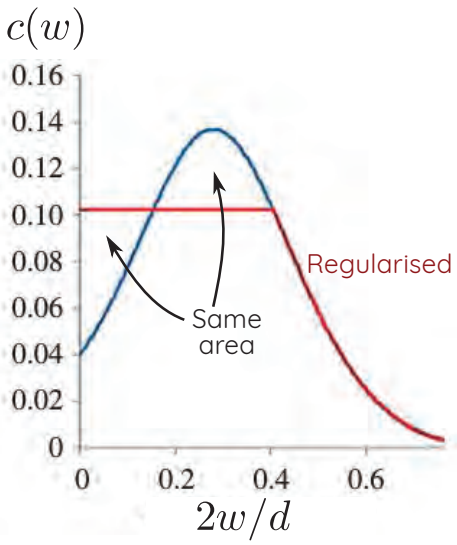

Figure 13: Example of regularisation of the velocity profile of the intrusion. The blue curve is computed from 26. The red curve is the regularised profile. Figure reproduced from Woods and Mingotti (2016).

4.2 A model for the depth-varying intrusion

The aim of this section is to provide a model describing the shape of the intrusion in the depth-varying Hele-Shaw cell. The derivation of this model relies on the total flux conservation across the channel. The velocities inside the intruding fluid u_1 and inside the preceding fluid u_2 along the x direction are related to the pressure field via a Darcy-type law:

$$\left\{ \begin{array}{lcl} u_1 & = & \dfrac{-b^2(y)}{12\mu_1}\partial_x p \ , \\ u_2 & = & \dfrac{-b^2(y)}{12\mu_2}\partial_x p \ , \end{array} \right. \tag{20}$$

where μ_1 and μ_2 are the respective viscosities of the two fluids. Because the channel is assumed to be long and thin, the pressure gradient is dominantly along channel, and leads to a simple model for the fractional flow of each fluid phase. The corresponding flux in each fluid Q_1 and Q_2 reads

$$\left\{ \begin{array}{lcl} Q_1 & = & \displaystyle\int_0^{w(x,t)} b(y)u_1(y)\mathrm{d}y \ = \ \frac{-1}{12\mu_1}\partial_x p \int_0^{w(x,t)} b(y)^3\mathrm{d}y \ = \ \frac{-1}{12\mu_1}\partial_x p f(0,w) \ , \\ Q_2 & = & \displaystyle\int_{w(x,t)}^{d/2} b(y)u_1(y)\mathrm{d}y \ = \ \frac{-1}{12\mu_1}\partial_x p \int_{w(x,t)}^{d/2} b(y)^3\mathrm{d}y \ = \ \frac{-1}{12\mu_2}\partial_x p f(w,d/2) \ , \end{array} \right. \tag{21}$$

where we have introduced the function

$$f : (r,s) \longmapsto \int_r^s b^3 \quad .$$

Combining flux conservation $Q_1+Q_2 = Q$ with the two equations (21) leads to an expression of $\partial_x p$ involving only viscosities, the flux Q and the function f. The intrusion flux Q_1 thus becomes

$$Q_1 = \frac{Q f(0,w)}{f(0,w) + \alpha f(w,d/2)} \ , \tag{22}$$

with $\alpha = \mu_1/\mu_2$ the viscosity ratio.

We may now write the flux conservation across a section of the intrusion, which merely reads

$$\frac{\partial}{\partial t}\int_0^{w(x,t)} b(y)\mathrm{d}y \ = \ -\frac{\partial Q_1}{\partial y} \ . \tag{23}$$

Using the relation

$$\frac{\partial f(0,w)}{\partial x} \ = \ \frac{\partial w}{\partial x} b^3(w) \ , \tag{24}$$

and a similar one for the left hand side of the flux conservation (23), we infer the following relation between spatial and temporal variation of w:

$$\frac{\partial w}{\partial t} \ = \ -Qb(w)^2 \frac{\alpha f(0,d/2)}{\left(f(0,w)+\alpha f(x,d/2)\right)^2} \ \frac{\partial w}{\partial x} \ , \tag{25}$$

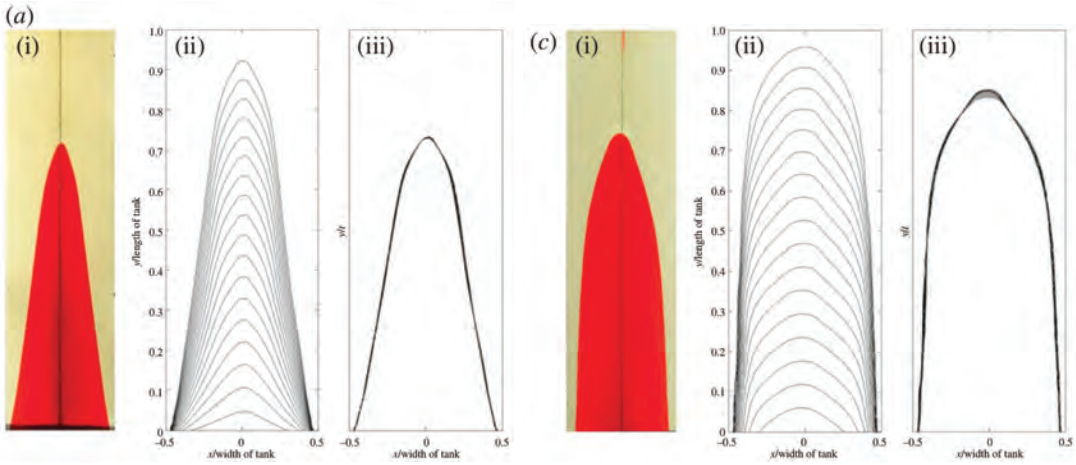

Figure 14: **a:** (i) visualisation, (ii) front position at different times and (iii) rescaling of the front position by time in the case of a low viscosity ratio. **b:** (i) visualisation, (ii) front position at different times and (iii) rescaling of the front position by time in the case of a large viscosity ratio. A shock type of finger develops such that the front is a travelling wave. Woods and Mingotti (2016).

which describes the propagation of the front with a width dependent velocity $c(w)$ such that

$$c(w) \;=\; Qb(w)^2 \frac{\alpha f(0,d/2)}{\left(f(0,w)+\alpha f(x,d/2)\right)^2} \quad . \tag{26}$$

Two possibilities can be regarded from (25). If the velocity $c(w)$ is a monotonic function of w, a finger intrudes the Hele-Shaw cell with a constant advection velocity along the $y = \overline{\text{cst}}$ lines. In the case where $c(w)$ is non-monotonic, a shock front develops and the solution needs regularisation to account for the effective propagation. We must therefore seek whether such shock solutions may develop and the corresponding physical configuration.

To gain a qualitative understanding of the variations of $c(w)$, we assume the Hele-Shaw cell has the following elliptical profile:

$$b(w) \;=\; b_0 \left(1 - \frac{2w}{d}\right)^{1/2} \quad . \tag{27}$$

After some algebra, one may find that a shock occurs provided that

$$\alpha = \frac{\mu_1}{\mu_2} \;>\; \frac{5}{2} > 1 \; . \tag{28}$$

We therefore conclude that shock solutions develop for a large viscosity ratio between the intruding fluid and the preceding fluid.

In the case of shock solutions, a regularisation must be applied, with the constraint that the flux must be conserved from the original solution to the regularised one, as illustrated in figure 13.

4.3 Experimental study of the finger intrusion

The viscous intrusion in a depth-varying Hele-Shaw cell has been investigated in Woods and Mingotti (2016). As shown in figure 14, the intrusion is highlighted by red dye, which allows tracking of the front of the finger. In the case of a low viscosity ratio, but still above 1 such that Saffman-Taylor instability does not interfere with the dynamics, the finger front is elongated over time – figure 14.a. Rescaling by time shows the very good collapse of all the profiles on a master curve, in accord with the theoretical development in the preceding paragraph.

In the case of large viscosity ratio, as seen in figure 14.b, the front does not elongate with time, but rather resembles a travelling wave, which is characteristic of a shock-like finger. Nevertheless, as suggested in figure 13, a shock solution should have a flat nose, which is not observed here. The fact that the model only accounts for velocities along the propagation direction may explain such a discrepancy. At the tip of the finger, the intruding fluid recirculates and is left behind. The detailed calculation of the shock structure would be an interesting development of the model.

5 Convection in a Porous Medium

To develop an understanding of convection in a porous medium, we must consider the conservation of both tracers (such as salt) and heat. We begin by considering conservation of a tracer through a simple 1D flux model for a volume element of width δx. If the concentration of the tracer in the liquid is c, the amount of tracer in the volume between x and $x + \delta x$ is then

$$c\phi\delta x, \tag{29}$$

per unit cross-sectional area. The net advective flux of tracer into the volume is

$$-\left\{uc|_{x+\delta x} - uc|_x\right\} = -u\frac{\partial c}{\partial x}\delta x, \tag{30}$$

assuming that the fluid is incompressible so $\nabla \cdot \boldsymbol{u} = 0$. For a macroscopic diffusivity D, the net diffusive flux of tracer is

$$\left\{ \phi D\frac{\partial c}{\partial x}\bigg|_{x+\delta x} - \phi D\frac{\partial c}{\partial x}\bigg|_x \right\} = \phi D\frac{\partial^2 c}{\partial x^2}\delta x. \tag{31}$$

Equating the fluxes to the rate of change of tracer in the small volume limit gives the full 3D equation for conservation of tracer:

$$\phi\frac{\partial c}{\partial t} + (\boldsymbol{u}\cdot\nabla)c = \phi D\nabla^2 c. \tag{32}$$

One important difference when considering the conservation of heat in a porous medium is the heat transfer that occurs from the liquid to the solid. This diffusion happens on a time scale of δ^2/κ where δ is the typical size of a grain and κ is the thermal diffusivity. The typical time for the fluid to flow past a grain is δ/v where v is a typical velocity scale. If the flow time is much greater than the thermal diffusion time (equivalent to $\kappa \gg \delta v$) then the fluid and grains can be assumed to be in thermal equilibrium. This is very typical of most porous media, since the condition only requires that grains are smaller than about 10cm.

Taking a similar approach to before, but with the assumption of thermal equilibration, we can derive an equation for the conservation of heat in a porous medium. In the volume between x and $x + \delta x$, the thermal energy per unit cross-sectional area is

$$\overline{\rho C_P}T\delta x, \tag{33}$$

where C_P is the heat capacity at constant pressure and T is the temperature. The overbar here denotes an average over the solid and liquid components of the volume in the sense

$$\overline{x} = (1-\phi)x_s + \phi x_l, \tag{34}$$

where the subscripts s and l denote values for the solid and liquid phases respectively. The net advective flux of heat into the volume is

$$-\left\{(\rho C_p)_l uT|_{x+\delta x} - (\rho C_p)_l uT|_x\right\} = -(\rho C_p)_l\left(u\frac{\partial T}{\partial x}\right). \tag{35}$$

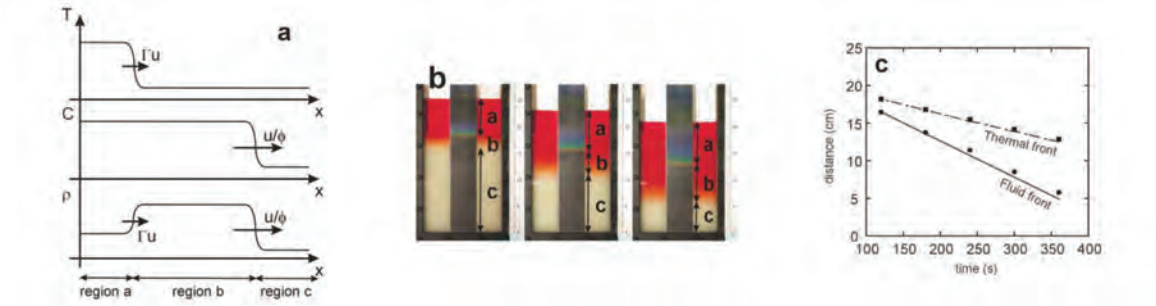

Figure 15: (a) Diagram showing the spatial distribution of temperature T, concentration c and density ρ, leading to three regions in which the fluid has different density. (b) Photographs from an experiment where hot, fresh water (dyed red) drained downwards through a bead pack initially saturated with cold, salty water. The red dye front indicates the front of fresh water, and the yellow line on the liquid crystal strip illustrates the leading edge of the thermal front. (c) The location of the dye front and thermal front from experimental data as dots, with straight lines showing theoretical predictions (Menand et al., 2003)

For an average thermal diffusivity $\overline{K}$, the net diffusive flux of heat is

$$\left\{ \overline{K}\frac{\partial T}{\partial x}\bigg|_{x+\delta x} - \overline{K}\frac{\partial T}{\partial x}\bigg|_{x} \right\} = \overline{K}\frac{\partial^2 T}{\partial x^2}. \tag{36}$$

As before, we can use the fluxes to now write down the 3D equation for conservation of heat

$$\overline{\rho C_p}\left(\frac{\partial T}{\partial t}\right) + \rho C_{pl}(\boldsymbol{u}\cdot\nabla T) = \overline{K}\nabla^2 T. \tag{37}$$

If we re-arrange both the conservation equations (32) and (37) into the form of an advection-diffusion equation,

$$\frac{\partial c}{\partial t} + \left(\frac{1}{\phi}\right)(\boldsymbol{u}\cdot\nabla)c = D\nabla^2 c, \tag{38}$$

$$\frac{\partial T}{\partial t} + \left(\frac{(\rho C_p)_l}{\overline{\rho C_p}}\right)(\boldsymbol{u}\cdot\nabla)T = \left(\frac{\overline{K}}{\overline{\rho C_p}}\right)\nabla^2 T, \tag{39}$$

then it is clear that the advection of tracer and heat occurs at different speeds. The advective speed of the tracer scales as the interstitial velocity u/ϕ, whereas the advective speed of heat is more similar to the Darcy velocity u (since the prefactor $\Gamma = (\rho C_p)_l/\overline{\rho C_p}$ in (39) is approximately one). The tracer therefore travels through the porous medium much faster than heat since it moves through the liquid phase only whereas a thermal anomaly must heat up the rock as it is being swept through the material by the liquid.

Menand et al. (2003) performed some experiments to show this behaviour. They placed hot, fresh water above a layer of cold, salty water in a bead pack, using dye to follow the spreading of salt through the porous medium and a liquid crystal strip to determine how the temperature front developed, as shown in figure 15b. The hot, fresh water is initially more dense than the water in the lower layer, but once thermal equilibrium has been reached

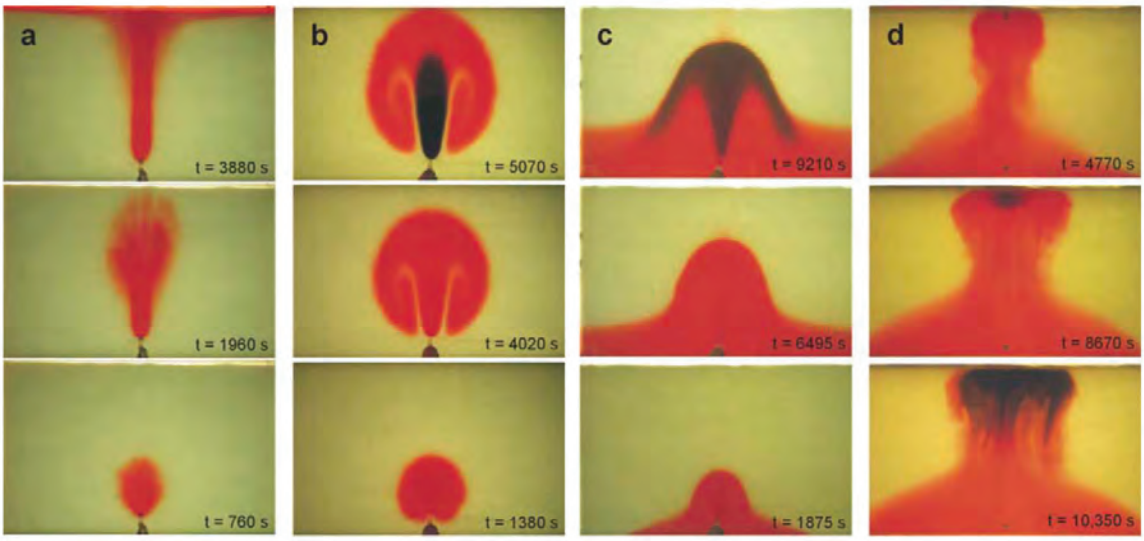

Figure 16: Photographs illustrating the flow patterns that arise when fluid of one temperature and salinity (dyed red) is continuously injected from a point source into a porous layer containing a fluid of different temperature and composition. (*a*) Fresh water injected into salty water, forming a plume. (*b*) Hotter fluid of the same salinity injected, which leads to a plume-like structure close to the source, and an effective mass source at the top of the plume. (*c*) Hotter, saltier water injected, leading to a fountain-like behaviour as the injected fluid loses its buoyancy. (*d*) Hotter, saltier water injected at the *top*, leading to sinking and formation of a gravity current. (Menand et al., 2003)

it will become less dense. As highlighted by figure 15a, the differences in salinity and temperature occur at fronts which move at the advective speeds calculated earlier. The difference in front speeds leads to three regions of different fluid density in the flow.

Injecting fluids with different combinations of temperature and salinity to an existing fluid in a porous medium will thus produce interesting behaviour. If the new fluid is hotter and saltier than the old fluid, it can initially be denser *or* lighter but will always end up more dense than the old fluid because of the fast equilibration of temperature. Figure 16 shows some interesting phenomena that can arise when injecting fluids of varying salinity and temperature into a porous medium. It is important to note that although the concepts of plumes and fountains can arise in these flows, viscosity is very important in problems of fluid in porous media and the motion is very slow compared to the turbulent problems discussed in earlier lectures. The fact that a combination of salt and heat lead to interesting dynamics here draws inevitable comparisons with the impact of double diffusion on flows. Since all of the dynamics here is controlled by the difference in *advection*, it would perhaps be apt to refer to these flows as affected by 'double advection'.

References

Bickle, M., A. Chadwick, H. E. Huppert, M. Hallworth, and S. Lyle
2007. Modelling carbon dioxide accumulation at Sleipner: Implications for underground carbon storage. *Earth and Planetary Science Letters*, 255(1-2):164–176.

Dudfield, P. and A. W. Woods
2013. On the use of seismic data to monitor the injection of CO2 into a layered aquifer. *Earth and Planetary Science Letters*, 368:132–143.

Farcas, A. and A. W. Woods
2015. Buoyancy-driven dispersion in a layered porous rock. *Journal of Fluid Mechanics*.

Menand, T., A. Raw, and A. W. Woods
2003. Thermal inertia and reversing buoyancy in flow in porous media. *Geophysical Research Letters*, 30(6):1291.

Nordbotten, J. M. and M. A. Celia
2006. Similarity solutions for fluid injection into confined aquifers. *Journal of Fluid Mechanics*, 561:307.

Woods, A. W.
2014. *Flow in Porous Rocks: Energy and Environmental Applications*. Cambridge University Press.

Woods, A. W., M. Hesse, R. Berkowitz, and K. W. Chang
2015. Multiple steady states in exchange flows across faults and the dissolution of co_2. *Journal of Fluid Mechanics*, 769:229–241.

Woods, A. W. and N. Mingotti
2016. Topographic viscous fingering: fluidfluid displacement in a channel of non-uniform gap width. *Phil. Trans. R. Soc. A*, 374(2078):20150427.

Lecture 10
Flow in Porous Rocks: The Influence of Temperature, Fluid-Rock Interactions and Viscous Instabilities

Notes by Edward Hinton and Bowen Zhao

June 29, 2018

1 Gravity Currents Driven by Variations in Temperature

Motivated by the geosequestration of carbon dioxide, we consider the flow of an injected fluid, which has different composition and temperature, to the ambient fluid within an inclined porous medium. Owing to the heat transfer between the fluid and the rock, the advection speed of the thermal energy is different to the fluid speed. The advection speed of the temperature front is given by [Phillips, 2009, Woods, 2014]

$$\Gamma u = \frac{\rho C_{pl}}{\overline{\rho C_p}} u \tag{1}$$

where u is the fluid velocity, C_p is the specific heat, C_{pl} is the specific heat of the liquid, and the overbar denotes a weighted average across the fluid and the solid matrix. Γ typically has values in the region $1.1 - 1.2$ depending on the porosity and specific fluids. The fluid front migrates with the interstitial speed u/ϕ which is much greater than Γu for typical values of the porosity, e.g. $\phi \approx 0.2$. The temperature front lags behind the fluid front.

We now apply this analysis to the injection of a cold fluid which is buoyant relative to the ambient fluid in an inclined aquifer [Rayward-Smith and Woods, 2011]. The injected fluid migrates away from the source with characteristic velocity U_1 and then acquires characteristic velocity U_2 at the thermal transition. The hot injectate travels faster ($U_2 > U_1$) and hence the depth of the current decreases across the transition (figure 1a). Mass conservation across the thermal transition is given by

$$U_1 H_1 - U_2 H_2 = \Gamma \phi U_1 (H_1 - H_2), \tag{2}$$

which can be rearranged to find the ratio of the depths,

$$\frac{H_2}{H_1} = \frac{1 - \Gamma\phi}{U_2/U_1 - \Gamma\phi}. \tag{3}$$

Next, we consider a hot buoyant injectate. This fluid cools after injection and subsequently migrates more slowly than the hot fluid near the source. The thermal transition will travel more slowly than the thermally adjusted injectate if the ambient fluid is not too cold (figure 1b). If the thermal transition travels faster than the thermally adjusted injectate then this adjusted injectate sinks relative to the original injectate, forming a layer below it (figure 1c).

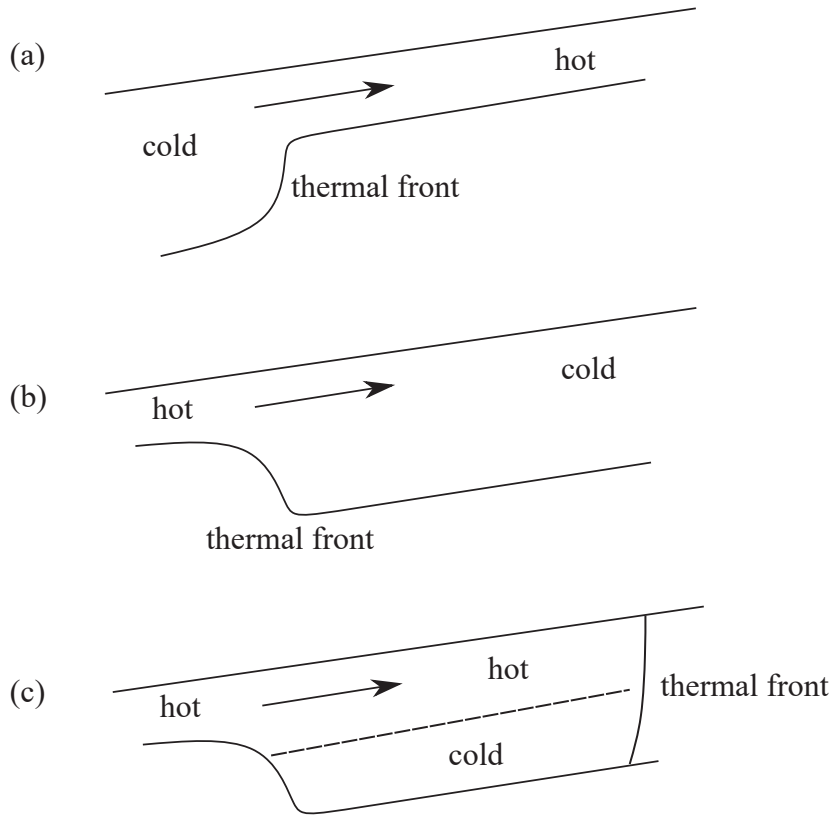

Figure 1: Migration of fluid and thermal fronts in an inclined aquifer. (a) Cold fluid accelerates across the thermal front. (b) Hot fluid decelerates across the thermal front when the thermal front travels more slowly than the thermally adjusted injectate. (c) For sufficiently high injection temperatures, the thermal front speeds exceeds the speed of the thermally adjusted injectate.

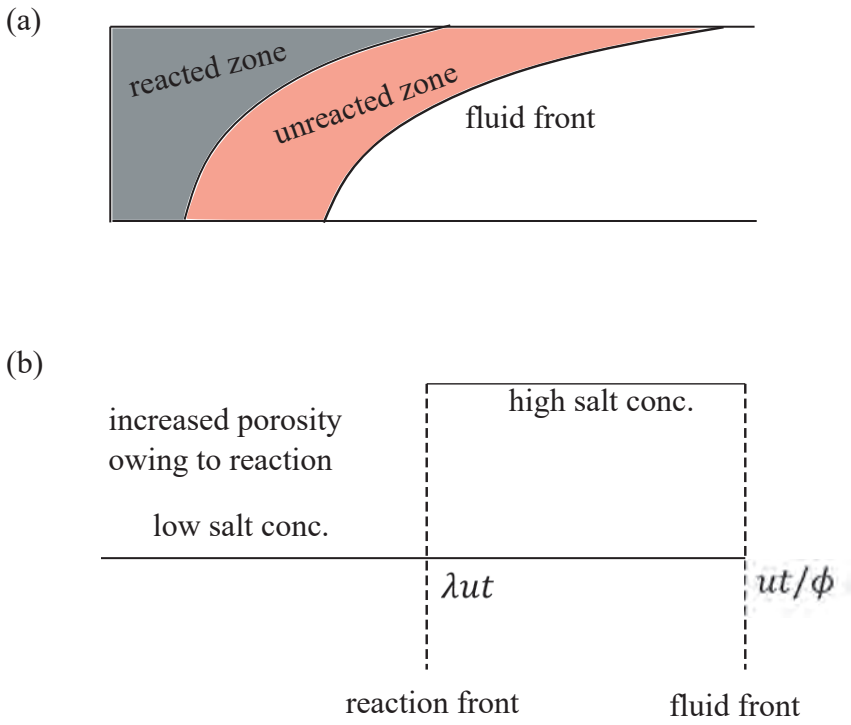

Figure 2: (a) Example flow structure for a reacting flow in a porous medium. (b) Salt concentration and location of the reaction front.

2 Reacting Flows in Porous Media

We consider the flow of reactive fluids through porous rock, important in the dissolution of mineral precipitate near oil wells [Verdon and Woods, 2007]. We suppose that there is a volume of salt $\epsilon \ll 1$, per unit volume of the rock, which is soluble in the liquid so that prior to the reaction, the solid volume fraction is $1-\phi$ and after the reaction, it is $1-\phi-\epsilon$ (see figure 2a). In order to calculate the speed of the front, we use a mass balance for the salt. The extent of the liquid zone is ut/ϕ and the extent of the salt-depleted rock is λut. The conservation of salt requires [Woods, 2014]

$$\lambda ut\epsilon(1-\phi) = (ut/\phi - \lambda ut)c_e\phi \tag{4}$$

where c_e is the concentration of the saturated salt in the liquid (see figure 2b). This gives the position of the reaction front

$$\lambda = \frac{c_e}{\phi c_e + \epsilon(1-\phi)}. \tag{5}$$

To calculate the shape of the current in figure 2a, we adopt the Boussinesq approximation, neglecting changes in density of the liquid except in the buoyancy forces, and we neglect changes in the porosity of the liquid except its impact on permeability [Verdon and Woods, 2007, Phillips, 2009]. The permeability in the reacted zone is k_u and the permeability in the unreacted zone is k_l. Let $y = h(x,t)$ be the depth of the reacted zone where y is

measured positive in the downwards direction. Mass continuity in the reacted zone implies

$$\frac{\partial h}{\partial t} = -\lambda \frac{\partial}{\partial x}\Big(u_u h\Big), \tag{6}$$

where u_u is the velocity of the unsaturated fluid (in the reacted zone). For the case of constant injection, Q, the flux across the aquifer satisfies,

$$Q = u_u h + u_l(H - h), \tag{7}$$

where u_l is the velocity in the saturated fluid, and H is the depth of the aquifer. Using the scalings [see Bear, 1971],

$$\mathcal{H} = h/H, \quad \xi = x/H, \quad \tau = Qt\lambda\beta/H^2, \tag{8}$$

we can combine equations (6) and (7) to find the dimensionless governing equation,

$$\frac{\partial \mathcal{H}}{\partial \tau} + \frac{\partial}{\partial \xi}\left(\frac{\mathcal{H}}{1 + (\beta - 1)\mathcal{H}}\right) = B\frac{\partial}{\partial \xi}\left(\frac{\mathcal{H}(1 - \mathcal{H})}{1 + (\beta - 1)\mathcal{H}}\frac{\partial \mathcal{H}}{\partial \xi}\right), \tag{9}$$

where $B = \Delta\rho g H k_l/\mu_l Q$ may be interpreted as a densimetric Froude number, being the ratio of the speed associated with the injection flux to the characteristic buoyancy speed [cf. Gunn and Woods, 2011]. $\beta = \mu_l k_u/k_l\mu_u$ is the mobility ratio across the reaction front. Pegler et al. [2014] found the same governing equation as (9) for the injection of a relatively buoyant fluid into an ambient fluid of different viscosity, with β replaced by the viscosity ratio.

For $B \ll 1$, we approximate (9) by neglecting the right-hand side. In the case $\beta > 1$, this leads to solutions in which the interface between the reacted and unreacted zones grows in proportion to time, τ. $\beta > 1$ is typical in a dissolution reaction. The growth of the interface implies that the significance of the diffusive term on the right-hand side of (9) decays relative to the advective term and can be neglected at times of order $\tau \gg B$, even when B is not small.

3 Inter-Seasonal Heat Storage

Many industrial plants, data centers and power stations generate large amounts of low-grade waste thermal energy. In winter months, there is a very high demand for thermal energy to heat buildings which is met mainly through burning fossil fuels. One strategy to reduce this consumption is to store waste thermal energy in permeable aquifers and extract it in the winter.

To gain insight into the efficiency of such thermal storage, we formulate a model for the periodic injection and extraction of fluid from a line well in a horizontal saturated aquifer [Dudfield and Woods, 2014]. The governing equation for the depth, $h(x, t)$, of the injectate in an aquifer of depth H is

$$\frac{\partial h}{\partial t} + \frac{Q(t)}{H\phi}\frac{\partial h}{\partial x} = S\frac{\partial}{\partial x}\left(h\left(1 - \frac{h}{H}\right)\frac{\partial h}{\partial x}\right), \tag{10}$$

where S is the characteristic buoyancy speed, and $Q(t)$ is the flux which alternates between positive and negative,

$$Q(t) = \begin{cases} Q & \text{if } 2n\tau < t \leq (2n+1)\tau, \\ -Q & \text{if } (2n+1)\tau < t \leq (2n+2)\tau \end{cases} \tag{11}$$

In the first injection period, in which $Q(t)$ is positive, the characteristic length which fluid travels into the aquifer is $L \sim Qt/\phi H$. The injected fluid cannot all be recovered, however, a greater fraction of the injected fluid is recovered after each cycle. There is a large oscillation in the flow near the source as fluid is injected and recovered, however, beyond this region, fluid spreads away from the source owing to buoyancy. The rate of this spreading of the nose can be obtained by balancing the buoyancy term in equation (10) with the time derivative which gives $x \sim t^{1/2}$. Dudfield and Woods [2015] extended this analysis to consider an inclined aquifer, and found that the fraction of injectate recovered decreases with each cycle owing to the advective nature of the buoyancy-driven flow away from the source.

4 Viscous Fingering in Porous Media

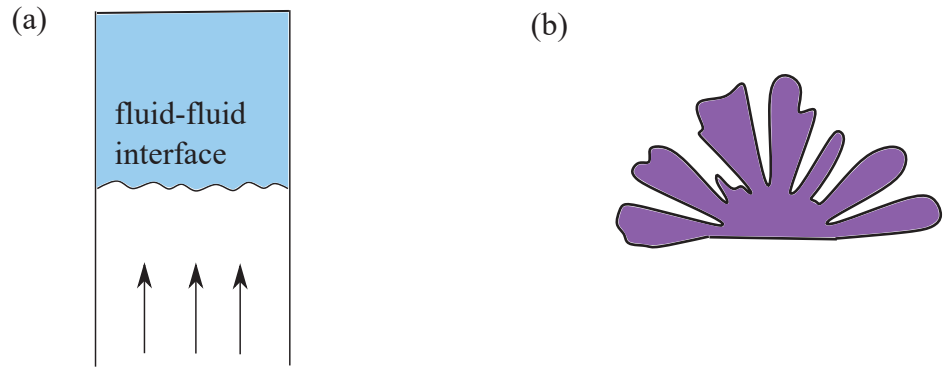

Figure 3: (a) The instability which occurs when a less viscous fluid is injected into a more viscous fluid. (b) Fractal pattern which arise in a Hele-Shaw cell.

The injection of a less viscous fluid into a more viscous fluid can lead to the onset of instabilities (see Homsy [1987] for a review). The less viscous fluid tends to penetrate or 'finger' through the more viscous fluid. We begin by considering injection in a Hele-Shaw cell. Darcy's law is

$$\frac{\mathrm{d}p}{\mathrm{d}x} = -\frac{\mu U}{k} + \rho g. \tag{12}$$

If we displace the interface between the two fluids by an amount δx, then the pressure on this displace fluid is

$$\delta p = (p_i - p_d) = \Big[(\mu_d - \mu_i)U/k + (\rho_i - \rho_d)g\Big]\delta x \tag{13}$$

where the subscripts i and d denote the injected and displaced fluids, respectively. If the net pressure is positive then a small displacement will amplify. If we consider horizontal

flow in which gravity can be neglected, the interface is unstable when $\mu_d > \mu_i$. Gravity stabilises this instability provided that

$$U < (\rho_d - \rho_a)gk/(\mu_d - \mu_a). \tag{14}$$

When a less viscous fluid is injected into an axisymmetric Hele-Shaw cell, beautiful fractal patterns occur owing to this instability (see figure 3b). At early times the radius of the injected fluid is small and surface tension stabilizes the interface suppresses the fingering. As the radius grows, the role of surface tension diminishes and the onset of fingering occurs. The fractal dimension of the shape is 1.7 which means that the area occupied by the pattern within a circle of radius r is proportional to $r^{1.7}$.

5 Pumice Eruptions

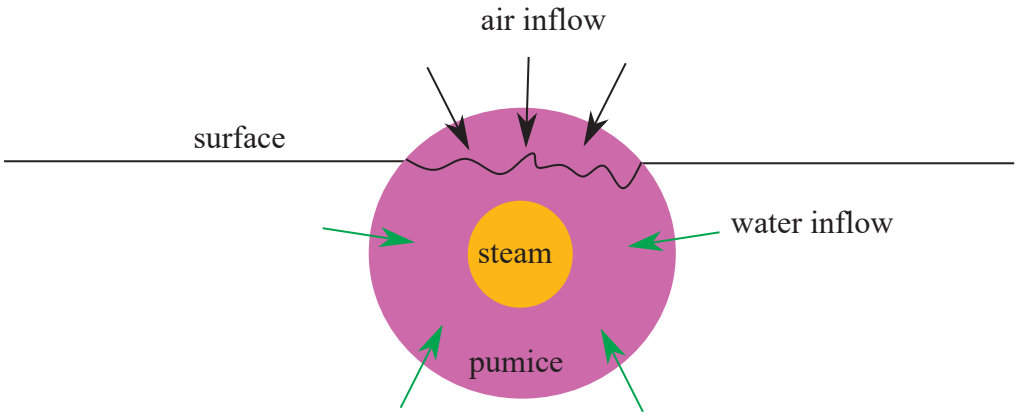

Figure 4: Schematic of the cooling mechanisms in a pumice 'lavaberg'.

The submerged Havre volcanoe, off the north coast of New Zealand, erupted in 2012 releasing large volumes of pumice into the ocean. Much of the pumice cooled as it rose and subsequently sank back to the seabed. However, there was a significant volume which accumulated on the surface forming a 'pumice raft' which took months to disperse. This surprising result could be caused by trapping of air within the pumice.

After eruption, the hot pumice is initially buoyant because it is filled with steam. As it rises, water flows into the pumice (see figure 4). When the pumice reaches the surface, air is drawn in as well as water. This air may be capillary trapped within the pumice before the steam has cooled sufficiently for the pumice to sink. This could enable long-term floating.

References

J. Bear. *Dynamics of flow in porous media*. Elsevier, 1971.

P. Dudfield and A. W. Woods. On the periodic injection of fluid into, and its extraction from, a confined aquifer. *Journal of Fluid Mechanics*, 755:111141, 2014. doi: 10.1017/jfm.2014.311.

P. Dudfield and A. W. Woods. Early-time periodic injection and extraction in an inclined confined aquifer. *Journal of Fluid Mechanics*, 776 (2015):430–457, 2015. ISSN 0022-1120. doi: 10.1017/jfm.2015.325. URL `http://www.journals.cambridge.org/abstract_S0022112015003250`.

I. Gunn and A. W. Woods. On the flow of buoyant fluid injected into a confined, inclined aquifer. *J. Fluid Mech*, 672:109–129, 2011. doi: 10.1017/S0022112010005896.

G. Homsy. Viscous Fingering in Porous media. *Annu. Rev. Fluid Mech*, pages 271–311, 1987.

S. S. Pegler, H. E. Huppert, and J. A. Neufeld. Fluid injection into a confined porous layer. *J. Fluid Mech.*, 745:592–620, 2014. ISSN 0022-1120. doi: 10.1017/jfm.2014.76.

O. M. Phillips. Geological Fluid Dynamics. In *Sub-surface Flow and Reactions*. Cambridge University Press, 2009.

W. J. Rayward-Smith and A. W. Woods. On the propagation of non-isothermal gravity currents in an inclined porous layer. *Journal of Fluid Mechanics*, 686:250271, 2011. doi: 10.1017/jfm.2011.327.

J. Verdon and A. W. Woods. Gravity-driven reacting flows in a confined porous aquifer. *Journal of Fluid Mechanics*, 588:2941, 2007. doi: 10.1017/S0022112007007069.

A. W. Woods. *Flow in Porous Rocks: Energy and Environmental Applications*. Cambridge University Press, 2014. doi: 10.1017/CBO9781107588677.

Horizontal Shear Instabilities in the Stellar Regime

Laura Cope

October 1, 2018

1 Introduction

Stratified shear flows are ubiquitous in geophysical fluids such as the Earth's atmosphere and oceans and astrophysical fluids such as stellar interiors. The stratification can arise due to thermal or compositional gradients, with strong and stable stratification providing a stabilizing effect against mixing. It is of interest to understand how much mixing and transport can occur in these flows in spite of the stratification.

In geophysical (atmospheric and oceanic) flows, the Prandtl number, defined to be the ratio of the kinematic viscosity to density diffusivity, is approximately of order unity. The stability of stratified horizontal shear flows within this context has been studied previously, for example by Lucas et al. [7] who were motivated by the 'zig-zag' instability (see [1, 2]) and the spontaneous layering of density fields often found in nature. In contrast, astrophysical (stellar) flows are characterised by very small Prandtl numbers leading to significantly different dynamics. The stability of stratified vertical shear flows to infinitesimal and finite amplitude perturbations was studied within this context, where it was found that vertical shears can be stabilized by sufficiently strong stratification (see [4] and references therein).

Bringing these ideas together, the main objective of our study is to investigate the stability and dynamics of stratified horizontal shear flows within an astrophysical regime. We are motivated by the solar interior which is composed of two layers: an inner radiative zone and a differentially rotating outer convective zone. A narrow transition region exists between these two layers, known as the solar tachocline, and is characterised by strong and stable stratification and combined horizontal and vertical shear. Ignoring the vertical shear for now, we use a combination of linear (infinitesimal) stability analysis and direct numerical simulations to study the stability of stratified horizontal shear flows and identify appropriate astrophysically motivated scaling regimes which permit theoretical estimates to be made about the mixing efficiency.

We begin in section 2 by introducing the mathematical model that will form the basis of our investigation. In section 3, we carry out a linear stability analysis of stratified horizontal shear flows. We consider the effects of the stratification and Prandtl number on the stability of the system and show that, in contrast to vertically sheared flows, the stability ultimately remains independent of both.

Direct numerical simulations allow us to study the nonlinear behaviour of the system in section 4, where we begin by exploring the effect of the geometry of the domain. The 'zig-zag' instability and density layering observed in [7] are found to be robust in a subset of domain sizes, findings which can be linked to our linear stability results. In addition, and

in a similar fashion to [3], we identify two scaling regimes of astrophysical interest, one of which we are able to demonstrate numerically. Future work hopes to explore the second of these two regimes. Predictions for the mixing efficiency in each regime are derived, where we demonstrate the potential for high mixing efficiency when the fluid viscosity is negligible.

2 Mathematical Model

2.1 Standard equations

We consider an incompressible, non-rotating, stably stratified Kolmogorov flow with streamwise velocity field aligned with the x-axis. The basic state comprises a density distribution $\rho_B(z)$ with reference density ρ_0 and linear vertical gradient β such that $\rho_B(z) = \rho_0 - \beta z$, and the body-forced laminar velocity field $\mathbf{u}_L(y)$ is monochromatic with cross-stream wavenumber n. The total density field, ρ, includes perturbations $\rho'(x, y, z, t)$ away from the basic state such that $\rho = \rho_B(z) + \rho'(x, y, z, t)$, and the three-dimensional velocity field is given by $\mathbf{u}(x, y, z, t) = u\mathbf{e}_x + v\mathbf{e}_y + w\mathbf{e}_z$. We impose triply-periodic boundary conditions on ρ' and $\mathbf{u}$ such that $(x, y, z) \in [0, L_x) \times [0, L_y) \times [0, L_z)$. Figure 1 illustrates the basic state in the case where $n = 1$.

We use the Boussinesq approximation in which density fluctuations are neglected except in the buoyancy force [9]. The governing equations are given by:

$$\frac{\partial \mathbf{u}}{\partial t} + \mathbf{u} \cdot \nabla \mathbf{u} + \frac{1}{\rho_0} \nabla p = \nu \nabla^2 \mathbf{u} - \frac{\rho' g}{\rho_0} \mathbf{e}_z + \chi \sin\left(\frac{2\pi n y}{L_y}\right) \mathbf{e}_x, \tag{1}$$

$$\frac{\partial \rho'}{\partial t} + \mathbf{u} \cdot \nabla \rho' - \beta w = \kappa \nabla^2 \rho', \tag{2}$$

$$\nabla \cdot \mathbf{u} = 0, \tag{3}$$

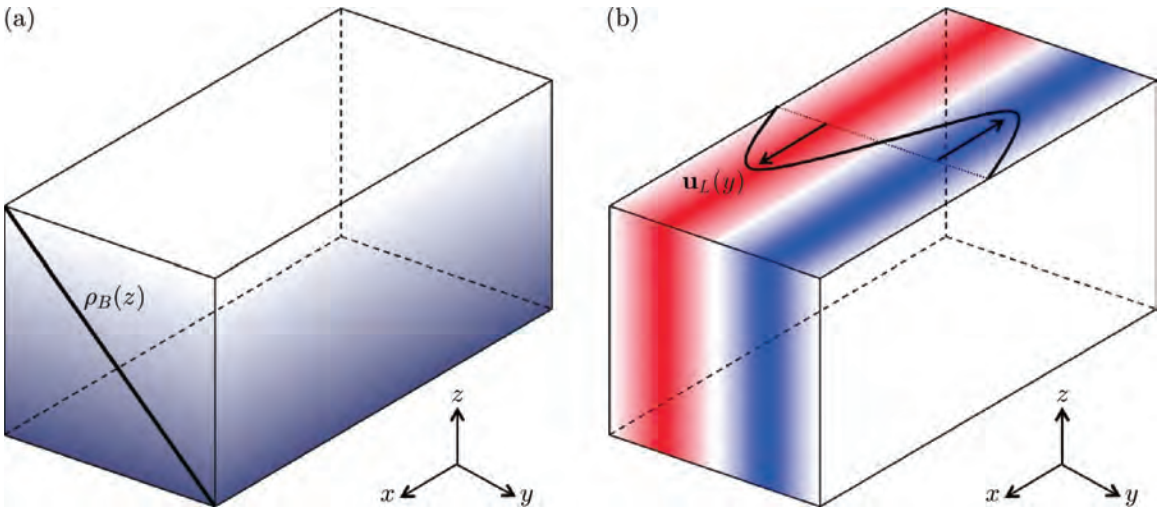

Figure 1: Schematic drawings of the basic state set-up showing (a) the density distribution $\rho_B(z)$ and (b) the laminar velocity profile $\mathbf{u}_L(y)$ with cross-stream wavenumber $n = 1$.

where ν is the kinematic viscosity, κ is the density diffusivity, χ is the forcing amplitude, p is the pressure and gravity g acts in the negative z-direction. In this study, we specify that $L_y = L_z$ while L_x may vary continuously such that the aspect ratio of the domain is given by $\alpha = L_x/L_y$. $\alpha > 1$ corresponds to domains which are longer in the streamwise direction.

In equilibrium, we anticipate a balance between the body force and fluid inertia such that $\mathbf{u} \cdot \nabla \mathbf{u} \sim \chi \sin(2\pi n y/L_y)\, \mathbf{e}_x$ in the streamwise direction. For a characteristic length scale $L_y/2\pi$, this gives a characteristic velocity scale $\sqrt{\chi L_y/2\pi}$ and a characteristic time scale $\sqrt{L_y/2\pi\chi}$. Combined with the vertical density gradient scale β, we use the same non-dimensionalisation as in [7] to give the following system of equations, in which all quantities are non-dimensional:

$$\frac{\partial \mathbf{u}}{\partial t} + \mathbf{u} \cdot \nabla \mathbf{u} + \nabla p = \frac{1}{Re} \nabla^2 \mathbf{u} - B\rho' \mathbf{e}_z + \sin(ny)\mathbf{e}_x, \tag{4}$$

$$\frac{\partial \rho'}{\partial t} + \mathbf{u} \cdot \nabla \rho' - w = \frac{1}{RePr} \nabla^2 \rho', \tag{5}$$

$$\nabla \cdot \mathbf{u} = 0. \tag{6}$$

We define three non-dimensional numbers, the Reynolds number Re, the buoyancy parameter B and the Prandtl number Pr, which determine the dynamics of the system:

$$Re := \frac{\sqrt{\chi}}{\nu} \left(\frac{L_y}{2\pi} \right)^{\frac{3}{2}}, \qquad B := \frac{g\beta L_y}{\rho_0 \chi 2\pi} = \frac{N_B^2 L_y}{2\pi\chi}, \qquad Pr := \frac{\nu}{\kappa}, \tag{7}$$

where $N_B = \sqrt{g\beta/\rho_0}$ is the (dimensional) buoyancy frequency associated with the background density field. It is convenient to introduce the Péclet number Pe, defined as

$$Pe := RePr = \frac{\sqrt{\chi}}{\kappa} \left(\frac{L_y}{2\pi} \right)^{\frac{3}{2}}. \tag{8}$$

Both sets of parameters, (Re, B, Pr) or (Re, B, Pe), uniquely define the system and will be used interchangeably throughout this report. Within this non-dimensional system, the domain is a cuboid and variables ρ' and $\mathbf{u}$ have triply-periodic boundary conditions such that $(x, y, z) \in [0, 2\pi\alpha) \times [0, 2\pi) \times [0, 2\pi)$. This system, defined by equations (4), (5) and (6), will henceforth be referred to as the standard system of equations.

2.2 Low-Péclet number equations

Systems in which a field diffuses on a timescale much shorter than the advective time enter a *quasi-static* regime in which there is a balance between the source and diffusive terms. Motivated by astrophysical applications, we consider the standard set of equations (4), (5) and (6) in the asymptotic limit of low Prandtl number, or correspondingly low Péclet number (LPN). This limit was studied by Speigel [8] in the context of thermal convection, and more recently by Lignières [6] in the context of stably stratified flows. Lignières proposed that the standard equations can be approximated by a reduced set of equations called the "low-Péclet number" equations (LPN equations hereafter), in which the density fluctuations are slaved to the vertical velocity field:

$$\frac{\partial \mathbf{u}}{\partial t} + \mathbf{u}\cdot\nabla\mathbf{u} + \nabla p = \frac{1}{Re}\nabla^2\mathbf{u} - B\rho'\mathbf{e}_z + \sin(ny)\mathbf{e}_x, \tag{9}$$

$$w + \frac{1}{Pe}\nabla^2\rho' = 0, \tag{10}$$

$$\nabla\cdot\mathbf{u} = 0. \tag{11}$$

These can be derived by assuming a regular asymptotic expansion of ρ' in powers of Pe, i.e. $\rho' = \rho'_0 + \rho'_1 Pe + \mathcal{O}(Pe^2)$, and by assuming that the velocity field is of order unity. At lowest order (Pe^{-1}), we get $\nabla^2\rho'_0 = 0$ implying that $\rho'_0 = 0$ under the boundary conditions, while at the next order (Pe^0), the equations yield $-w = \nabla^2\rho'_1 \approx Pe^{-1}\nabla^2\rho'$ as required.

Noting that equation (10) can be re-written as $\rho' = -Pe\nabla^{-2}w$, we derive the reduced set of LPN equations:

$$\frac{\partial \mathbf{u}}{\partial t} + \mathbf{u}\cdot\nabla\mathbf{u} + \nabla p = \frac{1}{Re}\nabla^2\mathbf{u} + BPe\nabla^{-2}w\mathbf{e}_z + \sin(ny)\mathbf{e}_x, \tag{12}$$

$$\nabla\cdot\mathbf{u} = 0. \tag{13}$$

These equations explicitly demonstrate that under the LPN approximation (and in contrast to the standard equations), there are only two non-dimensional parameters governing the flow dynamics, notably the Reynolds number Re and the product of the buoyancy parameter and either the Prandtl number, BPr, or equivalently the Péclet number, BPe.

Throughout this work, we will study both systems of equations, verifying the validity of the LPN equations where possible. For simplicity, we restrict all future analysis in this study to systems in which the cross-stream wavenumber $n = 1$.

3 Linear Stability Analysis

3.1 Standard equations

We consider the stability of the basic state to infinitesimal perturbations. The laminar solution $\mathbf{u}_L(y)$ satisfies $Re^{-1}\nabla^2\mathbf{u}_L + \sin(y)\mathbf{e}_x = 0$, hence it is given by

$$\mathbf{u}_L(y) = Re\sin(y)\mathbf{e}_x. \tag{14}$$

For small perturbations $\mathbf{u}'(x,y,z,t)$ away from the laminar solution, i.e. letting $\mathbf{u} = \mathbf{u}_L(y) + \mathbf{u}'(x,y,z,t)$, the linearised perturbation equations are:

$$\frac{\partial \mathbf{u}'}{\partial t} + Re\cos(y)v'\mathbf{e}_x + Re\sin(y)\frac{\partial \mathbf{u}'}{\partial x} + \nabla p = \frac{1}{Re}\nabla^2\mathbf{u}' - B\rho'\mathbf{e}_z, \tag{15}$$

$$\frac{\partial \rho'}{\partial t} + Re\sin(y)\frac{\partial \rho'}{\partial x} - w' = \frac{1}{Pe}\nabla^2\rho', \tag{16}$$

$$\nabla\cdot\mathbf{u}' = 0. \tag{17}$$

In this set of partial differential equations (PDEs), the coefficients are periodic in y but independent of x, z and t. Consequently, and in the conventional fashion, we consider normal mode disturbances of the form:

$$q(x, y, z, t) = \hat{q}(y) \exp[ik_x x + ik_z z + \sigma t], \tag{18}$$

where $q \in (u', v', w', \rho', p)$ and k_x and k_z are the perturbation wavenumbers in the x and z-directions, respectively. The geometry of the model set-up requires that $k_x \in \mathbb{R}$ and $k_z \in \mathbb{Z}$. We seek periodic solutions for $\hat{q}(y)$ given by

$$\hat{q}(y) = \sum_{m=-M}^{M} q_m e^{imy}. \tag{19}$$

Substituting this ansatz into equations (15), (16) and (17) and using the orthogonality property of complex exponentials, we obtain a $5 \times (2M + 1) = (10M + 5)$ algebraic system of equations for the u_m, v_m, w_m, ρ_m, p_m for $m \in (-M, M)$:

$$\frac{1}{2} Re k_x (u_{m+1} - u_{m-1}) - \frac{m^2 + k_x^2 + k_z^2}{Re} u_m - \frac{1}{2} Re (v_{m-1} + v_{m+1}) - ik_x p_m = \sigma u_m, \tag{20}$$

$$\frac{1}{2} Re k_x (v_{m+1} - v_{m-1}) - \frac{m^2 + k_x^2 + k_z^2}{Re} v_m - imp_m = \sigma v_m, \tag{21}$$

$$\frac{1}{2} Re k_x (w_{m+1} - w_{m-1}) - \frac{m^2 + k_x^2 + k_z^2}{Re} w_m - B\rho_m - ik_z p_m = \sigma w_m, \tag{22}$$

$$\frac{1}{2} Re k_x (\rho_{m+1} - \rho_{m-1}) + w_m - \frac{m^2 + k_x^2 + k_z^2}{RePr} \rho_m = \sigma \rho_m, \tag{23}$$

$$k_x u_m + m v_m + k_z w_m = 0. \tag{24}$$

This system can be re-formulated as a generalised eigenvalue problem for the complex growth rates σ,

$$\mathbf{A}(k_x, k_z, Re, B, Pr)\mathbf{X} = \sigma \mathbf{B}\mathbf{X}, \tag{25}$$

where $\mathbf{X} = (u_{-M}, ..., u_M, v_{-M}, ..., v_M, w_{-M}, ..., w_M, \rho_{-M}, ..., \rho_M, p_{-M}, ..., p_M)$, $\mathbf{A}$ and $\mathbf{B}$ are $(10M+5) \times (10M+5)$ square matrices and $\mathbf{B}_{i,j} = \{\delta_{ij},\ i, j \leq (8M+4);\ 0,\ \text{otherwise}\}$. For perturbation wavenumbers k_x and k_z and system parameters Re, B and Pr, the maximum value of the real part of the growth rates σ determines the linear stability. The eigenvalue problem can be solved numerically, with M chosen such that convergence is achieved. For example, for a 2D perturbation such that $k_x = 1$ and $k_z = 0$ and system parameters $Re = 50$, $B = 50$ and $Pr = 1$, we find that $(\text{Re}\ \sigma)_{max} = \sigma = -0.02$, i.e. this mode is stable to infinitesimal perturbations.

Maintaining temporary focus on the case when $B = 50$ and $Pr = 1$, we consider the linear stability of the system of equations across a range of Reynolds numbers and both 2D and 3D perturbation modes. Figure 2(a) shows the neutral stability curves ($\sigma = 0$) for a range of k_z modes ($k_z \in (0, ..., 6)$) across a spectrum of streamwise wavenumbers k_x and Reynolds numbers, matching results in [7]. Stability ($\sigma < 0$) is found to the left and above the curves while instability ($\sigma > 0$) exists to the right and below. The black curve illustrates the $k_z = 0$ mode (henceforth referred to as the 2D mode). For $Re \sim \mathcal{O}(1)$, this mode asymptotes to the line $Re = 1.19$, implying that the system is linearly stable when

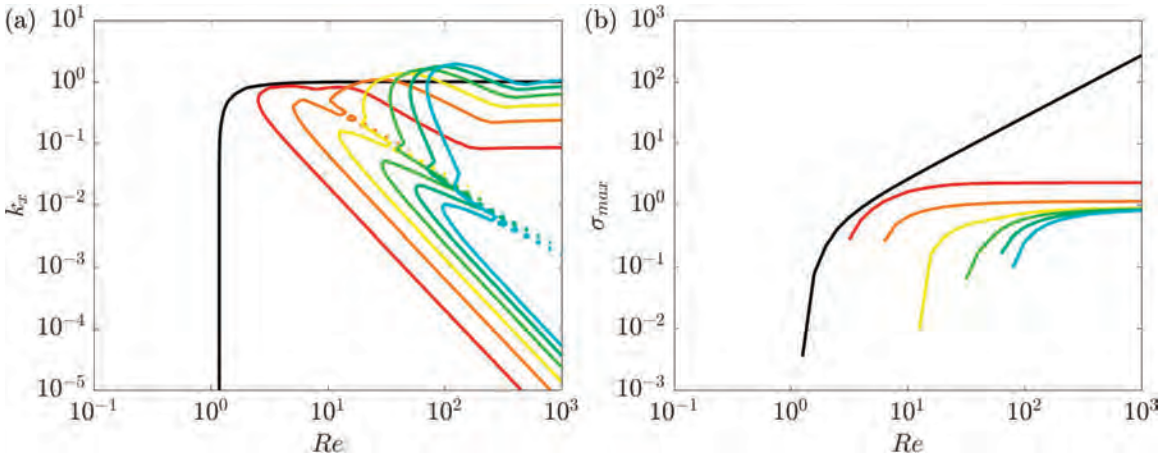

Figure 2: (a) Neutral stability curves for a range of k_z modes plotted against a spectrum of Reynolds numbers and k_x modes. Instability occurs to the right and below the curves. (b) The corresponding largest growth rates σ_{max} computed across a spectrum of k_x modes and plotted for a collection of k_z modes and a range of Reynolds numbers. The curves plotted include $k_z = 0$, 1, 2, 3, 4, 5, 6 and the standard equations were used with $B = 50$ and $Pr = 1$ fixed.

$Re < 1.19$. For large Re, it asymptotes to $k_x = 1$ but, crucially, always lies below this line, leading to the conclusion that domains such that $\alpha = L_x/L_y \leq 1$ are linearly stable to the 2D mode.

The coloured curves show the neutral stability curves for the first six 3D modes ($k_z \in (1, ..., 6)$). The onset of instability in the 3D modes occurs for higher Reynolds numbers than the 2D mode, and it would appear, at least from the selection of curves plotted in figure 2(a), that the critical Reynolds number for instability increases monotonously with increasing k_z. For $Re \sim \mathcal{O}(100)$, the 3D curves actually cross and lie above the line $k_x = 1$ implying that these modes are unstable for domains where $\alpha = 1$, i.e. cubic domains. The 2D mode, however only becomes unstable when $\alpha > 1$, posing the interesting question relating to the effect of the domain geometry on the dynamics. This question will be addressed in section 4.2.

A curious scaling emerges from figure 2(a), which is calculated to be $k_x \sim Re^{-4/3}$ ($k_z \geq 1$) on the lower branch of the neutral stability curves. Whilst we do not have an explanation for this scaling within this report, future work hopes to investigate this further within the system of equations.

Figure 2(b) further analyses the information in figure 2(a) by computing, for each Reynolds number and k_z, the largest growth rate σ_{max} across all values of k_x (only including $\sigma_{max} > 0$. It is clear that the 2D mode is always the most unstable mode, thus we would predict that this mode would dominate the dynamics in the system when it is unstable (i.e. for domain sizes such that $\alpha > 1$).

Having laid the foundations for our linear stability analysis, we now explore the effects of the buoyancy parameter and the Prandtl number on the overall picture, venturing closer towards the astrophysical regime. Figure 3 plots the neutral stability curves, in exactly

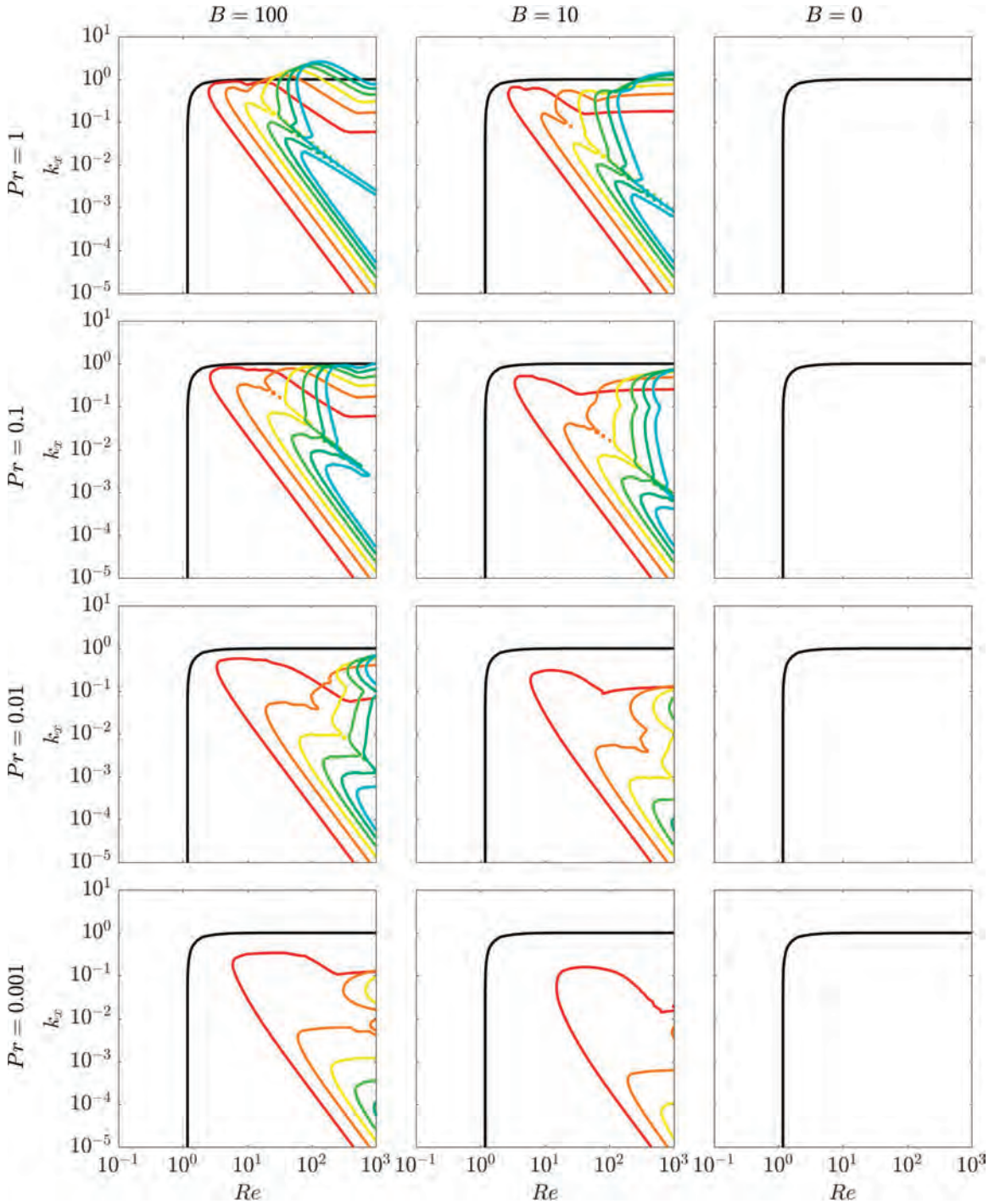

Figure 3: Neutral stability curves for a range of k_z modes plotted against a spectrum of Reynolds numbers and k_x modes. Instability occurs to the right and below the curves. Three different buoyancy parameters were used: $B = 100$ (first column), $B = 10$ (second column), $B = 0$ (third column), and four different Prandtl numbers: $Pr = 1$ (first row), $Pr = 0.1$ (second row), $Pr = 0.01$ (third row), $Pr = 0.001$ (fourth row). The curves plotted include $k_z = 0$, 1, 2, 3, 4, 5, 6 and the standard equations were used.

the same fashion as in figure 2(a), for three different buoyancy parameters: $B = 100$ (first column), $B = 10$ (second column), $B = 0$ (third column), and four different Prandtl numbers: $Pr = 1$ (first row), $Pr = 0.1$ (second row), $Pr = 0.01$ (third row), $Pr = 0.001$ (fourth row). Whilst the neutral stability curves are identical for the 2D mode, clear trends exist for the 3D modes. In the unstratified case ($B = 0$), no 3D modes are unstable. It can be seen that a reduction in the value of B shifts the critical Reynolds numbers for the onset of instability of the 3D modes towards higher values, thereby making these modes less unstable. We would anticipate this trend to continue as $B \to 0$ and the system approaches the unstratified limit.

A reduction in the Prandtl number also has the same effect. We speculate that as $Pr \to 0$, keeping B fixed and finite, the system also approaches a state in which only the 2D mode is unstable. Thus, $B \to 0$ (at fixed Pr) and $Pr \to 0$ (at fixed B) have the same effect: the 3D modes of instability are suppressed while the 2D mode remains unstable. The explanation for this emerges from equation (5). As the Prandtl number becomes very small (keeping the Reynolds number finite), the Péclet number becomes small and so the density diffusivity becomes large. In this case, a small parcel of fluid that is advected into surrounding fluid of a different density will adjust very rapidly to its surroundings, thereby reducing the buoyancy force and so approximating an unstratified system.

The modest selection of buoyancy parameters and Prandtl numbers explored in figure 3 suggests that the critical Reynolds number, Re_c, for the onset of linear instability, as given by the 2D mode, is independent of both of these parameters, and is fixed at $Re_c = 1.19$. In order to test this hypothesis, we compute Re_c numerically for a wide range of values of B and Pr. It is indeed found to be a constant, therefore we conclude that the critical Reynolds number is independent of the other two parameters in the system. This result differs quite substantially from that obtained in [4] for the case of a vertical shear, where stratification was found to be able to stabilize a system.

3.2 Low-Péclet number equations

We now examine the linear stability of the LPN equations, given by equations (12) and (13). We follow the same steps as in the previous section, however this time we find ourselves working with a reduced set of four equations rather than five. We obtain a $4 \times (2M + 1) = (8M + 4)$ algebraic system of equations for the u_m, v_m, w_m, p_m for $m \in (-M, M)$:

$$\frac{1}{2}Rek_x(u_{m+1} - u_{m-1}) - \frac{m^2 + k_x^2 + k_z^2}{Re}u_m - \frac{1}{2}Re(v_{m-1} + v_{m+1}) - ik_x p_m = \sigma u_m, \quad (26)$$

$$\frac{1}{2}Rek_x(v_{m+1} - v_{m-1}) - \frac{m^2 + k_x^2 + k_z^2}{Re}v_m - imp_m = \sigma v_m, \quad (27)$$

$$\frac{1}{2}Rek_x(w_{m+1} - w_{m-1}) - \frac{m^2 + k_x^2 + k_z^2}{Re}w_m - \frac{BPe}{k_x^2 + k_z^2}w_m - ik_z p_m = \sigma w_m, \quad (28)$$

$$k_x u_m + mv_m + k_z w_m = 0. \quad (29)$$

As before, this system can be re-formulated as a generalised eigenvalue problem for the complex growth rates σ,

$$\mathbf{A}(k_x, k_z, Re, BPr)\mathbf{X} = \sigma\mathbf{B}\mathbf{X}, \tag{30}$$

where $\mathbf{X} = (u_{-M}, ..., u_M, v_{-M}, ..., v_M, w_{-M}, ..., w_M, p_{-M}, ..., p_M)$, $\mathbf{A}$ and $\mathbf{B}$ are $(8M+4) \times (8M+4)$ square matrices and $\mathbf{B}_{i,j} = \{\delta_{ij},\ i, j \leq (6M+3);\ 0,\ \text{otherwise}\}$. For perturbation wavenumbers k_x and k_z and system parameters Re and BPr, the maximum value of the real part of the growth rates σ determines the linear stability. The eigenvalue problem can be solved numerically, with M chosen such that convergence is achieved.

Our initial focus is the validation of the LPN equations in terms of their ability to reproduce qualitative results from the standard equations in regions where the LPN approximation is deemed applicable. To this end, we choose to compare linear stability analysis results between the standard equations and the LPN equations across two sets of parameters.

Figure 4 illustrates this comparison, where on the first row we have plotted neutral stability curves from the standard equations and the second row shows the equivalent results from the LPN equations. Parameter values in the first column are $B = 50$ and $Pr = 0.1$ for the standard equations and $BPr = 5$ for the LPN equations, and in the second column they are $B = 50$ and $Pr = 0.01$ for the standard equations and $BPr = 0.5$ for the LPN equations. As before, we plot curves across a range of values of Re and k_x for the 2D mode (black) and the first six 3D modes (coloured). The regions in which we expect qualitatively similar results are highlighted with grey rectangles; these outline regions where $Pe = RePr < \mathcal{O}(1)$, a condition motivated by results in [4]. Excellent agreement between the linear stability analysis results of the LPN equations and the standard equations occurs for $Pe < \mathcal{O}(10^{-1})$, with moderately good agreement when $\mathcal{O}(10^{-1}) < Pe < \mathcal{O}(1)$. Outside of these regions, differences emerge as we would expect.

We now continue our validation of the LPN equations by considering the effect that the parameter BPr has on the stability of the system. Figure 5 plots the neutral stability curves for five different parameter values: (from left to right) $BPr = 5,\ 0.5,\ 0.05,\ 0.005,\ 0$. Similar patterns can be seen to those observed with the standard equations. In the unstratified case ($BPr = 0$), no 3D modes are unstable. It can be seen that a reduction in the value of BPr shifts the critical Reynolds numbers for the onset of instability of the 3D modes towards higher values, thereby making these modes less unstable. We would anticipate this trend to continue as $BPr \to 0$, which can be achieved by letting either $B \to 0$ or $Pr \to 0$ independently.

Each of the neutral stability curves for the 2D mode are identical, with the critical Reynolds number for the onset of linear instability being $Re_c = 1.19$. This prompts the question, as before, as to whether Re_c is indeed independent of the BPr parameter. We have tested this prediction and computed Re_c numerically for a range of values of BPr. Just as for the standard equations, we conclude that the critical Reynolds number is independent of BPe in the LPN system of equations. This differs from the result obtained in [4] for the case of a vertical shear in which Re_c was found to increase monotonically with increasing BPe.

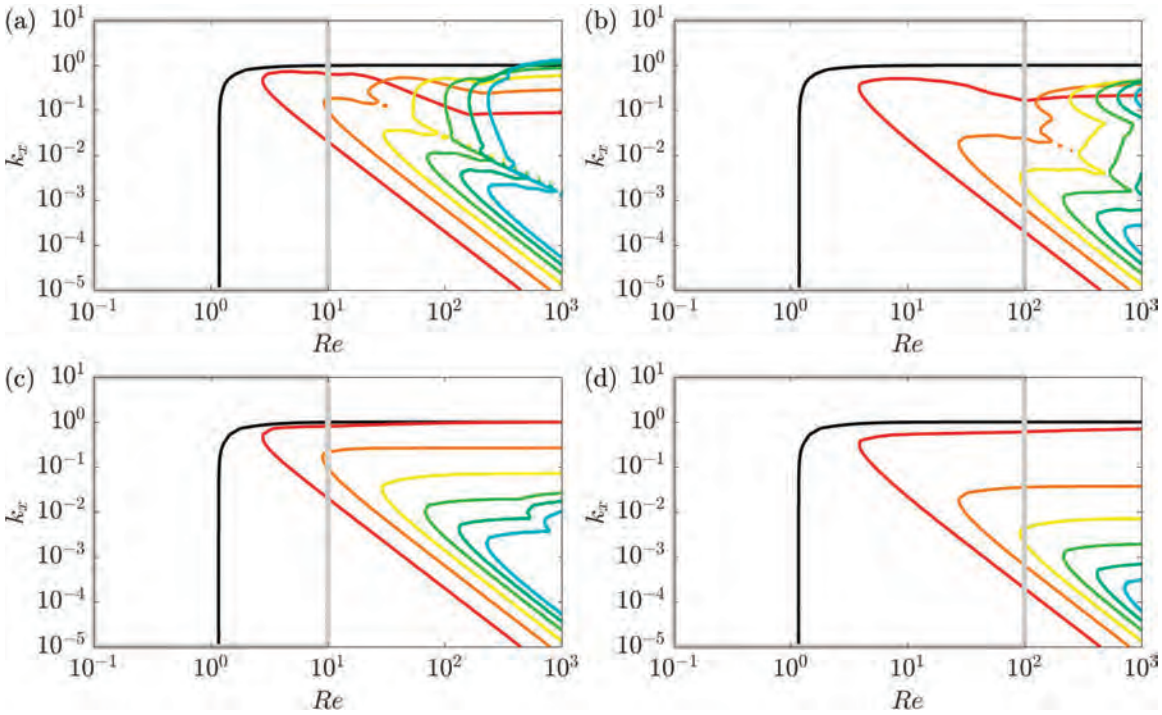

Figure 4: A comparison of linear stability analysis results between the standard equations (first row) and the LPN equations (second row). Neutral stability curves for a range of k_z modes ($k_z = 0$, 1, 2, 3, 4, 5, 6) are plotted against a spectrum of Reynolds numbers and k_x modes. Instability occurs to the right and below the curves. Parameter values used are (a) $B = 50$, $Pr = 0.1$, (b) $B = 50$, $Pr = 0.01$, (c) $BPr = 5$, (d) $BPr = 0.5$. Grey rectangles indicate regions where the LPN approximation is valid and hence where we would expect correspondence.

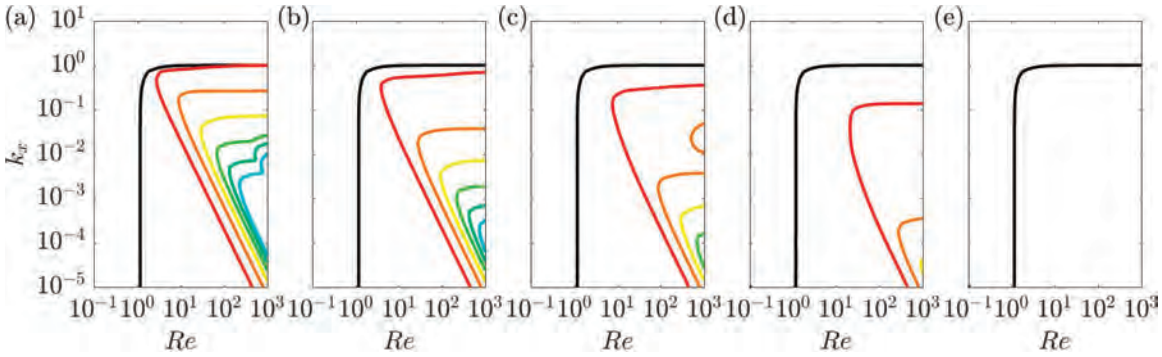

Figure 5: Neutral stability curves for a range of k_z modes plotted against a spectrum of Reynolds numbers and k_x modes. Instability occurs to the right and below the curves. Parameter values used are (a) $BPr = 5$, (b) $BPr = 0.5$, (c) $BPr = 0.05$, (d) $BPr = 0.005$, (e) $BPr = 0$. The curves plotted include $k_z = 0$, 1, 2, 3, 4, 5, 6 and the LPN equations were used.

4 Direct Numerical Simulations

Our work so far has focussed on the initial linear instabilities present within the standard and LPN systems of equations. While these results are of interest in terms of predicting when turbulent mixing may be expected, they do not predict the nature of the long-term equilibrium solutions. We now turn to direct numerical simulations (DNS) in order to retain all nonlinearities as we continue to study the properties of stratified horizontal shear flows in the astrophysical regime.

4.1 The numerical model

The standard equations (4), (5) and (6) are solved in a periodic domain of size $2\pi\alpha \times 2\pi \times 2\pi$ ($\alpha \in \mathbb{N}$) using a pseudo-spectral code that was originally developed by Stellmach to study double-diffusive convection [10] [11]. A small modification to the code has been made to include the Kolmogorov forcing. In terms of the resolution, we used 64 Fourier modes per 2π domain length, resulting in domain resolutions of $64\alpha \times 64 \times 64$. Small amplitude perturbations are initialised in the density field. We explore a range of values of $Re \leq 100$, B and $P\,r$ as we shall discuss, along with four different streamwise domain sizes ($2\pi\alpha$). Our simulations are run on the XSEDE supercomputing facilities (Stampede2 and Comet).

4.2 Effect of the domain geometry on the global solutions

We begin our study of the DNS results by considering the effect that the streamwise domain length (or equivalently the geometry of the domain) has on the solutions of the standard equations. Recent work by Lucas et al. [7] studied the zig-zag instability in cubic ($\alpha = 1$) domains with horizontal Kolmogorov forcing at $Pr = 1$. Motivated by our linear stability analysis results which hinted at the importance of the domain geometry on the linear instabilities and hence solutions of the equations, we seek to determine this effect when all nonlinearities are retained. This in turn will enable us to select an appropriate domain size to use for future simulations.

For this exercise, we choose to use the same parameters explored in [7], where we know that the zig-zag instability exists. We let $Re = 50$, $B = 50$ and $Pr = 1$ and we consider four different domain sizes such that $\alpha = 1, 2, 3, 4$. The first of these corresponds to a cube while the other three correspond to lengths that are $2\times$, $3\times$ and $4\times$ longer than a cube. For visualisation purposes, figure 6 shows snapshots, once the flow has equilibrated, of the streamwise component of the velocity field in each of the four simulations just described. The zig-zag instability can very clearly be seen in the cubic domain but is less apparent in the other three domain sizes.

We can continue to analyse the flow dynamics qualitatively in each of the four simulations by computing and plotting streamwise averages of variables. The top two rows in figure 7 show snapshots of the streamwise component of the velocity field u and the density perturbation field ρ' in the $y - z$ plane at $x = 0$ for the four geometries (left to right: increasing domain length) once the flow has equilibrated. The third and fourth rows plot the streamwise (x-) averages (denoted by $\langle\cdot\rangle_x$) of these fields at the same instances in time. There is a very clear zig-zag or chevron structure in the velocity field in the cubic domain, visible both in the snapshot at $x = 0$ and the streamwise average. Whilst smaller

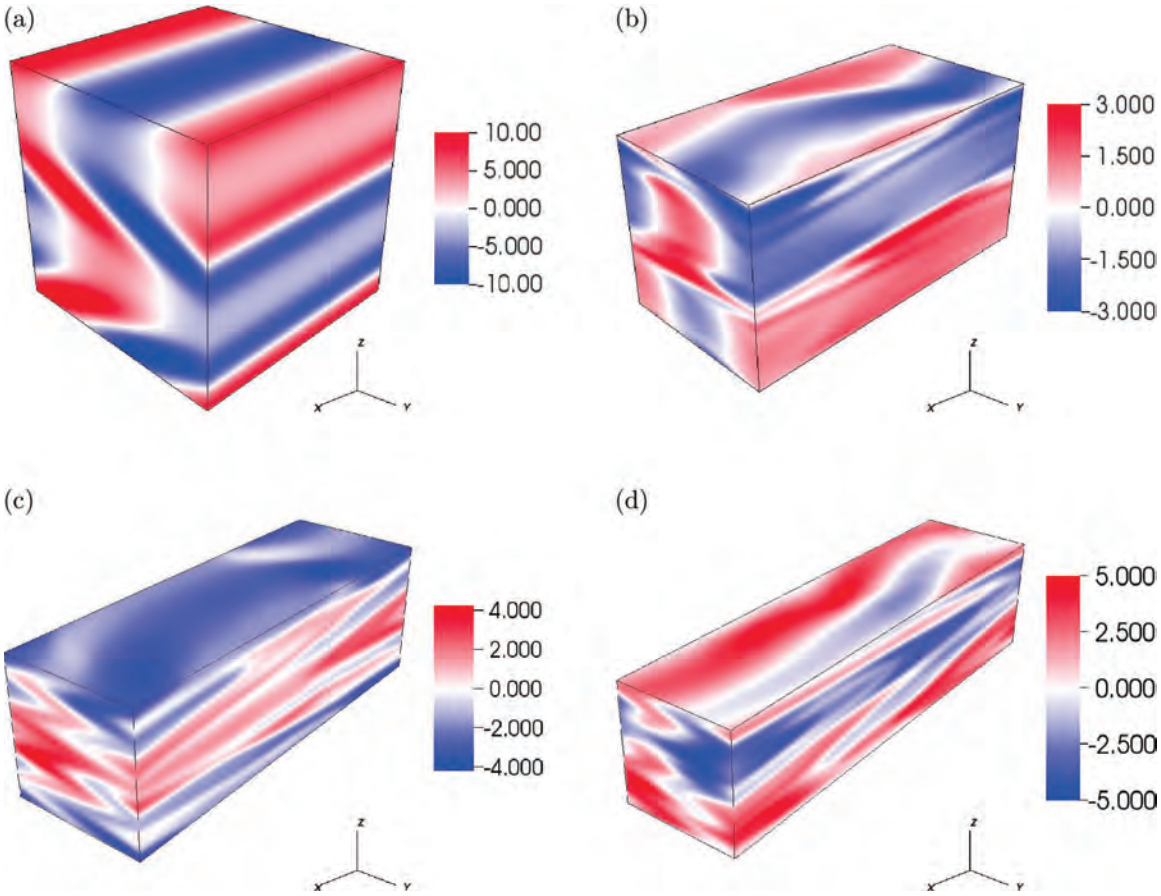

Figure 6: 3D snapshots of the streamwise (u) component of the velocity field in simulations that have equilibrated for domain sizes (a) $2\pi \times 2\pi \times 2\pi$, (b) $4\pi \times 2\pi \times 2\pi$, (c) $6\pi \times 2\pi \times 2\pi$, (d) $8\pi \times 2\pi \times 2\pi$. Parameters used were $Re = 50$, $B = 50$, $Pr = 1$.

scale zig-zags can be seen in the snapshots of the longer domains, these do not emerge in the streamwise averages. In addition, the clear layering of the density field in the cubic domain is not a feature that exists for longer domains, where smaller vertical length scales dominate.

It is clear that the inclusion of the 2D mode of linear instability in the longer domains does play a role in the dynamical attractor of the equilibrated solutions, and that no global attractor exists as a solution of the equations. The geometry of the domain, and hence the types of linear instabilities present, affect the transition of the system from a laminar flow into a more turbulent regime.

We conclude this section with a more quantitative analysis of the evolution and equilibration of the system in these four configurations. In figure 8 we plot the time evolution of domain averages (denoted by $\langle \cdot \rangle$) of u_{rms}, v_{rms}, w_{rms} and ρ'_{rms} for each simulation. The red curves represent the cubic domain simulation and deviate quite significantly from the other three curves, which to some degree closely approximate one another. Focussing initially on the simulations run in cuboid domains, we see that the initial linear instabilities take

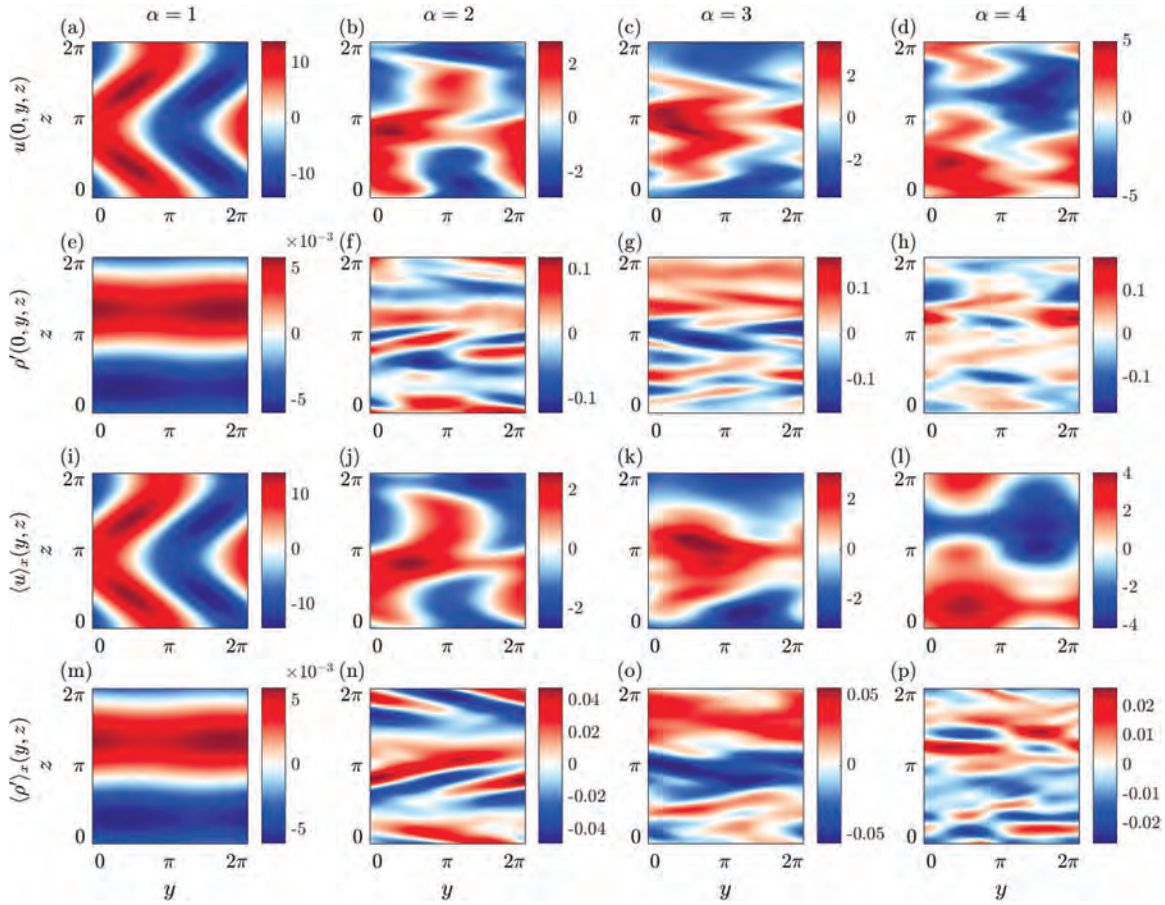

Figure 7: 2D plots of the $y-z$ plane showing $u(x=0,y,z)$ (first row), $\rho'(x=0,y,z)$ (second row), $\langle u\rangle_x(y,z)$ (third row), $\langle\rho'\rangle_x(y,z)$ (fourth row) for domain geometries $2\pi\times2\pi\times2\pi$ (first column), $4\pi\times2\pi\times2\pi$ (second column), $6\pi\times2\pi\times2\pi$ (third column), $8\pi\times2\pi\times2\pi$ (fourth column). $\langle\cdot\rangle_x$ denotes a streamwise (x-) average. All plots were taken from instances in time when the flow had equilibrated.

place almost immediately, with a sharp drop in $\langle u_{rms}\rangle$ and sharp increases in $\langle v_{rms}\rangle$, $\langle w_{rms}\rangle$ and $\langle\rho'_{rms}\rangle$. After a relatively short transition period, each simulation settles down to an equilibrium solution with only small variability due to gravity waves propagating through the system. It could be argued that the equilibrium in each of the three cases is equivalent.

Due to the very unstable (high growth rate, see figure 2(b)) 2D mode of instability present in each of these domains, the cuboid simulations de-laminarise in only a fraction of the time that it takes the cubic simulation to do so. Whilst energy builds up gradually in the v_{rms} and w_{rms} fields in the cubic simulation, the linear instability eventually takes place at about $t=35$. However, unlike the cuboid domains where the 2D mode of instability continues to dominate the dynamics, allowing an equilibrium to be reached, this mode is not present in the cubic domain. Consequently, we see that after the initial instability has taken place, the flow tries to relaminarise. We note that, whilst not visible in figure 8, the system never reaches a stable equilibrium but instead settles into a periodic pattern of sharp

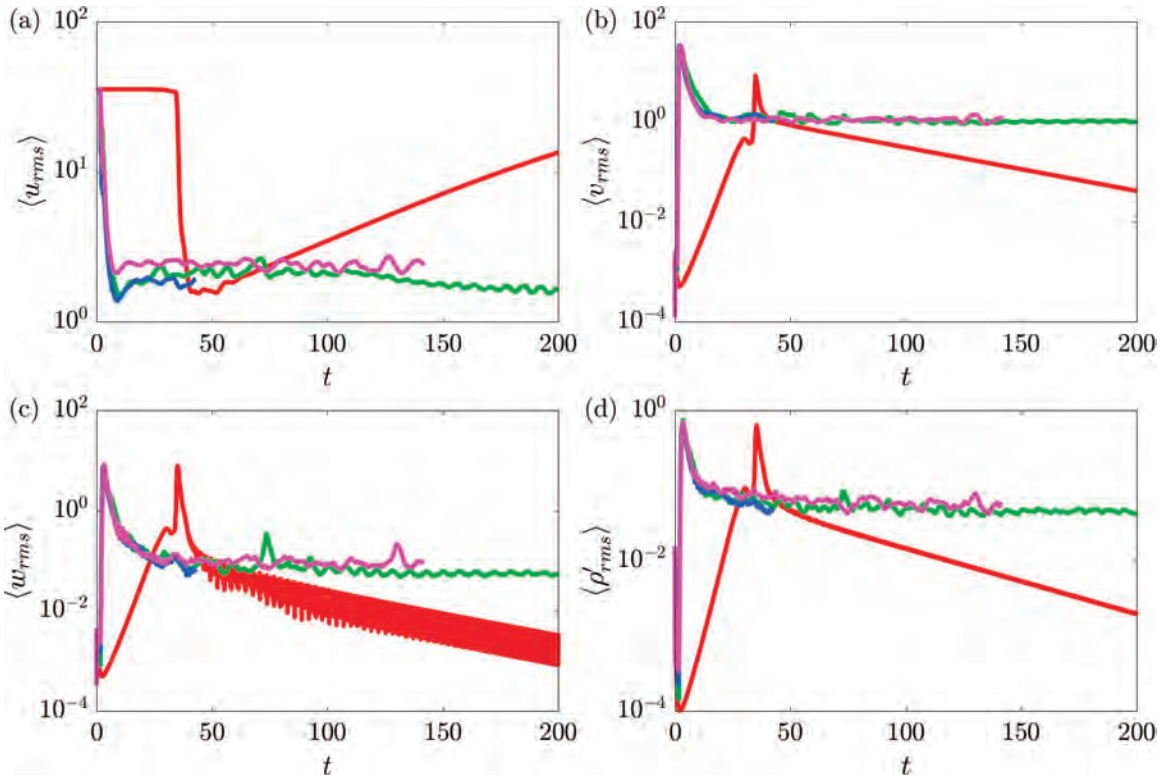

Figure 8: Time evolution plots of (a) $\langle u_{rms} \rangle$, (b) $\langle v_{rms} \rangle$, (c) $\langle w_{rms} \rangle$, (d) $\langle \rho'_{rms} \rangle$ for simulations run in domain sizes $2\pi \times 2\pi \times 2\pi$, $4\pi \times 2\pi \times 2\pi$, $6\pi \times 2\pi \times 2\pi$, $8\pi \times 2\pi \times 2\pi$. System parameters used were $Re = 50$, $B = 50$, $Pr = 1$. $\langle \cdot \rangle$ denotes a domain average.

'bursting' behaviour associated with an instability followed by gradual relaminarisation. The explanation for this is straightforward: the 3D modes of instability are unable to maintain the new turbulent state following an instability, instead only becoming active when a strong horizontal shear is present.

In conclusion, we acknowledge the importance of the geometry of the domain on the solutions of the equations. Moving forward, we choose to run all future simulations in a domain of size $4\pi \times 2\pi \times 2\pi$ ($\alpha = 2$), whose length is found to be sufficient to contain dynamics quantitatively similar to those of longer domains. We consider the cubic domain (and domains such that $\alpha < 1$) to be a special case where the 2D mode of instability cannot exist. Striving for the most generic set-up applicable to stellar interiors, and aiming for computational practicality, we consider this choice to be the most sensible option.

4.3 Scaling regimes in the low-Péclet number limit

The region of stellar interiors that motivates this study is characterised by strong stratification ($B \gg 1$), small Prandtl numbers ($Pr \ll 1$) and large Reynolds numbers ($Re \gg 1$). Within these constraints, and in a similar manner to the work carried out in [3] in which the focus was oceanographic ($Pr \gtrsim \mathcal{O}(1)$), we identify two scaling regimes which differ in dynamics due to the relative size of the Reynolds number.

4.3.1 Viscous regime

The first regime, which we call the viscous regime, considers viscosity to play an important role in the dynamics. Consequently, we seek an upper bound on the size of the Reynolds number. Based on the conditions $B \gg 1$, $Pr \ll 1$ and $1 \ll Re \ll ?$, where this upper asymptotic bound for Re is to be determined by our analysis, we make three assumptions. The first is that typical horizontal velocities $\mathbf{u}_h$ and horizontal length scales l_h satisfy $\mathbf{u}_h, l_h \sim \mathcal{O}(1)$ while vertical length scales l_v are much smaller: $l_v \ll 1$. By the continuity equation ($\nabla \cdot \mathbf{u} = 0$), it then follows that

$$w \sim l_v \ll 1. \tag{31}$$

In the second assumption, we focus on the vertical momentum equation (see equation (4)) and consider a dominant balance between the buoyancy force and viscous dissipation, consistent with our attempt to characterize a viscously dominated regime:

$$B\rho' \sim \frac{1}{Re}\nabla^2 w. \tag{32}$$

Implicit in this is that $\mathbf{u} \cdot \nabla w \ll Re^{-1}\nabla^2 w$. Finally, in the density equation (5) we consider the LPN approximation due to the low Prandtl number assumption, and thus arrive at the same balance as in section 2.2:

$$-w \sim \frac{1}{Pe}\nabla^2 \rho'. \tag{33}$$

Combining (31), (32) and (33) we are able to derive two predicted scalings, one for w and the other for ρ', that depend on the parameters in the system:

$$w \sim (BPeRe)^{-\frac{1}{4}}, \qquad \rho' \sim Pe^{\frac{1}{4}}(BRe)^{-\frac{3}{4}}, \tag{34}$$

from which it follows from (31) that $l_v \sim (BPeRe)^{-1/4}$. Associated with these three assumptions, there are three consistency criteria on the parameters in the system. These can be combined and equate to

$$\max\left(\frac{Pe}{B}, \frac{1}{BPe}\right) \ll Re \ll BPe, \tag{35}$$

providing the necessary criteria for the system to be in this astrophysically motivated viscous regime. Here, we see that the required condition on the Reynolds number is $Re \ll BPe$. Within the context of the LPN momentum equation (12), these conditions correspond to $Re^{-1}\nabla^2 w \sim -BPe\nabla^{-2} w$ where buoyancy is balanced by viscous dissipation.

DNS simulations allow us to validate the scalings derived in (34). We have run a selection of simulations using the standard equations in domain size $4\pi \times 2\pi \times 2\pi$ ($\alpha = 2$) for a variety of parameter values for B and Pr and two different Reynolds numbers: $Re = 50$ and $Re = 100$. Each simulation was run until a satisfactory equilibrium state was reached. We have categorised the simulations according to whether the consistency criteria (35), with inequalities replacing the asymptotic bounds, are met or not met, specifically:

$$\max\left(\frac{Pe}{B}, \frac{1}{BPe}\right) < Re < BPe. \tag{36}$$

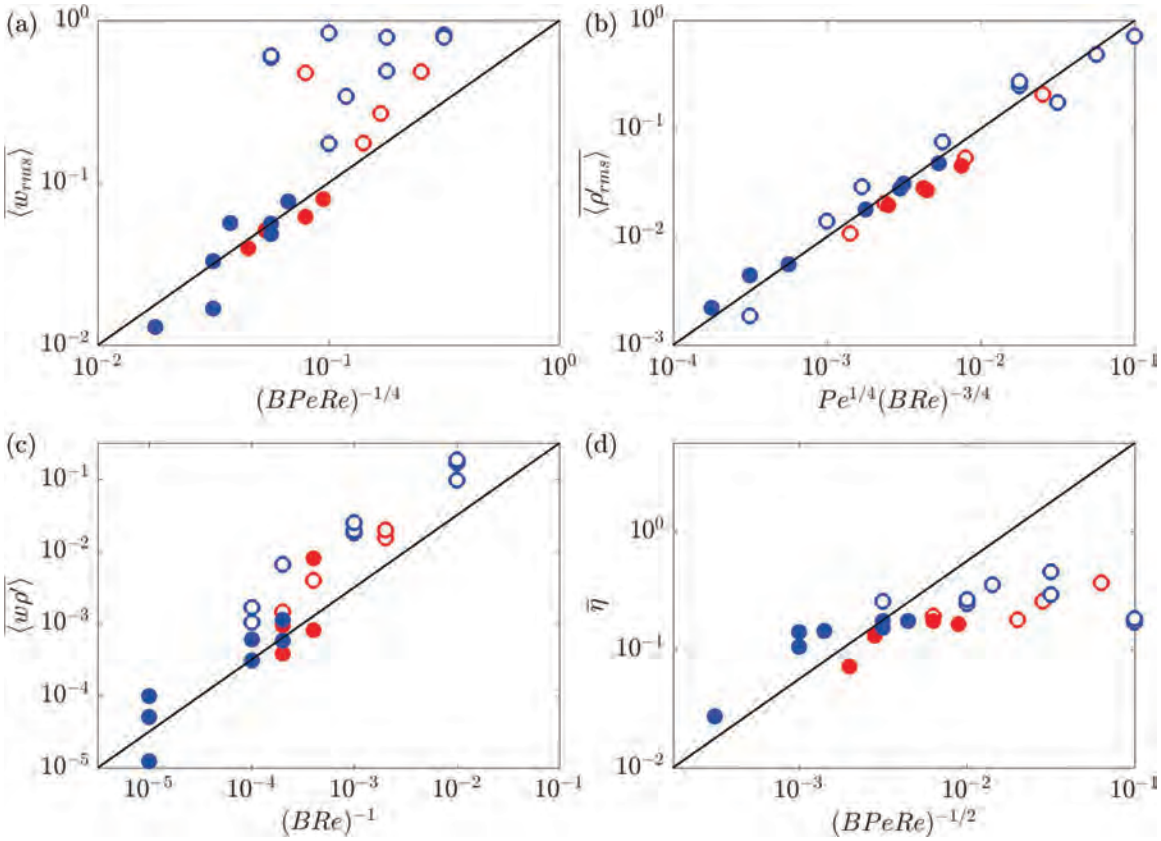

Figure 9: Plots showing the viscous regime scaling predictions against the DNS computed values for (a) $\overline{\langle w_{rms}\rangle}$, (b) $\overline{\langle \rho'\rangle}$, (c) $\overline{\langle w\rho'\rangle}$ and (d) $\overline{\eta}$. Red circles correspond to $Re = 50$ and blue circles correspond to $Re = 100$. Filled circles correspond to simulations where the inequalities in (35) are met and open circles correspond to simulations where the inequalities are not met. Plotted lines have slope equal to one and correspond to the predicted scalings in the viscous regime. $\langle\cdot\rangle$ denotes a domain average and $\bar{\cdot}$ denotes a time average.

Finally, we have computed time (denoted by $\bar{\cdot}$) and domain averages (once the simulations have reached equilibrium) of w_{rms}, ρ'_{rms} and the vertical buoyancy flux $w\rho'$ and have plotted these against the predicted scalings using the input parameters, where we assume that the predicted scaling for $w\rho'$ is simply the product of the scalings for w and ρ'. The results can found in figures 9(a), 9(b) and 9(c).

Denoted by filled circles, those simulations which meet the consistency criteria follow the predicted scalings and lie close to the plotted lines with slope equal to 1. It is interesting to comment on the fact that even those simulations which do not meet the consistency criteria would appear to follow the predicted scalings for ρ' and $w\rho'$, although this is not the case for w. A typical simulation within this regime can be seen in figure 10(a), in which the streamwise velocity is plotted. Here, we note the lack of small scale horizontal structures and the relatively smooth, non-turbulent appearance of the velocity field.

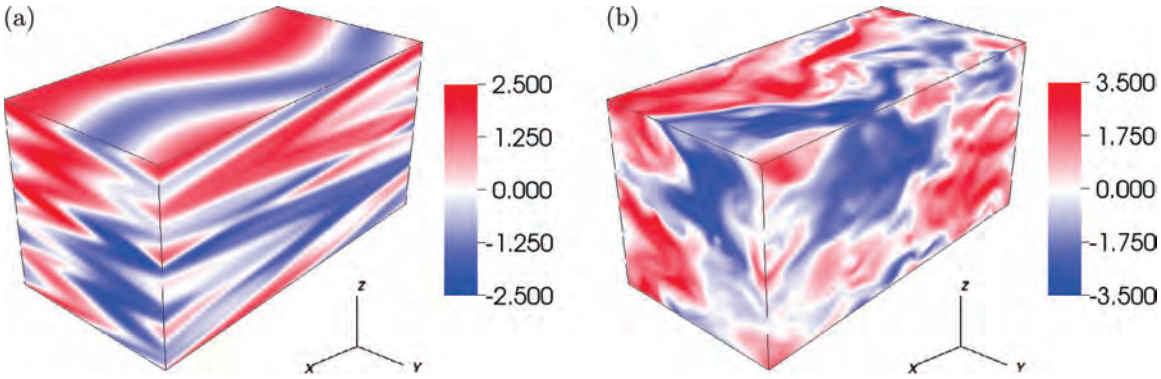

Figure 10: 3D snapshots of the streamwise (u) component of the velocity field in simulations that have equilibrated for (a) the viscous regime ($Re = 100$, $B = 1000$, $Pr = 0.1$) and (b) a set-up close to the inertial regime ($Re = 100$, $B = 10$, $Pr = 0.01$). The domain size was $4\pi \times 2\pi \times 2\pi$ in both cases.

4.3.2 Inertial regime

We now turn to the second regime, which we call the inertial regime. Here, we consider viscosity to be unimportant in the dynamics, and instead require that fluid inertia plays a dominant role. In contrast to the viscous regime, we seek a lower bound on the size of the Reynolds number. Based on the conditions $B \gg 1$, $Pr \ll 1$ and $1 \ll ? \ll Re$, where this lower asymptotic bound for Re is to be determined by our analysis, we make three assumptions. Two of these are identical to before, however for completeness, we explicitly describe each assumption in turn.

As before, the first is that typical horizontal velocities $\mathbf{u}_h$ and horizontal length scales l_h satisfy $\mathbf{u}_h, l_h \sim \mathcal{O}(1)$ while vertical length scales l_v are much smaller, i.e. $l_v \ll 1$, so that

$$w \sim l_v \ll 1. \tag{37}$$

The second assumption differs from the viscous regime. This time, we consider a dominant balance between the buoyancy force and the inertial term in the vertical momentum equation (4), consistent with our attempt to characterise a regime dominated by inertia:

$$\mathbf{u} \cdot \nabla w \sim -B\rho'. \tag{38}$$

Implicit in this is that $\mathbf{u} \cdot \nabla w \gg Re^{-1}\nabla^2 w$. Finally, in the density equation (5) we consider the LPN approximation due to the low Prandtl number assumption:

$$-w \sim \frac{1}{Pe}\nabla^2 \rho'. \tag{39}$$

Combining (37), (38) and (39) we derive two new predicted scalings, one for w and the other for ρ', that depend on the parameters in the system:

$$w \sim (BPe)^{-\frac{1}{2}}; \qquad \rho' \sim B^{-\frac{3}{2}}(Pe)^{-\frac{1}{2}}, \tag{40}$$

from which it follows from (37) that $l_v \sim (BPe)^{-1/2}$. As before, there are three consistency criteria on the parameters in the system, which can be combined and equate to

$$\max(1, Pe) \ll BPe \ll Re, \tag{41}$$

providing the necessary criteria for the system to be in this astrophysically motivated inertial regime. Here, we see that the required condition on the Reynolds number is $Re \gg BPe$. Within the context of the LPN momentum equation (12), these conditions correspond to $Re^{-1}\nabla^2 w \ll BPe\nabla^{-2}w$ where buoyancy is balanced by inertia.

Currently, we have not been able to validate this regime using data from DNS simulations, however this will be the focus of future work. In the meantime, we display a visualisation in figure 10(b) of the streamwise velocity of a simulation which fulfills the consistency criteria (41) where the asymptotic bounds are replaced by inequalities. Until we obtain sufficient data to validate the magnitude differences required on the bounds in (41), we cannot be 100% confident that this simulation is close to the regime of interest. However, it does show significant differences from the smooth appearance of the viscous regime, appearing to be more turbulent with smaller scale structures appearing.

4.3.3 Mixing efficiency in the viscous and inertial regimes

Having introduced the existence of two new astrophysically motived scaling regimes, we now take a moment to consider the amount of mixing, or vertical transport of buoyancy, that is theoretically possible in each. In a stratified system, the mixing efficiency is defined as the ratio of the net change in potential energy to the energy used for mixing or vertical buoyancy transport. In other words, it quantifies how much of the energy that is injected into the system is used for transporting buoyancy compared with being dissipated due to viscosity. In terms of our model, the mixing efficiency can be defined mathematically as

$$\eta = \frac{B\langle w\rho'\rangle}{B\langle w\rho'\rangle + \frac{1}{Re}\langle|\nabla\mathbf{u}|^2\rangle}. \tag{42}$$

In the viscous regime, using the scalings calculated in (34), we determine the mixing efficiency to scale as

$$\eta \sim \frac{1}{(BPeRe)^{\frac{1}{2}}}. \tag{43}$$

Since one of the consistency criteria for this regime was that $1 \ll BPeRe$, we see immediately that $\eta \ll 1$. Thus, vertical buoyancy transport and mixing is very inefficient when viscous effects are important. We are able to validate this scaling using data from DNS simulations; the results are presented in figure 9(d) and show a consistency for those simulations (closed circles) which belong in the viscous regime.

We now consider the inertial regime. Here, we use the scalings calculated in (40) to determine the scaling for the mixing efficiency to be

$$\eta \sim \frac{1}{1 + \frac{(BPe)^2}{Re}} = \frac{1}{1 + BPe\frac{BPe}{Re}}. \tag{44}$$

From the consistency criteria for this regime, we know that $Re \gg BPe$. However, we have no condition on the magnitude of BPe and hence $(BPe)^2/Re$ could be either large or small. We conclude that $0 \leq \eta \leq 1$ and hence, theoretically, we could have $\eta \sim \mathcal{O}(1)$. This is a fundamental difference from the viscous regime and could have strong astrophysical implications. Future work aims to explore this prediction using DNS simulation data.

4.4 Standard versus low-Péclet number equations comparison

Simulation of the inertial scaling regime will likely require Reynolds numbers to be in excess of those that we have considered so far. Modest increases in the Reynolds number have indicated that increased resolution is required to adequately resolve the smaller scale dynamics that begin to emerge. This, in turn, requires more computational resources and thus can become expensive. The LPN equations, however, pose a viable alternative. Provided we can demonstrate their validity, this reduced set of equations will allow the system parameters to be pushed further into the inertial regime and provide a better prospect of demonstrating the predicted scalings.

A modification in the code to the momentum equation allowed it to be adapted to solve the LPN equations, just as in [4]. We have run one simulation using the standard code with a selection of parameters chosen such that the LPN approximation should be valid ($Re = 100$, $B = 1000$, $Pr = 0.0001$, $BPe = 1$). In addition, we have run a second simulation using the LPN code with equivalent parameters ($Re = 100$, $BPe = 1$). We would expect the results to be very close, and find that this is the case. Figure 11 shows a selection of diagnostics from each of the two simulations, where we see virtually identical results. In addition, figure 12 shows snapshots of the streamwise velocity field in the $y - z$ plane taken at $x = 0$, where the flow structure appears to be qualitatively the same. Combined with the results from our linear stability analysis of the LPN equations which demonstrated their validity, we are confident in their use for our future purposes.

4.5 Vertical versus horizontal shear comparison

We conclude this study with a comparison between vertical shear and horizontal shear instabilities. We are fortunate to obtain a data set used in [4] for stratified vertically sheared simulations. The data collected in that study used the same code as discussed here, with the only difference being the orientation of the shear. Thus the two data sets use the same parameters and are comparable in the sense that they both consider cuboid domains.

In figure 13 we plot time and domain averages of $\mathbf{u}_{rms}$ against BPe for a variety of vertically sheared simulations (red) and horizontally sheared simulations (blue). For simulations in which $BPe < \mathcal{O}(1)$, both vertical and horizontal shearing is broken down by instabilities to produce turbulent behaviour with large reductions in the value of $\langle \mathbf{u}_{rms} \rangle$ away from its laminar value. However, for $BPe > \mathcal{O}(1)$, the behaviour of the two types of shearing diverge. The horizontally sheared simulations continue to exhibit turbulent behaviour, since Re_c is parameter independent and the 2D mode of linear instability is always present. On the other hand, the turbulent stresses in the vertically sheared simulations begin to the feel effects of stratification, hence these flows become less turbulent and more laminar.

	Re	B	Pr	Pe	BPe	$\overline{\langle \mathbf{u}_{rms} \rangle}$	$\overline{\langle u_{rms} \rangle}$	$\overline{\langle v_{rms} \rangle}$	$\overline{\langle w_{rms} \rangle}$	$\overline{\langle \lvert\nabla \mathbf{u}\rvert^2 \rangle}$
Standard	100	10^3	10^{-4}	0.01	1	2.27	1.41	1.56	0.79	46.1
LPN	100				1	2.25	1.42	1.51	0.79	46.1

Figure 11: Data from a standard and a LPN simulation with equivalent parameters chosen such that the LPN approximation is valid and $BPe = 1$ in each. Various time and domain-averaged diagnostics are compared to demonstrate the validity of the LPN approximation.

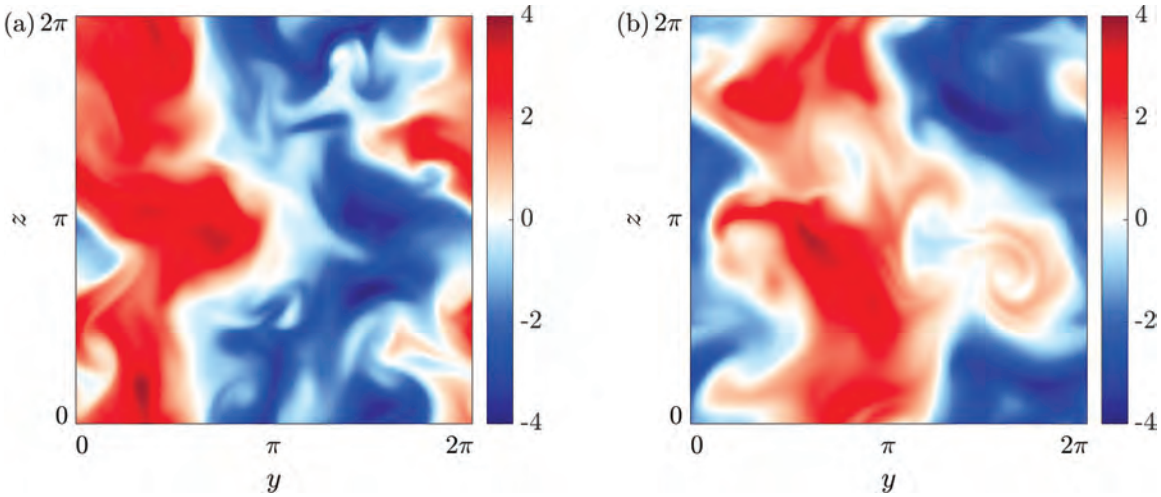

Figure 12: Plots of the $y - z$ plane showing $u(x = 0, y, z)$ in simulations run using (a) the standard equations with $Re = 100$, $B = 1000$, $Pr = 0.0001$ and (b) the LPN equations with $Re = 100$, $BPe = 1$. The plots were taken from instances in time after equilibration.

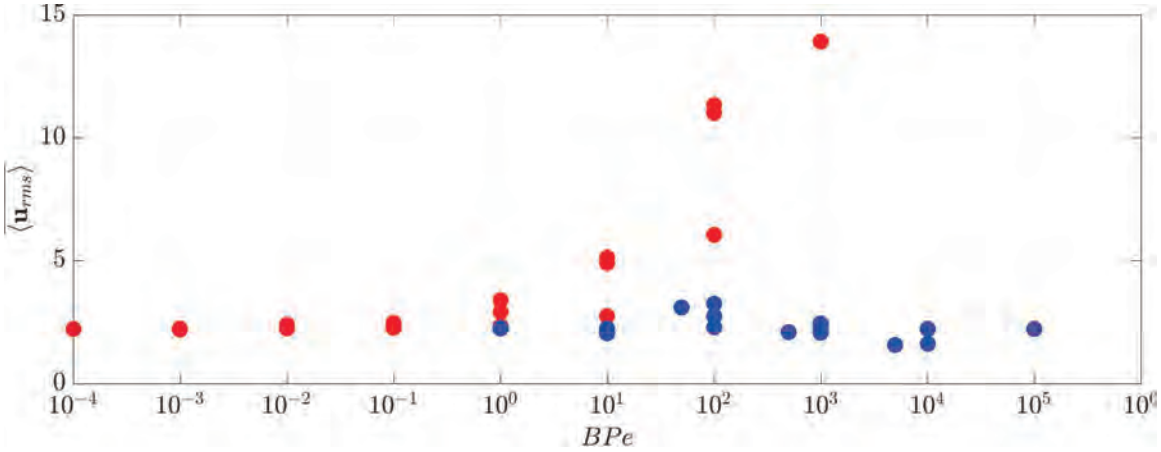

Figure 13: Data from vertically sheared and horizontally sheared simulations showing $\overline{\langle \mathbf{u}_{rms} \rangle}$ plotted against BPe for a variety of parameter values and cuboid domains. The standard code was used for all simulations. $\langle \cdot \rangle$ denotes a domain average and $\bar{\cdot}$ denotes a time average.

5 Discussion

Our goal in this work was the study of the stability and dynamics of stably stratified horizontal shear flows, primarily within an astrophysical regime characterised by strong stratification and low Prandtl numbers. Through a combination of linear stability analyses and direct numerical simulations, our objectives were three-fold: (1) to explore the effect of the domain geometry, (2) to identify astrophysically relevant scaling regimes which allow mixing efficiency predictions, and (3) to test the validity of the LPN equations.

Results from our linear stability analysis showed that the stability of horizontal shear flows is independent of the system parameters, provided the computational domain is longer in the streamwise than spanwise direction, with the critical Reynolds number for the onset of instability always being of order one, irrespective of the stratification or the Prandtl number. In addition, we showed that in the limit of small Prandtl numbers, the system behaves like an unstratified system, with the only unstable perturbation modes being 2D. As the stratification or Prandtl number increases, so do the number of 3D perturbation modes which are unstable at any fixed Reynolds number.

Using direct numerical simulations, we explored the nonlinear behaviour of our system of equations. We began by exploring the effect that the geometry of the domain has on the solutions. This was motivated by results from the linear stability analysis which revealed that the 2D mode, whilst being much more unstable than 3D modes, was only unstable for domains in which $\alpha = L_x/L_y > 1$. Consequently, we found that the 'zig-zag' instability and density layering were much more pronounced in a cubic domain than in longer domains where other dynamics also occur. This dependence on the geometry, and hence the linear instabilities, demonstrated that there is no global attractor within the system of equations.

We proceeded to seek astrophysically motivated scaling regimes, characterised by strong stratification and small Prandtl numbers. In doing so, we identified two regimes of interest: one in which viscosity was dominant and the other in which inertia was dominant. The viscous regime was identified and confirmed numerically, with results agreeing well with the predicted scaling laws. The mixing efficiency of each regime was investigated, where it was found that although the viscous regime inhibits mixing, the inertial regime doesn't eliminate the possibility of high mixing efficiencies and large vertical transport.

Moving forward, we intend to use the LPN equations to simulate the inertial regime, which will require numerical simulations to be run at much higher Reynolds numbers. The validity of the LPN equations was tested through a combination of linear stability analyses and direct numerical simulations; these will allow a larger range of parameters to be explored with fewer computational resources. This work is presently under way, and the results will be presented elsewhere.

An interesting extension to this study would be to consider the stability of shear flow that has both a horizontal and vertical component. Our results show an interesting difference in the behaviour of vertically and horizontally sheared flows: vertical shears can be stabilized with sufficiently strong stratification whilst horizontal shears are always unstable, provided that $Re \gtrapprox 1$. It is unknown, for example, how a small amount of horizontal shear can affect the stability of a vertical shear; this is a question of astrophysical importance.

6 Acknowledgements

First and foremost, I would like to thank my two supervisors, Pascale Garaud and Colm-cille Caulfield, for their energy and enthusiasm towards this project and their patience during our countless discussions. It was truly a pleasure to work with both of them. I would also like to thank the two directors, Neil Balmforth and Colm-cille Caulfield, for organising a very diverse programme of seminars, and to Andrew Woods for a fascinating collection of principal lectures. Last, but certainly not least, my thanks go out to the group of GFD fellows with whom I spent a very enjoyable and extremely memorable summer.

References

[1] P. Billant and J.-M. Chomaz, *Experimental evidence for a new instability of a vertical columnar vortex pair in a strongly stratified fluid*, Journal of Fluid Mechanics, 418 (2000), pp. 167–188.

[2] ——, *Theoretical analysis of the zigzag instability of a vertical columnar vortex pair in a strongly stratified fluid*, Journal of Fluid Mechanics, 419 (2000), pp. 29–63.

[3] G. Brethouwer, P. Billant, E. Lindborg, and J.-M. Chomaz, *Scaling analysis and simulation of strongly stratified turbulent flows*, Journal of Fluid Mechanics, 585 (2007), pp. 343–368.

[4] P. Garaud, B. Gallet, and T. Bischoff, *The stability of stratified spatially periodic shear flows at low Péclet number*, Physics of Fluids, 27 (2015).

[5] P. Garaud and L. Kulenthirarajah, *Turbulent transport in a strongly stratified forced shear layer with thermal diffusion*, The Astrophysical Journal, 821 (2016).

[6] F. Lignières, *The small-Péclet-number approximation in stellar radiative zones*, Astronomy and Astrophysics, 348 (1999), pp. 933–939.

[7] D. Lucas, C. P. Caulfield, and R. R. Kerswell, *Layer formation in horizontally forced stratified turbulence: connecting exact coherent structures to linear instabilities*, Journal of Fluid Mechanics, 832 (2017), pp. 409–437.

[8] E. Spiegel, *Thermal turbulence at very small prandtl number*, Journal of Geophysical Research, 67 (1962), pp. 3063–3070.

[9] E. A. Spiegel and G. Veronis, *On the boussinesq approximation for a compressible fluid*, The Astrophysical Journal, 131 (1960), pp. 442–447.

[10] A. Stellmach, P. Traxler, P. Garaud, N. Brummell, and T. Radko, *Dynamics of fingering convection. Part 2. The formation of thermohaline staircases*, Journal of Fluid Mechanics, 677 (2011), pp. 554–571.

[11] P. Traxler, A. Stellmach, P. Garaud, T. Radko, and N. Brummell, *Dynamics of fingering convection. Part 1. Small-scale fluxes and large-scale instabilities*, Journal of Fluid Mechanics, 677 (2011), pp. 530–553.

How Mixed is the Ocean Mixed Layer?

Neeraja Bhamidipati

October 24, 2018

1 Introduction

The ocean mixed layer is the region in the ocean directly underneath the air-sea interface. Because of the high heat capacity of water, the upper 2.5 m of the ocean contains the same amount of heat as the entire atmosphere above it. Oceans act as heat reservoirs, gaining heat during spring-summer and losing it slowly during fall-winter. The ocean mixed layer mediates the exchange of mass, momentum and energy between the ocean and the atmosphere [6]. The depth of these layers is typically $\mathcal{O}(10 - 1000$ m), and exhibits large seasonal variations depending on the latitude. The mixing, however, is driven by a range of factors. In the winter or at night, the mixing is largely driven by the convection due to radiative heat loss to the atmosphere, whereas during the summer, the mixing is mainly shear-driven, since the wind stress at the surface is the primary mixing agent. Although the surface wind stress acts to stir light water downwards, most of this energy dissipates rapidly within the top $25 - 30$ m of the ocean. Figure 1 shows the variation of the mixed layer depth in the mid-latitudes, illustrating the effect of convection in producing deeper mixed layers.

The ocean is heated near the surface by both short-wave and long-wave radiative fluxes, and deeper in the water column from solar radiation in the visible part of the spectrum penetrating into the water. This solar heating produces a diurnal cycle that varies in importance and magnitude over the course of a year. The surface cooling, however, is driven by radiative and evaporative losses at the surface to the atmosphere. Seasonal variation of the mixed layer depth due to radiative heating is also important, although the importance depends on the latitude. As the sea-surface cools at night or over the winter, the water may become denser than the underlying fluid. If the isopycnals are perturbed from level, horizontal buoyancy gradients are produced which, in turn, begin to produce vorticity. The flows will further lift the light fluid and draw the heavier fluid down; the layer tries to overturn. This process is retarded by viscosity, but also by conduction which reduces the density contrast. The deepest mixed layers, which exceed 2000 m in regions such as the Labrador Sea, are formed through this process, which is a type of convective instability.

Figure 2 shows the regionally averaged variations in mixed layer depth over a year, highlighting large variations in the North Atlantic which has a strong deepening of the mixed layer in the winter. In the boreal winter, convection acts to deepen the mixed layer in the regions around close to the North pole, dominantly around Labrador and Greenland seas, whereas in the boreal summer, convection is strongest close to the south pole, producing deeper mixed layers close to the Antarctic. Figure 3 shows the global mixed layer depth

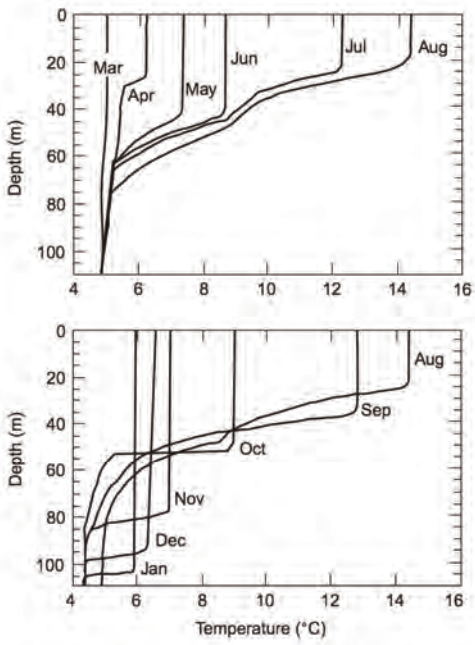

Figure 1: Seasonal evolution of temperature in the mid-latitude upper ocean. Shallow, warm mixed layers during spring-summer alternate with cold, deep ones during fall-winter. (Source: Kantha and Clayson, 2000 [6])

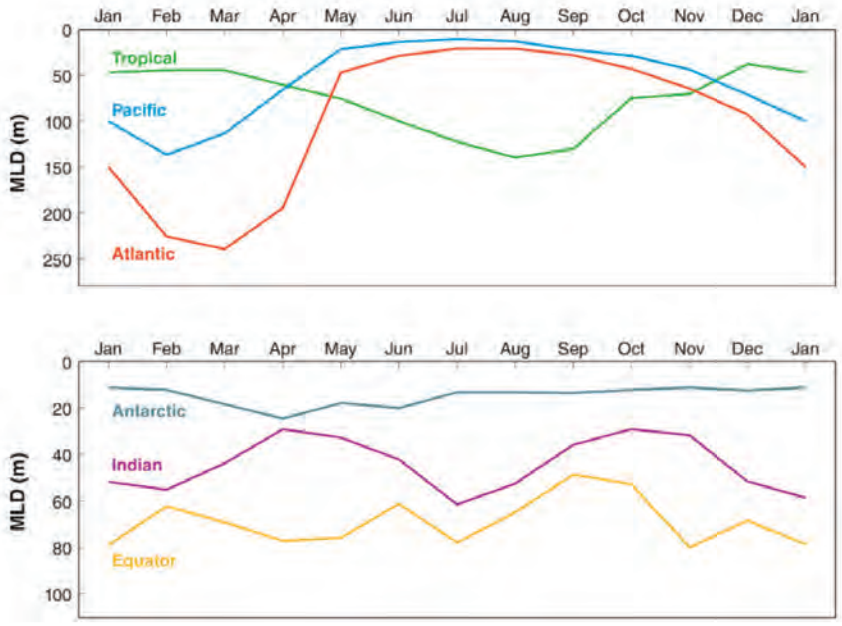

Figure 2: Example of regional variations in mixed layer depth over the year. Mixed layer depths can, regionally, become much deeper when convective processes are active. (Source: Kara et al., 2003 [7], Modified by: Wunsch, 2015 [18])

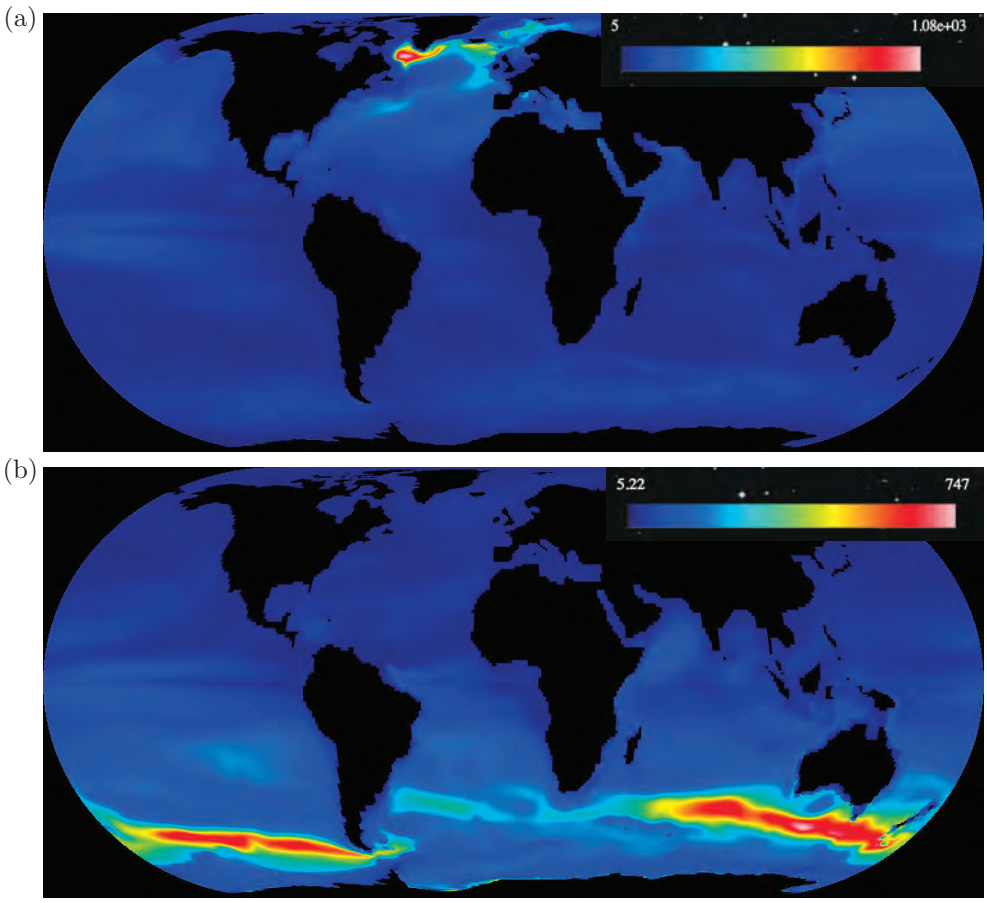

Figure 3: Surface mixed layer depth (metres) in (a) January, and (b) August. (Source: `http://eddies.mit.edu/esglobe/`)

in January and August, illustrating that the mixed layer depth is in fact greater in winter than summer in each hemisphere. During the summer, increased solar heating of the surface water leads to more stable density stratification, reducing the penetration of wind-driven mixing. Because seawater is most dense just before it freezes, wintertime cooling over the ocean always reduces stable stratification, allowing a deeper penetration of wind-driven turbulence but also generating turbulence that can penetrate to great depths.

The mixed layer is characterized by properties such as temperature and salinity which are nearly uniform throughout the layer. At the bottom of the mixed layer, there exists a region where there is a sharp change in temperature, called a thermocline; sometimes there may be a rapid salinity change called a halocline that occurs as well. The combined influence of temperature and salinity changes results in an abrupt density change, or pycnocline. The ocean mixed layer is nutrient-poor, and its depth determines the average level of light seen by phytoplankton. Therefore, the mixing at the base of the ocean mixed layer is crucial for biological productivity. Since marine biological net primary production is the first step in the food chain of marine organisms, its decline could have severe consequences for fish stock and fisheries [9]. Biological productivity is also important from a climatic point of

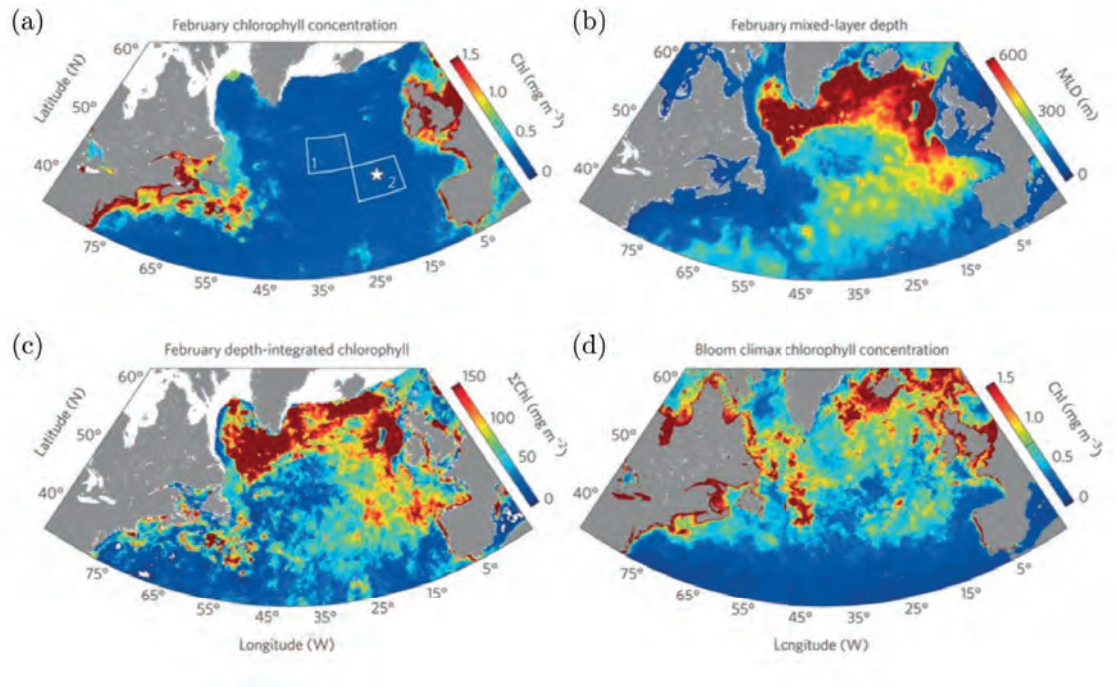

Figure 4: (a) February surface-chlorophyll concentration. (b) February mixed-layer depth. (c) February water-column chlorophyll inventory integrated from the surface to the mixed layer depth. (d) Maximum chlorophyll concentration achieved during the spring/summer bloom climax. (Source: Behrenfeld, 2014 [1])

view over time scales of decades or more. Carbon fixing constitutes a biological pathway for removing some of the anthropogenic CO_2 introduced into the atmosphere. Therefore the primary production is also of considerable interest to oceanographers because it contributes significantly to global photosynthesis and ocean carbon uptake [17].

Mixed-layer deepening along with decreasing sunlight in the wintertime in the North Atlantic is therefore associated with a strong reduction in surface chlorophyll a because of a decline in phytoplankton division rates. In the subarctic Atlantic, the winter transition from mixed-layer deepening to shoaling occurs around February. At this time, chlorophyll concentrations are at their annual minimum and, seaward of the continental margins, show little spatial variability across the basin (figure 4a). Figure 4b shows that this has a stark contrast to patterns in physical properties, particularly the depth of the mixed layer at that time. However, this deep mixing also replenishes near-surface nutrient stocks. Thus when the mixed layer becomes shallow in the spring, and light levels increase, there is often a concomitant increase of phytoplankton biomass, known as the "spring bloom". In the subarctic Atlantic, this link between physics and ecology allows water-column-integrated phytoplankton populations to increase in size while division rates are decreasing, with greater accumulations corresponding to deeper mixing (figure 4b,c).

At polar and subpolar latitudes the annual phytoplankton biomass cycle is dominated by the spring bloom, which occurs in response to increases in mean irradiance of the mixed

layer. The need for an energy source in producing biomass restricts primary production to the upper few tens of meters (the euphotic or photic zone), in which the solar insolation is strong enough to assist carbon fixation [6]. At lower latitudes of the subtropics, a biomass peak (much reduced in comparison to high-latitude spring blooms) occurs during winter, when mixing by winds and thermal convection replenishes the euphotic zone with plant nutrients. When viewed from space, the North Atlantic spring bloom is among the largest mass greenings observed on the Earth surface extending over scales of more than 2000 km [19]. Ferrari et al. (2015) [4] observe that surface phytoplankton increase rates are very high through the subpolar North Atlantic when convection stops, and argue that convection shutdown and lower mixing rates are a trigger of surface blooms even though the mixed layer has not shallowed. An important aspect of this relationship is its implication that dampened high-latitude winter mixing with climate warming will decrease annual maxima in depth-integrated phytoplankton biomass. For the subarctic Atlantic, this decrease has recently been estimated at an average of approximately 40% by the end of the coming century [2].

In the geophysical context, mixed layers play an important role in global climate and carbon-dioxide induced global warming. Mixed layers are are a key element to our understanding of processes such as the El Niño Southern Oscillation (ENSO) and thus to climatic fluctuations on both short and long time scales [16]. During El Niño events on interannual timescales, a weakening of the wind stress to positive sea surface temperature (SST) anomalies as less cold water is pumped upwards from below the surface of the ocean. Those positive anomalies in the surface temperature further weaken the wind stress. This effect could increase under climate change because of the reduced mixed-layer depth that arises as a result of the reduced mean trade wind strength, and increased thermal stratification [13]. Wind stress anomalies could become more effective at exciting SST anomalies; in addition, the wind stress response to SST anomalies can become stronger in regions where SST increases are largest, that is, on the equator. Both effects would tend to amplify ENSO [3].

Air-sea exchanges involve not only momentum, heat, and water vapour, but also photochemically produced and other greenhouse gases [6]. The transfer and exchange of greenhouse gases such as CO_2 between the ocean and the atmosphere has important implications for climate change. Some of these gases are brought to the ocean mixed layer by the deepening of the seasonal thermocline, and are eventually degassed into the atmosphere when the mixed layer becomes shallower. Additionally, CO_2 induced warming of sea surface temperature is delayed markedly in the North Atlantic and the Circumpolar Ocean of the Southern Hemisphere due to the deep mixing of heat trapped by the increased greenhouse gas [11]. However, this exchange with the atmosphere depends on the difference across the sea-surface. But the value near the surface depends on how the dissolved gas is fluxed vertically. In addition, the dynamics of mixing within the mixed layer also determines the dispersal of pollutants in the upper ocean since most of the pollution in the global ocean takes place through the ocean mixed layer [6; 5].

Ocean mixing is an essential ingredient in determining the thermohaline structure of the ocean. Thermohaline circulation is that part of the ocean circulation which is driven by fluxes of heat and freshwater across the sea surface and subsequent interior mixing of heat and salt [15]. One of the key features of thermohaline circulation is the deep water

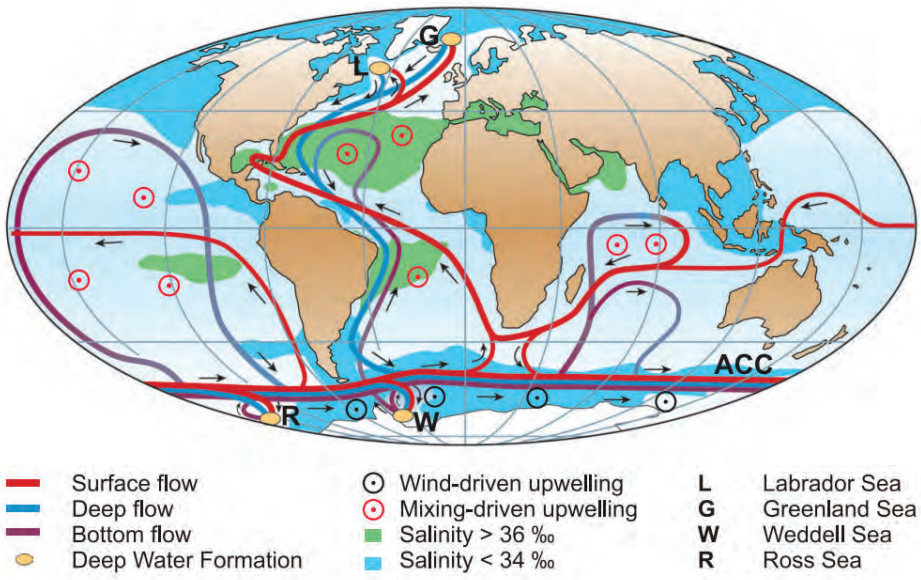

Figure 5: Schematic representation of the global thermohaline circulation. Surface currents are shown in red, deep waters in light blue and bottom waters in dark blue. The main deep water formation sites are shown in orange. (Source: Rahmstorf, 2006 [15])

formation in high latitudes where surface waters sink down to supply the ocean with its deep water masses [9]. The North Atlantic Deep Water (NADW) is closely associated with convection and vertical mixing in areas such as Labrador and Greenland seas, which in turn drives circulation (figure 5). This is the energy supply of the thermohaline circulation: in an energetic sense, it is driven by turbulent mixing in the ocean's interior [15]. Due to global warming, a decrease in the mixed layer depth and vertical mixing would not only reduce the deep water formation and affect the thermohaline circulation, but it would also cut the supply of nutrients from the deep water masses to the upper layer of the ocean where the nutrients are consumed. The result would be a declining phytoplankton population, with possible impacts on all the subsequent links of the food chain. Kuhlbordt et al. (2009) [9] predict that the effect of global warming on the net primary production of the Atlantic is stronger than on the shutdown of thermohaline circulation. Additionally, this implies that the oceanic carbon uptake would be regionally lowered by such a reduction of the mixed layer depth.

In summary, proper parameterisation of turbulent mixing in the surface mixed layer is crucial to simulate dynamics in the ocean interior, air-sea exchanges, and sea surface temperature correctly. Although several parameterisations are currently in use, common to several of these schemes is the assumption that turbulent diffusion, like molecular diffusion, depends linearly on the property gradient, with an appropriate constant of proportionality, which is the eddy diffusivity [10]. This is known as the non-local K-Profile Parameterisation (KPP) scheme which unifies the treatment of a variety of unresolved processes involved in vertical mixing. Other parameterisations have represented the turbulent diffusion as a

function of the Richardson number [8]. KPP has a local part and the Mellor-Yamada scheme is local [12], but KPP also has a non-local term. Non-local effects have also been incorporated into schemes other than KPP such as the bulk mixed-layer models [14], but these are ad-hoc. This work focuses on a formulation of the flux which is a functional of the local property gradient, using high resolution simulations to determine the form of the functional. §2 discusses the basic equations governing the 2D system and derives an equation for the mixed layer depth, ignoring the effects of wind stress. Although 3D effects appear soon after the instability, the 2D problem can describe both the instability and some of the effects of non-linearity. We also present some results of the 2D simulations to describe the evolution of the temperature profile, which then forms the basis for the formulation of eddy flux using a passive tracer in §3. In §4, we discuss the conclusions of this work and the direction for future work. §5 presents some additional mathematical formulations and ideas that arose while working on this project.

2 Governing Equations

We use the incompressible Navier-Stokes equation under the Boussinesq approximation. The advection-diffusion equation governing the temperature field has an added source term to account for internal heating due to solar radiation. The penetrative solar radiation decays exponentially with depth and is also also time-dependent, but here we study the quasi-steady state problem with a constant solar insolation and study the evolution of the temperature and velocity fields in the domain.

The continuity equation,

$$\underline{\nabla}.\underline{u} = 0 \tag{1}$$

The Navier-Stokes equation with the buoyancy term,

$$\frac{\partial \underline{u}}{\partial t} + (\underline{u}.\underline{\nabla})\underline{u} = -\underline{\nabla} p + \nu \nabla^2 \underline{u} + \alpha g T \hat{z} \tag{2}$$

The advection-diffusion equation for temperature with an added source term,

$$\frac{\partial T}{\partial t} + \underline{u}.\underline{\nabla} T = \kappa \nabla^2 T + \underline{\nabla}.\underline{Q} \tag{3}$$

where $\underline{u} = (u, w)$ is the fluid velocity, p is its pressure, α is the coefficient of thermal expansion defined so that the density is assumed to vary linearly with temperature ($\rho = \rho_o(1 - \alpha(T - T_o))$), ν is the kinematic viscosity of the fluid, and κ is its thermal diffusivity. The internal heating due to penetrative solar radiation, given by $\underline{Q} = Q_o e^{z/l}\hat{z}$, decays exponentially with depth over a length scale l, where $Q_o = \frac{H}{\rho C_p}$, and C_p is the specific heat capacity of the fluid. Typical values of the surface heat flux H are of the order 100 W/m^2. Here we consider only the shorter wavelength blue radiation which has the greatest penetration depth ($l \approx 20$ m). The longer wavelength red light gets absorbed over a much shallower depth ($l \approx 0.6$ m). The red spectrum has around 60% of the heat flux and the blue around 40%.

Note that the velocity of the fluid is given by the perturbation velocity $\underline{u}'$ since there is zero base flow ($\underline{u} = \underline{0} + \underline{u}'$, $\underline{u}' = (u', w')$). The boundary conditions for the system are no-slip

and impermeable boundaries at the top and bottom. The flux at the bottom boundary is given by the stratification frequency of the thermocline. The boundary conditions are given by

$$w = 0, \qquad \frac{\partial u}{\partial z} = 0, \qquad \frac{\partial(\alpha g T)}{\partial z} = N^2 \qquad \text{at} \quad z = -H \tag{4}$$

$$w = 0, \qquad \frac{\partial u}{\partial z} = 0 \qquad \text{at} \quad z = 0 \tag{5}$$

The boundary condition for temperature at the top boundary at $z = 0$ is found by taking the horizontal average of equation (3), and assuming a quasi-steady temperature evolution so that $\frac{\partial \langle T \rangle}{\partial t} = 0$ where $\langle * \rangle$ denotes horizontal average of $*$ given by $\langle * \rangle = \frac{1}{L}\int_0^L * \mathrm{d}x$. Taking the horizontal average of equation (3) gives

$$\kappa \frac{\partial^2 \langle T \rangle}{\partial z^2} = -\frac{\mathrm{d}}{\mathrm{d}z}(Q_o e^{z/l}) - \frac{\partial}{\partial}\langle w'T' \rangle \tag{6}$$

where $T'(x, z, t)$ is the temperature perturbation ($T = \langle T \rangle(z, t) + T'(x, z, t)$). Integrating over the depth of the domain from $z = -H$ to $z = 0$ gives the boundary condition for temperature at $z = 0$,

$$\left.\frac{\partial \langle T \rangle}{\partial z}\right|_{z=0} = \frac{N^2}{\alpha g} - \frac{Q_o}{\kappa}(1 - e^{-H/l}) \tag{7}$$

The boundary conditions for temperature at the top and bottom boundaries specify the value of the fluxes at these boundaries. At the bottom boundary, this implies the stratification frequency of the thermocline. At the top boundary, the boundary condition is given by the heat flux lost at the top boundary (i.e., the surface of the ocean) so that the net flux in the domain is zero, in order to have a quasi-steady temperature evolution in the domain. For example, this could be a radiative heat loss at the surface of the ocean during the winter when the ocean surface loses heat radiatively to the cold air above it.

If $\frac{\partial T}{\partial z} < 0$ at the top boundary, we have colder fluid overlying hotter fluid. Therefore, $\frac{Q_o(\alpha g)}{\kappa N^2} > 1$ is a necessary condition for convection to occur, but it is not a sufficient condition since the fluid also needs to overcome viscous forces. This is given by the Rayleigh number, which is the ratio of buoyancy forces to viscous forces, and is defined below.

The following dimensionless parameters are defined to non-dimensionalise the governing equations and boundary conditions for the simulations,

$$\tilde{t} = \frac{t\kappa}{l^2}, \qquad \underline{\tilde{u}} = \frac{\underline{u}\kappa}{l}, \qquad \widetilde{T} = \frac{T}{\Delta}, \qquad \tilde{p} = \frac{p\kappa^2}{l^3} \tag{8}$$

The dimensionless equations are (dropping the tildes),

$$\underline{\nabla}.\underline{u} = 0 \tag{9}$$

$$\frac{\partial \underline{u}}{\partial t} + (\underline{u}.\underline{\nabla})\underline{u} = -\nabla p + Pr\nabla^2\underline{u} + PrRaT\hat{z} \tag{10}$$

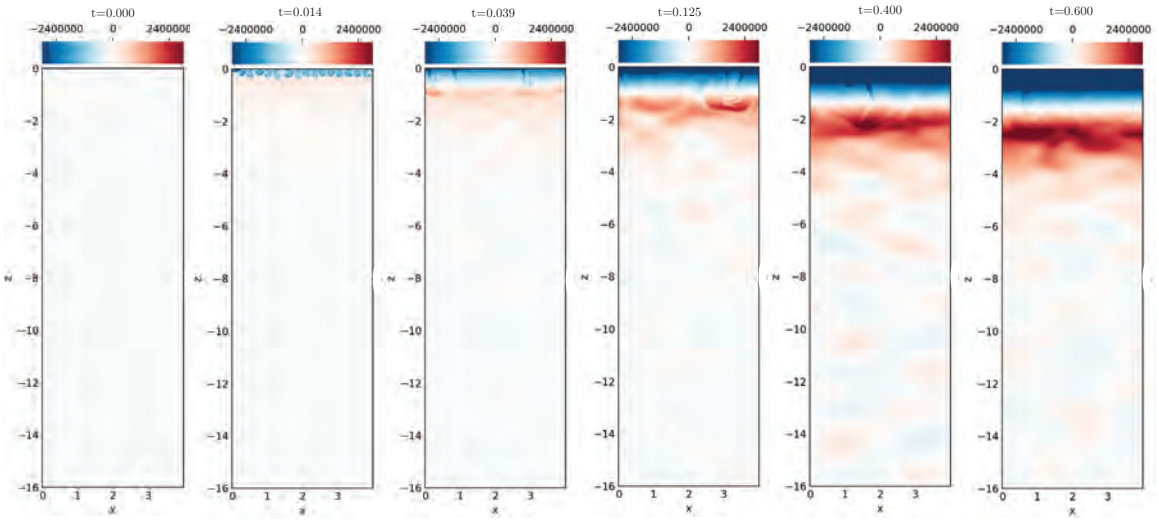

Figure 6: The panels show the evolution of the temperature anomaly ΔT in the domain and the deepening of the mixed layer, where ΔT is the temperature anomaly between the instantaneous temperature and the initial linear temperature profile.

$$\frac{\partial T}{\partial t} + \underline{u}.\underline{\nabla} T = \nabla^2 T + \frac{\partial}{\partial z}(Fe^z) \tag{11}$$

where the following non-dimensional parameters are defined

$$F = \frac{Q_o l}{\kappa \Delta}, \qquad Pr = \frac{\nu}{\kappa}, \qquad Ra = \frac{\alpha g l^3 \Delta}{\nu \kappa}, \qquad \Phi = \frac{N^2 l}{\alpha g \Delta} \tag{12}$$

where Pr and Ra are the Prandtl and Rayleigh numbers, respectively. The dimensionless boundary conditions are now given by,

$$w = 0, \qquad \frac{\partial u}{\partial z} = 0, \qquad \frac{\partial T}{\partial z} = \Phi \qquad \text{at} \quad z = -L_z \tag{13}$$

$$w = 0, \qquad \frac{\partial u}{\partial z} = 0, \qquad \left.\frac{\partial \langle T \rangle}{\partial z}\right|_{z=0} = \Phi - F(1 - e^{-L_z}) \qquad \text{at} \quad z = 0 \tag{14}$$

where $L_z = H/l$ is the dimensionless depth of the domain. In order to mitigate the effects of internal gravity waves reflecting off the bottom boundary, we would need a semi-infinite domain. However, for simulations, we use an artificial bottom boundary with $H \gg l$ so the effect of internal gravity waves on convection is negligible. The domain is defined so that it is periodic in the horizontal x-direction. The simulations use Chebyshev polynomials to discretise the domain in the vertical direction so that the grid is highly resolved close to the bottom and top boundaries. The dimensional depth of the domain is $H = 320\ m$, and $l = 20\ m$, so that $L_z = H/l = 16$. In this case, the smallest length scales in the vertical direction are in the range $5 - 10$ mm.

Figure 6 shows the time-evolution of the temperature in the domain. The panels show the convective plumes descending downwards from the surface and driving mixing within

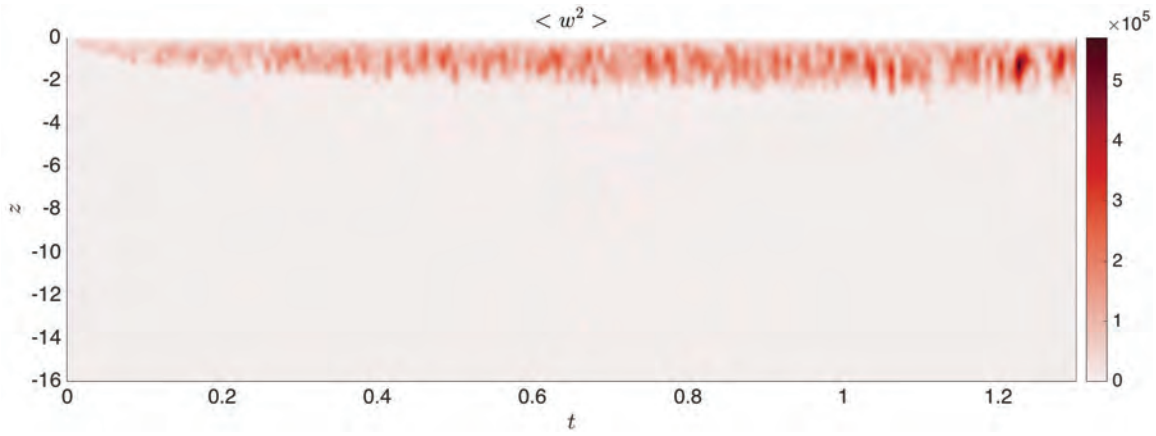

Figure 7: Horizontally averaged value of variance of vertical velocity $\langle w^2 \rangle$ plotted against depth z and time t.

the mixed layer. At later times, we also observe internal gravity waves generated by the plumes in the stratified region below the mixed layer and reflecting off the bottom boundary. Figure 7 shows the horizontally averaged vertical velocity variance in the domain; it decays rapidly below the mixed layer. In a shallower domain, the internal gravity waves would have a noticeable effect below the mixed layer. Figure 8 shows the deepening of the mixed layer, starting with an initially linear temperature profile, and the penetrative convection is shown by the overshoot of the vertical uniform temperature profile within the convective region below the initial linear profile. The depth of the mixed layer is defined as the distance below the top of the domain where the temperature becomes stably stratified, i.e., $\frac{\partial \langle T \rangle}{\partial z} > 0$ at $z = -h$.

The depth of the mixed layer can be estimated by noting that the deep solution is just the diffusive one and is given by setting the right hand side of equation 3 to zero since the velocities below the mixed layer are negligible and the convection is limited to the region within the mixed layer. The diffusive solution implies that

$$\frac{\partial^2 T}{\partial z^2} + \frac{\mathrm{d}}{\mathrm{d}z}(Fe^z) = 0 \tag{15}$$

The solution to this equation is the diffusive profile given shown in figure 10. Integrating this below the convecting layer from $z = -H$ to $z = -h$, and noting that within the mixed layer, the temperature is uniform with depth, gives the mixed layer depth,

$$h = -\ln\left(\frac{F}{\Phi}\right) \tag{16}$$

The layer mixes to the depth where the diffusive solution becomes neutral. The mixed layer depth is plotted against time in figure 9, which shows an initial $\sqrt{t}$ growth as expected of penetrative convection, but eventually deepens and settles at the constant value given by equation (16) for $t \geq 1.4$. Figure 11 shows the deepening of mixed layer when the surface radiative heat flux is increased relative to the stratification of the thermocline in accordance with equation (16).

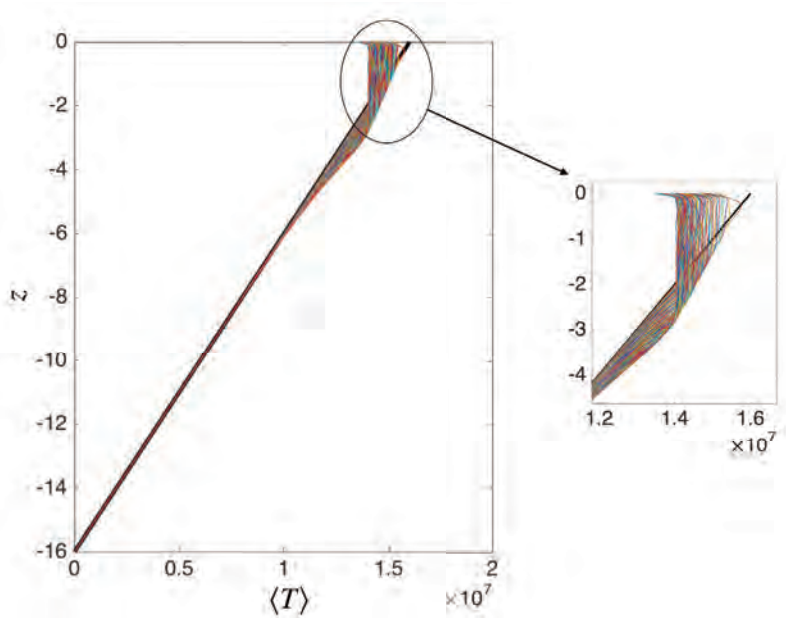

Figure 8: Time-evolution of the horizontally averaged temperature $\langle T \rangle$ plotted against depth z. The black profile is the initial linear temperature profile given by $T = \Phi(z - H)$.

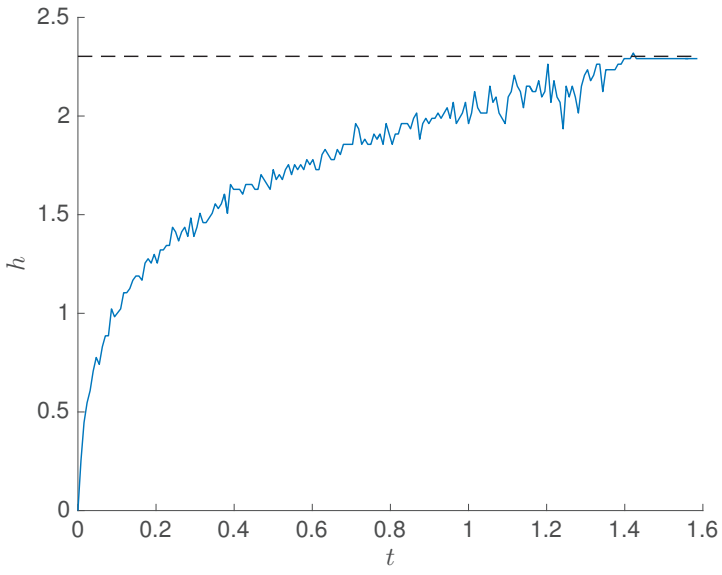

Figure 9: The variation of mixed layer depth h with time t. The black dotted line shows the theoretical value of mixed layer depth.

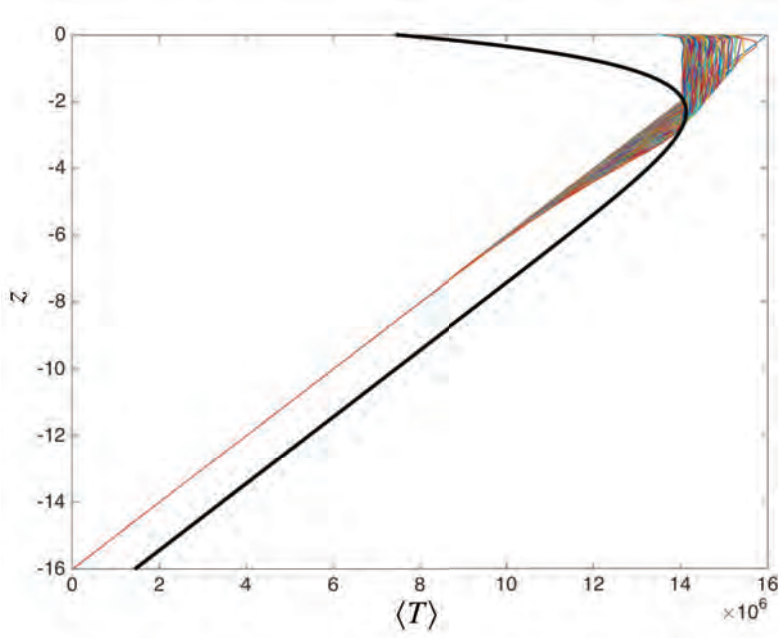

Figure 10: Time-evolution of the horizontally averaged temperature $\langle T \rangle$ plotted against depth z, where the black profile is the diffusive temperature profile when convective effects are absent.

3 Eddy Flux

We begin with the advection-diffusion equation for temperature,

$$\frac{\partial T}{\partial t} + \underline{u}.\underline{\nabla} T = \nabla^2 T + \frac{\mathrm{d}}{\mathrm{d}z}(Fe^z) \tag{17}$$

Splitting the temperature into a horizontally averaged part $\langle T \rangle$ and a fluctuating part T', and taking a horizontal average of equation (17) gives the mean equation,

$$\frac{\partial \langle T \rangle}{\partial t} = \frac{\partial^2 \langle T \rangle}{\partial z^2} + \frac{\mathrm{d}}{\mathrm{d}z}(Fe^z) - \frac{\partial}{\partial} \langle w'T' \rangle \tag{18}$$

and the fluctuation equation,

$$\frac{\partial T'}{\partial t} + \underline{u}.\underline{\nabla} T' - \kappa \nabla^2 T' - \langle w'T' \rangle = -w' \frac{\partial}{\partial z} \langle T \rangle \tag{19}$$

Note that T' satisfies the no-flux condition at the top and bottom boundaries.

$$\frac{\partial T'}{\partial z} = 0 \qquad \text{at}_{\partial z}\, z = 0, -H \tag{20}$$

Equation (17) is analogous to the advection-diffusion equation for a passive scalar given by

$$\frac{\partial c}{\partial t} + \underline{u}.\underline{\nabla} c = \nabla^2 c + \frac{\mathrm{d}}{\mathrm{d}z}(f(z)) \tag{21}$$

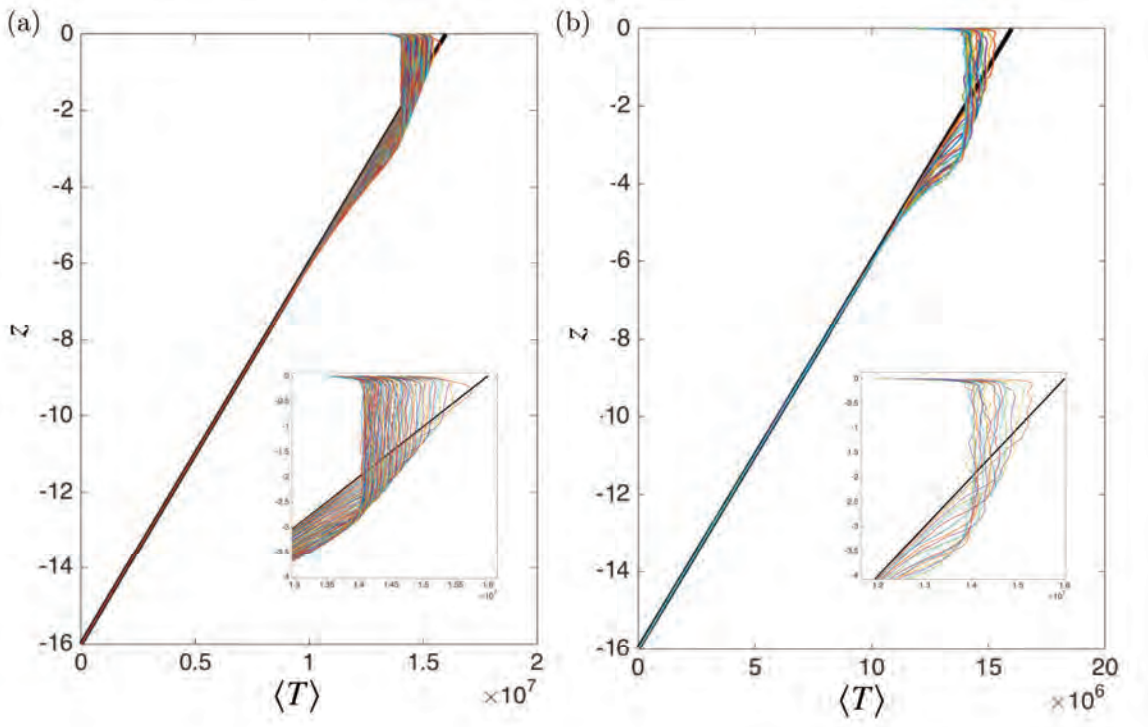

Figure 11: Time-evolution of the horizontally averaged temperature $\langle T \rangle$ plotted against depth z for (a) $F/\Phi = 10$ and (b) $F/\Phi = 50$.

where $f(z)$ is a forcing function or a source term for the tracer. Additionally, we define the boundary conditions for the tracer concentration c as,

$$\frac{\partial c}{\partial \mathrm{z}} = 0 \qquad \text{at} \quad z = 0, -H \tag{22}$$

Taking a horizontal average of equation (21) and using the continuity of velocity gives,

$$\frac{\partial \langle c \rangle}{\partial t} + \frac{\partial}{\partial z}\langle w'c' \rangle = \frac{\partial^2 \langle c \rangle}{\partial z^2} + \frac{\mathrm{d}}{\mathrm{d}z}(f(z)) \tag{23}$$

where $\langle * \rangle$ denotes horizontal average of $*$. Splitting the concentration into a horizontally averaged part and a fluctuating part,

$$c = \langle c \rangle + c' \tag{24}$$

and substituting this into the equation for tracer concentration (21) gives

$$\frac{\partial c'}{\partial t} + \underline{u}.\underline{\nabla} c' - \nabla^2 c' - \frac{\partial}{\partial z}\langle w'c' \rangle = -w' \frac{\partial \langle c \rangle}{\partial z} \tag{25}$$

Linearity implies that, if we have a specified flow field, c' and $F_c \equiv \langle w'c \rangle = \langle w'c' \rangle$ will be linear functionals of $g_c \equiv -w' \frac{\partial \langle c \rangle}{\partial z}$.

$$c' = -\int \mathrm{d}\underline{x}' \mathrm{d}t' G(\underline{x}, t | \underline{x}', t') w'(\underline{x}', t') \frac{\partial \langle c \rangle}{\partial z'} \tag{26}$$

where G is the Green's function response to a delta function forcing in $\underline{x}$ and t.

$$\left(\frac{\partial}{\partial t} + (\underline{u}.\underline{\nabla}) - \nabla^2 \right) G(\underline{x}, t | \underline{x}', t') = \delta(\underline{x} - \underline{x}') \delta(t - t') \tag{27}$$

Multiplying equation (26) by w' and taking an average over x and t gives,

$$F_c \equiv \langle w'c' \rangle = -\int \mathrm{d}z' \widehat{w'(\underline{x}, t) \int \mathrm{d}x' \mathrm{d}t' G(\underline{x}, t | \underline{x}', t') w'(\underline{x}', t')} \frac{\partial \langle c \rangle}{\partial z'} \tag{28}$$

$$= -\int \mathrm{d}z' R(z|z') \frac{\partial \langle c \rangle}{\partial z'} \tag{29}$$

with $\widehat{*}$ here being the average of $*$ over x and t.

We solve from zero initial conditions, holding f fixed, and compute to a statistical steady state to find the eddy diffusivity kernel R for the mixing of a passive tracer.

$$\langle w'c' \rangle = -\int \mathrm{d}z' R(z|z') \frac{\partial \langle c \rangle}{\partial z'} \tag{30}$$

The boundary conditions for c also imply constraints on selection of the forcing function $f(z)$. For example, $f(z)$ could be a delta function forcing centred at z_c. Integrating equation (21) over the domain and noting the periodicity in the x-direction shows that $f(z)$ needs to vanish on the top and bottom boundaries, and the domain average of $\frac{\mathrm{d}}{\mathrm{d}z} f(z)$ is required to be zero in order for the domain-averaged concentration to be constant in time. Here we

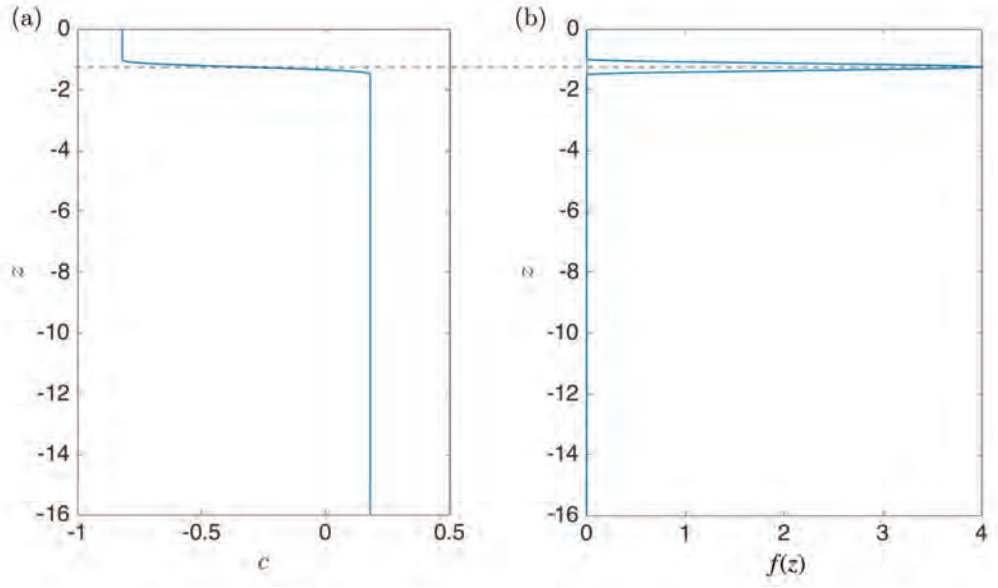

Figure 12: (a) The profile of tracer concentration c at $t = 0$, and (b) the profile of the forcing function $f(c)$ when the centre of the forcing function $z_c = -1.25$.

define $f(z)$ to be a cubic piece-wise polynomial centred at z_c, with compact support. The initial value of c is chosen to be the diffusive value given by

$$\frac{\mathrm{d}^2}{\mathrm{d}z^2}c + \frac{\mathrm{d}}{\mathrm{d}z}f(z) = 0 \tag{31}$$

$$c = -\int f(z)\mathrm{d}z \tag{32}$$

Example profiles of $f(z)$ with the centre at $z_c = -1.25$, and the initial value of c used for the simulations, are plotted in figure 12. Figures 13-15 show the response of the tracer concentration to three different locations z_c of the forcing function (see equation (32)). When the forcing function is centred within the mixed layer, the maximum gradient of tracer concentration is initially within the mixed layer. The tracer within the mixed layer is mixed by the convective plumes, and so the maximum gradient in tracer concentration is shifted to the base of the convection zone (figures 13,14). However, if the forcing function is centered just below the mixed layer, the maximum gradient in the tracer concentration remains unperturbed by the mixing within the mixed layer (note that we are starting with a diffusive profile so the the tracer concentration within the mixed layer is already well mixed). Figures 16a-d and 17a-d show the variation of the horizontally averaged values of the eddy flux and the gradient of the tracer concentration with time, which illustrate the effects described above.

Placing the forcing function at several locations within the domain and computing to a statistically steady state, allows us to estimate the eddy flux kernel given by equation (30). In the discrete form, equation (30) can be written as,

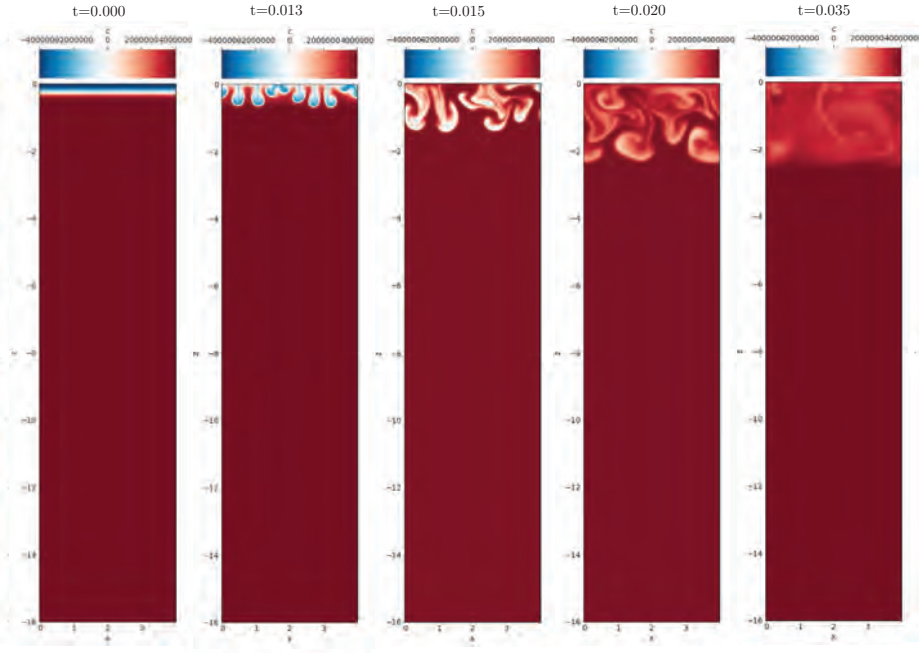

Figure 13: Evolution of the tracer concentration in time t for $z_c = -0.25$.

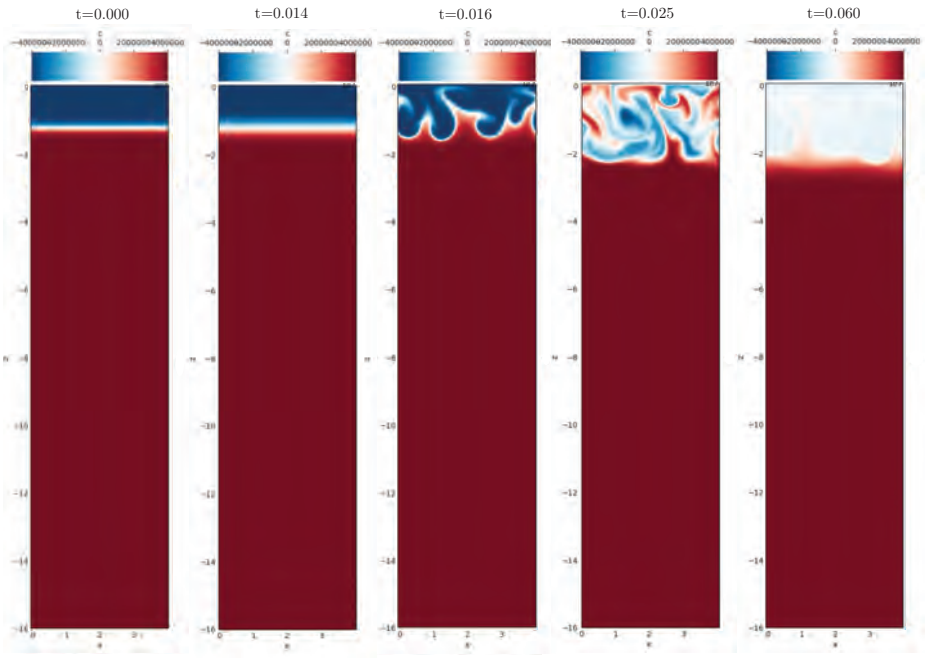

Figure 14: Evolution of the tracer concentration in time t for $z_c = -1.25$.

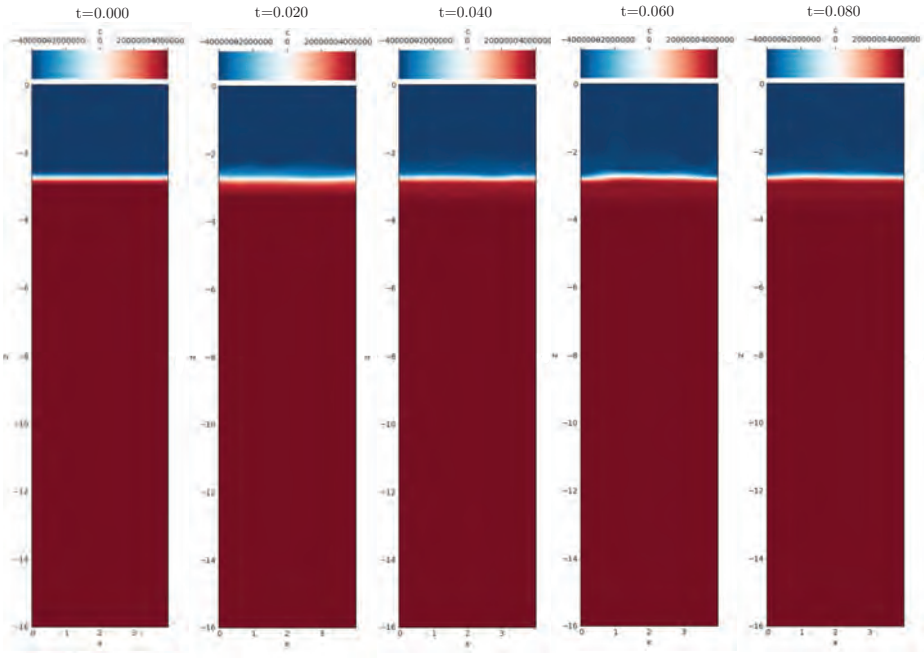

Figure 15: Evolution of the tracer concentration in time t for $z_c = -2.75$.

$$\langle w'c' \rangle_{ij} \ = -\mathrm{d}z R_{ik} \langle c_z \rangle_{kj} \tag{33}$$

where R can be determined using a least-squares fit of the discrete data. This is plotted in figure 18a where the horizontal axis gives the center of the forcing, and the vertical the response. Figure 18a shows that the mixing is strongest within the mixed layer, but illustrates both local and non-local effects of mixing within the convective region (since R is not just a diagonal matrix). The local effects of mixing can be seen from the diagonal elements of R (figure 18b). However, more interestingly, we observe the non-local effects of mixing in figure 18c. show that the flux has contributions from the gradient at that level but also has contributions from the region closer to the surface due to the convective plumes having a greater momentum, and weak contributions from below as well. Figure 19 shows the very weak eddy flux associated with the internal gravity waves in the region below the mixed layer. We also see a weak dependence on the location of the forcing function based on the discrete peaks along the diagonal, but we would obtain a smoother profile by performing higher resolution simulations and sampling the forcing function at more depths.

4 Conclusions and Future work

The mixing of a passive tracer in the the surface mixed layer of the ocean is given by a parameterisation of the eddy flux in terms of the mean gradient. Although this is similar to several parameterisations defined in literature, we define the eddy flux to be a functional of the gradient, given by the eddy flux kernel. This describes both the local and non-local effects of mixing, illustrating that the non-local effects are strongest closer to the surface

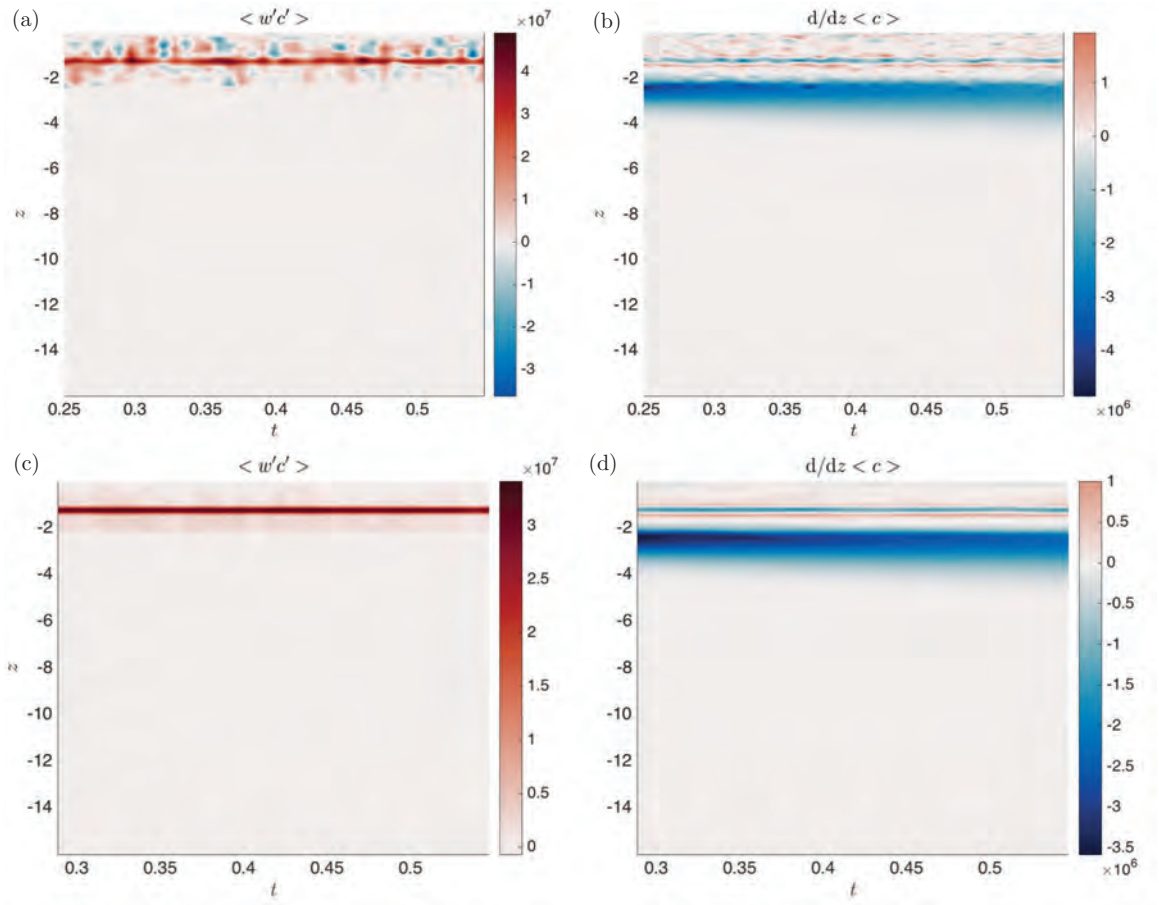

Figure 16: $z_c = -1.25$. Variation of the horizontally averaged quantities with time (a) eddy flux and (b) tracer concentration. (c) and (d) are moving averages of (a) and (b) over a few eddy turnover times.

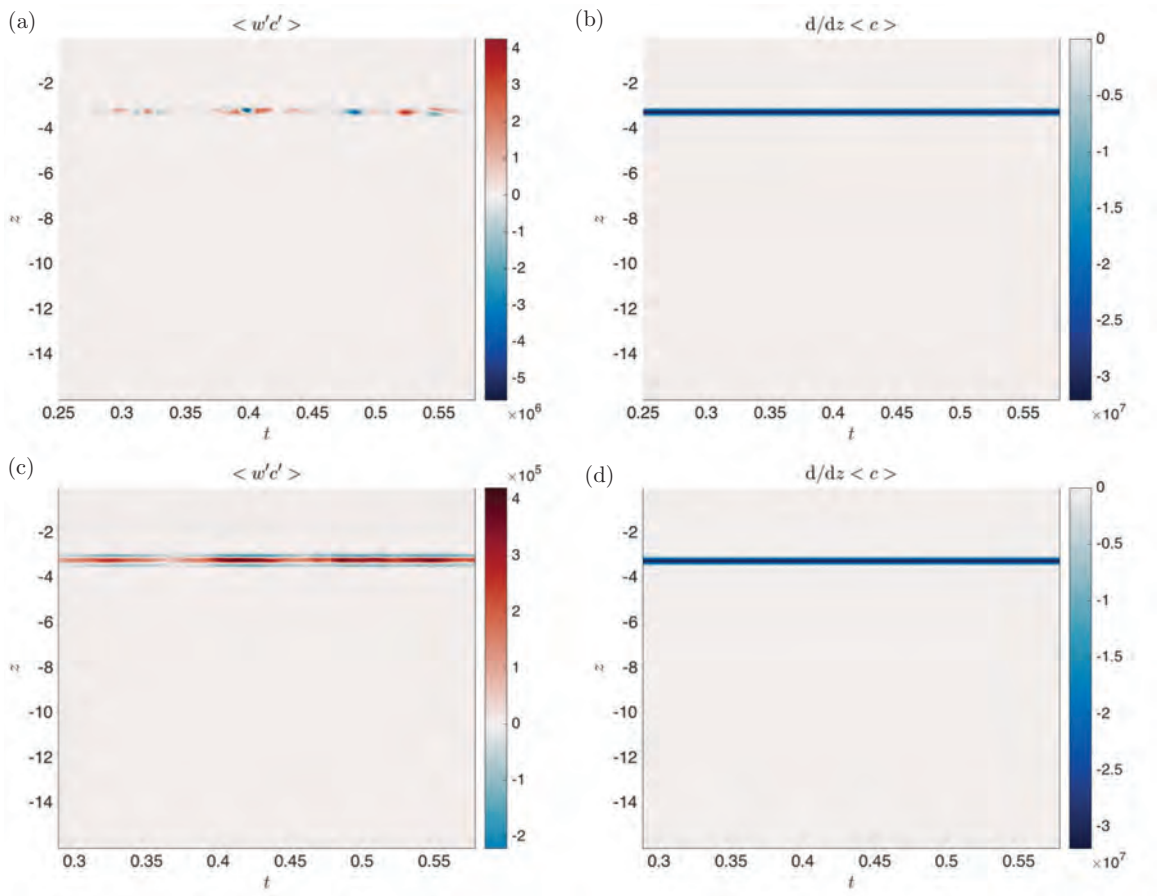

Figure 17: $z_c = -3.5$. Variation of the horizontally averaged quantities with time (a) eddy flux and (b) tracer concentration. (c) and (d) are moving averages of (a) and (b) over a few eddy turnover times.

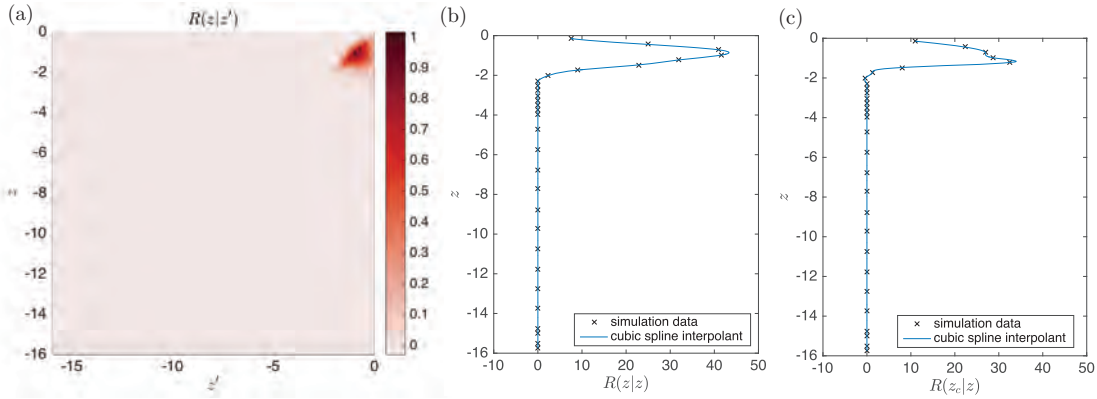

Figure 18: (a) The eddy flux kernel R. (b) Taking the diagonal values in (a) gives the local effects of mixing ($z = z'$). (c) Taking a horizontal slice in (a) at $z = 1.25$ gives the non-local effects of mixing at that location.

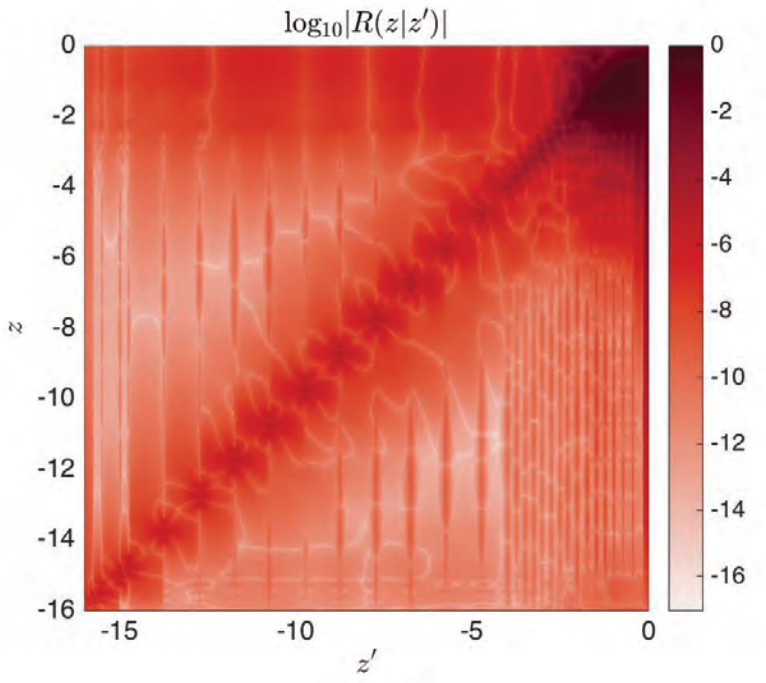

Figure 19: Logarithm of the eddy flux kernel R. Note that the mixed layer depth is $h \approx 2.3$.

because of the energy of the convective plumes detaching from the surface. An extension of this work would be to examine the dependence of the kernel on problem parameters. The ansatz for this particular convectively forced problem would be that the kernel is proportional to the kinetic energy of the eddies produced by the forcing and depends on z/h, z'/h with h the convective adjustment depth.

We have also shown conclusively that the mixed layer depth does indeed grow as the surface fluxes are increased relative to the buoyancy fluxes at the thermocline in accordance with the theoretical formulation of the mixed layer depth. At early times, the mixed layer depth is observed to grow as the square root of time, but eventually settles to a near constant value with some fluctuations due to turbulence. One further development could be to study seasonal variations of mixed layer depth by adding a time-varying surface insolation.

5 Appendix

5.1 An alternative approach to determine the eddy flux kernel

The advection-diffusion equation for a tracer can given by

$$\frac{\partial c}{\partial t} + \underline{u}.\underline{\nabla} c = \nabla^2 c + \lambda(f(z) - c) \tag{34}$$

where $f(z)$ is a forcing function or a source term for the tracer and λ is a relaxation parameter.

Doing this for a range of delta functions at different location helps estimate a kernel for the flux of tracer.

$$\langle w'c' \rangle = -\int \kappa(z|z') \frac{\partial c}{\partial z'} \mathrm{d}z' \tag{35}$$

Define $d = c - \tilde{f}(z)$ so that

$$\frac{\partial d}{\partial t} + \underline{u}.\underline{\nabla} d = \nabla^2 d - \lambda d - w \frac{\mathrm{d}\tilde{f}(z)}{\mathrm{d}z} + \lambda f(z) - \lambda \tilde{f}(z) + \kappa \frac{\mathrm{d}^2 \tilde{f}(z)}{\mathrm{d}z^2} \tag{36}$$

This equation is analogous to equation (19) for T' if $\tilde{f}(z)$ is defined such that

$$\lambda f(z) - \lambda \tilde{f}(z) + \kappa \frac{\mathrm{d}^2 \tilde{f}(z)}{\mathrm{d}z^{\,2}} = 0 \tag{37}$$

Integrating equation (34) over the domain and noting that $\frac{\mathrm{d}c}{\mathrm{d}z}\big|_{z=0,-H} = 0$, and $u|_{x=0} = u|_{x=L_x}$, $w|_{z=0,-H} = 0$,

$$\frac{\partial \overline{c}}{\partial t} = \lambda(\overline{f}(z) - \overline{c}) \tag{38}$$

$$\int_0^{\overline{c}_o} \frac{\mathrm{d}\overline{c}}{\lambda(\overline{f}(z) - \overline{c})} = \int_0^t \mathrm{d}t \tag{39}$$

$$\overline{c} = \overline{c}_o e^{-\lambda t} + \overline{f}(z)(1 - e^{-\lambda t}) \tag{40}$$

Hence the relaxation parameter λ needs to be defined so that the solution for mean concentration of tracer decays to a constant value over a time scale comparable to the time scale of adjustment of the mean temperature profile to the steady-state solution.

References

[1] M. J. Behrenfeld, *Climate-mediated dance of the plankton*, Nature Climate Change, 4 (2014), p. 880.

[2] M. J. Behrenfeld, S. C. Doney, I. Lima, E. S. Boss, and D. A. Siegel, *Annual cycles of ecological disturbance and recovery underlying the subarctic atlantic spring plankton bloom*, Global biogeochemical cycles, 27 (2013), pp. 526–540.

[3] M. Collins, S.-I. An, W. Cai, A. Ganachaud, E. Guilyardi, F.-F. Jin, M. Jochum, M. Lengaigne, S. Power, A. Timmermann, et al., *The impact of global warming on the tropical pacific ocean and el niño*, Nature Geoscience, 3 (2010), p. 391.

[4] R. Ferrari, S. T. Merrifield, and J. R. Taylor, *Shutdown of convection triggers increase of surface chlorophyll*, Journal of Marine Systems, 147 (2015), pp. 116–122.

[5] L. H. Kantha and C. A. Clayson, *An improved mixed layer model for geophysical applications*, Journal of Geophysical Research: Oceans, 99 (1994), pp. 25235–25266.

[6] L. H. Kantha and C. A. Clayson, *Small scale processes in geophysical fluid flows*, vol. 67, Elsevier, 2000.

[7] A. B. Kara, P. A. Rochford, and H. E. Hurlburt, *Mixed layer depth variability over the global ocean*, Journal of Geophysical Research: Oceans, 108 (2003).

[8] E. B. Kraus and J. S. Turner, *A one-dimensional model of the seasonal thermocline ii. the general theory and its consequences*, Tellus, 19 (1967), pp. 98–106.

[9] T. Kuhlbrodt, S. Rahmstorf, K. Zickfeld, F. B. Vikebø, S. Sundby, M. Hofmann, P. M. Link, A. Bondeau, W. Cramer, and C. Jaeger, *An integrated assessment of changes in the thermohaline circulation*, Climatic Change, 96 (2009), pp. 489–537.

[10] W. G. Large, J. C. McWilliams, and S. C. Doney, *Oceanic vertical mixing: A review and a model with a nonlocal boundary layer parameterization*, Reviews of Geophysics, 32 (1994), pp. 363–403.

[11] S. Manabe and R. J. Stouffer, *Century-scale effects of increased atmospheric c02 on the ocean–atmosphere system*, Nature, 364 (1993), p. 215.

[12] G. L. Mellor and T. Yamada, *Development of a turbulence closure model for geophysical fluid problems*, Reviews of Geophysics, 20 (1982), pp. 851–875.

[13] S. Philip and G. J. Van Oldenborgh, *Shifts in enso coupling processes under global warming*, Geophysical Research Letters, 33 (2006).

[14] J. F. Price, R. A. Weller, and R. Pinkel, *Diurnal cycling: Observations and models of the upper ocean response to diurnal heating, cooling, and wind mixing*, Journal of Geophysical Research: Oceans, 91 (1986), pp. 8411–8427.

[15] S. Rahmstorf, *Encyclopedia of quaternary sciences, chapter thermohaline ocean circulation*, SA Elias Elsevier, Amsterdam, (2006).

[16] N. R. Smith, *Ocean modeling in a global ocean observing system*, Reviews of Geophysics, 31 (1993), pp. 281–317.

[17] T. Takahashi, S. C. Sutherland, R. Wanninkhof, C. Sweeney, R. A. Feely, D. W. Chipman, B. Hales, G. Friederich, F. Chavez, C. Sabine, et al., *Climatological mean and decadal change in surface ocean pco2, and net sea–air co2 flux over the global oceans*, Deep Sea Research Part II: Topical Studies in Oceanography, 56 (2009), pp. 554–577.

[18] C. Wunsch, *Modern observational physical oceanography: Understanding the global ocean*, Princeton University Press, 2015.

[19] J. A. Yoder, C. R. McClain, G. C. Feldman, and W. E. Esaias, *Annual cycles of phytoplankton chlorophyll concentrations in the global ocean: A satellite view*, Global Biogeochemical Cycles, 7 (1993), pp. 181–193.

Defending Against Lava Flows

Edward Hinton

September 18, 2018

1 Introduction

Lava flows, which develop when magma erupts from a volcano, can migrate into populated areas and cause significant damage to homes and infrastructure, costing millions of dollars to local economies [Williams and Moore, 1983]. Concerns about the impact of lava flows have led to the construction of barriers to divert the flow [Colombrita, 1984, Scifoni et al., 2010]. However, these attempts have had limited success. Whilst there have been some simulations and laboratory studies on controlling and diverting lava flows [Fujita et al., 2009, Dietterich et al., 2015], there has been little theoretical analysis of how barriers and obstructions ought to be designed.

Theoretical analysis of lava flows is challenging because lava is a complex fluid [Griffiths, 2001]. As it cools, lava becomes more viscous and subsequently solidifies, and it has a yield strength which varies across time and space [Sparks et al., 1976, Takagi and Huppert, 2010]. Kerr et al. [2006] showed that the formation of crust at the lateral edges of a downslope lava flow confines the lava in a channel of constant width. Over a significant range of temperatures, lava behaves like a viscoplastic fluid, with internal stresses having a significant influence on its gravity-driven flow [see Balmforth et al., 2002]. A key challenge for creating simplified models of lava is determining which of its non-Newtonian properties is the most important physical process in any given situation [Balmforth et al., 2000].

The interaction between a lava flow and an obstruction adds an extra layer of complexity to the modelling of this fluid which exhibits a multiplicity of behaviours. In order to gain insight into the role of obstructions, we consider a simplified model of lava as an isothermal Newtonian fluid. Such viscous Newtonian flows have been studied in the absence of obstructions on a horizontal plane by Huppert [1982a], and an inclined plane by Huppert [1982b] and Lister [1992] who showed that flow from a line source becomes steady with constant depth far behind the contact line. We will analyse how this steady flow is perturbed by an obstruction. The study of this fluid-solid interaction is also important for ice flows over and around topography, although the slow travelling ice is often modelled as a non-Newtonian viscous fluid using the power-law model [Glenn, 1955, Hutter, 1982].

In section 2, we consider obstructions with vertical boundaries which are sufficiently high that no overtopping occurs. Examples include cement casings of electrical pylons such as those employed in Pahoa, Hawaii. We carried out a series of laboratory experiments with a constant flux line source and a cylindrical obstruction downstream of the source. This identified that there may be dry regions downstream of the obstruction depending on the slope angle, cylinder radius, and upstream flow depth. To make progress in understanding

Far upstream depth (cm)	Slope angle (^{o})	Max. depth (cm)	Min. depth (cm)
0.72	5.0	1.14	0.43
0.98	3.5	1.20	0.56
1.32	3.5	1.72	0.80
0.85	5.3	1.20	0.52
1.05	11.0	1.69	0.50
0.55	11.0	1.02	0
0.60	11.0	1.05	0

Table 1: Depth of the steady flow past a cylinder of radius 4.8cm.

the shape of the dry region, we consider flow from a partial line source; we blocked part of the line source so that the upstream boundary is partitioned into a region with constant flux and a region with no flux. We measure the steady contact line which develops as fluid slumps cross-slope from the partial line source.

Next, we reproduce Lister's governing equation for downslope flow, and introduce a no-flux condition at the vertical boundaries of the obstruction. Using a finite-element method, we solve this system numerically and compare the simulations to our experimental results for the contact heights at the edge of the cylinder. In the case where the cylinder has a small influence on the flow depth, we find an asymptotic expansion which agrees well with our numerical results, providing a useful check on our numerical simulations. To make progress in the other regime in which there is a dry region, we derive similarity solutions to describe flow from a partial line source and compare these to our experiment.

In section 3, motivated by the problem of diverting lava flows and understanding the influence of topography, we turn our attention to flow over and around axisymmetric mounds. Viscous flows over topography have been studied extensively in the limit where surface tension dominates the flow, motivated by coating processes [see for example Huppert, 1982b, Stillwagon and Larson, 1988]. Since lava flows consist of dense fluid and have large length scales relative to the capillary length, we assume surface tension is negligible. The problem of flow over a mound has three lengthscales: the depth of the far-field flow, and the horizontal and vertical dimensions of the mound. In the limit of a shallow oncoming flow relative to the horizontal length of the mound, we determine mound aspect ratios for which the flow goes only around the mound and there is a dry region at the peak. We also find a range of mound aspect ratios for which fluid 'ponds' upstream of the mound.

2 Flow Around Obstructions with Vertical Boundaries

2.1 Laboratory technique

We carried out a series of laboratory experiments in an inclined tank of width 39.6cm and length 115.6cm in the downslope direction. Karo syrup was released from a lock gate behind which a fixed depth of syrup was maintained to provide a constant head (see figure 1). The downslope flow from a constant-flux line source evolves into a steady current with depth

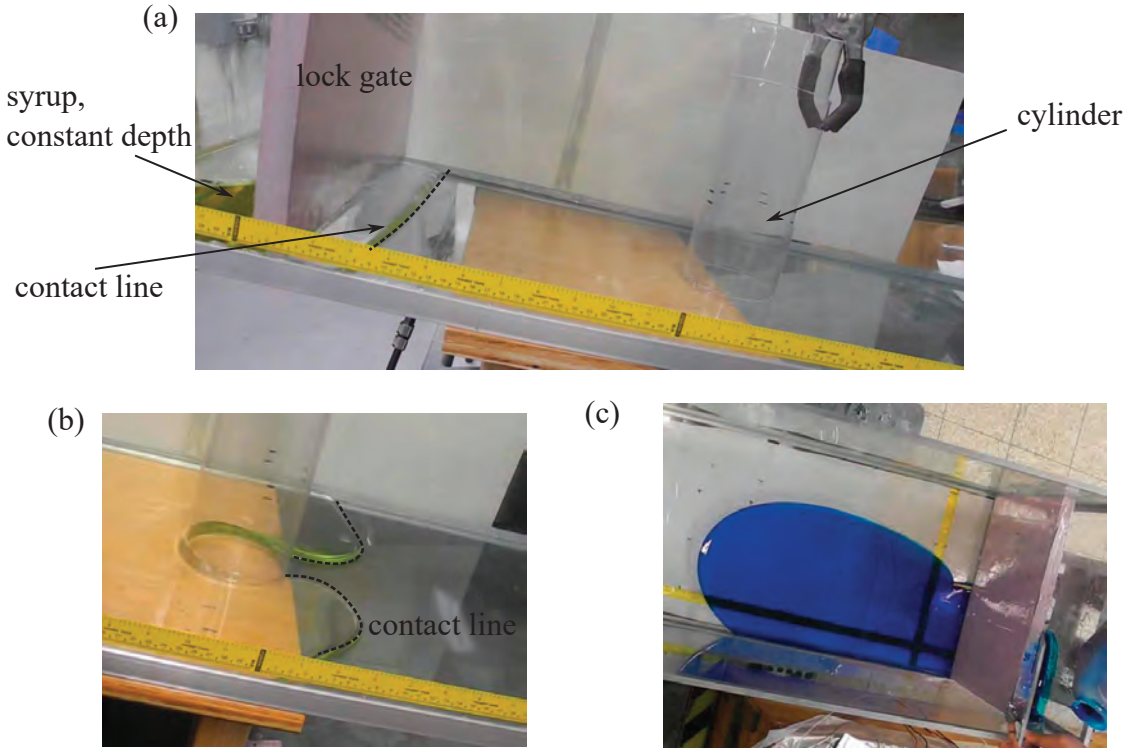

Figure 1: Laboratory setup. (a) Photograph of syrup flowing towards the cylinder from a constant-depth reservoir. (b) Photograph after the contact line passes the cylinder. (c) Photograph from above the tank of our partial line source experiment.

[Lister, 1992]

$$H_\infty = \left(\frac{3\mu Q}{\Delta\rho g \sin\beta} \right)^{1/3}, \tag{1}$$

where Q is the flux per unit width, μ the dynamic viscosity, and $\Delta\rho$ the density difference between the syrup and the air. A cylinder of radius 4.8cm was held fixed in the centre of the tank and we measured the flow depth, H_∞, far upstream of the cylinder. We define the contact line as the set of points at the edge of the flow at which the depth is zero. This line passes the cylinder, and then after a sufficiently long period, the flow around the cylinder becomes steady. We observed that the far upstream, constant depth flow is perturbed in a neighbourhood of the cylinder. The flow deepens upstream and becomes shallower downstream of the cylinder.

The minimum and maximum depth of the steady flow occurs at the edge of the cylinder, at the most downstream and most upstream points, respectively. We performed a series of experiments in which we varied the inclination of the plane and the source flux per unit width, and measured the far upstream, minimum and maximum depths of the flow using a camera and ruled markings. The results are shown in table 1.

Our results demonstrate that, for the same slope angle, shallower oncoming flows are perturbed more relative to the far upstream depth than deeper oncoming flows. When this

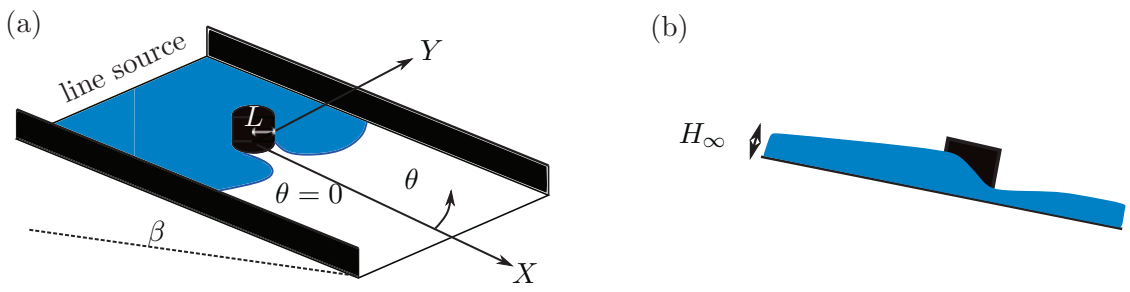

Figure 2: (a) Schematic for flow past a cylinder of radius L. (b) Side view showing oncoming far-field depth, H_∞.

perturbation is large enough, the minimum flow depth is 0 and we observe a dry region downstream of the cylinder (figure 2). This occurs because the cross-slope, gravity-driven slumping of the syrup is insufficient in comparison to the downslope flow to drive the fluid across the downstream edge of the cylinder. Determining the shape of the dry region by comparing the significance of these two physical ingredients is complicated by the geometry of the cylinder, the influence of no-slip on the edge of the cylinder and the significance of surface tension at the contact line (these are discussed further in section 2.5).

To simplify the problem, we consider flow from a partial line source (see figure 1c). This is analagous to flow past a long cuboid with free-slip along the boundary (i.e. the flow past the rectangle is independent of cross-channel position). We performed an experiment in which a 14cm block was added behind the gate to restrict the flow from the source to one side of the channel. Using a camera mounted above the tank, we measured the shape of the contact line in the steady state, plotted in figure 6. This setup allows us to isolate the influence of the balance between cross-channel slumping and downslope gravity-driven flow, aiding our understanding of the shape of the dry region downstream of a cylinder. We investigate the balance theoretically in section 2.6.1.

The main challenges in our experimental procedure were maintaing a constant flux and supplying that flux for a sufficiently long time to reach the steady states. Maintaining constant flux was difficult because we did not have access to pumps with sufficient flux for our line source and instead we poured syrup into the reservoir behind the lock gate and attempted to maintain a constant depth by eye with a marked level on the tank. We had only five litres of syrup which constrained the duration of our experiments and the flow may have still been slowly adjusting at the end of some of the experiments, particularly those with a dry region downstream of the cylinder.

2.2 Formulation

We consider the flow of a fluid of dynamic viscosity μ down a rigid inclined plane at an angle β to the horizontal. We denote the downslope coordinate by X, the cross-slope coordinate by Y, the normal distance above the inclined plane by Z and time by T. The depth of the fluid is given by $H(X, Y, T)$. We assume that the fluid is sufficiently viscous that the effects

of both inertia and surface tension can be neglected (i.e. Reynolds and capillary numbers are sufficiently small). We assume that the flow is predominantly parallel to the plane and hence the pressure within the fluid is hydrostatic [Batchelor, 1965],

$$P = P_0 + \Delta\rho g(H - Z)\cos\beta, \tag{2}$$

where $\Delta\rho$ is the density difference between the fluid and the ambient and P_0 is the ambient pressure, assumed a constant. The fluid velocity in the X and Y directions is given by

$$\begin{aligned} U &= \tfrac{\Delta\rho g}{2\mu} Z\big(Z - 2H\big)\bigg(\tfrac{\partial H}{\partial X}\cos\beta - \sin\beta\bigg), \\ V &= \tfrac{\Delta\rho g}{2\mu} Z\big(Z - 2H\big)\tfrac{\partial H}{\partial Y}\cos\beta, \end{aligned} \tag{3}$$

respectively [Lister, 1992]. Local mass conservation is expressed by

$$\frac{\partial H}{\partial T} + \frac{\partial}{\partial X}\bigg(\int_0^H U\,\mathrm{d}Z\bigg) + \frac{\partial}{\partial Y}\bigg(\int_0^H V\,\mathrm{d}Z\bigg) = 0. \tag{4}$$

Then using our expressions for the velocities (3), we obtain

$$\frac{\partial H}{\partial T} + \frac{\Delta\rho g}{3\mu}\frac{\partial}{\partial X}\bigg[\bigg(\sin\beta - \frac{\partial H}{\partial X}\cos\beta\bigg)H^3\bigg] - \frac{\Delta\rho g}{3\mu}\frac{\partial}{\partial Y}\bigg[\frac{\partial H}{\partial Y}H^3\cos\beta\bigg] = 0. \tag{5}$$

We consider a line-source at $X = 0$ supplying a flux of Q per unit width. Lister [1992] showed that after an initial transient and away from the contact line, the flow advances with constant depth, given by equation (1). We consider the interaction between this flow and obstructions with lengthscale L measured parallel to the inclined plane. We assume that the channel is much wider than the obstruction so that it may be considered isolated. We have used the lubrication approximation, neglecting the component of velocity normal to the plane in (2), which is equivalent to assuming $H_\infty/L \ll 1$.

In this section we restrict our attention to obstructions which have vertical boundaries and are sufficiently high that there is no overtopping (this is examined in section 3). We introduce the following dimensionless variables

$$x = X/L, \quad y = Y/L, \quad z = Z/H_\infty, \quad t = LH_\infty T/Q. \tag{6}$$

Using equation (5), we find the following governing equation for the dimensionless depth, h(x,y,t),

$$\frac{\partial h}{\partial t} + \frac{\partial h^3}{\partial x} = \Lambda\bigg[\frac{\partial}{\partial x}\bigg(h^3\frac{\partial h}{\partial x}\bigg) + \frac{\partial}{\partial y}\bigg(h^3\frac{\partial h}{\partial y}\bigg)\bigg], \tag{7}$$

where

$$\Lambda = \frac{H_\infty}{L\tan\beta} = \bigg(\frac{3\mu Q}{(\Delta\rho g\sin\beta)L^3\tan^3\beta}\bigg)^{1/3} \tag{8}$$

quantifies the importance of the diffusive terms on the right-hand side of (7), associated with the gravity-driven slumping of the fluid, relative to the downslope advective term on the left-hand side of (7), associated with the gravity-driven flow down the plane.

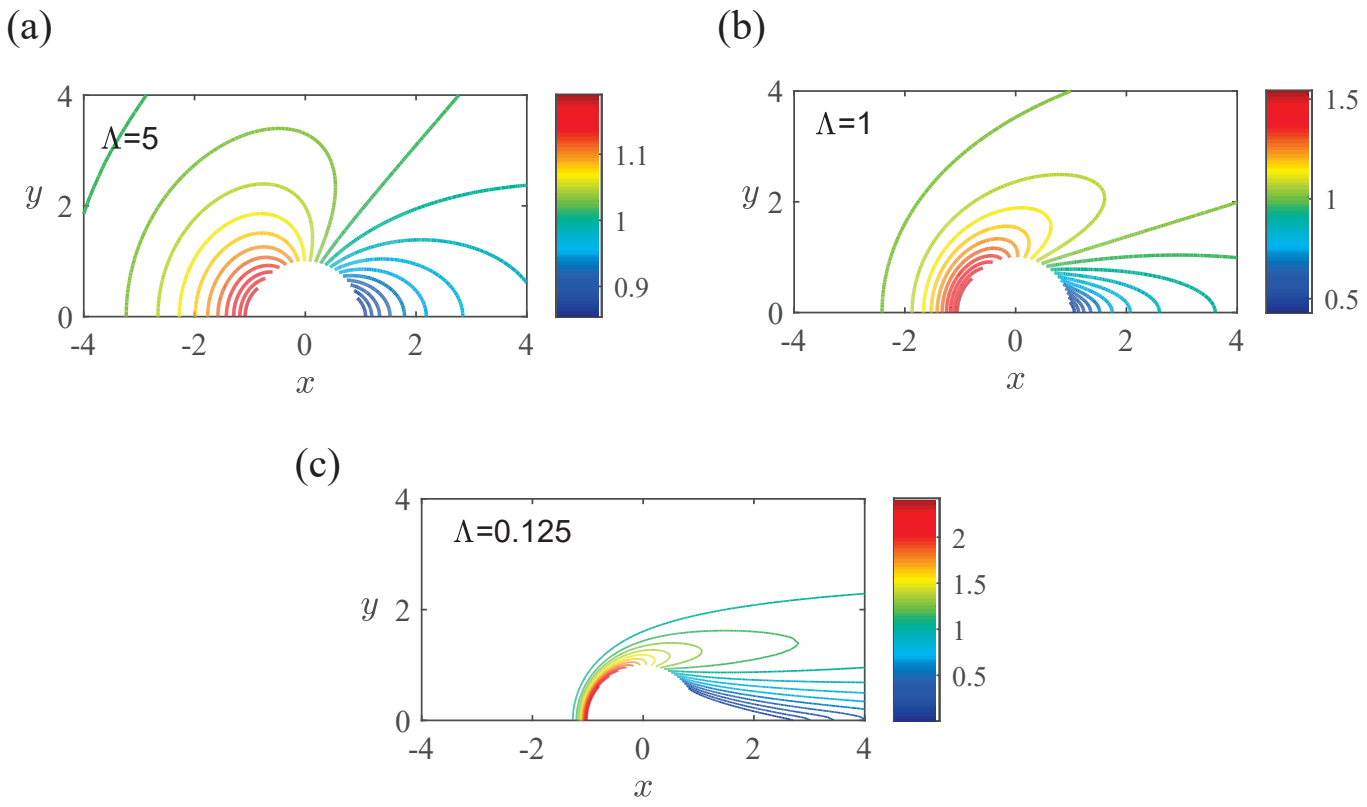

Figure 3: Contour plots of the depth for steady downslope flow past a cylinder centred on $x = 0$, $y = 0$ (flow is in the increasing x direction). (a) ($\Lambda = 5$) The flow deepens slightly upstream of the cylinder, and similarly downstream of the cylinder the flow is shallower than far upstream. (b) ($\Lambda = 1$) For this smaller value of Λ (owing to a wider cylinder, for example) the obstruction leads to a larger perturbation of the depth. (c) ($\Lambda = 0.125$) Flow detachment occurs as Λ is decreased further and a 'dry' region downstream of the cylinder develops.

We impose a no-flux boundary condition at the edge of the obstruction, $\mathbf{u}\cdot\mathbf{n} = 0$, where $\mathbf{n}$ is the outward pointing normal, and

$$\mathbf{u} = \frac{3}{2}z(z-2h)\left(1-\Lambda\frac{\partial h}{\partial x}, -\Lambda\frac{\partial h}{\partial y}\right) \tag{9}$$

is the dimensionless velocity. We allow free-slip on the obstruction. The region in which this a good approximation is calculated in appendix 4.

Throughout this report, we focus on the steady solution which develops long after the current first passes the obstruction.

2.3 Numerical technique

We used MATLAB's Partial Differential Equation Toolbox$^{\mathrm{TM}}$ to solve the steady version of equation (7) with a no-flux boundary condition on the obstruction walls. The program uses a finite-element method and performs adaptive mesh generation. The system was solved in the half-domain $y > 0$, with no-flux imposed on $y = 0$ and on a far-field boundary $y = a$. We also applied a constant flux boundary condition on an upstream boundary $x = -b$, and a free flux condition on $x = b$. For each Λ, the domain size was increased until the results became independent of further increases to it. For example, with the choice $\Lambda = 1$, we used $a = 6$, $b = 10$.

Contour plots of our numerical results of the depth of the fluid are shown in figure 3 for steady flow past a cylinder. Smaller values of Λ correspond to a wider cylinder, a shallower oncoming flow, or a steeper slope (cf. equation 8). For smaller Λ, the presence of the cylinder leads to a larger perturbation to the far-field depth (see figure 3a and 3b). The downstream depth decreases with decreasing Λ and there is a critical value ($\Lambda \approx 0.47$) below which the flow detaches from the cylinder (see figure 3c and figure 4) and there is a dry region downstream of the cylinder. The numerical method was not effective when there were dry regions and we therefore added a small source on the edge of the cylinder, altering the boundary condition on $r = 1$ to $\mathbf{u} \cdot \mathbf{n} = \epsilon$. The magnitude of this source ϵ, was chosen to be as small as possible whilst still providing an 'imaginary' thin film of fluid coating all of the dry region in order that the governing equation (7) could be solved everywhere. The fluid depth in the dry region is approximately constant and this can be used to determine the edge of the dry region.

2.4 Steady flow with no dry regions

We consider steady flow past a cylinder of radius L. For $\Lambda \gg 1$, the flow remains attached to the cyclinder, i.e. there are no dry regions downstream, and the upstream increase in depth owing to the cylinder is small relative to the far upstream depth and restricted to a region near the cylinder (see figure 3a). This motivates seeking an expansion for h in the case $\Lambda \gg 1$, about the far-field depth, $h = 1$, of the form

$$h = 1 + \Lambda^{-1} h_1 + \Lambda^{-2} h_2 + \cdots \tag{10}$$

In polar coordinates, with the origin at the centre of the cylinder, the steady version of the governing equation (7) is

$$\cos\theta \frac{\partial h^3}{\partial r} - \frac{\sin\theta}{r} \frac{\partial h^3}{\partial \theta} = \tfrac{1}{4} \Lambda \nabla^2 h^4, \tag{11}$$

and the no-flux boundary condition at the edge of the cylinder, $r = 1$, is

$$h^3 \left(\Lambda \frac{\partial h}{\partial r} - \cos\theta \right) = 0. \tag{12}$$

At $\mathcal{O}(1)$, equation (11) is

$$\nabla^2 h_1 = 0, \tag{13}$$

subject to boundary conditions

$$\frac{\partial h_1}{\partial r} = \cos\theta \quad \text{at } r = 1, \tag{14a}$$

$$h_1 \to 0 \quad \text{as } r \to \infty. \tag{14b}$$

Seeking a separable solution in r and θ, we find

$$h_1 = -r^{-1}\cos\theta. \tag{15}$$

At $\mathcal{O}(\Lambda^{-1})$, equation (11) leads to

$$\nabla^2 h_2 = 3\cos\theta\frac{\partial h_1}{\partial r} - 3\frac{\sin\theta}{r}\frac{\partial h_1}{\partial \theta} - \frac{3}{2}\nabla^2 h_1^2. \tag{16}$$

With our expression (15) for h_1, we obtain

$$\nabla^2 h_2 = 3r^{-2}\cos 2\theta - 3r^{-4}. \tag{17}$$

The boundary conditions for h_2 are

$$\frac{\partial h_2}{\partial r} = 0 \quad \text{at } r = 1, \tag{18a}$$

$$h_2 \to 0 \quad \text{as } r \to \infty. \tag{18b}$$

The general solution to equation (17) is

$$h_2 = A_0\log(r) + B_0 + \sum_{n=1}^{\infty}\left(A_n r^n + B_n r^{-n}\right)\left[C_n\cos n\theta + D_n\sin n\theta\right] - \frac{3}{4}\cos 2\theta - \frac{3}{4}r^{-2}. \tag{19}$$

We impose $A_n = 0$ $(n \geq 1)$ because h_2 cannot grow algebraically in the far-field if it is to match with $h_2 \to 0$ as $r \to \infty$. Applying the boundary condition at $r = 1$ (equation 18a), we find $A_0 = -3/2$ and $B_n = 0$ $(n \geq 1)$, yielding

$$h_2 = -\frac{3}{2}\log(r) + B_0 - \frac{3}{4}\cos 2\theta - \frac{3}{4}r^{-2}. \tag{20}$$

Hence it is not possible to apply the boundary condition as $r \to \infty$ (equation 18b) because $A_0 \neq 0$ and hence $h_2 \sim \log r$.

Instead in the regime $\Lambda \gg 1$, the solution forms two asymptotic regimes close to and far from the cylinder. When the radial distance is $\mathcal{O}(\Lambda)$, the advective terms of (11) are comparable with the diffusive terms. The problem is therefore singular [Hinch, 1991] and its asymptotic solution comprises an 'inner' region close to the cylinder which is matched to an 'outer' region far from it.

Next, we seek an asymptotic expansion for the depth in the outer region where the advective and diffusive terms balance.

2.4.1 Outer region

The distinguished limit for the outer region of equation (11) occurs when we rescale r with Λ given by

$$r = \Lambda \hat{r}, \tag{21}$$

where $\hat{r}$ is order 1, and $\hat{x}$ and $\hat{y}$ are defined similarly. Equation (11) in the rescaled coordinates is

$$\frac{\partial h^3}{\partial \hat{x}} = \left[\frac{\partial}{\partial \hat{x}} \left(h^3 \frac{\partial h}{\partial \hat{x}} \right) + \frac{\partial}{\partial \hat{y}} \left(h^3 \frac{\partial h}{\partial \hat{y}} \right) \right], \tag{22}$$

Seeking an outer solution of the form $h = 1 + \delta(\Lambda)\hat{h}$, where $\delta(\Lambda) \ll 1$ is to be determined, we find $\hat{h}$ satisfies

$$3\frac{\partial \hat{h}}{\partial \hat{x}} = \nabla^2 \hat{h}. \tag{23}$$

By letting $\hat{h} = \psi(\hat{r}, \theta) e^{3\hat{x}/2}$, equation (23) is transformed into a more familiar equation for $\psi(\hat{r}, \theta)$ [see chapter 5 of Hinch, 1991]

$$(\nabla^2 - \tfrac{9}{4})\psi = 0. \tag{24}$$

Since $\hat{h} \to 0$ at infinity, we require that decays faster than $e^{-3\hat{x}/2}$. Equation (24) has separable solutions

$$= \left[a_m \cos(m\theta) + b_m \sin(m\theta) \right] \Psi(\hat{r}), \tag{25}$$

where

$$\hat{r}^2 \Psi'' + \hat{r}\Psi' - (9\hat{r}^2/4)\Psi - m^2 \Psi = 0. \tag{26}$$

This has general solution

$$\Psi = P_m I_m \left(3\hat{r}/2 \right) + Q_m K_m \left(3\hat{r}/2 \right), \tag{27}$$

where I_m and K_m are modified Bessel functions of the first and second kind, respectively and P_m and Q_m are constants. The function I_m grows as $\hat{r} \to \infty$, which imposes $P_m = 0$. For $\hat{r} \gg 1$ [Abramowitz and Stegun, 1965]

$$K_m \left(3\hat{r}/2 \right) \sim \sqrt{\frac{\pi}{3\hat{r}}} e^{-3\hat{r}/2}, \tag{28}$$

which implies that $\hat{h}$ decays as $\hat{r}^{-1/2}$ as $\hat{r} \to \infty$. Putting this together, the outer solution is

$$h = 1 + \delta(\Lambda)\hat{h} = 1 + \delta(\Lambda) \sum_{m=0}^{\infty} \left[a_m \cos(m\theta) + b_m \sin(m\theta) \right] K_m \left(3\hat{r}/2 \right) e^{3\hat{x}/2}. \tag{29}$$

We now use the limit of this solution as $\hat{r}$ tends to zero to determine the constants in the inner solution.

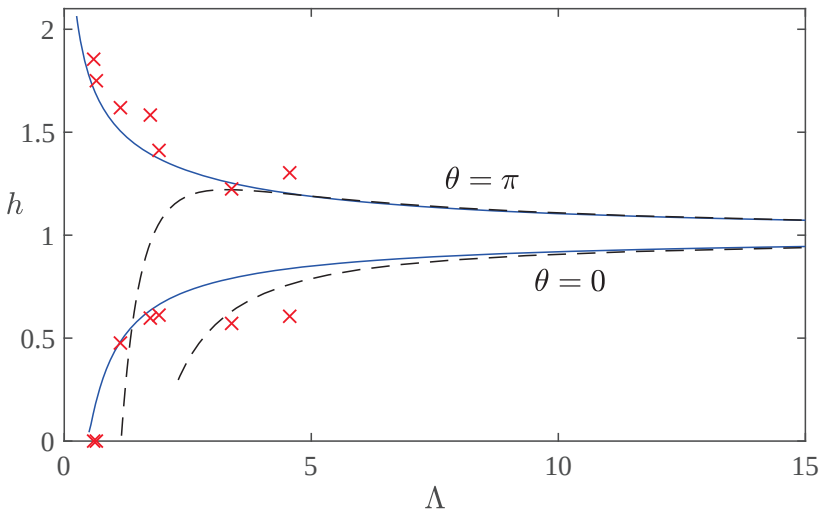

Figure 4: Upstream ($\theta = \pi$) and downstream ($\theta = 0$) flow heights at the edge of a cylinder in steady state. The solid blue lines show numerically calculated predictions, the dashed lines are the asymptotic approximations (equation 37). Experimental data from table 1 is shown as red crosses, where a height of zero corresponds to a dry region downstream of the cylinder. For further details of the experimental procedure, see section 2.1.

2.4.2 Matching

For matching, we recall the behaviour of the modified bessel functions K_m as $\hat{r} \to 0$ [Abramowitz and Stegun, 1965],

$$K_0\left(3\hat{r}/2\right) \sim -\log(3\hat{r}/4) - \gamma, \qquad K_m\left(3\hat{r}/2\right) \sim [(m-1)!/2]\left(3\hat{r}/4\right)^{-m} \tag{30a,b}$$

We keep just K_0 and K_1. It will become clear when matching that the later terms grow too fast as $\hat{r} \to 0$. With this choice the outer solution is

$$h = 1 + \delta\left[a_0 K_0\left(3\hat{r}/2\right) + a_1 \cos\theta K_1\left(3\hat{r}/2\right)\right] e^{(3\hat{r}\cos\theta)/2} \tag{30}$$

and the inner solution is

$$h = 1 - \frac{\cos\theta}{r\Lambda} + \Lambda^{-2}\left[B_0 - \frac{3}{2}\log(r) - \frac{3}{4}\cos 2\theta - \frac{3}{4}r^{-2}\right]. \tag{31}$$

We now match these using an intermediate variable,

$$\rho = r\Lambda^{-\alpha} = \hat{r}\Lambda^{1-\alpha} \tag{32}$$

with ρ fixed as $\Lambda \to \infty$ and α between 0 and 1. The leading order term of both expressions is 1 and the next term in the inner expansion is $\mathcal{O}\left(\Lambda^{-1-\alpha}\right)$. The second order term in the outer solution arises from K_1 and is $\mathcal{O}\left(\delta\Lambda^{1-\alpha}\right)$. Hence to match we choose

$$\delta = \Lambda^{-2}. \tag{33}$$

To order $\Lambda^{-1-\alpha}$, mathcing implies that

$$a_1 = -3/2. \tag{34}$$

To order Λ^{-2}, we find

$$-a_0 \log(\tfrac{3}{4}) - \gamma a_0 - a_0 \log(\rho) - a_0(\alpha - 1)\log(\Lambda) + \tfrac{a_1}{2} = B_0 - \tfrac{3}{2}\alpha \log(\Lambda) - \tfrac{3}{2}\log(\rho). \tag{35}$$

We determine

$$a_0 = \frac{3}{2}, \quad B_0 = -\frac{3}{2}\log\left(\frac{3}{4\Lambda}\right) - \frac{3\gamma}{2} - \frac{3}{4}, \tag{36}$$

where $\gamma \approx 0.577$ is the Euler constant. The inner solution is

$$h = 1 - \frac{\cos(\theta)}{\Lambda r} - \frac{3}{4\Lambda^2}\left[2\log\left(\frac{3r}{4\Lambda}\right) + 2\gamma + 2\cos^2(\theta) + r^{-2}\right]. \tag{37}$$

We use (37) to evaluate the height on the cylinder ($r = 1$) at the upstream stagnation point ($\theta = \pi$) and the dowstream point ($\theta = 0$) (see figure 4). These give the maximum and minimum perturbations to the depth of the flow in the regime $\Lambda \gg 1$. We also plot the maximum and minimum depths of the numerical solution of the governing equation (11) and the experimental data. We note that the asymptotic solution accurately captures the numerical results and that there is reasonable agreement with the experimental measurements.

2.5 Discussion of numerical and experimental data

In addition to the difficulties which arose in our experimental procedure described at the end of section 2.1, the difference between numerical and experimental data may be ascribed to limitations of our model. In particular, we neglected surface tension and allowed free slip on the cylinder boundary. We discuss the importance of each of these in turn. We find that both effects lead to dry regions occuring at higher values of Λ than is predicted by our numerical results. This is consistent with figure 4.

It is well known that in a viscous gravity-driven flow in which the Bond number $B = \Delta\rho g H_\infty^2/\sigma \gg 1$, surface tension only plays a significant role near the contact line where the gradients of the depth are large [Huppert, 1982a]. In our experiments, surface tension is important at the contact line between the syrup and the base of the channel, and at the contact between the syrup and the cylinder walls. As the two flows from either side of the cylinder first join up downstream of the cylinder, there is always a small dry region between the contact point and the cylinder and this region may subsequently be enclosed by the flow (see figure 1b). During the transition to the steady state, the flow into this dry region is inhibited by surface tension and this may cause dry regions to occur in our experiments when they are not predicted by our model.

The flow near the cylinder wall is also influenced by no-slip which our model neglected. Its influence in the case of flow past a rectangle is analysed in appendix 4. As with surface tension, no-slip inhibits the flow into the dry region, which may also contribute to the occurence of dry regions even when not predicted by our model.

Finally, we note briefly that surface tension has an important impact on the shape of the dry region. The curvature of the contact line is largest at the downstream corner where the two flows from either side of the cylinder meet. Surface tension could be very significant here and leads to shortening of the dry region.

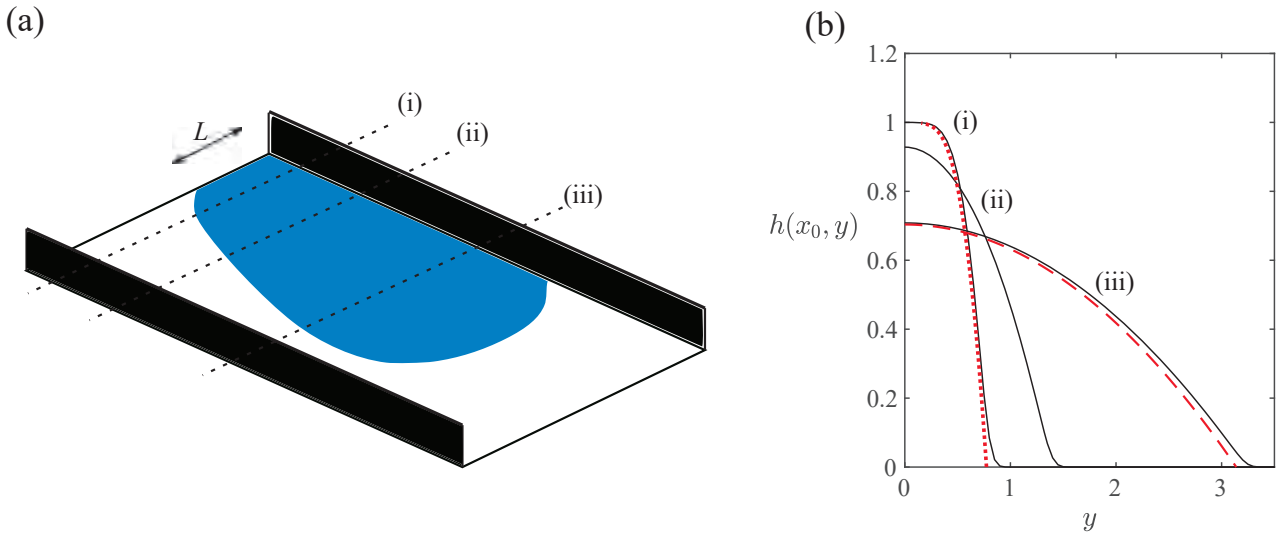

Figure 5: (a) Schematic of flow from a partial line source, the three dashed lines correspond to the plots in (b). (b) Numerical solution to equation (38) at three downstream positions (black lines). The red dotted line is the similarity solution in which the depth tends to 1 at infinity (equation 39), the red dashed line is the similarity solution for a point source at (equation 45).

2.6 Dry wakes downstream of obstructions

In the case of $\Lambda \ll 1$ (corresponding to a wider cylinder relative to the upstream depth, for example), we anticipate that the flow depth becomes 0 in a region downstream of the cylinder (see figure 3c). The boundary condition at the edge of the cylinder (12) is now $h = 0$ in a downstream region, and $\Lambda \partial h/\partial r = \cos\theta$ elsewhere. To make progress in understanding the shape of the dry region, we consider the simpler problem of a line source in a channel which is wider than the source (eg. figure 5a). This provides insight into how the fluid spreads into the 'shadow' region downstream of the cylinder.

2.6.1 Steady solution for a partial line source

We begin by considering a semi-infinite line source ($-\infty < y < 0$) in an infinitely wide channel. There is no lengthscale parallel to the plane and hence the choice of L is arbitrary. In the region of large negative y, the flow behaves as if there was a full line source, having constant depth $h = 1$ and advancing with the downstream distance x growing in proportion to t [Lister, 1992].

Far behind the leading edge of the current, the flow is steady and has spread into $y > 0$. The steady flow in a neighbourhood of $y = 0$ is controlled by a balance between the cross-channel slumping of the current and the downslope component of gravity,

$$\frac{\partial h^3}{\partial x} = \Lambda \frac{\partial}{\partial y}\left(h^3 \frac{\partial h}{\partial y}\right). \tag{38}$$

We have neglected the downslope diffusive term which is small for $x \gg \Lambda$, i.e. everywhere except in a region close to the source. The boundary condition for equation (38) is $h \to 1$ as $y \to -\infty$, owing to the constant depth flow in the far-field. This leads to the scaling $y \sim (\Lambda x)^{1/2}$, and equation (38) has a similarity solution with variable, $\eta = y/(\Lambda x)^{1/2}$. Then $h(x, y) = \chi(\eta)$ satisfies

$$-\tfrac{1}{2}\eta(\chi^3)' = (\chi^3\chi')', \tag{39}$$

with boundary conditions, $\chi(\eta_0) = 0$ and $\chi \to 1$ as $\eta \to -\infty$ so that the boundary condition as $y \to \infty$ is attained. To solve this system numerically we shoot from $\chi = 0$ and iterate to determine η_0. Shooting from $\chi = 0$ requires a second boundary condition at $\eta = \eta_0$, which we determine by letting $\chi \to 0$ which gives the behaviour for small χ,

$$\chi \sim \frac{\eta_0}{2}(\eta_0 - \eta). \tag{40}$$

We find $\eta_0 \approx 1.578$. Our solution for the depth, $h(x, y)$, is plotted at a fixed downstream position x_0 as a red dotted line in figure 5b. The shape of the contact line is

$$y = \eta_0(\Lambda x)^{1/2}. \tag{41}$$

This solution is valid for $x \ll t$ so that the steady solution has developed. The predicted scaling for the contact line agrees well with or our experimental results (see figure 6).

2.6.2 Steady solution for two separated line sources

We can apply the results above to the problem of two semi-infinite line sources separated by a distance L to find the shape of the dry region. The two parabolic contact lines touch at

$$x = \frac{1}{4\eta_0^2\Lambda} \approx 0.1\Lambda^{-1}, \tag{42}$$

which is the furthest extent of the dry region.

2.6.3 A finite width line source

We next consider a finite line source of length L at one side of a channel. The similarity solution above with $y \sim (\Lambda x)^{1/2}$ becomes invalid far downstream because the condition that $h \to 1$ far away from the edge of the current cannot be imposed. This is because the flow has begun to slump away from the wall further downstream. Our similarity solution implied that the cross-slope length of the region in which the depth is not 1 grows in proportion to $(\Lambda x)^{1/2}$ and hence, for a line source of dimensionless width 1, the condition $h \to 1$ at the wall cannot be applied for

$$x \gg \Lambda^{-1}. \tag{43}$$

Beyond this distance, but still far behind the front $x_f = t$, the flow transitions to the similarity solution for a point source found by Smith [1973]. The solution can be obtained by observing that instead of applying $h \to 1$ we impose constant flux across the current because the flow is steady,

$$\int_0^{Y_0} h^3 \mathrm{d}y = 1. \tag{44}$$

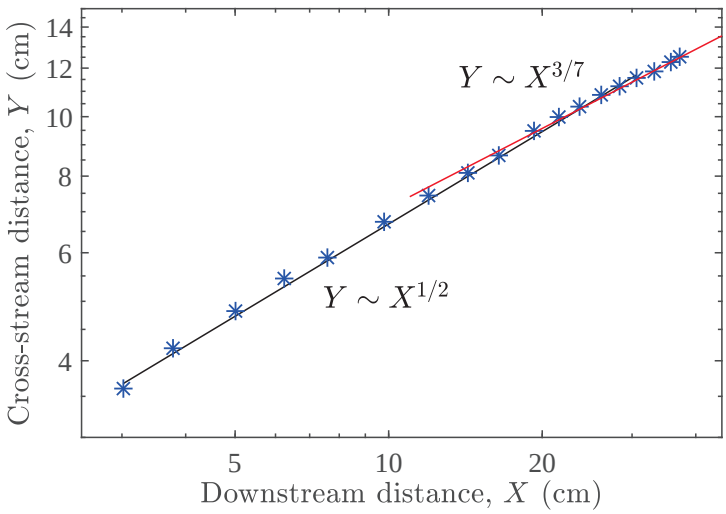

Figure 6: The cross-stream distance that the line source has spread, Y, as a function of downstream distance, X. The stars show experimental measurements of the position of the steady contact line. There is a transition from the similarity solution for a semi-infinite line source (41), $Y \sim X^{1/2}$, to the similarity solution for a point source (equation 45), $Y \sim X^{3/7}$.

Combined with equation (38), this leads to the solution,

$$h = \frac{3}{7}(\Lambda x)^{-1/7}\left(P^2 - y^2/(\Lambda x)^{6/7}\right), \tag{45}$$

where $P = (12005/108)^{1/7} \approx 1.96$. This is compared with the numerical solutions to equation (38) in figure 5b, and the scaling for the contact line, $y \sim x^{3/7}$, is compared to experimental results in figure 6.

3 Flow Over and Around Mounds

In section 2, we analysed the flow around obstructions with vertical boundaries which were sufficiently deep that there was no overtopping. In the present section, we consider how the flow interacts with a smooth mound. The flow may go over the mound, or there may be a dry region around the peak, with the fluid flowing either side of the mound. It is a key aim to determine what controls which of these situations occur. We will focus on the case of a Gaussian mound which leads to some general principles for determining flow overtopping, and our techniques may be applied to any axisymmetric mound.

3.1 Formulation

We consider a mound with peak height D, horizontal lengthscale L and profile $Z = Df(\mathbf{x}/L)$, where f is dimensionless and $f(0) = 1$, $f \to 0$ as $r \to \infty$ (see figure 7). We again consider a line source far upstream of the mound. Measuring the depth of the flow

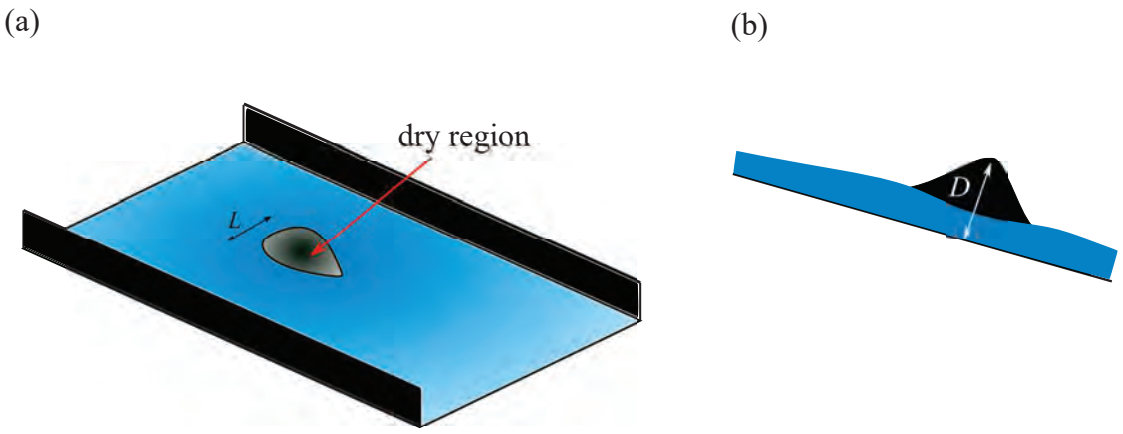

Figure 7: (a) Schematic of flow around a mound. (b) Side view in the case that flow goes around but not over the mound.

from the base of the mound, the hydrostatic pressure (equation 2) is adjusted to include the influence of the topography

$$P = P_0 + \Delta\rho g\big[H(X,Y) + Df(X,Y) - Z\big]\cos\beta. \tag{46}$$

Following the method of section 2.2, we find the dimensionless steady equation for the depth is

$$\frac{\partial h^3}{\partial x} = \Lambda\nabla^2 h^4/4 + \Gamma\left[\frac{\partial}{\partial x}\left(h^3\frac{\partial f}{\partial x}\right) + \frac{\partial}{\partial y}\left(h^3\frac{\partial f}{\partial y}\right)\right], \tag{47}$$

where Λ is as before (8) and there is another dimensionless parameter, Γ, which measures the amplitude of the obstacle relative to its width and the slope of the underlying boundary,

$$\Gamma = \frac{D}{L\tan\beta} \tag{48}$$

There are now two dimensionless groups as we have introduced a third lengthscale, the height of the mound, D. The only boundary condition is the far-field condition $h \to 1$ as $r \to \infty$.

We will focus on the limit of a shallow oncoming flow ($\Lambda \ll 1$) since this regime leads to wake formation with the obstacle. To identify some of the important aspects of the problem, we begin with the one-dimensional problem of a Gaussian bump which spans the channel in the y direction.

3.2 One-dimensional bump

In the one-dimensional problem fluid always flows over the top of the bump. The governing equation is

$$\frac{\mathrm{d}h^3}{\mathrm{d}x} = \Lambda\frac{\mathrm{d}}{\mathrm{d}x}\left(h^3\frac{\mathrm{d}h}{\mathrm{d}x}\right) + \Gamma\frac{\mathrm{d}}{\mathrm{d}x}\left(h^3\frac{\mathrm{d}f}{\mathrm{d}x}\right). \tag{49}$$

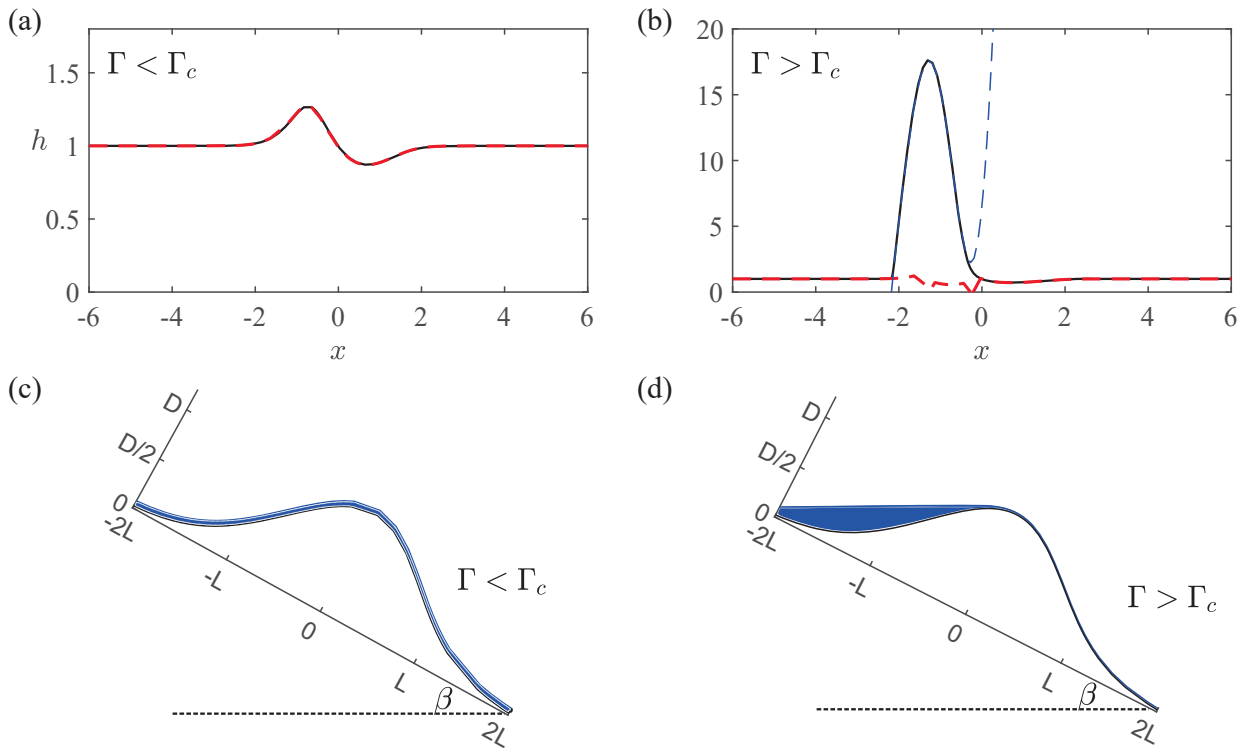

Figure 8: Flow over a one-dimensionsal Gaussian bump for $\Lambda = 0.03$. (a) $\Gamma = 0.6 < \Gamma_c$, the depth is order 1 everywhere, the asymptotic expansion from equation (52) (red dashed line) agrees well with the numerical solution (solid black line). (b) $\Gamma = 2 > \Gamma_c$, the flow deepens upstream of the bump and the first asymptotic expansion (red dashed line) becomes invalid in this deep region. Our expansion for the regions where $h \sim \Lambda^{-1}$ (equation 66) is plotted as a blue dashed line and agrees well with the numerical results in the deep region. (c) Dimensional plot corresponding to (a), where we have rotated the axes through an angle β. The black line shows the bump topography and the blue region represents the fluid. (d) Dimensional plot corresponding to (b), the fluid ponds upstream of the bump.

We examine topography with $f(x) = e^{-x^2}$, but note that our analysis would apply to any bump. Integrating equation (49) and using the constant flux condition for steady flow, we find

$$h^3\big[1 - \Gamma f'(x)\big] = 1 + \Lambda h^3 \frac{\mathrm{d}h}{\mathrm{d}x}. \tag{50}$$

To solve this ODE numerically, we shoot from $x = +\infty$ with the boundary condition $h \to 1$ at $+\infty$. Our numerical results are plotted as black lines in figure 8a and 8b for $\Lambda = 0.03$ and are typical of the regime $\Lambda \ll 1$ corresponding to shallow oncoming flow. There is a critical value of Γ, denoted Γ_c, associated with the height of the bump, at which there is a qualitative change in the numerical results. For Γ less than the critical value, the flow depth is order 1 everywhere (see figure 8a and 8c), whilst for Γ larger than the critical value, the flow pools upstream of the bump (see figure 8b and 8d).

To investigate these two regimes we naively seek an asymptotic expansion in the limit

$\Lambda \ll 1$

$$h = h_0 + \Lambda h_1 + \cdots \tag{51}$$

Substituting into equation (50) and applying the far-field condition, we find that

$$h_0 = \big[1 - \Gamma f'(x)\big]^{-1/3}, \quad h_1 = \Gamma f''(x)\big[1 - \Gamma f'(x)\big]^{-8/3}/9, \tag{52}$$

and the asymptotic expansion for h is

$$h \sim \big(1 - \Gamma f'(x)\big)^{-1/3} + \Lambda \frac{\Gamma f''(x)}{9}\big(1 - \Gamma f'(x)\big)^{-8/3} + \cdots \tag{53}$$

The depth at leading order is independent of Λ. This asymptotic expansion is plotted as a red dashed line in figure 8a and agrees well with the numerical solution. At leading order, this solution neglects the diffusive slumping term in the governing equation (49). This is valid when the gradients in h are small.

However, the leading term in the expansion, h_0, will become singular if there exists a solution to $1 - \Gamma f'(x) = 0$. For the case $f(x) = e^{-x^2}$ there are no solutions to this equation, and hence no singular points, for

$$\Gamma < \Gamma_c = \left(\frac{e}{2}\right)^{1/2} \approx 1.17\ldots \tag{54}$$

and in this case, the expansion (53) is a good approximation to the solution everywhere.

For $\Gamma > \Gamma_c$, the expansion (53) has two singular points which lie in $x < 0$. The second term in the expansion, h_1, is more singular than h_0 at these points and hence the expansion breaks down, which is illustrated in figure 8b ($\Gamma > \Gamma_c$), where we have plotted the expansion as a red dashed line.

Our expansion needs revisiting for $\Gamma > \Gamma_c$ because as we approach the singular point, the left-hand side of equation (50) becomes small and can no longer be compared with the 1 on the right-hand side. Instead, we need an expansion which balances the second term on the right-hand side of (50) with the left-hand side because as the singular point is approached the gradients in h become large. We must capture the diffusive slumping term. This motivates seeking

$$h = \Lambda^{-1}\hat{h}_{-1} + \epsilon(\Lambda)\hat{h}_0 + \cdots \tag{55}$$

where $\epsilon \ll \Lambda^{-1}$ is to be determined. This expansion cannot satisfy the boundary condition $h \to 1$ at $\pm\infty$ and instead it will be valid in a neighbourhood of the singular points and must be matched with our earlier asymptotic expansion (equation 53) which is valid away from the singular points. Substituting (55) into the governing equation (50), we find

$$\hat{h}_{-1} = x - \Gamma f(x) + c_{-1} \qquad \hat{h}_0 = c_0, \tag{57a,b}$$

where c_{-1} and c_0 are to be determined using matching.

3.2.1 Matching

The outer expansion (53) becomes invalid as we approach the singularity x_0, which satisfies

$$f'(x_0) = \Gamma^{-1}. \tag{56}$$

Note that this equation has two solutions. We take x_0 to be the greater solution.

The outer expansion (53) stops being asymptotic near x_0 because the second order term is more singular than the first. To determine the region in which the first and second term are of the same order, we rescale $x = x_0 + \Lambda^\alpha \xi$ in (53), and choose $\alpha = 3/7$ to balance the terms. Then in these rescaled coordinates the outer solution (53) is

$$h \sim \Lambda^{-1/7}\left\{ \big[-\Gamma f''(x_0)\big]^{-1/3}\xi^{-1/3} + \Gamma f''(x_0)\big[-\Gamma f''(x_0)\big]^{-8/3}\xi^{-8/3}/9 \right\}. \tag{57}$$

In the same overlap region, $x = x_0 + \Lambda^{3/7}\xi$, the inner solution (57a,b) takes the form

$$h \sim \Lambda^{-1}\big[x_0 - \Gamma f(x_0) + c_{-1}\big] + \Lambda^{-1/7}\big[-\Gamma\xi^2 f''(x_0)/2\big] + \epsilon c_0. \tag{58}$$

Expansions (57) and (58) must be equivalent in the overlap region and in particular they must have the same magnitude at leading order. Therefore, the first term in (58) must vanish and we obtain

$$c_{-1} = -x_0 + \Gamma f(x_0). \tag{59}$$

To determine ϵc_0, we analyse the governing equation (50) in the overlap region using the rescalings

$$h = \Lambda^{-1/7} H \qquad x = x_0 + \Lambda^{3/7}\xi. \tag{62a,b}$$

Then, at leading order, the governing equation in the overlap region is

$$\frac{\partial H}{\partial \xi} = -H^{-3} - \Gamma f''(x_0)\xi. \tag{60}$$

Note that $f''(x_0) < 0$. As $\xi \to -\infty$, $H \to \infty$ to match with the inner solution (equation 55). This motivates seeking a balance between the left-hand side of (60) with the second term on the right-hand side in the limit of large, negative ξ. We find

$$H \sim -\frac{\Gamma f''(x_0)\xi^2}{2} + a_0, \tag{61}$$

where a_0 is the constant of integration. Comparing (61) with the expansion in the inner region near the singular points (equation 58), we find that $\epsilon = \Lambda^{-1/7}$ and $a_0 = c_0$. The problem is now to determine a_0. We do this by numerically shooting in equation (60) from $\xi = +\infty$. To determine the boundary condition at $\xi = +\infty$, we seek a balance in equation (60) in the limit of large positive ξ. In this region H decays and hence we balance the two terms on the right-hand side of equation (60), leading to

$$H \sim \big[-\xi\Gamma f''(x_0)\big]^{-1/3} = A\xi^{-1/3}. \tag{62}$$

where $A = [-\Gamma f''(x_0)]^{-1/3}$. Then, by substituting $H = \xi^{-1/3}(A + B\xi^{-n})$ into the full equation in the overlap region (60), we determine B and find

$$H = A\xi^{-1/3} - A^5\xi^{-8/3}/9, \tag{63}$$

which we use as our boundary condition. The expansion (63) matches with the outer solution (53) as $\xi \to \infty$, as expected. We can now use (63) to shoot in equation (60). In order to carry out this shooting only once for any value of Γ, we make a rescaling in order to solve a canonical problem with no Γ,

$$H = A^{3/7}H^0, \quad \xi = A^{12/7}\xi^0. \tag{64}$$

Then shooting to determine H^0 and comparing the solution at $\xi^0 = -\infty$ (61), we find

$$c_0 = 1.611A^{3/7} = 1.611\big[-\Gamma f''(x_0)\big]^{-1/7}. \tag{65}$$

The inner expansion is

$$h \sim \Lambda^{-1}\big[x - x_0 + \Gamma f(x_0) - \Gamma f(x)\big] + 1.611\Lambda^{-1/7}\big[-\Gamma f''(x_0)\big]^{-1/7}. \tag{66}$$

This is plotted as a blue dashed line in figure 8b and agrees well with numerical results in the region of large h.

We have found that the depth of the flow is critically dependent on Γ in the limit $\Lambda \ll 1$. For $\Gamma < \Gamma_c$ the shape becomes independent of Λ in the limit of small Λ. However, for $\Gamma > \Gamma_c$, the shape has a region in which the depth is of order Λ^{-1}. Our results suggest that for bumps which have a small aspect ratio relative to the slope gradient ($\Gamma < \Gamma_c$, recall equation 48), the current deepens slightly upstream to overtop the bump (figure 8a and 8c), and provided Γ is constant, the upstream depth is independent of the bump height d. However, for a steeper bump relative to the slope gradient ($\Gamma > \Gamma_c$), fluid accumulates upstream forming a pond and for constant Γ, the upstream depth grows in proportion to the bump height d (figure 8b and 8d). We anticipate that there will be a similar critical dependence on Γ in the 2d problem.

We note briefly that for $\Gamma > \Gamma_c$, the gradients in h become large (see figure 8b) and our lubrication approximation may break down. However, the conclusion of ponding in this case is physically sound. When the flow is not shallow, it must deepen to the depth of the bump in order to flow over the top (see figure 8d).

3.3 Two-dimensional mounds

We recall the governing equation for steady flow over a mound

$$\Lambda\nabla^2\frac{h^4}{4} + \frac{\partial}{\partial x}\left[h^3\big(\Gamma\frac{\partial f}{\partial x} - 1\big)\right] + \Gamma\frac{\partial}{\partial y}\left[h^3\frac{\partial f}{\partial y}\right] = 0. \tag{67}$$

We again consider the limit $\Lambda \ll 1$, noting that the flow need not go over the bump in the two-dimensional geometry; the flow can go only around the mound. We adapted our numerical technique from section 2.3 to solve the governing equation (47) for flow over an axisymmetric mound with $f = e^{-r^2}$. Contours of constant depth from our numerical results

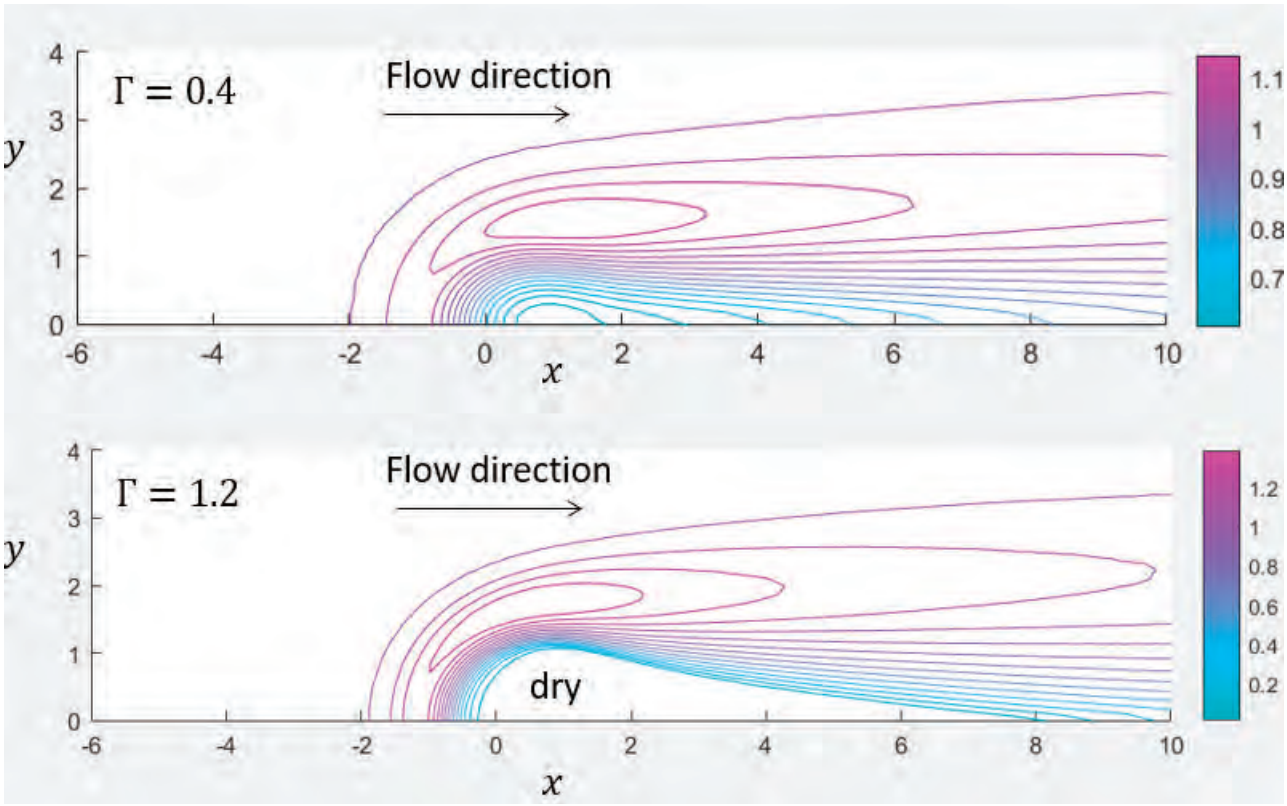

Figure 9: Contour plots of the numerical solutions for flow over an axisymmetric gaussian mound with $\Lambda = 0.05$. For $\Gamma > \Gamma_c$ there is a dry region around the mound. Note that the maximum depth occurs away from the centreline and slightly downstream from the peak of the mound.

are shown in figure 9. Note that the max depth does not occur on the symmetry axis as it did for flow past a cylinder. When a dry region occurs we introduce a small line source along $y = 0$ to create a thin film (see section 2.3).

We follow the same analysis as we did for the one-dimensional problem to determine how the size of the mound controls the steady flow and in particular finding when dry regions occur. Naively seeking an order 1 expansion as before

$$h = h_0 + \Lambda h_1 + \cdots , \tag{68}$$

then at leading order we find the first-order equation for h_0

$$\left[1 - \Gamma \frac{\partial f}{\partial x}\right] \frac{\partial h_0^3}{\partial x} - \Gamma \frac{\partial f}{\partial y} \frac{\partial h_0^3}{\partial y} = \Gamma h_0^3 \nabla^2 f. \tag{69}$$

This equation neglects the diffusive slumping terms in the governing equation (67). We use the method of characteristics to find the following solution to (69)

$$\frac{\mathrm{d}x}{\mathrm{d}s} = 1 - \Gamma \frac{\partial f}{\partial x}, \quad \frac{\mathrm{d}y}{\mathrm{d}s} = -\Gamma \frac{\partial f}{\partial y}, \quad \frac{\mathrm{d}\log(h_0^3)}{\mathrm{d}s} = \Gamma \nabla^2 f, \tag{70}$$

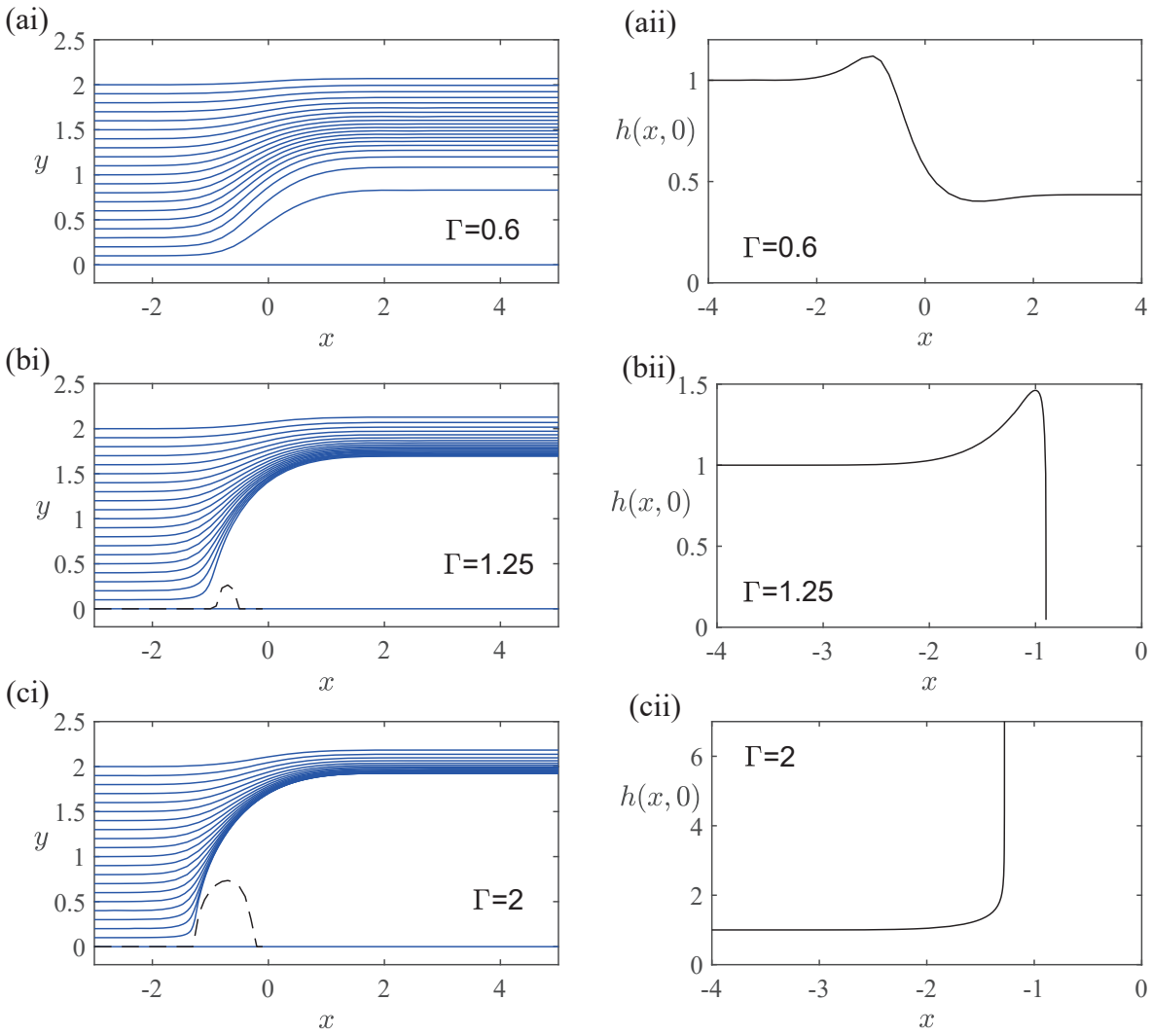

Figure 10: Characteristics in the plane in the limit $\Lambda \ll 1$ (left-hand column) and slices through $y = 0$ of the characteristic solution to equation (69) (right-hand column). (a) $\Gamma < \Gamma_c$, the characteristic solution maintains order 1 depth over the bump (similar to 1d case). (b) $\Gamma_c < \Gamma < \Gamma_d$, there is a region not accessed by the characteristics and the depth decays at the edge of this region. This arises because $\mathrm{d}x/\mathrm{d}s = 0$ at x_1. (c) $\Gamma > \Gamma_d$, the depth grows as x_1 is approached.

where s parametrises the characteristics. We observe that for $\Gamma < \Gamma_c$, $\mathrm{d}x/\mathrm{d}s$ is nowhere 0. We begin by analysing this regime and consider $\Gamma > \Gamma_c$ later.

In the plane, the shape of the characteristic curves is given by

$$\frac{\mathrm{d}y}{\mathrm{d}x} = \frac{2\Gamma y e^{-r^2}}{1 + 2\Gamma x e^{-r^2}}. \tag{71}$$

These are plotted in figure 10a for $\Gamma = 0.6$. The depth far upstream is 1 and the characteristics carry this data over and around the bump and there are no dry regions. Far

downstream, the characteristic solution converges to a shape which is independent of x since $\mathrm{d}y/\mathrm{d}s$ and $\mathrm{d}h/\mathrm{d}s$ tend to zero. This far downstream shape is plotted in figure 11a which illustrates that the depth converges to 1 as $y \to \infty$ but not as $x \to \infty$. Therefore, the characteristic solution cannot be matched with the far-field condition, $h \to 1$, which suggests there is an outer region in which the diffusive slumping terms are important and our current asymptotic expansion is not valid.

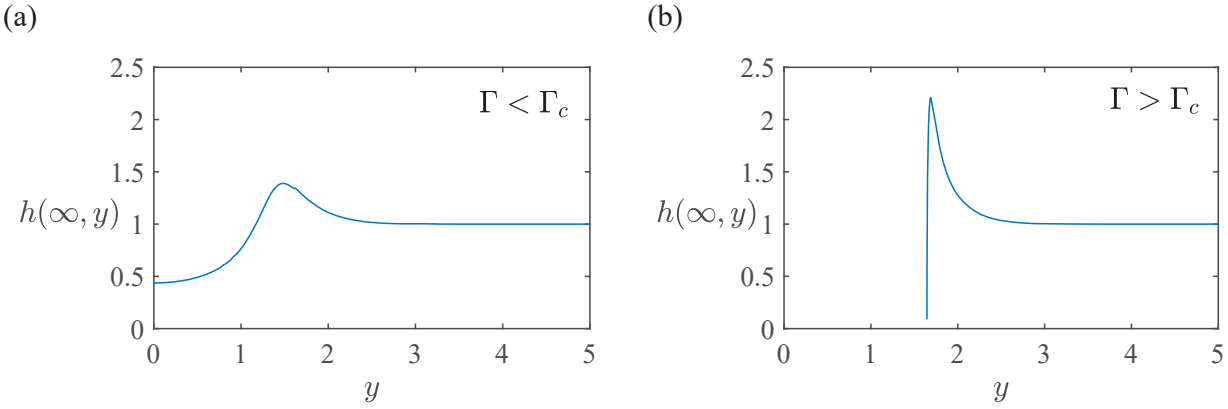

Figure 11: Far downstream cross-channel depth profile for the leading order term in the expansion (68) for (a) $\Gamma = 0.6$ and (b) $\Gamma = 1.2$. The depth becomes independent of x.

3.3.1 Outer region

When x is large and positive, the asymptotic expansion described above converges to a fixed shape in y (figure 11a). Cross-channel diffusive slumping, which was neglected in our asymptotic expansion above, smoothes this shape so that the depth tends to 1 everywhere as $x \to \infty$. This motivates an outer region in which we rescale only the downstream coordinate x by

$$\hat{x} = \Lambda x. \tag{72}$$

Then at leading order the governing equation (67) is

$$\frac{\partial^2 h^4/4}{\partial y^2} = \frac{\partial h^3}{\partial \hat{x}} \tag{73}$$

which represents a balance between the downslope advective term and the term associated with cross-channel diffusive slumping. We use the shape from the limit as $x \to \infty$ of our inner asymptotic solution (see figure 11a) as the 'initial' condition at $\hat{x} = 0$ to solve the nonlinear diffusion equation (73) numerically. The solution converges to $h = 1$ everywhere, satisfying the far-field boundary conditions.

We compare this outer asymptotic approximation with our numerical solution to the full governing equation (67) in figure 12 for $\Gamma = 0.6$. The depth of the numerical solution along the centreline is plotted as a blue dashed line whilst the inner and outer asymptotic approximations are in black and red solid lines, respectively. The inner expansion converges to a constant, whilst the outer solution converges to $h = 1$ far downstream.

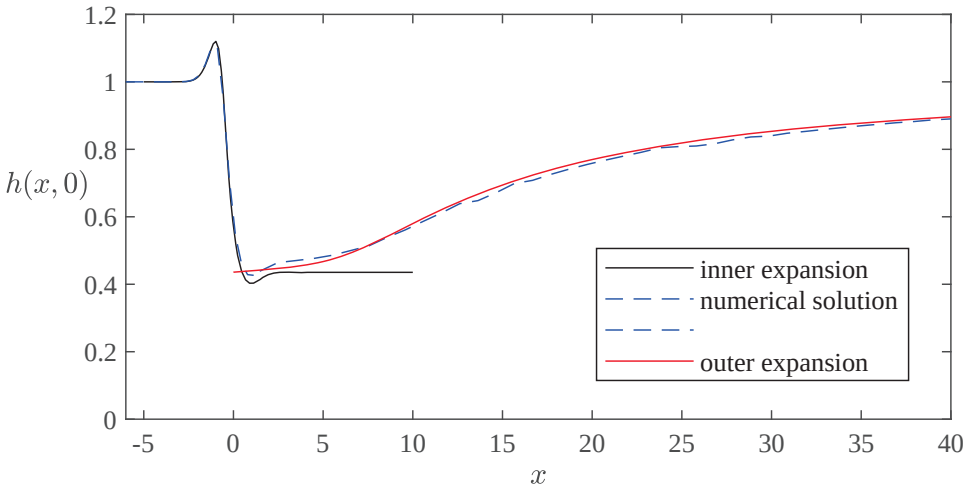

Figure 12: Depth along the centreline ($y = 0$) for $\Gamma = 0.6$. The inner asymptotic approximation (black line) is calculated from equation (69), whilst the outer asymptotic approximation (red line) is calculated from equation (73), using the limit of the innner solution as the boundary condition.

3.3.2 Dry regions ($\Gamma > \Gamma_c$)

We have shown that for $\Gamma < \Gamma_c$, the depth is nowhere zero because the characteristics of the inner asymptotic solution travel over all of the mound. However, as in the 1d problem, there is a regime change at Γ_c. For $\Gamma > \Gamma_c$, $\mathrm{d}x/\mathrm{d}s$ vanishes for the inner expansion (see equation 69) and there is a region not accessed by the characteristics (see left-hand column of figure 10). There is a line on which $\mathrm{d}x/\mathrm{d}s$ is first zero,

$$y = \pm\sqrt{\log(-2\Gamma x) - x^2}, \tag{74}$$

which is plotted as a dashed line in the left-hand column of figure 10. Our aim is to determine the depth in the region which is not accessed by the characteristics. From our numerical simulations (see figure 9), we anticipate that the depth in this region is 0. To confirm this, we show that the depth along the centreline at the edge of the unaccessible region is 0 when downslope diffusive terms are reintroduced, and then observe that the characteristics carry this depth along the edge of the unaccessible region. As we travel further downstream, the characteristics become parallel to the x axis and the cross-slope diffusive term becomes important and this will close up the dry region (see figure 9).

We begin by analysing the depth of the inner asymptotic approximation along the centreline ($y = 0$) which is plotted in figures 10bii and 10cii. According to the solution from the characteristic method, the depth along the centreline is given by

$$\frac{\mathrm{d}\log(h^3)}{\mathrm{d}x} = \frac{4\Gamma(x^2-1)e^{-x^2}}{1+2\Gamma x e^{-x^2}}. \tag{75}$$

As we approach the point at which $\mathrm{d}x/\mathrm{d}s$ first vanishes, which we call x_1 (the smaller root

of $1 + 2\Gamma x e^{-x^2} = 0$), we can approximate (75) by

$$\frac{\mathrm{d}\log(h^3)}{\mathrm{d}x} = \frac{2(x_1^2 - 1)}{(1 - 2x_1^2)(x - x_1)}. \tag{76}$$

Then the behaviour near x_1 is

$$h \sim (x_1 - x)^k \tag{77}$$

where

$$k = \frac{2(x_1^2 - 1)}{3(1 - 2x_1^2)}, \tag{78}$$

which is weakly dependent on Γ. Note that k changes sign as x_1 crosses -1. In terms of Γ this corresponds to

$$k > 0 \quad \text{for } \Gamma < \Gamma_d \approx 1.36, \tag{79a}$$

$$k < 0 \quad \text{for } \Gamma > \Gamma_d. \tag{79b}$$

Hence there is a change in behaviour at Γ_d (see figure 10bii and 10cii). In both cases, the x gradients in h become large, which leads to a recognition that the downslope diffusive slumping term cannot be neglected in a neighbourhood of x_1 along the centreline. To reintroduce this term we make the rescaling

$$x = x_1 + \Lambda^\alpha \xi, \quad h = \Lambda^{\alpha k} H, \tag{80}$$

where the scaling for h is motivated by the behaviour of the innner expansion (equation 77). Using the governing equation (67) we find that along the centreline H satisfies

$$\frac{\partial^2 H^4/4}{\partial \xi^2} + A_\Gamma \xi \frac{\partial H^3}{\partial \xi} + B_\Gamma H^3 = 0, \tag{81}$$

where we have chosen

$$\alpha = \frac{1}{2 - k}, \tag{82}$$

for a balance, and

$$A_\Gamma = -2\Gamma(1 - 2x_1^2)e^{-x_1^2}, \quad B_\Gamma = 4\Gamma(x_1^2 - 1)e^{-x_1^2} \tag{83}$$

are constants. The boundary condition for (81) as $\xi \to -\infty$ is provided by the limiting behaviour of the innner expansion given by (77). Writing this in terms of H and ξ, we find that

$$H = C_\Gamma(-\xi)^k, \tag{84}$$

where C_Γ is a constant which can be determined from the numerical solution for the characteristics. We solve for H by assuming H has compact support and then shooting from $H(\xi_0) = 0$ and iterating to find ξ_0 by matching with the boundary condition (84) at $-\infty$. To shoot from $H = 0$ we need two boundary conditions. Taking the limit of small H in equation (81), we determine the behaviour to be

$$H \sim 2A_\Gamma \xi_0(\xi_0 - \xi). \tag{85}$$

In figure 13, we plot the limiting behaviour of the inner expansion in ξ coordinated as dashed and dotted-dashed lines for $\Gamma = 1.25$ and $\Gamma = 2$, respectively. The outer expansion, described above, which is the solution to equation (81), and which matches with the inner solution is plotted as blue and red solid lines. This expansion includes the x diffusive terms and confirms that the depth becomes 0 at the edge of the inaccessible region in both cases $k < 0$ and $k > 0$.

There is, however, an important physical distinction as k changes sign, equivalent to crossing $\Gamma = \Gamma_d$ (equation 79). The depth in a neighbourhood of x_1 is given by the scaling in (80),

$$h = \Lambda^{k/(2-k)} H. \tag{86}$$

The exponent of Λ changes sign as k changes sign. For $\Gamma < \Gamma_d$, the exponent is positive and the depth of the flow is at most order 1. For a higher mound ($\Gamma > \Gamma_d$), the depth along the centreline near x_1 is of order $\Lambda^{k/(2-k)}$ which grows as Λ becomes smaller. This is somewhat analagous to the one-dimensional problem and corresponds to pooling upstream of the mound.

Further downstream, the cross-stream diffusive terms become important. The same analysis as in section 3.3.1 can be performed; we take the downstream limit of the inner solution for $\Gamma > \Gamma_c$ (figure 11b) as the initial condition for the nonlinear diffusion equation (73). The dry region is closed up and much further downstream, the depth converges to 1.

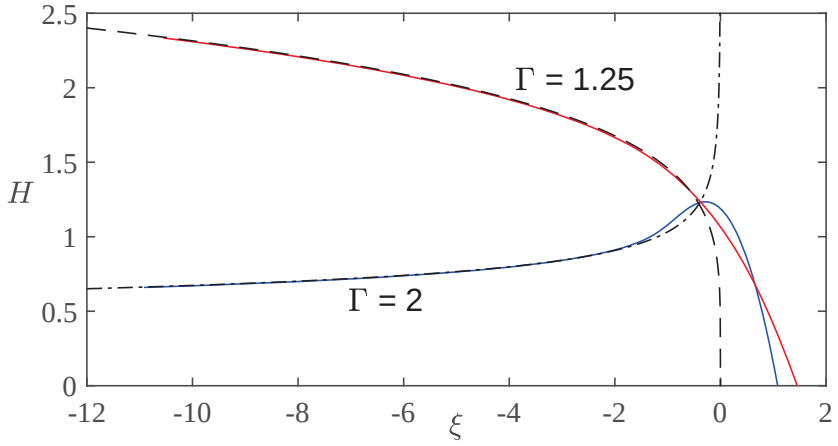

Figure 13: Matching with the limit of the characteristic solution (equation 77), dashed line. The red and blue lines show the numerical solution to (81) shooting with (85).

3.3.3 Summary

We have found three regimes for a shallow oncoming flow ($\Lambda \ll 1$) over an axisymmetric mound.
For $\Gamma < \Gamma_c$ flow goes over and around the mound and there are no dry regions.
For $\Gamma_c < \Gamma < \Gamma_d$ there is a dry region and the depth remains order 1 with respect to Λ.
For $\Gamma > \Gamma_d$ there is a dry region and the depth upstream of the mound increases as $\Lambda^{k/(2-k)}$, with $k < 0$ (can be determined by (80)).

4 Conclusion and Discussion

We have quantified the steady free-surface flow of viscous fluid around a cylinder and found parameter values for which there is a dry region downstream of the cylinder. Upstream of the cylinder, the flow deepens and in the case where there is a dry region, the flow depth can more than double upstream. This deepening should be considered when designing obstructions to lava flows; the barriers must be significantly higher than the anticipated flow depth. We have analysed the shape and extent of dry regions which occur downstream of wide obstructions.

Our work has also shown that shallow flow over topography can be critically dependent on the height of the topography, and steeper mounds can lead to significant upstream deepening of the flow.

Acknowledgements

I would like to thank Andrew Hogg and Herbert Huppert for their guidance and advice, it was a great pleasure to work with them over the summer. I am also grateful to Andy Woods for a fascinating set of lectures, and Neil Balmforth and Colm-cille Caulfield for organising a very stimulating program with an excellent series of talks.

Appendix A: Flow near a wall

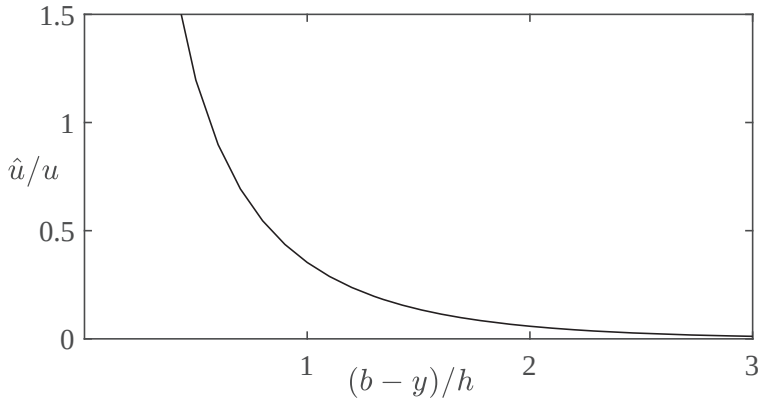

Figure 14: Influence of the no-slip condition on the flow velocity near the wall. The walls are at $\pm b$, and the flow depth is h. Note that $\hat{u}/u$ as a function of $(b-y)/h$ is independent of b and h.

We consider the steady flow in a channel between two walls at $y = \pm b$ assuming that the depth, $h(x)$, is independent of cross-channel position and the flow is unidirectional in the downslope direction. A similar problem for modelling a paint-brush was considered by Batchelor [1965], in which the depth is infinite. The x-component of the momentum

equation is

$$\frac{\partial p}{\partial x} = \mu\left(\frac{\partial^2 u}{\partial y^2} + \frac{\partial^2 u}{\partial z^2}\right), \tag{87}$$

where u is the downslope velocity. Since there is no flow in the y and z directions, the pressure gradient is

$$\frac{\partial p}{\partial x} = -\rho g \sin\beta. \tag{88}$$

Equating (87) and (88), we find an equation for u,

$$\mu\left(\frac{\partial^2 u}{\partial y^2} + \frac{\partial^2 u}{\partial z^2}\right) = -\rho g \sin\beta. \tag{89}$$

We decompose u into the contribution from no-slip on the walls, $\hat{u}$, and the contribution from the hydrostatic pressure,

$$u = \frac{\rho g \sin\beta}{2\mu} z(2h - z) + \hat{u}. \tag{90}$$

We now find $\hat{u}$ to determine the influence of no-slip. From our decomposition, the governing equation for $\hat{u}$ is

$$\left(\frac{\partial^2 \hat{u}}{\partial y^2} + \frac{\partial^2 \hat{u}}{\partial z^2}\right) = 0. \tag{91}$$

There is no-slip ($u = 0$) at the base of the channel,

$$\hat{u} = 0 \quad \text{on } z = 0. \tag{92}$$

No-slip at the walls of the channel imposes

$$\hat{u} = -\frac{\rho g \sin\beta}{2\mu} z(2h - z) \quad \text{on } y = \pm b. \tag{93}$$

Finally, zero stress at the surface $z = h$ becomes

$$\frac{\partial \hat{u}}{\partial z} = 0 \quad \text{on } z = h. \tag{94}$$

This system has separable solutions,

$$\hat{u} = \sum_{n=0}^{\infty} c_n \cosh[(n + 1/2)\pi y/h] \sin[(n + 1/2)\pi z/h]. \tag{95}$$

We use the boundary condition at $y = \pm b$ to determine the coefficients. We compare the series for $\hat{u}$ (95) with (93) on the domain $(0, 4h)$ for z, since $\hat{u}$ is $4h$-periodic. Let $\phi = \pi z/(4h)$, and,

$$d_n = c_n \cosh[(n + 1/2)\pi b/h]. \tag{96}$$

Then

$$\sum_{n=0}^{\infty} d_n \sin[(4n + 2)\phi] = -\frac{\rho g \sin\beta}{2\mu}\left[\frac{8h^2}{\pi}\phi - \frac{16h^2}{\pi^2}\phi^2\right]. \tag{97}$$

We find the coefficients are

$$c_n = -\frac{2\rho g h^2 \sin\beta}{\mu\pi(2n+1)\cosh((n+1/2)\pi b/h)}. \tag{98}$$

This can be used to determine the influence of the walls on the flow velocity. The ratio $\hat{u}/u$ quantifies the significance of the no-slip condition on the velocity field. We plot $\hat{u}/u$ at the surface $z = h$ as a function of cross-slope position divided by the flow depth, h in figure 14. Using this we can identify the lengthscale over which the walls influence the flow. For example the walls have a 10% influence ($\hat{u}/u = 0.1$) at a distance $b - y \approx 1.68h$ from the wall.

References

M. Abramowitz and I. A. Stegun. *Handbook of mathematical functions with formulas, graphs and mathematical tables*. Dover books on intermediate and advanced mathematics. Dover, New York, 1965. ISBN 9780486612720.

N. J. Balmforth, A. S. Burbidge, R. V. Craster, J. Salzig, and A. Shen. Visco-plastic models of isothermal lava domes. *Journal of Fluid Mechanics*, 403:37–65, 2000. ISSN 00221120. doi: 10.1017/S0022112099006916.

N. J. Balmforth, R. V. Craster, and R. Sassi. Shallow viscoplastic flow on an inclined plane. *Journal of Fluid Mechanics*, 470:1–29, 2002. ISSN 00221120. doi: 10.1017/S0022112002001660.

G. K. Batchelor. *An introduction to fluid dynamics G. K. Batchelor.* Cambridge Mathematical Library. Cambridge University Press, Cambridge, 1965. ISBN 9780511800955.

R. Colombrita. Methodology for the construction of earth barriers to divert lava flows: the Mt. Etna 1983 eruption. *Bulletin Volcanologique*, 47(4):1009–1038, 1984. ISSN 02588900. doi: 10.1007/BF01952358.

H. R. Dietterich, K. V. Cashman, A. C. Rust, and E. Lev. Diverting lava flows in the lab. *Nature Geoscience*, 8(7):494–496, 2015. ISSN 17520908. doi: 10.1038/ngeo2470.

E. Fujita, M. Hidaka, A. Goto, and S. Umino. Simulations of measures to control lava flows. *Bulletin of Volcanology*, 71(4):401–408, 2009. ISSN 02588900. doi: 10.1007/s00445-008-0229-7.

J. W. Glenn. The creep of polycrystalline ice. *Proceedings of the Royal Society of London A: Mathematical, Physical and Engineering Sciences*, 228 (1175):519–538, 1955. ISSN 0080-4630. doi: 10.1098/rspa.1955.0066. URL `http://rspa.royalsocietypublishing.org/content/228/1175/519`.

R. W. Griffiths. The Dynamics of Lava Flows. *Annu. Rev. Fluid Mech*, WP01/05(1):4–25, 2001. ISSN 0066-4189. doi: 10.1146/annurev.fluid.32.1.477.

E. J. Hinch. *Perturbation methods.* Cambridge texts in applied mathematics. Cambridge University Press, Cambridge, 1991. ISBN 0521378974.

H. E. Huppert. Viscous Gravity Currents Over a Rigid Horizontal Surface. *J. Fluid Mech*, 121, 1982a.

H. E. Huppert. Flow and instability of a viscous current down a slope. *Nature*, 300(5891): 427–429, 1982b. ISSN 00280836. doi: 10.1038/300427a0.

K. Hutter. Dynamics of Glaciers. pages 245–256, 1982. URL `http://link.springer.com/10.1007/978-90-481-2642-2_127`.

R. C. Kerr, R. W. Griffiths, and K. V. Cashman. Formation of channelized lava flows on an unconfined slope. *Journal of Geophysical Research: Solid Earth*, 111(10):1–13, 2006. ISSN 21699356. doi: 10.1029/2005JB004225.

J. R. Lister. Viscous flows down an inclined plane from point and line sources. *Journal of Fluid Mechanics*, 242:631–653, 1992. doi: 10.1017/S0022112092002520.

S. Scifoni, M. Coltelli, M. Marsella, C. Proietti, Q. Napoleoni, A. Vicari, and C. Del Negro. Mitigation of lava flow invasion hazard through optimized barrier configuration aided by numerical simulation: The case of the 2001 Etna eruption. *Journal of Volcanology and Geothermal Research*, 192(1-2):16–26, 2010. ISSN 03770273. doi: 10.1016/j.jvolgeores.2010.02.002. URL `http://dx.doi.org/10.1016/j.jvolgeores.2010.02.002`.

P. C. Smith. A similarity solution for slow viscous flow down an inclined plane. *Journal of Fluid Mechanics*, 58(2):275–288, 1973. doi: 10.1017/S0022112073002594.

R. S. J. Sparks, H. Pinkerton, and G. Hulme. Classification and formation of lava levees on Mount Etna, Sicily. *Geology*, 4(5):269–271, 1976. ISSN 00917613.

L. E. Stillwagon and R. G. Larson. Fundamentals of topographic substrate leveling. *Journal of Applied Physics*, 63(11):5251–5258, 1988. ISSN 00218979. doi: 10.1063/1.340388.

D. Takagi and H. E. Huppert. Initial advance of long lava flows in open channels. *Journal of Volcanology and Geothermal Research*, 195(2-4):121–126, 2010. ISSN 03770273. doi: 10.1016/j.jvolgeores.2010.06.011. URL `http://dx.doi.org/10.1016/j.jvolgeores.2010.06.011`.

R. Williams and J. Moore. Man Against Volcano : The Eruption on Heimaey, Vestmennaeyjar, Iceland. *Report USGS General Interest Publication*, pages 1–26, 1983. ISSN 1437900429. URL `http://pubs.usgs.gov/gip/heimaey/`.

Centrifugally Forced Viscous Rayleigh-Taylor Instability: Growth Rates of Varicose Modes

Sutirtha Sengupta

October 1, 2018

1 Motivation

The study of the classical Rayleigh-Taylor instability has wide-ranging applications in day-to-day observed phenomena involving mixing of two fluids of differing densities in a gravitational field, e.g. simply mixing milk in coffee to cloud patterns in the sky. The growth of this instability and its inhibition in the presence of rotation has recently been studied in both experiments ([1, 6]) and numerical simulations ([2]). This study is primarily motivated by the recent work of [7] on the growth of Rayleigh-Taylor instabilities in a rotating cylindrical geometry (as illustrated in Fig 2.1) for a two-fluid setup in absence of a gravitational field. Their work considered the case of azimuthal perturbations to the interface in a two-dimensional setup. This study explores the full three-dimensional problem taking into account both the azimuthal and axial (varicose) perturbations of the interface (denoted by $\mathscr{I}$), both from the point of view of linear theory to predict growth rates of the unstable modes in inviscid as well viscous scenarios, and with help of preliminary numerical simulations to test the predictions of the linear theory and gain insights into the full non-linear evolution of the growing instabilities in the system.

This report presents a summary of the work describing the model setup for the 3D-"varicose centrifuge" problem followed by the analytical tools used to perform a linear stability analysis (both for inviscid and viscous setups) that are subsequently compared with numerical simulations performed with the help of the open-source software package OpenFoam. The report concludes with some interesting observations from the set of numerical simulations performed which seem to hint at the emergence of an inherent length scale in the problem independent of initial conditions and various parameters of the system. These parameters were studied systematically to quantify any influence on the growth of the varicose modes in the system.

2 Model

2.1 Governing equations

We chose a rotating cylindrical coordinate system with $\mathbf{r} = (r, \theta, z)$ in which the fluid is being described by the incompressibility and momentum equations:

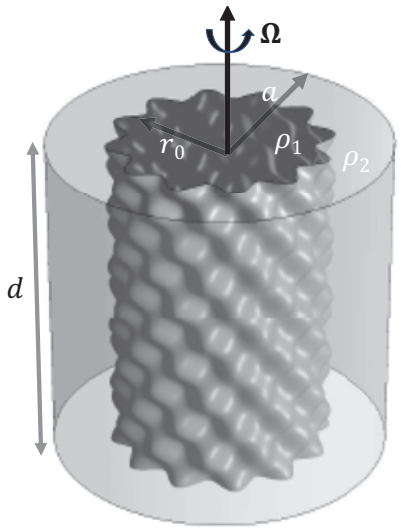

Figure 2.1: Cartoon illustrating the flow setup of the two-fluid system rotating with an angular frequency Ω with the fluid density and dynamic viscosity in the inner ($r < r_0$) and outer ($r > r_0$) layers being ρ_1, μ_1 and ρ_2, μ_2, respectively.

$$\nabla \cdot \mathbf{u}_j = 0 \tag{2.1}$$

$$\rho_j \frac{\mathrm{D}\mathbf{u}_j}{\mathrm{D}t} = -\nabla p_j - \rho_j \mathbf{\Omega} \times (\mathbf{\Omega} \times \mathbf{r}) - 2\rho_j \mathbf{\Omega} \times \mathbf{u}_j + \mu_j \nabla^2 \mathbf{u}_j + 2\underline{\underline{e}}_j \cdot \nabla \mu_j \tag{2.2}$$

with $j = 1$ and 2 corresponding to the inner and outer fluid, respectively, ρ_j and μ_j being the densities and viscosities of the respective fluids (assumed to be constant in each layer for simplicity) and the rate of strain tensor given by

$$\underline{\underline{e}}_j = \frac{1}{2}\left(\nabla \mathbf{u}_j + \nabla \mathbf{u}_j^T\right), \tag{2.3}$$

and $\mathbf{\Omega} = \Omega \hat{\mathbf{e}}_z$ is the rotation vector.

2.2 Non-dimensionalisation

We non-dimensionalise time by the angular velocity Ω and length by the radial extent a of the domain. The density and viscosity in each layer are non-dimensionalised by the average of the values in each layer, respectively,

$$\rho_0 = \frac{1}{2}(\rho_1 + \rho_2),\ \mu_0 = \frac{1}{2}(\mu_1 + \mu_2). \tag{2.4}$$

The governing equations in each fluid layer then reduce to

$$\nabla \cdot \mathbf{u}_j = 0, \tag{2.5}$$

$$\frac{\mathrm{D}\mathbf{u}_j}{\mathrm{D}t} = -\frac{1}{\rho_j}\nabla p_j + r\hat{\mathbf{e}}_r - 2\hat{\mathbf{e}}_z \times \mathbf{u}_j + \frac{\mu_j}{\rho_j}\mathrm{Ek}\nabla^2\mathbf{u}_j, \tag{2.6}$$

where the Ekman number, $\mathrm{Ek} = \frac{\mu_0}{\rho_0 \Omega a^2}$ describes the ratio of the viscous to the Coriolis forces.

2.3 Velocity potential function

Following [5], we adopt the following ansatz for the velocity in each of the two layers in terms of potential functions, ϕ_j, as

$$\begin{aligned}\mathbf{u}_j = \epsilon \left\{1 + \frac{1}{4}\left(\frac{\partial}{\partial t} - \frac{\mu_j}{\rho_j}\mathrm{Ek}\nabla^2\right)^2\right\}\nabla\phi_j - \frac{1}{2}\left(\frac{\partial}{\partial t} - \frac{\mu_j}{\rho_j}\mathrm{Ek}\nabla^2\right)(\hat{\mathbf{e}}_z \times \nabla\phi_j) \\ + \hat{\mathbf{e}}_z \times (\hat{\mathbf{e}}_z \times \nabla\phi_j) \\ = \epsilon\left[\left(1 + \mathcal{L}^2\right)\nabla\phi_j - \mathcal{L}\left(\hat{\mathbf{e}}_z \times \nabla\phi_j\right) + \hat{\mathbf{e}}_z \times (\hat{\mathbf{e}}_z \times \nabla\phi_j)\right]\end{aligned} \tag{2.7}$$

where $\epsilon \ll 1$ and $\mathcal{L} = \frac{1}{2}\left(\frac{\partial}{\partial t} - \frac{\mu_j}{\rho_j}\mathrm{Ek}\nabla^2\right)$. Using this, the incompressibility condition (2.5) yields a governing equation for ϕ_j in each layer

$$\left(1 + \mathcal{L}^2\right)\nabla^2\phi_j - \left(\nabla^2 - \frac{\partial^2}{\partial z^2}\right)\phi_j = 0. \tag{2.8}$$

In order to satisfy no-flow conditions through the top and bottom boundaries, we seek solutions of the form

$$\phi_j(r, \theta, z, t) = \psi_j(r)\cos\left(\frac{n\pi z}{\delta}\right)\exp\left(i(m\theta + \omega t)\right), \tag{2.9}$$

where $m, n \in \mathbb{N}$ are respectively the azimuthal and vertical wavenumbers, $\delta = \frac{d}{a}$ is the aspect ratio of our domain and $\omega \in \mathbb{C}$, such that $\mathcal{I}m(\omega) < 0$ gives an unstable mode. Defining

$$\mathcal{D}^2[\phi] \coloneqq \left[\frac{d^2}{dr^2} + \frac{1}{r}\frac{d}{dr} - \frac{m^2}{r^2} - \frac{n^2\pi^2}{\delta^2}\right]\phi \tag{2.10}$$

$$\mathcal{D}_H^2[\phi] \coloneqq \left[\frac{d^2}{dr^2} + \frac{1}{r}\frac{d}{dr} - \frac{m^2}{r^2}\right]\phi, \tag{2.11}$$

(2.8) then reduces to

$$\left[\left\{1 + \frac{1}{4}\left(i\omega - \nu_j\mathrm{Ek}\mathcal{D}^2\right)^2\right\}\mathcal{D}^2 - \mathcal{D}_H^2\right]\psi_j = 0. \tag{2.12}$$

with the kinematic viscosity of each layer given by $\nu_j = \frac{\mu_j}{\rho_j}$. Using (2.9) in (2.7), we can write the components of the velocity field in the following form

$$\mathbf{u}_j = \epsilon\begin{pmatrix} \mathcal{L}^2\frac{\partial\phi_j}{\partial r} + \mathcal{L}\left(\frac{1}{r}\frac{\partial\phi_j}{\partial\theta}\right) \\ \mathcal{L}^2\left(\frac{1}{r}\frac{\partial\phi_j}{\partial\theta}\right) - \mathcal{L}\frac{\partial\phi_j}{\partial r} \\ \left(1 + \mathcal{L}^2\right)\frac{\partial\phi_j}{\partial z} \end{pmatrix}. \tag{2.13}$$

The total pressure in each layer is the sum of the hydrostatic contribution and a perturbation term, P_j, given by

$$p_j(r) = p_0 + \rho_j \int_0^r r' dr' + P_j \tag{2.14}$$

where $p_0 = p(r = 0)$ and ρ_j is the initial density in each layer. We use the form for the pressure perturbation in each layer as in [5] for rotating fluids in terms of the aforementioned potential function, and can be expressed in the above notation as

$$P_j = -2\epsilon\rho_j \left(1 + \mathcal{L}^2\right) \mathcal{L}\phi_j. \tag{2.15}$$

2.3.1 Inviscid solutions:

We first consider the inviscid problem ($\nu_j = 0$) in which case the Eq (2.12) can be reduced to

$$\left[\frac{d^2}{dr^2} + \frac{1}{r}\frac{d}{dr} - \left\{\frac{m^2}{r^2} + (1 - \frac{4}{\omega^2})\frac{n^2\pi^2}{\delta^2}\right\}\right] \psi_j = 0 \tag{2.16}$$

which has solutions of the form

$$\psi_j(r) = C_{j1}\mathcal{J}_m(\lambda r) + C_{j2}\mathcal{Y}_m(\lambda r), \tag{2.17}$$

with

$$\lambda = \frac{n\pi}{\delta}\sqrt{1 - \frac{4}{\omega^2}} = \delta_n^{-1}\sqrt{1 - \frac{4}{\omega^2}} \tag{2.18}$$

using Miles' notation of $\delta_n = \frac{\delta}{n\pi}$. For the inviscid flow field given by

$$\mathbf{u}_j = \epsilon \begin{pmatrix} \left(-\frac{m\omega\psi_j}{2r} - \frac{1}{4}\omega^2\psi_j'\right)\cos\left(\delta_n^{-1}z\right) \\ \left(-\frac{1}{4}im\omega^2\frac{\psi_j}{r} - \frac{1}{2}i\omega\psi_j'\right)\cos\left(\delta_n^{-1}z\right) \\ -\frac{1}{4}k(4 - \omega^2)\psi_j \sin\left(\delta_n^{-1}z\right) \end{pmatrix} \exp\left(i(m\theta + \omega t)\right), \tag{2.19}$$

we now impose the following boundary conditions:

Velocity regularity at $r = 0$: Using the form of the solution for ψ_j given by (2.17), for $\mathbf{u}_1(r = 0) \cdot \hat{\mathbf{e}}_r < \infty$, we require $C_{11} = 0$. Thus,

$$\psi_1(r) = C_{11}\mathcal{J}_m(\lambda r) \tag{2.20}$$

$$\psi_2(r) = C_{21}\mathcal{J}_m(\lambda r) + C_{22}\mathcal{Y}_m(\lambda r). \tag{2.21}$$

which also ensures regularity for the azimuthal and vertical components of the velocity field.

No penetration at $r = 1$ and $z = \pm\delta$: Setting the radial component of the velocity field at $r = 1$ to zero, we obtain

$$\left\{m(\omega + 2)\mathcal{J}_m(\lambda) - \lambda\omega\mathcal{J}_{m+1}(\lambda)\right\} C_{21} + \left\{m(\omega + 2)\mathcal{Y}_m(\lambda) + \lambda\omega\mathcal{Y}_{m+1}(\lambda)\right\} C_{22} = 0 \tag{2.22}$$

The condition for no penetration at $z = \pm\delta$ is automatically satisfied by the ansatz 2.9. We further introduce the following functions

$$f(r) = m\,(\omega+2)\,\mathcal{J}_m\,(\lambda r) - \lambda\omega r_0 \mathcal{J}_{m+1}\,(\lambda r) \tag{2.23a}$$

$$g(r) = m\,(\omega+2)\,\mathcal{Y}_m\,(\lambda r) + \lambda\omega r_0 \mathcal{Y}_{m+1}\,(\lambda r)\,, \tag{2.23b}$$

which then reduces (2.22) to

$$f(1)C_{11} + g(1)C_{22} = 0. \tag{2.24}$$

Kinematic condition at the interface: The linearized kinematic condition requires the fluid to move with the velocity of the interface defined by

$$\mathscr{I} \coloneqq r = r_0\left\{1 + \epsilon\cos\left(\delta_n^{-1}z\right)\exp\left(i(m\theta+\omega t)\right)\right\} \tag{2.25}$$

which implies

$$\omega\psi_j^{'}(r_0) + \frac{2m\psi_j(r_0)}{r_0} = -4ir_0. \tag{2.26}$$

Using the form of the solution given by (2.20) and (2.21) for the inner and outer fluid layers, we respectively obtain

$$f(r_0)C_{11} = -4ir_0^2 \tag{2.27a}$$

$$f(r_0)C_{21} + g(r_0)C_{22} = -4ir_0^2 \tag{2.27b}$$

which gives

$$\psi_1(r) = -\frac{4ir_0^2\mathcal{J}_m\,(\lambda r)}{f(r_0)} \tag{2.28a}$$

$$\psi_2(r) = \frac{4ir_0^2\left[g(1)\mathcal{J}_m\,(\lambda r) - f(1)\mathcal{Y}_m\,(\lambda r)\right]}{f(1)g(r_0) - f(r_0)g(1)}. \tag{2.28b}$$

Stress continuity at the interface: For the inviscid case, we have pressure continuity across the interface in absence of surface tension. Using the expression for the pressure perturbation given by Eq 2.15, and equating the pressure on the interface (given by 2.25), to the leading order in ϵ, we obtain

$$4\rho_1 r_0^2 + i\omega(\omega^2-4)\rho_1\psi_1(r_0) = 4\rho_2 r_0^2 + i\omega(\omega^2-4)\rho_2\psi_2(r_0) \tag{2.29}$$

which can be written in terms of the Atwood number, $\mathscr{A} = \frac{\rho_2-\rho_1}{\rho_2+\rho_1}$ to yield the dispersion relation as

$$\omega(\omega^2-4)\left[\frac{1+\mathscr{A}}{\mathscr{A}}\psi_2(r_0) - \frac{1-\mathscr{A}}{\mathscr{A}}\psi_1(r_0)\right] = 8ir_0^2. \tag{2.30}$$

Using (2.28a) and (2.28b), for $\omega \neq 0$ or ± 2, this can be written in the form

$$\frac{1+\mathscr{A}}{\mathscr{A}}\frac{g(1)\mathcal{J}_m\,(\lambda r_0) - f(1)\mathcal{Y}_m\,(\lambda r_0)}{f(1)g(r_0) - f(r_0)g(1)} + \frac{1-\mathscr{A}}{\mathscr{A}}\frac{\mathcal{J}_m\,(\lambda r_0)}{f(r_0)} = \frac{2}{\omega(\omega^2-4)}. \tag{2.31}$$

Fig 2.2 shows the solutions for ω for the above dispersion relation for two values of the azimuthal wavenumber m, as a function of the vertical wavenumber n for a negative Atwood

number $\mathscr{A} = -0.5$ - the negative root giving the unstable growing mode. For $n \to 0$, we approximately recover the growth rates for the azimuthal perturbations for $m \to \infty$ as in [7] given by

$$\omega \sim -\mathscr{A} \pm \{\mathscr{A}(\mathscr{A} + m)\}^{\frac{1}{2}} . \tag{2.32}$$

Special case for $\mathscr{A} = 0$: inertial oscillations We test the predictions of the linear theory developed thus far for the inviscid case against the findings of [4] for the case of spin up of a single fluid in a cylindrical container. The modes of pressure perturbations in such a system were also found to be stable. Also, for axially symmetric perturbations, their eigenvalue spectrum had limit points at ± 2 and had a dense distribution in the interval bound by these two limits. We recover these results in the limit of $\mathscr{A} \to 0$ when the two fluids with identical densities essentially behave as a single fluid, as illustrated shown in Fig 2.3.

2.3.2 Viscous case:

For the full viscous problem, we seek general solutions of the sixth-order ode in r given by (2.12), of the form

$$\psi_j(r) = c_{j1i}\mathcal{J}_m\left(k_{ji}r\right) + c_{j2i}\mathcal{Y}_m\left(k_{ji}r\right) \tag{2.33}$$

where we use Einstein notation with $i \in [1, 3]$, and k_{ji} are roots of the cubic polynomial in λ^2 obtained by using the inviscid solution ansatz given by (2.17). Using the notation introduced in Section 2.3, the viscous flow field can be written as

$$\mathbf{u}_j = \epsilon \begin{pmatrix} \left\{\frac{im}{2}\left(i\omega - \nu_j \mathrm{Ek}\mathcal{D}^2\right)\frac{\psi_j}{r} + \frac{1}{4}\left(-\omega^2 - 2i\omega\nu_j\mathrm{Ek}\mathcal{D}^2 + \nu_j^2\mathrm{Ek}^2\mathcal{D}^4\right)\psi_j'\right\}\cos\left(\frac{z}{\delta_n}\right) \\ \left\{\frac{im}{4}\left(-\omega^2 - 2i\omega\nu_j\mathrm{Ek}\mathcal{D}^2 + \nu_j^2\mathrm{Ek}^2\mathcal{D}^4\right)\frac{\psi_j}{r} - \frac{1}{2}\left(i\omega - \nu_j\mathrm{Ek}\mathcal{D}^2\right)\psi_j'\right\}\cos\left(\frac{z}{\delta_n}\right) \\ -k\left\{1 + \frac{1}{4}\left(-\omega^2 - 2i\omega\nu_j\mathrm{Ek}\mathcal{D}^2 + \nu_j^2\mathrm{Ek}^2\mathcal{D}^4\right)\right\}\psi_j\sin\left(\frac{z}{\delta_n}\right) \end{pmatrix} \exp\left(i(m\theta + \omega t)\right) \tag{2.34}$$

For the above flow field to be well-behaved at $r = 0$, we require $c_{12i} = 0$, leaving us with 9 independent constants, which requires the following 10 conditions to get a dispersion relation:

No-penetration in radial direction at $r = 1$ and in vertical direction at $z = \pm\delta$: For the radial condition at $r = 1$, we need

$$\begin{gathered} \mathbf{u}_2(r=1).\hat{\mathbf{e}}_r = 0 \\ \Rightarrow \frac{im}{2}\left(i\omega - \nu_j\mathrm{Ek}\mathcal{D}^2\right)\frac{\psi_2}{r}\bigg|_{r=1} = \frac{1}{4}\left(\omega^2 + 2i\omega\nu_j\mathrm{Ek}\mathcal{D}^2 - \nu_j^2\mathrm{Ek}^2\mathcal{D}^4\right)\psi_2'\big|_{r=1} . \end{gathered} \tag{2.35}$$

As for the inviscid case, the ansatz 2.9 ensures no flow through the upper and lower walls of the domain at $z = \pm\delta$.

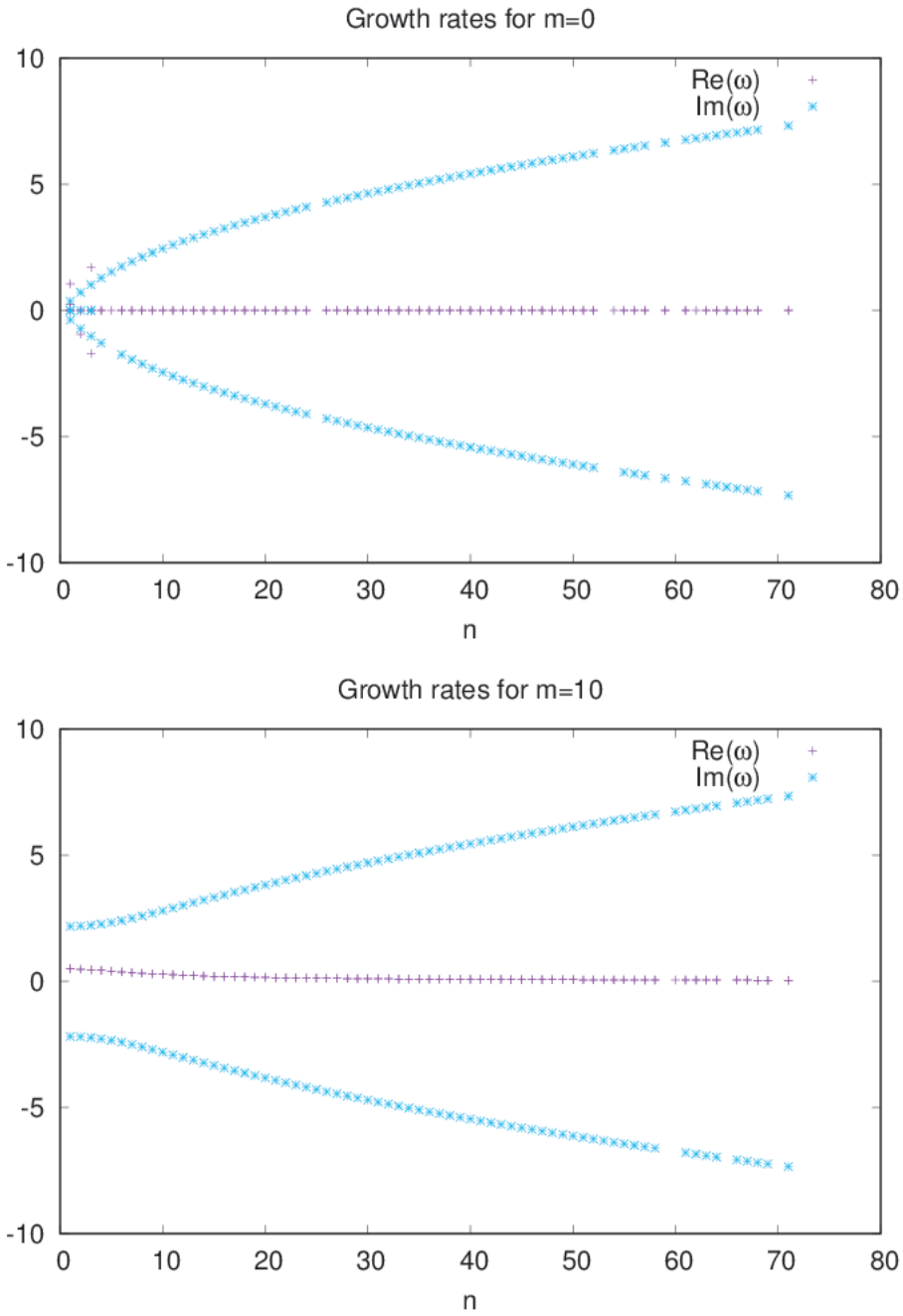

Figure 2.2: Solutions obtained for real and imaginary part of the growth rate ω as a function of vertical wavenumber n for two values of $m = 0, 10$ with $\mathscr{A} = -0.5$, $\delta = 1$, $\nu_j = 0$.

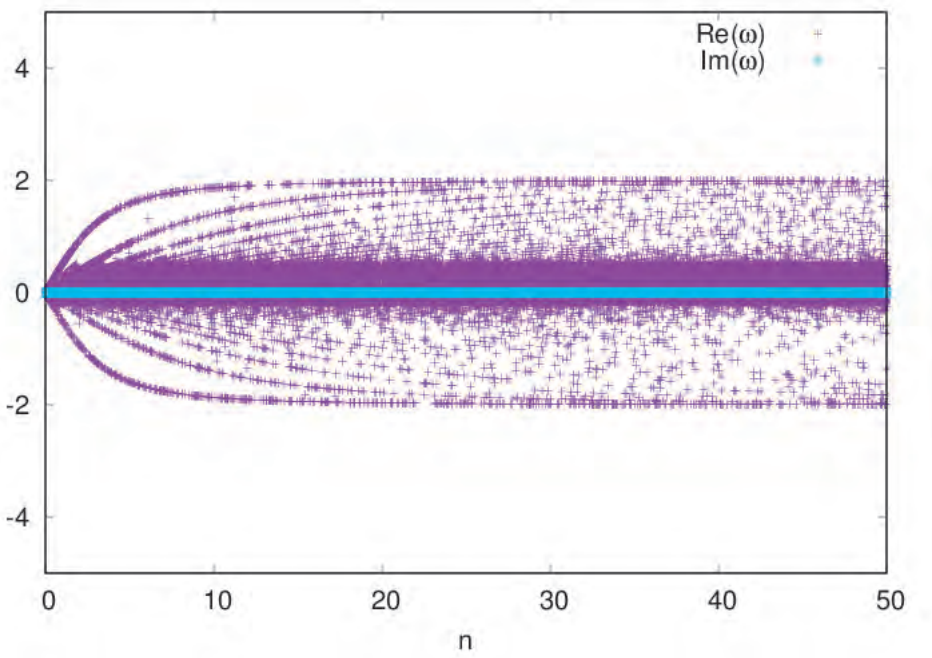

Figure 2.3: Solutions obtained for real and imaginary part of the growth rate ω as a function of vertical wavenumber n with $\mathscr{A}=0$.

No-slip in tangential and vertical components at $r=1$: In the case of a viscous fluid, we must additionally satisfy no-slip boundary conditions in the azimuthal and vertical flow at $r=1$, which implies

$$\mathbf{u}_2(r=1).\hat{\mathbf{e}}_\theta = 0$$
$$\Rightarrow -\frac{im}{4}\left(\omega^2 + 2i\omega\nu_j \mathrm{Ek}\mathcal{D}^2 - \nu_j^2\mathrm{Ek}^2\mathcal{D}^4\right)\frac{\psi_2}{r}\bigg|_{r=1} = \frac{1}{2}\left(i\omega - \nu_j\mathrm{Ek}\mathcal{D}^2\right)\psi_2'\big|_{r=1} \tag{2.36}$$

and

$$\mathbf{u_2}(r=1).\hat{\mathbf{e}}_z = 0$$
$$\text{i.e. } \psi_2|_{r=1} = \left\{\frac{1}{4}\left(\omega^2 + 2i\omega\nu_j\mathrm{Ek}\mathcal{D}^2 - \nu_j^2\mathrm{Ek}^2\mathcal{D}^4\right)\right\}\psi_2|_{r=1}. \tag{2.37}$$

Kinematic condition at the interface: The linearized kinematic condition requires

$$\left\{\frac{im}{2}\left(i\omega - \nu_j\mathrm{Ek}\mathcal{D}^2\right)\frac{\psi_j}{r} + \frac{1}{4}\left(-\omega^2 - 2i\omega\nu_j\mathrm{Ek}\mathcal{D}^2 + \nu_j^2\mathrm{Ek}^2\mathcal{D}^4\right)\psi_j'\right\}\bigg|_{r=r_0} = i\omega r_0, \tag{2.38}$$

which give one constraining equation in each layer of fluid.

Continuity condition at the interface: (2.38) ensures the continuity of the radial components of the velocity field. For a viscous fluid, we also require continuity of the tangential and vertical components i.e.

$$\frac{im}{4}\left(-\omega^2-2i\omega\nu_1\mathrm{Ek}\mathcal{D}^2+\nu_1^2\mathrm{Ek}^2\mathcal{D}^4\right)\frac{\psi_1}{r}\bigg|_{r=r_0}-\frac{1}{2}\left(i\omega-\nu_1\mathrm{Ek}\mathcal{D}^4\right)\psi_1^{'}\bigg|_{r=r_0}$$
$$=\frac{im}{4}\left(-\omega^2-2i\omega\nu_2\mathrm{Ek}\mathcal{D}^2+\nu_2^2\mathrm{Ek}^2\mathcal{D}^4\right)\frac{\psi_2}{r}\bigg|_{r=r_0}-\frac{1}{2}\left(i\omega-\nu_2\mathrm{Ek}\mathcal{D}^4\right)\psi_2^{'}\bigg|_{r=r_0} \quad (2.39)$$

and

$$\left\{1+\frac{1}{4}\left(-\omega^2-2i\omega\nu_2\mathrm{Ek}\mathcal{D}^2+\nu_2^2\mathrm{Ek}^2\mathcal{D}^4\right)\right\}\psi_1=\left\{1+\frac{1}{4}\left(-\omega^2-2i\omega\nu_2\mathrm{Ek}\mathcal{D}^2+\nu_2^2\mathrm{Ek}^2\mathcal{D}^4\right)\right\}\psi_2, \quad (2.40)$$

Stress continuity at the interface: This condition may be expressed as

$$\triangle\left\{\underline{\underline{\sigma}}\cdot\hat{\mathbf{n}}\right\}=0, \quad (2.41)$$

where $\triangle\{\cdot\}$ indicates the jump in the quantity in $\{\}$ from the outer fluid to the inner fluid, in absence of any surface tension, across the interface $\mathscr{I}$, where the non-dimensional stress tensor in each fluid layer is given by

$$\underline{\underline{\sigma}}_j=-p_j\underline{\underline{I}}+2\mu_j\mathrm{Ek}\underline{\underline{e}}_j, \quad (2.42)$$

with the rate of strain tensor, $\underline{\underline{e}}_j$ in each fluid layer given by (2.3). The unit vector normal to the interface (given by 2.25) directed outward (from fluid 1 into fluid 2) is given by

$$\hat{\mathbf{n}}=\frac{\nabla\left(r-r_0\left\{1+\epsilon\cos\left(\frac{n\pi z}{\delta}\right)\exp\left(i(m\theta+\omega t)\right)\right\}\right)}{\left|\nabla\left(r-r_0\left\{1+\epsilon\cos\left(\frac{n\pi z}{\delta}\right)\exp\left(i(m\theta+\omega t)\right)\right\}\right)\right|}$$
$$=\left(1+\mathcal{O}(\epsilon^2)\right)\hat{\mathbf{e}}_r+\left(\frac{imr_0}{r}\epsilon\cos\left(\frac{n\pi z}{\delta}\right)\exp\left(i(m\theta+\omega t)\right)+\mathcal{O}(\epsilon^2)\right)\hat{\mathbf{e}}_\theta$$
$$+\left(-\frac{n\pi}{\delta}r_0\epsilon\sin\left(\frac{n\pi z}{\delta}\right)\exp\left(i(m\theta+\omega t)\right)+\mathcal{O}(\epsilon^2)\right)\hat{\mathbf{e}}_z. \quad (2.43)$$

and the pressure in each layer is given by (2.14).
To compute the second term in (2.42), we note that for the viscous flow field of (2.13), (2.3) gives an expression $\mathcal{O}(\epsilon)$ for $\underline{\underline{e}}_j$. Hence, to the leading order in ϵ, only non-zero contribution to the term $\underline{\underline{e}}_j\cdot\hat{\mathbf{n}}$ come from the radial terms. Furthermore, the pressure in each layer at the interface to the leading order in $\epsilon$is given by

$$p_j=\frac{1}{2}\rho_1r_0^2+\epsilon\rho_j\cos\left(\frac{n\pi z}{\delta}\right)\exp\left(i(m\theta+\omega t)\right)+P_j \quad (2.44)$$

where P_j is the Hart-like pressure perturbation (given by Eq 2.15). Hence, we can simplify Eq 2.41 at order ϵ as

$$\triangle\left\{-\epsilon\begin{pmatrix}\rho_j\left\{\cos\left(\frac{n\pi z}{\delta}\right)\exp\left(i(m\theta+\omega t)\right)-2\left(1+\mathcal{L}^2\right)\mathcal{L}\phi_j\right\}\\-\frac{1}{2}\rho_1r_0^2im\cos\left(\frac{n\pi z}{\delta}\right)\exp\left(i(m\theta+\omega t)\right)\\\frac{1}{2}\rho_1r_0^3\frac{n\pi}{\delta}\sin\left(\frac{n\pi z}{\delta}\right)\exp\left(i(m\theta+\omega t)\right)\end{pmatrix}+\mu_j\mathrm{Ek}\underline{\underline{e}}_{\mathrm{j}}\cdot\hat{\mathbf{e}}_{\mathrm{r}}\right\}=0. \quad (2.45)$$

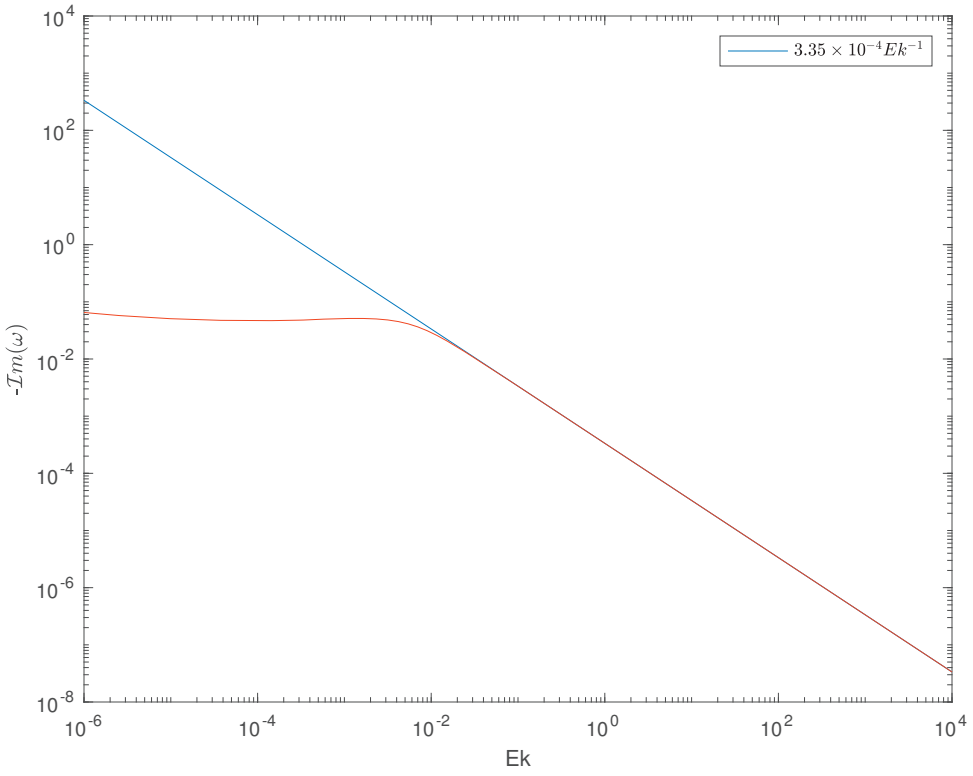

Figure 2.4: Viscous growth rates given by $-\mathcal{I}m(\omega)$ as a function of Ek obtained by numerically solving for the viscous dispersion relation (see text) showing an asymptotic behavior of Ek^{-1} indicated by the blue straight line.

The above set of 10 linear equations in the coefficients c_{jli} $(l = 1, 2)$ can be solved using standard methods to give the coefficients in terms of the Bessel functions involving k_{ji}, r_0, μ_j, Ek and the wavenumbers m and n of the varicose modes. Any of the above equations may be used to obtained the dispersion relation which gives the value of the growth rates as a function of m and n. For example, for $m = 0$ and $n = 6$, choosing $\nu_j = 1$, $r_0 = \frac{1}{\sqrt{2}}$, $\delta = 1$ and $\mathscr{A} = -0.018$, Fig 2.4 shows the growth rate of perturbations to the interface (given by $-\mathcal{I}m(\omega)$) satisfying the above set of equations, which exhibits a clear scaling behavior of

$$\omega \sim -3.35 \times 10^{-4} \mathrm{iEk}^{-1} \text{ for } \mathrm{Ek} \gtrsim 1. \tag{2.46}$$

Interestingly, for this particular choice of parameter, initial investigations reveal a non-monotonic behavior in the growth rates for $\mathrm{Ek} < 10^{-2}$ with a local minima in the growth rate for $\mathrm{Ek} \sim 10^{-4}$. On the following section, we attempt to investigate this particular choice of system parameters from a numerical perspective in order to test the predictions of the linear theory developed thus far.

3 Numerical Simulations with OpenFoam

In order to test the predictions of the linear theory developed in the preceding section, we used the interFoam package available with the OpenFoam distribution [3] modified in [7] to account for rotation in a cylindrical two-fluid setup, as illustrated in Fig 3.1.

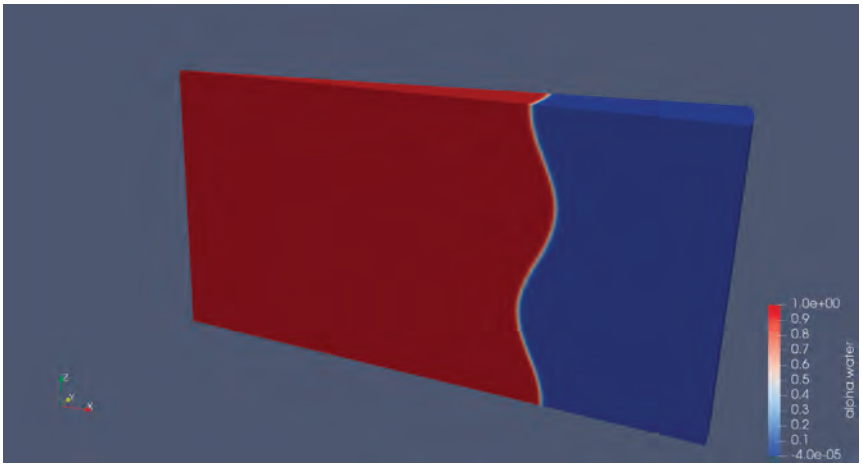

Figure 3.1: Sample initial setup in Openfoam showing fluid interface

3.1 Test of linear theory predictions:

The interface is initialized with the shape given by Eq 2.25 for a specific choice of the wavenumbers m and n with $r_0 = \frac{1}{\sqrt{2}}$ and ϵ is chosen to set the initial amplitude of the interfacial waves.

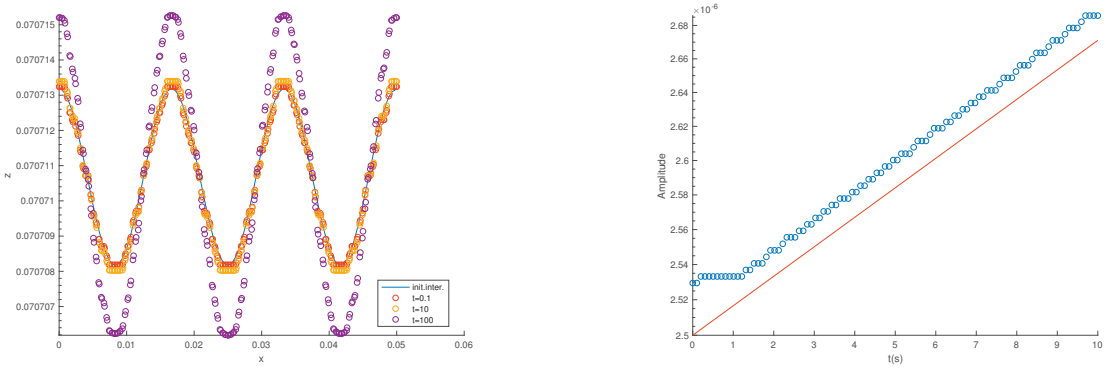

Figure 3.2: (Top) Time evolution of the shape of the interface in a rotating OpenFoam run initialized according to Eq 2.25 with $m = 0$, $n = 6$ for $\epsilon = 2.5 \times 10^{-5} \times \frac{a}{r_0}$, $\Omega = 2\pi$, $\delta = 0.5$, $\mathscr{A} \simeq -0.018$ and Ek ~ 0.16; (Bottom) Comparison against the viscous linear theory predictions -for same fluid parameters, we obtain a (non-dimensional) growth rate given by $\mathscr{I}m(\omega) \simeq -0.0493254$ which is the straight line (plotted on a semi-log axis in y).

The left panel of Fig 3.2 shows the gradual growth in amplitudes of the initial interface

Figure 3.3: Evolution of the perturbation to the interface for two OpenFoam runs with $\epsilon = 2.5 \times 10^{-5} \times \frac{a}{r_0}$, $\mathscr{A} \simeq -0.018$ and Ek $\sim 1.6 \times 10^{-5}$ at $\Omega = 2\pi$ rad/s (left) and 4π rad/s (right) demonstrating the effect of increasing rotation on the emergence of smaller scales in the growth of the perturbations.

for a particular choice of $m = 0$, $n = 6$ in a OpenFoam run with $\epsilon = 2.5 \times 10^{-5} \times \frac{a}{r_0}$, $\Omega = 2\pi$ rad/s, $\mathscr{A} \simeq -0.018$ and Ek ~ 0.16. The right panel shows the comparison with the prediction from the viscous linear theory described at the end Section 2.3, which for the case with equal fluid viscosities and a choice of $\mathscr{A} \simeq -0.018$ and Ek ~ 0.16 yields a solution for the system with $\mathcal{I}m(\omega) \simeq -0.0010533$. Following an initial transient phase (up to $t \simeq 1$), the rate of growth of the amplitude of the sinusoidal shape of the interface roughly agrees with the linear theory value. This is indicative that the linear theory developed in Section 2.3 can correctly predict the early time evolution of this system. Further exploration of the parameter space in $\mathscr{A}$ and Ek is part of currently ongoing work to confirm a robust test of any scaling with these quantities, which at least seems to emerge with Ek > 1 from the viscous theory predictions.

3.2 Effect of rotation

Using our OpenFoam rotating cylindrical setup, we performed a systematic exploration of the parameter space in rotation rates and Atwood numbers for our problem to see the evolution of the varicose instabilities through the linear growth phase before the runs become fully nonlinear. Beyond verifying our linear theory, these simulations were performed with the aim of understanding how rotation affects the evolution of the interface and if it possibly leads to complete suppression of the basic instability for any regime of our chosen set of parameter space.

3.2.1 $\mathscr{A} = -0.018$ runs

Firstly, we performed a simulation with the identical setup as the one described in Section 3.1 at double the rotation rate i.e. for $\Omega = 4\pi$. Fig 3.3 shows contours slices of the interface before nonlinear effects start to dominate and break up any small scales in the simulations. The comparison of the two runs for two different rotation rates qualitatively demonstrates the effect of increasing rotation in driving the growth of perturbations towards smaller scales.

3.2.2 $\mathscr{A} = -0.5$ runs

While it was possible to predict and compare our linear theory predictions for small values of the Atwood number ($\mathscr{A} \ll 1$), we could only probe larger values of the density contrast ($\mathscr{A} \sim 1$) with the help of simulation which show the onset of nonlinearity very early on in the runs. Fig 3.4 presents two such simulations with $\mathscr{A} = 0.5$ for two different rotation rates of Ω=2π and 4π. The figure shows the contour of the interface shape at early times in each simulation. These contours exhibit a similar behavior, with the emergence of smaller scale perturbation with increasing rotation.

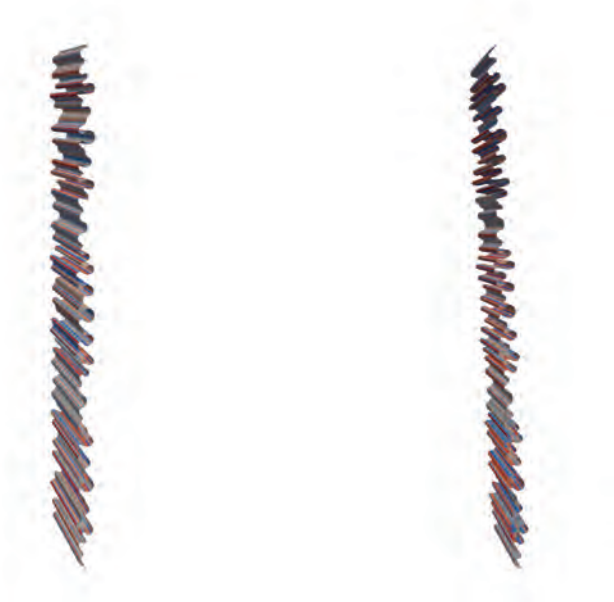

Figure 3.4: Evolution of the perturbation to the interface for two OpenFoam runs with $\epsilon = 2.5 \times 10^{-5} \times \frac{a}{r_0}$, $\mathscr{A} \simeq -0.5$ and Ek $\sim 1.6 \times 10^{-5}$ at $\Omega = 2\pi$ rad/s (left) and 4π rad/s (right) demonstrating the effect of increasing rotation on the emergence of smaller scales in the growth of the perturbations.

3.3 Effect of initial conditions

We also investigate the dependence of the growth of the interface on the initial shape by chasing a different value of $\epsilon = 0.1$ as described in the earlier section. As shown in Figure 3.5, we see the evolution of an interface starting from a sinusoidal wave-like pattern (left panel)

to the phase of growth of small scale patterns (right panel) in this setup. This shows further evidence of the choice of a particular underlying lengthscale in the fluid that is independent of the choice of initial shape of perturbations to the interface.

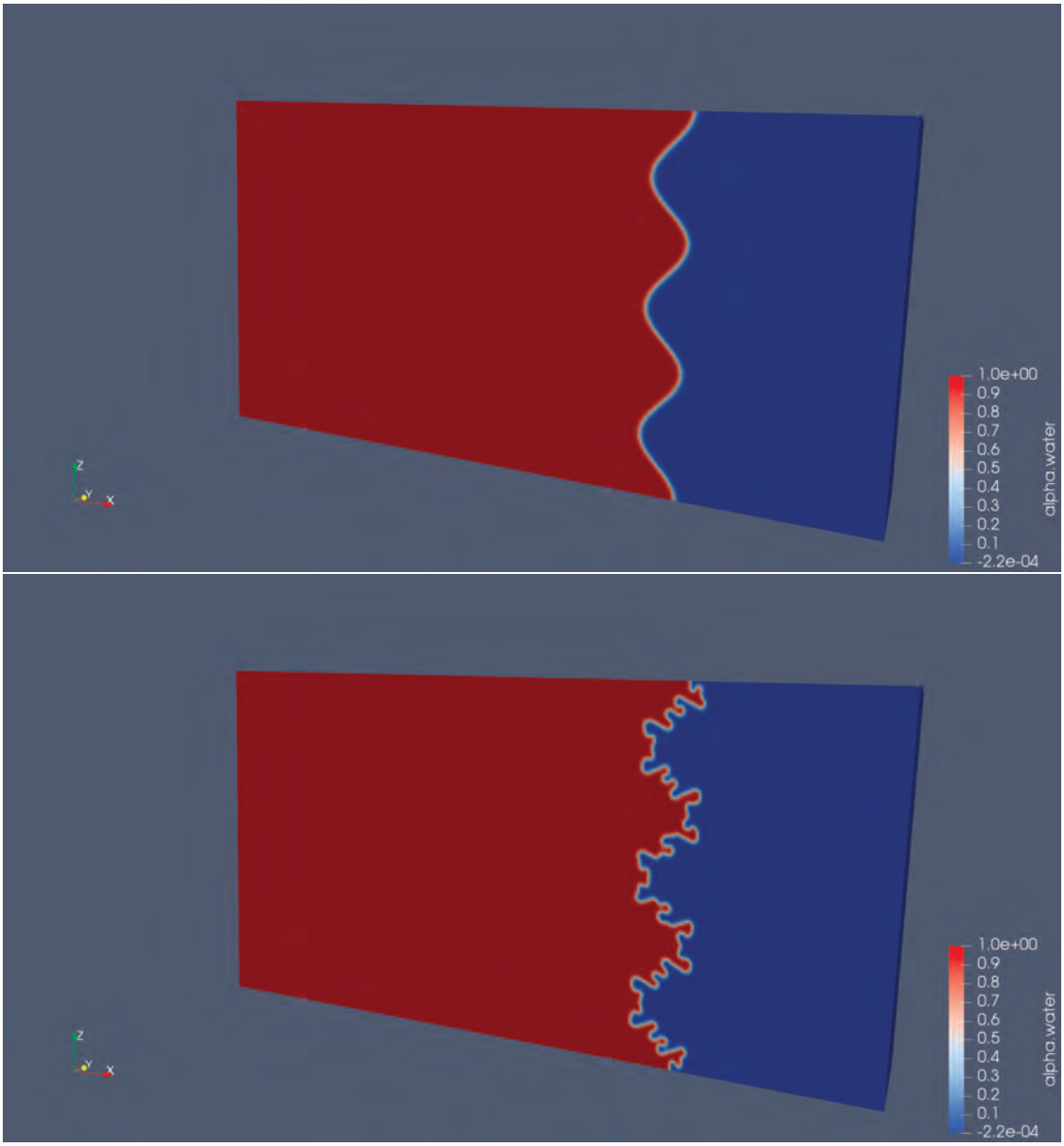

Figure 3.5: (Top) Initial interface between the two fluids of with equal viscosity for $\mathscr{A} = -0.018$, $\Omega = 2\pi$ and $\mathrm{Ek} \simeq 1.6 \times 10^{-5}$ (Bottom)

4 Summary

In this study, we considered a two-fluid rotating setup in a cylindrical geometry and studied the linear stability of the interface separating the two fluids for both azimuthal and axial perturbations. Our linear theory predictions for growing modes are shown to agree with the conclusions derived by [4] for essentially a continuum of a single fluid in the limit of vanishing density contrast ($\mathscr{A} = 0$). For the full viscous problem, initial solutions of the full set of governing equations satisfying all imposed boundary conditions at low $\mathscr{A}$ exhibit a clear scaling with viscosity for Ek > 1. Preliminary results of numerical simulations performed within the OpenFoam framework has been shown to give decent agreement with the linear theory growth rates for Ek $= 0.6, \mathscr{A} = -0.018$. We have also qualitatively explored the effects of rotation at two different values of $\mathscr{A}$ which all seem to hint towards the emergence of a preferred length scale for growth of the varicose modes for the perturbations to the interface, irrespective of the initial shape of the interface. Further work is ongoing to quantify this length scale and its possible dependence on the basic physics governing the evolution of the Rayleigh-Taylor instability.

4.1 Future work: measure of curvature of the interface

As is evident from the preliminary simulations presented in Sections 3.2 and 3.3, the growing perturbations at the interface of the two fluids seem to evolve naturally towards an inherent length scale which is expected to be controlled by the balance of the physical forces governing the motion of the fluids - i.e. viscosity and rotation. In order to extract a quantitative measure of this anticipated dependence, we plan to compute the radius of curvature of the interface from our numerical data by fitting a circle with three neighboring points along the position of the curved interface during the linear phase of evolution of the simulations.

Acknowledgements The work has been made possible through the generous support and auspices provided by the directors and hosts of the Woods Hole GFD summer program, to whom I am deeply thankful for providing me this opportunity to meet some wonderful people and work in a truly unique environment. I also wish to thank my fellow GFD fellows for all the good times in "the barn" and with softball and helping each other through some challenging times. I hope to continue our friendship for many years to come. Last and most importantly, the effort and persistence from my project supervisor, Dr. Matt Scase, has been instrumental in pushing this work forward and I thank him for teaching me the tricks and tools of his trade. I am also thankful for useful feedback and suggestions from Joe Pedlosky, Jack Whitehead, Glenn Flierl and others and their appreciation of this work.

References

[1] K. A. Baldwin, M. M. Scase, and R. J. A. Hill, *The Inhibition of the Rayleigh-Taylor Instability by Rotation,* Scientific Reports, 5 (2015), p. 11706.

[2] G. Boffetta and A. Mazzino, *Incompressible Rayleigh-Taylor Turbulence*, Annual Review of Fluid Mechanics, 49 (2017), pp. 119–143.

[3] S. S. Deshpande, L. Anumolu, and M.F. Trujillo, *Evaluating the performance of the two-phase flow solver interFoam*, Computational Science and Discovery, 5 (2012), p. 014016.

[4] H. P. Greenspan, *On the transient motion of a contained rotating fluid,* Journal of Fluid Mechanics, 20 (1964), pp. 673–696.

[5] R. W. Hart, *Generalized scalar potentials for linearized three-dimensional flows with vorticity*, Physics of Fluids, 24 (1981), pp. 1418–1420.

[6] M. M. Scase, K. A. Baldwin, and R. J. A. Hill, *Rotating Rayleigh-Taylor instability*, Physical Review Fluids, 2 (2017), p. 024801.

[7] M. M. Scase and R. J. A. Hill, *Centrifugally forced Rayleigh-Taylor instability,* Journal of Fluid Mechanics, 852 (2018), pp. 543–577.

Viscoplastic Flow Around a Cylinder: Nuggets or No Nuggets?

Rohit Supekar

October 2018

1 Introduction

From food pastes and cosmetic fluids in our everyday life, to mud and lava flow in the context geophysical or environmental flows, viscoplastic fluids can be found in a variety of scenarios around us. This has generated interest in their study in practical scenarios as well as in the context of classical fluid mechanics problems, such as the flow around a cylinder. The problem of Newtonian flow around a cylinder is associated with the famous Stokes' paradox which states that there is no solution at zero Reynolds number for this problem in an infinite domain. To resolve the paradox, inertial effects need to be considered far away from the cylinder. The viscoplastic version of the same problem has received a lot of attention, for example, by Tokpavi et al. [2008] and most recently by Chaparian and Frigaard [2017]. The characteristic feature of viscoplastic fluids is their yield stress (τ_Y); they flow only when the stresses exceed this critical value. Viscoplasticity thus also offers a resolution for the Stokes' paradox because when the stress falls below the yield stress sufficiently far away from the cylinder, the flow gets localized.

Beyond theoretical interest, the problem of viscoplastic flow around a cylinder is very relevant in practical scenarios. In this report, we consider problems that are applicable to three different settings. Firstly, in the oil industry, yield-stress fluids (drilling muds) are used to flush out rock cuttings to the surface from bore-wells (Okrajni and Azar [1986]). The yield stress of the fluid enhances transport of the rock cuttings when it flows but prevents sedimentation of the cuttings when the flow is stopped for repair purposes. In the sedimentation scenario, calculations of the drag force on circular particles are useful in the limit when the yield stress is large (or equivalently, the sedimentation velocity is small). Secondly, in the civil engineering industry, calculation of the collapse loads of partially rough cylindrical pipes in cohesive soil, which can be modeled as a perfectly plastic material, is a topic of wide interest (Aubeny et al. [2005], Randolph and Gourvenec [2011]). Viscoplastic computations performed in the limit of high yield stress can facilitate such calculations. Lastly, in a rather different physical setting, this problem is also relevant to cylindrical models of micro-organisms swimming in viscoplastic fluids such as mud. Historically, cylinders with an imposed surface velocity have been taken to be models (commonly referred to as squirmers) for swimming micro-organisms in Newtonian or viscoelastic fluids (Blake [1971], Lighthill [1952], Yazdi et al. [2014]). However, there have been no such studies of squirmers in viscoplastic fluids.

In this report, we address the fundamental problem of viscoplastic flow around a cylinder in the limit of large yield stress. We study this problem for different surface boundary conditions, viz., no-slip, partial roughness and imposed tangential velocity. While these scenarios are applicable to different physical problems discussed earlier, the framework we develop can be easily modified to address them. The no-slip case is relevant to understanding sedimentation of particles in viscoplastic fluids. Despite being such a fundamental problem, there are some discrepancies in the literature about the comparison of viscoplastic computations at a large yield stress with the corresponding plastic solution (see figure 1). We address this discrepancy in this report. The case of partially rough cylinders is directly applicable to calculating collapse loads of pipes in plastic materials. Lastly, imposing surface velocity on the cylinder helps us develop a model for swimming micro-organisms (squirmers) in viscoplastic fluids.

This report is structured as follows: we describe the mathematical model and associated methods in §2. The problem with no-slip boundary conditions is considered in §3, where we discuss the surprising differences between the viscoplastic and plastic solution related to rigidly rotating plugs, which we refer to as *the nuggets*. We extend our analysis to account for partially rough cylinders in §4. In §5, we develop a viscoplastic model for squirmers and find the swimming speed for an imposed tangential velocity profile. Finally, we present our conclusions in §5.

2 Mathematical Model

Neglecting inertia and gravity, we consider a cylinder of radius $\mathcal{R}$ moving through an incompressible Bingham fluid with velocity $\mathcal{U}\hat{e}_x$. To obtain a dimensionless set of equations, we use $\mathcal{R}$ and $\mathcal{U}$ to remove the dimensions of length and velocity, respectively. Pressure and stresses are scaled by the characteristic viscous stress $\mu\mathcal{U}/\mathcal{R}$ where μ is the (plastic) viscosity of the fluid. In the polar coordinate system (r, θ) with the origin at the center of the cylinder, the governing equations for the dimensionless fluid velocity $(u(r,\theta), v(r,\theta))$ and pressure $p(r,\theta)$ are given by,

$$\frac{1}{r}\frac{\partial}{\partial r}(ru) + \frac{1}{r}\frac{\partial v}{\partial \theta} = 0 \tag{1}$$

and,

$$\frac{\partial p}{\partial r} = \frac{1}{r}\frac{\partial}{\partial r}(r\tau_{rr}) + \frac{1}{r}\frac{\partial}{\partial \theta}\tau_{r\theta} - \frac{\tau_{\theta\theta}}{r}, \tag{2a}$$

$$\frac{1}{r}\frac{\partial p}{\partial \theta} = \frac{1}{r^2}\frac{\partial}{\partial r}(r^2\tau_{r\theta}) + \frac{1}{r}\frac{\partial}{\partial \theta}\tau_{\theta\theta} \tag{2b}$$

where τ_{ij} is the deviatoric stress tensor such that $\tau_{rr} + \tau_{\theta\theta} = 0$. Equation (1) enforces incompressibility and (2a), (2b) are the momentum equations.. We use the Bingham law to relate the stress to the strain rate $\dot{\gamma}_{ij}$ so that

$$\begin{aligned} \tau_{ij} = \left(1 + \frac{\mathrm{Bi}}{\dot{\gamma}}\right)\dot{\gamma}_{ij} \qquad &\text{for} \qquad \tau > \mathrm{Bi}, \\ \dot{\gamma}_{ij} = 0 \qquad &\text{for} \qquad \tau \leq \mathrm{Bi}. \end{aligned} \tag{3}$$

The strain rate is related to the velocity components as follows:

$$\{\dot{\gamma}_{ij}\} = \begin{pmatrix} 2u_r & v_r + (u_\theta - v)/r \\ v_r + (u_\theta - v)/r & 2(v_\theta + u)/r \end{pmatrix}, \tag{4}$$

where the subscripts r and θ denote partial derivatives with respect to r and θ respectively. $\dot{\gamma} = \sqrt{\frac{1}{2}\dot{\gamma}_{ij}\dot{\gamma}_{ij}}$ and $\tau = \sqrt{\frac{1}{2}\tau_{ij}\tau_{ij}}$ denote the second invariants of the the strain rate and stress tensors (following the Einstein summation notation). The above system has only one dimensionless number, the Bingham number:

$$\mathrm{Bi} = \frac{\tau_Y \mathcal{R}}{\mu \mathcal{U}}. \tag{5}$$

For imposing no-slip on the cylinder surface, we set the following boundary condition:

$$(u, v) = (\cos\theta, -\sin\theta) \qquad \text{at} \qquad r = 1. \tag{6}$$

If the surface of the cylinder is partially rough, we impose:

$$u = \cos\theta \qquad \text{and} \qquad \frac{|\tau_{r\theta}|}{\tau} = \frac{|\dot{\gamma}_{r\theta}|}{\dot{\gamma}} = \varrho \qquad \text{at} \qquad r = 1, \tag{7}$$

where ϱ represents the roughness factor that varies between 0 and 1. $\varrho = 0$ is the same as allowing free slip on the cylinder surface and $\varrho = 1$ corresponds to the no-slip condition that is equivalent to equation (6).

In section (5), for developing a model for a squirmer, we impose a prescribed surface velocity which has a characteristic velocity scale $\widehat{\mathcal{U}}$. The velocity variables are now rescaled using $\widehat{\mathcal{U}}$, in which case, the surface velocity becomes $(U_p(\theta), V_p(\theta))$ and the swimming speed is given by U_s. The boundary conditions thus become

$$(u, v) = (U_p(\theta) + U_s\cos\theta, V_p(\theta) - U_s\sin\theta) \qquad \text{at} \qquad r = 1. \tag{8}$$

Far away from the cylinder, the stresses fall to zero and hence the flow is expected to be localized. We thus choose a large enough computation domain with radius R_0 and set the velocity to $(u, v) = (0, 0)$. If the domain boundary is well beyond the outermost yield surface, its exact location will not have any effect on the solution we obtain.

2.1 Numerical method

We solve the viscoplastic equations using the augmented Lagrangian scheme that is used by Hewitt and Balmforth [2017]. We shall provide only preliminary details of the numerical method in this report as further details of the scheme can be found in the reference. The Stokes equations with the Bingham law (equations (1), (2a), (2b) and (3)) are solved in terms of the stream function $\psi(r, \theta)$ such that

$$(u, v) = \left(\frac{1}{r}\frac{\partial\psi}{\partial\theta}, -\frac{\partial\psi}{\partial r}\right). \tag{9}$$

The elimination of pressure from the momentum equations leads to a bi-harmonic equation for ψ. Instead of solving this nonlinear bi-harmonic equation directly, the problem is solved

in its weak form by writing a Lagrangian and minimizing it. This minimization results in algebraic nonlinear equations and a linear bi-harmonic equation that is solved iteratively. The iterations are stopped when, for example,

$$\max_{r,\theta} |\dot{\gamma}_n - \dot{\gamma}_{n-1}| < 10^{-7},$$

where n and $n-1$ represent the iteration numbers. We have imposed two classes of boundary conditions for the problems discussed in this report. For the cases in which the boundary velocities are specified, the implementation is done directly in terms of the boundary value of the stream function and its derivatives. For the cases where the ratio of the strain rates is specified as in equation (7), the boundary condition is implemented iteratively. In the presence of viscoplastic boundary layers on the cylinder surface, a stretched grid in the r-direction was used so as to sufficiently resolve the boundary layers.

2.2 Slipline theory: $\mathrm{Bi} \to \infty$

Despite neglecting inertia, this problem is highly nonlinear due to the $\dot{\gamma}$ term in the Bingham law given by equation (3). However, analytic progress is possible when $\mathrm{Bi} \to \infty$, that is, the fluid is perfectly plastic (Hill [1950]). In this case, the relation between the stress and the strain rate becomes

$$\tau_{ij} = \frac{\mathrm{Bi}}{\dot{\gamma}} \dot{\gamma}_{ij}, \tag{10}$$

which leads to the following yield condition that the stress components satisfy:

$$\tau^2 = \tau_{xx}^2 + \tau_{xy}^2 = \mathrm{Bi}^2. \tag{11}$$

For simplicity, we now switch to the (x, y) coordinate system. The momentum equations become

$$\frac{\partial \tau_{xx}}{\partial x} + \frac{\partial \tau_{xy}}{\partial y} = \frac{\partial p}{\partial x}, \tag{12a}$$

$$\frac{\partial \tau_{xy}}{\partial x} - \frac{\partial \tau_{xx}}{\partial y} = \frac{\partial p}{\partial y}. \tag{12b}$$

The stress components can now be written in terms the local slip angle ϑ as

$$(\tau_{xx}, \tau_{xy}) = \mathrm{Bi}(-\sin 2\vartheta, \cos 2\vartheta). \tag{13}$$

Substituting the above expressions into equations (12a) and (12b), one can deduce that the problem for the stress field is hyperbolic. The characteristics of the hyperbolic problem (usually referred to as the sliplines) are given by:

$$\alpha\text{-lines:} \qquad \frac{dy}{dx} = \tan\vartheta, \qquad p + 2\mathrm{Bi}\vartheta = \text{constant}, \tag{14}$$

$$\beta\text{-lines:} \qquad \frac{dy}{dx} = -\cot\vartheta, \qquad p - 2\mathrm{Bi}\vartheta = \text{constant}. \tag{15}$$

The angle ϑ is the anti-clockwise angle of the α-line as measured from the x-axis. The sliplines are essentially a set of mutually orthogonal lines along which the shear stress is the

maximum and the normal stresses are zero. In other words, if $[R(\vartheta)]$ denotes the rotation matrix, then,

$$[R(\vartheta)][\tau][R(\vartheta)]^T = \begin{bmatrix} 0 & \pm\mathrm{Bi} \\ \pm\mathrm{Bi} & 0 \end{bmatrix}. \tag{16}$$

For a given problem, the stress field can be constructed from the slipline pattern by satisfying the boundary conditions. For example, if the cylinder is perfectly rough, one set of sliplines must emerge tangentially from the cylinder surface.

The velocity field for a perfectly plastic flow is totally independent of the stress field. The components of the velocity field along the sliplines (u_α, u_β) satisfy

$$\frac{\partial u_\alpha}{\partial s_\alpha} = \frac{\partial u_\beta}{\partial s_\beta} = 0, \tag{17}$$

where s_α and s_β are the coordinates along the respective sliplines. In other words, the component of the velocity along a slipline is constant for a particular slipline. The above equation also ensures that the velocity field is divergence free.

2.2.1 Bounds for slipline solutions

A feature of the hyperbolic problem for a perfectly plastic flow is that multiple stress and velocity solutions can be obtained that satisfy the specified boundary conditions. Thus, in order to bound the true solution, it is a common practice to find the lower and upper bound to the net drag force on a body moving through a perfectly plastic fluid (Randolph and Houlsby [1984]).

Lower bound analysis involves finding stress solutions that satisfy equations (14) and (15), and the imposed boundary conditions. Assuming the body is in equilibrium, the calculation of the drag force from the stress solution serves as the lower bound for the true value. Upper bound analysis is done by finding a velocity solution that satisfies equation (17) and the imposed boundary conditions. Using the velocity solution, the dissipation in the flow can be calculated and related to the work done by the drag force on the cylinder. The calculated value of this drag force serves as an upper bound for the true value. If the calculated values of the drag force for the lower bound and the upper bound analysis match, the stress and the velocity solutions must be the true solutions. However, if the bounds don't match, uncertainty about the true solution remains.

3 Fully Rough (No-Slip) Cylinder

In this section, we compute and analyze the viscoplastic flow around a fully rough cylinder. This is equivalent to imposing a no-slip boundary condition on the cylinder surface. Figure 1a shows the plot of $\log_{10}\dot{\gamma}$ that is numerically computed for $\mathrm{Bi} = 2^{14}$. The regions indicated in black correspond to either stationary, linearly translating or rigidly rotating plugs.

3.1 Plastic solution ($\mathrm{Bi} \to \infty$)

For the limit $\mathrm{Bi} \to \infty$, the slipline pattern for this problem was obtained by Randolph and Houlsby [1984]. The solution they obtained is shown in figure 1b in terms of the α and β

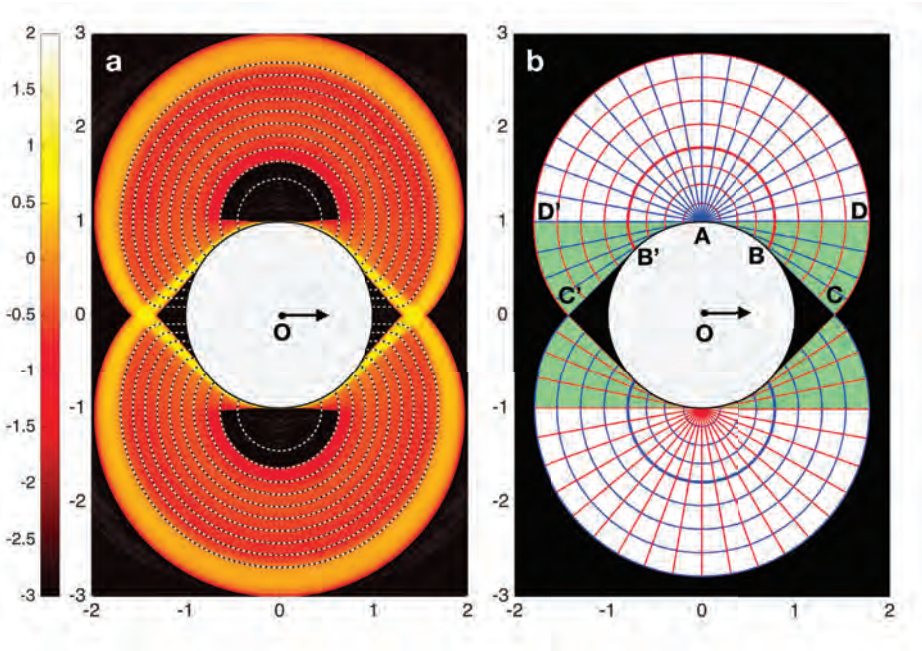

Figure 1: Comparison of the numerical solution and the slipline pattern for a fully rough cylinder. (a) is a plot of $\log_{10}(\dot{\gamma})$ of the numerical solution for $\mathrm{Bi} = 2^{14}$. The dotted lines are the streamlines of the flow. (b) Red and blue represent the α-lines and β-lines and the black regions are plugs. The $\alpha-$lines are involutes in the green region and circular arcs in the white region. Arrows indicate the direction of motion of the cylinder. Notice that the rigidly rotating plugs (*nuggets*) above and below the cylinder in the numerical solution are not predicted by the slipline pattern.

lines. Since the solution has top-bottom symmety, we will only discuss the upper half of the solution. The slipline pattern consists of a semi-circular centered fan on the top of the cylinder with the center A $(0, 1)$ and radius of $1 + \pi/4$. The β-lines form the spokes and α-lines form the circular arcs of the fan. Below line AD, the α-lines become involutes to the cylinder so that the $\beta-$lines emerge out tangentially. This ensures that the normal stress on the cylinder surface is zero as it is fully rough. In the first quadrant, the involutes are described by the parametric form,

$$\begin{pmatrix} x \\ y \end{pmatrix} = \begin{pmatrix} \cos\theta' - (\theta_s - \theta')\sin\theta' \\ \sin\theta' + (\theta_s - \theta')\cos\theta' \end{pmatrix}, \tag{18}$$

where θ_s is the polar angle of the intersection of the involute on the cylinder surface and θ' is the parametric angle that goes from θ_s to $\pi/2$. The limiting β-line BC makes an angle of $\pi/4$ owing to the symmetry condition on the x-axis and intersects it at the point $(\sqrt{2}, 0)$. This leads to rigid plugs on the front and back of the cylinder, and also determines the outermost yield surface beyond which there is no deformation in the fluid. As expected, the flow is localized around the cylinder.

To find the velocity field in the deformed region, the normal velocity on the cylinder surface is matched with v_α. From equation (17), this velocity magnitude is carried around

through the respective α line. Since only the normal velocity is matched, there is a tangential velocity slip on the surface of the cylinder. For the α-lines that emerge out from the rigid plug in the front, $v_\alpha = 1/\sqrt{2}$. Thus, the slipline solution allows for a finite velocity jump of $1/\sqrt{2}$ on the outermost yield surface.

The local angle of the α-line, $\vartheta(x, y)$, can now be used to determine the stress and the pressure field. Along the β-lines, the Riemann invariant $p - 2\mathrm{Bi}\vartheta$ is constant. We assume $p = 0$ at the vertical symmetry line or at $\theta_A = \pi/2$ where (r_A, θ_A) are the polar coordinates centered at A. Since, $p + 2\mathrm{Bi}\vartheta$ is constant along the α-lines, $p = 2\mathrm{Bi}\pi - 2\mathrm{Bi}\vartheta$ everywhere in the deformed region. In the semicircular fan, the pressure just depends on the angle $\theta_A = \vartheta - \pi/2$ such that $p = \mathrm{Bi}(\pi - 2\theta_A)$. In the region where the α-lines are involutes, the pressure is given by $p = 2\mathrm{Bi}(\pi - \theta)$ where θ is the angle of the point at which the corresponding β-line is tangent to the cylinder. Thus, the pressure on the surface of the cylinder is given by

$$p(1, \theta) = 2\mathrm{Bi}(\pi - \theta) \qquad \text{for} \qquad 0 < \theta < \pi/2, \qquad \text{and} \tag{19}$$

$$p(1, \theta) = 2\mathrm{Bi}(\pi - \theta) + 2\mathrm{Bi}\pi \qquad \text{for} \qquad \pi/2 < \theta < \pi. \tag{20}$$

The above equation indicates that there is a pressure jump of $\mathrm{Bi}\pi$ across point A since the α-lines curve around and change their angle from $\vartheta = \pi/2$ to $\vartheta = 3\pi/2$. Integrating the force around the cylinder, we can obtain the drag coefficient (Randolph and Houlsby [1984])

$$C_d = \frac{F_x}{2\mathrm{Bi}} = 2(\pi + 2\sqrt{2}) \simeq 11.94. \tag{21}$$

3.2 Viscoplastic vs plastic solution: *Nuggets*

Comparing the slipline and the numerical solution at a large Bi in figure 1, it can be seen that both the solutions lead to the same size for the deformed region. The plugs in front and behind the cylinder also match. The regions where there is a velocity jump in the slipline solution are replaced by viscoplastic shear layers that change the velocity jump into a smooth transition due to viscosity. These shear layers are reflected in the numerical solution through high values of $\dot{\gamma}$ indicated in yellow. Similarly, there are viscoplastic boundary layers on the cylinder surface where free slip is not allowed due to viscosity. However, there is a major difference between the two solutions despite the value of Bi being quite large. On the top and bottom of the cylinder, there are two rigidly rotating plugs that the slipline solution does not have. These plugs, which we will refer to as *nuggets* hereafter, sit above thin viscoplatic boundary layers that exist due to the no slip boundary condition. These nuggets have been observed in the solutions obtained by Tokpavi et al. [2008] and Chaparian and Frigaard [2017], which are computed using different numerical schemes. Thus, it is certain that they are not an artifact of the numerical scheme. This difference in the viscoplastic solution and the slipline solution is puzzling, since Randolph and Houlsby [1984] have shown that the upper bound and the lower bound calculation for this solution match. Hence, in the limit $\mathrm{Bi} \to \infty$, it is expected that the viscoplastic solution converges to the slipline solution, and that the nugget shrinks to zero. As shown in figure 4b, we find that the size of the nugget asymptotically decreases to zero albeit very weakly as $\mathrm{Bi} \to \infty$. In the next section, we develop a boundary layer theory to predict these weak

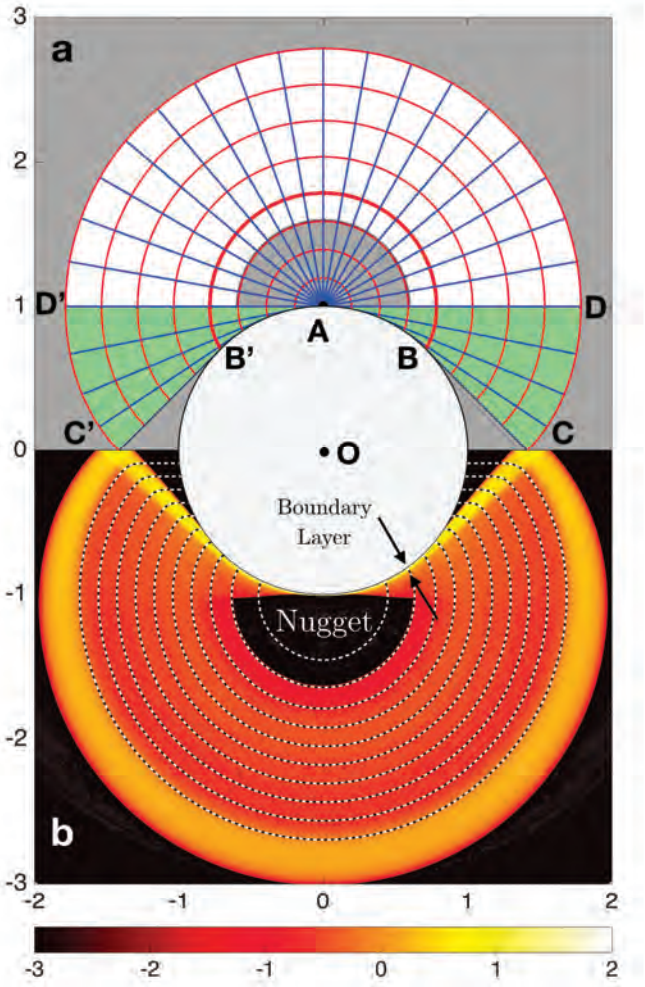

Figure 2: Comparison of the slipline pattern and the numerical solution. (a) The slipline pattern in figure 1 that is now superimposed with a nugget. Gray indicates plugs, and green (white) indicates the regions where $\alpha-$ lines are involutes (circular arcs). (b) Plot of $\log_{10}\dot{\gamma}$ obtained from the numerics with the nugget and the boundary layers as shown.

scalings so as to reconcile the expectation that the viscoplastic solution must match the plastic solution in the limit $\mathrm{Bi} \to \infty$.

3.3 Boundary layer theory

In figure 2, we present a detailed comparison of the slipline and the numerical solution. The boundary layer structure against the cylinder surface is highlighed by the regions $\log_{10}\dot{\gamma}$ takes the largest values. Numerically, it is observed that away from the Nugget region, the viscoplastic solution agrees well with the slipline solution. We thus superimpose the nugget (plugged) region (indicated in gray in figure 2a) over the slipline pattern. Away from the nugget and the viscoplastic boundary layers, we assume the plastic deformation to be close to the slipline solution. On carefully examining the numerical solution, it can be noted that

there is a region where the nugget directly attaches to the boundary layer. Away from this region, it detaches from the boundary layer leaving a region of plastic deformation between the nugget and the boundary layer.

3.3.1 Away from the nugget

We first concentrate on the viscoplastic boundary layer on the surface of the cylinder in a region that is not under the nugget. To leading order, the balance of forces is given by

$$p_r \sim 0 \qquad \text{and} \qquad p_\theta \sim (r^2 \tau_{r\theta})_r, \qquad \text{where} \qquad \tau_{r\theta} \sim v_r + \mathrm{Bi}\,\mathrm{sgn}(v_r), \tag{22}$$

such that $\tau_{r\theta} \sim \mathcal{O}(\pm\mathrm{Bi})$, and $p = \mathcal{O}(\mathrm{Bi})$ and is given by equations (19) and (20). Imposing no-slip at $r = 1$ and $v(r_b) = v_r(r_b) = 0$, where r_b is the edge of the boundary layer, we obtain

$$v = -2\mathrm{Bi}(r_b - r)^2\ \mathrm{sgn}(\sin\theta), \qquad r_b = 1 + \mathrm{Bi}^{-1/2}\sqrt{\frac{1}{2}|\sin\theta|}. \tag{23}$$

Thus, the thickness of the boundary layer is $\mathcal{O}(\mathrm{Bi}^{-1/2})$.

3.3.2 Under the nugget

As indicated by equations (19) and (20), the slipline solution allows for a pressure jump on the surface of the cylinder at point A ($\theta = \pi/2$). However, at a finite but large Bi, viscosity must smooth out this pressure jump. This introduces a smoothing region with an additional angular scale which is relatively wide as compared to the boundary layer (figure 3). This smoothing increases the pressure gradient, thus the flow through the boundary layer. If the net transport of mass within the boundary layer is the same as that away from the nugget, it is expected that the boundary layer under the nugget is thinner than $\mathcal{O}(\mathrm{Bi}^{-1/2})$.

We now focus on the 1st and the 2nd quadrant of the solution ($y > 0$) and rescale the variables so that

$$(r, \theta) = \left(1 + \mathrm{Bi}^{-a}\xi, \frac{\pi}{2} - \mathrm{Bi}^{-b}\Theta\right), \tag{24}$$

where η and Θ are $\mathcal{O}(1)$. It is expected that $a > \frac{1}{2}$ so that the boundary layer is thinner than $\mathcal{O}(B^{-1/2})$, and $b > 0$. To satisfy the continuity equation to leading order, the velocity variables are rescaled as

$$[u, v] \sim [\mathrm{Bi}^{b-a}U(\xi, \Theta), V(\eta, \Theta)]. \tag{25}$$

Similarly, the pressure and the stress are rescaled as

$$p \sim \mathrm{Bi}P(\xi, \Theta) \qquad \text{and} \qquad \tau_{\xi\Theta} \sim \mathrm{Bi}^a V_\xi - \mathrm{Bi} \tag{26}$$

Force balance from equation (22) now becomes

$$P_\eta \sim 0 \qquad \text{and} \qquad -\mathrm{Bi}^{1+b}P_\Theta = \mathrm{Bi}^{2a}V_{\xi\xi}. \tag{27}$$

Balancing the orders of the terms, we demand

$$1 + b = 2a. \tag{28}$$

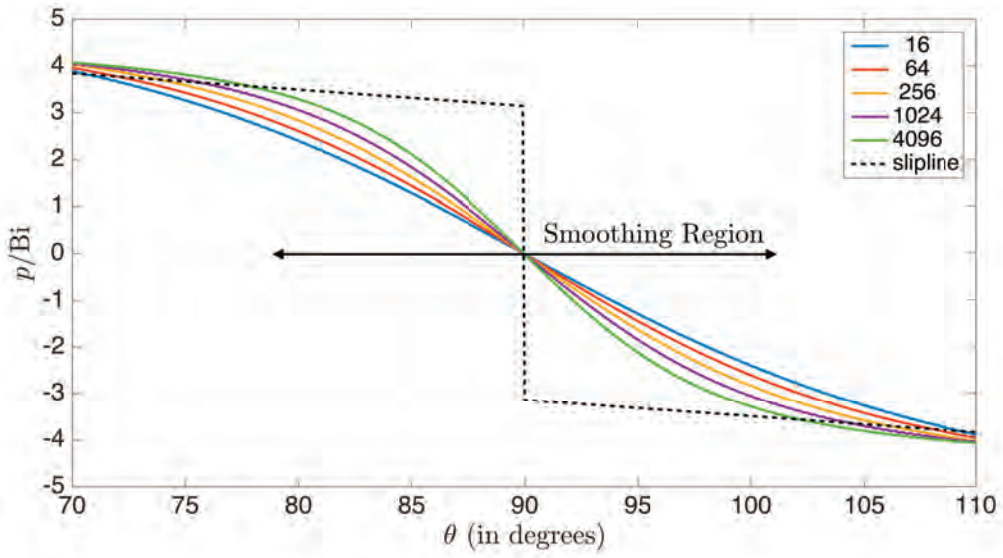

Figure 3: Pressure variation over the cylinder normalized by Bi. The legend indicates different values of Bi. The dotted line is the pressure from the slipline solution given by equations (19) and (20). The smoothing region over which the pressure differs from the slipline solution is marked.

We solve for $V(\xi, \Theta)$ by integrating the above equation and imposing $(V, V_\xi) = (0, 0)$ at $\xi = \Xi(\Theta)$ to obtain the following quadratic profile

$$V \sim -\left(1 - \frac{\xi}{\Xi}\right)^2, \tag{29}$$

while the pressure gradient is given by

$$P_\Theta = \frac{2}{\Xi^2}. \tag{30}$$

The upper nugget is centered at $(x, y) = (0, 1)$ and is taken to rotate at a rotation rate $\omega \sim 1 - \mathrm{Bi}^{-c}\Omega$. We observe from the numerics that $\Omega > 0$ (figure 4a). The velocity field in the nugget can be written as $(u, v) = \omega(\cos\theta, r - \sin\theta)$. Integrating the continuity equation, $U_\Xi - V_\Theta \sim 0$, over the boundary layer from $\xi = 0$ to $\xi = \Xi$ leads to

$$\left[\int_0^\Xi \left(1 - \frac{\xi}{\Xi}\right)^2 d\xi\right]_\Theta = \frac{1}{3}\Xi_\Theta = U(0, \Theta) - U(\Xi, \Theta). \tag{31}$$

The radial velocity at the edge of the boundary layer can now be matched to the nugget velocity, that is, $u(\mathrm{Bi}^{-a}\Xi, \theta) = \omega\cos\theta$. From the no penetration condition on the cylinder surface, we also have that $u(0, \theta) = \cos\theta$. Putting these conditions together, we obtain

$$\mathrm{Bi}^{b-a}\left[U(0, \Theta) - U(\Xi, \Theta)\right] \sim \mathrm{Bi}^{-b-c}\Omega\Theta. \tag{32}$$

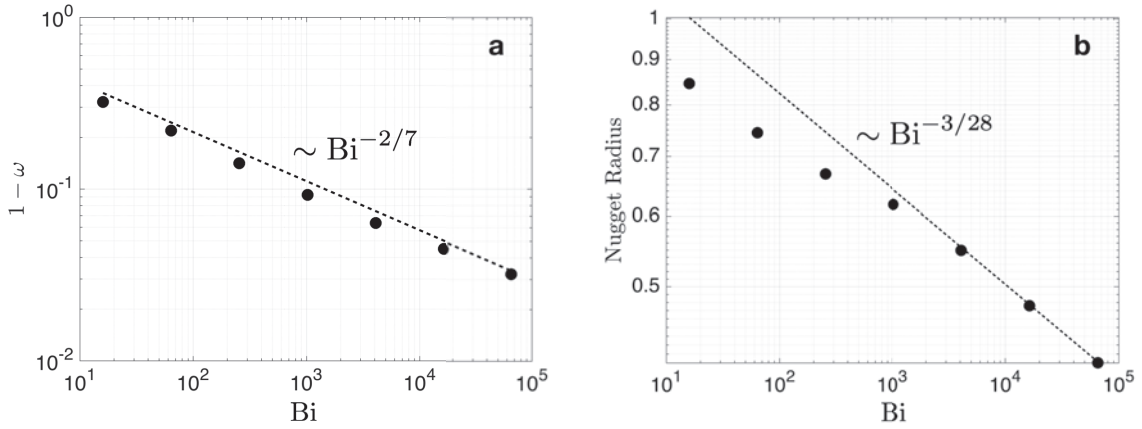

Figure 4: (a) The variation of the nugget's rotation rate ω plotted as $1-\omega$ which scales as $\mathrm{Bi}^{-2/7}$. (b) The variation of the radius of the nugget which scales as $\mathrm{Bi}^{-3/28}$.

To satisfy the above balance, we need

$$2b + c = a. \tag{33}$$

Letting $\Xi_A \equiv \Xi(0)$, we can integrate equation (31) to find the boundary layer thickness to be

$$\Xi = \Xi_A + \frac{3}{2}\Omega\Theta^2. \tag{34}$$

Clearly, the bounday layer width has a minima at $\Theta = 0$ and it increases away from $\theta = \pi/2$. Note that this is different from the $\mathrm{Bi}^{-1/2}$ layer which increases in thickness as $\left|\frac{\pi}{2} - \theta\right|$ decreases (from equation (23)).

We now consider the region beyond the point where the nugget detaches. In this region, there is an intervening window between the boundary layer and the bottom of the nugget where the deformation is purely plastic. Since this widow is very small, the $\alpha-$lines remain close to the ones given by the involutes (equation (18) and as in the green region in figure 2a). The involute that begins at the angular location $\theta = \frac{\pi}{2} - \mathrm{Bi}^{-b}\Theta$ reaches the base of the nugget at $y = 1$ and $x = \mathrm{Bi}^{-b}\Theta$. We assume that the $\alpha-$line remains close to this curve with some additional correction. With this additional correction, the velocity at the edge of the boundary layer can now be matched to the base of the nugget as $\mathrm{Bi}^{b-a}U(\Xi,\Theta) \sim \mathrm{Bi}^{-b}\omega\Theta - \mathrm{Bi}^{b-a}\varpi(\Theta)$. Therefore,

$$\begin{aligned}\frac{1}{3}\Xi_\Theta &\sim U(0,\Theta) - U(\Xi,\theta)\\ &\sim \mathrm{Bi}^{a-b}\sin(\mathrm{Bi}^{-b}\Theta) - (\mathrm{Bi}^{-2b+a}(1-\mathrm{Bi}^{-c}\Omega)\Theta - \varpi(\Theta)).\end{aligned}$$

Expanding the $\sin(\mathrm{Bi}^{-b}\Theta)$ term and using equation (33), we get

$$\frac{1}{3}\Xi_\Theta \sim \varpi(\Theta) + \Omega\Theta - \frac{1}{6}\mathrm{Bi}^{a-4b}\Theta^3. \tag{35}$$

This expression suggests that

$$a - 4b = 0, \tag{36}$$

since all the terms must come in at the same order of Bi because the boundary layer remains continuous across the point of detachment from the nugget. Using equations (28), (33) and (36), we obtain

$$a = \frac{4}{7}, \qquad b = \frac{1}{7} \qquad \text{and} \qquad c = \frac{2}{7}. \tag{37}$$

Thus, the boundary layer thickness scales as $\mathrm{Bi}^{-4/7}$, the angular width of the smoothing region scales as $\mathrm{Bi}^{-1/7}$ and the rotation rate of the nugget approaches 1 with a scaling of $\mathrm{Bi}^{-2/7}$ (figure 4a). The boundary layer profile now gets modified to

$$\Xi(\Theta) \sim \Xi_* + \int_{\Theta_*}^{\Theta} \varpi d\Theta - \frac{1}{8}(\Theta^4 - \Theta_*^4) + \frac{3}{2}\Omega\Theta^2, \tag{38}$$

where Θ_* denotes the angular location at which the nugget detaches and the corresponding boundary layer thickness is Ξ_*. We note that due to the Θ^4 term in the above expression, $\Xi(\Theta) \to 0$ as Θ gets larger than Θ_*. This is unexpected since the boundary layer must thicken to become $\mathcal{O}(\mathrm{Bi}^{-1/2})$ from being $\mathcal{O}(\mathrm{Bi}^{-4/7})$ under the nugget. Thus, the only resolution to this issue is to choose $\varpi(\Theta)$ such that

$$\int_{\Theta_*}^{\Theta} \varpi d\Theta \sim \frac{1}{8}(\Theta^4 - \Theta_*^4), \tag{39}$$

which implies that the profile in (34) remains throughout the smoothing region. The constants, Ξ_A and Ω are to be determined. From the numerics, we find $\Omega \simeq 0.68$. To determine Ξ_A, we use equation (30) and impose the following pressure jump condition for the slipline solution as specified by equations (19) and (20):

$$[p]_{\theta=\pi/2^-}^{\theta=\pi/2^+} = 2\pi\mathrm{Bi} \implies \int_{-\infty}^{+\infty} P_\Theta d\Theta = \int_{-\infty}^{+\infty} \frac{2}{\left(\Xi_A + \frac{3}{2}\Omega\Theta^2\right)^2} d\Theta = 2\pi. \tag{40}$$

The above integral can be evaluated using the method of residues and we subsequently obtain

$$\Xi_A = \left(\frac{1}{6\Omega}\right)^{1/3} \simeq 0.63. \tag{41}$$

Using this value and the scalings we have found, the boundary layer profiles are plotted in figure 5. The thickness of the numerical boundary layers is calculated by fitting the quadratic velocity profile in equation (29). The numerical profiles show an asymptotic collapse towards the analytic profile, which qualitatively captures their quadratic nature. Since the scalings are so weak, computations for larger values of Bi are needed for a quantitative agreement with the analytic profile. For this, the smoothing region must be small enough so that $\mathrm{Bi}^{-1/7} \ll 1$, or $\mathrm{Bi} \gg 10^7$. For such large values of Bi, the simulations need to be highly resolved due to very thin viscoplastic boundary layers on the cylinder surface and the convergence of the numerical method was found to be slow.

We can now determine the radius of the nugget. The boundary layer under the nugget must smoothly join the boundary layer away from it which is $\mathcal{O}(\mathrm{Bi}^{-1/2})$. This happens when $\mathrm{Bi}^{-a}(\Xi_A + \frac{3}{2}\Omega\Theta^2) \sim \mathrm{Bi}^{-1/2}$ which implies that $\Theta = \mathcal{O}(\mathrm{Bi}^{(a-1/2)/2}) = \mathcal{O}(\mathrm{Bi}^{-3/28})$. Thus, the radius of the nugget is $\sim (\pi/2 - \theta) \sim \mathcal{O}(\mathrm{Bi}^{-3/28})$. We find that this scaling captures the numerical values for the radius of the nugget very well (figure 4b).

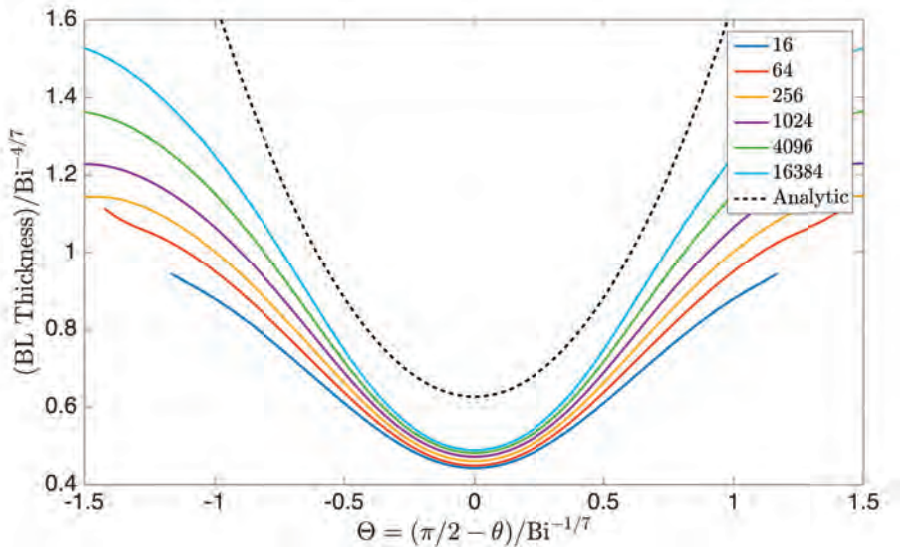

Figure 5: Boundary layer profiles for different values of the Bingham number Bi. The boundary layer thickness is rescaled by $\mathrm{Bi}^{-4/7}$ and $\pi/2 - \theta$ is rescaled by $\mathrm{Bi}^{-1/7}$. The legend indicates different values of Bi, where the dotted line is the analytic function given by equation (34).

4 Partially Rough Cylinder

In this section, we will consider the cylinder to be partially rough so that $|\tau_{r\theta}|/\tau = \varrho$ on the cylinder surface, where ϱ is the roughness factor (equation (7)). The no-slip (or fully rough) case discussed in the previous section corresponds to $\varrho = 1$. Here, we shall present solutions for $0 \leq \varrho < 1$ in the limit $\mathrm{Bi} \to \infty$. While $\varrho \neq 0$ is more relevant for applications in solid mechanics where ϱ can be related to the friction factor on the cylinder surface, $\varrho = 0$ is relevant in cases where wall slip is experimentally observed in viscoplastic fluids (as an example, in the experiments by Aktas et al. [2014]).

4.1 Plastic solution ($\mathrm{Bi} \to \infty$)

In addition to $\varrho = 1$ case discussed in the previous section, Randolph and Houlsby [1984] also presented analytical solutions for $\varrho < 1$. For their proposed mechanism, they showed that the upper bound and the lower bound calculations for the drag coefficient C_d match. However, Murff et al. [1989] pointed out a mistake in their upper bound calculation, which on being corrected leads to a mismatch of the upper and lower bound calculations except for $\varrho = 1$, the perfectly rough case that we discussed in the previous section.

In order to better bound the unknown true solution, Martin and Randolph [2006] proposed an alternative mechanism. They showed that for all values of $\varrho < 1$, their mechanism leads to a smaller (better) upper bound value of C_d. The mechanism they proposed is shown in figure 6 for a general value of ϱ. For simplicity, only the 1st quadrant of the solution is shown and the complete solution can be constructed by assuming a left-right and top-bottom symmetry. In the region ABCHFJI, the $\alpha-$lines are circular arcs with the

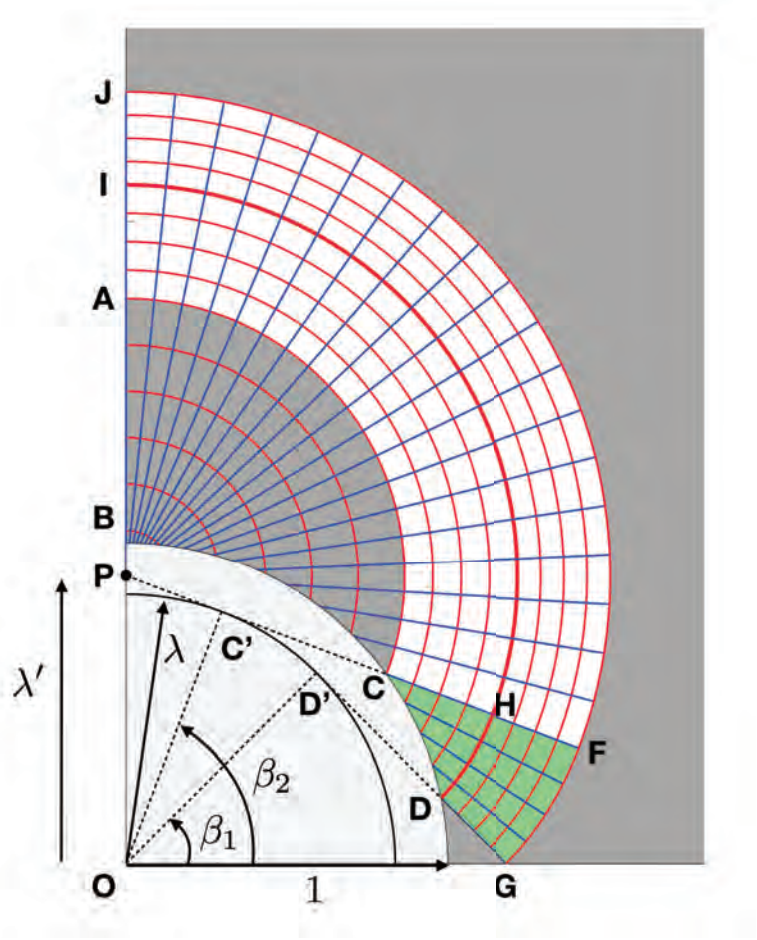

Figure 6: The slipline pattern proposed by Martin and Randolph [2006] for a general value of the roughness factor ϱ and the parameter β_2, with $\beta_1 = \pi/4$. The α and β lines are marked by red and blue, respectively. Gray indicates plugs and green represents the region in which the $\alpha-$lines are involutes to the inner circle. The thick red line marks the $\alpha-$line with a velocity jump.

center P. In a subset of this region, the gray region ABC, the flow is in rigid body rotation and is thus plugged. For this construction, another inner circle of radius λ is used, where λ is related to the roughness factor ϱ as

$$\lambda = \cos\left(\frac{\cos^{-1}\varrho}{2}\right). \tag{42}$$

Beyond the limiting radial line PC that is parameterized by the angle β_2, the $\alpha-$lines become the involutes to this inner circle (the green region CDGFH). The length of line OP, λ' can thus be geometrically found to be

$$\lambda' = \frac{\lambda}{\sin\beta_2} = \frac{1}{\sin\beta_2}\cos\left(\frac{\cos^{-1}\varrho}{2}\right). \tag{43}$$

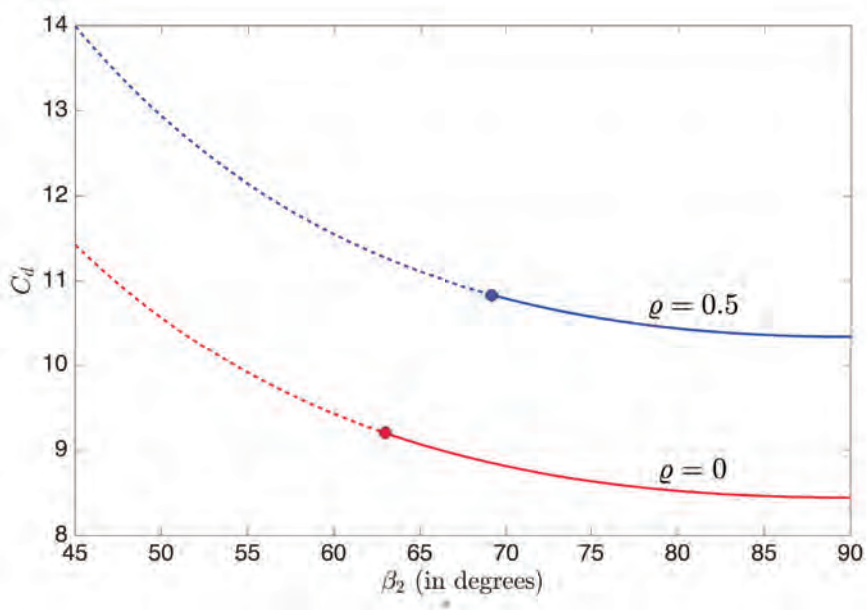

Figure 7: Variation of the drag coefficient with the angle β_2 for $\varrho = 0$ (red) and $\varrho = 0.5$ (blue). The dotted lines indicate the cases where the stress solution is perhaps not valid. The blue and red circles are the optimized values for the upper bound calculations by Martin and Randolph [2006], which lie on the analytical curves obtained from our lower bound calculation.

This construction ensures that the $\alpha-$lines originate from the surface of the cylinder at an angle $(\pi/4 - \Delta/2)$, where

$$\Delta = \sin^{-1} \varrho. \tag{44}$$

As a result, the boundary condition $|\tau_{r\theta}|/\tau = \varrho$ is satisfied on the cylinder surface CD. Note that this boundary condition need not be satisfied on the cylinder surface BC since the flow is plugged, hence the stress field within this region is not defined. The involute region is bounded below by the limiting line DG that is parameterized by the angle β_1. β_1 is chosen to be $\pi/4$ so that DG makes an angle $\pi/4$ with the x-axis to ensure zero shear stresses on the symmetry line. This leads to a rigid plug in the front of the cylinder. To find the velocity field, v_α is found by matching the normal velocity on the surface of the cylinder, and $v_\beta = 0$ everywhere. Interestingly, along with the velocity jump at the outermost yield surface, this mechanism also has a velocity jump on DHI (the thick red $\alpha-$line) which lies within the deformed region.

Using this mechanism, Martin and Randolph [2006] performed an upper bound analysis by considering the velocity solutions and optimized the angle β_2 numerically so as to minimize the dissipation. As an example, for $\varrho = 0$ (free slip), they found $C_d = 9.20$ and the optimized value $\beta_2 = 63.0^o$. For $\varrho = 0.5$, they found $C_d = 10.83$ and the optimized value $\beta_2 = 69.2^o$. These values are plotted in figure 7.

4.2 Stress solution: lower bound calculation

Martin and Randolph [2006] proposed the mechanism in figure 6, but only did an upper bound analysis. In this section, we perform a lower bound analysis by calculating the drag coefficient on the cylinder by considering the stress solution. As in the previous section, we assume the pressure p to be zero on the y-axis. Since $p + 2\text{Bi}\vartheta$ is constant on the $\alpha-$lines, where ϑ is the local angle from the x-axis, and $\vartheta = \pi$ on the y-axis, the pressure is $p = 2\text{Bi}\pi - 2\text{Bi}\vartheta$ in the deformed regions of the flow. The stress or the pressure field is not defined within the plugged regions. We thus calculate the drag force on the cylinder by integrating over the lines AC, CD and DG. Since the flow is inertia free, this is equivalent to computing the force directly on the cylinder surface. Therefore, the drag coefficient is given by

$$C_d = \frac{-F_x}{2\text{Bi}} = \frac{-1}{2\text{Bi}} \left(4 \int\limits_{\text{AC, CD, DB}} f_x dl \right), \tag{45}$$

where f_x is the force per unity length in the x-direction. The factor of 4 comes from the left-right and top-bottom symmetry of the flow due to which the force calculated from the first quadrant is a quarter of the total force.

The curve AC is a circular arc with center P and radius

$$R_P = \lambda' \sin\left(\frac{\pi}{2} - \beta_2\right) + \sqrt{1-\lambda^2} = \lambda \cot\beta_2 + \sqrt{1-\lambda^2}. \tag{46}$$

In the polar coordinate system (r_P, θ_P) centered at P, the traction force on AC is

$$\{f\}_{\text{AC}} = \begin{bmatrix} -p & -\text{Bi} \\ -\text{Bi} & -p \end{bmatrix} \begin{bmatrix} 1 \\ 0 \end{bmatrix} = \begin{bmatrix} -p \\ -\text{Bi} \end{bmatrix} \tag{47}$$

The slipline angle ϑ is related to the polar angle θ_P by $\vartheta = \pi/2 + \theta_P$. Thus, the force in the x-direction on curve AC ($f_x = -p\cos\vartheta - \text{Bi}\cos\vartheta$) can be integrated to obtain the total force

$$\begin{aligned} \frac{F_{\text{AC}}}{\text{Bi}} &= \int_{\beta_2}^{\pi} (-(2\pi - 2\vartheta)\cos\vartheta - \cos\vartheta) R_P d\vartheta \\ &= -R_P \left[2(\pi - \beta_2)\cos\beta_2 + \sin\beta_2\right] \end{aligned} \tag{48}$$

On curve CD that can be parameterized by the polar coordinates $(1, \theta)$, the local slipline angle is $\vartheta = \theta + (\pi/4 - \Delta/2)$ and hence, the pressure is $p = 2\text{Bi}(\pi - \vartheta) = \text{Bi}(3\pi/2 - 2\theta + \Delta)$. The traction force on this curve in the x-y coordinate system is

$$\{f\}_{\text{CD}} = \begin{bmatrix} -p - \text{Bi}\sin 2\vartheta & \text{Bi}\cos 2\vartheta \\ \text{Bi}\cos 2\vartheta & -p + \text{Bi}\sin 2\vartheta \end{bmatrix} \begin{bmatrix} \cos\theta \\ \sin\theta \end{bmatrix}, \tag{49}$$

which can be used to find $f_x = -p\cos\theta - \text{Bi}\cos(\Delta - \theta)$. The limits on the angle θ are $(\beta_1 - \Delta^*)$ and $(\beta_2 - \Delta^*)$ corresponding to points C and D, respectively, where Δ^* is the angle between OD' and OD (OC' and OC) given by

$$\Delta^* = \cos^{-1}\lambda = \frac{\cos^{-1}\varrho}{2}. \tag{50}$$

Thus, the total force on CD in the x-direction can be calculated as

$$\frac{F_{\mathrm{CD}}}{\mathrm{Bi}} = \int_{\beta_1-\Delta^*}^{\beta_2-\Delta^*} \left(-\left[\frac{3\pi}{2} - 2\theta + \Delta\right]\cos\theta - \cos(\Delta-\theta)\right) d\theta$$

$$= -\left(\frac{3\pi}{2}+\Delta\right)\left(\sin\left(\beta_2-\Delta^*\right) - \sin\left(\frac{\pi}{4}-\Delta^*\right)\right) - \sin\left(\beta_2-\Delta^*-\Delta\right) + \sin\left(\frac{\pi}{4}-\Delta^*-\Delta\right)$$

$$+2\left(\left(\beta_2-\Delta^*\right)\sin\left(\beta_2-\Delta^*\right) - \left(\frac{\pi}{4}-\Delta^*\right)\sin\left(\frac{\pi}{4}-\Delta^*\right) + \cos\left(\beta_2-\Delta^*\right) - \cos\left(\frac{\pi}{4}-\Delta^*\right)\right), \tag{51}$$

where β_1 is set to $\pi/4$.

Finally, on the surface DG, the slipline angle is $\vartheta = \pi/4$. Thus, the pressure is constant and is equal to $3\pi\mathrm{Bi}/2$. The traction force in the x-direction is $f_x = -(1/\sqrt{2})\mathrm{Bi} - (1/\sqrt{2})p$ and the length of DG is $(\lambda - \sqrt{1-\lambda^2})$. Hence, the force acting on DG can be found to be

$$\frac{F_{\mathrm{DG}}}{\mathrm{Bi}} = -\left(\frac{2+3\pi}{2\sqrt{2}}\right)(\lambda - \sqrt{1-\lambda^2}). \tag{52}$$

Combining equations (45), (48), (51) and (52), we can obtain the drag coefficient as a function of the angle β_2 and the roughness factor ϱ:

$$C_d(\beta_2, \varrho) = \frac{-2}{\mathrm{Bi}}(F_{\mathrm{AC}} + F_{\mathrm{CD}} + F_{\mathrm{DG}}) \tag{53}$$

The above function is plotted in figure 7 for two values of the roughness factor. It is interesting to note that the curves for C_d monotonically decrease with increasing β_2. Furthermore, these curves pass through the optimized values that Martin and Randolph [2006] found for their upper bound analysis. This implies that for these optimized values, the upper bound and lower bound calculation for C_d match each other. Thus, the mechanism that Martin and Randolph [2006] proposed is not just an upper bound as they thought to be, but actually the exact solution. In the next section, we compare our numerical viscoplastic solutions for $\mathrm{Bi} \to \infty$ and provide further evidence that this mechanism is the true solution. For values of β_2 lower than the optimal values (indicated by dotted lines in the figure), the lower bound calculation yields a higher value than the upper bound. Since this is not possible, we conclude that the stress solution must not be valid for these values of β_2. It is perhaps the case that the rigidly rotating plugs becomes over-stressed and thus can no longer be deformation-free.

4.3 Comparison with numerics

With the boundary conditions in equation (7), we numerically computed the viscoplastic solutions as for $\mathrm{Bi} \gg 1$. A comparison of the numerical solution and the slipline pattern is shown in figure 8 for $\varrho = 0$ (free slip case). In the limit $\mathrm{Bi} \to \infty$, it is clear that the solution approaches the mechanism discussed in the previous section. The only difference in the two solutions is the viscoplastic shear layer at the periphery which is a result of the finite velocity jump in the plastic solution. Figure 9 compares the two solutions for $\varrho = 0.5$. Here

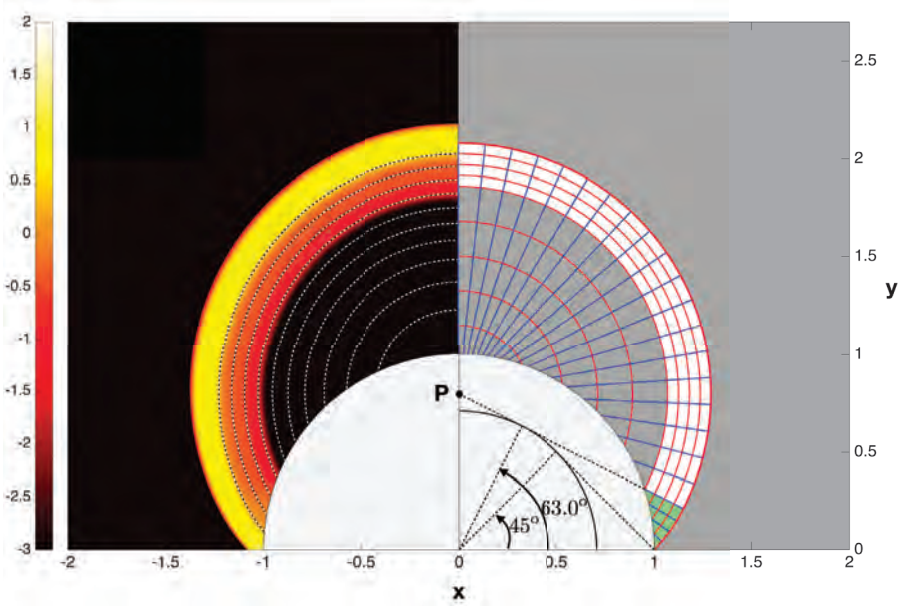

Figure 8: Comparison of the numerical solution and the plastic solution for $\varrho = 0$. Left: plot of $\log_{10} \dot{\gamma}$ for $\mathrm{Bi} = 2^{14}$. The dotted lines indicate the streamlines. Right: the slipline pattern found with the construction in figure 6 with $\beta_1 = 45^{\mathrm{o}}$ and $\beta_2 = 63.0^{\mathrm{o}}$, the optimized values found by Martin and Randolph [2006].

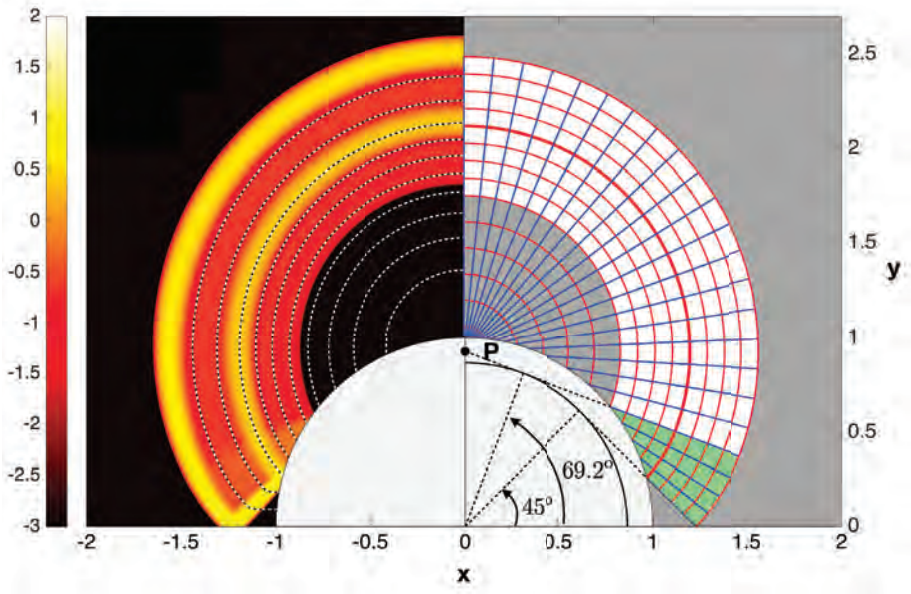

Figure 9: Comparison of the numerical solution and the plastic solution for $\varrho = 0.5$. Left: plot of $\log_{10} \dot{\gamma}$ for $\mathrm{Bi} = 2^{18}$. The dotted lines indicate the streamlines. Right: the slipline pattern found with the construction in figure 6 with $\beta_1 = 45^{\mathrm{o}}$ and $\beta_2 = 69.2^{\mathrm{o}}$, the optimized values found by Martin and Randolph [2006].

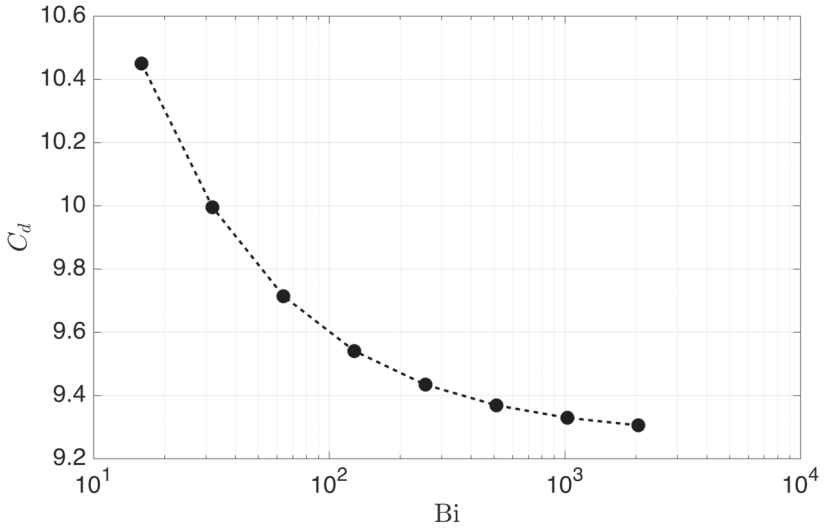

Figure 10: The variation of the drag coefficient with Bingham number Bi for the roughness factor $\varrho = 0$ (free slip). The curve asymptotes to the value 9.20, which is the drag coefficient obtained from the plastic solution shown in figure 9.

again, the numerical solution matches very well with the slipline pattern in terms of the size of the rigidly rotating plug and the plugged wedges in front of the cylinder. For this case, in addition to the velocity jump on the outermost yield surface, the plastic solution has an intermediate line with a velocity jump that is indicated by the thick red $\alpha-$line. This jump is smoothed out by an intermediate viscoplastic shear layer which lies at the same location as the velocity jump in the plastic solution.

5 Squirmer Model

In this section, we develop a model for a swimming micro-organism (a squirmer) in a viscoplastic fluid based on the early studies by Lighthill [1952] and Blake [1971] for Newtonian fluids. The bounday conditions (8) are imposed with $U_p = 0$ and a general profile for $V_p(\theta)$ which is responsible for propelling the squirmer. The results of the numerical simulations for $V_p(\theta) = \sin\theta$ and different values for the swimming speed U_s are shown in figure 11. For zero swimming speed, a large scale plastic deformation exists around the swimmer in order to allow for a return flow to support the net flow imposed cylinder surface. As the swimmer starts to move, however, the plastic deformation as well as the drag force on the swimmer reduces. As there are no external forces on a freely swimming swimmer, this state must correspond to zero drag force and the corresponding value of U_s is the true swimming speed. From the simulations, we observe that in this state, the flow is totally localized in a viscoplastic boundary layer that is attached to the swimmer. The streamlines originate on the surface in front of the swimmer and terminate behind it. Hence, the volume flux is balanced within the boundary layer itself and no large scale plastic deformation is needed. In the next subsection, we utilize this localized nature of the flow and develop a boundary

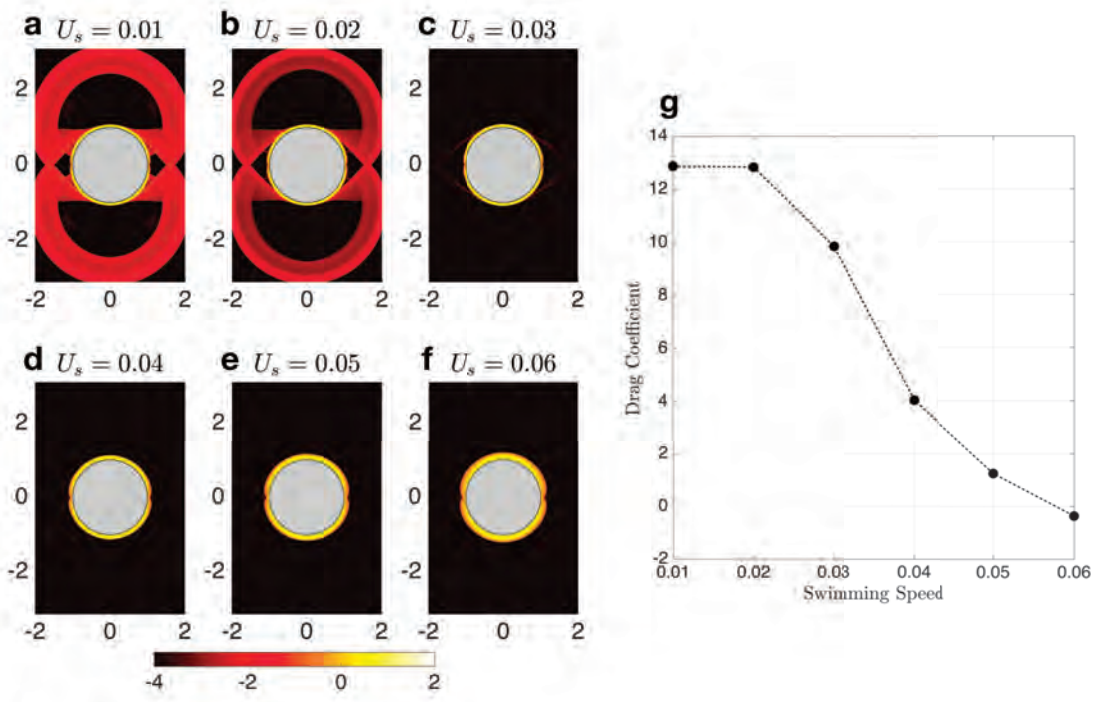

Figure 11: Simulations and the corresponding drag coefficient values for $U_p = 0$ and $V_p(\theta) = \sin\theta$ for different values of the swimming speed U_s. (a) to (f) are plots of $\log_{10}\dot{\gamma}$ for different swimming speeds at $\mathrm{Bi} = 30$. The flow gets localized within a boundary layer for $U_s \geq 0.03$. (g) plots the variation of the the drag coefficient with the swimming speed.

layer theory to find the swimming speed for an imposed tangential velocity.

5.1 Boundary layer theory: swimming speed

In the limit of a large Bingham number ($\mathrm{Bi} \gg 1$), we assume that the imposed surface velocity $(U_p(\theta), V_p(\theta))$ and the swimming speed U_s are such that the flow is localized within a viscoplastic boundary layer attached to the cylinder surface. We now rescale the radial coordinate to zoom into the boundary layer by letting $r = 1 + \delta\eta$, where η is $\mathcal{O}(1)$. Making this substitution, the force balance in equation (22) holds. We subsequently obtain

$$\frac{1}{\delta^2}\frac{\partial^2 v}{\partial \eta^2} + 2\mathrm{Bi}\ \mathrm{sgn}\left(\frac{\partial v}{\partial \eta}\right) = \frac{\partial p}{\partial \theta}. \tag{54}$$

We now focus on the upper half of the solution such that $\mathrm{sgn}(\partial v/\partial\eta) < 0$. The tangential velocity v and the swimming speed U_s are expressed as a regular perturbation expansions in δ so that

$$v = v_0 + \delta v_1 + \ldots, \tag{55}$$

and

$$U_s = \delta U_1 + \ldots \tag{56}$$

Setting $\delta = \mathrm{Bi}^{-1/2}$ and rescaling pressure as $p = \mathrm{Bi}P$, to leading order, equation (54) becomes

$$\frac{\partial^2 v_0}{\partial \eta^2} = 2 + \frac{\partial P}{\partial \theta}. \tag{57}$$

We rewrite the boundary conditions in equation (8) in expanded form here. The boundary conditions for the tangential velocity are

$$v = V_p(\theta) - U_s \sin\theta \text{ at } \eta = 0 \qquad \text{and} \qquad (v, v_\eta) = (0,0) \text{ at } \eta = \eta_b, \tag{58}$$

and for the radial velocity are

$$u = U_s \cos\theta \text{ at } \eta = 0 \qquad \text{and} \qquad u = 0 \text{ at } \eta = \eta_b, \tag{59}$$

where $\eta_b(\theta)$ marks the edge of the boundary layer. Integrating equation (57) with the above boundary conditions, leads to the velocity profile

$$v_0 = V_p(\theta)\left(1 - \frac{\eta}{\eta_b}\right)^2, \tag{60}$$

where η_b is given by

$$\eta_b(\theta) = \sqrt{\frac{2V_p(\theta)}{2 + P_\theta}}. \tag{61}$$

Integrating the continuity equation, $v_\theta + (1/\delta)u_\eta \sim 0$ across the boundary layer and using the boundary conditions gives us

$$\frac{\partial}{\partial \theta}\left[\frac{\eta_b V_p(\theta)}{3}\right] - U_1 \cos\theta = 0, \tag{62}$$

which can be integrated further by assuming $V_p(0) = 0$ due to symmetry. Hence,

$$\eta_b(\theta) = \frac{3U_1 \sin\theta}{V_p(\theta)}. \tag{63}$$

For making the swimmer force free, we demand

$$\int_0^\pi f_x d\theta = \int_0^\pi (-P\cos\theta + \sin\theta) d\theta = 0. \tag{64}$$

In the above equation, the pressure $P(\theta)$ is obtained from equations (61) and (63). On evaluating this integral to get U_1, the swimming speed U_s is subsequently found to be

$$U_s = \frac{\mathrm{Bi}^{-1/2}}{3}\sqrt{\int_0^\pi \frac{V_p(\theta)^3}{\sin\theta} d\theta}. \tag{65}$$

In the special case where $V_p(\theta) = \sin\theta$, the swimming speed is $U_s = \sqrt{\pi/18}\mathrm{Bi}^{-1/2}$ and the boundary layer thickness does not vary with θ (equation (61)). For $\mathrm{Bi} = 2^7$, the numerical value of the swimming speed was found to be 0.03 ± 0.01. The numerical solution for this case is shown in figure (12)d. The corresponding analytic prediction is 0.037, which is very close to the numerical value. It can also be seen that the boundary layer is uniform in thickness, as predicted from the theory.

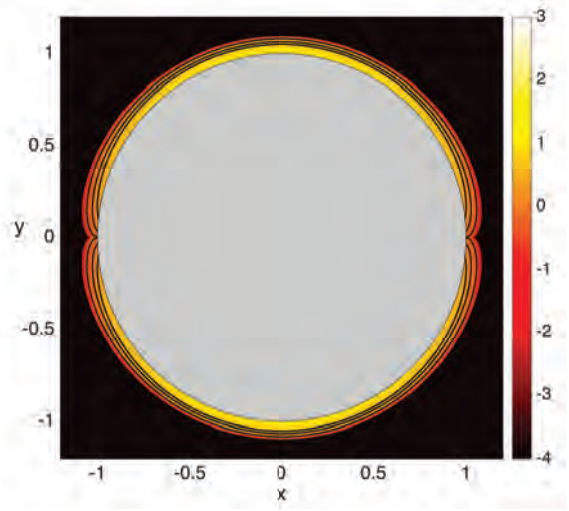

Figure 12: Plot of $\log_{10}\dot{\gamma}$ for the numerical solution of a squirmer with $V_p = \sin\theta$ for $\mathrm{Bi} = 2^7$ at $U_s = 0.03$ such that $C_d \simeq 0$. The black lines are the streamlines of the flow.

6 Conclusions

In this report, we have investigated the problem of viscoplastic flow around a cylinder in the limit of large yield stress. In the case of no-slip on the cylinder surface, we compared analytic plastic solutions with viscoplastic computations which show significant differences due to the presence of rigidly rotating plugs (*nuggets*) above and below the cylinder even at a large Bingham number. By developing a boundary layer theory, we corroborated the existence of such features and analytically derived the scalings with which these features vanish (as expected) in the limit $\mathrm{Bi} \to \infty$. These scalings compare very well with the numerical findings. We then modified the problem by allowing for partial slip on the sur-face of the cylinder. For purely plastic flow, Martin and Randolph [2006] had proposed a mechanism for this case but had only performed an upper bound analysis. By considering the stress solution for their mechanism, we performed a lower bound analysis and showed that it matches with their upper bound calculation. Since the bounds match, we concluded that their solution is not just an upper bound but actually the true solution to this prob-lem, which was previously unknown. Our viscoplastic computations in the limit $\mathrm{Bi} \to \infty$ compare well with this true solution. Finally, we further modified this problem by imposing surface velocity on the cylinder surface in order to model swimming micro-organisms in viscoplastic fluids (squirmers). Computations for such squirmer models suggested that the flow gets localized to a viscoplastic boundary layer attached to the squirmer. Utilizing this observation, we developed a boundary layer theory to analytically determine the swimming speed of the squirmer, which compares well with the numerical value.

Acknowledgements

I sincerely thank my advisors, Duncan Hewitt and Neil Balmforth, for their guidance, enthusiasm and inspiration throughout this work. I want to thank the program directors, Neil

Balmforth and Colm-cille Caulfield, for a fantastic summer and a great learning experience. I would also like to acknowledge Shreyas Mandre for his advice, interest and willingness to discuss my work. Lastly, all the fellows made the GFD program very enjoyable (especially the softball games) and I would like to thank all of them for their support and companionship.

References

Seda Aktas, Dilhan M. Kalyon, Benjamín M. Marín-Santibáñez, and José Pérez-González. Shear viscosity and wall slip behavior of a viscoplastic hydrogel. *Journal of Rheology*, 58 (2):513–535, 2014.

C. P. Aubeny, H. Shi, and J. D. Murff. Collapse Loads for a Cylinder Embedded in Trench in Cohesive Soil. *International Journal of Geomechanics*, 5(4):320–325, 2005.

J. R. Blake. Self propulsion due to oscillations on the surface of a cylinder at low Reynolds number. *Bulletin of the Australian Mathematical Society*, 5(2):255–264, 1971.

Emad Chaparian and Ian A. Frigaard. Yield limit analysis of particle motion in a yield-stress fluid. *Journal of Fluid Mechanics*, 819:311–351, 2017.

D R Hewitt and N J Balmforth. Taylor's swimming sheet in a yield-stress fluid. *Journal of Fluid Mechanics*, pages 33–56, 2017.

Rodney Hill. *The Mathematical Theory of Plasticity*. Oxford University Press, 1950.

M. J. Lighthill. On the squirming motion of nearly spherical deformable bodies through liquids at very small reynolds numbers. *Communications on Pure and Applied Mathematics*, 5(2):109–118, 1952.

C. M. Martin and M. F. Randolph. Upper-bound analysis of lateral pile capacity in cohesive soil. *Geotechnique*, 56(2):141–145, 2006.

J D Murff, D A Wagner, and M. F. Randolph. Pipe penetration in cohesive soil. *Geotechnique*, 39(2):213–229, 1989.

Slavomir Okrajni and J J Azar. The Effects of Mud Rheology on Annular Hole Cleaning in Directional Wells. *SPE Drilling Engineering*, 1(04):297–308, 1986.

M. F. Randolph and G T Houlsby. The limiting pressure on a circular pile loaded laterally in cohesive soil. *Geotechnique*, 34(4):613–623, 1984.

Mark F. Randolph and Susan Gourvenec. *Offshore Geotechnical Engineering*. Spon Press, 2011.

Dodji Léagnon Tokpavi, Albert Magnin, and Pascal Jay. Very slow flow of Bingham viscoplastic fluid around a circular cylinder. *Journal of Non-Newtonian Fluid Mechanics*, 154(1):65–76, 2008.

Shahrzad Yazdi, Arezoo M. Ardekani, and Ali Borhan. Locomotion of microorganisms near a no-slip boundary in a viscoelastic fluid. *Physical Review E - Statistical, Nonlinear, and Soft Matter Physics*, 90(4):1–11, 2014.

Spooky Mixing at a Distance: Nonlocal Mixing from Stochastic Advection

Tyler Lutz

October 18, 2018

1 Introduction

Turbulent fluid flows generally exhibit complex dynamical behavior across a broad range of length scales. Numerical models of such flows are typically unable to explicitly model the full range of these dynamics, either due to limited spatial resolution or the computational costs associated with modeling nonlinear dynamics. In ocean or climate simulations, turbulent flow dynamics often make substantial contributions to the dispersion of passive tracers, which may include environmental toxins or biological organisms. Without fully resolving the turbulent flows in all of their complexity, one would like to be able to make predictions about their effects on the dispersion of tracers.

It is conventional to model the mixing intensity as proportional to concentration gradients of the tracer, in close analogy to the case of molecular diffusion; one typically fits the effect of the turbulent mixing to an effective diffusivity, κ_{eff}. By considering a stochastic advecting flow field, we show here that this approximation is only valid when the typical length scale associated with a turbulent eddy is much smaller than the typical length scale associated with the mean concentration structure. For larger eddies, the flux of tracer anomaly due to turbulent flow—the so-called eddy flux—at a given point depends not only on the concentration gradient at that point, but also on the gradients at points far away from it. We undertake here an investigation of the weighting function that determines how distant regions factor into the eddy flux at a given point.

G. I. Taylor was one of the first to characterize the diffusion of a passive tracer due to turbulent flows; in 1921 (3), he constrained the spatial distribution of tracers that are initially close to each other as a function of time. Unfortunately, this formulation does not help determine how well-mixed a given region of the domain is; we're interested in the obverse problem of determining how far separated starting points of tracer particles were, provided that they all pass through a particular region of the domain at a given time.

Kraichnan (2) demonstrated the value of modeling mixing from a Lagrangian perspective. We follow here a broadly similar tack to Kraichnan, but we work instead in a Eulerian frame. The Eulerian setting allows us to address a unique set of questions; we can constrain, for instance, the likelihood of fluctuations away from a mean concentration of passive tracers at a particular grid point in a large ocean simulation.

2 Posing the Problem

The evolution of the concentration of a passive, scalar tracer carried along by a fluid flow can be modeled by the advection-diffusion equation,

$$\partial_t c(\mathbf{x},t) + \nabla \cdot (\mathbf{u}(\mathbf{x},t)c(\mathbf{x},t)) - \kappa \nabla^2 c(\mathbf{x},t) = s(\mathbf{x},t), \tag{1}$$

where c represents the tracer concentration, s accounts for sources and sinks of tracer concentration, and $\mathbf{u}$ is the velocity field of the advecting flow. Assuming that the molecular (or at least sub-grid-scale) diffusivity of the tracer is spatially homogenous and isotropic, we've written the diffusion coefficient κ as a scalar.

Employing the additional simplifying assumptions of a time-independent source and an incompressible fluid,

$$\nabla \cdot \mathbf{u} = 0, \tag{2}$$

we arrive at an advection-diffusion equation of the form

$$\partial_t c(\mathbf{x},t) + \mathbf{u}(\mathbf{x},t) \cdot \nabla c(\mathbf{x},t) - \kappa \nabla^2 c(\mathbf{x},t) = s(\mathbf{x}), \tag{3}$$

which holds for domains of an arbitrary number of dimensions. Given s and $\mathbf{u}$, solving this equation would determine the tracer concentration as a function of space and time.

We are interested in advection due to turbulent velocity fields. These fields may have a mean component that can be constrained and written down explicitly, but they also contain a fluctuating component that, by hypothesis, can not be modeled explicitly and must instead be considered to be "random" in a sense we'll pin down below.

The tracer concentration, in turn, can be decomposed into mean and fluctuating components; disentangling the time evolutions of these two components would involve solving a system of coupled partial differential equations. To see this explicitly, we write $c = \overline{c} + c'$ and $\mathbf{u} = \overline{\mathbf{u}} + \mathbf{u}'$, insert them into equation (3), and take the ensemble mean of the whole equation to arrive at

$$\partial_t \overline{c} + \nabla \cdot \overline{\mathbf{u}'c'} - \kappa \nabla^2 \overline{c} = s. \tag{4}$$

In order to focus strictly on the effects of the fluctuating component of the velocity field, we consider a mean-zero field, by virtue of which we were able to eliminate the $\overline{\mathbf{u}} \cdot \nabla \overline{c}$ from (4). The important thing to notice here is that the mean concentration is coupled to the eddy diffusivity, $\nabla \cdot \overline{\mathbf{u}'c'}$, which quantifies the average flux of concentration anomaly due to the fluctuating fluid velocity component.

If we could constrain this eddy diffusivity term, we would have a model for how the mean concentration depends on the fluctuating fluid velocity. The conventional way to do this is to posit that concentration anomalies diffuse, on average, at a rate proportional to local gradients in the mean concentration. In analogy to the diffusive flux of the tracer, one could consider writing the eddy flux as

$$\nabla \cdot \overline{\mathbf{u}'c'} \to -\kappa_{eff} \nabla^2 \overline{c}, \tag{5}$$

where κ_{eff} is an effective diffusion constant that depends on the particular statistical properties of the velocity field under consideration. We expect this replacement to be valid in the regime in which the characteristic length scale of the eddies—or, alternatively, the mean

free path of the concentration anomaly—is small relative the domain size. As soon as the mean free path becomes comparable to the domain size, a given region of space may receive an influx of tracer advected from points far away from it. In such cases, the eddy flux can no longer be thought of as a function of the mean concentration gradients in the region's immediate vicinity, but instead depends on what's happening at points spatially distant from it within the domain; we thus speak in such cases of a nonlocal eddy diffusivity.

As in the case of molecular diffusion, this eddy diffusivity still depends on the mean concentration gradient, which we demonstrate below. What needs to be constrained in such cases is the particular weights to be assigned to distant points throughout the domain in determining the eddy diffusivity at any particular location.

To show that the mean concentration gradient is still the quantity of interest, we subtract (4) from (3) to obtain an equation for the fluctuating component of the tracer concentration:

$$\partial_t c' + \mathbf{u}'\nabla\overline{c} - \nabla\cdot\overline{\mathbf{u}'c'} + \mathbf{u}'\cdot\nabla c' - \kappa\nabla^2 c' = 0., \tag{6}$$

or, grouping like terms,

$$(\partial_t + \mathbf{u}'\cdot\nabla - \kappa\nabla^2)c' - \nabla\cdot\overline{\mathbf{u}'c'} = -\mathbf{u}'\nabla\overline{c}. \tag{7}$$

We observe that left hand side is linear in c', by virtue of which we expect to be able to write

$$c' = -\int\int dx'dt' G(x,t|x',t')\mathbf{u}'\cdot\nabla\overline{c}., \tag{8}$$

and hence

$$\overline{\mathbf{u}'c'} = -\overline{\int\int dx'dt' \mathbf{u}' G(x,t|x',t')\mathbf{u}'\cdot\nabla\overline{c}}. \tag{9}$$

Recalling the form of the eddy flux term, we thus expect to be able to write it as the divergence of the convolution of an integral kernel with the concentration gradient, consistent with what Kraichnan obtains in (2). The kernel weights each location in the domain according to its effect on the local eddy flux. Note that in the particular case for which the full integral operator approaches a delta function, the eddy flux recovers the form of a local, scalar diffusivity, $\kappa_{eff}\nabla^2\overline{c}$.

Our goal is to determine the form of this integral kernel for an arbitrary source. Though writing down a formal expression for this integral kernel is feasible in many circumstances, we can make progress towards writing it down in closed form by recasting the problem in terms of stochastic differential equations.

3 Stochastic Calculus Approach

We're assuming that we can't model u' explicitly, which motivates treating it as a random variable. We don't want to just use any old random variable, of course; eventually we'd like u' to have similar statistical properties—things like the variance and the Lagrangian autocorrelation—to the flow field under consideration.

To define the randomness of u' precisely, we reformulate the problem as a stochastic process. For simplicity, we begin by considering a one-dimensional domain with periodic boundary conditions; in order to maintain incompressibility, the advecting velocity must be spatially uniform.

3.1 Blob formulation

Consider tracking the position and concentration of a single infinitesimal blob of advected by the flow that gains or loses concentration as it traverses the domain depending how much time it spends in "source" and "sink" regions, respectively. The Langevin equations describing this blob can then be written as:

$$dx = udt + \sqrt{2\kappa}\ dW_1, \tag{10}$$

$$du = -\gamma u dt + \sqrt{2\epsilon}\ dW_2, \tag{11}$$

$$dc = s(x)\ dt. \tag{12}$$

The stochastic element in these equations comes from the dW terms, which describe independent Weiner processes. One can think of dW as sampling from a normally distributed, mean-zero, and unit standard deviation random variable for each infinitesimal increment of time, dt. The parameter ϵ gives us a knob with which to adjust the strength of the forcing.

We've chosen to describe the stochastic velocity field as a mean zero Ornstein-Uhlenbeck process both because of its generality and because of the simplicity of adapting it to measured properties of real-world flows—we'll see below that the time constant for the decay in Lagrangian auto-correlation is just γ.

Writing the Fokker-Planck equation for this system,

$$\partial_t \rho + u\partial_x \rho - \kappa \partial_x^2 \rho + \partial_c s\rho + \mathcal{F}_u[\rho] = 0, \tag{13}$$

gives us an equation for the joint probability density $\rho(x, u, c, t)$. $\mathcal{F}_u$, defined as

$$\mathcal{F}_u = \partial_u - \epsilon \partial_u^2, \tag{14}$$

is a differential operator corresponding to the Ornstein-Uhlenbeck process.

Note that the Fokker-Planck equation for just the dx and dc equations alone is identical to the advection-diffusion equation (3) for the mean concentration; multiplying the Fokker-Planck through by c and integrating over c yields (3) once we make the identification

$$\int c\rho dc \equiv \overline{c}. \tag{15}$$

3.2 Scalar field formulation

It's worth noting that discrete blobs of concentration isn't the only way of parameterizing the system. Noting the linearity of (3), we could instead immediately resolve both the source and concentration terms into Fourier modes

$$c = \sum_{n=1}^{\infty} s_n(t)\sin(k_n x) + c_n(t)\cos(k_n x), \tag{16}$$

assuming the spatial average of the concentration is zero, and

$$s = \sum_{n=1}^{\infty} a_n \sin k_n x + b_n \cos k_n x, \tag{17}$$

with $k_n = \frac{2\pi n}{\Gamma}$ for a domain of size Γ.

The linearity of (3) in the source term allows us to focus on a single source mode at a time. By plugging these into (3) we can immediately write down an alternative set of Langevin equations for each mode:

$$ds_n = (uk_n c_n - \kappa k_n^2 s_n + a_n)dt, \tag{18}$$

$$dc_n = (-uk_n s_n - \kappa k_n^2 c_n + b_n)dt, \tag{19}$$

$$du = -\gamma u dt + \sqrt{2\epsilon}\, dW, \tag{20}$$

where we again posit an Ornstein-Uhlenbeck process for the advecting velocity.

We can simplify these further by assuming periodic boundary conditions, the translational symmetry of which enables us to drop the cosine terms of the source, $b_n \to 0$, without loss of generality. Employing this simplification, the Fokker-Planck equation corresponding to this set of Langevin equations reads:

$$\partial_t \rho_n + \partial_{s_n}(uk_n c_n - \kappa k_n^2 s_n + a_n)\rho_n + \partial_{c_n}(-uk_n s_n - \kappa k_n^2 c_n)\rho_n + \mathcal{F}_u[\rho_n], \tag{21}$$

with $\mathcal{F}_u[\rho]$ defined as above and $\rho_n(s_n, c_n, u)$ the joint probability density for the nth Fourier mode of the source.

Rather than modeling the individual trajectories of tracer blobs that collect or lose concentration as they traverse the domain, this formulation constrains the evolution of a whole field of concentration values; instead of the position and concentration of a single blob, we're tracking here the amplitudes of the sine and cosine modes of the concentration over the whole domain. The two formulations lead to identical predictions for the mean concentrations in the steady state of the system.

Because of the ease of carrying through the following manipulations on it, we will focus primarily on the blob formulation described by (13) in what follows, though it's conceptually helpful to keep both pictures in mind.

3.3 Source term

For forcing functions that depend on space alone, the variance of the concentration grows unbounded in time for the $\kappa = 0$ case. Given that each parcel of fluid is undergoing a random walk in concentration space, some parcels will persistently walk in the same direction—always gaining or losing concentration each step—causing the variance to grow without bound.

In order to ensure statistical stationarity, we insert

$$s(x) = \lambda\left(r(x) - c(x,t)\right). \tag{22}$$

The parameter λ sets the timescale for which a non-advected, non-diffusing tracer concentration would settle down to a reference profile $r(x)$. Physically, we can imagine such an equation being relevant to biological populations, the density of which typically hovers about some fixed equilibrium set by external conditions (nutrient fluxes, predator concentration, etc.)

As before, the linearity of the problem makes it natural to decompose both the equilibrium and the concentration into Fourier modes and to consider the equations for each mode individually,

$$r(x) = \sum_{n=1}^{\infty} a_n \sin(k_n x) + b_n \cos(k_n x), \tag{23}$$

where we're again at liberty to take $b_n \to 0$ by translational symmetry.

4 N-state Velocity Model

We make progress on solving (13) by reparameterizing the velocity field. Determining the full form of ρ for arbitrary times gives us more information than we need; we instead restrict our attention to steady states of the system, which sets $\partial_t \rho$ to zero.

As time tends to infinity, the probability density of the velocity in an Ornstein-Uhlenbeck process approaches a Gaussian, the width of which is a function of both γ and ϵ. One can imagine decomposing this continuous probability distribution into a discrete one; what this looks like physically is constraining the velocity to take on one of a finite number of possible velocity states at any given time. The limit as the number of states goes to infinity recovers the full, continuous probability density distribution of the Ornstein-Uhlenbeck process.

In this approach, (13) can be decomposed into N independent equations, one for the probability density of each velocity state. We can think of it, in other words, as a matrix equation with

$$\rho = \begin{pmatrix} \rho_{u_0} \\ \rho_{u_1} \\ \vdots \\ \rho_{u_N} \end{pmatrix}. \tag{24}$$

In this context, the Ornstein-Uhlenbeck operator $\mathcal{F}_u$ is naturally represented as a transition matrix that couples the different velocity states to each other. Following (1), the entries of the transition matrix T for N velocity states are taken to be

$$T_{ij} = \frac{1}{2}\left[-(N-1)\delta_{ij} + k\delta_{j+1,k} + (N-1-k)\delta_{j-1,k}\right], \tag{25}$$

with $j, k = 0, 1, 2, \ldots N-1$

The matrix is tridiagonal—we force the velocity to transition only between neighboring states—with entries that quantify the rates associated with moving up or down by one state or remaining in the same state.

The spacing between successive velocity states is constant and equal to $\frac{2\sigma}{\sqrt{N}}$, where σ sets the standard deviation of the probability density function for the velocities. The velocity spacing decreases as N increases, which must be the case if models containing different numbers of states are to approximate the same velocity distributions; without the $\frac{1}{\sqrt{N}}$ dependence in the spacing, the $N+1$-state model would correspond to a velocity probability distribution with a higher standard deviation than the N-state model.

4.1 Moments of the Fokker-Planck equation

Rather than solve the Fokker-Planck for each ρ_{u_i} in all of its dependencies, we construct the nth moment of ρ by multiplying (13) by c^n and integrating over c, defining

$$P^n_{u_i} = \int dc\, c^n \rho_{u_i}. \tag{26}$$

For the 0th moment we obtain, dropping the explicit velocity state indices:

$$\partial_t P^0 + u\partial_x P^0 - \kappa\partial_x^2 P^0 + \mathcal{F}_u[P^0] = 0, \tag{27}$$

where we've stipulated that ρ disappear at positive and negative infinity in c.

To obtain an equation for the first moment, we multiply first by c then carry out the integration, yielding

$$\begin{aligned} \partial_t P^1 + u\partial_x P^1 - \kappa\partial_x^2 P^1 + \mathcal{F}_u[P^1] &= -\int dc\, c\partial_c s\rho \\ &= cs\rho|_{-\infty}^{\infty} + \int dc\, s\rho \\ &= sP^0 \end{aligned} \tag{28}$$

The first moment has the natural interpretation of the mean of c, and we find it depends on the zeroth moment. This is generally the case; the nth moment will contain a P^{n-1} term arising from the $\partial_c s$ in the original Fokker Planck:

$$\partial_t P^n + u\partial_x P^n - \kappa\partial_x^2 P^n + \mathcal{F}_u[P^n] = snP^{n-1} \tag{29}$$

We proceed by solving these matrix equations in ascending order—using each previous moment as input for the next equation—for each Fourier mode of the forcing. We are primarily interested in the first three moments, recognizing $P^2 - (P^1)^2$ as the variance.

Focusing on individual Fourier modes allows us to decompose each of the $P^n_{u_i}$ into their respective sine and cosine modes as well; the spatial derivatives in (29) act to multiply $P^n_{u_i}$ by the wavenumber of the forcing (since no other wavenumbers survive) and, in the case of the advection term, interchange the sine and cosine modes.

Considering the 3-state system and a forcing wavenumber of k_n and typical velocity scale u, for instance, we find

$$\begin{aligned} \bar{c} &\equiv P^1_{-u} + P^1_0 + P^1_u \\ &= \frac{\lambda \sin(k_n x)\left(6\gamma^2 + 9\gamma\left(k^2\kappa + \lambda\right) + 3\left(k^2\kappa + \lambda\right)^2 + 2k^2u^2\right)}{\left(\gamma + k^2\kappa + \lambda\right)\left(3\left(k^2\kappa + \lambda\right)\left(2\gamma + k^2\kappa + \lambda\right) + 4k^2u^2\right)} \end{aligned} \tag{30}$$

4.2 Convergence

The algebraic form of the moments becomes successively more complicated as we increase the number of velocity states. The convergence to the full Ornstein-Uhlenbeck process is generally slow for the N-state model, motivation for trying a different way of packaging the equations.

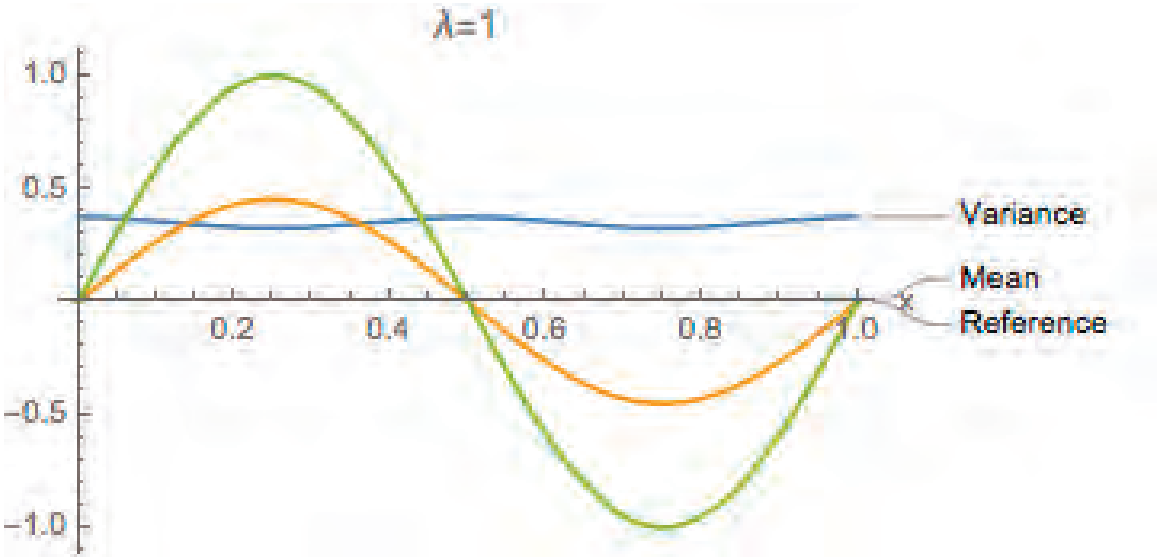

Figure 1: For moderate λ, the variance (blue) is highest at the nodes of the mean concentration (orange), suggesting that the advection is winning out over the forcing; the dominant source of jitter is the phase shift in the mean coming from the stochastic advection. The relative weakness of the forcing is also reflected in the fact that the amplitude of the mean concentration is roughly half that of the reference profile $r(x)$ (green) the forcing is trying to relax to.

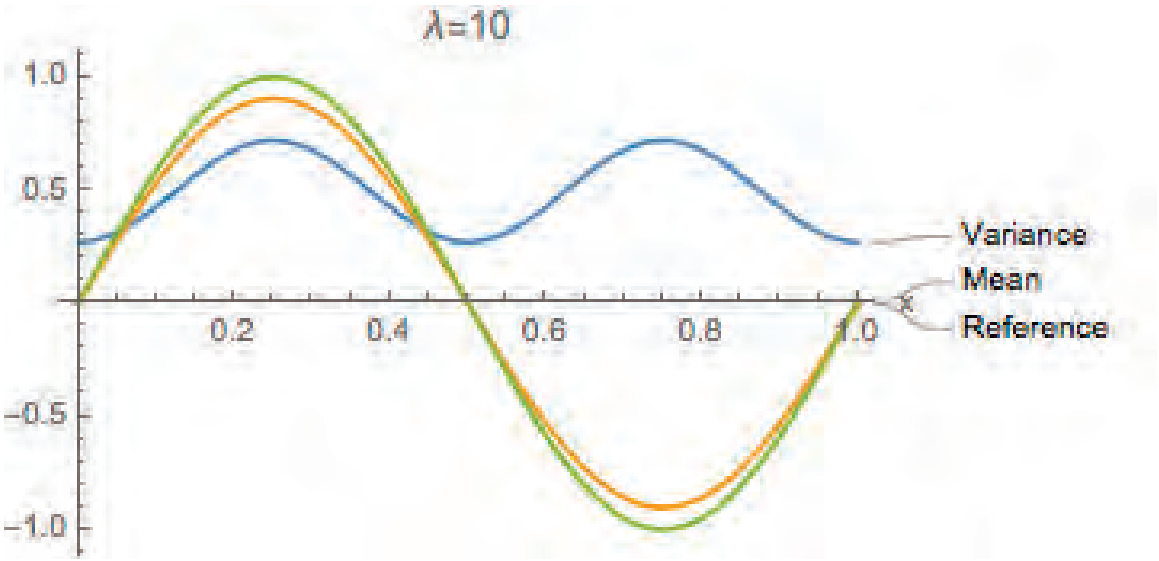

Figure 2: At higher λ, the variance peaks at the extrema of the mean, points where the forcing is strongest. The variance is exhibited primarily in the amplitude of the mean. The forcing is sufficiently strong to make the mean concentration (orange) nearly match the reference profile $r(x)$ (green).

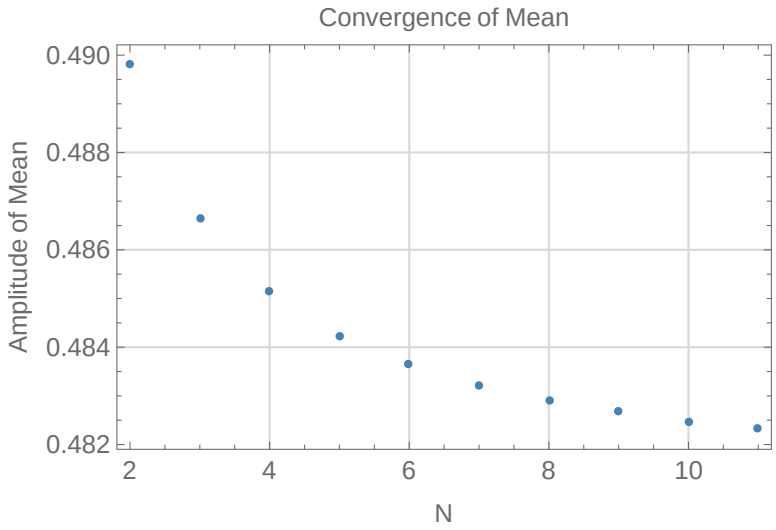

Figure 3: Even at 10 velocity states, the amplitude of the mean for the N-state model is still 10% away from the value it eventually converges to, 0.437.

5 Hermite Basis

5.1 Method

The N-state model helps us develop intuitions for the behavior of the system, but its slow convergence makes it poorly suited for complicated calculations—to get any sensible results, we'd have to use a large number of velocity states, which significantly increases the computational expense.

The way forward is to implement a spectral method using the eigenfunctions of the Fokker-Planck operator as a basis.

The Hermite polynomials scaled by exponentials provide exactly the basis we're after. Note:

$$\mathcal{F}_u[e^{-\frac{u^2}{2}} H_n(u)] = -ne^{-\frac{u^2}{2}} H_n(u). \tag{31}$$

We can now decompose the ρ into N Hermite Polynomial terms. The mixing between successive Hermite modes now comes from the advection term and the fact that

$$uH_n(u) = H_{n+1} + nH_{n-1}. \tag{32}$$

Equipped with these basis functions, we can proceed to calculating the moments of the Fokker-Planck equation (13) as in the N-state model, only now decomposing ρ into N Hermite modes rather than N velocity states.

5.2 Convergence

This trick substantially enhances the speed of calculation—which is unsurprising given that it constitutes a spectral method.

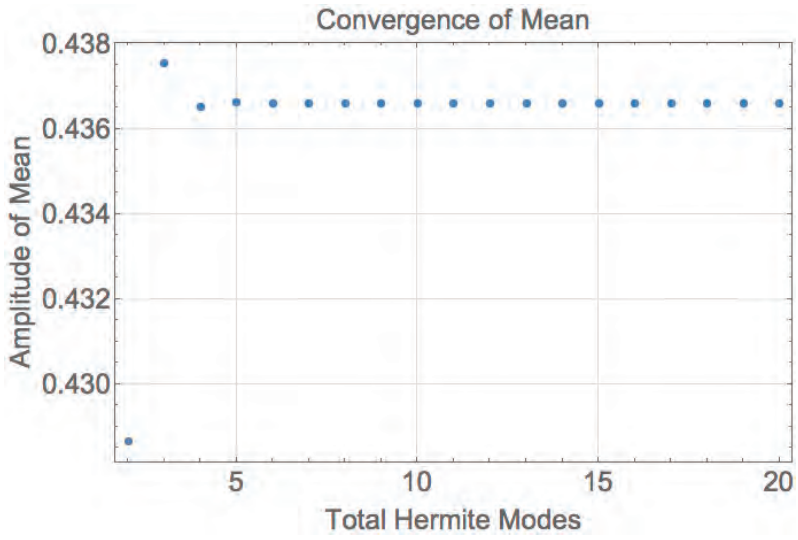

Figure 4: The mean is well-converged within 10 Hermite Modes.

This speed-up comes at the cost of the interpretability of the modes; the basis functions no longer correspond to intuitive statements about, e.g., the number of accessible velocity states. We will move between these two distinct methods in what follows depending on whether computational efficiency or an intuitive picture of the system is called for.

5.3 Effective diffusivity

We've been arguing that the eddy flux can not be written as a constant times the concentration gradient. Having considered the special case of a sinusoidal forcing—which constitutes a basis for an arbitrary forcing—we discover that we can in fact think of the eddy flux as corresponding to a constant effective diffusivity times the concentration gradient.

The special ingredient here is the fact that the mean turns out to be proportional to the forcing; this allows dividing $\sin(kx)$ from both sides of the steady state equation:

$$(\kappa + \kappa_{eff})k^2\overline{c} = \lambda(r(x) - \overline{c}), \tag{33}$$

or

$$\kappa_{eff} = \frac{\lambda(1 - |\overline{c}|)}{(k^2|\overline{c}|)} - \kappa, \tag{34}$$

where we've written the amplitude of the mean as $|\overline{c}| \equiv \frac{\overline{c}}{\sin(kx)}$.

As we increase the wavenumber of the forcing, tracer particles have less time to build up concentration anomaly before being pushed to the next region of the forcing, making the advection less effective at mixing. Similarly, as kappa is increased for a fixed wavenumber, the particles become progressively more "leaky" and lose memory of where they were before they can be advected any appreciable distance—again this dampens the magnitude of the eddy flux.

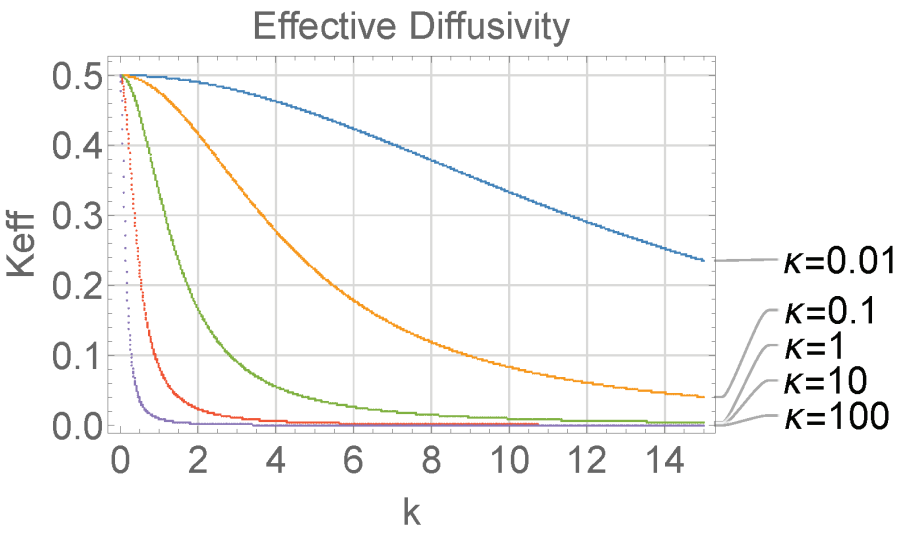

Figure 5: As κ increases, tracer particles lose memory of the concentration they'd picked up, making the advection less effective at mixing over mean concentration gradients. $\lambda = 1$.

5.4 Nonlocality

The only spatial input to κ_{eff} is the forcing wavenumber, k; if κ_{eff} becomes independent of k, the effective diffusivity no longer depends on the large-scale structure of the forcing, rendering it uniform across the domain. Consequently, we can determine the degree of nonlocality represented by κ_{eff} by examining what parameter regimes make it relatively more or less sensitive to k.

For the 2-velocity system ($\pm u$ are the accessible velocities) in particular, we find

$$\kappa_{eff} = \frac{u^2}{2\left(\gamma + k^2\kappa + \lambda\right)}. \tag{35}$$

Noting that $k = \frac{2\pi n}{\Gamma}$, where Γ represents the (periodic) domain size, allows us to devise a dimensionless parameter,

$$Nl = \frac{\kappa}{\Gamma^2(\lambda + \gamma)}, \tag{36}$$

that determines whether the k^2 term wins out over the constant term in the denominator. For $Nl \gg 1$ the nonlocal effects cannot be ignored, while for $Nl \ll 1$ we can treat the κ_{eff} as a constant, meaning that its transform looks like a delta function.

Note that the κ_{eff} becomes independent of k as $\kappa \to 0$ and, moreover, that the u^2 appears only as an overall scaling and does not influence the width of the kernel. Both of these are unique features of the 2-state system.

For the 3-velocity system, on the other hand,

$$\kappa_{eff} = \frac{2u^2\left(2\gamma + k^2\kappa + \lambda\right)}{6\gamma^2 + 9\gamma\left(k^2\kappa + \lambda\right) + 3\left(k^2\kappa + \lambda\right)^2 + 2k^2u^2}. \tag{37}$$

This allows us to write a similar parameter by completing the square in the denominator: we find the k-dependent term in the denominator looks like

$$3\kappa\left(k^2+\frac{2u^2+9\gamma\kappa+6\kappa\lambda}{6\kappa}\right)^2, \tag{38}$$

and thus that the k-dependence in the denominator can be switched on or off according to

$$Nl_{denom}=\frac{6}{\Gamma^2(6\lambda+9\gamma+2\frac{u^2}{\kappa})}. \tag{39}$$

As long as this number is sufficiently larger than 1, we expect to see k-dependence in the κ_{eff} and, thus, significant nonlocal effects. The new effects that enter at the 3-state level are that k-dependence is still possible even as $\kappa\to 0$ and that the scale of the random velocity field u, which can be thought of as the standard deviation of the velocity magnitude, now enters into the determination of locality as well. In particular, if u is especially large, we find that it washes away the k-dependence in the denominator; what's happening here is that tracers are being pulled along so quickly that they scarcely feel the forcing anymore—the alternating crests and troughs become blurred out.

5.5 Integral kernel

Equipped with the effective diffusivity for each wavenumber, we know how to weight each Fourier mode of an arbitrary concentration gradient in frequency space to determine the total effective diffusivity. In particular, we write the total eddy flux for an arbitrary concentration gradient as

$$\int\int \kappa_{eff}(k)\cos[k(x-x')]\partial_x\bar{c}dx'dk. \tag{40}$$

Performing just the k integral gives us an integral kernel that we convolve with the concentration gradient over all space to find the eddy flux at a given point.

$$\int \widetilde{\kappa_{eff}}(x-x')\partial_{x'}\bar{c}dx'. \tag{41}$$

Focusing on the N-state model with $N=3$, $\kappa=0$, and $\lambda=\gamma=1$, the integral kernel takes the simple form

$$\widetilde{\kappa_{eff}}(x-x')=\sqrt{\frac{\pi}{2}}e^{-3|x-x'|}. \tag{42}$$

6 Stochastically Oscillating Velocity Field

In real flow fields, the Lagrangian autocorrelation of the velocities is often not monotonically decaying but in fact may oscillate around zero. Such statistical flow structures are not inconsistent with our intuitions about how eddies work—if we follow a parcel of fluid initially moving in a particular direction, we might expect to find it moving in the opposite direction

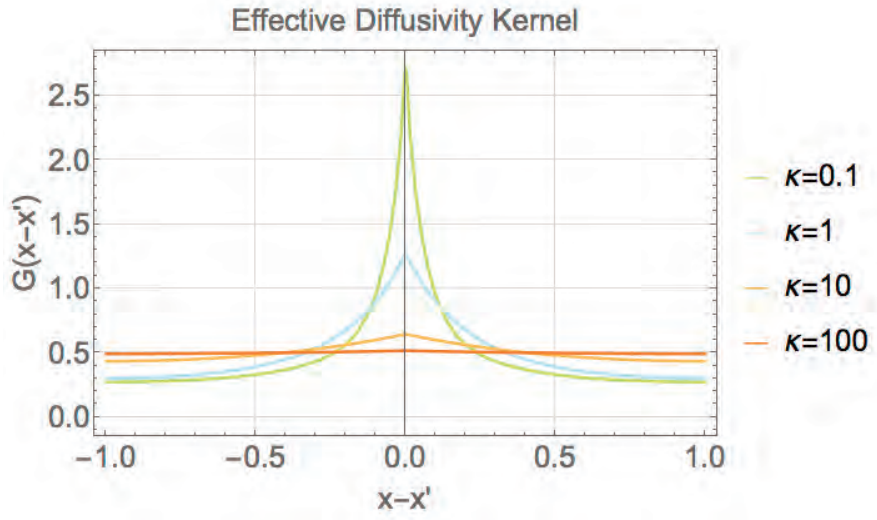

Figure 6: As κ increases, $\kappa_{eff}(k)$ becomes more peaked in structure; its Fourier transform thus approaches a flat line. For small values of κ, on the other hand, $\kappa_{eff}(k)$ flattens as a function of k, yielding a delta-function-like kernel. Loosely speaking, the width of the kernel corresponds to the mean free path of tracer anomaly.

a determinate time later. They have also been measured in real flow fields in the ocean, for instance in Figure 7.

In order to allow the Lagrangian autocorrelation in our original stochastic system to oscillate we allow the velocity to take on complex values:

$$du = -\gamma u dt + i\omega u dt + \sqrt{2\xi} dW \tag{43}$$

We see that this system is indeed oscillating by calculating the covariance:

$$\begin{aligned} \langle u(t)u(t+\tau)\rangle &\approx \langle u(t)(u(t) + \tau \frac{du}{dt}|_t)\rangle \\ &\approx \langle u(t)(u(t) + \tau/N \frac{du}{dt}|_t)^N\rangle \\ &\approx \langle u^2(t) e^{(-\gamma+i\omega)\tau}\rangle \\ &\approx e^{(-\gamma+i\omega)\tau}\langle u^2(t)\rangle \end{aligned} \tag{44}$$

We can think of this as constituting two coupled velocity fields corresponding to the real and imaginary components of u, in which only Re(u) is advecting. An equivalent way to write this is to keep everything real and add in an additional, non-advecting velocity v that couples to u according to:

$$du = -\gamma u dt + \omega v dt + \sqrt{2\xi} dW \tag{45}$$

$$dv = -\gamma v dt - \omega u dt + \sqrt{2\xi} dW \tag{46}$$

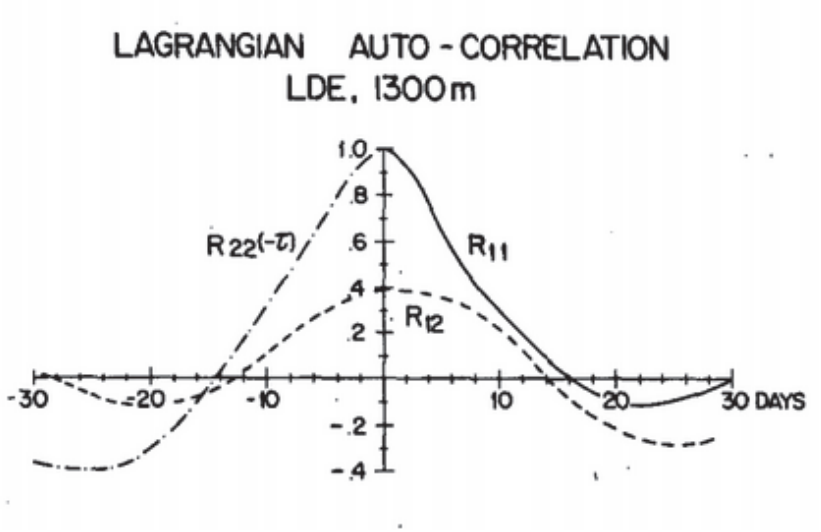

Figure 7: Oscillations are built into the otherwise exponentially-decaying Lagrangian autocorrelation of fluid parcels in the ocean. From: Rossby et al., 1984.

6.1 Fokker-Planck term

Given

$$du = (-\gamma u + \omega v)dt + \sqrt{2\xi}dW_1 \tag{47}$$

and

$$dv = (-\gamma v - \omega u)dt + \sqrt{2\xi}dW_2, \tag{48}$$

the Fokker-Planck operators become:

$$\mathcal{D}_u = \gamma\partial_u(u\rho) - \omega\partial_u(v\rho) + \xi\partial_{uu}\rho \tag{49}$$

$$\mathcal{D}_v = \gamma\partial_v(v\rho) + \omega\partial_v(u\rho) + \xi\partial_{vv}\rho \tag{50}$$

We show that the eigenfunctions of these differential operators are infinite sums of products of Hermite polynomials in u and v scaled, as before, by the appropriate Gaussians

$$\rho_{nm} = e^{-u^2/2}e^{-v^2/2}H_n(u)H_m(v) \tag{51}$$

Consider first the Fokker-Planck operator for u:

$$\mathcal{D}_u\rho_{nm} = \gamma u\partial_u(\rho_{nm}) + \gamma\rho_{nm} - \omega v\partial_u(\rho_{nm}) + \xi\partial_{uu}\rho_{nm} \tag{52}$$

We find after some algebra that:

$$\mathcal{D}_u\rho_{nm} = \omega\left(\rho_{n+1,m+1} + m\rho_{n+1,m-1}\right) - n\xi\rho_{n,m}, \tag{53}$$

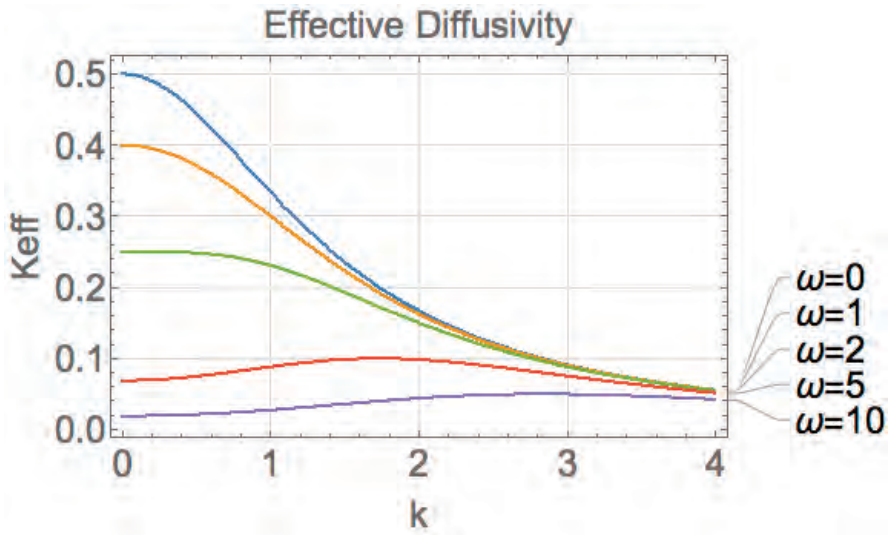

Figure 8: For sufficiently large values of ω, the effective diffusivity develops a peak.

where we used the facts that the Hermite polynomials are an Appell sequence—i.e. $\partial_u H_n(u) = nH_{n-1}(u)$—and that $H_n(x)$ is a solution to the differential equation $\partial_{xx}y(x) - x\partial_x y(x) + ny(x) = 0$.

Proceeding likewise for $\mathcal{D}_v$, we find that

$$\mathcal{D}_v \rho_{nm} = -\omega\left(\rho_{n+1,m+1} + n\rho_{n-1,m+1}\right) - m\xi\rho_{n,m}. \tag{54}$$

Grouping like terms after applying the differential operators to $\sum_n \sum_m \rho_{nm}$, we find that the ρ_{nm} terms resulting from the action of $\mathcal{D}_u$ on this series receive contributions from what were initially $\rho_{n-1,m-1}$ and $\rho_{n-1,m+1}$ terms, with weights that can be determined by reindexing (53) and (54) in n and m.

As before, we will need to truncate the series in ρ_{nm} in order to keep the equations numerically tractable. Given that higher order modes make increasingly modest changes to the final calculation, we find that the error associated with throwing out the m+1st mode by truncation becomes vanishingly small for increasingly large mode numbers.

6.2 Integral kernel

The effect is something like that of a bandpass filter; there's a "resonant" wavelength that is disproportionally emphasized. Roughly speaking, this is the wavelength such that the stochastically oscillating flow advects parcels between neighboring crests in the time it takes the flow to oscillate.

7 Quasi-2D Case

The machinery developed above carries over unproblematically to higher dimensions. The primary difficulty lies in defining a stochastic flow field that remains incompressible at all

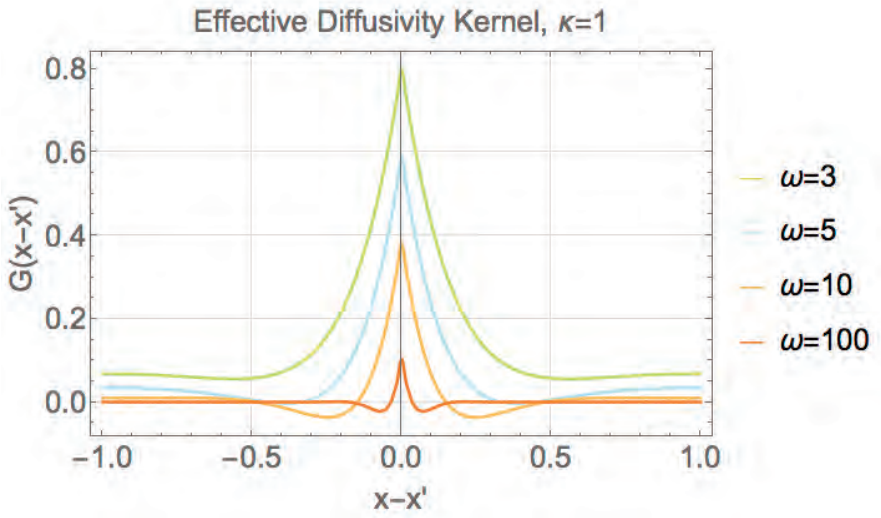

Figure 9: The effect of the "resonance"—forcing wavelengths that maximize effective diffusivity by being in phase with the stochastic velocity oscillations—is manifested in negative lobes in the kernel.

times and which is nonetheless sufficiently complex to describe flows encountered in the real world.

We can straightforwardly extend the work above to two dimensions by considering stacking an infinite series of the one-dimensional domains we'd originally looked at on top of each other such that the amplitude of the stochastic advecting flow field varies periodically in the vertical dimension. This corresponds to an advecting flow constrained to one dimension but with a stochastic amplitude that varies in the other dimension. By adding in an additional spatial dimension to our domain, we can explore what happens if we bake in a *spatially* varying velocity field.

The advection-diffusion equation for this domain reads:

$$\partial_t c + \mathbf{u}(t) \cdot \nabla c - \kappa \nabla^2 c = \sin(kx), \tag{55}$$

now with $c = c(\mathbf{x}, t)$. We choose $\mathbf{u}(t) = (A(t)\sin(ly), 0)$ and $s = \sin(kx)$, yielding

$$\partial_t c + A(t)\sin(ly)\partial_x c - \kappa \nabla^2 c = \sin(kx) \tag{56}$$

Following the Fokker-Planck formalism from before, we can represent this system using the Langevin equations

$$d\mathbf{x} = Au(\mathbf{x})dt + \sqrt{2\kappa}\, d\mathbf{W_1}, \tag{57}$$

$$dA = -Adt + \sqrt{2}\, dW_2, \tag{58}$$

$$dc = s(x)dt, \tag{59}$$

from which we can write the Fokker-Planck equation,

$$\partial_t \rho + a(t)\mathbf{u} \cdot \nabla \rho - \kappa \nabla^2 \rho = -\partial_c \sin(kx) + \mathcal{F}_A[\rho], \tag{60}$$

and solve the corresponding equations for the moments as above.

7.1 Sine and cosine modes

The Fokker-Planck operator in A motivates using the Hermite eigenfunctions as before. We decompose the spatial dependence in ρ into an infinite series of products of sines and cosines. Using trigonometric addition formulas, we find that the advection term converts $\sin(nly)$ into $\cos((1 \pm n)ly)$ terms, and likewise $\cos(nly) \to \sin((1 \pm n)ly)$ In order to match the forcing, the lowest order mode in y must be:

$$\rho_0 = \cos(0)\sin(kx)H_m[A] \tag{61}$$

with

$$H_m[A] \equiv e^{-\frac{A^2}{2}} h_m(A) \tag{62}$$

Working up from here, we can construct an infinite ladder of trigonometric product terms,

$$\rho = \sum_{n=0}^{\infty}\sum_{m=0}^{\infty} \left(s_n \cos(nly)\sin(kx) + c_n \sin(nly)\cos(kx)\right) H_m(A). \tag{63}$$

The boundary condition forces $s_n = 0$ whenever n is odd, and $c_n = 0$ for n even, halving the number of terms we need to consider. By inserting this expansion into (60), we can again solve for the moments of ρ and from them deduce the κ_{eff} and integral kernel.

We find that the effective diffusivities remain monotonic in k but not, however, in l; for a fixed forcing wavenumber, they attain a maximum for a value of l that is generally nonzero. For this 2D domain, computing the integral kernel requires computing a 2D Fourier transform of $\kappa_{eff}(k, l)$; we expect thus to find negative lobes in the y-projection of the kernel but no such lobes in the x-projection.

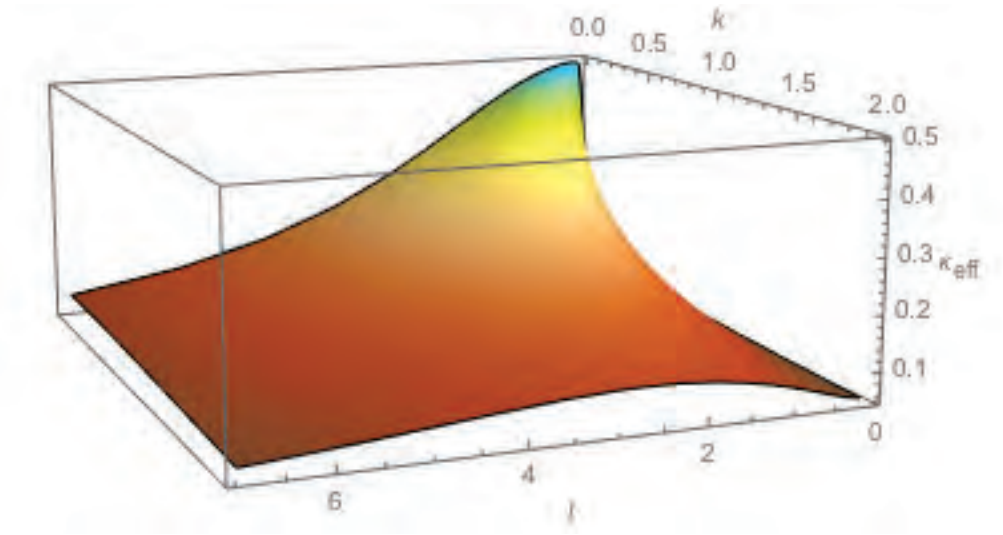

Figure 10: The effective diffusivities are monotonically decreasing in the forcing wavenumber k. At a given forcing wavenumber, however, diffusivity is not monotonic in l—the wavenumber of the velocity structure—but rather reaches a maximum at a generally nonzero value of l. $\kappa = 0.1$, $n_{max} = 8$, and $m_{max} = 5$.

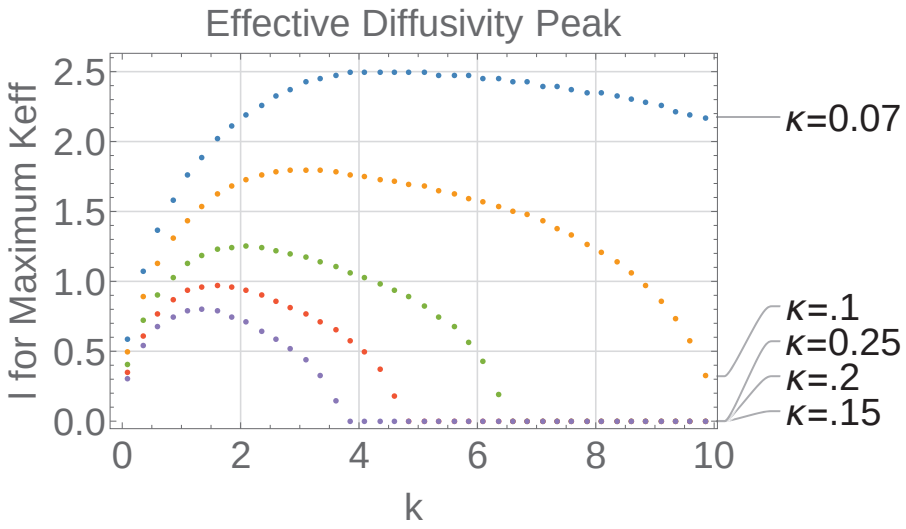

Figure 11: The forcing and oscillation structure wavenumbers corresponding to maximal effective diffusivity initially scale linearly with each other; as the forcing wavelengths decrease beyond a given threshold, however, the highest effective diffusivities are achieved by decreasing the oscillation wavelength.

References

[1] P. S. Hagan, C. R. Doering, and C. D. Levermore, *The distribution of exit times for weakly colored noise*, Journal of Statistical Physics, 54 (1989), pp. 1321–1352.

[2] R. Kraichnan, *Eddy viscosity and diffusivity: Exact formulas and approximations*, Complex Systems., 1 (1987), pp. 805–820.

[3] G. Taylor, *Diffusion by continuous movements*, Proc. R. Soc. London, Ser. 2, 20 (1921), p. 196.

Destabilization of Vortices by Topography

Bowen Zhao

October 1, 2018

1 Introduction

Vortices are ubiquitous in fluid dynamics. Geophysical examples include Gulf Stream rings in the ocean and the Red Spot in the Jupiter atmosphere. As vortices propagate they transport energy, material and fluid properties, such as temperature, along with them; during the decay, vortices deposit their energy, material and fluid properties into the surroundings and hence can be regarded as local sources. Agulhas Rings exemplify how vortices transport contribute to exchange across ocean basins (Goni et al., 1997): after detachment from the Agulhas Current, Agulhas Rings propagate northwestward and bring relatively warm and salty Indian ocean water into the South Atlantic Ocean and hence play an important role in the Atlantic Ocean heat and salt balance. However, satellite altimeter data revealed that many Agulhas Rings are destroyed around the Walvis Ridge region probably due to interaction with the bottom topography, leading to strong deposit of Indian ocean water locally (Schouten et al., 2000). Several laboratory and numerical studies support the idea that topography could strongly influence vortex trajectories and even lead to disintegration (Beismann et al., 1999; Van Geffen and Davies, 2000; Sansón, 2002). Adams and Flierl (2010) however showed that vortices with baroclinic structure could cross the topography relatively easily while the topography effect is mostly felt by the bottom layer. This study aims to examine the linear stability of vortices above a topography using a two-layer quasi-geostrophic model.

Linear as well as nonlinear instabilities of barotropic and baroclinic, quasi-geostrophic vortices were examined extensively by Flierl (1988). This study builds on Flierl (1988) to consider the effect of topography on vortices' linear stability.

2 Two-layer Quasi-geostrophic Contour Dynamics Model

In the contour dynamics model, a vortex is configured as concentric circular regions of piecewise uniform potential vorticity (PV; Fig. 1). At each PV discontinuity/jump (Δ_i, inward PV minus outward PV), we place a material contour that can be subject to displacement, η. The stability problem is then to consider under what conditions contour displacements (η_i) could grow. We embed the contour dynamics model into a two layer, equal depth (H), quasi-geostrophic model. In the upper layer, we impose two PV jumps at $r = r_1$ and $r = r_2$, and correspondingly there are two contours whose displacements are denoted by η_1 and η_2, respectively. In the lower layer, we place a top-hat topography (h_t) at $r = r_t = r_1$. The PV jump associated with the topography ($\frac{fh_t}{H}$) is denoted as Δ_t. Accordingly, we place a contour at the edge of topography, whose displacement is denoted by η_t. Note Δ_t could

be either positive or negative. Negative topography with a cyclonic vortex will give the same growth rates as positive topography with an anticyclone (i.e. "parity asymmetry" of quasi-geostrophic model).

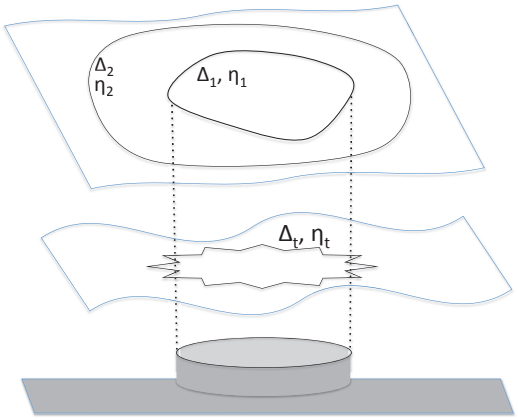

Figure 1: Schematic drawing of the experimental set up.

Then the system is governed by the two-layer quasi-geostrophic PV equation:

$$\begin{aligned} q_1 &= \nabla^2\psi_1 - F(\psi_1 - \psi_2) = \Delta_j \mathcal{H}(r_j + \eta_j - r) \\ q_2 &= \nabla^2\psi_2 + F(\psi_1 - \psi_2) + \Delta_t \mathcal{H}(r_t - r) = \Delta_t \mathcal{H}(r_t + \eta_t - r), \end{aligned} \tag{1}$$

where $j \in \{1, 2\}$ refers to the upper layer contour and repeated indices implies summation (i.e. Einstein notation is implied). Below we will use index $i \in \{1, 2, t\}$ to refer to all three contours. $2F = 2\frac{f^2}{g'H} = \frac{1}{R_d^2} = k_d^2$ with R_d and k_d denoting the Rossby Deformation Radius and its inverse. $\mathcal{H}(\cdot)$ denotes the Heaviside step function. Note $r_t = r_1$. Motivated by the Agulhas Ring example, we define our mean field (η_i=0) with no presence of topography (i.e. the vortex state before encountering any topography):

$$\begin{aligned} \nabla^2\overline{\psi}_1 - F(\overline{\psi}_1 - \overline{\psi}_2) &= \Delta_j \mathcal{H}(r_j - r) \\ \nabla^2\overline{\psi}_2 + F(\overline{\psi}_1 - \overline{\psi}_2) &= 0. \end{aligned} \tag{2}$$

The linearized perturbation field then follows:

$$\begin{aligned} \nabla^2\psi_1' - F(\psi_1' - \psi_2') &= \Delta_j \eta_j \delta(r_j - r) \\ \nabla^2\psi_2' + F(\psi_1' - \psi_2') &= \Delta_t \eta_t \delta(r_t - r). \end{aligned} \tag{3}$$

The kinematic condition at each contour closes the problem:

$$\frac{\partial \eta}{\partial t} + \frac{\overline{v}}{r}\frac{\partial \eta}{\partial \theta} = u' = -\frac{1}{r}\frac{\partial \psi'}{\partial \theta} \tag{4}$$

Hereafter, it's assumed that $\overline{(\cdot)}$ denotes mean field variable while lower case letter (prime dropped) denotes the perturbation field variable. Also, we use bold symbols to denote

a matrix and a vector that incorporates values for all three contours, for example, $\boldsymbol{\eta} = \begin{bmatrix}\eta_1 & \eta_2 & \eta_t\end{bmatrix}^T$, $\boldsymbol{\Delta} = \begin{bmatrix}\Delta_1 & \Delta_2 & \Delta_t\end{bmatrix}^T$.

We normalize lengths by r_1 so that Δ_1 and Δ_t are upper and lower layer PV jumps at $r = 1$ while Δ_2 is the PV jump at $r = b = \frac{r_2}{r_1}$. After normalization, F indicates the vortex size relative to the Rossby Deformation Radius, R_d. We also normalize the streamfunction ψ by some mean value such that the nondimensionalized version of above equations retains the form.

Assuming wave-like solutions, i.e. $\eta_i = \hat{\eta}_i e^{im(\theta - ct)}$ (hereafter hat $\hat{\cdot}$ is dropped and lower case letters indicate wave amplitude), we can formulate an eigenvalue problem for $\boldsymbol{\eta}$:

$$c\boldsymbol{\eta} = \boldsymbol{L}\boldsymbol{\eta}. \tag{5}$$

$\boldsymbol{L}$ contains Green's functions which are defined as

$$\nabla^2 G_{nl} + (-1)^n F(G_{1l} - G_{2l}) = \delta_{nl} \cdot \delta(r - r'); \qquad n \in \{1, 2\}; l \in \{1, 2\}. \tag{6}$$

where n indicates the layer for which we are calculating the response while l indicates the system with upper layer PV forcing ($l = 1$) or lower layer PV forcing ($l = 2$). Note that G_{ln} also depends on mode m due to the ∇^2 operator.

Noticing that the mean velocity field and the upper layer PV jumps are closely related (2), we can reduce the phase space dimension by constraining the upper layer mean velocity such that $\begin{bmatrix}\overline{v}_1(1) \\ \overline{v}_1(b)\end{bmatrix} = \begin{bmatrix}1 \\ 0\end{bmatrix}$. This choice corresponds to realistic scenarios where the vortex velocity at large distance reduces to background values. We can still vary the mean flow shear by varying the outer contour radius b. Although we constrain $\overline{v}_1$ or Δ_1 to be positive (i.e. cyclone), our conclusion on stability can equivalently apply to the anticyclone case by simply reversing the sign of topography Δ_t. Then parameters that remain to consider include F (or R_d), m, b and Δ_t (or $\frac{\Delta_t}{\Delta_1}$).

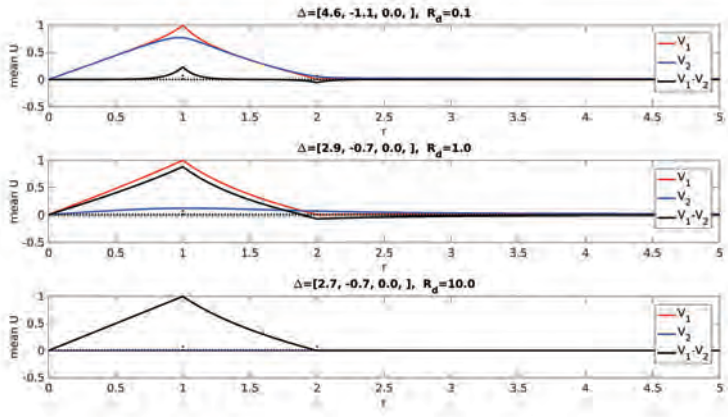

Figure 2: Mean velocity field for upper layer (red) and lower layer (blue) as well as the mean shear (black) for different R_d: $R_d = 0.1$ for top panel, $R_d = 1$ for middle panel and $R_d = 10$ for bottom panel.

Before we proceed to the stability analysis, it is worthwhile to take a look at the mean velocity field for different R_d (or F). As R_d denotes the Rossby Deformation Radius relative to the vortex size, increasing R_d or decreasing F should lead to weakening of layer coupling and vice versa. While the upper layer mean velocity is uniquely decided for given b, the lower layer mean velocity decreases remarkably as the layer coupling decreases (Fig. 2). This implies that varying R_d (or F) would dramatically change the lower layer wave phase speed and hence the stability.

3 Growth Rate

Let's first look at the $m = 1$ mode. When $m = 1$,

$$\boldsymbol{L} = \begin{bmatrix} -b\Delta_2 G_{11}(1,b) & b\Delta_2 G_{11}(1,b) & \Delta_t G_{12}(1,1) \\ \frac{\Delta_1}{b} G_{11}(1,b) & -\frac{\Delta_1}{b} G_{11}(1,b) & \frac{\Delta_t}{b} G_{12}(1,b) \\ \Delta_1 G_{21}(1,1) & b\Delta_2 G_{21}(1,b) & \Delta_t G_{22}(1,1) - \Delta_1 G_{12}(1,1) - b\Delta_2 G_{12}(1,b) \end{bmatrix}, \quad (7)$$

where $m = 1$ is implied in the Green's functions ($G_{11} = \frac{1}{2}[-I_m(k_d r_<)K_m(k_d r_>)) - \frac{1}{2m}(\frac{r_<}{r_>})^m]$ for example). It is easy to see that the matrix only admits real eigenvalues when $\Delta_t = 0$ (i.e. $m = 1$ stable) while topography could generally destabilize the $m = 1$ mode (Fig. 3). However, at small R_d limit or large F limit, only negative topography destabilizes the $m = 1$ mode whereas at large R_d limit, almost all topography destabilizes the $m = 1$ mode regardless of the sign and the magnitude. Also note that the growth rate becomes much smaller as R_d increases. We will offer an explanation for these features soon below.

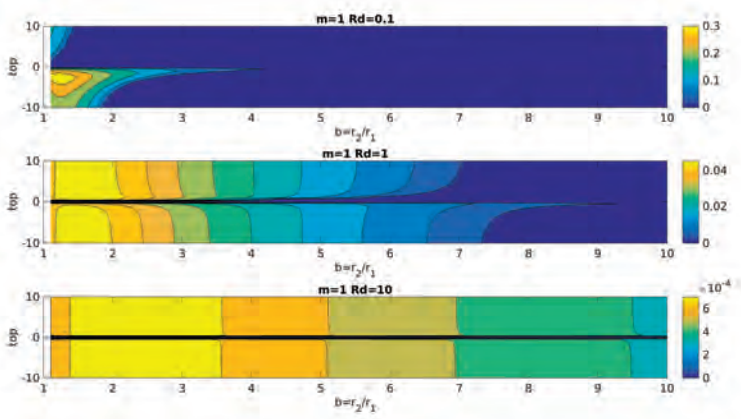

Figure 3: Growth rate of $m = 1$ mode as a function of outer contour radius b and topography Δ_t. The three panels are for different R_d: from top to bottom $R_d = 0.1, 1, 10$.

In comparison, $m = 2$ and higher modes are unstable even without topography. Notably, the instability region of $m = 2$ mode shrinks toward smaller b or larger mean horizontal shear such that most of the phase space to the right of $b = 2$ is stable (Fig. 4). Higher mode growth rates are similar to the $m = 2$ mode except the unstable region further shrinks toward smaller b values (not shown). Due to the successive shrinking of unstable regions

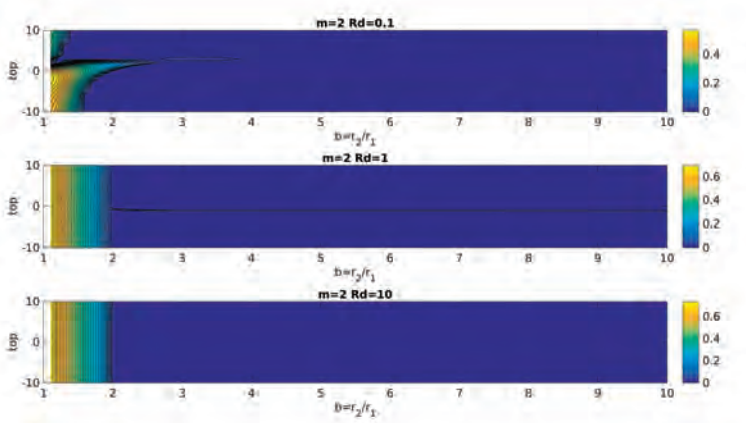

Figure 4: Similar to Fig. 3 except for $m = 2$.

in higher modes, $m = 1$ is almost the only mode that could be destabilized by topography once $b > 2$. In a nonlinear simulation for the part of phase space where linear stability analysis only renders $m = 1$ unstable, we find that the $m = 1$ mode (the "shift mode") is indeed destabilized first while higher modes get excited later (Fig. 5). Another feature that deserves attention is the narrow unstable arm that extends toward the right from $b \approx 2$ for $R_d \geq\sim 1$(for R_d=10 in Fig. 4, the unstable arm breaks into discrete patches and is not revealed in the plot). This unstable arm turns out to be a different instability regime from the bulk and will be discussed in details in section 4. Lastly, we observe that the growth rate for higher modes is less sensitive to the topography at large R_d while more sensitive to the topography at small R_d, similar as we noted for the $m = 1$ model.

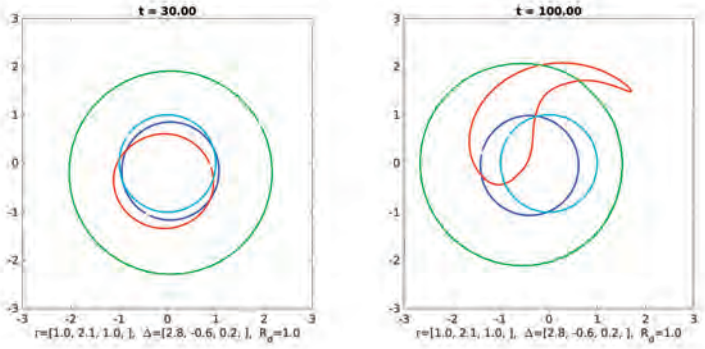

Figure 5: A nonlinear calculation for the case of $b = 2.1$ and $R_d = 1$. The blue and green contours are associated with the upper layer PV jump while the red contour is associated with the lower layer PV jump. The cyan contour denotes the topography, which is fixed. Run time is labelled above each plot.

Next, we offer an explanation for features described above, especially for the differing

topography influences at small versus large R_d values. Because all modes possess similar transition from small R_d to large R_d, we will focus on $m = 1$ mode. The idea is to employ perturbation method, that is, expand $\boldsymbol{L}$, $\boldsymbol{\eta}$ and c as a power of some small parameter ϵ and then match the order of ϵ. For small F limit, $\epsilon = F$ we have $c = c_0 + \epsilon c_1 + \epsilon^2 c_2 + \ldots$ and similarly for $\boldsymbol{L}$ [1] and $\boldsymbol{\eta}$.

3.1 Large R_d, small F limit

When we take $F \to 0$ or $R_d \to \infty$, the two layers become nearly independent and we are left with two uncoupled, barotropic layers. The zero-th order $\boldsymbol{L}$ matrix is

$$\boldsymbol{L_0} = \begin{bmatrix} \frac{1}{1-b^2} & -\frac{1}{1-b^2} & 0 \\ \frac{1}{1-b^2} & -\frac{1}{1-b^2} & 0 \\ 0 & 0 & -\frac{\Delta_t}{2} \end{bmatrix}. \tag{8}$$

One eigenvalue is $-\frac{\Delta_t}{2}$ with corresponding eigenvector $\begin{bmatrix} 0 & 0 & 1 \end{bmatrix}^T$, which is clearly a pure lower layer eigenmode, actually a topographic Rossby wave. In the absence of mean velocity (Fig. 2), the topographic Rossby wave propagates with shallow water (high PV) on the right, thus positive topography yield clockwise waves or negative phase speed and vice versa. Further, topographic Rossby wave phase speed is proportional to the magnitude of topography, consistent with the eigenvalue of $-\frac{\Delta_t}{2}$. The other eigenvalue 0 is degenerate (i.e. 0 is a double root of the characteristic equation), the corresponding right eigenvector ($\boldsymbol{\eta}_0$) and left eigenvector ($\boldsymbol{\alpha}_0$) have no projection in the lower layer:

$$\boldsymbol{\eta}_0 = \begin{bmatrix} 1 \\ 1 \\ 0 \end{bmatrix}, \boldsymbol{\alpha}_0 = \begin{bmatrix} 1 \\ -1 \\ 0 \end{bmatrix}. \tag{9}$$

Clearly, this eigenpair is a pure upper layer eigenmode. Biebuyck (1986) showed that when $\overline{v}_1(b) \neq 0$ the degenerate eigenvalue 0 manifests as two distinguishing eigenvalues: eigenvalue 0 corresponds to displacing the upper layer two contours by the same amount in the same direction (i.e. displacing the whole vortex trivially) while the other non-zero eigenvalue ($\frac{\overline{v}_1(b)}{b}$) corresponds to a rotation mode resulting from displacing the upper layer two contours relative to each other (i.e. has some amplitude in $\begin{bmatrix} 1 & -1 & 0 \end{bmatrix}^T$). Further, the rotation mode was shown to rotate with a radius $R \propto \frac{1-\overline{v}_1(b)}{\overline{v}_1(b)}$, which clearly turns into a translation mode when $\overline{v}_1(b) = 0$, corresponding to our degenerate 0 eigenvalue.

As F increases or R_d decreases, the two layers couple weakly and we expect the upper layer mode to become unstable; that is, we expect the eigenvalue 0 to split into a complex conjugate pair. Thus, we look for the first order correction to the 0 eigenvalue. The first order equation reads as

$$\boldsymbol{L}_0\boldsymbol{\eta}_1 + \boldsymbol{L}_1\boldsymbol{\eta}_0 = c_0\boldsymbol{\eta}_1 + c_1\boldsymbol{\eta}_0 = c_1\boldsymbol{\eta}_0, \tag{10}$$

[1] As the reader may note that Δ_1 and Δ_2 also depend (weakly) on R_d or F, we actually consider $\frac{\boldsymbol{L}}{\Delta_1}$ and expand $\frac{\Delta_2}{\Delta_1}$. The instability conditions are the same and the results are similar.

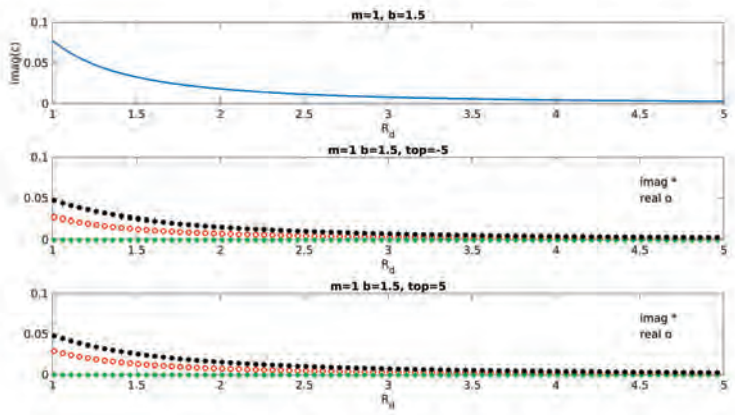

Figure 6: Compare the growth rate, i.e. the imaginary part of phase speed c from first order correction (top panel) and from direct numerical calculation ("$*$" in bottom two panels). Note the x-axis starts from $R_d = 1$. $\Delta_t = \pm 5$ is used in numerical calculation. $b = 1.5$ is used in all three panels.

where $\boldsymbol{L_1}$ is the first order correction for $\boldsymbol{L}$. Focusing on the lower layer contour component (i.e. the third row), we have

$$-\frac{\Delta_t}{2}\boldsymbol{\eta}_1(3) + \boldsymbol{L_1}(3,1)\boldsymbol{\eta}_0(1) + \boldsymbol{L_1}(3,2)\boldsymbol{\eta}_0(2) = 0, \tag{11}$$

where the first term indicates wave self-propagation due to PV anomalies associated with the topography while the last two terms on the left hand side indicate wave propagation due to upper layer PV anomalies (i.e. upper layer contour displacements). It follows from (11) that a wave at the lower layer contour is required to remain stationary (i.e. zero phase speed) in the first order correction, which allows it to phase lock with the upper layer mode, whose phase speed is 0 on the zero-th order, and hence enables perturbation growth. Note this sets $\Delta_t\boldsymbol{\eta}_1(3)$ to be a constant (up to a weak dependence on R_d), which is crucial in explaining the insensitivity of growth rate to topography at large R_d (see below). Of course, $\boldsymbol{\eta}$ as an eigenmode which only indicates the relative displacement of contours and what we really meant is that $\Delta_t\frac{\boldsymbol{\eta}_1(3)}{\boldsymbol{\eta}_1(1)}$ is a constant (up to a weak dependence on R_d). Projecting the first order equation onto the corresponding eigevector $\boldsymbol{\eta}_0$ yields

$$c_1 = \frac{1}{1-b^2}[\eta_1(1) - \eta_1(2)]. \tag{12}$$

That is, the first order correction to the 0 eigenvalue is proportional to the relative displacement of upper layer two contours, suggesting an emergence of a weak rotation mode in view of the previous discussion.

As in the usual procedure, we project the first order equation onto the left eigenvector $\boldsymbol{\alpha}_0$, which however vanishes trivially. Thus it is necessary to go to the second order and we get a quadratic equation for c_1:

$$c_1^2 - [\boldsymbol{L}_1(1,1) - \boldsymbol{L}_1(2,1)]c_1 + \frac{1}{b^2-1}\boldsymbol{\eta}_1(3)[\boldsymbol{L}_1(1,3) - \boldsymbol{L}_1(2,3)] = 0, \tag{13}$$

which clearly admits complex roots and hence unstable modes. Note that $\boldsymbol{L_1}(1,3)$ and $\boldsymbol{L_1}(2,3)$ describe Δ_t influence on upper layer contour displacements and are both proportional to Δ_t. As we noted above $\Delta_t \boldsymbol{\eta}_1(3)$ is a constant (up to a weak dependence on R_d), c_1 thus turns out to be independent of Δ_t, explaining the feature seen in Fig. 3 at large R_d. However, it is clear from (13) that there will be no complex roots if there is no topography (i.e. the constant term is zero). The imaginary part of c ($c \approx F c_1$ as $c_0 = 0$) calculated from (13) is compared with direct numerical calculation in Fig. 6. It seems that the first order correction yields good approximation for $R_d > 1.5$.

Let us summarize the physics by considering a vortex with net vorticity (i.e. $\overline{v}_1(b) \neq 0$). The eigenvalue variation for the case of $\overline{v}_1(b) = 0.2$ is partially shown in Fig. 7 (the $-\frac{\Delta_t}{2}$ eigenvalue is not shown due to the y-axis scale). At the large R_d limit, there are two distinguishing eigenvalues: 0 and $\frac{\overline{v}(b)}{b}$. As R_d decreases, it appears that the zero eigenvalue increases toward the non-zero eigenvalue; when the two eigenvalues merge, the modes phase lock and instability yields (Schmidt and Johnson, 1997). Physically, instability arises as the trivial "shift" mode turns into a rotation mode under the influence of topography and phase lock with the original rotation mode (the translation mode when $\overline{v}_1(b) = 0$). Apparently the "shift" mode is forced to rotate in the same sense as the net vorticity (i.e. $\overline{v}_1(b)$) thus the zero eigenvalue increases for both signs of topography, which explains the growth rate being insensitive to the sign of the topography at large R_d (Fig. 3). Note that the increase in 0 eigenvalue is very slow such that the merging actually happens at $R_d < 1$. In the $\overline{v}_1(b) = 0$ case, the merging would happen right away as the two eigenvalues are same to start with. In short, the appearance of topography is crucial to rotate the "shift mode," yet the sign or magnitude of the topography does not influence the growth rate because the contour displacements adjust accordingly to match the zero phase speed constraint. In the end the growth rate is solely decided by the coupling strength, i.e. R_d or F.

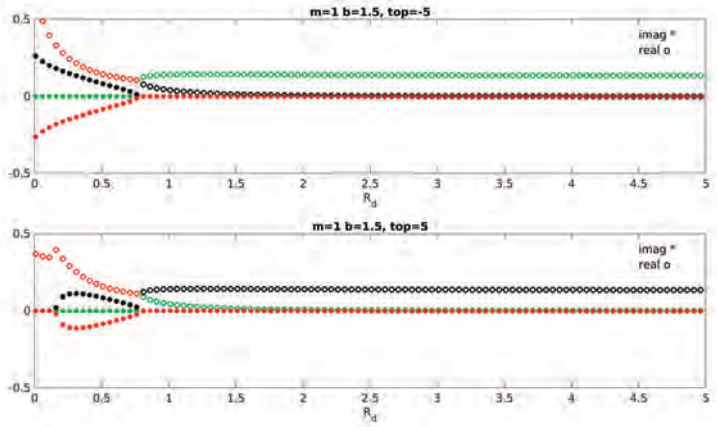

Figure 7: Growth rate for a vortex whose upper layer mean velocity is $[1, 0.2]$. Note the x-axis starts from $R_d = 0$. "$\circ$" denotes real part while "$*$" denotes imaginary part. $\Delta_t = \pm 5$ and $b = 1.5$ are used.

Now we briefly comment on the $m = 2$ and higher modes by analogy. A single-layer, barotropic vortex can have strong $m = 2$ and higher instability from coupling of the upper

layer two contours with opposite PV jumps. This corresponds to the instability of $m = 2$ and higher modes at large R_d limit (and the instability at small R_d limit with $\Delta_t = 0$). As R_d decreases, the influence of topography is weak such that the original large growth rate is barely changed. Therefore, the growth rate is essentially independent of topography (Fig. 4).

3.2 Small R_d, large F limit

When we take $F \to \infty$ or $R_d \to 0$, the two layers are strongly coupled such that we essentially have a single barotropic layer. Instead of employing perturbation method, i.e. expanding $\boldsymbol{L}$ in terms of $\frac{1}{F}$, we proceed with a slightly different approach to reveal more physics.

Define $\phi = \psi_1 - \psi_2$: Then (1) can be rewritten as

$$\begin{aligned} \nabla^2\psi_2 + F\phi &= \Delta_t\mathcal{H}(r_t + \eta_t - r) - \Delta_t H(r_t - r) \\ \nabla^2\phi - 2F\phi &= \Delta_j\mathcal{H}(r_j + \eta_j - r) - \Delta_t\mathcal{H}(r_t + \eta_t - r) + \Delta_t\mathcal{H}(r_t - r) \end{aligned} \tag{14}$$

The perturbation field of $O(1)$ reads:

$$\begin{aligned} -2F\phi &= \Delta_j\eta_j\delta(r_j - r) - \Delta_3\eta_3\delta(r_3 - r) \\ \nabla^2\psi_2 &= \frac{1}{2}\Delta_j\eta_j\delta(r_j - r) + \frac{1}{2}\Delta_3\eta_3\delta(r_3 - r). \end{aligned} \tag{15}$$

The $\boldsymbol{L}$ matrix for the zero-th order problem becomes

$$\boldsymbol{L_0} = \begin{bmatrix} \frac{1}{1-b^2} & -\frac{1}{1-b^2} & -\frac{\Delta_t}{4} \\ \frac{1}{1-b^2} & -\frac{1}{1-b^2} & -\frac{\Delta_t}{4b^2} \\ \frac{b^2}{1-b^2} & -\frac{1}{1-b^2} & 1 - \frac{\Delta_t}{4} \end{bmatrix}. \tag{16}$$

The eigenvalues are

$$\lambda_1 = 1, \quad \lambda_{2,3} = \pm\frac{\sqrt{\frac{\Delta_t}{4}(\frac{\Delta_t}{4}b^2 + 4)} - \frac{\Delta_t}{4}b}{2b}. \tag{17}$$

The eigenvector corresponding to $\lambda_1 = 1$ is $\begin{bmatrix} -\frac{\Delta_t}{\Delta_1} & 0 & 1 \end{bmatrix}^T$. Clearly this eigenmode is associated with the tilting of the inner column such that the PV anomalies at upper layer and lower layer are of same magnitude. Eigenvalues $\lambda_{2,3}$ could be a complex conjugate pair when $\frac{\Delta_t}{4}(\frac{\Delta_t}{4}b^2 + 4) < 0$, corresponding to an unstable mode. The corresponding eigenvector reveals that the inner column is displaced as a whole (i.e. $\eta_1 = \eta_t$). The range of topography that could destabilize the mode thus corresponds to configurations that waves on the inner contour and outer contour could phase lock.

4 Energetics

In this section we examine the energy source for modes growth, i.e. contrast barotropic conversion versus baroclinic conversion. The eddy kinetic energy (EKE) and eddy available

potential energy (EAPE) growth in the quasi-geostrophic two-layer model are governed by

$$\begin{aligned}\frac{1}{H}\frac{\partial}{\partial t}K' &= \int \overline{v}_1 u_1 \zeta_1 + \int \overline{v}_2 u_2 \zeta_2 + \frac{f}{H}\int w(\psi_1 - \psi_2) \\ \frac{1}{H}\frac{\partial}{\partial t}A' &= \frac{F}{2}\int (\overline{v}_1 - \overline{v}_2)(u_1 + u_2)(\psi_1 - \psi_2) - \frac{f}{H}\int w(\psi_1 - \psi_2)\end{aligned} \tag{18}$$

while the total eddy energy growth is obtained by adding the above two equations,

$$\frac{1}{H}\frac{\partial}{\partial t}(K' + A') = \sum_i \int \overline{v}_i u_i q_i. \tag{19}$$

Barotropic conversion refers to $\sum_i \int \overline{v}_i u_i \zeta_i = \sum_i \int \overline{v}_i u_i q_i - \frac{F}{2}\int (\overline{v}_1 - \overline{v}_2)(u_1 + u_2)(\psi_1 - \psi_2)$ while baroclinic conversion refers to $\frac{F}{2}\int (\overline{v}_1 - \overline{v}_2)(u_1 + u_2)(\psi_1 - \psi_2)$.

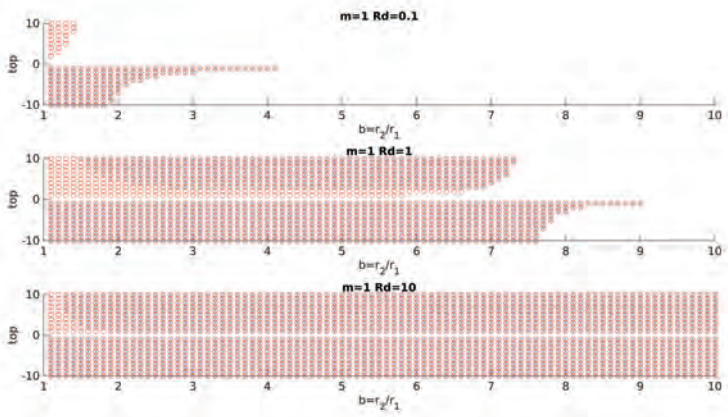

Figure 8: Energetics of $m = 1$ mode as a function of outer contour radius b and topography Δ_t. Circles are filled with blue crosses when baroclinic conversion happens while circles are painted red when barotropic conversion dominates baroclinic conversion. The three panels are for different R_d: from top to bottom $R_d = 0.1, 1, 10$.

As shown in Fig. 8, barotropic conversion dominates over baroclinic conversion throughout the $\{\Delta_t, b, R_d\}$ phase space. We confirmed the dominance of barotropic conversion for an arbitrarily chosen configuration with nonlinear calculation. The same is true for $m = 2$ and higher modes except at the previously noted narrow arm region (Fig. 9), where baroclinic conversion dominates (barotropic conversion still takes place). This baroclinic conversion dominant region lying in the negative topography quadrant is consistent with the traditional notion that baroclinic conversion happens when upper layer and lower layer mean PV gradient (jump) are of opposite sign. We also note that only when the upper layer contour separation is large enough will baroclinic conversion dominate. Consistently, when the topography is of same sign as upper layer inner contour PV jump and the upper layer contour separation is small, baroclinic conversion vanishes and we have pure barotropic conversion.

We suspect that the the general dominance of barotropic conversion is due to the strong mean horizontal shear. We first tried to remove the PV jump at the upper layer outer

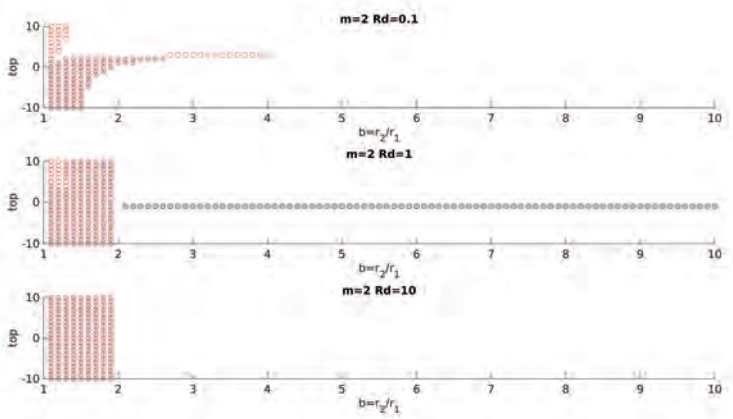

Figure 9: Same as Fig. 8 except for $m = 2$. Note there are discrete patches of baroclinic conversion dominant instability for $R_d = 10$ but not revealed by our integer topography step.

contour, yet still observe the barotropic conversion dominance. Further noticing that there is horizontal shear inherent in the circular contour curvature, we consider the piece-wise uniform quasi-geostrophic jet setup (Meacham, 1991), where the vortex radius is relaxed to infinity. The rectilinear setup does provide crucial insight into the energetics discussed above.

4.1 Rectilinear case

We retain our configuration of two contours in the upper layer while one contour in the lower layer as before and merely let the contour radius goes to infinity. However, the system is now set up in the Cartesian coordinate: we align the x-axis along the unperturbed contour and put the origin on the upper layer inner contour (i.e. $y_1 = 0$), then the coordinate of upper layer outer contour is denoted as $y_2 > 0$. Same as before, the topography is right below the inner contour (i.e. $y_t = 0$). The PV jumps associated with the three contours are still denoted as Δ_1, Δ_2 and Δ_t. Then (1) modifies to

$$\begin{aligned} \nabla^2\psi_1 - F(\psi_1 - \psi_2) &= \Delta_j \mathcal{H}(y - \eta_j) \\ \nabla^2\psi_2 + F(\psi_1 - \psi_2) &= \Delta_t \mathcal{H}(y - \eta_t) - \Delta_t \mathcal{H}(y). \end{aligned} \tag{20}$$

The mean field is still defined without topography. But we have to specify the mean field PV jumps differently now: the mean PV jump at $y_1 = 0$ (i.e. Δ_1) is set to be 1. We vary Δ_2 to consider two configurations with different horizontal shear strength: one case with $\Delta_2 = 0$ while the other case with $\Delta_2 = -1$. In addition, lengths are now normalized with respect to the Rossby Deformation Radius R_d. We further arbitrarily set $y_2 = 2$ (i.e. $2R_d$) in the following results as varying y_2 does not change our conclusion. Then we can obtain an eigenvalue problem in the exactly same way as in the vortex case.

The mean velocity field for the two cases are shown in Fig. 10. As expected, the horizontal shears in both layers are enhanced with the addition of an opposite sign PV

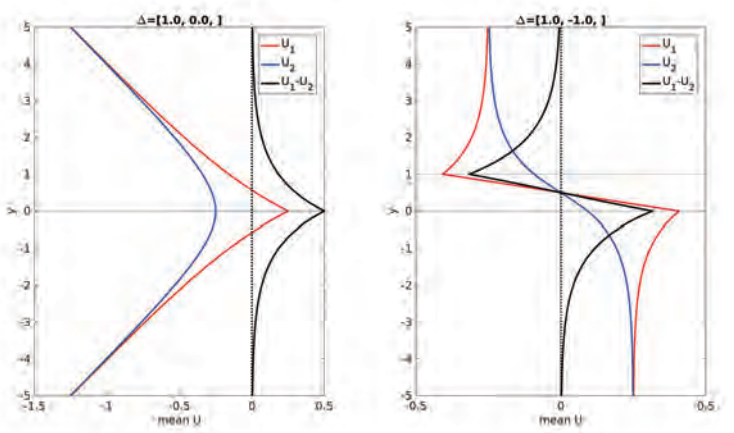

Figure 10: Mean velocity for the two rectilinear cases: (left) $\Delta_2 = 0$ and (right) $\Delta_2 = -1$. The red, blue and black curves are for the upper layer mean velocity, lower layer mean velocity and mean velocity vertical shear. Locations of upper layer PV jumps are labelled by horizontal dotted line.

jump (i.e. Δ_2). Correspondingly, the growth rate in the two cases exhibit different regimes (Fig. 11). For $\Delta_2 = 0$, there exist local growth rate maxima which shift toward shorter wave lengths as the topography is enhanced. The apparent quantization arises from the coupling between upper layer and lower layer waves. This regime of instability is dominated by baroclinic conversion while barotropic conversion still takes place (Fig. 11). The ratio of barotropic conversion and baroclinic conversion, $\frac{(\mu-k)(\mu+k+\gamma)}{\gamma^2} - 1$, is clearly less than 1, where k is the wavenumber, $\gamma^2 = 2F$ and $\mu^2 = k^2 + \gamma^2$. As the mean horizontal shear increases due to the addition of an opposite sign PV jump ($\Delta_2 = -1$), the baroclinic conversion dominant regime persists while a new regime at larger wave scales appear. In this new regime, barotropic conversion dominates. Comparison of the two rectilinear cases clearly indicates that horizontal shear enhancement would promote barotropic conversion dominance. The coexistence of a baroclinic conversion dominant regime and a barotropic conversion dominant regime is also reminiscent of the vortex case (with relatively large R_d).

5 Conclusion

We examine the linear stability of vortices above a topography with a two-layer, quasi geostrophic contour dynamics model. It is found that topography exerts strong influence on the vortex when the two layers are strongly coupled. Further when the two layers are weakly coupled, topography could destabilize the $m = 1$ mode in particular through triggering the "shift mode" to rotate. For most of the instability growth, barotropic conversion dominates baroclinic conversion. Meanwhile, there also exists a narrow region in the phase space where baroclinic conversion dominates. This regime corresponds to opposite PV gradients in the upper layer and lower layer and relatively weak horizontal shear (i.e. relatively large contour separation in the upper layer). We then show that there is close analog in the rectilinear set up where the baroclinic conversion dominant region coexists with the barotropic

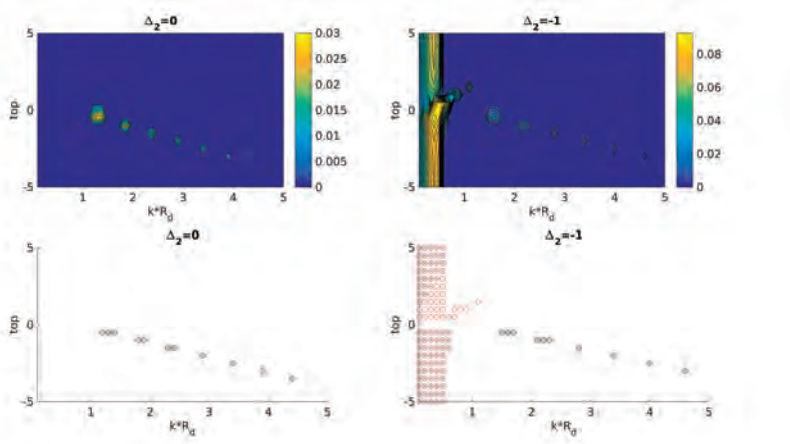

Figure 11: Growth rate (top) and energetics (bottom) for the two rectilinear cases: (left) $\Delta_2 = 0$ and (right) $\Delta_2 = -1$. X-axis is wavenumber normalized by R_d while Y-axis is topography. $y_2 = 2$ is used. Clearly, varying y_2 in the $\Delta_2 = 0$ case does not make any difference while increasing y_2 in the $\Delta_2 = -1$ case merely shrinks the instability band close to $kR_d = 0$ and shifts growth rate local maxima.

conversion dominant region, the latter of which only arises when the horizontal shear is strong enough.

Our results are generally consistent with earlier studies about eddies crossing a topography (Beismann et al., 1999; Van Geffen and Davies, 2000; Sansón, 2002; Adams and Flierl, 2010). We expect our general conclusions extend to various layer depth ratios and topography shapes but further study is required to fully address these issues.

Acknowledgement

I greatly thank Glenn Flierl for advising me and inspiring me throughout the summer. Glenn is a great advisor and a great friend. I also thank Joe Pedlosky, Ian Hewitt, Thomas Evans and others for discussions with me.

References

Adams, D. K. and Flierl, G. R. (2010). Modeled interactions of mesoscale eddies with the east pacific rise: Implications for larval dispersal. *Deep Sea Research Part I: Oceanographic Research Papers*, 57(10):1163–1176.

Beismann, J.-O., Käse, R. H., and Lutjeharms, J. R. (1999). On the influence of submarine ridges on translation and stability of agulhas rings. *Journal of Geophysical Research: Oceans*, 104(C4):7897–7906.

Biebuyck, G. L. (1986). Self propagation of a barotropic circular eddy. *WoodsHole Oceanographic Institution Tech.Rep*, WHOI-86-45:193–197.

Flierl, G. R. (1988). On the instability of geostrophic vortices. *Journal of fluid mechanics*, 197:349–388.

Goni, G. J., Garzoli, S. L., Roubicek, A. J., Olson, D. B., and Brown, O. B. (1997). Agulhas ring dynamics from topex/poseidon satellite altimeter data. *Journal of Marine Research*, 55(5):861–883.

Meacham, S. (1991). Meander evolution on piecewise-uniform, quasi-geostrophic jets. *Journal of physical oceanography*, 21(8):1139–1170.

Sansón, L. Z. (2002). Vortex–ridge interaction in a rotating fluid. *Dynamics of atmospheres and oceans*, 35(4):299–325.

Schmidt, G. and Johnson, E. (1997). Instability in stratified rotating shear flow along ridges. *Journal of marine research*, 55(5):915–933.

Schouten, M. W., Ruijter, W. P., Leeuwen, P. J., and Lutjeharms, J. R. (2000). Translation, decay and splitting of agulhas rings in the southeastern atlantic ocean. *Journal of Geophysical Research: Oceans*, 105(C9):21913–21925.

Van Geffen, J. and Davies, P. (2000). A monopolar vortex encounters a north–south ridge or trough. *Fluid Dynamics Research*, 26(3):157.

Turbulent Point Source Plumes in Confined, Rotating Environments

Christopher J. Howland

September 2018

1 Introduction

Turbulent buoyant plumes are prolific in geophysical and environmental flows. They exist over a wide range of scales, from the small wisps of smoke rising above a fire to the massive ash clouds from the eruption of a volcano. On the largest geophysical scales, both rotation and stratification affect the development of a plume. In some cases, plumes can be produced in regions of low stratification, and so rotation is thought to have a more dominant effect on their development. For example, plumes of dense water can be formed at high latitudes in regions of weak stratification due to sea ice formation [16]. Astrophysicists have also hypothesised that plumes produced at the base of the well-mixed subsurface ocean of Europa are affected strongly by rotation [11].

In the case of sea ice formation, one can think of multiple sources of dense water forming in the marginal ice zone which can lead to nearby plumes interacting with each other. The combined effects of interaction of the plumes and rotation on entrainment will control the amount of mixing that the dense water undergoes on its journey to the bottom of the ocean. The properties of this bottom water are thus closely linked to the plume dynamics, and understanding these external effects on the plume is important for gaining insight into abyssal water formation which helps drive the meridional overturning circulation.

Two previous research projects at the WHOI GFD Program have used laboratory experiments to investigate these problems. In 2009 Yamamoto, Cenedese and Caulfield performed experiments with a pair of axisymmetric, turbulent plumes in a rotating environment and varied the separation distance of the plume sources as well as the rotation rate. They focused on the early time behaviour of the plume and observed qualitative differences in the flow depending on whether the plumes merged before being affected by rotation or vice versa [22]. If the plumes merged at early times, a single cyclonic vortex was generated in the ambient fluid, whereas two vortices appeared if the rotation rate was sufficiently high.

The second project took a more systematic approach in order to quantify the effect on entrainment of the interaction of two plumes in a non-rotating frame. Cenedese and Linden [4] carried out experiments in 2013 based on the ventilated filling box technique first implemented by Baines (1983) [1]. They formulated and verified a simple model based on conservation of mass and self-similarity of merged plumes to compare the "effective" entrainment of the merging plumes against the entrainment that would occur from two independent plumes with the same source properties.

The development of a plume can also be affected by the presence of a nearby vertical boundary. The interaction of point source plumes with adjacent walls has been studied less than merging plumes, but still has important geophysical applications [5, 7, 19]. Following research on turbulent wall jets [14], turbulent plumes are expected to become asymmetric, spreading more across the wall than away from it. This is due to the creation of streamwise vorticity near the boundary when the no-slip condition is enforced. The effect of rotation on this problem has not yet been tested and is currently unknown.

The aim of this study is to use a similar type of filling box experiment to that in [4] to precisely quantify the effect of rotation on the entrainment of turbulent plumes. However, we find that the lower boundary of the tank has a strong influence on the development of the filling box, making the measurement of entrainment from this method practically impossible. We also perform further experiments to investigate the effect of rotation on point source wall plumes, using the development of the plume shape to measure effects on dispersion and identify mechanisms by which the plume may *detrain* fluid.

The rest of this report is organised as follows. In section 2 the classical theory of point source, axisymmetric plumes will be introduced, followed by a brief overview of the existing literature on the effects of rotation and studies of turbulent wall plumes. We will then outline the experimental setups used for the various experiments in section 3, and delve deeper into the issues that hindered the filling box experiments. The results of the wall plume experiments will then be presented in section 4, before we finally discuss the implications of our findings and the potential avenues for future research in section 5.

2 Theory and Literature

2.1 Classical plume theory

Many developments in the field of turbulent plumes have stemmed from the groundbreaking paper of Morton, Taylor and Turner (1956) [18]. They considered the axisymmetric, statistically steady state with plume radius $b(z)$ arising from a maintained source of constant buoyancy flux and made use of four key assumptions:

- self-similarity: the profiles of vertical velocity $u(z)$ and buoyancy $g'(z) = g(\rho_a - \rho(z))/\rho_0$ are the same at all heights;
- linear entrainment: the rate of entrainment of fluid is proportional to the vertical velocity at all heights ($u_e = \alpha u$);
- incompressibility: fluid does not change volume on mixing;
- the Boussinesq approximation holds: local variations in density are small compared to some reference density ($\rho - \rho_a \ll \rho_0$).

Using these assumptions, and further assuming 'top-hat' profiles for u and g', we can write down the following equations for conservation of volume, momentum and buoyancy

$$Q = \pi b^2 u, \qquad \frac{dQ}{dz} = 2\pi b\alpha u = 2\pi^{1/2}\alpha M^{1/2}, \tag{1}$$

$$M = \pi b^2 u^2, \qquad \frac{dM}{dz} = \pi b^2 g' = \frac{BQ}{M}, \tag{2}$$

$$B = \pi b^2 u g' \qquad \frac{dB}{dz} = 0, \tag{3}$$

where Q, M and B are volume flux, momentum flux and buoyancy flux. In the final equation, we have also assumed that the ambient fluid is homogeneous, i.e. ρ_a does not vary with height. These equations can be easily solved, revealing that the plume radius takes the form $b = \frac{6}{5}\alpha z$. The time-averaged shape of a plume therefore provides a measure of the entrainment coefficient α, which decades of experiments have found to be approximately constant and equal to 0.1 ± 0.01 [21].

An alternative method for inferring the entrainment rate of a turbulent plume was devised by Baines and Turner in 1969 [2]. As shown in figure 1, dense plume fluid injected from a point source will descend to the bottom of an enclosed container, spread out and form a front which will rise as the plume fluid fills the tank. By conservation of mass, the net volume flux at the height of the front must be zero and hence

$$Q = (A - A_p)w_f. \tag{4}$$

Here A and A_p are the cross-sectional areas of the tank and the plume, respectively, w_f is the speed of the front, and Q is the volume flux of the plume. It is typically assumed that $A_p \ll A$, so Q can be computed just from measurements of the front speed. The

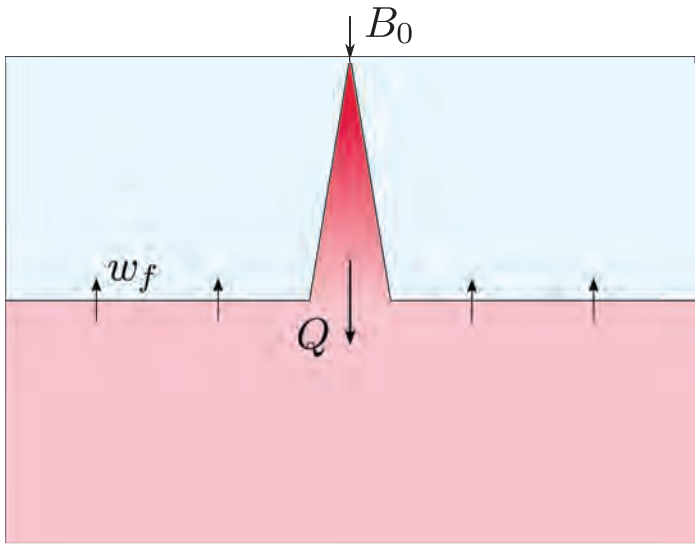

Figure 1: Schematic of a filling box experiment with a source of constant buoyancy flux B_0 as described in [2].

entrainment coefficient α can then be inferred from this measurement by comparing the observed variation of the volume flux with the prediction from classical theory:

$$Q = \left(\frac{9}{10}\right)^{1/3} \frac{6}{5}\pi^{2/3}\alpha^{4/3}B_0^{1/3}z^{5/3}. \tag{5}$$

Baines later improved the accuracy of measuring the volume flux in this way by ventilating the tank [1]. This was done by adding a source of constant volume flux to the upper ambient fluid and pumping fluid out of the bottom of the tank at the same rate. In this setup, the interface between the ambient fluid and the mixed fluid will move to and remain at an equilibrium height where the volume flux in the plume is precisely the volume flux being added to and removed from the tank. By adjusting the rate at which fluid is pumped in or out of the tank, it is possible to accurately measure the volume flux in the plume at all heights. One further advantage of this technique is that the two-layer stratification can be set up before the plume is running, resulting in a sharper front. This type of experiment was used by Cenedese and Linden in their study on merging plumes [4].

2.2 The effects of rotation

Many simple results in classical plume theory can be obtained by dimensional analysis, noting that the only conserved quantity is the buoyancy flux B_0, which has dimensions L^4T^{-3}. The steady state plume dynamics are well described by scaling laws that come about from combining B_0 and the local height z. When ambient rotation is non-negligible, a new timescale is introduced to the problem, namely the inertial period of rotation $T_f = 2\pi/f$ where f is the Coriolis parameter. The introduction of f also suggests the importance of a new length scale $L_f = (B_0/f^3)^{1/4}$. Identifying how these scales affect the dimensional analysis requires experimental data. The Coriolis force will also strongly affect the plume dynamics directly as follows. For a non-rotating plume, entrainment draws ambient fluid towards the plume. When rotation is added, the Coriolis force acts on this motion in the ambient fluid, deflecting the flow into a cyclonic circulation (if $f > 0$) around the plume.

A number of experimental and numerical studies have been performed to gain insight on the effect of rotation on turbulent plumes and quantify the importance of these processes and scales [8, 9, 10, 11, 12, 20, 22]. Of the laboratory studies, Fernando, Chen and Ayotte (1998) were the first to investigate the development of a plume in a rotating but unstratified fluid [9]. They found that rotational effects become important after a time $0.764T_f$, before which the plume behaves as if no rotation is present. After $1.75T_f$, the lateral growth of the plume is restricted and the plume reaches a maximum width of $b_c \approx 2.35L_f$. This restriction implies that there is *no* entrainment below a certain height of the plume, which we had hoped to verify with our own experiments.

When the plume reached the bottom of the tank, Fernando et al. observed more interesting behaviour. As plume fluid continues to be injected, the plume spreads radially inducing an anticyclonic circulation near the base of the tank. After some time, this eddy reaches a size where it becomes baroclinically unstable and sheds from the main structure of the plume. This behaviour was also observed in an earlier study where the ambient was stratified, and the plume spread out above the neutral height rather than the solid boundary [12].

Lateral deflection of the plume was also observed, but not explained in the Fernando et al. study. It is now thought that the deflection of the plume is in fact regular, anticyclonic precession [8, 10]. Frank et al. (2017) performed experiments with a plume in a rotating, homogeneous ambient for a wide range of buoyancy fluxes, rotation rates, and water depths, finding that after one rotation period the plume moves about the vertical axis at a precession frequency of $\omega \approx 0.2f$. Fascinatingly, this frequency appears to be independent of the source size, buoyancy flux or water depth, implying that if rotation is present, it will always affect the dynamics.

2.3 Wall plumes

Turbulent wall plumes are often studied in the context of natural ventilation or melting glaciers [15, 17]. However, these papers usually consider the effect of a vertically distributed or planar source of buoyancy rather than a point source. Motivated by the plumes that rise up from subglacial meltwater channels along the side of a glacier, recent studies have modified the classical plume equations (1)-(3) to account for the effect of an adjacent wall [5, 7, 19]. By modifying the geometry to a half-cone and adding a quadratic drag force along the wall, the plume equations become

$$Q = \frac{\pi b^2}{2} u, \qquad \frac{dQ}{dz} = \pi b \alpha u = \sqrt{2\pi}\alpha M^{1/2}, \tag{6}$$

$$M = \frac{\pi b^2}{2} u^2, \qquad \frac{dM}{dz} = \frac{\pi b^2}{2} g' - 2c_d b u^2 = \frac{BQ}{M} - \frac{2^{3/2} c_D}{\sqrt{\pi}} \frac{M^{3/2}}{Q}, \tag{7}$$

$$B = \frac{\pi b^2}{2} u g' \qquad \frac{dB}{dz} = 0. \tag{8}$$

Despite the changes to the equations, the far-field asymptotic solution for the velocity follows the same scaling as the classical theory but has an extra pre-factor to account for the drag [7].

The effect of rotation on these wall plumes is currently unknown. Since the entrainment of a wall plume is asymmetric and the net flow induced by entrainment is towards the wall, the Coriolis force will generate a cross-flow along the wall when rotation is present. Purely due to geometrical constraints, there is potential for the precession observed in rotating plumes to be suppressed by the presence of the wall, and the lack of ambient circulation may affect the growth and breakup of baroclinic eddies.

3 Experimental Setup

3.1 Filling box experiments

The laboratory setup of the initial filling box experiments is shown in the schematic of figure 2. A transparent, cubic tank of dimensions $60\text{cm} \times 60\text{cm} \times 60\text{cm}$ was filled to a depth of approximately 50cm with fresh water of density $\rho_a = 0.998\text{g}\,\text{cm}^{-3}$. The tank was placed on a rotating table which was rotated at Coriolis parameters of $f = 0\text{s}^{-1}$, $f = 0.5\text{s}^{-1}$ and $f = 1\text{s}^{-1}$. The table was spun up for at least 30 minutes before each experiment to ensure that the fluid in the tank was very close to solid body rotation. Filtered seawater of density

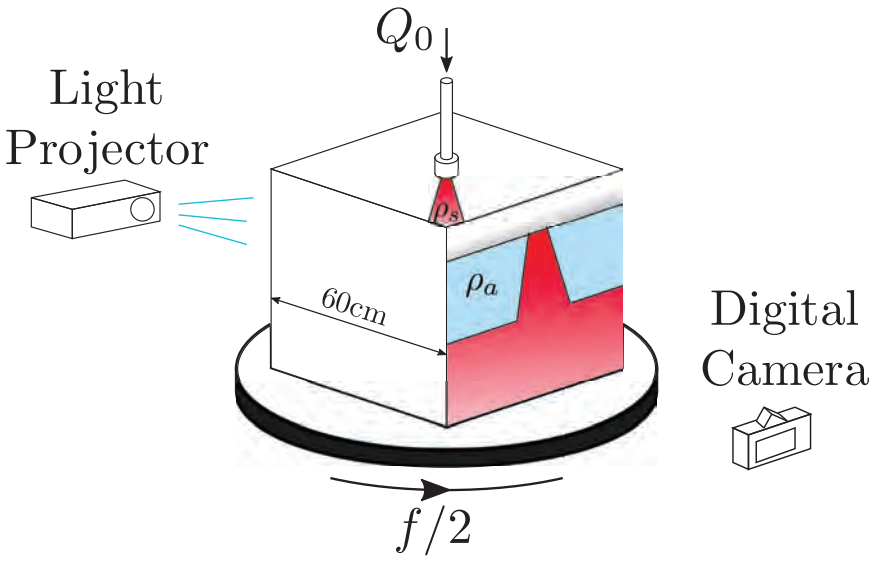

Figure 2: Schematic of the filling box setup.

$\rho = 1.02\mathrm{g\,cm^{-3}}$ was injected through a Cooper nozzle[1] of radius 2.65mm that was placed just below the surface of the water. A gear pump was used to pump the seawater through the nozzle at a constant volume flux Q_0, which was varied between 1 and $2\mathrm{cm^3\,s^{-1}}$ for different experiments. This gave a range of buoyancy fluxes of $B_0 = 20 - 40\mathrm{cm^4\,s^{-3}}$.

The seawater was dyed using red food dye so that the plume could be visualised easily using a shadowgraph technique. A light projector illuminated the experiment, and was placed approximately 2m away from the edge of the tank to prevent parallax issues in visualisation. One face of the tank was covered with a translucent sheet of paper to act as the recording plane for the shadowgraph. The experiment was recorded by an Olympus OM-D E-M10 Mark II digital camera attached to a tripod approximately 2m from the tank, directly opposite the light projector. Since neither the camera nor the projector were rotating with the tank, only one frame per rotation period could be used for analysing the experiment.

3.2 Filling box issues

In the non-rotating filling box experiments, the videos were processed as follows to obtain an entrainment coefficient α and a virtual origin correction z_0. In the regions to the left and right of the plume, the height of the front was determined in each pixel column by a threshold value for the reduction in blue light intensity. This height was then averaged across the pixel columns in each frame to obtain a time series for the front height $z_f(t)$. A polynomial fit was then used to interpolate the data, and this was numerically differentiated to give a front speed $w_f(t)$ and in turn a volume flux $Q = Aw_f$. Since the front height is known at all times, Q can also be plotted as a function of z. Rearranging (5) and accounting

[1]This type of nozzle uses a recirculation chamber and wire mesh to ensure turbulent outflow, and was first designed by Professor Paul Cooper, University of Wollongong, Australia.

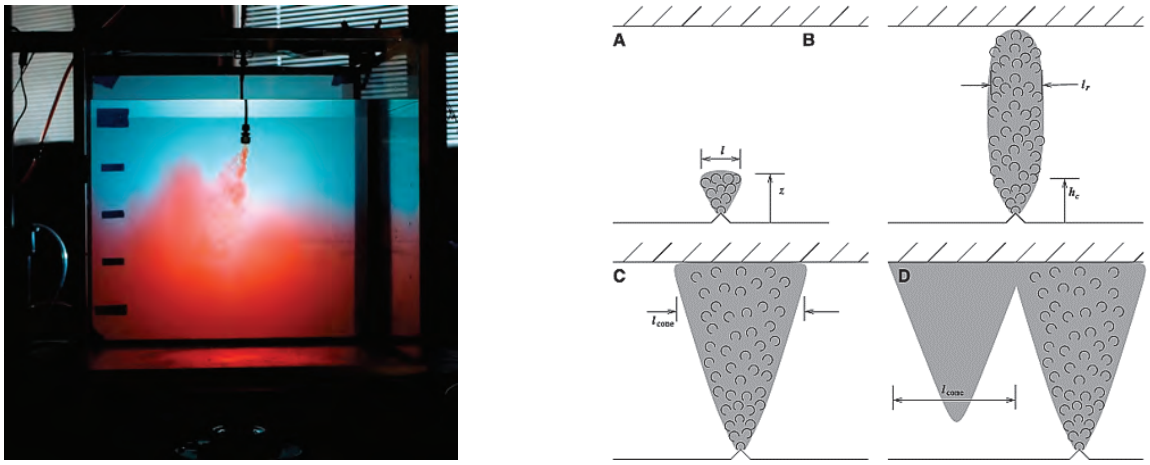

(a) (b)

Figure 3: (a) A picture of the experiment running with $f = 0.5$, showing plume deflection and a cone of dyed fluid indicative of a baroclinic eddy or possibly a 'heton'. (b) Schematic from Goodman et al. (2004) [11]: "Stages in the evolution of a buoyant convecting plume." A: Free turbulent convection. B: Rotationally controlled cylindrical plume. C: Baroclinic cone. D: Baroclinic instability."

for a virtual origin gives

$$z = \alpha^{-4/5} \left(\frac{Q}{c_1 B_0^{1/3}} \right)^{3/5} - z_0, \tag{9}$$

where $c_1 = \left(\frac{9}{10}\right)^{1/3} \frac{6}{5}\pi^{2/3}$. Thus α and z_0 can be estimated by a linear fit for the above equation. Typical values computed for these parameters were $\alpha = 0.12$ and $z_0 = 1$cm.

Figure 3a highlights some of the difficulties in applying this method to the case of rotating plumes. Firstly, the plume can be seen to deflect due to the precession identified in [10], which makes identifying regions over which to average a front height more challenging. Of greater concern is the shape of the front itself. The fact that there is not a clear, horizontal boundary between the dyed fluid and the clear ambient implies that the assumption of uniform upflow required for the filling box experiment is not valid. The mound of fluid that can be seen to the left of the plume propagates around the tank and is reminiscent of the anticyclonic eddies mentioned in section 2.2 and observed in previous studies [9, 11, 12]. Helfrich and Battisti (1991) suggest that the combination of this anticyclonic eddy with the cyclonic flow around the plume forms a 'heton' [12]. This term was first used by Hogg and Stommel (1985) to describe a pair of counter-rotating geostrophic vortices across a density interface which becomes pulled up or down depending on the sign of the vortices. [13]. Goodman et al. (2004) simply associate the shedding of a cone structure (as shown in figure 3b) with spreading of the dense fluid to a scale comparable to the Rossby radius of deformation $r_D = \sqrt{g'H}/f$, where H is the water depth [11].

Regardless of the origin of the tall cone of fluid, its presence in all of the rotating experiments makes the use of a filling box measurement to infer entrainment impossible. This

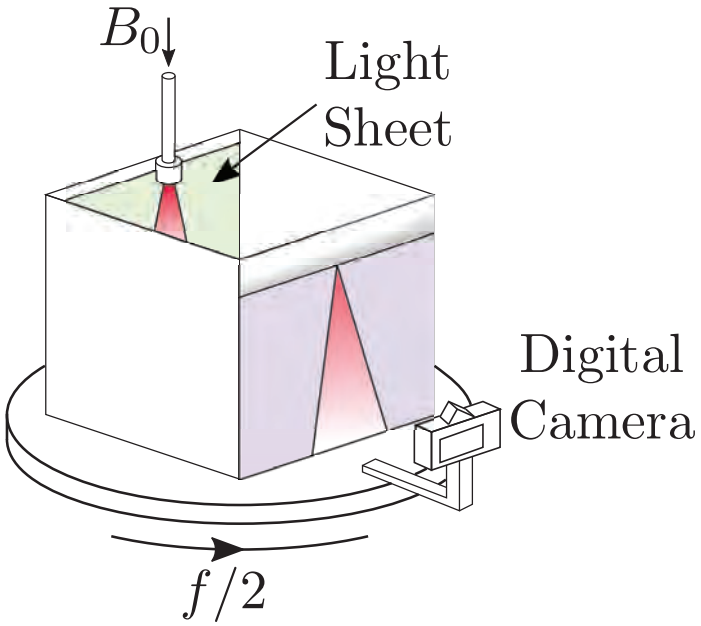

Figure 4: Schematic of the wall plume experimental setup when capturing the front view development of the wall plume.

led us to attempt an alternative experimental setup. Inspired by [3], where instantaneous measurements from a simple shadowgraph of the plume were used to determine properties of the mean flow, we prepared a setup similar to that shown in figure 4, but with the plume far from the boundaries of the tank. Unfortunately, the observed plume precession prevented accurate measurement of the plume width and hence hindered us from obtaining useful statistics of the flow. Qualitatively, it was interesting to observe *detrainment* of plume fluid into the ambient at all heights, although this exacerbated the problem of detecting the edge of the plume. Further investigation of the flow field in a rotating plume is needed to shed light on this behaviour. One possibility is that the detrainment could be related to the combination of the rigid boundary at the bottom of the tank and the Taylor–Proudman theorem, which together would hinder vertical motion in a rotating frame.

3.3 Wall plume experiments

The second experimental setup, used to investigate point source wall plumes in a rotating environment, is shown in figure 4. In contrast to the previous setup, both the digital camera and light source were attached to the rotating table to allow for a greater time resolution of 25fps in videos of the experiment. A projector and translucent sheet were not used for these experiments. Instead, electroluminescent Light Tape® attached to one face of the tank provided a uniform light source. The digital camera was attached to an arm on the rotating table approximately 60cm from the edge of the tank. Since we were only interested in the fluid near the plume, and not the entire width of the tank, the shorter distance between the camera and the tank edge did not lead to issues with parallax.

The same tank was used as in the filling box experiments, again filled with approximately

Volume flux Q_0 [$\mathrm{cm}^3\,\mathrm{s}^{-1}$]	Source density ρ_s [$\mathrm{g}\,\mathrm{cm}^{-3}$]	Coriolis parameter f [s^{-1}]
$2 - 2.5$	$1.02, 1.05$	$0, 0.5, 1, 2$

Table 1: Parameter values used for the wall plume experiments.

50cm of fresh water. For half of the wall plume experiments, extra salt was added to the seawater to increase its density, thus changing the buoyancy flux without altering the volume flux or momentum flux. A density meter measured the density of both the ambient fresh water and the source fluid before each experiment. The full range of parameter values used in the experiments can be found in table 1.

The plume source was attached to the illuminated side of the tank using filament tape such that the plume was directed vertically down the wall. The nozzle was placed a short distance below the surface of the water and halfway along the length of the wall to avoid the effect of the other boundaries of the tank. This setup provided a visualisation of the 'front view' describing how the plume spread along the wall. However due to the asymmetric development of wall plumes, we needed to repeat each experiment to also obtain a 'side view' showing how the plume spread away from the wall. For this setup, the plume source was attached to one of the walls adjacent to the illuminated side and the camera was moved so that it captured a view down that wall. Extra perspex sheets were added along the side with the plume to ensure that the view down the inner wall was not obscured by the corner of the tank.

The videos produced during the experiments were analysed using bespoke MATLAB scripts. Since the red dye concentration is linked to the reduction in blue light intensity, frame-by-frame analysis of the videos allows us to determine vertical profiles of the instantaneous width of the plume. The edges of the plume were defined at each height by locating the longest sequence of pixels where the blue light intensity was less than a given tolerance level. This tolerance was computed to be 80% above the minimum blue light intensity at each height relative to the background (maximum) light intensity.

4 Results

Due to the size and shape of the nozzle, the plume fluid did not exit the source attached to the boundary in the wall plume experiments. However, since entrainment induces areas of low pressure surrounding the top of the plume, the ambient pressure away from the wall pushes the plume onto the wall. This is known as the Coandă effect, which leads to the plume becoming attached to the wall within the top few centimetres. In the non-rotating experiment, once the plume was attached to the wall it remained attached for the duration of its descent to the bottom of the tank. The plume developed into a steady state where the width measured along the wall (in front view) was a linear function of height. The leftmost panel of figure 5 shows the instantaneous width of the plume over a 3-minute time window of the experiment. This shows that the instantaneous profiles never deviate significantly from the mean. The gradient of the instantaneous half-width db_x/dz was found to be approximately 0.184, which is larger than typical values for unconfined plumes and suggests increased along-wall entrainment.

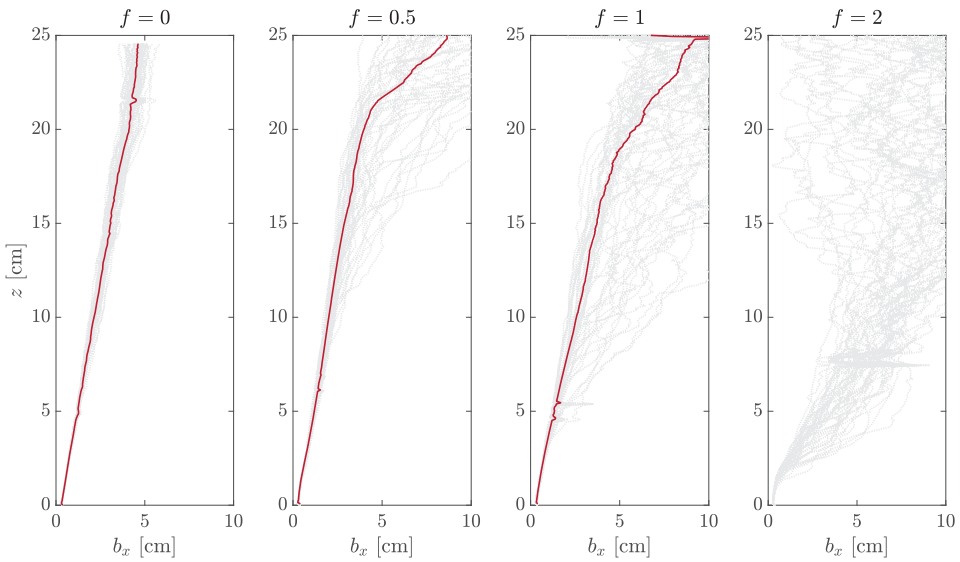

Figure 5: Vertical profiles of instantaneous plume half-width along the wall (in front view) over the course of four experiments with a volume flux of $Q_0 = 2\text{cm}^3\,\text{s}^{-1}$ and source density of $\rho_s = 1.023\text{g}\,\text{cm}^{-3}$. Profiles are only plotted for $t > 30$s to ignore the initial transient features of the plume. Each width is also averaged over 4s time intervals of 100 frames to smooth the data. Red lines indicate the time-mean of the instantaneous profiles that are considered to be in a 'quasi-steady' state.

The side view reveals that the steady state of the point source wall plume is unsurprisingly asymmetric. The vertical profile of the plume width away from the wall is however not a simple linear profile. Instead, the plume spreads out quickly within the top 3-4cm before descending with an almost constant width from the wall, as seen in the leftmost panel of figure 6. The fast spreading towards/away from the wall near the source may be attributed to Coandă-like effects which seem to be dominant in this region. The growth of turbulent eddies that engulf and entrain ambient fluid in a plume could be reduced in the direction perpendicular to the wall purely due to confinement. This would explain a reduction in entrainment away from the wall, but not the constant-width shape of the plume. One possibility is that the fluid entrained towards the wall squeezes the plume against the wall, leading to further spreading *along* the wall instead of growth away from it. This would be consistent with the generation of streamwise vorticity near the boundary observed for turbulent wall jets with no buoyancy [14].

Figures 5 and 6 compare the vertical profiles obtained at different rotation rates for a fixed volume flux and buoyancy flux. At early times and intermittently throughout the experiment, the plumes in rotating frames with $f = 0.5$ and $f = 1$ resemble the steady state found in the non-rotating experiment. We refer to the plume as being in a 'quasi-steady' state during these times, which can be identified as periods in which the fluctuations of the width in time are small. In figure 5, a fraction of the instantaneous profiles in grey for $f = 0.5$ and $f = 1$ are concentrated around an approximately linear profile associated with this quasi-steady state. The red lines are obtained by taking a time-mean of the profiles

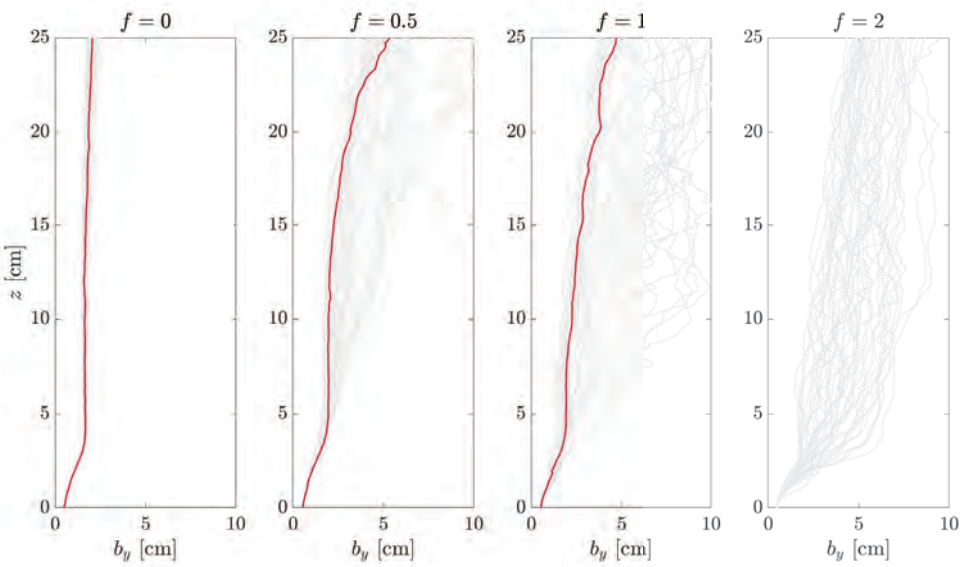

Figure 6: Vertical profiles of instantaneous plume width away from the wall (in side view) similar to figure 5. These experiments had an initial volume flux of $Q_0 = 2.15\text{cm}^3\,\text{s}^{-1}$.

considered to be in the quasi-steady state, and these profiles have similar gradients to the non-rotating steady state ($db_x/dz \approx 0.177$ for $f = 0.5$ and $db_x/dz \approx 0.2387$ for $f = 1$). The increase in gradient for $f = 1$ may simply be due to detraining dyed fluid, making it hard to identify the edge of the plume. Beyond a certain distance from the source, the plume is not consistent with a linear profile, and this distance reduces as the rotation rate increases. Bottom boundary effects becoming more important as rotation increases may explain these shrinking quasi-steady regions. At $f = 2$ no quasi-steady behaviour is observed, as can be seen in the rightmost panels of figures 5 and 6.

The vertical profiles from the side view in figure 6 have similar properties to those from the front view. At intermittent times throughout the experiments for $f = 0.5$ and $f = 1$, the plume exhibits a quasi-steady state but its connection to the non-rotating steady state is a little different. Both experiments show a rapid spreading near the source as in the non-rotating case, which stops at a width just below 2cm. Moving vertically away from the source, the quasi-steady profile has a region where the width remains approximately constant before further spreading occurs. The size of the region of constant width decreases with rotation rate, again indicative of increasingly important bottom boundary effects.

Inspecting video snapshots from the experiments provides us with some understanding of the plume dynamics during the times when it is not in a quasi-steady state, and reveals remarkable quasi-periodic behaviour. As shown in figures 7b and 7d, the upper section of the plume occasionally detaches fully from the wall and moves to the left in the front view. This intriguingly means that the plume moves in the opposite direction along the wall to the cross flow that is induced by entrainment. After a short period of time being detached from the wall, the plume typically reattaches to the wall and adjusts back to the quasi-steady state seen in figures 7a and 7c. In the detached state, the upper plume fluid appears to become arrested at a certain height from the source, and figure 7b also shows

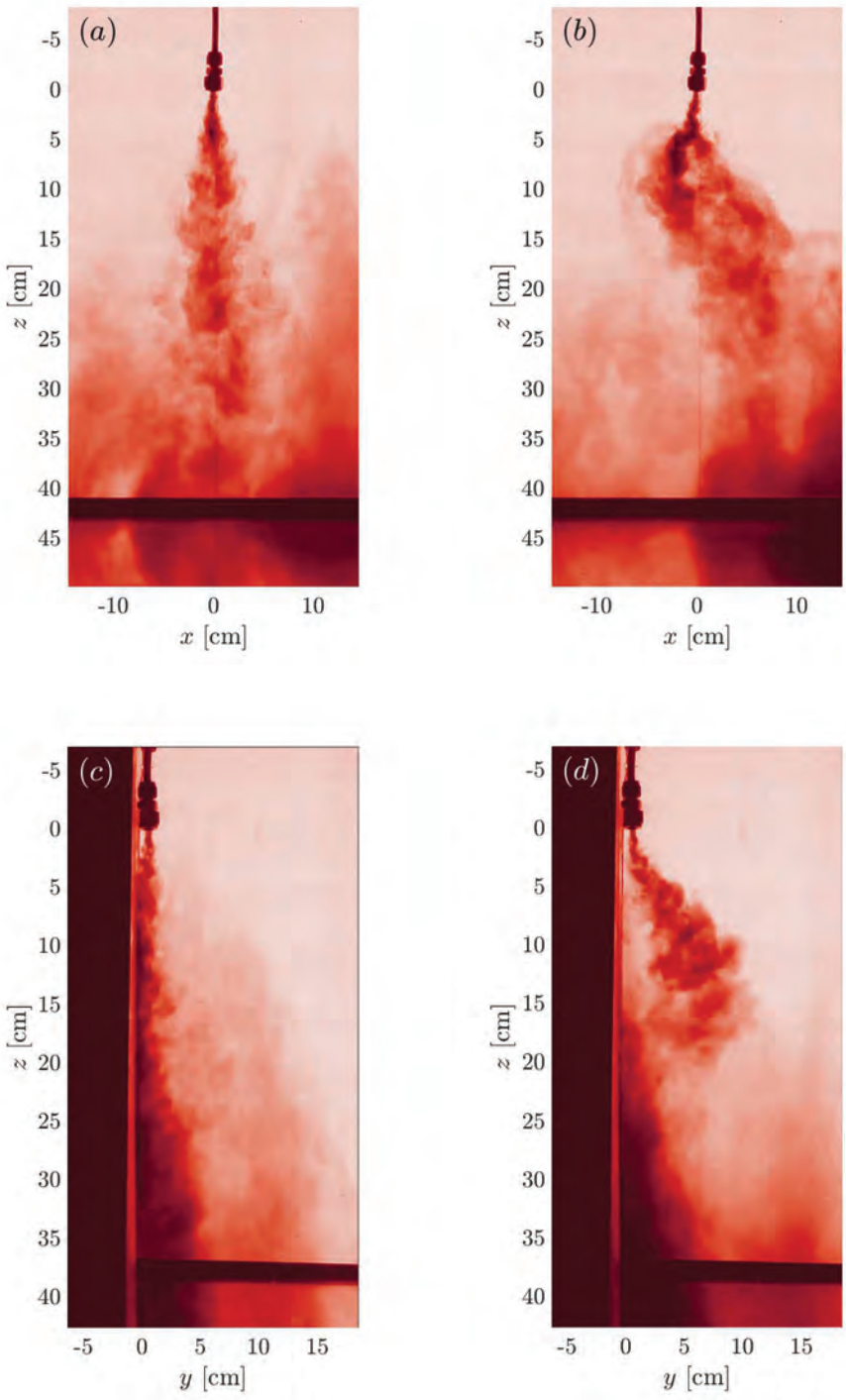

Figure 7: False colour images of blue light intensity from two experiments rotating at $f = 1$ with a source density of $\rho_s = 1.023\mathrm{g\,cm^{-3}}$. (a) and (b) show the front view at times $t = 60\mathrm{s}$ and $t = 100\mathrm{s}$, respectively, for volume flux $Q_0 = 2\mathrm{cm^3\,s^{-1}}$. (c) and (d) show the side view (flipped left to right) at times $t = 50\mathrm{s}$ and $t = 80\mathrm{s}$, respectively, for volume flux $Q_0 = 2.15\mathrm{cm^3\,s^{-1}}$.

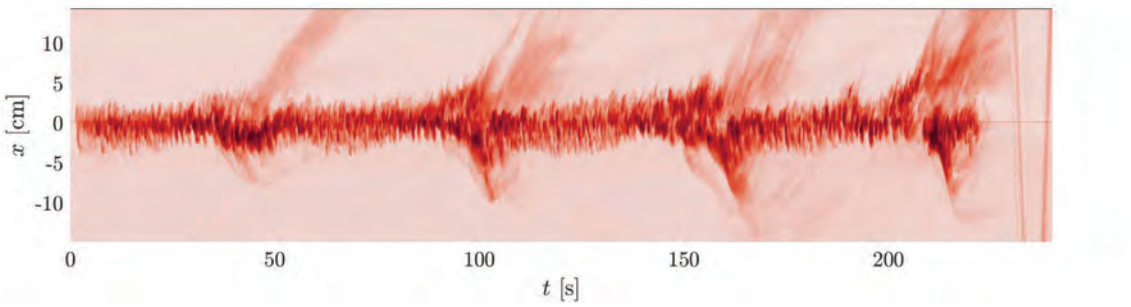

Figure 8: Time series of a horizontal slice of blue light intensity 10cm below the source level in front view for the same experiment as figures 7a and 7b.

that plume fluid further from the source is advected to the right along the wall. Videos of the experiment show that significant amounts of the fluid moving to the right are detrained from the plume while it is detached from the wall. This is clearly visualised in figure 8 by a time series of a horizontal slice 10cm below the plume. Large, diffuse patches propagating upwards in this figure correspond to fluid detraining to the right, and these coincide with the sudden deflections of the darker region associated with the plume.

A similar analysis for the side view experiment is shown in figure 9, which presents a time series of a vertical slice against the wall. The light space at the top of the figure shows that the plume does not leave the source attached to the wall and adjusts over a distance of 1-2cm. Detachment events can be seen clearly in figure 9 as the lighter patches descending over time. Although the front view and side view experiments were run with comparable parameters, the times of detachment are not consistent, suggesting that the mechanism is very sensitive to the experimental conditions or somewhat chaotic. This makes it difficult to determine whether the buoyancy flux has any effect on the frequency of detachment, but there is a clear trend for increasing rotation rate to increase the frequency of detachment as shown by figure 10.

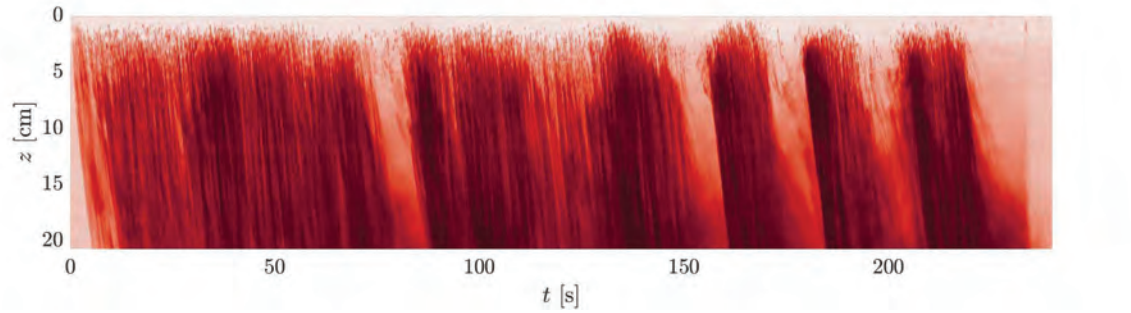

Figure 9: Time series of a vertical slice of blue light intensity between the source and the wall from the side view. The experimental parameters are identical to those in figures 7c and 7d.

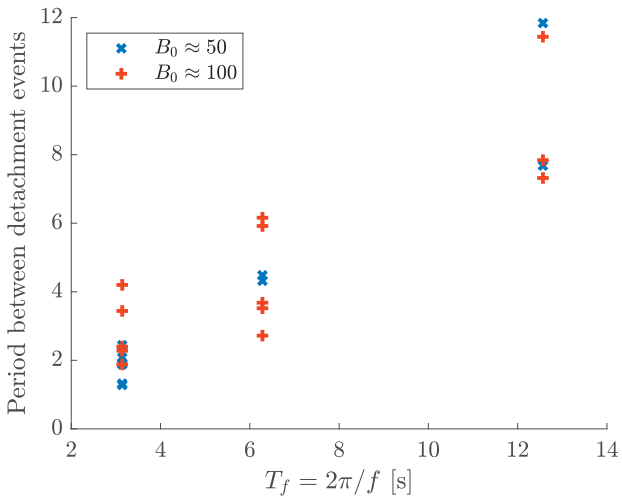

Figure 10: Scatter plot of time periods measured between detachment events against the inertial period of rotation. Only side view experiments were used to obtain these values.

5 Discussion

The results of our experiments leave many open questions for the effects of rotation and confinement on turbulent plumes. Even without the presence of rotation, the shape of the steady state formed by a point source plume along a wall is surprising. The results of a recent numerical study [7] do not appear to match the profile of close to constant width from the wall found in figure 6, and it remains important to understand this discrepancy. The difference between the numerics and our experiments may also have implications for the use of the half-cone model (6)-(8) in modelling glacial meltwater plumes. Quantifying the variation in the volume flux with height experimentally for this flow would be useful in determining whether the model can accurately represent the asymmetric plume dynamics. We only performed the non-rotating experiment at a single volume flux and source density, so there is plenty of scope for further investigation of this flow in various parameter regimes.

One caveat for our results in the non-rotating experiments is the position of the source nozzle. As discussed earlier, the dynamics near the source are thought to be dominated by the Coandă effect and the downstream impact of this is unknown. Replacing the source with a simple pipe outflow attached to the wall would remove these effects, but it is likely that the flow from this source would be laminar. Obtaining geophysically relevant parameters would be difficult in this case, but possible with a sufficiently deep tank that allows for the laminar-turbulent transition region.

The addition of rotation to the wall plume experiments resulted in frequent deviations from the steady state. The movement of the plume away from the wall and the detrainment that occurs during these detachment events has a strong impact on the amount of mixing that occurs between the plume and the ambient. Figure 11 shows the time-averaged front view of plumes at four different rotation rates for a buoyancy flux of $B_0 \approx 47.5\text{cm}^4\,\text{s}^{-3}$. Despite the difference in dye concentration between the non-rotating and rotating experiments, a clear trend is visible with the dye becoming more diffuse at higher rotation rates.

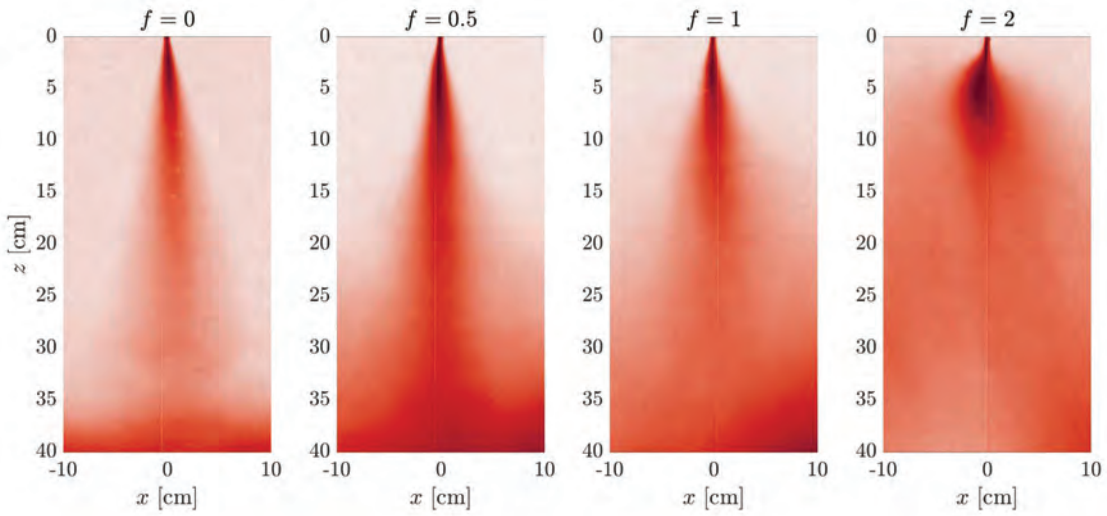

Figure 11: 3-minute time averages of the reduction in blue light intensity for four experiments in front view at various rotation rates. The time average is taken over a period that begins 20s after the start of each experiment, so effects of initial transients are not seen. Note that the dye concentration in the $f = 0$ experiment is half of that in the other experiments.

The lateral spreading of dyed fluid is also greater as f increases.

This increased dispersion can be quantified by considering a Gaussian profile fit to the light intensity deficit at each height. For a given row of pixels, we fit the profile

$$I = Ae^{-\frac{(x-\mu)^2}{2\sigma^2}}, \tag{10}$$

by taking the maximum intensity deficit to be equal to A and finding the first two data points away from this maximum to have $I < A/e$, i.e. the points that are an e-folding distance from the maximum. We then assume these points are at $x = \mu \pm \sqrt{2}\sigma$, from which we obtain the mean of the Gaussian μ, and the standard deviation σ. Vertical profiles of $\sigma(z)$ provide a useful measure of dispersion to compare the different experiments with. Figure 12 plots these profiles for both the experiments shown in figure 11 and those run with a higher buoyancy flux. The profiles show a striking dependence on the rotation rate of the experiment, with the change in buoyancy flux having practically no impact on the dispersion observed. This is despite the fact that the frequency of detachment was not totally consistent between experiments with the same rotation and varying buoyancy flux.

This apparent independence of buoyancy flux for long term mixing poses an interesting question as to how wall jets without any buoyancy would develop in this rotating system. Turbulent jets initially lead to confined cylindrical structures at sufficiently high rotation

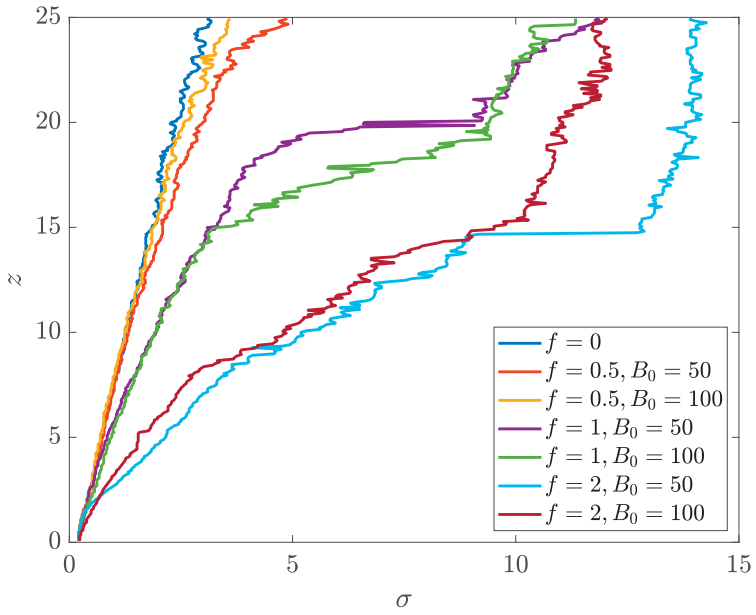

Figure 12: Plot of Gaussian standard deviation $\sigma(z)$ from 3-minute averages.

rates (see GFD Report of Lehn, 2018), but the interaction of these structures with the wall is unknown. Finding out whether a turbulent wall jet has the same detachment behaviour would be useful for further understanding the dynamics. Another process in rotating plumes found to be independent of the buoyancy flux is the precession of an axisymmetric plume in a rotating environment. The precession frequency was found in [10] to *only* rely on the rotation rate and not the buoyancy flux of the plume or the total depth of the water. This suggests that the process of detachment from the wall may be related to the free plume precession, and gaining further insight on the wall plume dynamics could help our understanding of the laterally unconfined plumes.

The fact that the wall plume reverts to a quasi-steady state between detachment events could be indicative of bistability in the system. The existence of multiple steady states for an unconfined plume in a rotating (and stratified) environment was discovered by Deremble [6]. This study used a continuation method to numerically compute the steady states of an LES-type model where turbulent processes are parameterised by an eddy viscosity. Without rotation the method identifies the steady state solutions described by classical plume theory. Once rotation is added, a steady state similar to the classical solution is found as well as second state that exhibits very different circulation patterns. This solution has fluid *upwelling* along the vertical axis beneath the plume, and the outflow of plume fluid is deflected. If similar steady states exist for the wall plume this could explain the attachment/detachment behaviour, so a further study on steady states for this problem would provide a lot of insight into the dynamics.

The influence of the bottom boundary on the wall plume is not fully understood. At higher rotation rates the more rapid lateral spreading appears to coincide with hindered vertical motion, as can be seen in figure 11 when $f = 2$. In the video for this experiment,

detrained fluid is seen to arrange itself into Taylor columns, indicating that the Taylor–Proudman theorem is affecting the dynamics and that velocity is close to uniform with height. The combination of the bottom boundary condition and the Taylor–Proudman theorem would explain this restriction on vertical motion. However,the precise effect that the bottom of the tank has on the detaching behaviour is unknown. Plume precession in [10] was found to be independent of the depth of the water, and testing whether the wall plume motion also has this property would provide further evidence to determine if the detachment is a signal of the precession.

One key result from [10] comes about because the precession is solely dependent on the rotation rate. Since precession occurs in every experiment after approximately one rotation period, rotation will always affect the dynamics as long as the source is maintained for a sufficiently long period of time. We have not quite shown that the dynamics of the wall plume are only dependent on the rotation rate, but we can hypothesise that since it is independent of the buoyancy flux similar results may apply. This would have implications for geophysical flows with sustained sources, such as glacial meltwater plumes and dense water currents running into undersea canyons. As we have seen above, plumes affected by rotation mix and disperse laterally to a greater extent than expected from a plume in a non-rotating environment, leading to changes in the long-time effects of these flows.

6 Acknowledgements

I would like to thank Craig McConnochie for advising me on this project and providing endless support, guidance and enthusiasm through the many twists and turns of my research over the summer. I would also like to thank Andrew Woods both for his series of inspiring and insightful lectures, and for the many useful discussions that helped steer my research down interesting new avenues. I am grateful too for the guidance of Claudia Cenedese, who did not let being on a different continent prevent her from providing good advice for the experiments. This summer was a phenomenal experience for me, which was in no small part due to the staff and visitors of the GFD Program. I am particularly grateful to the directors Colm Caulfield and Neil Balmforth, who helped create a wonderful atmosphere in which to do research. Finally, I want to extend my gratitude to the other Fellows on the Program, without whom this summer would not have been the same.

References

[1] W. D. Baines, *A technique for the direct measurement of volume flux of a plume*, Journal of Fluid Mechanics, 132 (1983), pp. 247–256.

[2] W. D. Baines and J. S. Turner, *Turbulent buoyant convection from a source in a confined region*, Journal of Fluid Mechanics, 37 (1969), pp. 51–80.

[3] H. C. Burridge, J. L. Partridge, and P. F. Linden, *The fluxes and behaviour of plumes inferred from measurements of coherent structures within images of the bulk flow*, Atmosphere - Ocean, 54 (2016), pp. 403–417.

[4] C. Cenedese and P. F. Linden, *Entrainment in two coalescing axisymmetric turbulent plumes*, Journal of Fluid Mechanics, 752 (2014), p. R2.

[5] T. Cowton, D. Slater, A. Sole, D. Goldberg, and P. Nienow, *Modeling the impact of glacial runoff on fjord circulation and submarine melt rate using a new subgrid-scale parameterization for glacial plumes*, Journal of Geophysical Research: Oceans, 120 (2015), pp. 796–812.

[6] B. Deremble, *Convective plumes in rotating systems*, Journal of Fluid Mechanics, 799 (2016), pp. 27–55.

[7] E. Ezhova, C. Cenedese, and L. Brandt, *Dynamics of three-dimensional turbulent wall plumes and implications for estimates of submarine glacier melting*, Journal of Physical Oceanography, 48 (2018), pp. 1941–1950.

[8] A. Fabregat Tomàs, A. C. Poje, T. M. Özgökmen, and W. K. Dewar, *Effects of rotation on turbulent buoyant plumes in stratified environments*, Journal of Geophysical Research: Oceans, 121 (2016), pp. 5397–5417.

[9] H. J. S. Fernando, R.-r. Chen, and B. A. Ayotte, *Development of a point plume in the presence of background rotation*, Physics of Fluids, 10 (1998), pp. 2369–2383.

[10] D. Frank, J. R. Landel, S. B. Dalziel, and P. F. Linden, *Anticyclonic precession of a plume in a rotating environment*, Geophysical Research Letters, 44 (2017), pp. 9400–9407.

[11] J. C. Goodman, G. C. Collins, J. Marshall, and R. T. Pierrehumbert, *Hydrothermal plume dynamics on Europa: Implications for chaos formation*, Journal of Geophysical Research, 109 (2004), p. E03008.

[12] K. R. Helfrich and T. M. Battisti, *Experiments on baroclinic vortex shedding from hydrothermal plumes*, Journal of Geophysical Research, 96 (1991), p. 12511.

[13] N. G. Hogg and H. M. Stommel, *The heton, an elementary interaction between discrete baroclinic geostrophic vortices, and its implications concerning eddy heatflow*, Proceedings of the Royal Society A: Mathematical, Physical and Engineering Sciences, 397 (1985), pp. 1–20.

[14] B. E. Launder and W. Rodi, *The turbulent wall jet measurements and modeling*, Annual Review of Fluid Mechanics, 15 (1983), pp. 429–459.

[15] P. F. Linden, G. F. Laneserff, and D. A. Smeed, *Emptying filling boxes - the fluid-mechanics of natural ventilation*, Journal of Fluid Mechanics, 212 (1990), pp. 309–335.

[16] J. Marshall and F. Schott, *Open-ocean convection: Observations, theory, and models*, Reviews of Geophysics, 37 (1999), pp. 1–64.

[17] C. D. McConnochie and R. C. Kerr, *The turbulent wall plume from a vertically distributed source of buoyancy*, Journal of Fluid Mechanics, 787 (2015), pp. 237–253.

[18] B. R. Morton, G. Taylor, and J. S. Turner, *Turbulent gravitational convection from maintained and instantaneous sources*, Proceedings of the Royal Society A: Mathematical, Physical and Engineering Sciences, 234 (1956), pp. 1–23.

[19] D. A. Slater, D. N. Goldberg, P. W. Nienow, and T. R. Cowton, *Scalings for submarine melting at tidewater glaciers from buoyant plume theory*, Journal of Physical Oceanography, 46 (2016), pp. 1839–1855.

[20] K. G. Speer and J. Marshall, *The growth of convective plumes at seafloor hot springs*, Journal of Marine Research, 53 (1995), pp. 1025–1057.

[21] A. W. Woods, *Turbulent plumes in nature*, Annual Review of Fluid Mechanics, 42 (2010), pp. 391–412.

[22] H. Yamamoto, C. Cenedese, and C. P. Caulfield, *Laboratory experiments on two coalescing axisymmetric turbulent plumes in a rotating fluid*, Physics of Fluids, 23 (2011), p. 056601.

On Turbulent Fountains with Background Rotation

Andrea M. Lehn

September 29, 2022

1 Introduction

Turbulent fountains are ubiquitous in natural systems as well as in industrial processes [7]. Fountains occur when there is a reversal or arresting of fluid motion due to buoyancy differences between the fluid in the fountain and the ambient environment. A turbulent fountain occurs when a fluid of non-neutral buoyancy is injected form a localized source with sufficient momentum to be driven initially against gravity and to become turbulent. Consider a jet of salty water injected at the bottom of a tank of fresh water. Initially, the salt water will be driven upwards, against gravity, if there is sufficient momentum to make the jet turbulent. The fluid will rise, entraining fresh water along the way, until it can no longer rise. The diluted salty fluid at the top of the fountain then overturns, driven downwards by gravity. The fluid may fall completely to the bottom or intrude horizontally in the ambient if a background density stratification is present.

The role of rotation on the dynamics of turbulent fountains has not been detailed in scientific literature, although it is relevant for geophysical processes. For some natural processes involving turbulent fountains, such as cloud formation or volcanic eruptions, the Earth's rotation may influence the dynamics. This report presents experimental results investigating the role of rotation on turbulent fountains.

1.1 Laminar vs. Turbulent Fountains

The Froude number (Fr) is the non-dimensional group which determines whether or not a fountain will be turbulent or laminar. Consider a circular source with radius R and mean source velocity $\bar{u}$, injecting buoyant fluid with a modified gravitational acceleration $g' = (\Delta\rho/\rho_0)\, g$, where $\Delta\rho$ is the density difference between the two fluids, ρ_0 is a reference density, and g is acceleration due to gravity. Fr represents the ratio of inertial forcing to gravitational forcing for the fountain and is defined as

$$Fr = \frac{\bar{u}}{\sqrt{g'R}}. \tag{1}$$

For $Fr >> 1$ a fountain becomes turbulent while for $Fr = O(1)$ it remains laminar. Qualitatively and quantitatively there are differences between turbulent and laminar fountains. Before overturning, laminar fountains rise to a height, h, which is on the order of R, the source radius. This result may be obtained from dimensional analysis. For a laminar fountain with four variables, h, R, g' and $\bar{u}, h \sim R$ for a source with a fixed g' and $\bar{u}$. There

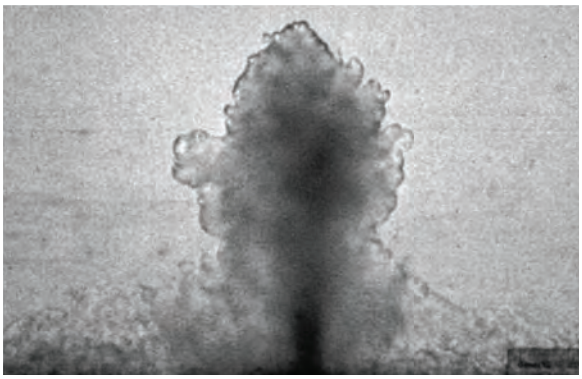

Figure 1: A turbulent fountain rising. Dense, salty water is injected upwards into a fresh ambient from a high Fr source. Image from Bloomfield and Kerr [3].

is little to zero entrainment of the surrounding fluid and the laminar fountain has memory of the source conditions, i.e., the penetration height is totally dependent upon source conditions. Burridge and Hunt [4] have systematically investigated the behavior of fountains at low and very low Fr source values. Overall, these systems are well studied.

The behavior of high $F\ r$ sources, i.e. negatively buoyant sources driven by source momentum, was initially studied by Turner in 1966 [8]. Turbulent fountains have little memory of the source conditions due to turbulent entrainment of ambient fluid, which causes the fountain to penetrate such that $h >> R$. An example of a turbulent fountain is shown in Figure 1. Heavy fluid is injected from a point source upwards into a still body of ambient fluid. Turbulence enhances mixing of the lighter ambient into the injected fluid, which reduces the buoyancy, allowing the fluid to rise higher before overturning and falling back down.

The important parameters for turbulent fountains are the buoyancy flux, B, and the momentum flux, M. M is the volume flux of the source times the mean outlet velocity with units of $\mathrm{L}^4/\mathrm{T}^2$ and B is the volume flux of the source times g', with units of $\mathrm{L}^4/\mathrm{T}^3$. For a source with a circular cross section,

$$M = \pi \mathrm{R}^2 \bar{u}^2 \tag{2}$$

and

$$B = \pi \mathrm{R}^2 \bar{u} g'. \tag{3}$$

Both of these variables include information about source conditions g', $\bar{u}$ and R; however, these parameters alone do not determine the fountain height, as they do for a low Fr source fountain.

Bloomfield and Kerr [3] determined a power law for the mean height of rise of a turbulent fountain, based on original work by Turner [8]. The height, H_f depends solely upon M and B. For a turbulent fountain,

$$H_f = 1.6 M^{3/4} B^{-1/2}. \tag{4}$$

This non-rotating, turbulent H_f is useful as a characteristic length scale. The height of the fountain oscillates about a mean height with relatively large amplitudes. Eddies where

mixing occurs are visible along the sides of the fountain and at the top, as shown in Figure 1. Once the fountain overturns, a curtain partially shields the sides of the rising fountain, preventing the rising fluid from entraining the ambient fluid. The dynamics of turbulent fountains have been well studied for a range of conditions, including turbulent fountains in multi-layer cross-flows [1] and fountains impinging on a density interface [2].

1.2 Low *Fr* Sources with Rotation

Griffiths and Linden [6] investigated the stability of two-layer density stratified systems with ambient rotation. A curved density interface forms due to the buoyancy difference between the two fluids, and eventually the system becomes unstable under the influence of the Coriolis force. The constant flux experiments performed by Griffiths and Linden are related to the present investigation. A buoyant fluid was injected at the free surface of a homogeneous body of fluid which had been spun-up to rigid body rotation. A circular cross-section, porous source of 1 cm diameter was positioned at the free surface. A constant volume of buoyant fluid was injected for the duration of the experiment, and the radial and vertical growth of a vortex was observed. The $F\,r$ values for these experiments are relatively low, ranging from 10^{-3} to 5, so that the flow remains laminar.

A key feature that differentiates the Griffiths and Linden experiments from those presented in this report is that upon injection there is no large vertical penetration of the fluid. For turbulent fountains, there is a large change in height of injected fluid due to source momentum and subsequent entrainment of ambient fluid. The momentum of the source for the Griffiths and Linden experiments, indicated by Fr, is not sufficiently large to create turbulent entrainment of the ambient fluid. In the constant flux experiments, a geostrophic vortex grows, surrounded by the ambient fluid. There is very little mixing. A side-view image showing vertical penetration of a geostrophic vortex is shown in Figure 2.

The streamlines of the flow are solely determined by rotational effects, the Coriolis and centrifugal forces, and the modified gravity, g', between the two fluids. Eventually, the vortex becomes unstable to rotation and higher order modes occur. A top view of an unstable configuration is shown in Figure 3. The vortex that forms from injected fluid forms a smooth boundary with the ambient fluid since there is negligible mixing at the density interface. The density difference between the two fluids is maintained as the vortex grows. A key result of Griffiths and Linden's work is that the radius, $R \sim t^{1/4}$ and the height, $h \sim t^{1/2}$.

1.3 Objective: Behavior of Turbulent Fountains with Rotation

How the current investigation is situated with published scientific literature can be visualized as table with two options, rotation or no rotation and laminar or turbulent. This grid is shown in Figure 4. Laminar and turbulent fountains have been well characterized and rotating currents with a low Fr have been studied, filling in three quadrants of the grid. Conversely, constant source volume flux, turbulent fountains with background rotation have yet to be studied. This project is situated in the bottom right corner of this grid. The dynamics of the turbulent fountain are studied by systematic experiments over a parameter space determined by important dimensionless groups, as discussed below.

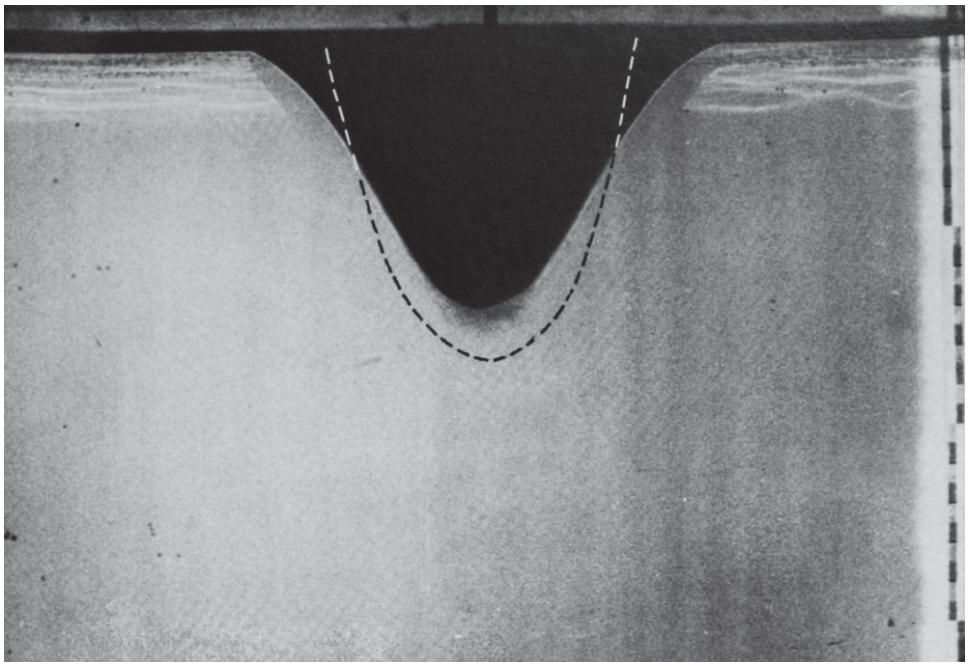

Figure 2: Side view of a vortex forming from Griffiths and Linden [6]. The dark vortex is buoyant fluid injected from a low Fr source. Dotted lines are theoretical predictions of the vortex location. The tank is rotating anti-cyclonically and the vortex is rotating cyclonically.

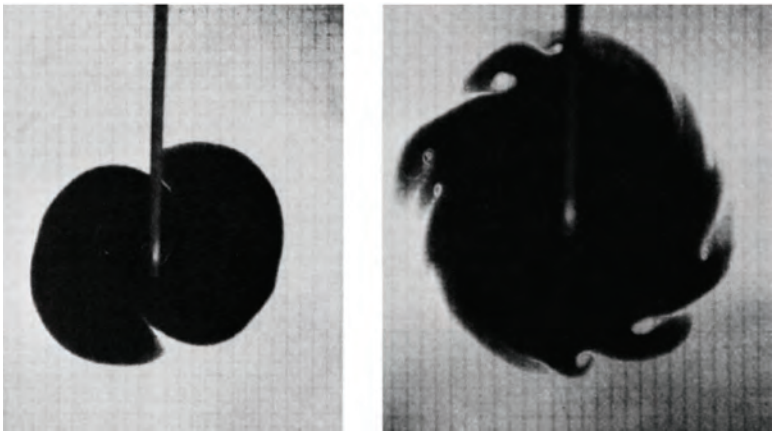

Figure 3: Top view of the onset of instabilities with different azimuthal wave numbers in experiments by Griffiths and Linden [6].

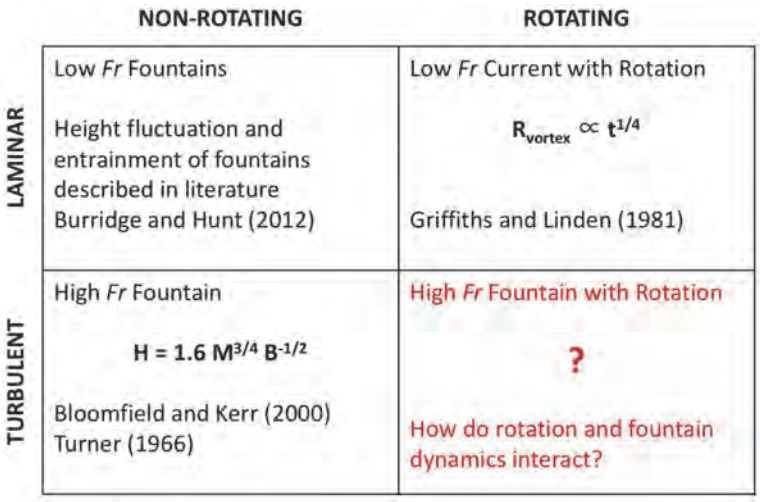

Figure 4: The scientific context of this project fits into the bottom right quadrant of this grid. The dynamics of rotating, turbulent fountains are investigated for the first time in this project.

2 Dimensional Analysis

Dimensional analysis was used to determine a parameter space for experiments. Although dimensional analysis is useful, knowing the relevant physical variables is crucial for determining appropriate dimensionless groups. Based on expected behavior of rotating systems and turbulent fountains, relevant physical variables are determined and scaling is performed to derive three dimensionless Π groups.

Based on the power law produced by Turner [8] and verified by Bloomfield and Kerr [3] there is a time scale for the turbulent fountain. A relevant time scale for the time it takes a fluid parcel to rise to the top of the fountain is the ratio of momentum flux to buoyancy flux, M/B. For a turbulent fountain, recall that momentum flux and buoyancy flux are the relevant parameters for predicting fountain behavior. The Coriolis parameter, f, has units of T^{-1}. It is the appropriate rotational time scale. The Coriolis parameter is equal to twice the rotational frequency of the experimental table: $f = 2\Omega$. In terms of the period of the table's rotation, T_{table}, $\Omega = 2\pi/T_{table}$. Thus, the period of rotation is $4\pi/f$ s.

Since the system is rotating, there is an added stiffness to the fluid due to its vorticity. This can be understood by considering the Taylor-Proudman Theorem. A fluid parcel that is displaced in a direction parallel to the axis of rotation will be forced back to its initial location by rotation. The faster the rotation rate, the more vertical displacement of fluid parcels is suppressed. An alternative argument is that in the limit of rapid rotation, the Taylor-Proudman Theorem gives $\partial w/\partial z = 0$ where w is the velocity in the vertical direction, z. Since there is no vertical flux through the bottom of the tank, $w = 0$, the vertical velocity must be zero everywhere.

Using the Buckingham Pi Theorem and intuition about the system based on the Taylor-Proudman Theorem and on behavior of non-rotating turbulent fountains, three Π groups are determined for the rotating fountain system. There are five relevant variables in the system,

f, M, B, the height of the fountain, H_f and the initial depth of the ambient, H_T. Since there are two dimensions, three Π groups exist. The groups are $\Pi_1 = fM/B$, $\Pi_2 = H_f/H_T$ and $\Pi_3 = M/f^2H_T^4$. The first group, fM/B represents a ratio of the two important time scales of the problem, the fountain rise time to the rotational time. The third group can be thought of as a ratio of the momentum imparted to the fountain and the resistance to vertical penetration. For simplicity, given the time constraint of the GFD program, the ratio of fM/B was varied systematically for fixed values of M. The height of the tank H_T was also fixed. Based on the parameter space, the rotation time scale, $1/f$ was slower than the fountain time scale, M/B. Thus, it was anticipated that the fountain dynamics would dominate the system before rotation.

3 Experimental Setup

3.1 Laboratory Apparatus

Experiments were performed in the Geophysical Fluid Dynamics Laboratory at the Woods Hole Oceanographic Institution. A 91 cm diameter cylindrical plastic tank was placed on a direct-drive rotating table and filled with sea water to $H_T = 35$ cm. A pump was used to inject a constant flux of dyed fluid through a 0.5 cm diameter copper pipe, which was positioned in the center of the tank, just below the free surface. An acrylic lid with a small circular opening for the source was placed on top of the tank for rotating experiments. This was so the air layer above the free surface was also brought up to solid body rotation, to create a nearly stress free boundary between the water and air.

Instrumentation for collecting digital video data from the side view and top view were attached to the rotating table. From the top, a Basler imager was positioned to provide a top view of the entire tank. A Windows machine equipped with software to control the top view camera was mounted to the rotating frame and used to acquire images. Images were collected as single page tifs at a rate of five frames per second. The side view was filmed on a Nikon Coolpix P7000. The collection rate was 24 frames per second. Start times were synchronized using coordinated verbal and visual cues. For the side view, illumination was provided using Light Tape, a flexible electro-luminescent panel, which was aligned flush with the curved tank wall. Pictures of the experimental setup are shown in Figure 5.

3.2 Experimental Parameter Space

A total of 20 experiments were conducted to investigate the role f and B on the behavior of turbulent fountains. The volume flux of the source, Q_0, M and H_T were fixed at $Q_0 = 5.11$ cm^3/s, $M = 133$ cm^4/s^2 and $H_T = 35$ cm for all experiments. To compare the fountain rise time and rotation time f and B were systematically varied. For the rotating experiments the table was rotated at $f = [0.5, 1.0, 2.0 \text{ and } 3.0]$ s^{-1}. Another set of experiments examined the non-rotating case, f=0. For all five rotation rates, fluids of four different densities were injected to investigate the role of buoyancy. Four values of B were examined, $B/Q_0 =$ [0, 0.2, 0.5, 1] g_0' where $g_0' \approx 25$ cm^{4}s^{-3}. The case of $B = 0$ is a jet purely driven by momentum, since there is negligible buoyancy. In terms of the dimensionless parameter fM/B, which represents the ratio of rotational time to fountain rise time, the fountain

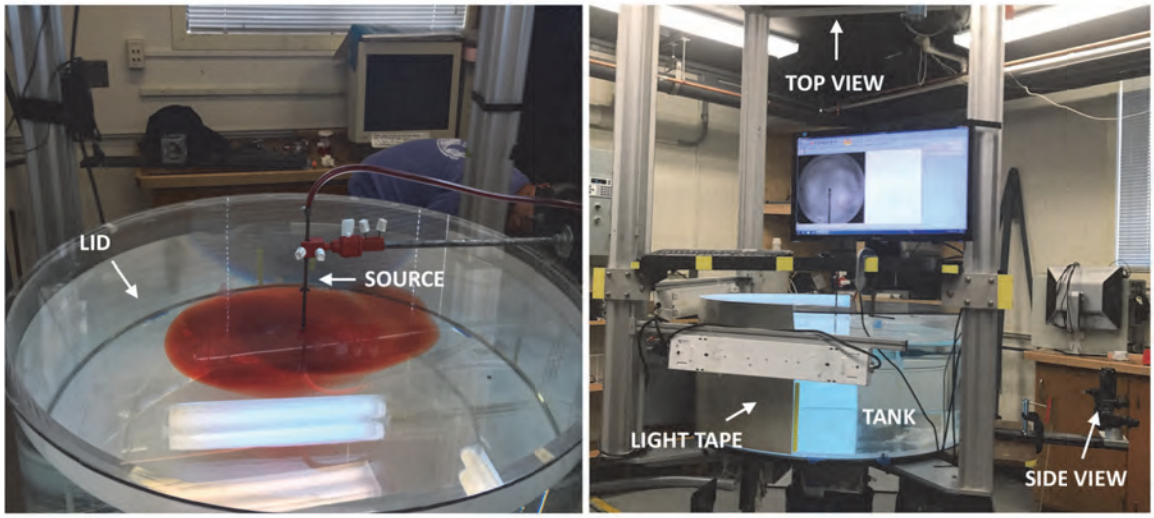

Figure 5: The experimental apparatus used to study rotating fountains. Left: the top view of the rotating system showing the tank lid and source. Right: a side view of the system showing the location of the two camera views as well as the lighting, provided by flexible electro-luminescent lighting (Light Tape).

dynamics are expected to set in before rotation. The Rossby number, Ro is represented by $(fM/B)^{-1}$ for this problem. Ro is a ratio of the rotation time, $1/f$ s to the advective time, M/B s for the initial values of the flow. So, $Ro = B/fM$ for the turbulent fountain with background rotation. The experimental parameter space is shown graphically in Figure 6. The horizontal axis is the reciprocal Ro and the vertical axis is the theoretical fountain height, computed from equation 4, normalized by H_T.

4 Results

4.1 Role of Rotation in Turbulent Fountains

The first experiments were performed by varying f with a fixed B and M. The buoyancy difference was set by the difference between sea water and fresh water, which was the maximum buoyancy flux tested, $B/Q_0 = g'_0$. The role of rotation significantly influences the system dynamics. Figure 7 is a time series comparing a non-rotating turbulent fountain to a turbulent fountain with background rotation. In the non-rotating case, the injected fluid spreads radially as it penetrates the ambient. Billows at the interface of the two fluids indicate turbulent mixing, whereby denser ambient fluid mixes with the fountain, decreasing it buoyancy. With reduced buoyancy, the fountain touches the bottom boundary of the tank and then returns to the surface, driven by buoyancy. The same source conditions with background rotation produced a fountain with a smoother interface and with significantly decreased penetration. The vortex formed in the rotating case prevents the newly injected fluid from mixing with the ambient, thus stifling penetration. Figure 8 shows the fluid interactions occurring in the interior of a surface vortex, formed once the fountain has

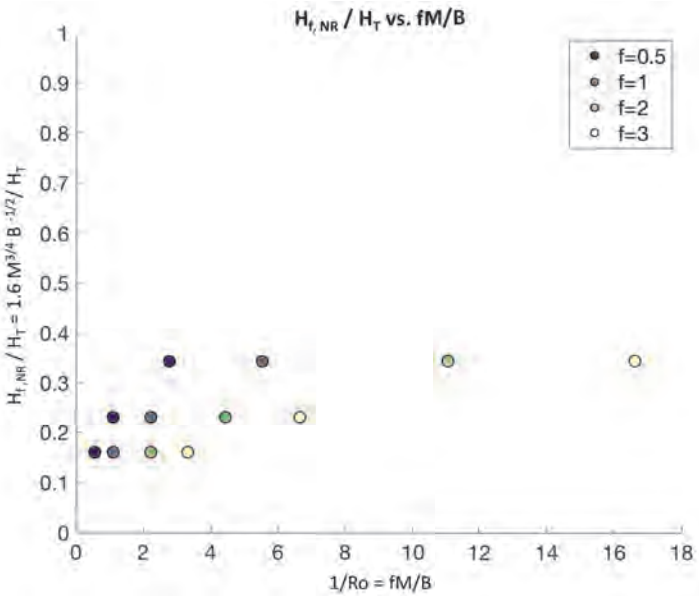

Figure 6: Experimental parameter space for non-zero buoyancy flux and non-zero rotation rate. The vertical axis is H_f based on scaling by Bloomfield and Kerr [3] given in equation 4, scaled by the depth of the ambient, H_T. The horizontal axis is the reciprocal Ro, fM/B.

turned around and risen due to its buoyancy. The injected fluid is initially colored yellow but then dyed red after the vortex has established. The red fluid shows the fountain still exists but is contained within the vortex. A small region at the center of the fountain may punch through the vortex, but largely the fountain is contained within the vortex. Since the newly injected fluid is largely shielded from the ambient by the established vortex, it may only entrain fluid of similar density, leaving its buoyancy relatively unchanged. Without the reduction in buoyancy, the fountain penetrates less deeply. It is too buoyant to continue further and must rise.

For all non-zero rotation rates, rotation systematically decreases the vertical fountain penetration. Figure 9 shows the height of the fountain as a function of time for a fixed value of $B/Q_0 = g_0'$ and four non-zero f values. Data is plotted until a consistent fountain depth is established. As f increases, the initial entrainment and penetration depth are systematically decreased. Before the vortex has begun to shield the incoming fluid from the ambient, entrainment and mixing occur, as in the non-rotating case. The vortex establishes more rapidly at higher f, decreasing the time available for fluid to entrain the denser ambient. Thus, the buoyancy remains unchanged and the fountain does not penetrate as deeply. The average fountain height obtained from data presented in Figure 9, scaled by the height of a non-rotating turbulent fountain, $H_f = 1.6M^{3/4}B^{-1/2}$ is plotted against fM/B in Figure 10. This non-dimensional plot shows that the penetration of the fountain is substantially reduced with increasing rotation. By comparing the volume of the vortex with time to the injected volume, it is clear that rotation systematically suppresses entrainment, as shown in Figure 11. Overall, the entrainment is small relative to the injected volume and only occurs at early times, when the fountain is initiated, before the vortex partially

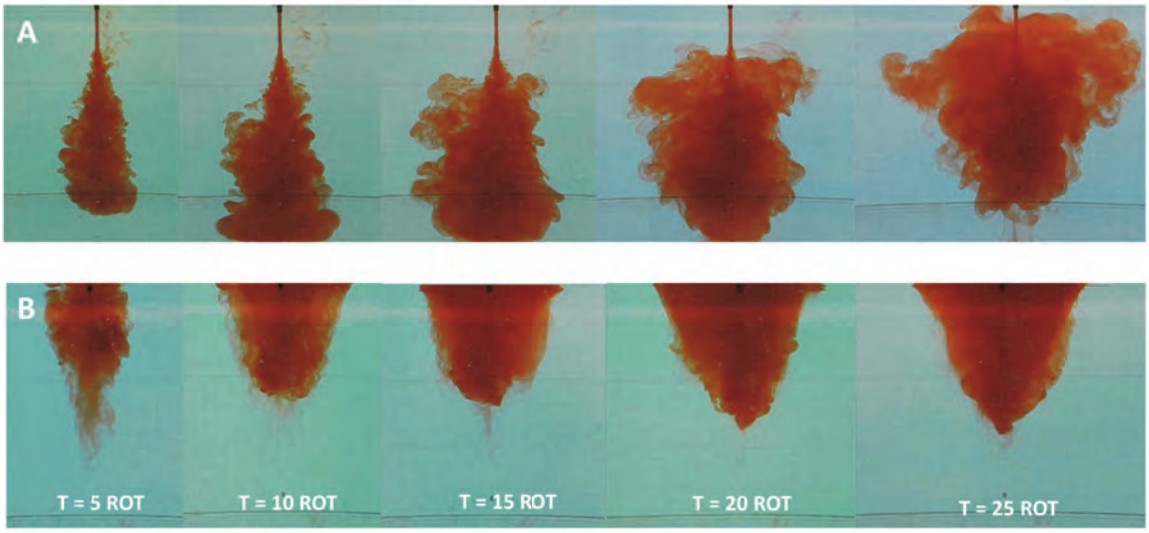

Figure 7: A time series showing the influence of rotation on turbulent fountain dynamics. Panel A shows a turbulent fountain with no background rotation. The fountain becomes turbulent, hits the bottom of the tank, and eventually rises back up to the surface. Panel B shows the same fluid being injected with identical source conditions, $B/Q_0 = 0.5g_0' = 12.5$ cm^{4}s^{-3} and $M = 133$ cm^{4}s^{-2}, but with a background rotation of $f = 3.0$ s^{-1}. The period of one rotation (T = 1 ROT) was 4.2 s.

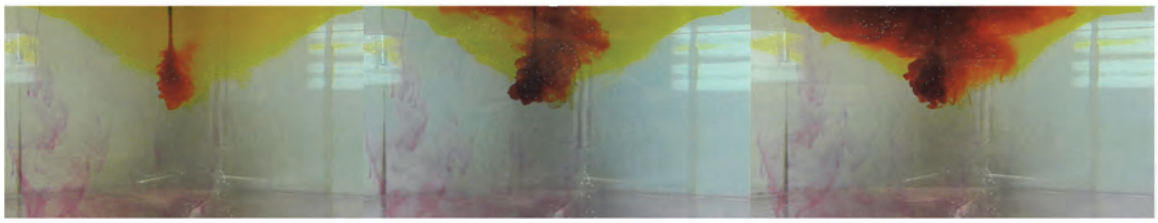

Figure 8: A time series revealing fountain behavior in an established vortex. The fountain color is changed from yellow to red after the vortex has established. The interior behavior of the vortex-fountain system is qualitatively shown to be complex, including stratification and circulation. Source conditions were $B/Q_0 = g_0' = 25$ cm^{4}s^{-3} and $M = 133$ cm^{4}s^{-2} with a background rotation of $f = 0.5$ s^{-1}.

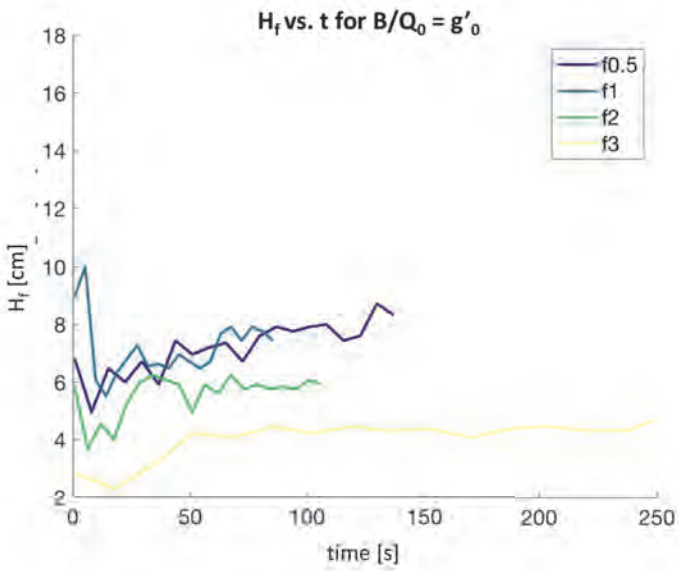

Figure 9: Height of the fountain versus time for increasing f at a fixed B. Source conditions were $B/Q_0 = g'_0 = 25$ cm^{4}s^{-3} and $M = 133$ cm^{4}s^{-2}.

encapsulates the fountain. Entrainment of ambient fluid subsidies as more fluid is injected because the fountain is contained within the growing vortex, shown qualitatively in Figure 8. The fountain is entraining fluid of a density close to that of itself, which doesn't enhance mixing with the ambient and maintains a large g'.

Unexpectedly, the radius of the vortex which develops at the surface grows with $t^{1/2}$. A log-log plot of radius versus time is shown for all g$'$ values with varying f in Figure 12. Since this collapses well to a line with slope of a half, this suggests that $R(t) \sim t^{1/2}$. This is robust for all non-zero values of f and B examined. Notably, this behavior is different than the $t^{1/4}$ scaling demonstrated by Griffiths and Linden [6]. A scaling for R as a function of f was estimated by plotting the vertical intercepts of the log-log R vs.t plots and assuming a power law scaling of the form $R \sim t^{1/2} f^{\beta}$. This power law can be determined by plotting the vertical intercepts of the lines of slope $m = 1/2$, shown as dotted lines on Figure 13. Plotting these vertical intercepts against log f would produce a line should a power law scaling be correct. Figure 13 shows the intercepts used to determine the value of β. Figure 14 shows the intercepts plotted against log f. Two dotted lines are plotted to serve as visual aids, one of slope $m = -1/3$ and one of $m = -1/2$. A similar approach was applied for the B, using data from cases with varying g', to find that $R \sim B^{1/3}$.

The power law for $R \sim f^{\beta}$ is not obvious. There is support for $\beta = -1/3$ and for $\beta = -1/2$, but it is not clear which is correct given the limited amount of data currently available. A value of $\beta = -1/3$ would be consistent with a $-1/3$ power law for the dimensionless group fM/B since $R \sim B^{1/3}$. A linear least squares fit produced a slope of $\beta = -0.44$ with a R-squared error $R^2 = 0.99$ and an RMS error of 0.042. Since there are only four data points, this power law is not yet definitive. However, a power law of $\beta = -0.44$ is consistent with expected values based on dimensional analysis and physical reasoning, as discussed further

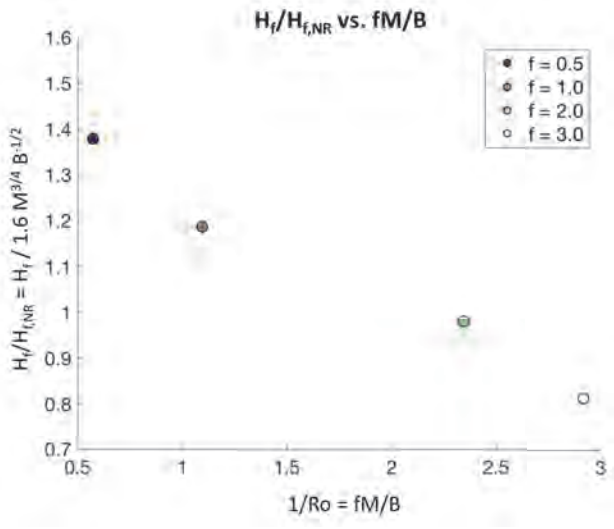

Figure 10: Average fountain height after long times normalized by the non-rotating fountain height, plotted against fM/B for one value of $B/Q_0 = g_0'$. Average H_f values are obtained from data shown Figure 9.

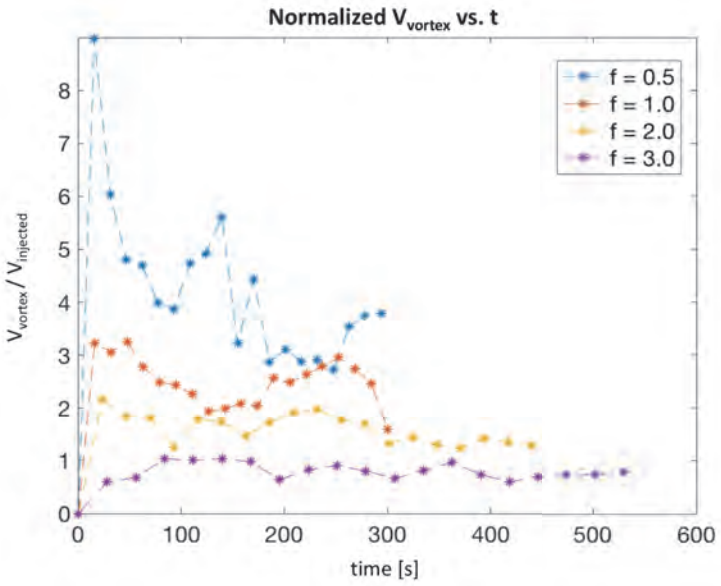

Figure 11: The volume of the vortex that develops plotted against total injected volume as a function of time. The initial entrainment, indicated by the large increase in volume at early times, is decreased with increasing f. Source conditions were $B/Q_0 = g_0' = 25\ \mathrm{cm^4 s^{-3}}$ and $M = 133\ \mathrm{cm^4 s^{-2}}$.

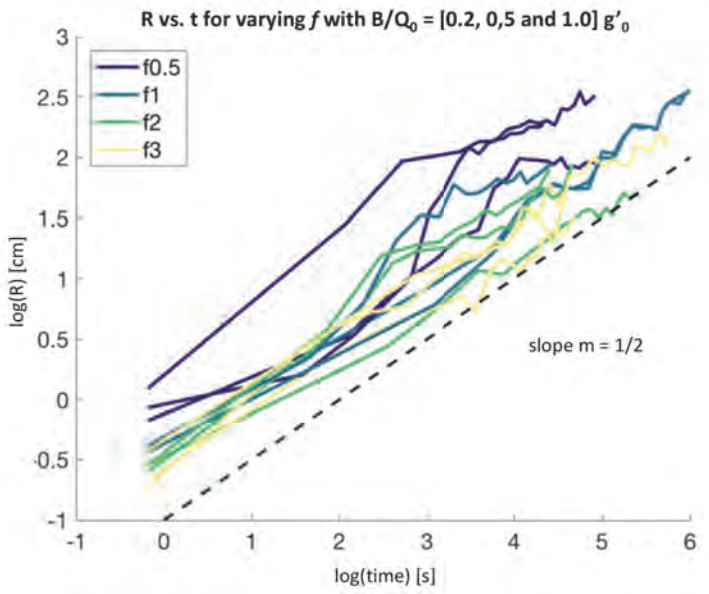

Figure 12: A log-log plot of R vs. t for varying f and three non-zero values of $B/Q_0 = [0.2, 0.5 \text{ and } 1.0]g_0'$ where $g_0' = 25$ cm^{4}s^{-3}. A line of slope $m = 1/2$ is shown as a dotted line for comparison to the data. The scaling of $R \sim t^{1/2}$ is robust for the 12 experiments represented here.

in § 4.2.

Plots collapsing the radius according to the scaling relationships $R \sim t^{1/2}B^{1/3}f^{-1/3}$ and $R \sim t^{1/2}B^{1/3}f^{-1/2}$ are presented in Figures 15 and 16, respectively. Both of these plots collapse the data relatively well. Since M and H_T were not varied due to time constraints, there is not enough information to determine a complete scaling for radial growth of the vortex at the surface. However, there has been progress toward determining a comprehensive power law. An interesting finding that is strongly supported by this data set is that the radius grows with $t^{1/2}$ rather than $t^{1/4}$, as was determined by Griffiths and Linden [6].

4.2 Turbulence versus Rotation in Rotating Jets

In order to further understand how rotation impacts the fountain, the simplified case of a pure momentum source (i.e. a jet) with background rotation was studied. The experimental setup was the same, except salt water was injected into salt water, so there was no buoyancy flux. The experiment was repeated for the same rotation rates, $f = [0.5, 1.0, 2.0 \text{ and } 3.0]$ s^{-1}. As expected from the previous experiments, rotation plays a critical role. A time series of the early time behavior of a jet with and without rotation is shown in Figure 17. The jets subjected to background rotation are contained to a vertical column almost immediately. The non-rotating jet expands laterally and reaches the bottom. Background rotation influences the jet by constraining radial growth to a vertical column. The jet with rotation penetrates the ambient, but does not descend to the bottom of the tank as the jet does. As more fluid is added, the column grows radially and the vertical interface with the ambient fluid is maintained. The fluid appears to be forced into a Taylor column at very

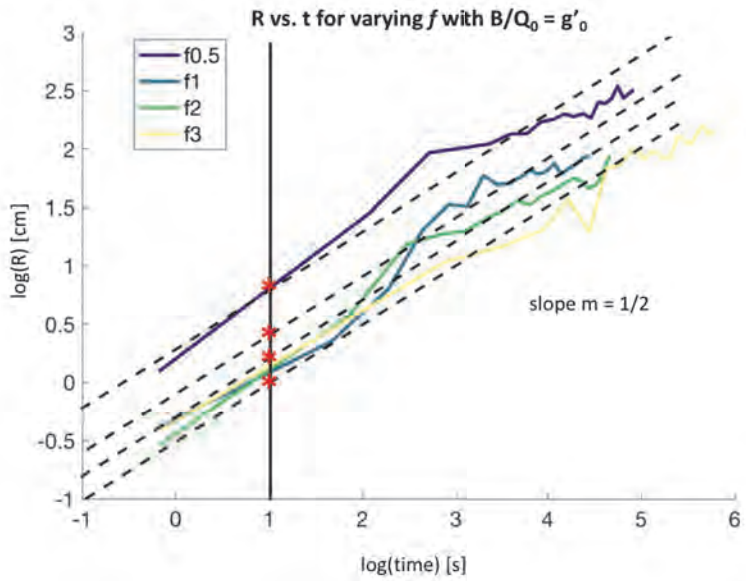

Figure 13: To estimate a power law for $R \sim f^{\beta}$ the vertical intercepts of the dotted lines, indicated by red asterisks, are plotted against log f in Figure 14. Source conditions were $B/Q_0 = g_0' = 25$ cm^{4}s^{-3} and $M = 133$ cm^{4}s^{-2}.

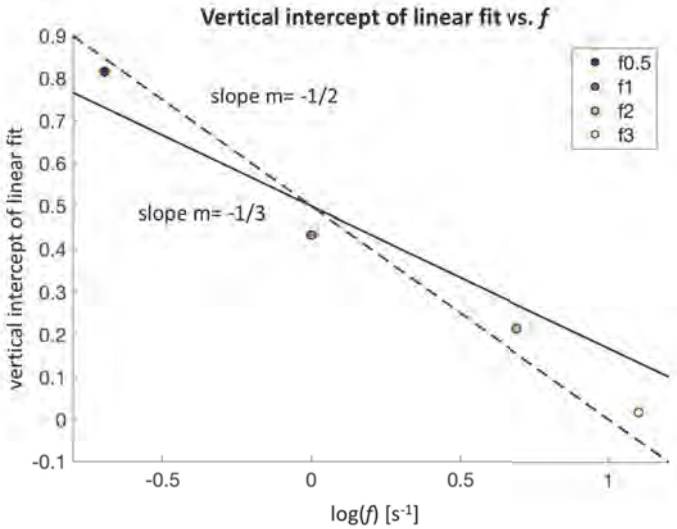

Figure 14: A plot of the vertical intercepts in Figure 13 versus log f. Source conditions were $B/Q_0 = g_0' = 25$ cm^{4}s^{-3} and $M = 133$ cm^{4}s^{-2}. Lines of slope $m = -1/2$ and $m = -1/3$ are shown for comparison. A least squares analysis produces a slope of $m = -0.44$ with an R-squared fit of $R^2 = 0.99$ and an RMS error of 0.042.

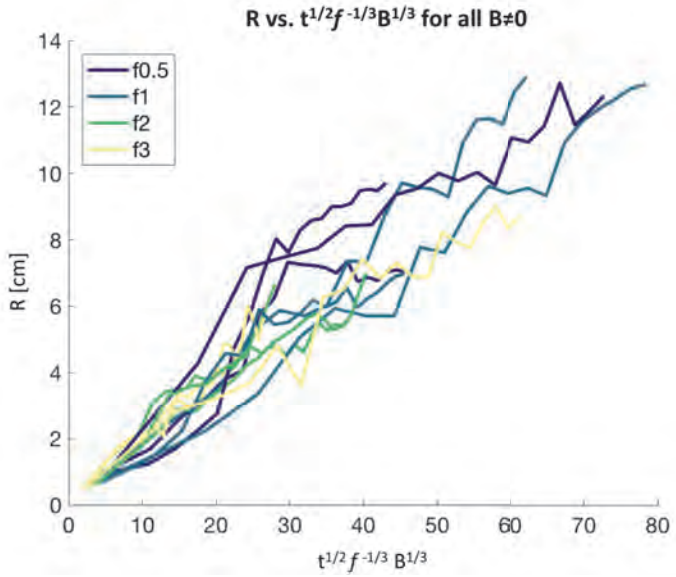

Figure 15: Collapse of R data for cases of non-zero f and B. Data is fit according to the scaling $R \sim t^{1/2} f^{-1/3} B^{1/3}$, which has dimensions of $\mathrm{T}^{-1/6}\mathrm{L}^{4/3}$. $B/Q_0 = [0.2, 0.5 \text{ and } 1.0] g_0'$ where $g_0' = 25$ cm^{4}s^{-3}.

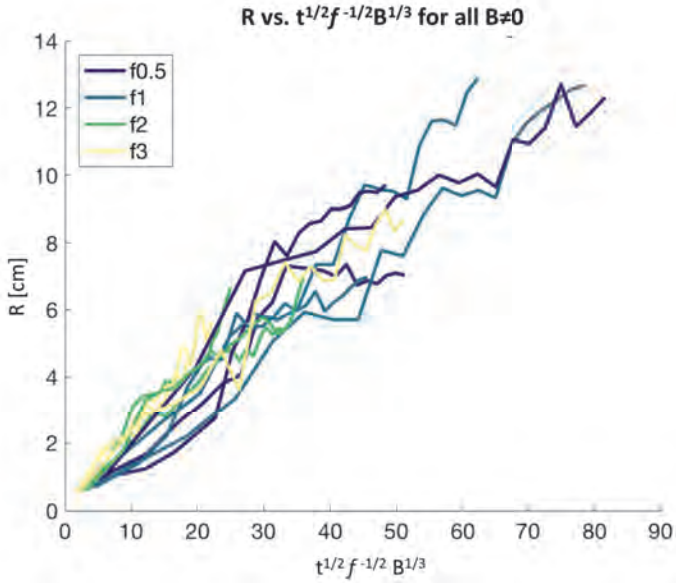

Figure 16: Collapse of R data for cases of non-zero f and B. Data is fit according to the scaling $R \sim t^{1/2} f^{-1/2} B^{1/3}$ which has dimensions of $\mathrm{T}^{-1/2}\mathrm{L}^{4/3}$. Source conditions were $B/Q_0 = [0.2, 0.5 \text{ and } 1.0] g_0'$ where $g_0' = 25$ cm^{4}s^{-3}.

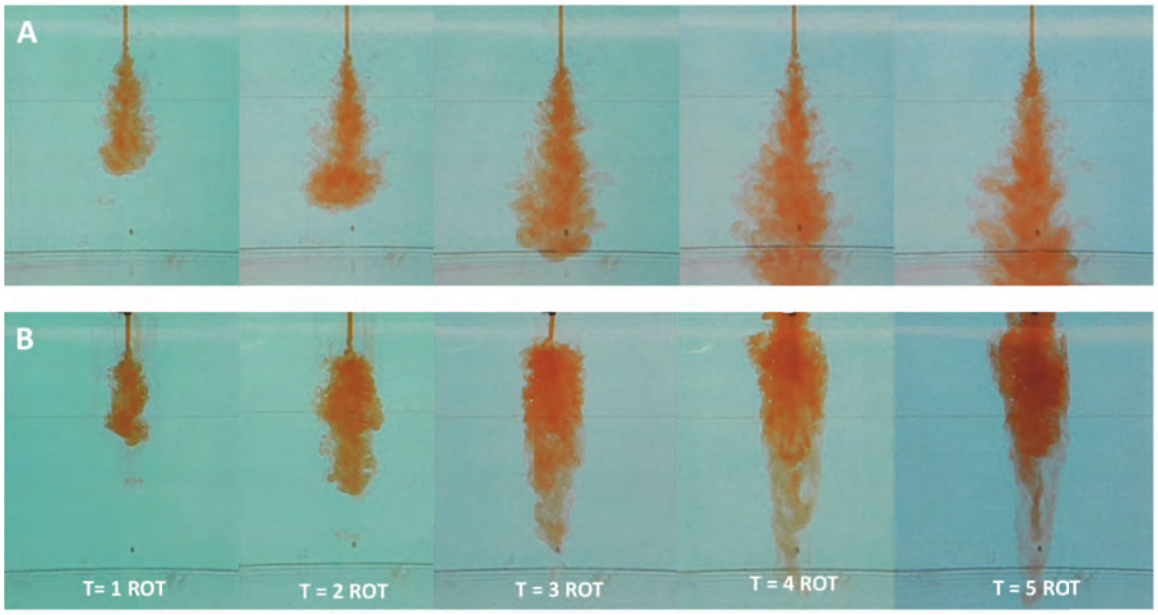

Figure 17: A time series comparing a turbulent jet with no background rotation (A) and with background rotation (B). The rotation rate is $f = 3.0$ s^{-1}, corresponding to one rotational period (T = 1 ROT) of 4.2 s. Snapshots are taken after 1,2,3,4 and 5 rotational periods. Source conditions were $B = 0$ and $M = 133$ cm^{4}s^{-2}.

early times, as soon as two rotational periods. In order to quantify the role of rotation, the radius of the initial Taylor column, R_{TC}, was plotted against f. An example measurement R_{TC} is shown in Figure 18.

From dimensional analysis an expected scaling for f can be obtained. For a non-buoyant ($B = 0$), turbulent jet with background rotation the meaningful physical parameters are R_{TC}, f, and M. From this, $R_{TC} \sim f^{-1/2}M^{1/4}$ is expected. A dotted line of slope $m = -1/2$ is plotted along with the experimental results in Figure 19. This fits the data well and is consistent with the proposed scaling. A linear least squares analysis yielded a power law exponent of -0.46 with and R-squared error $R^2 = 0.96$ and an RMS error of 0.089. This result agrees with a study of rotating jets by Etling and Fernando, [5]. This scaling of $f^{-1/2}$ may be influencing the radial growth of the vortex for the buoyant cases. This finding supports the scaling of $R \sim f^{-1/2}$, although more data is necessary to validate the relationship.

5 Conclusion and Future Work

The dynamics of turbulent fountains and jets with background rotation was investigated by varying the non-dimensional parameter, fM/B, which represents a ratio of the fountain time to the rotation time. Key results of this project are shown in Figure 20. Although more rigorous statistical analysis is ongoing to clarify and validate the scaling laws presented in this report, many trends have been observed clearly. For cases where $B \neq 0$, once the

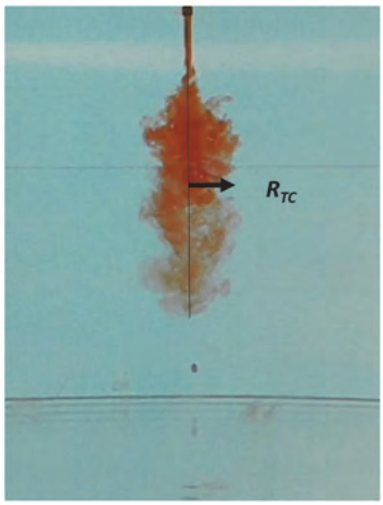

Figure 18: The distance treated as the radius of the Taylor column, R_{TC}, for jets with background rotation. The source conditions were $B = 0$ and $M = 133$ cm^{4}s^{-2} with a background rotation of $f = 3.0$ s^{-1}.

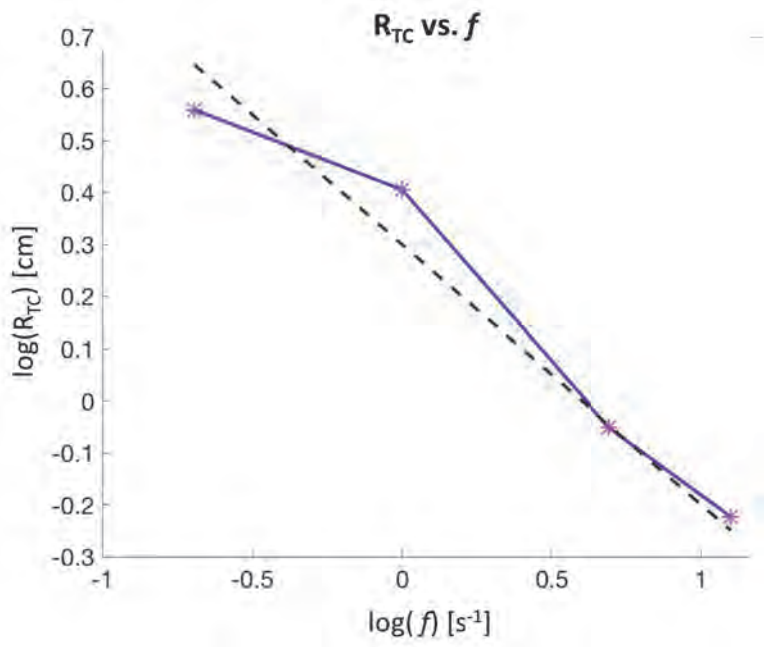

Figure 19: A log-log plot of the radius of the Taylor column versus f. A dotted line of slope $m = -1/2$, which is expected from dimensional analysis, is shown for comparison. The source conditions were $B = 0$ and $M = 133$ cm^{4}s^{-2}.

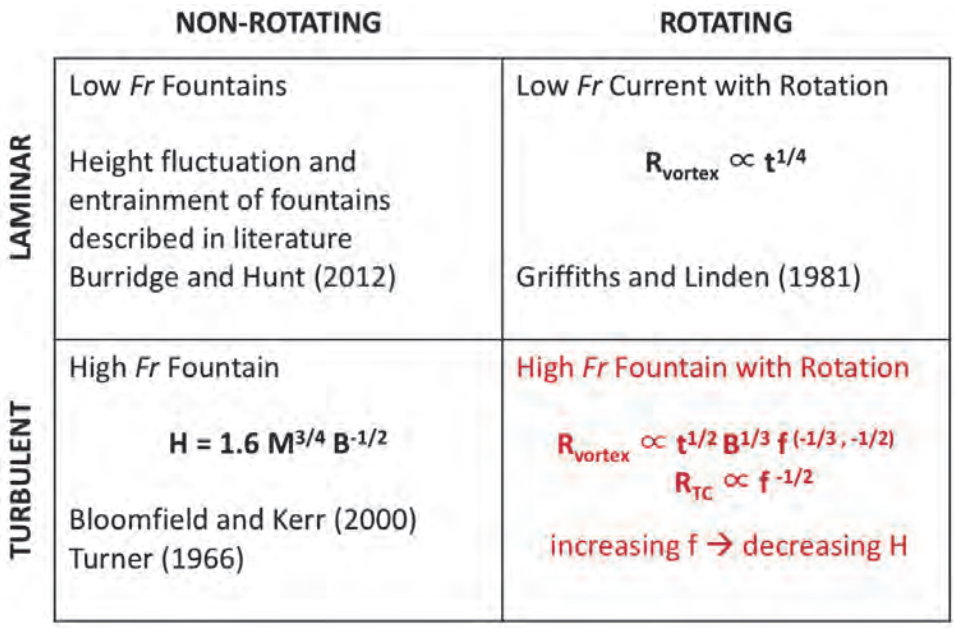

Figure 20: As a follow up to the diagram shown in Figure 4, the results of this project have begun to populate the bottom right quadrant.

fountain returns to the surface, the radius of the vortex grows as $R \sim t^{1/2}$. Comparing cases with varying B showed $R \sim B^{1/3}$; however, the dependence on rotation is less clear, leaving $R \sim f^{-1/2}$ and $R \sim f^{-1/3}$ as possible power laws. There is support for both of these laws. More data is necessary to clarify the dependence on f. It could be argued that $R \sim f^{-1/2}$ based on evidence that a Taylor column with $R_{TC} \sim f^{-1/2}$ establishes at early times.

Experiments varying H_T and M will be performed in the near future. H_T appears to matter for the fountain system. This is in contrast to Bloomfield and Kerr [3], where the penetration height H_f does not depend on H_T. Solid-body rotation introduces a stiffness to the ambient fluid which strongly discourages vertical motion, in accordance with the Taylor-Proudman Theorem. This is apparent by how rotation systematically suppresses fountain penetration. The fluid appears to be forced into a Taylor column after just a few rotation periods. R_{TC} appears to scale according to $R_{TC} \sim f^{-1/2}$.

Another ongoing aspect of this project is investigating the onset of instability once the vortex becomes unstable to rotation. A picture demonstrating the onset of different instabilities shown from the top view is show in Figure 21. For a turbulent source with background rotation, higher order azimuthal wave numbers are observed, as they are in Griffiths and Linden [6]. Further characterization of these instabilities will be the topic of future work.

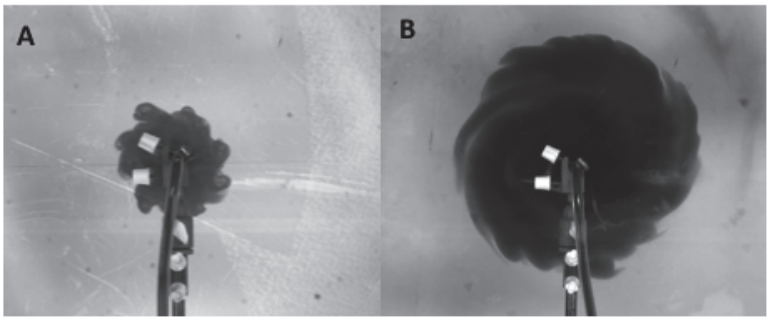

Figure 21: Once the fluid returns to the surface, the vortex becomes unstable to rotation. Characterization of this unstable behavior is ongoing. Panel A shows source conditions of $B/Q_0 = 0.2g_0' = 4.9$ cm^{4}s^{-3} and $M = 133$ cm^{4}s^{-2}, with a background rotation of $f = 2.0$ s^{-1}. Panel B shows source conditions of $B/Q_0 = 0.2g_0' = 4.9$ cm^{4}s^{-3} and the same M with a background rotation of $f = 0.5$ s^{-1}.

References

[1] J. K. Ansong, A. Anderson-Frey, and B. R. Sutherland, *Turbulent fountains in one- and two-layer crossflows.*, Journal of Fluid Mechanics, 689 (2011), p. 254.

[2] J. K. Ansong, P. J. Kyba, and B. R. Sutherland, *Fountains impinging on a density interface.*, Journal of Fluid Mechanics, 595 (2008), pp. 115 – 139.

[3] Bloomfield and Kerr, *A theoretical model of a turbulent fountain*, Journal of Fluid Mechanics, 424 (2000), pp. 197–216.

[4] H. C. Burridge and G. R. Hunt, *The rise heights of low- and high-froude-number turbulent axisymmetric fountains*, Journal of Fluid Mechanics, 691 (2012), p. 392416.

[5] D. Etling and H. Fernando, *On the influence of background rotation on turbulent jets*, Recent Research Advances in the Fluid Mechanics of Turbulent Jets and Plumes, (1994), pp. 401–411.

[6] R. Griffiths and P. Linden, *The stability of vortices in a rotating, stratified fluid.*, Journal of Fluid Mechanics, 105 (1981), pp. 283 – 316.

[7] G. Hunt and H. Burridge, *Fountains in industry and nature*, Annual Review of Fluid Mechanics, 47 (2015), pp. 195–220.

[8] J. Turner, *Jets and plumes with negative or reversing buoyancy*, Journal of Fluid Mechanics, 26 (1966), pp. 779 – 792.

Swimming with Posts

Sara Lenzi

August 23, 2018

1 Introduction and Motivations

Biological problems regarding microorganisms moving into viscous fluid are interesting fields of research since the second half of 1900s [1][2]. The case in which such organisms are embedded in a fluid in presence of a microstructure is particularly useful for the study of fundamental biological phenomena but differs from the classical continuous fluid dynamics problem because of the presence of obstacles comparable in size with the swimmers themselves.
Some examples can be [3][5]:

- *mammalian sperm in the viscous vaginal mucus : where the swimmer (sperm) is constrained to move across a fibrous fluid (mucus)*;

- *nematode moving in the soil*;

- *diseases diffusion, like malaria, occurs when male gametocyte parasite Plasmodium navigates a dense suspension of red blood cells in the digestive tract of the mosquito as it searches for its female counterpart.*

For all these reasons the analysis of the ondulatory motion of microorganisms at low Re numbers still arouses the interest of scientists. About this an important experimental work has been developed by Majmudar et al. [3] to infer which is the optimal swimming wavelength for an organism embedded in a fluid or how the swimmer motion/speed is affected by obstacle spacing.
Results reported by Majmudar et al. [3] show that the presence of obstacles, against which the swimmer can push or pull, generally enhances swimmer velocity.

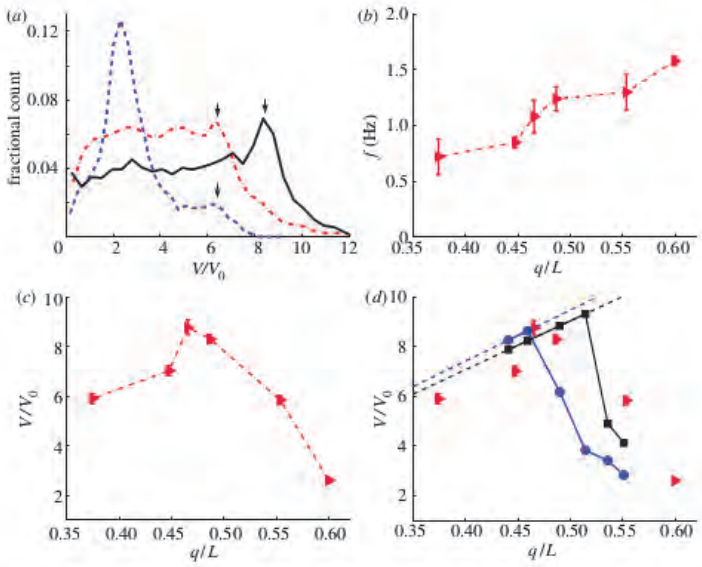

Figure 4. Velocity and frequency variations in experiments and simulations. (*a*) The fractional count of V/V_0 from the experiments. Each curve corresponds to one of the different values of q/L: $q/L = 0.37$ (dash-dotted line), $q/L = 0.47$ (solid line) and $q/L = 0.55$ (dashed line). The arrows point to the peaks associated with swimming along the lattice diagonals. Values below $V/V_0 = 1$ correspond to situations when the worm is 'trapped' and moves even slower than the free-swimming case. (*b*) Experimental data for the nematode's average undulation frequency f as a function of q/L; f monotonically increases with increasing q/L. (*c*) The experimentally measured values of enhanced velocity, V/V_0, when the worm moves along the diagonal, are shown as a function of q/L. V/V_0 exhibits non-monotonic behaviour and reaches a peak value of $V/V_0 \approx 9$ when $q/L = 0.47$. (*d*) The solid lines with symbols show the enhanced velocity given by the mechanical worm model and are compared with the corresponding experimental values (solid triangles). The solid line with squares indicates the enhanced velocity for the simulations where $\mathcal{W} = 11.3$, whereas the solid line with the circles corresponds to those where $\mathcal{W} = 15.1$. The dashed lines indicate speeds given by $V = \sqrt{2}qf$; for both values of $\mathcal{W}$, the simulation data for V/V_0 follow this relation until V/V_0 reaches its peak value.

Figure 1: Some experimental results from Majmudar et al.
Note in the bottom panels the velocity reaches its maximum for $\frac{q}{L} \approx 0.5$.

Even if maintaining a fixed shape, the swimmer changes motion frequency in function of viscosity (decreasing frequency for increasing viscosity and vice versa).
In particular, it approaches the crawling frequency when the structure spacing is smaller and an increased one for higher spaced obstacles.

In [3] is shown how, in certain conditions, the swimmer maximizes its speed for $\frac{q}{L} \approx 0.5$ where $\frac{q}{L}$ is the ratio between the swimmer length (q) and the spacing between obstacles (L) (see fig.1). In our work, due to our different definitions that will be shown later, we replaced this ratio with κ.
Moreover, it has been observed that changes in swimmer speed are not correlated to maximizing efficiency or locomotion but only to surrounding environment changes (ex. viscosity).

In this work the following are assumed:

- **swimmer interacts with topography only on one side**. Top and bottom bounds of 2D domain correspond to the swimmer and the topography, respectively;

- **no head/tail for the swimmer**. Ignoring as a first approximation the particular interaction of extremities with the fluid field;

- **periodic topography**. Domain contains a periodic portion of both topography and swimmer;

- **small gap**. Small distance between the swimmer and the topography;

- **no inertia for both swimmer** (organism with very small m) **and fluid** ($Re \to 0$).

On the other side we focused on some aspects we identified as interesting to be explored:

- **fixed/flexible swimmer shape**. What if the swimmer is able to maintain a constant shape against fluid's pressure during its motion? What if the profile can be modified by external forces?

- **shape of topography**. How does the particular choice of topography influence the motion? Does a different topography affect swimmer velocity?

- **finite/periodic swimmer length**. What if we consider a finite/infinite length for the swimmer?

2 Setting the Problem

Let's consider the following 2D domain in which the upper boundary is represented by the swimmer and the lower represents the topography:

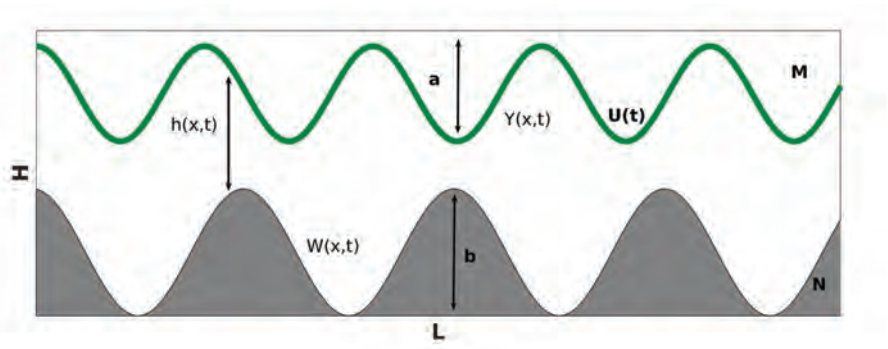

Figure 2: Sketch of domain

L is the domain length, H is the vertical dimension, h(x,t) is the mean separation between the swimmer and the wall, Y and W are the swimmer and the wall profiles, respectively.
We assume the swimmer produces a backward wave of velocity c to propel itself forward with velocity U(t).
The domain contains exactly M wavelengths of the swimmer profile and N wavelengths of the wall where M and N are different integers.
If $\lambda = \frac{2\pi}{k}$ and $\lambda_w = \frac{2\pi}{K}$ are the wavelengths of the swimmer and the wall, respectively, we obtain the following relation:

$$L = M\lambda = N\lambda_w = M\frac{2\pi}{k} = N\frac{2\pi}{K} \tag{1}$$

Furthermore, in the reference frame of the swimmer, for the swimmer and the wall profile :

$$\begin{cases} Y = a\cos k(x+ct) + H \\ W = b\cos K\left(x + \int_0^t U(t')dt'\right) \end{cases} \tag{2}$$

with velocity boundary conditions:

$$\begin{cases} \vec{v}(x,Y,t) = (0, Y_t) \\ \vec{v}(x,W,t) = (-U(t), 0) \end{cases} \tag{3}$$

at the top and bottom profiles, being Y_t the time derivative.

The equations of dynamics for the 2D Newtonian inertia-less fluid are the following:

$$\begin{cases} p_x = \mu(u_{xx} + u_{yy}) \\ p_y = \mu(v_{xx} + v_{yy}) \\ u_x + u_y = 0 \end{cases} \tag{4}$$

mass and momentum conservation in the $Re \to 0$ approximation written in the x-y space. Since we consider the case of small gap ($H \ll L$ lubrication theory) the non-dimensional problem is described using different length scale for the x and y directions and as time scale the time the wave needs to move through the domain :

$$\hat{x} = kx \quad \hat{y} = y/H \quad \hat{t} = tck \quad \hat{u} = u/c \quad \hat{v} = v/cHk \tag{5}$$

respect to these variables the domain is $L = 2\pi M$, the non-dimensional equations for the profiles are

$$W = \hat{b}cos\kappa \left(\hat{x} + \int_0^t \hat{U}(\hat{t}) \right) \tag{6}$$

$$Y = 1 + \hat{a}cos(\hat{x} + \hat{t}) \tag{7}$$

and for eq.(4) we obtain

$$\hat{p}_x = (u_{yy} + \epsilon^2 u_{xx}) = u_{yy} + o(\epsilon) \tag{8}$$

$$\hat{p}_y = \epsilon(\epsilon^2 v_{xx} + v_{yy}) = o(\epsilon) \tag{9}$$

$$\hat{u}_x + \hat{v}_y = 0 \tag{10}$$

where we defined

$$\hat{a} = a/H \quad \hat{b} = b/H \quad \hat{\kappa} = K/k \quad \hat{p} = p\frac{\mu c}{kH^2} \quad \hat{U} = U/ck \quad \epsilon = kH \ll 1 \tag{11}$$

representing non-dimensional amplitudes for swimmer and topography, non-dimensional topography wavenumber, pressure and swimmer velocity,respectively.
We also add the small-ratio condition for lubrication theory.
Note that the non-dimensional $\kappa = \frac{K}{k}$ is not only the ratio of the two wavenumbers but also of the two wavelengths $\lambda = \frac{2\pi}{k}$ and $\lambda_w = \frac{2\pi}{K}$.
In the following we will use this parameter in analogy with the $\frac{q}{L}$ ratio used by Majmudar et al. with the difference that since our spacing between obstacles is $\frac{\lambda_w}{2}$ our analog reference value will be doubled.
So, while the original reference [3] is to $\frac{q}{L} \approx 0.5$, we will focus on $\kappa = 1$.

3 Swimmer Dynamics

We analyze now the force balance of the system. The normal force balance along the swimmer profile is dictated by the Euler-Bernoulli beam theory:

$$p = DY_{xxxx} - f_d \tag{12}$$

where D is the swimmer stiffness and we assume the swimmer produces wave moving backward with velocity c with the associated non-dimensional driving force:

$$f_d(x,t) = aD\cos(x+t)\,. \tag{13}$$

For $D \to \infty$ eq.(12) can be re-written as:

$$\frac{p}{D} = Y_{xxxx} - \frac{f_d}{D} \tag{14}$$

when the first term vanishes and

$$Y_{xxxx} = \frac{f_d}{D} \tag{15}$$

which after integration gives the constrain of a fixed shape condition:

$$Y \approx 1 + a\cos(x+t). \tag{16}$$

and justifies the assumption of eq.(2) for swimmer profile.
Since we solve the instantaneously no-inertia swimmer problem (in the limit of $m \to 0$) we know that $\forall t\ F = 0$ along the swimmer profile:

$$F|_{y=Y} = \int_0^{2\pi M} f dx = 0 \quad . \tag{17}$$

Considering the non-dimensional argument the non-dimensional normalized vector normal to the swimmer surface is:

$$\hat{n} = \frac{(-Y_x, 1)}{\sqrt{{Y_x}^2 + 1}} = \frac{(-\epsilon Y_x, 1)}{\sqrt{1 + \epsilon^2 {Y_x}^2}} \sim (-\epsilon Y_x, 1) \tag{18}$$

where we recalled for simplicity all the non-dimensional variables without hat and the subscript is the space derivative.
The stress tensor for the Newtonian problem is represented by the following :

$$\overline{\sigma} = \begin{pmatrix} -p + 2\mu u_x & \mu(u_y + v_x) \\ \mu(u_y + v_x) & -p + 2\mu u_y \end{pmatrix} \tag{19}$$

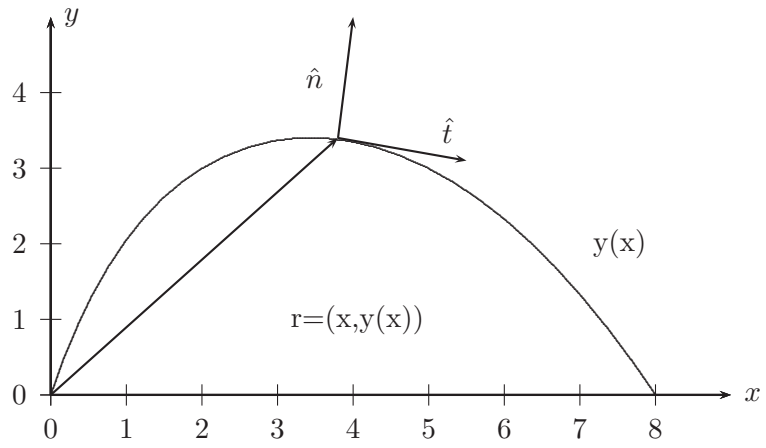

Figure 3: Tangent and normal vectors. $\hat{t} = r_x = (1, Y_x)$ and $\hat{n} = (-Y_x, 1)$ since $\hat{n} \cdot \hat{t} = 0$

where the normal components are represented by σ_{ii} and the shear components by σ_{ij}. The non-dimensional stress tensor can be expressed as :

$$\overline{\sigma} = \begin{pmatrix} -p + o(\epsilon) & \epsilon u_y \\ \epsilon u_y & -p + o(\epsilon) \end{pmatrix} \tag{20}$$

from which we can derive the x-component of the force:

$$f|_{y=Y} = \begin{pmatrix} -p & \epsilon u_y \\ \epsilon v_y & -p \end{pmatrix} \begin{pmatrix} -\epsilon Y_x \\ 1 \end{pmatrix} = \epsilon \left(p Y_x + u_y \right). \tag{21}$$

In this case the total force along x-direction can be written (see eq.(17))

$$F|_{y=Y} = \int_0^{2\pi M} p Y_x + u_y dx \tag{22}$$

using the explicit form for the local force f.
We remark that since we assume infinite stiffness for the swimmer (see eq.(13)) we didn't consider the y-component of F that is equivalent to assume that swimmer profile doesn't change shape with time (see eq.(16)).

4 Solving the Problem

To solve the problem we need now an expression for both u_y and p.
We derive an equation for the velocity field integrating eq.(8) across the domain and forcing with the boundary conditions:

$$u(y = Y) = 0 \quad and \quad u(y = W) = -U \tag{23}$$

to obtain the following expression for the fluid velocity:

$$u = -\frac{p_x}{2}(Y - y)(y - W) - U\frac{(Y - y)}{(Y - W)} \quad . \tag{24}$$

Furthermore, explicit integration of the continuity equation across the gap using eq.(24):

$$\int_W^Y u_x + v_y dy = \int_W^Y u_x dy + v(Y) - v(W) = 0 \tag{25}$$

becomes :

$$Y_t + \frac{\partial}{\partial x}\left[-\frac{p_x}{12}(Y - W)^3 - U\frac{(Y - W)}{2} - UW\right] = 0 \tag{26}$$

which (note that for the swimmer profile $Y_t = Y_x = -a\sin(x + t)$) gives us a conservation law for some quantity that can eventually depend also on time:

$$Q(t) = Y - UW - \frac{p_x h^3}{12} - \frac{Uh}{2} \tag{27}$$

where $h = Y - W$ is the gap.
With these equations it's possible to calculate the velocity field from the :

$$\begin{cases} u = -\frac{p_x}{2}(Y - y)(y - W) - U\frac{(Y-y)}{(Y-W)} \\ Q(t) = Y - UW - \frac{p_x h^3}{12} - \frac{Uh}{2} \\ f|_{y=Y} = (pY_x + u_y)|_{y=Y} \end{cases} \tag{28}$$

Assuming the no-inertia condition for the swimmer:

$$F|_{y=Y} = \int_0^{2\pi M} pY_x + u_y dx = 0 \tag{29}$$

and

$$\int_0^{2\pi M} p_x dx = 0 \tag{30}$$

(because of our choice of periodicity for p) eq.(28) becomes:

$$\begin{cases} u|_{y=Y} = \frac{p_x h}{2} + \frac{U}{h} \\ p_x = \left[-Q + Y - UW - \frac{Uh}{2}\right] \frac{12}{h^3} \\ \int_0^{2\pi M} pY_x + u_y dx = 0 \end{cases} \tag{31}$$

and from the lasts of the (31) we obtain an equation for U and Q that can be replaced into the third of the (31) to get a final equation for the swimmer velocity :

$$U = \frac{I_3^1(I_2^0 - 2I_3^1) + I_3^0(2I_3^2 - 2I_2^1)}{2I_3^2(I_2^0 - 2I_3^1) + 2I_3^0(I_3^2 - I_2^1 + \frac{I_1^0}{3}) - \frac{(I_2^0)^2}{2}} \tag{32}$$

where we defined :

$$I_n^m(t) = \int_0^{2\pi M} \frac{[1 + a\cos(x+t)]^m}{[1 + a\cos(x+t) - b\cos\kappa(x+\Psi)]^n} dx \tag{33}$$

with $\Psi = \int_0^t \hat{U}(\hat{t})d\hat{t}$.
Note that in the limit of $b \to 0$ (non wavy surface), $Y \to h$ and $I_n^m \to I_{n-m}^0$.
In this case we have :

$$U = \frac{6I_3^0 I_1^0 - 6(I_2^0)^2}{4I_3^0 I_1^0 - 3(I_2^0)^2} \tag{34}$$

that is the result predicted from the theory [5].
Plot of the instantaneous swimmer velocity is shown in fig.4 for different values of κ:

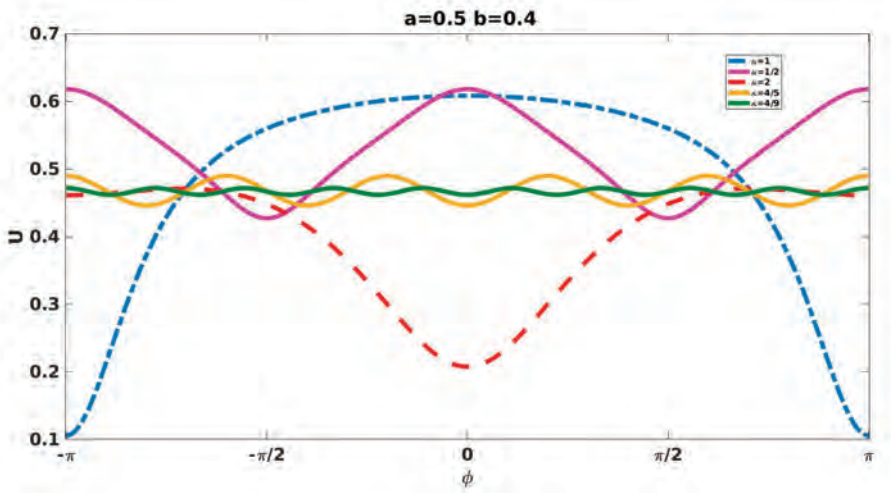

Figure 4: Example of different instantaneous velocity $U(\phi)$ for $a = 0.5$ and $b = 0.4$ and different values of κ.

The expression for the mean velocity is:

$$\bar{U} = \frac{1}{T}\int_0^T U(t')dt' = \frac{\int_0^{2\pi} \frac{U(\phi)}{\kappa(U-1)}d\phi}{\int_0^{2\pi} \frac{d\phi}{\kappa(U-1)}} \tag{35}$$

where we defined $d\phi = \kappa(U-1)dt$ to consider the net phase difference from the swimmer and the wall that is $\phi = \kappa\int_0^t \hat{U}(\hat{t})d\hat{t} - t$.
With this change of variable eq.(33) becomes:

$$I_n^m(t) = \int_0^{2\pi M} \frac{[1+a\cos\xi]^m}{\left[1+a\cos\xi - b\cos\kappa(\xi - t + \int_0^t U(t'))dt'\right)\right]^n}d\xi \tag{36}$$

then

$$I_n^m(\phi,\kappa) = \int_0^{2\pi M} \frac{[1+a\cos\xi]^m}{[1+a\cos\xi - b\cos(\kappa\xi+\phi))]^n}d\xi \tag{37}$$

where $\xi = x + t$ and $\bar{U}(t) \to \bar{U}(\phi)$.
Plot for the mean velocity, gives us:

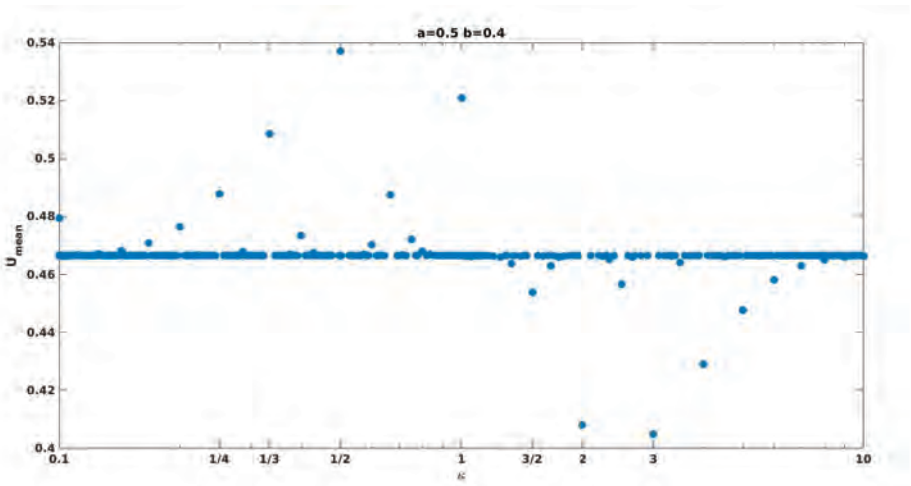

Figure 5: U_{mean} velocity for different values of κ, $a = 0.5$ and $b = 0.4$. The velocity is a discontinuous function of κ: for $\kappa > 1$ is positive, for $\kappa < 1$ is negative.

that is independent on ϕ, since we integrated on this variable, and surprisingly also on the wavenumber κ.

In particular we notice some discontinuities for certain values of κ and in general $\bar{U}$ is positive for $\kappa > 1$ while for $\kappa < 1$ is negative.
This is a non-obvious result since from the eq.(37) the dependence on κ is clear. In the following a main goal will be to understand why $\bar{U}$ is in general a constant, except for some

discrete points in correspondence of small values of κ.

4.1 Explaining U behavior

Since we want to explain the discontinuous behavior of U we considered the general integral analytically:

$$I_n^m(\phi,\kappa) = \int_0^{2\pi M} \frac{[1+a\cos x]^m}{[1+a\cos x - Y_p(\kappa x+\phi)]^n} dx \tag{38}$$

where Y_p is a general periodic function representing the topography.
Rewriting it like a sum the integral becomes:

$$\sum_{j=1}^{M} \int_{2\pi(j-1)}^{2\pi j} \frac{[1+a\cos x]^m}{[1+a\cos x - Y_p(\kappa x+\phi)]^n} dx \tag{39}$$

and operating a shift with the change of variable $\tilde{x} = x - 2\pi(j-1)$ we obtain

$$\sum_{j}^{M} \int_0^{2\pi} \frac{[1+a\cos(\tilde{x}+2\pi(j-1))]^m}{[1+a\cos(\tilde{x}+2\pi(j-1)) - Y_p(\kappa(\tilde{x}+2\pi(j-1))+\phi)]^n} d\tilde{x} \tag{40}$$

where the upper and lower limits are now independent of j. Commuting, and because of the periodicity of $\cos x$ we obtain:

$$= M \int_0^{2\pi} \frac{1}{M} \sum_{j}^{M} \frac{[1+a\cos\tilde{x}]^m}{[1+a\cos\tilde{x} - Y_p(\kappa\tilde{x}+2\kappa\pi(j-1)+\phi)]^n} d\tilde{x} = \tag{41}$$

where the argument of cos still maintains a j-dependence.

Note that until now we used an exact representation for the integral. We re-write the inner sum like:

$$\sum_{j}^{M} \frac{[1+a\cos\tilde{x}]^m}{[1+a\cos\tilde{x} - Y_p(z_j+\gamma)]^n} d\tilde{x} \tag{42}$$

where we recalled for simplicity $z_j = 2\kappa\pi(j-1)$ and $\gamma = \kappa\tilde{x}+\phi$.

Note that in the limit of $M \gg 1$ this inner sum is the Riemann integral between the two limits a and b with M the number of intervals and $\Delta\tilde{x} = \frac{b-a}{M}$ the length of the intervals.
From that assumption the argument of cos goes from $a = \kappa\tilde{x}+\phi$ $(j=1)$ and $b =$

$\kappa\tilde{x} + \phi + 2\pi M\kappa$ ($j = M + 1$ in b) and the integral (42) becomes:

$$\approx \frac{1}{2\pi} \int_{\kappa\tilde{x}+\phi}^{\kappa\tilde{x}+\phi+2\pi M\kappa} \frac{[1 + a\cos\tilde{x}]^m}{[1 + a\cos\tilde{x} - Y_p(z)]^n} d\tilde{x} \tag{43}$$

$$= N\frac{1}{2\pi} \int_0^{2\pi} \frac{[1 + a\cos\tilde{x}]^m}{[1 + a\cos\tilde{x} - Y_p(z)]^n} d\tilde{x} \tag{44}$$

remainding that $\kappa = \frac{N}{M}$ and because of the 2π-periodicity of $\cos x$.

Note that in the $M \gg 1$ limit the integral **is independent of** κ and so the final form for eq. (41) is:

$$= N \int_0^{2\pi} dx \frac{1}{2\pi} \int_0^{2\pi} \frac{[1 + a\cos\tilde{x}]^m}{[1 + a\cos\tilde{x} - Y_p(z)]^n} d\tilde{x} \tag{45}$$

This approach is extremely useful and explains why the mean velocity is not a function of κ except for small values of M.

4.2 Extension to irrational

Because the previous argument is valid only for rational values of κ we introduce the continued fractions argument to generalize the solution to all irrational numbers. Continued fractions method is useful to address an univocal representation of a real number. This method is based on the possibility of splitting a real number in its integer part q $\in \mathbb{N}$ and a rest r $\in \mathbb{R}$:

$$m = q + r \tag{46}$$

to obtain an expression through an iterative fraction as we can see in the following.
More precisely : given $(m, r_i) \in \mathbb{R}$ and $q_i \in \mathbb{N}$ $\forall m$ $\exists!(r_i, q_i) : m = q_i + r_i$ where q_i is the integer part and r_i is the rest of i-th iteration.
With this method we can iteratively split m in q_i and r_i but since :

$$r_i = \frac{1}{\frac{1}{r_i}} \tag{47}$$

and observing that by definition $r_i < 1$ and $\frac{1}{r_i} > 1$ we can iteratively apply the method defining the next $q_{i+1} = \frac{1}{r_i} > 1$. The final result is :

$$m = q_0 + \cfrac{1}{q_1 + \cfrac{1}{q_2 + \cfrac{1}{q_3 + \cfrac{1}{\cdots + \cfrac{1}{\cdots + \cfrac{1}{q_i + \cfrac{1}{\ldots + \cfrac{1}{q_n}}}}}}}} \tag{48}$$

Collecting all the q_i values m can be represented with the sequence $S = [q_0\ q_1\ q_2\ \ldots\ q_n]$.
If m is rational $\exists$ two *finite* sequences to represent this number : these sequences differ only for the last coefficient q_n and conventionally the number is represented by the truncated sequence $S = [q_0\ q_1\ q_2\ \ldots\ q_{n-1}]$.
Instead, *in the case of irrational m,* $\exists! S : S = [q_0\ q_1\ q_2\ \ldots\ q_n\ \ldots]$ *of an infinite number of coefficients* to represent it.
So, for this second case, we can use a *truncated sum as an approximation for irrationals*, knowing that in the limit of $n \to \infty$

$$\lim_{n\to\infty} \sum_{k=0}^{n} (\ldots) = \sum_{0}^{\infty} (\ldots) \tag{49}$$

we obtain a better approximation the bigger value of n we choose.
A detailed example for the irrational κ in function of q_i is:

$$\kappa = \lim_{n\to\infty} \sum_{i=0}^{n} q_i (1)^{-i}. \tag{50}$$

In conclusion, since rationals approximate irrationals, we can apply the previous argument to irrationals replacing them with a limit of truncated sums.
The assumption of $M \gg 1$ and N, M with no common factors is valid to furnish an exhaustive explanation also for irrationals to explain why for M very large we obtain a constant values for U (fig.5).
Indeed, for big M, the rational $\kappa = \frac{N}{M}$ is closer and closer to an irrational number and only small Ms furnish higher or smaller values of the mean velocity (discontinuities of $\bar{U}$ in fig.5).

5 Velocity as a Function of a & b

Summarizing what we noticed until now for the case of sinusoidal topography and fixed shape for the swimmer we observe:

- for $M \gg 1 \quad \overline{U} = f(a, b)$ the mean velocity doesn't depend on κ ($\forall \kappa : \kappa = \frac{N}{M}$).

- for $M = O(1) \quad \overline{U} = f(a, b, \kappa)$.

A brief overview on the $\bar{U}$ behavior in function of a and b is shown in fig.5
We can generally conclude that the mean velocity is a non-trivial function of a and b and that for $\kappa = n$ with n $\in$ N, $\overline{U}$ has negative sign, while for $\kappa = \frac{1}{n}$ it assumes positive values. Moreover, we can also affirm that generally the resonance ($\kappa = 1$) isn't the better condition for the velocity and some other values of the wavenumber can provide a higher velocity (for example $\kappa = \frac{1}{2}$) depending on a and b values (behavior to be explored deeper, see fig.5 and fig.6).

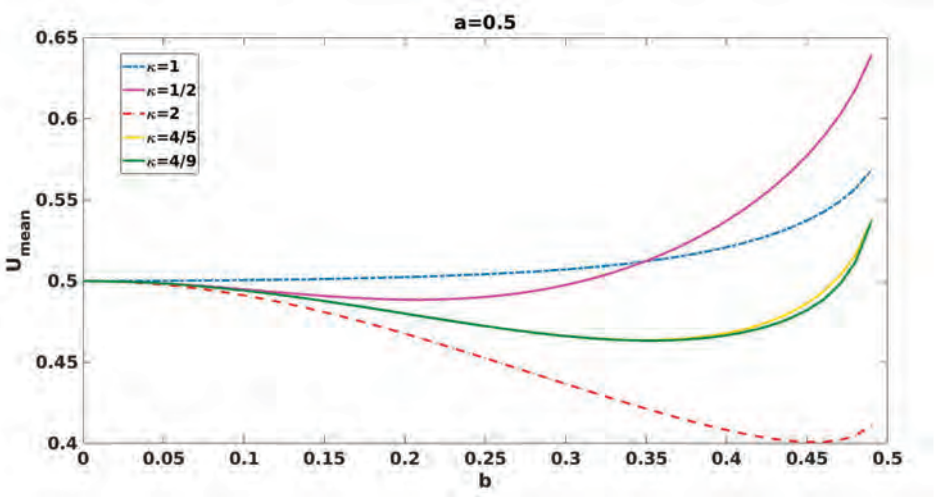

Figure 6: U_{mean} velocity in function of increasing b for different values of κ and $a = 0.5$. The plot show that the best κ depends on the value of b.

Plot of $\bar{U}$ for fixed value of a varying b show that the higher value of the mean velocity depends on the amplitude of topography (fig.6). The same can be noticed for $\bar{U}$ in function of varying a for fixed value of b (fig.5).

Although $U(\phi)$ behavior is not surprising for $a < 1 - b$, meaning that for all the values of phase the swimmer can freely move along the gap, this behavior changes for values of $a > 1 - b$. This last case is shown in fig.8 where instantaneous velocity is plotted against phase for different values of a. From the plot is clear that if for example $a = 0.9$ the swimmer velocity is smaller than the topography velocity for all values of initial phase. Because of this non zero relative velocity the swimmer will reach the topography independently of

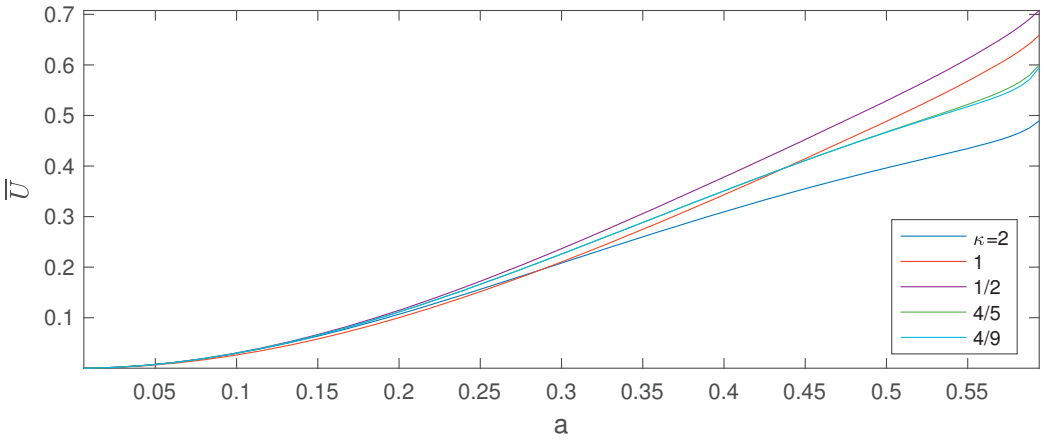

Figure 7: U_{mean} velocity in function of increasing a for different values of κ and $b = 0.4$. The plot shows that the best κ depends on the value of a.

the value of the initial phase. The reached state is a locked state with contact,where we define a locked state as that state in which the swimmer is moving with the same velocity of the topography.

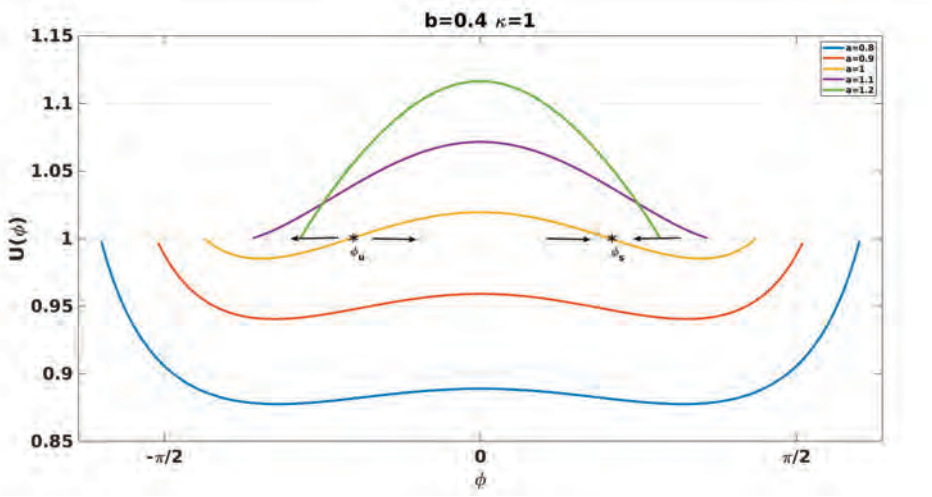

Figure 8: Instantaneous velocity against phase for $b = 0.4$ and $\kappa = 1$ with varying a. Stable and unstable states are marked with stars. For positive phases the swimmer is in a stable equilibrium (approaching the locked state), for negative phases the equilibrium is unstable and the swimmer departs from the initial phase. In this second case two different developments take place : for $\phi > \phi_u$ the swimmer moves to the stable attraction basin while for $\phi < \phi_u$ it crash against topography.

Non-trivial results can be observed for bigger values of a (example $a = 1.1$). In fig.8 two

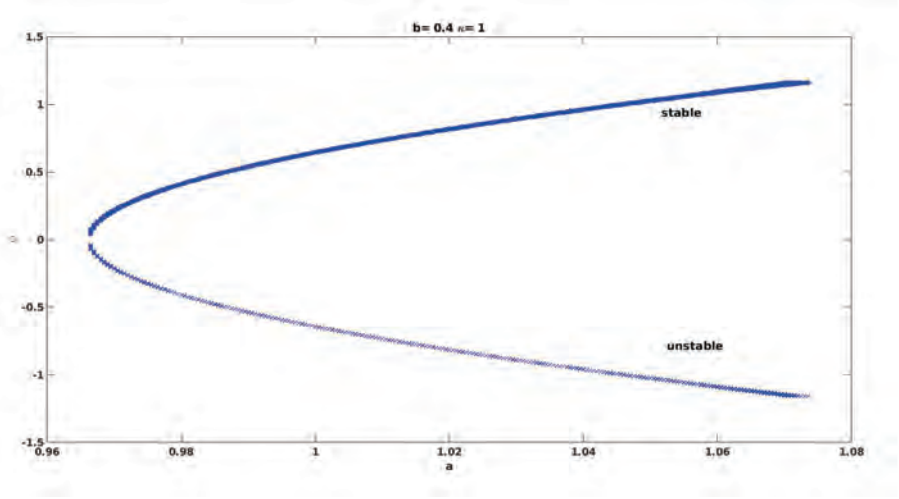

Figure 9: Bifurcation diagram: for positive phases the swimmer is in a stable equilibrium, for negative phases the equilibrium is unstable and the swimmer departs from the initial phase.

different value of phase are marked : both of them are locked state since their velocity is $U = 1$.
The locked state for $\phi < 0$ describes a swimmer profile shifted on the right with respect to the topography, in this case, increase in phase brings increase in velocity (i.e. moving away from the locked state) and the same for phase decrease which brings to a lower velocity. We can then affirm that the locked state with negative phase is an unstable state, marking it as ϕ_u. For positive ϕ the swimmer is shifted to the left (see eq.(13)), and in this case an increasing in phase is linked to a decreasing in velocity and the other way around for decreasing in phase. For this reason the $\phi > 0$ locked state is a stable state (ϕ_s).

In conclusion, the general behavior of the system is the following : for initial phases bigger than ϕ_u the velocity of the swimmer increases and decreases to reach the topography velocity (in the wave reference frame) and moves with that: this kind of locked state is **without contact** since the swimmer maintains a phase difference with the topography. For an initial phase smaller than ϕ_u, the swimmer is not able to synchronize with the topography and will reach the topography (locked state **with contact**). Bifurcation diagram for this problem is shown in fig.9. Note that the considered range of a-values is very small, meaning that it's unlikely to find these kind of states.

6 Swimming with Posts

We approach now the problem with posts to study how the topography affects the velocity field. The swimmer still has an infinite stiffness so its shape doesn't change with time. The new domain is shown in fig.10 :

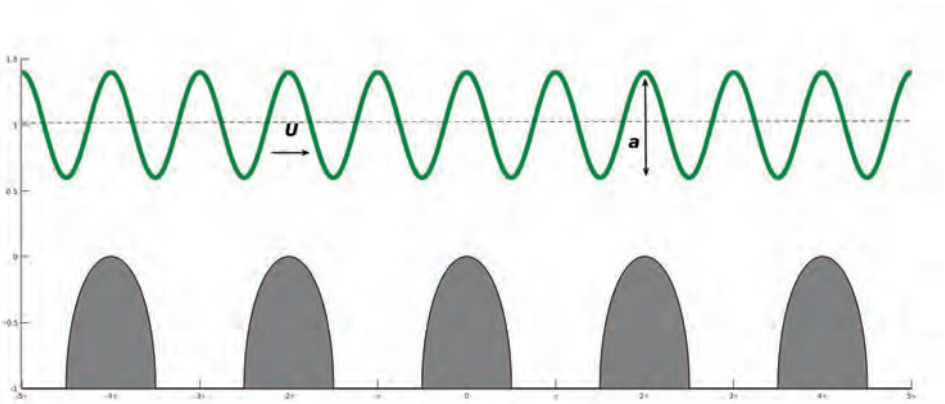

Figure 10: Picture of the domain with posts.

where posts are represented as regular semicircular structures separated by variable depth troughs (choice of using half-circle shape is due to the mathematical limits of defining circular posts).
Even if, in the regions where troughs are present, lubrication theory is not valid anymore, we assume in that part of domain interactions are negligible and results confirm that. Moving in the posts reference frame with the change of variable $x = \kappa\bar{x} + \phi$ we obtain for profiles:

$$\begin{cases} Y = 1 + a\cos((x-\phi)/\kappa) \\ Y_p = \left[\sqrt{max(0, 1 - \frac{4}{\pi^2}(x-2n\pi)^2)} - 1\right] \frac{1-\mathrm{sgn}\,(|x-2n\pi|-\frac{\pi}{2})}{2} - \frac{1+\mathrm{sgn}(|x-2n\pi|-\frac{\pi}{2})}{2} \cdot b \end{cases} \tag{51}$$

now the swimmer is moving forward and the increasing b determines the increasing of the trough between two posts.
We assess the problem as before to calculate the U field after the redefinition of the I_n^m integrals :

$$I_n^m = \int_{-\pi M}^{\pi M} ... = \int_0^{2\pi M} ... = \int_0^{2\pi N} \frac{(1 + a\cos(\frac{\tilde{x}}{\kappa} - \tilde{\phi}))^m}{(1 + a\cos(\frac{\tilde{x}}{\kappa} - \tilde{\phi}) - Y_p)^n} \frac{d\tilde{x}}{\kappa} \tag{52}$$

where $\tilde{x} = \kappa x + \phi$ and $\tilde{\phi} = \frac{\phi}{\kappa}$.
Because of numerical problems due to the alignment of the grid and the posts we shifted the domain from $[0, 2\pi M]$ to $[-\pi M, \pi M]$ such that jumps of topography do not fall between

two grid points giving rise to convergence problem.
Moreover, numerical results confirmed the assumptions we made to use lubrication theory and also that the assumptions that there are negligible interactions in the trough zone between the swimmer and the posts in the limit of high depth was correct.

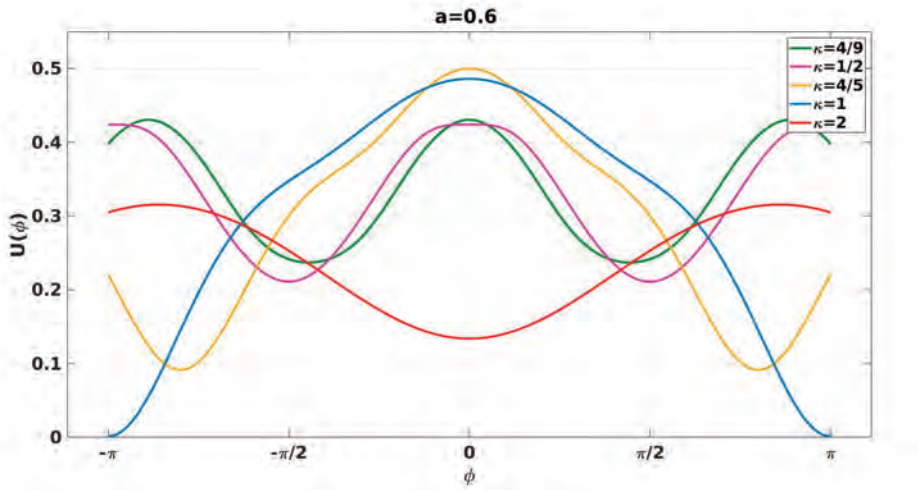

Figure 11: Instantaneous velocity against phase for different κ

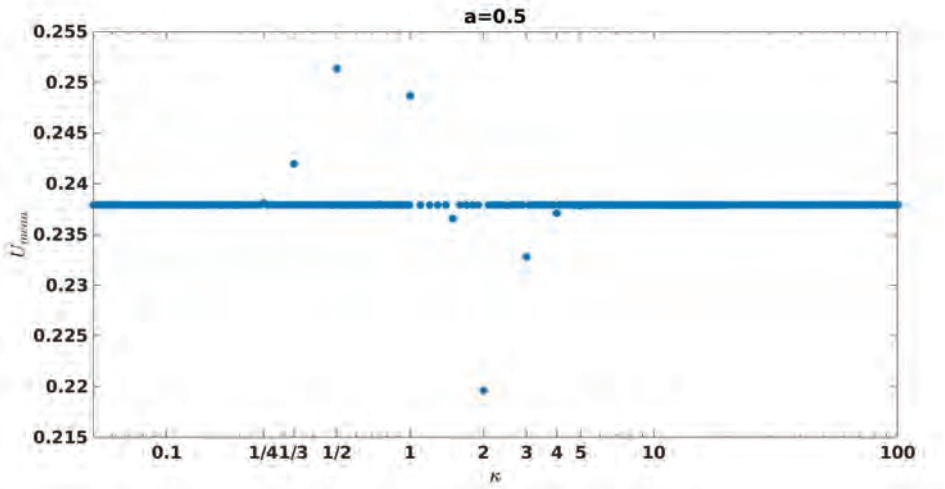

Figure 12: Mean velocity in function of κ.

The behavior of the instantaneous velocity is plotted in fig.11 and for mean velocity we observe a qualitatively similar behavior to the previous case with several discontinuities for some special values of κ (fig.12).

6.1 Increasing depth

Even if not systematically explored, we also observed the general convergent behavior of velocity for increasing depth between posts that is, in the limit of large depth, bottom doesn't interact with the swimmer.
In the following, some examples are reported to catch this general behavior (see fig.13 for instantaneous velocity, fig.14 for mean velocity and fig.15 for a bigger range of b).

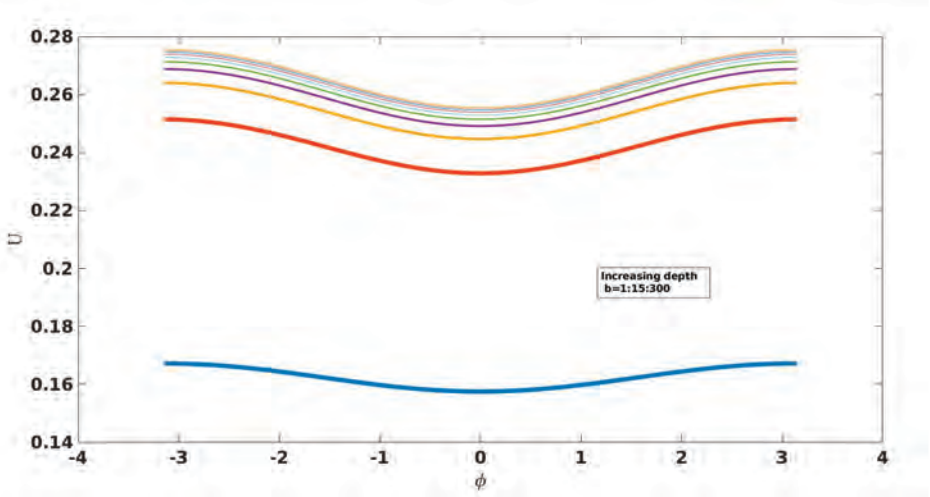

Figure 13: Example of convergent instantaneous velocity for increasing depth.

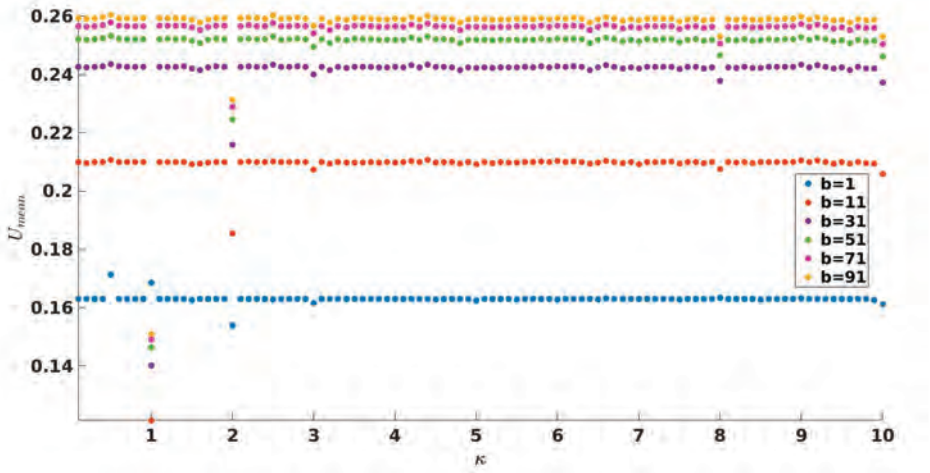

Figure 14: Example of convergent U_{mean} in function of (a small range of) κ for increasing depth.

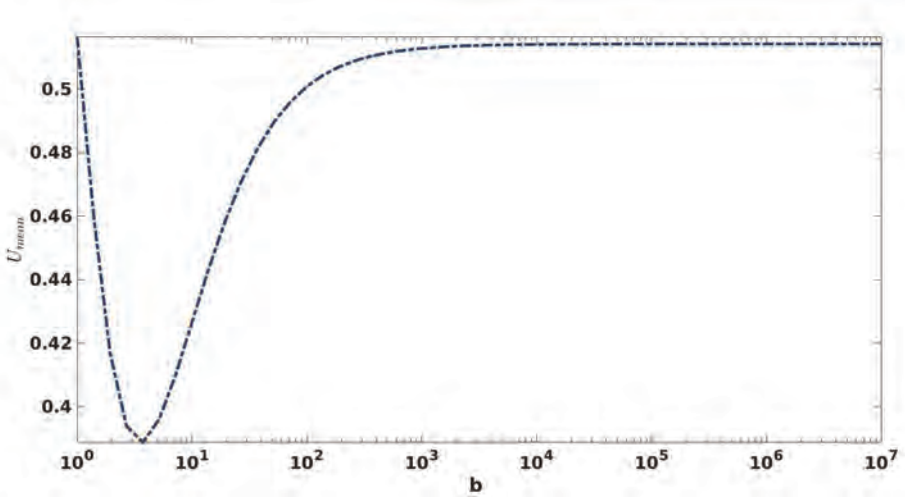

Figure 15: Example of convergent U_{mean} in function increasing depth.

Moreover, mean velocity behavior in function of variable resolution has been explored. Results shows that for increasing grid points the mean velocity profile is not affected by the particular choice of resolution, ensuring we chose adequate resolution for the computation and then the reliability of our results.

6.2 Explanation of results

As in paragraph 4.1, where we focused on the sinusoidal topography case, we can develop an integral argument to analytically explain κ dependence of $\bar{U}$ also for posts case.
Even if we don't go further into this topic, since it's formally the same as previously discussed in the no-posts case, again, also in this case, the $M \gg 1$ argument is the only one we need to explain the $\bar{U}$ behavior against κ.

7 Is $\kappa = 1$ the better condition for $\overline{U}$?

In their experimental work Majmudar et al. observed that the swimmer maximizes its speed for $\frac{q}{L} \approx 0.5$ where $\frac{q}{L}$ is the ratio between the swimmer length (q) and the spacing between obstacles (L). As already hinted at the beginning of this work, due to different definitions the $\frac{q}{L}$ ratio corresponds to our $\frac{\kappa}{2}$. Consequently in the following we will refer to $\kappa \approx 1$ instead of $\frac{q}{L} \approx 0.5$ as the best value of wavenumber to maximize the mean velocity.
Referring to those results our work is focused on looking for a mathematical model confirming Majmudar et al. observations.
In the following we report different graphs for $\overline{U}$ in function of κ to summarize our outcomes. From these graphs emerges a non-obvious mean velocity behavior as a function of

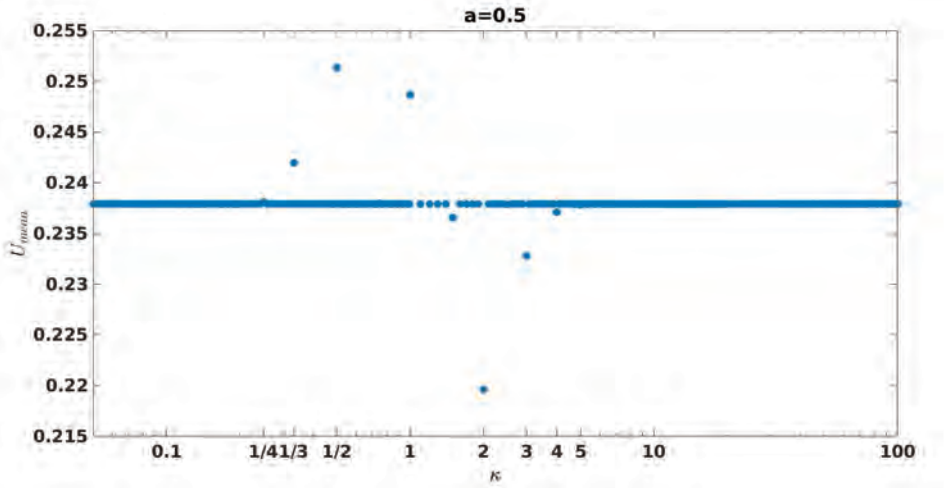

Figure 16: Mean velocity against κ, for $a = 0.5$.

wavenumber: for almost all values of κ, it is clear that $\overline{U}$ is constant except for a discrete number of κ where a discontinuous behavior is evident. For wavenumber like $\kappa = 1/4, 1/2, 1, 2, 3$ we observe a different value of $\overline{U}$ and in particular, the value $\kappa = 1$ (resonance, same number of wavelength for swimmer and topography) doesn't furnish the the higher value for the mean velocity.
Furthermore, fig.17 shows a different behavior for the posts case with respect to the previous: the mean velocity is now independent on b for big enough b and, again, $\kappa = 1$ is not the best choice for wavenumber since the $\kappa = \frac{4}{9}$ seems to furnish the higher value of $\bar{U}$ for all b.

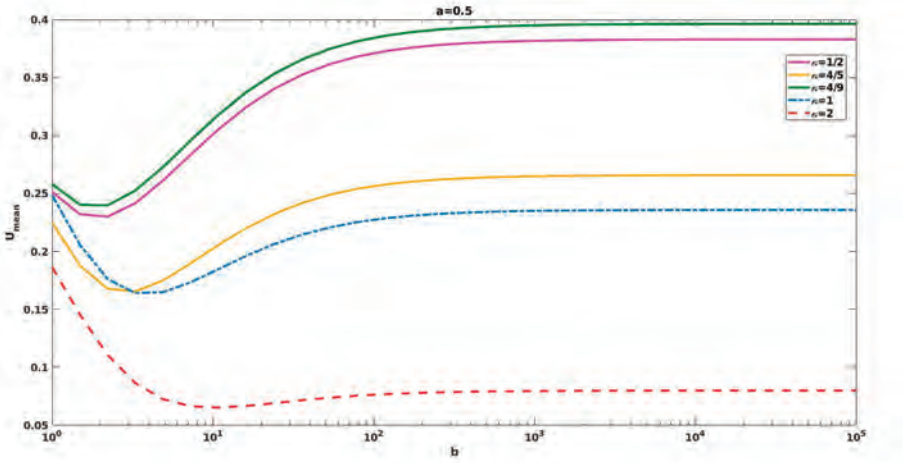

Figure 17: Mean velocity against b for $a = 0.5$ for different κ.
The best value κ seems to be $\kappa = 4/9$. Note that $\bar{U}$ reaches a constant value for big enough b.

8 Results: Instantaneous and Mean Velocity

Also in this case we briefly summarize what we noticed :

- $\overline{U} = f(a, b)\ \forall \kappa : \kappa = \frac{N}{M}$ with $M \gg 1$.

- $\overline{U} = f(a, b, \kappa)$ if $M = O(1)$.

- $\overline{U} = f(a) = \overline{U}_\infty$ for $b \to \infty\ \forall \kappa : \kappa = \frac{N}{M}$ with $M \gg 1$.

Where the last one is the converging velocity behavior we observed for increasing depth. We report now some examples for instantaneous and mean velocity as a function of a and b with an interpretation also for the case with posts.

8.1 Locked states

Also in the presence of posts we observe locked states.
In the following pictures locked states are shown for the particular value of trough depth $b = 1$:

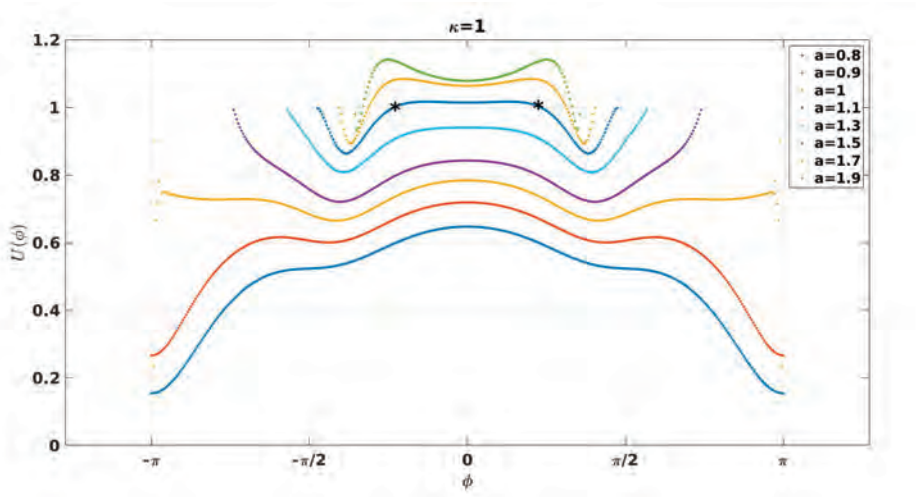

Figure 18: Instantaneous velocity against phase for $b = 1$ and $\kappa = 1$ with varying a. Locked states are marked with stars.

and for a bigger depth ($b = 10$) :

Bifurcation diagram (fig.20) shows stable and unstable states as a function of the control parameter a. Note that contrary to the previous case we observe a larger validity range for a.

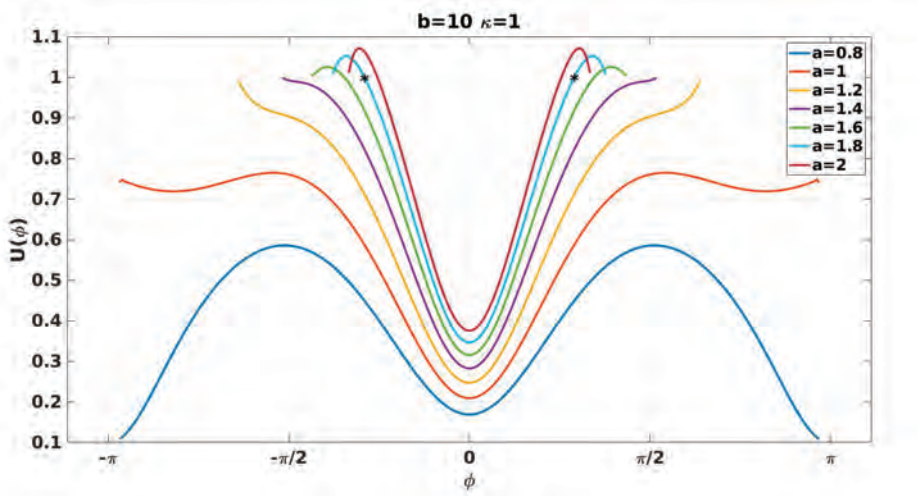

Figure 19: Instantaneous velocity against phase for $b = 10$ and $\kappa = 1$ with varying a. Example of locked states is marked with stars.

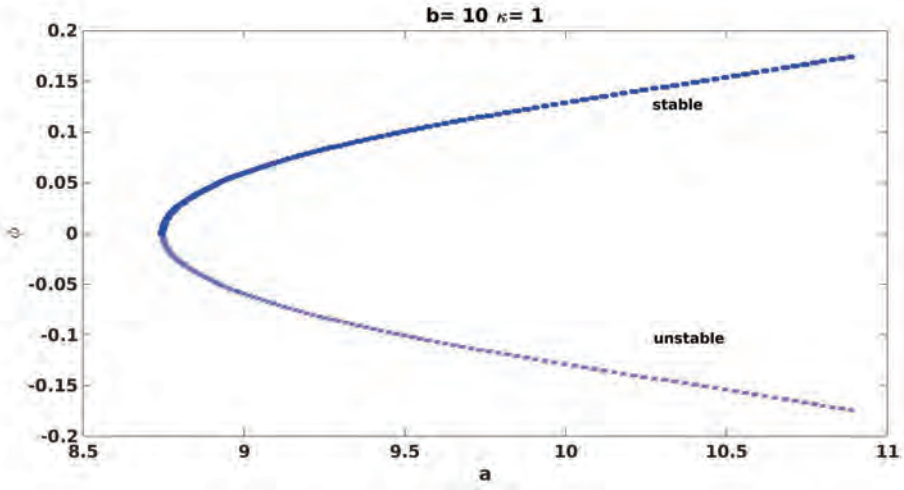

Figure 20: Bifurcation diagram: for positive phases the swimmer is in a stable equilibrium, for negative phases the equilibrium is unstable and the swimmer departs from the initial phase.

9 Finite-length Swimmer

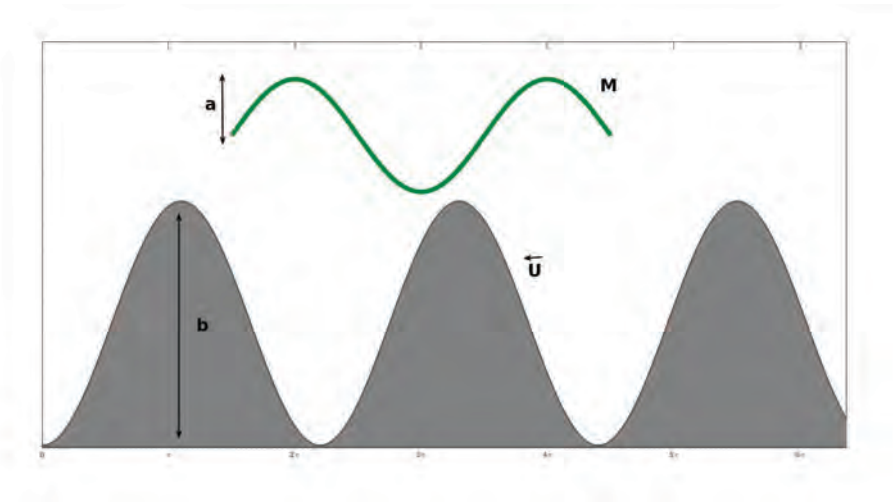

Figure 21: Sketch of finite length domain.

Another aim of this work is to understand what happens in the more realistic situation of finite length.
In this case the number of swimmer's wavelengths could be any number, that is, the topography and the swimmer are not periodic anymore. We assume $p = 0$ at the organism extremities and we come back to the fixed-shape swimmer (infinite stiffness case).
As at the beginning, we assume the no-inertia limit :

$$m\frac{dU}{dt} = F = \int_0^{2\pi} f(x)dx = 0 \tag{53}$$

with the only difference that we are now considering a finite length organism and we restrict our calculation to a wavelength for the swimmer ($M = 1 \rightarrow$ integration from 0 to 2π).
Because of the periodicity of p (infinite domain):

$$\int_0^{2\pi M} p_x dx = 0 \tag{54}$$

and for the local force:

$$f|_{y=Y} = \epsilon \left(pY_x + u_y\right) \tag{55}$$

So, for the finite length problem, if we assume that the ends make no other contribution, formulas for infinite stiffness (i.e., Y prescribed) are unchanged from the periodic problem. Plot of instantaneous velocity in function of ϕ is reported in fig.22 for different values of κ.

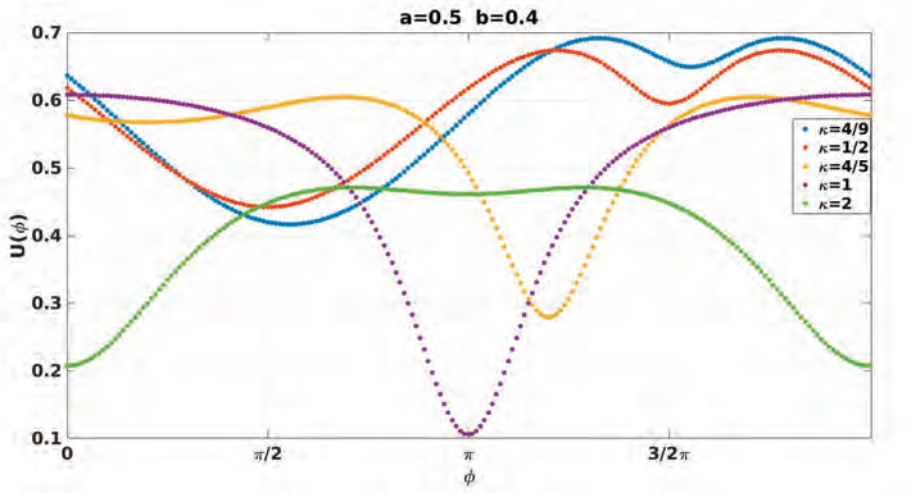

Figure 22: Instantaneous velocity against phase for $a = 0.5$, $b = 0.4$ and varying κ.

In this case the I_n^m integrals in x are only over 2π if there is exactly one wavelength along the length of the swimmer. Moreover, the $I_n^m(a, b)$ are clearly periodic in ϕ with period 2π. This gives a slightly different problem than the first periodic one. The mean speed becomes a continuous function of κ (see blue line in fig.23) and for increasing value of M it approaches the discontinuous case of infinite length (see different values of M in fig.23).

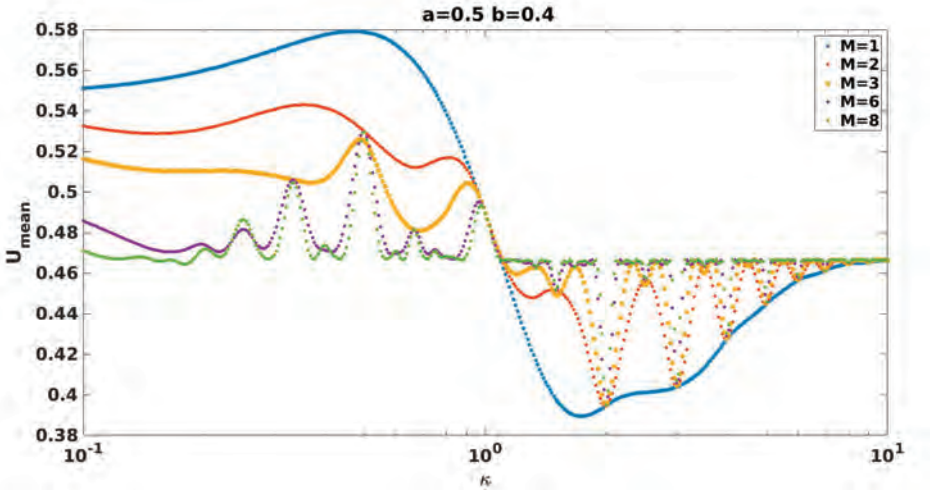

Figure 23: U_{mean} velocity in function of increasing κ for the finite length case. Different values of M represent different values of κ. Note that for increasing values of M the mean velocity is more similar to the infinite length discontinuous case.

10 Flexible Swimmer

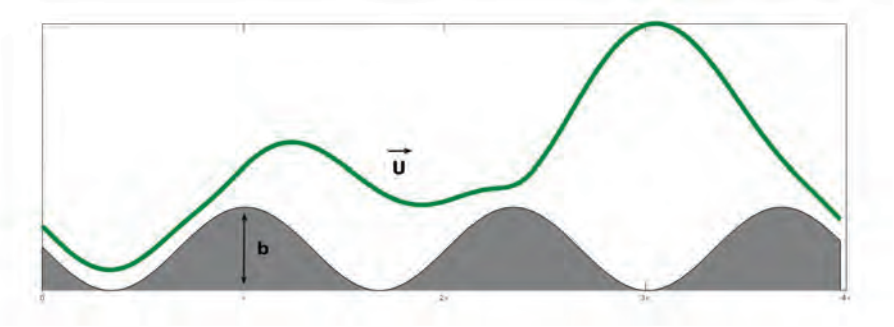

Figure 24: Domain fot the flexible case

Until now we considered the case in which the swimmer is able to maintain its shape or equivalently the case in which the swimmer is always able to exert the same force against the fluid (we didn't consider F_y contribution).
We want now to approach the case in which the swimmer is not able to exert all possible forces anymore or that it is deformable.
In this case the equations of dynamics are the same as before (see eq.(4)) since we are still considering a Newtonian fluid.
The velocity boundary conditions are:

$$\begin{gathered} u(x,W,t) = v(x,W,t) = 0 \\ u(x,Y,t) = U \qquad v(x,Y,t) = Y_t + UY_x \end{gathered} \tag{56}$$

and the force balance provides:

$$p = DY_{xxxx} - f_d \tag{57}$$

obtained referring to the *Euler-Bernoulli beam theory* which is based on evenly distributed forces along the body.
The force driving the swimmer in the swimmer's reference is

$$f_d(x,t) = A\cos\left[x + t - \int_0^t U(t')dt'\right] \tag{58}$$

and if we consider the effective inertia at the swimmer profile $y = Y$:

$$m\frac{dU}{dt} = F = \int_0^{2\pi M} f(x)dx = 0. \tag{59}$$

With the same assumptions of the beginning the integration of continuity equation across

the gap furnishes:

$$Y_t = -\frac{\partial}{\partial x}\int_W^Y u dy, \tag{60}$$

integration of momentum (see eq.(9)) gives :

$$u = -\frac{p_x}{2}(Y-y)(y-W) + \frac{y-W}{h}U \tag{61}$$

from which we obtain a formula for Y_t and Q(t):

$$Q(t) = -\frac{h^3}{12}p_x - H + (H - \frac{1}{2}h)U. \tag{62}$$

to set the problem in analogy with the initial one.

10.1 Very stiff swimmer

In the case of large stiffness the swimmer is able to equilibrate most part of the fluid force so, for a vary large stiffness $D \gg 1$, we should obtain coherent results with the first case in which we assumed a fixed shape.
Moreover, we note that for the case of flexible swimmer ($D < \infty$) because the only physical solutions are for $h > 0$, the locked states are **without contact!**
This can be appreciated from p_x equation :

$$p_x = \frac{12}{h^3}\left[Q(t) - Y + UW + \frac{Uh}{2}\right] \tag{63}$$

where we have to require $h > 0$ to ensure physical values for p_x.
Eq.(57) can be re-written as:

$$\frac{p}{D} = Y_{xxxx} - \frac{f_d}{D} \tag{64}$$

the first term goes to 0 for $D \gg 1$ and

$$Y_{xxxx} = \frac{f_d}{D} \tag{65}$$

which after integration gives the constrain for a fixed shape:

$$Y \approx 1 + a\cos(x+\phi). \tag{66}$$

that is coherent with the initial case (infinite stiffness).
A main difference is that in this case the swimmer reaches the topography moving with

that (the locked state) without contact.
A clear example of that is shown in fig.25 . The top of the figure shows the swimmer profile against time with yellow corresponding to the maximum swimmer profile while blue to the minimum. The swimmer (bottom-right in orange) is approaching the locked state which is moving with the topography (bottom-right in blue).
An example of the approach of the locked state is shown in the bottom-left sketch where velocity is reaching $U = 1$, meaning the swimmer is moving at the same velocity of the topography in the wave reference frame.

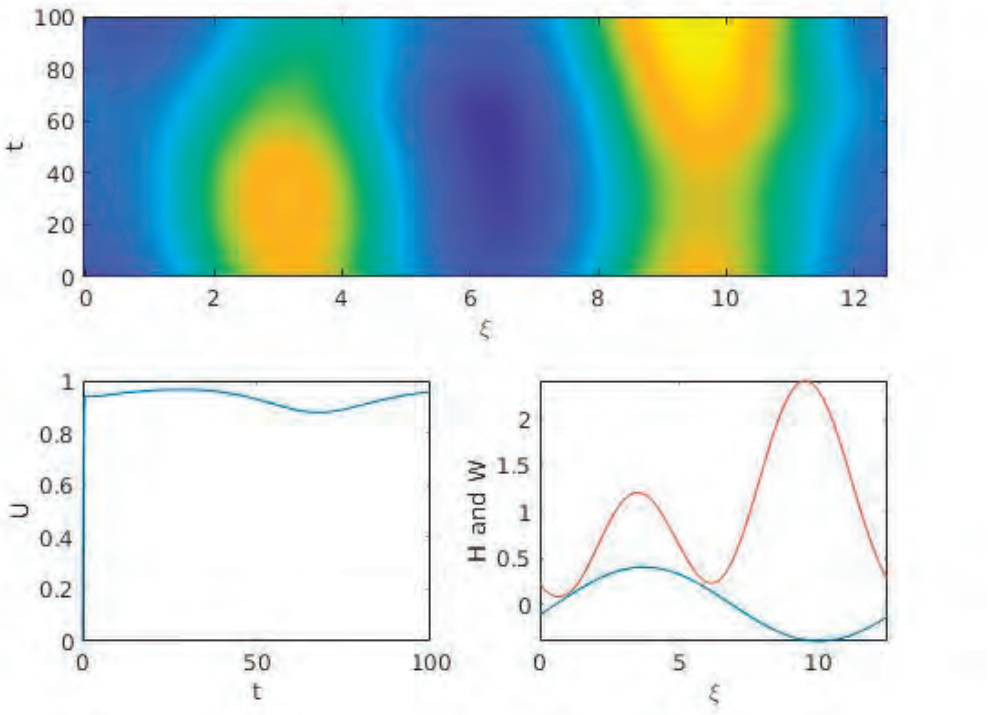

Figure 25: Top: Map of swimmer profile in function of space, ξ, and time.
Lighter areas are peaks and blue areas are troughs of the swimmer profile.
Bottom left: Example of velocity evolution with time.
Bottom right: Example of locked state: swimmer profile in orange, topography in blue.

Time evolution of swimmer profile close to the locked state is shown in fig.26 : starting with a certain phase difference, the swimmer approaches the topography reaching a *contactless* locked state.

In figs. 27, 28 some plots for the mean velocity for different stiffness and different κ are reported.

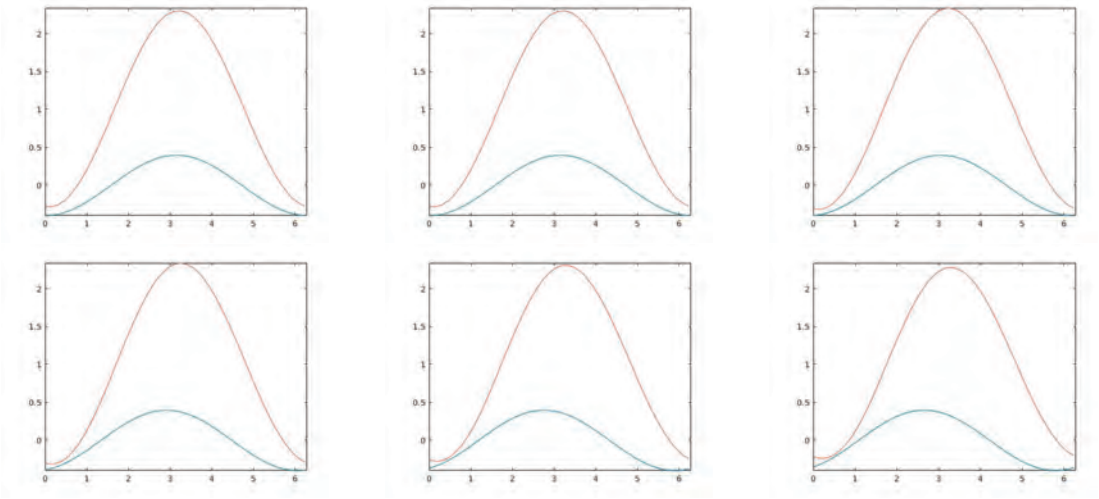

Figure 26: Evolution of swimmer profile (orange) approaching the topography (blue). From top left to bottom right : $t = 5$, $t = 15$, $t = 25$,$t = 40$, $t = 60$, $t = 80$.

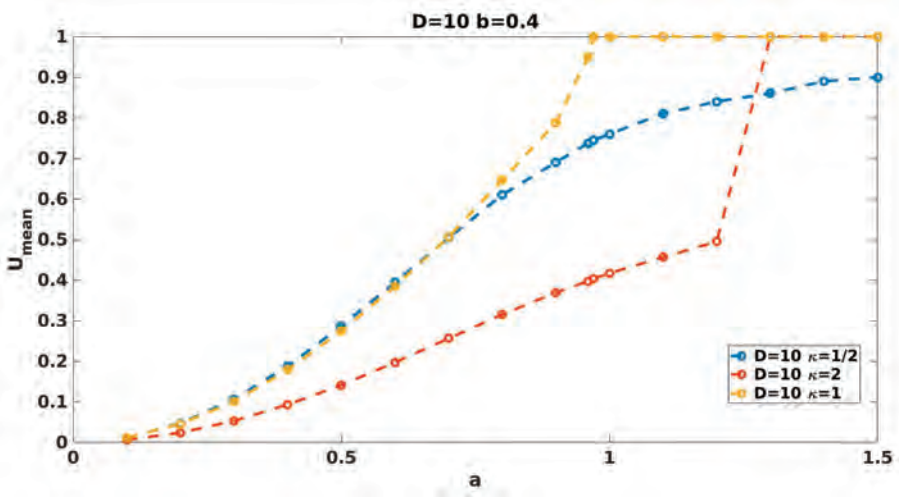

Figure 27: U_{mean} velocity in function of increasing a for finite stiffness $D = 10$ and different κ.

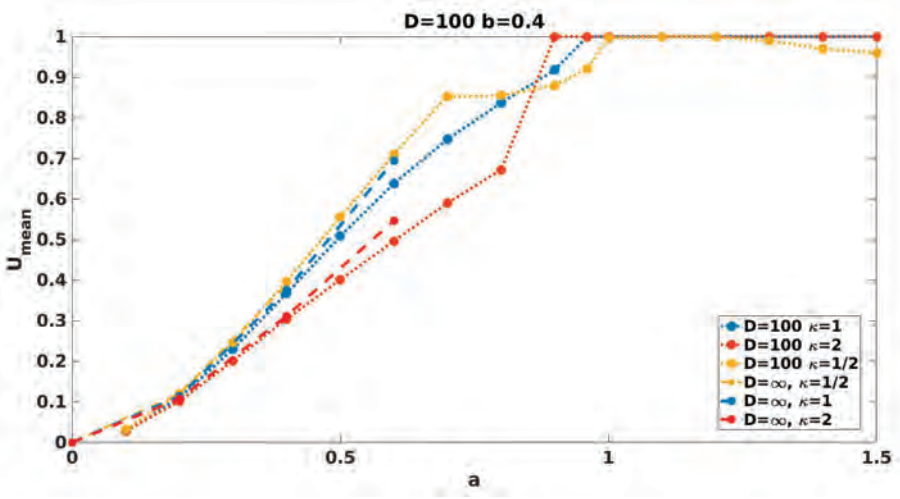

Figure 28: U_{mean} velocity in function of increasing a for infinite and finite stiffness ($D = 100$) for different κ.
The case for infinite stiffness approaches the finite stiffness case for big values of D.

Mean velocity shows both some values of stiffness for which the locked state can't be reached (see fig.27 $\kappa = 1/2$) and others for which it can.
Also in this case, for both cases of locked and not locked state, **we can't observe the higher value of velocity** in correspondence of $\kappa = 1$.

11 Conclusions and Future Works

Since our work results don't match with Majmudar et al. we need to better understand the model we built.
Several assumptions have been done and some of them could affect our results:

- **one side swimmer** : since we neglected contributions from a second side, this assumption probably leads to underrate the net velocity that generally increases in the presence of obstacles.

Further work should be focused on introduction of two side models for the topography. In this case the swimmer, interacting on both sides with topography, should increase its velocity and, in principle, change the dominant wavenumber. This change could be useful to better reproduce the C. Elegans velocity obtained by Majmudar et al.

- **no head/tail** : contributions from the extremities can deeply affect the resulting motion. For this reason further work could be focused on modeling this aspect.

- **lubrication theory** : lubrication theory is an appropriate assumption if the domain shows different scales for the two principal dimensions.
But probably, in real case, conduits along which the organisms have to move are not well represented by this approximation.

A new analysis in the absence of lubrication theory could be interesting to understand which are the limits of this theory and how accurate is the small gap assumption to describe the problem.

Acknowledgments

I'd like to thank Neil J. Balmforth and Shreyas Mandre for their fundamental support.

References

[1] Katz, D. (1974). On the propulsion of micro-organisms near solid boundaries. Journal of Fluid Mechanics, 64(1), 33-49.

[2] G. I. Taylor. (1951). Analysis of the swimming of microscopic organisms. Proc. R. Soc. London, Ser. A 209, 4447.

[3] Trushant Majmudar, Eric E. Keaveny, Jun Zhang, Michael J. Shelley. (2018). Experiments and theory of undulatory locomotion in a simple structured medium. J. R. Soc. Interface.

[4] Balmforth, N. J., Coombs, D., & Pachmann, S. (2010). Microelastohydrodynamics of swimming organisms near solid boundaries in complex fluids. Quarterly journal of mechanics and applied mathematics, 63(3), 267-294.

[5] Chan, Brian and Balmforth, N. J. and Hosoi,A. E. (2005). Building a better snail: Lubrication and adhesive locomotion. Physics of Fluids, 17(11), 113101.

[6] Batchelor, G. (2000). An Introduction to Fluid Dynamics (Cambridge Mathematical Library). Cambridge: Cambridge University Press.

Porous Convection with Internal Heating: Understanding Enceladus Hydrothermal Activity

Thomas Le Reun

October 3, 2018

1 Introduction

Enceladus, a 500 km diameter icy satellite orbiting Saturn, has drawn a lot of attention since the first flybys operated by the Cassini probe in 2005. Pictures and *in situ* astrochemical measurement have revealed the presence of a water vapour and ice plume ejected into outer space, as represented in figure 1 [26]. It emerges along fractures in the ice crust at the South Pole of Enceladus and is associated with a large heat flux anomaly of 12.5 GW. [26]. Later analyses have revealed that the ejected material contains silicate particles of nanometric size whose chemistry indicates that the water contained in the plume has been previously hot, liquid, and in contact with silicate rocks [17]. Enceladus plumes have since then been interpreted as evidence for hydrothermal activity occurring below the ice crust of Enceladus. This remains nonetheless surprising and paradoxical as, unlike the Earth, Enceladus has radiated away all its initial heat, and its small size makes internal heating by radiogenic elements insufficient to explain the abnormal heat flux [5].

Recently, Choblet *et al.* [5] have proposed a self-consistent model to explain the hydrothermal activity based on internal heating by tides in Enceladus' water-saturated porous core. Because of the small gravity intensity within the moon, its silicate core, depicted in figure 2, is thought to be unconsolidated [28, 5]. As an example, the pressure at the centre of the core is around 2 MPa, which is well below the typical fracture stress of silicate rocks encountered in planetary interiors [28]. Based on Enceladus' density and moment of inertia, researchers propose that the core porosity ranges from 20% to 30% [5]. In addition, it is also proved from tracking of Enceladus' librations that between the core and the ice crust lies a global ocean [29] whose thickness varies from 30 km to around 5 km in the model proposed in [5], the ocean's liquid water permeates and saturates the porous core. Flowing of water inside Enceladus' core may then be driven by tidal heating giving rise to instabilities. Enceladus has a short period and eccentric orbit around Saturn which exerts a huge gravitational torque because of the gigantic mass ratio between the two bodies. The spin and the orbit of the moon are synchronised. If the orbit was perfectly circular, the tidal bulge of Enceladus would always point towards Saturn, but eccentricity changes this picture as it forces periodic misalignment of the tidal bulge, leading to oscillations of the shape of the core. This periodic deformation is associated with dissipation and net heating in the bulk of the core over one period. With these three ingredients, it is proposed in [5] that as water flows inside the core, tidal heating causes its temperature to rise, thus leading to upwelling of hot plumes through the porous matrix. This process is summarised schematically in

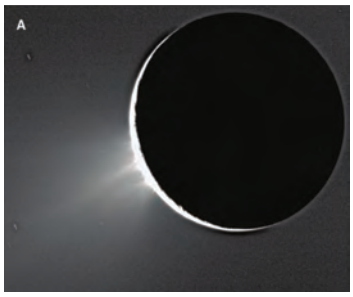

Figure 1: Picture of Enceladus' vapour and ice plume taken by Cassini, adapted from [26].

figure 2. Choblet *et al.* [5] provide a thorough numerical study of the porous convection with internal heating process in conditions similar to Enceladus' interior. They observe that this phenomenon is able to drive hydrothermal activity which is consistent with Cassini's observations. Interestingly, they showed in their simulations that the flow organises in narrow upwelling sheets that focus heat flux anomalies along lines at the surface of the core.

Yet, convective instabilities in internally heated porous layers far from the onset of motion has received little attention. Several experimental and numerical studies, mostly carried out by researchers interested in nuclear accident prevention, were focused on the onset of convective instabilities or on averaged heat transport through closed porous layers [3, 24, 13, 19, 8]. To the best of our knowledge there is no quantitative study describing flow structures inside such a porous layer and the associated thermal anomalies at the top boundary. In addition, Enceladus' core includes additional complexity as it communicates with a layer of unconfined liquid water: the subsurface ocean. Heat and mass transport are coupled between the two media and their behaviours are governed by very different physics. Studies of instabilities driven by temperature differences have been carried out in the context of nuclear accident prevention, waste storage in deep geological repositories or solidification of binary alloys [1, 2, 20]. Yet they are restrained to quantifying either the onset of instabilities [4, 16], or to heat transfer close or far from the onset of motion [1]. Other numerical works, mostly carried out in a geophysical fluid dynamics context, have proposed a simplification to the issue of two layers coupling: they focus on the porous medium only and apply a special boundary condition that allows for heat and mass transfers at the top as a parameterisation for the coupling with the above layer [27, 22, 6, 5].

In the present proceeding, we introduce an idealised model for Enceladus' core as a two dimensional internally heated porous layer with an open top boundary. With this set-up, we aim to understand the flow structures close and far from the onset of convective motion, and to quantify heat transfer efficiency and heat flux anomalies in such a system. We thus seek to bridge the gap between idealised and mathematical studies of the related Rayleigh-Bénard problem in porous media [25, 14, 15] and complex numerical simulations of planetary interiors [22, 5].

This report starts with a short introduction on the idealised system used here. We discuss in particular the choice of the thermal boundary conditions at the top of the layer and the expected balances at stake to adequately scale the governing equations. We then present a brief stability analysis of the considered system, and explore the different regimes above

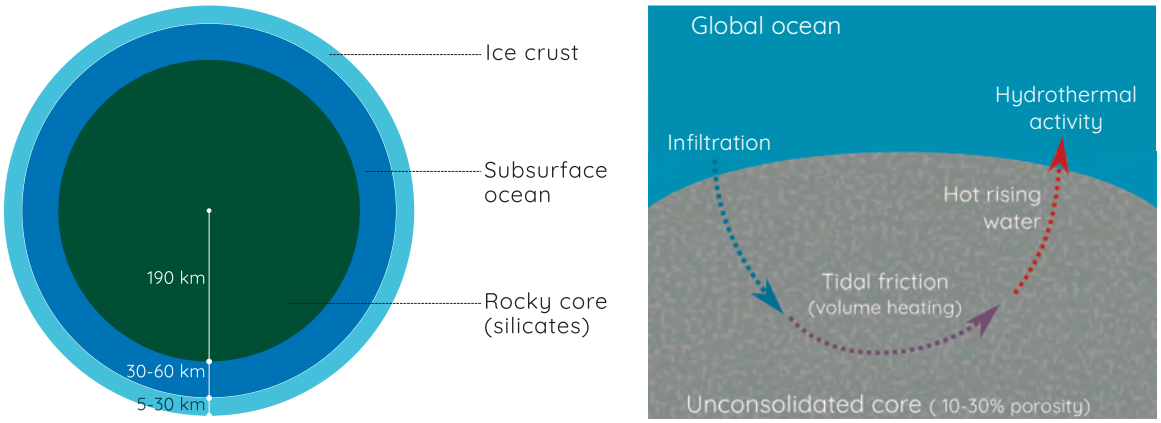

Figure 2: **Right:** schematic view of Enceladus' interiors. The entire surface is covered by a thick ice sheet; underneath lies a global water ocean and a silicate core. Due to the low gravity, large deviations are observed in the topography of these layers: the thickness of the ocean is thought to vary between 30 to 60 km. **Left:**A cartoon of the model proposed in [5] to explain hydrothermal activity inside Enceladus. The rocky core is porous, saturated with the ocean's water and heated by tidal friction. Heating forces the ascent of buoyant hot fluid then giving rise to hydrothermal activity.

the onset of convection. The core of this proceeding is devoted to investigate the principal scalings and balances at play in the non-linear regime and the how the flow organises to carry the internal heat away. We then study the influence of large-scale variations of the volume heat production to account for a tidal-like heating and compare the driven flow to the homogeneous case. Lastly, we discuss the relevance of this simple model to describe the interior of Enceladus; we include estimates of the hydrothermal activity driven by convection in the core of Enceladus that are consistent with those provided in [5].

2 A Simple Model for the Interior of Enceladus

2.1 The model and its governing equations

The core of Enceladus is modelled by a two-dimensional porous medium of permeability k, which is saturated with water of viscosity μ. It lies beneath an ocean that we assume to be well mixed with a global temperature T_0 —see figure 3. The flow $\boldsymbol{U} = (U, W)$ inside the porous core is modelled by Darcy's law:

$$\boldsymbol{U} = \frac{k}{\mu}\left(-\boldsymbol{\nabla} P + \rho \boldsymbol{g}\right) \tag{1}$$

where P is the pressure, ρ is the density of water and $\boldsymbol{g}$ is the gravity field, which we assume to be vertical and constant throughout the layer. Note that this is not the case in Enceladus' core as the gravitational field intensity increases linearly with radius. Moreover, since it is a small 500 km moon, the strength of gravity on Enceladus is about a hundred times smaller than on the Earth. In addition to Darcy's law, the flow is assumed to be

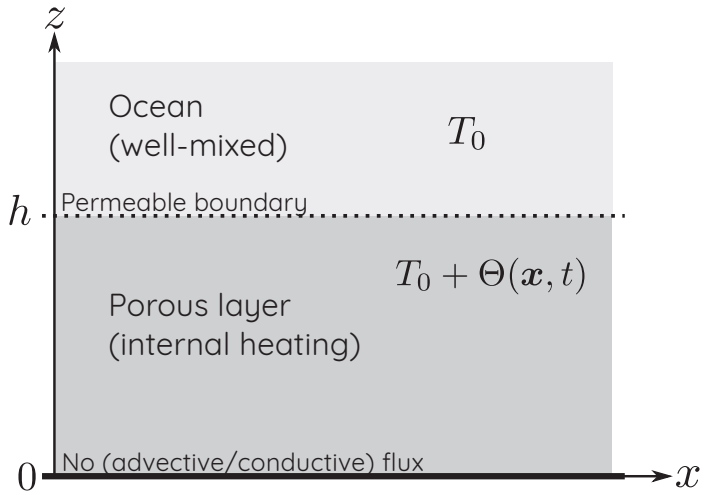

Figure 3: An idealised 2d model to describe porous convection inside Enceladus' core in interaction with the subsurface ocean. The bottom of the porous layer models the centre of the moon, there is no heat and mass flux at this height. Mass exchange between the ocean and the porous core are allowed with a free vertical velocity at the top.

incompressible, so that it must also satisfy a continuity equation:

$$\partial_x U + \partial_z W = 0 \ . \tag{2}$$

Water motion inside the core is driven by buoyancy and temperature differences. We model the effects of temperature on density assuming linear expansion of the fluid with temperature under the Boussinesq approximation, such that $\rho = \rho_0(1 - \alpha(T - T_0))$ where ρ_0 is a reference density and α the thermal expansion coefficient. Darcy's law may thus be written as:

$$\boldsymbol{U} \ = \ \frac{k}{\mu}\left(-\boldsymbol{\nabla} P' + \rho_0 g \alpha \Theta \boldsymbol{e}_z\right) \tag{3}$$

where $P' = P + \rho_0 g z$ and $\Theta \equiv T - T_0$

The flow being driven by thermal anomalies Θ, we must introduce an equation modelling the transport of heat inside the porous medium. This is achieved using thermal energy conservation, in which a source term accounting for volume heat production is included:

$$\partial_t \Theta + \boldsymbol{U} \cdot \boldsymbol{\nabla} \Theta \ = \ \kappa \nabla^2 \Theta + q \tag{4}$$

with κ the heat diffusivity inside the porous medium —*i.e.* of both water and the porous matrix together— and q is the internal heat source term. The latter is related to the volume heat production by tidal heating Q_V via $q = Q_V/(\rho c_p)$ where c_p is the heat capacity per unit of mass of the porous medium and ρ its density.

2.2 Boundary conditions

From a mathematical point of view, Darcy's l aw is a first order equation with two components, two boundary conditions must therefore be applied to the velocity field $\boldsymbol{U}$. The

temperature field is governed by a second order equation and two boundary conditions must also be imposed on Θ.

The bottom of the porous layer roughly corresponds to the core centre, we thus assume that there is no heat and mass flux crossing the bottom boundary, that is:

$$\partial_z \Theta(z=0) \;=\; 0 \quad \text{and} \quad W(z=0) = 0 \tag{5}$$

The top of the layer at $z = h$ is in contact with the ocean and must allow mass exchange between the core and the ocean. This is achieved by imposing a purely vertical velocity at the top, *i.e.* :

$$U(z=h) = 0 \; . \tag{6}$$

The two layers are also thermally coupled. One first natural choice for the top boundary condition is to impose the top temperature to be the temperature of the ocean, *i.e.* $\Theta(z = h) = 0$. However, the advective heat flux driving hydrothermal activity $W\Theta(z = h)$ across the interface would vanish. Another condition should then be considered as the water coming out the porous layer may drive a buoyant plume rising in the ocean. In such a configuration, the water coming out of the core would keep its temperature as it crosses the boundary between the two domains, that is:

$$\partial_z \Theta(z=h) = 0 \; . \tag{7}$$

Such a condition cannot be applied everywhere at the top boundary as the temperature of the water flowing in would not be controlled. We must therefore impose the temperature of the incoming fluid to be the same as in the ocean. To summarise, the other boundary condition that is used hereafter is:

$$\begin{cases} \text{if } W > 0, \; \partial_z \Theta(z=h) = 1 \\ \text{else } \Theta(z=h) = 0 \; . \end{cases} \tag{8}$$

Such a discontinuous boundary condition introduces an additional non-linearity in the system which may be difficult to handle. In addition, one may wonder whether the elliptic problem (4) with the boundary conditions (8) is well posed; this issue will be discussed below.

The boundary conditions (8) and (6) may be regarded as two end-members of the fully coupled problem of the core-ocean interaction. In the case of slow ascent in the porous medium, diffusion from the ocean inside the core causes the temperature inside the porous medium to drop in the top boundary vicinity. Conversely, if the upwelling is fast, diffusion is not able to affect the temperature inside the ascending plume. As a side note, intermediary situations where $\partial_z \Theta(z = h) = -\beta$ with $\beta > 0$ could also be considered. Nevertheless, choosing between the two boundary conditions or parameterisation β would require a demanding study of the fully coupled system involving both the ocean and the porous core.

2.3 Scaling the problem: dimensionless equations

In this paragraph, we aim at writing dimensionless equations driving the porous convection with internal heating. First, all considered lengths are normalised by the height of the

porous layer h. We must also define a velocity and a temperature scale, respectively, denoted as U^* and $\Delta\Theta$.

Darcy's law (3) gives a simple relation between these two scales

$$U^* = \frac{k}{\mu}\rho_0 \alpha g \Delta\Theta \ . \tag{9}$$

Another relation can be inferred from the advection-diffusion equation and several balances may be considered: advection and diffusion, diffusion and heat production or advection and heat production. We predict that in the non-linear regime, heat production and advection will be the dominant balance, leading to the following relation between velocity and temperature:

$$U^*\Theta^* = hq \, . \tag{10}$$

Both scales are then expressed as a function of physical parameters as follows:

$$\left\{ \begin{array}{rcl} U^{*2} & = & \dfrac{k}{\mu}\rho_0 \alpha g h q \\ \Delta\Theta & = & \sqrt{\dfrac{\mu h q}{k \rho_0 \alpha g}} \end{array} \right. \tag{11}$$

We finally find that the system considered here is governed by only one dimensionless parameter, a Rayleigh number comparing the relative importance of advection and diffusion[1]:

$$Ra \ \equiv \ \frac{hU^*}{\kappa} \ = \ \left(\frac{k\alpha g}{\kappa \nu} \frac{q h^2}{\kappa} h \right)^{1/2} . \tag{12}$$

Note that other definitions have been considered for the Rayleigh number, depending in particular on the expected balance at play. For instance, Buretta & Berman [3] choose velocity and temperature scales based on advection and diffusion balance, leading to a Rayleigh number $Ra_{bb} = Ra^2$.

Introducing the dimensionless temperature $\theta = \Theta/\Delta\Theta$ and velocity $\boldsymbol{u} = \boldsymbol{U}/U^*$, the dimensionless governing equations for a porous layer with internal heating are:

$$\left\{ \begin{array}{rcl} \boldsymbol{\nabla} \cdot \boldsymbol{u} & = & 0 \\ \boldsymbol{u} & = & -\boldsymbol{\nabla} p + \theta \boldsymbol{e}_z \\ \partial_t \theta + \boldsymbol{u} \cdot \boldsymbol{\nabla}\theta & = & \dfrac{1}{Ra} \nabla^2 \theta + 1 \end{array} \right. \tag{13}$$

where the pressure is rescaled by hU^* and time by h/U^*. The flow being incompressible and 2d, it is particularly convenient to introduce a stream function ψ such that $\boldsymbol{u} = \boldsymbol{\nabla} \times (-\psi \boldsymbol{e}_y)$. The governing equations (13) are then transcribed as:

$$\left\{ \begin{array}{rcl} \nabla^2 \psi & = & -\partial_x \theta \\ \partial_t \theta + J(\psi, \theta) & = & \dfrac{1}{Ra} \nabla^2 \theta + 1 \\ J(\psi, \theta) & \equiv & \partial_z \psi \partial_x \theta - \partial_x \psi \partial_z \theta \end{array} \right. \tag{14}$$

[1] It can thus also be regarded as a Peclet number.

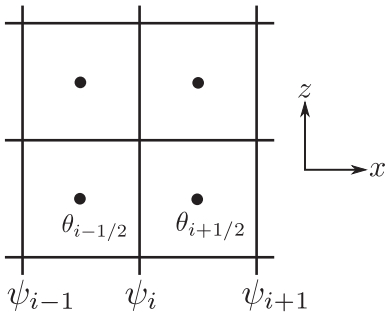

Figure 4: Schematic cartoon of the staggered grids used in the numerical code showing the relative locations of the computed values of the stream function ψ and the temperature θ. ψ is evaluated at the nodes of the lattice, whereas temperature is computed at the squares' centres.

Lastly the boundary conditions are, for the velocity:

$$\begin{cases} w(z=0) &= 0 \\ u(z=1) &= 0 \end{cases} \tag{15}$$

and for the temperature:

$$\text{BC 1:} \quad \begin{cases} \text{if } w>0,\ \partial_z\theta(z=1)=1 \\ \text{else } \theta(z=1)=0\ . \end{cases} \qquad \text{BC 2:} \quad \theta(z=1)=0\ . \tag{16}$$

2.4 Numerical code

In the following, we investigate numerically the non-linear behaviour of porous convection with internal heating. We use a code that was introduced by Hewitt *et al.* [14] to study Rayleigh-Bénard convection in porous media. The code solves the governing equations of the temperature and stream function (14) in a rectangular domain of aspect ratio L with periodic boundary conditions in x. It proceeds using a Fourier transform in the x direction and finite differences in z and time. The code evaluates temperature and velocity at the nodes of two staggered grids —see figure 4— allowing the numerical scheme to be flux conservative and second order accurate in time and space.

3 The Onset of Convection

In this section, we investigate both theoretically and numerically the critical value of the Rayleigh number Ra above which a convective instability develops. We also study the motion the flow structure at onset, which is in particular helpful to benchmark the numerical scheme.

3.1 The diffusive base state

We seek a base state $(\boldsymbol{u}_b, \theta_b)$ for which there is no velocity ($\boldsymbol{u}_b = 0$), which corresponds to a balance between heat production and diffusion:

$$\nabla^2 \theta_b + 1 = 0 \ . \tag{17}$$

The system is invariant along the x direction and taking into account the boundary conditions —either BC 1 or BC 2 in (16)— yields:

$$\theta_b(z) = \frac{Ra}{2}\left(1 - z^2\right) \ . \tag{18}$$

3.2 Linear perturbations to the base state

We look for perturbations of the base state of the form:

$$\psi = \psi_1(\boldsymbol{x}) e^{\sigma t} \quad \text{and} \quad \theta = \theta_b + \theta_1(\boldsymbol{x}) e^{\sigma t} \tag{19}$$

such that $|\psi_1|,\ |\theta_1| \ll \theta_b$. The exponential terms allow to account for the existence of convective instability characterised by $\mathsf{Re}(\sigma) > 0$. Using the ansatz (19), the equations (14) written at order one are:

$$\nabla^2 \psi_1 \ = \ -\partial_x \theta_1 \tag{20}$$

$$\sigma \theta_1 + Ra z \partial_x \psi_1 \ = \ Ra^{-1} \nabla^2 \theta_1 \ . \tag{21}$$

Taking the x derivative of (21) and substitution with (20) gives a single equation on the stream function:

$$\nabla^4 \psi_1 = Ra\sigma \nabla^2 \psi_1 - z Ra^2 \partial_{xx} \psi_1 \tag{22}$$

As the system is invariant along the x direction, ψ_1 is assumed to be a plane wave along x, that is $\psi_1 = \psi_{01}(z)\exp(ikx)$ —and consequently $\theta_1 = \theta_{01}(z)\exp(ikx)$. The equation (22) with the plane wave assumption yields the following ordinary differential equation on the function ψ_{01}:

$$\psi_{01}^{(4)} - (2k^2 + Ra\sigma)\psi_{01}^{(2)} + (k^4 + Ra\sigma k^2 - z Ra^2 k^2)\psi_{01} = 0 \tag{23}$$

where σ is also unknown. This boundary value problem has five boundary conditions:

- $w(z=0) = 0 \longrightarrow \psi_{01}(0) = 0$
- $u(z=1) = 0 \longrightarrow \psi'_{01}(1) = 0$
- $\theta(z=1) = 0 \longrightarrow \psi''_{01}(1) = k^2$
- $\partial_x \theta(z=0) = 0 \longrightarrow \psi_{01}^{(3)}(0) = 0$
- $\psi_{01}(1) = 1$ to set the amplitude of the solution

where we have used the boundary condition BC 2 for the temperature at the top of the domain. This is justified as we consider the onset of motion and upwelling is by construction very slow close the threshold.

3.3 Theoretical solving

The equation (23) is solved numerically with the SciPy routine `solve_bvp` [18, 7]. The input parameters are the Rayleigh number Ra and the wave number k. These two values are explored to find the range of parameters for which the instability grows. A plot of the critical values of the Rayleigh number above which the instability grows as a function of the wave number is given in figure 5 left. From this numerical solving, we find the lowest value of the Rayleigh for which $\sigma = 0$ to be $Ra = Ra_c = 5.894$ at $k = k_c = 1.751$. The temperature field and streamlines of the unstable mode at onset are represented in figure 5 right. The vertical structure functions ψ_{01} and θ_{01} are plotted in figure 6.

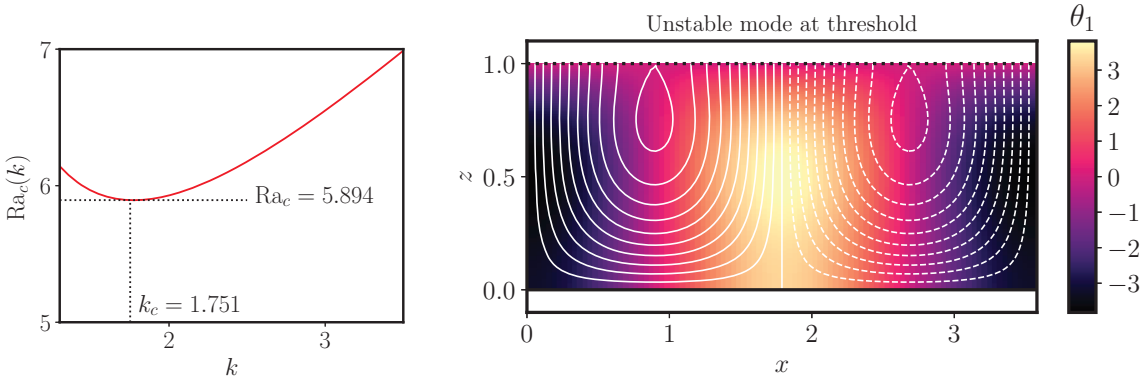

Figure 5: **Left:** Curve of the critical Rayleigh number $Ra_c(k)$ above which the instability grows as a function of the horizontal wave number k. **Right:** temperature heat map and velocity streamlines of the most unstable mode at the threshold of the instability.

In their experimental set-up with closed top boundary Buretta & Berman [3] predicted, and found experimentally their critical Rayleigh number to be $Ra_{bb,c} \simeq 32.8$. To compare their values to ours, we must remember that $Ra_{bb} = Ra^2$, and here we find that $Ra_c^2 \simeq 34.7$; this is slightly above $Ra_{bb,c}$, but remains similar.

3.4 Benchmarking the numerical code

The theoretical investigation of the onset of convection is used to benchmark the numerical code. Simulations are carried out at values of the Rayleigh number Ra very close to the onset —$|Ra - Ra_c| \leq 10^1$ typically. The aspect ratio L of the box in the x direction is chosen to match twice the critical wave length, *i.e.* $L = 2 \times 3.580$. Computations are initiated with a diffusive temperature profile (18) plus a relatively small noise. We observe an exponential growth or decay of the kinetic energy and the thermal energy of the perturbation to the diffusive base state. The growth rate found numerically is reported in figure 7. It is compared to the theoretical value of the growth rate at the same Rayleigh numbers and at the critical wave number k_c. The agreement between the two methods appears to be satisfying: the relative error between both growth rates is within 2%, apart from the closest value of Ra to Ra_c, for which it is difficult to measure precisely the growth rate.

The agreement between the numerical computation is sufficient to use it confidently for the study of the non-linear behaviour of the instability above the threshold, provided the

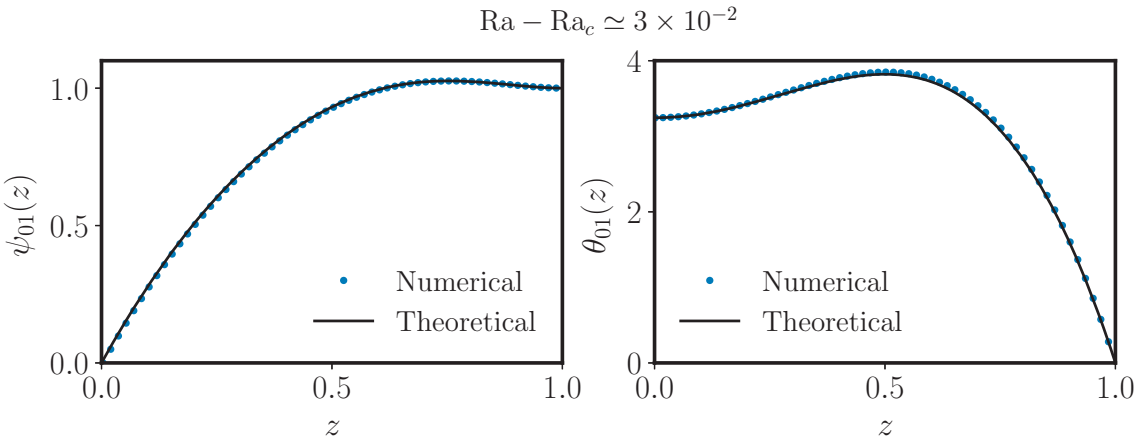

Figure 6: Vertical structure function of the stream function $\psi_{01}(z)$ and the temperature $\theta_{01}(z)$ obtained by solving the boundary value problem (23) (black line) and extracted from a numerical simulation of the instability close to the threshold ($Ra - Ra_c \simeq 3 \times 10^{-2}$).

spatial and time resolution are sufficient to well resolve the dynamics.

4 The Non-linear Behaviour of Internally Heated Convection

4.1 Organisation of the flow: structures and scales

4.1.1 Illustrating the non-linear behaviour

To introduce to the non-linear behaviour of the instability driven by internal heating, we propose to illustrate typical patterns observed at different Rayleigh numbers. Figures 8 and 9 are typical snapshots of the temperature field and streamlines, and figure 10 shows the mean temperature difference between the bottom and the top of the porous layer as a function of Ra. At low Rayleigh number, *i.e.* for $Ra_c \leq Ra \lesssim 40$, the convection reaches a steady state with few rolls, be it for boundary condition BC 1 or BC 2 —see (16). For larger Rayleigh numbers, the flow exhibits a chaotic behaviour where two or three modes with different periodicity —or plume numbers— are in competition. This situation ceases for $Ra \gtrsim 600$, at least for an aspect ratio $L = 4$: higher values of the Rayleigh number give rise to steady solutions with a large number of narrow plumes. This transition is also noticeable in the temperature difference —figure 10— where the emergence of steady plumes is associated with a sudden decrease in the temperature difference.

The only noticeable difference between the two boundary conditions is the existence of thin thermal boundary layer when the top temperature is imposed —BC 2. Its thickness of order Ra^{-1} is set by a balance between vertical advection and diffusion. In addition, the high degree of similarity between the simulations carried out with different boundary conditions suggests that the mixed boundary condition —BC 1— is reliable. Note that this is not the case below the threshold of the instability where flows that are highly sensitive to initial conditions are observed. We therefore choose to use both boundary conditions in the study hereafter, as long as $Ra > Ra_c$; the condition BC 1 is particularly convenient in

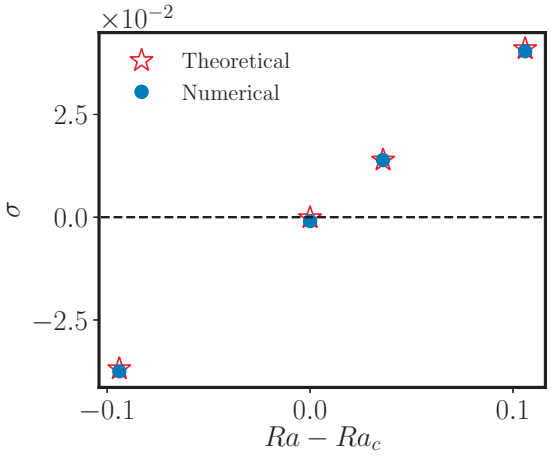

Figure 7: Growth rate computed from numerical simulations and comparison with the expected theoretical value obtained solving the boundary value problem (23). For the theoretical computation, the wave number k is chosen such that $k = k_c$.

terms of resolution as it does not produce a sharp boundary layer at the top of the domain.

Lastly, we notice on these snapshots that $(\theta, |\boldsymbol{u}|) = \mathcal{O}(1)$, and more quantitatively on the plot of the mean temperature difference between the top and the bottom of the layer —figure 10. This is the case even close to the instability threshold at Rayleigh numbers as low as 10. It confirms that the balance between advection and heat production drives the dynamics. In addition, in the steady saturated state of the convective instability, the temperature anomaly θ is positive. This is a theoretical constraint given by the extremum principle applying on elliptic and parabolic partial differential equations —the interested reader may refer to a short demonstration in [12].

4.1.2 Typical plume size and distances

The snapshots presented in figures 8 and 9 show that, as the Rayleigh number is increased, the typical extent is reduced, as observed for instance in [5] for the case of internal heating, and also in [14] and [15]. We also notice that the number of plumes increases.

In this paragraph, we aim at better quantifying the typical plume size ℓ_p and separation Δx_p as a function of the Rayleigh number. This is achieved from measurements of the heat flux J_t at the top of the porous layer,

$$J_t = \left(\overline{w\theta} - \frac{1}{Ra} \frac{\partial \overline{\theta}}{\partial z} \right) \Big|_{z=1} \tag{24}$$

where the horizontal bar denotes a horizontal averaging. J_t involves both an advective and a diffusive contribution, and we recall that for the case of fixed temperature at the top —BC 2—, the advective part of J_t vanishes.

J_t peaks at the core of upwelling zones, and we define the typical plume scale ℓ_p as the full width at half maximum of these peaks. For one simulation, J_t is recorded every quarter time unit —while a simulation is typically a hundred time units— ℓ_p is the ensemble average

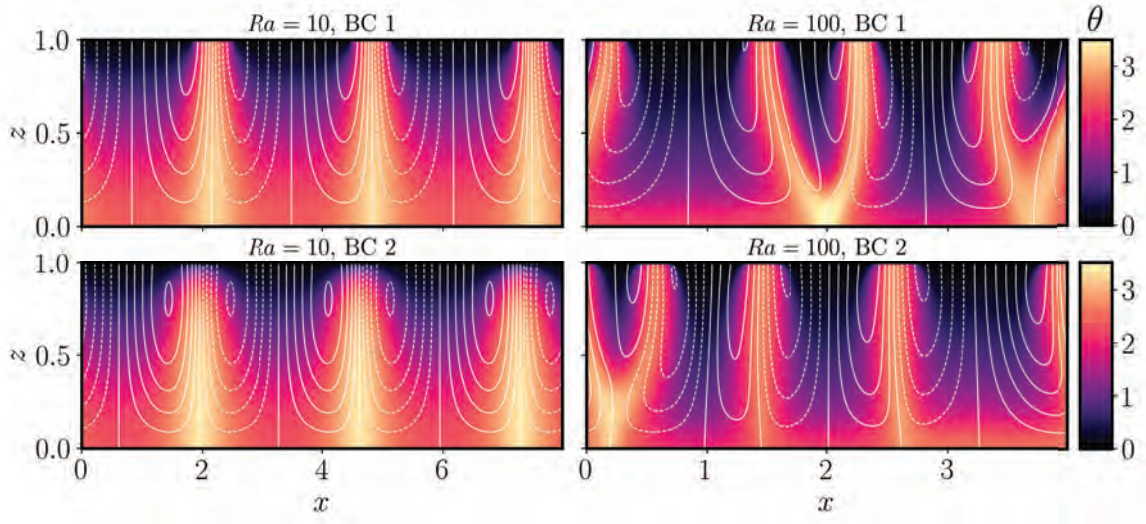

Figure 8: Snapshots of the temperature field θ (heat map) and the stream lines of the flow at $Ra = 10$ (**left**) and $Ra = 100$ (**right**) for boundary condition BC 1 (**top**) and BC 2 (**bottom**). Both states have reached a statistically steady state but the overall behaviour is chaotic. The resolution for both simulations is 512×300 ($x \times z$). Note that the aspect ratio is decreased by a factor two between the two Rayleigh numbers.

Figure 9: Snapshots of the temperature field θ (heat map) and at $Ra = 1000$ for boundary condition BC 1 (**top**). The resolution for both simulations is 1024×300 ($x \times z$).

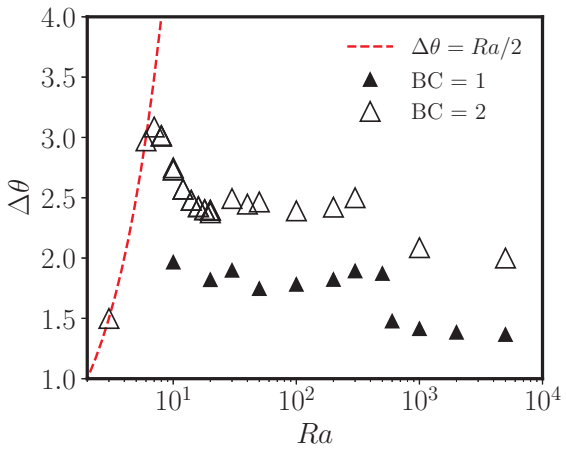

Figure 10: Mean temperature difference between the bottom and the top of the porous layer $\Delta\theta$ as a function of the Rayleigh number Ra, for both boundary conditions and for an aspect ratio $L = 4$. The diffusive temperature difference $\Delta\theta = Ra/2$ is shown for comparison.

over every peak of all snapshots. The same process is used to determine the typical plume separation Δx_p. The result of this processing is shown in figure 11: both the plume width and separation exhibit the same scaling with the Rayleigh number, that is $\ell_p, \Delta x_p \propto Ra^{-1/2}$, even close to the threshold. It indicates that although the plumes become narrower with increasing Ra, their density and aspect ratio remains unchanged. This power law can't be explained by linear theory, even at low Ra, as the mean separation between plumes does not coincide with the most unstable mode predicted by linear stability analysis —see figure 11.

The $Ra^{-1/2}$ power low describing plume size and separation may be explained by deriving a relation between the mean temperature field and the mean temperature gradients [9]. Multiplying the energy conservation relation in (13) by the temperature θ yields:

$$\frac{1}{2}\partial_t\theta^2 + \theta\boldsymbol{\nabla}\cdot(\boldsymbol{u}\theta) = \frac{1}{Ra}\theta\boldsymbol{\nabla}^2\theta + \theta \ . \tag{25}$$

Taking the time and volume average, denoted as $\langle \ \cdot \ \rangle$, and assuming the system has reached a statistically steady state, leads to the following relation:

$$\frac{1}{2}\left.\overline{w\theta^2}\right|_{z=1} = \frac{1}{Ra}\left\langle\theta\boldsymbol{\nabla}^2\theta\right\rangle + \langle\theta\rangle \tag{26}$$

where the left hand side term is an energy leak term at the top boundary averaged in x. It vanishes for boundary condition BC 2 where $\theta(z = 1) = 0$. Integration by parts of the term $\left\langle\theta\boldsymbol{\nabla}^2\theta\right\rangle$ finally gives the following identity:

$$\langle\theta\rangle = Ra^{-1}\left\langle|\boldsymbol{\nabla}\theta|^2\right\rangle + \frac{1}{2}\left.\overline{w\theta^2}\right|_{z=1} \ . \tag{27}$$

w and θ are both order one quantities because of the physical balance between heat production and advection. As a consequence, the gradients are order $Ra^{1/2}$ which explains the scaling observed in figure 11.

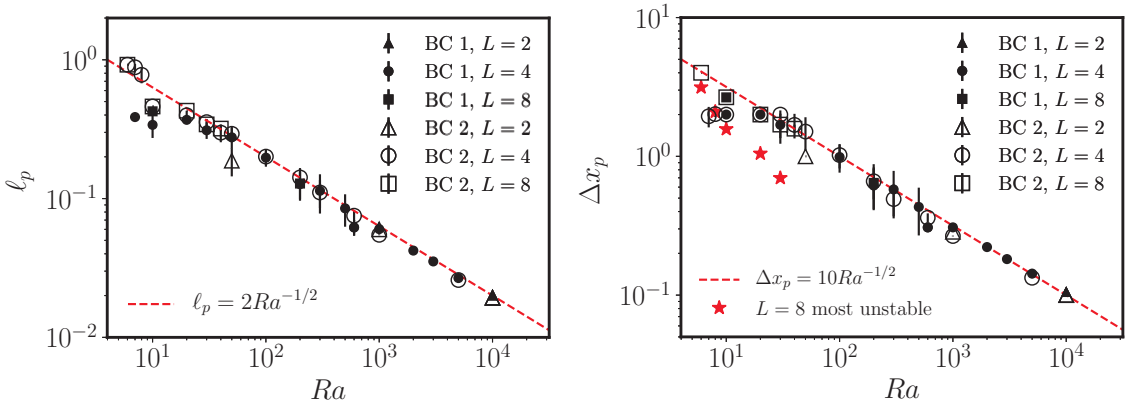

Figure 11: Typical plume size ℓ_p (**left**) and plume separation Δx_p (**right**) for several simulations with both boundary conditions BC 1 and BC 2 at different aspect ratios ranging from 2 to 8. Both quantities scale with the Rayleigh number as $Ra^{-1/2}$. The error bars are determined by the standard deviation of the mean plume width and separation over a data set containing every plumes of all snapshots. The red stars indicate the plume separation expected for the most unstable mode fitting in an aspect ratio $L = 8$ domain inferred from linear theory by solving the boundary value problem (23).

4.2 Describing the asymptotic regime of porous convection with internal heating

In the previous section, we have illustrated the heat transporting structures in the non-linear regime of the convective instability through snapshots. We have also characterised shape properties such as their typical width and distance. In this section, we present a thorough characterisation of the asymptotic regime in terms of heat transport and physical balances. In particular, we derive a steady non-linear solution for plumes at high Rayleigh numbers that we compare with what is observed in simulations.

4.2.1 The flux conservation equation to characterise heat transport

The horizontally averaged vertical heat flux, including advection and diffusion, writes:

$$J(z) = \overline{w\theta}(z) - \frac{1}{Ra}\frac{\partial \overline{\theta}}{\partial z} \ . \tag{28}$$

Thermal energy conservation (13) prescribes a balance between vertical heat transport and volume heat production such that:

$$J(z) = z \tag{29}$$

In the asymptotic regime of high Rayleigh number, we expect that the heat produced is carried away by advection only, except in a boundary layer when they exist —*i.e.* for boundary condition BC 2—, that is:

$$\overline{w\theta}(z) = z \tag{30}$$

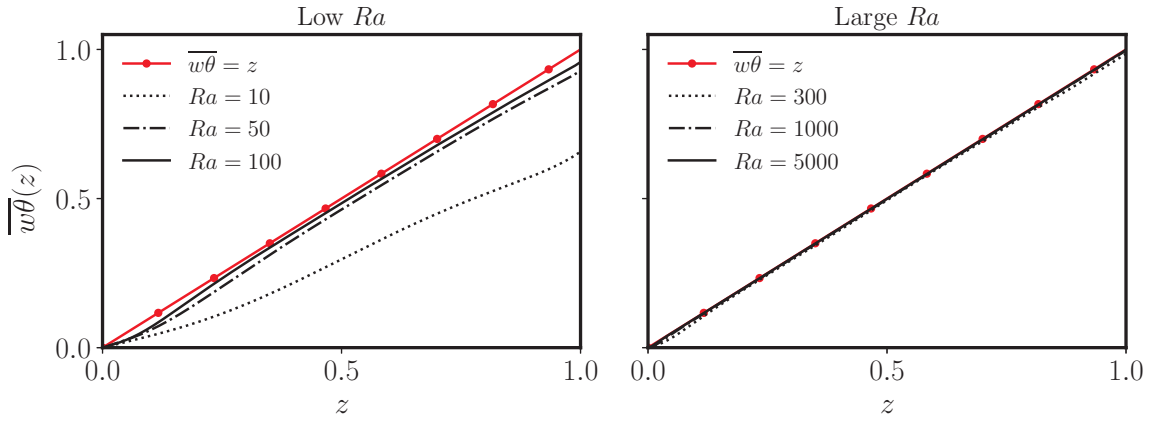

Figure 12: Vertical variations of the horizontally-averaged advective heat flux in the case of both low and high Rayleigh numbers, for boundary condition BC 1 and aspect ratio $L = 4$. Note that the results are very similar for BC 2 apart from the presence of a top boundary layer of thickness $\mathcal{O}(Ra^{-1})$ where the advective flux drops to zero as θ vanishes. The asymptotic law $\overline{w\theta} = z$ is given for reference.

As it can be noticed in figure 12, the advective heat flux tightly follows the asymptotic law (30) even at Rayleigh numbers as low as $Ra = 50$. This balance is broken when $\theta = 0$ is imposed everywhere at the top boundary —BC 2—: the advective flux is converted into conductive heat flux over a layer of thickness $\mathcal{O}(Ra^{-1})$ as illustrated in figure 15. Nevertheless, heat transport in the bulk is dominated by advection at high Rayleigh numbers, as expected.

4.2.2 The evolution of temperature with height

Convection being efficient in transporting heat away, one may wonder how it mixes the thermal energy in the porous layer, which is characterised by the horizontally averaged temperature profile. In the case of Rayleigh-Bénard convection in porous media, in the asymptotic regime of high Ra, the temperature is constant in the bulk [14]. That is also an observation made in classical convection with internal heating, where the quadratic temperature profile at low Ra flattens towards constant temperature across the domain —see [11] and references therein.

In figure 13, at low Rayleigh number —here $Ra = 10$— the temperature profile bears a quadratic shape reminiscent of the diffusive base state (18). Conversely, at high Ra, we observe homogenisation convergence towards an asymptotic profile for which the temperature increases with depth in the porous medium. The temperature difference being $\mathcal{O}(1)$, it is reduced by a factor $\mathcal{O}(Ra^{-1/2})$ compared to the diffusive base state. In that respect, the non-linear regime of our convection setup is similar to those mentioned above in terms of internal energy mixing.

We also quantify the lateral variations of the temperature and represent in 14 the horizontal variance of the temperature field, that is $\overline{\theta^2} - \overline{\theta}^2$. Surprisingly, it seems to converge towards a linear profile, exactly like the advective flux. The origin of this particular law will

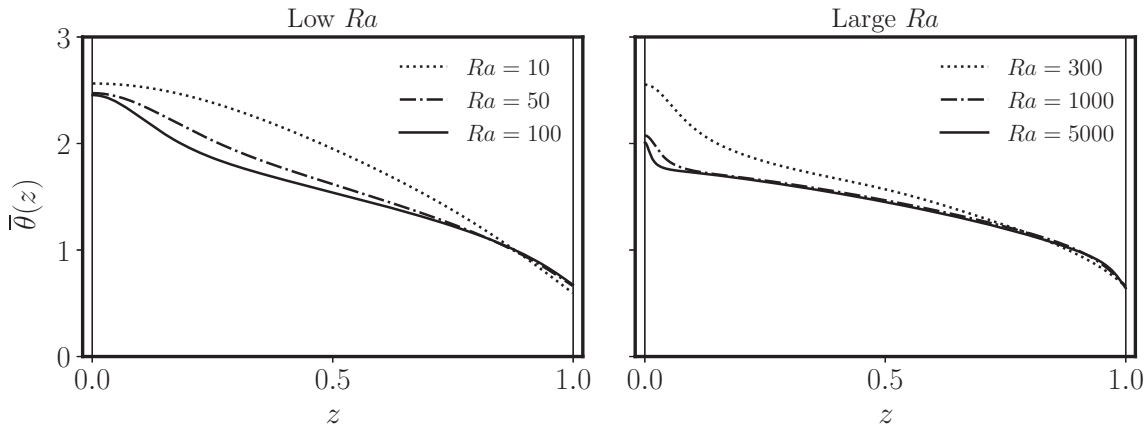

Figure 13: Vertical variations of the horizontally-averaged temperature flux for boundary condition BC 1 and aspect ratio $L = 4$. Note at $Ra = 10$ a quadratic profile that is reminiscent of the diffusive steady state (18)

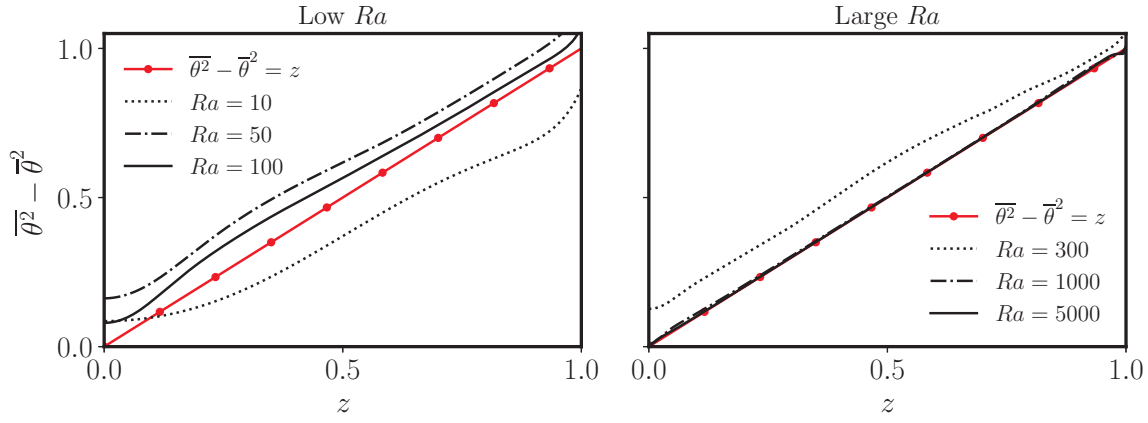

Figure 14: Horizontal variance of the temperature as a function of z for boundary condition BC 1 and aspect ratio $L = 4$ at low and high Ra. The line $\overline{\theta^2} - \overline{\theta}^2$ is given for reference in both cases.

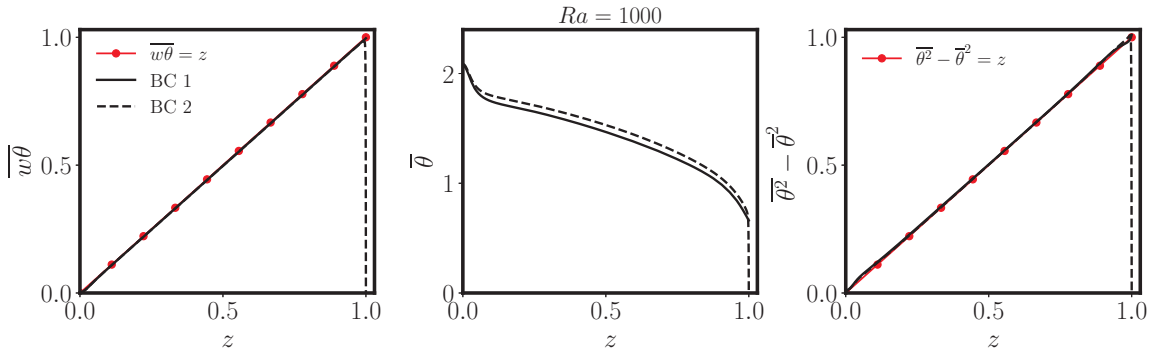

Figure 15: Comparison between the two boundary conditions BC 1 and BC 2 of the advective flux, average temperature and horizontal variance profiles at $Ra = 1000$ for an aspect ratio $L = 4$. This figure highlights the similarities between the profiles apart from the top boundary layer.

be explicited in the next paragraph. The variance increase with height is consistent with the observation from snapshots in 8 and 9 that the temperature contrast between upwelling and downwelling zones increases with height, as cold water flows in and hot water is expelled.

4.2.3 Analysing scalings and balances in the high Rayleigh number regime

In the preceding paragraphs, we have exhibited the statistical features of the asymptotic regime of high Rayleigh numbers in terms of plume dimensions, heat transport and temperature variations. We would like to provide a theoretical understanding of these properties; we thus propose to analyse the governing equations (13) for $Ra \gg Ra_c$.

We know after paragraph 4.1.2 that horizontal gradients are order $Ra^{1/2}$: this forces introducing a rescaled horizontal variable $\hat{x} = Ra^{1/2}x$. The continuity equation then compels $|u|/|w| \sim Ra^{-1/2}$, we thus also define a rescaled horizontal velocity $\hat{u} = Ra^{1/2}u$. With these rescaled variables, velocity components, temperature and gradients are all $\mathcal{O}(1)$.

The curl of Darcy's law in (14) gives:

$$\partial_x w - \partial_z u \;=\; \partial_x \theta \tag{31}$$

or equivalently with rescaled variables:

$$Ra^{1/2}\partial_{\hat{x}} w - Ra^{-1/2}\partial_z \hat{u} \;=\; Ra^{1/2}\partial_{\hat{x}}\theta \tag{32}$$

which yields at leading order in Ra:

$$\partial_{\hat{x}} w = \partial_{\hat{x}}\theta \tag{33}$$

and thus, taking into account vertical mass flux conservation:

$$w = \theta - \overline{\theta}(z)\ . \tag{34}$$

The advective heat flux may therefore be recast as:

$$\overline{w\theta} = \overline{\theta^2 - \overline{\theta}\theta} = \overline{\theta^2} - \overline{\theta}^2 \tag{35}$$

which explains the similarity observed between figures 12 and 14. The equivalence between temperature fluctuations and heat advection is a consequence of Darcy's law and of the $\mathcal{O}(Ra^{1/2})$ scaling for the plume dimensions.

Lastly, note that the advection-diffusion equation in not easily reduced in the asymptotic regime of high Ra. Horizontal and vertical advection, lateral diffusion and heat production are all of the same order when rescaled variables are used.

4.2.4 A non-linear solution in the high Rayleigh number regime

With the help of the scalings expressed in the preceding paragraph, we derive in the present a fully non-linear solution to the equations (13) in the high Rayleigh number regime. We look for a low order solution that is steady and harmonic with wave number $k = Ra^{1/2}\hat{k}$. The ansatz for the velocity field is therefore:

$$\left\{ \begin{array}{rcl} \hat{u} & = & \hat{u}_0(z)\sin(\hat{k}\hat{x}) \\ w & = & w_0(z)\cos(\hat{k}\hat{x}) \end{array} \right. \tag{36}$$

for which there is no mean vertical or horizontal mass flux. For this ansatz to satisfy the continuity equation, the following relation is required:

$$w_0' = -\hat{k}\hat{u}_0 \ . \tag{37}$$

We must also introduce an assumption for the structure temperature field. It may be found by analysing the advection-diffusion equation (13) transcribed in rescaled variables $\hat{x}$ and $\hat{u}$, and keeping the highest order terms only:

$$\hat{u}\partial_{\hat{x}}\theta + w\partial_z\theta = \partial_{\hat{x}\hat{x}}\theta + 1 \ . \tag{38}$$

θ must contain a harmonic part for the temperature fluctuations to match the velocity field (36), but a component depending on z only must also be added for the diffusion term in (38) to be balanced by the non-linear term. Our ansatz for the temperature is therefore:

$$\theta = f(z) + w_0(z)\cos(\hat{k}\hat{x}) \tag{39}$$

which automatically satisfies the velocity-temperature fluctuations relation provided by Darcy's law (34).

To determine the functions w_0 and f, we must use the advection-diffusion equation (38), which contains a mean and two harmonic ($\hat{k}$ and $2\hat{k}$) terms. Balancing the mean terms and using the continuity relation (37) simply yields a balance between vertical heat advection and heat production, that is:

$$\frac{\mathrm{d}w_0^2}{\mathrm{dz}} = 2 \quad \textit{i.e. } w_0 = \sqrt{2z} \tag{40}$$

The harmonic $\hat{k}$ terms transcribe a balance between horizontal diffusion and the vertical advection of the average thermal energy —or temperature— profile:

$$w_0 f' = -\hat{k}^2 w_0 \quad \textit{i.e. } f(z) = f_0 - \hat{k}^2 z \ . \tag{41}$$

The latter balance is particularly important, without any *a priori* knowledge of the dependence of k with the Rayleigh number, it sets $k \propto Ra^{1/2}$. In other words, an alternative way to derive the structure of the temperature and velocity fields would have been to use first a similar ansatz to (36) and (39) but without any assumption on the relative scalings between the two components of the velocity or the dependence of k with Ra. The balance between vertical advection and lateral diffusion would have imposed $k \propto Ra^{1/2}$, and consequently the relative scalings of the preceding paragraph.

Lastly, the harmonic $2k$ terms coming from the non-linear term leads to exactly the same balance as Darcy's law, which is automatically satisfied by our ansatz.

To summarise, the fully non-linear low-order solution to the internally heated porous convection in its expanded form is:

$$\begin{cases} u &= -\dfrac{Ra^{-1/2}}{\hat{k}\sqrt{2z}}\sin(Ra^{1/2}\hat{k}x) \\ w &= \sqrt{2z}\cos(Ra^{1/2}\hat{k}x) \\ \theta &= f_0 - \hat{k}^2 z + \sqrt{2z}\cos(Ra^{1/2}\hat{k}x) \end{cases} \tag{42}$$

where $\hat{k}$ and f_0 are $\mathcal{O}(1)$ but *a priori* unknown. Note that this solution only satisfies one boundary condition: the absence of mass flux at the bottom of the porous layer. The remaining boundary conditions, be it the absence of bottom heat flux, the purely vertical velocity at the top, or any of the thermal boundary conditions BC 1 or BC 2, are all unmatched with the solution. Although the non-linear solution predicts a decrease of temperature with height, the obtained linear trend obviously does not match the more complex master curve observed in figure 13.

Figure 16 provides a comparison between plumes extracted from the simulations at two different Rayleigh numbers with a synthetic plume corresponding to the solution 42. The overall behaviour of the two fields are the same, but the theoretical solution does not capture the shrinking of the plumes close the the top boundary. To draw a more quantitative comparison between the non-linear solution and the flow in one plume, we plot in figure 17 several horizontal cuts at different heights of the vertical and horizontal velocity. We find that in the bulk, the theoretical solution adequately describes the amplitude of the velocity variations despite the above-mentioned discrepancies. As indicated by the highest profile in figure 17, refining the model would require including higher harmonics which become predominant at the top boundary, which is difficult to implement because of non-linearities.

4.2.5 Conclusions

To conclude on the asymptotic behaviour of the instability, we have derived a steady, periodic and fully non-linear solution of the equations (13) under the assumption of high Rayleigh number. It has highlighted the main balance at play in the layer between heat production and the vertical advective flux, and between the horizontal diffusion and the advection of the average thermal energy. Although the non-linear solution is too simple and does not satisfy the majority of the imposed boundary conditions, it does capture the

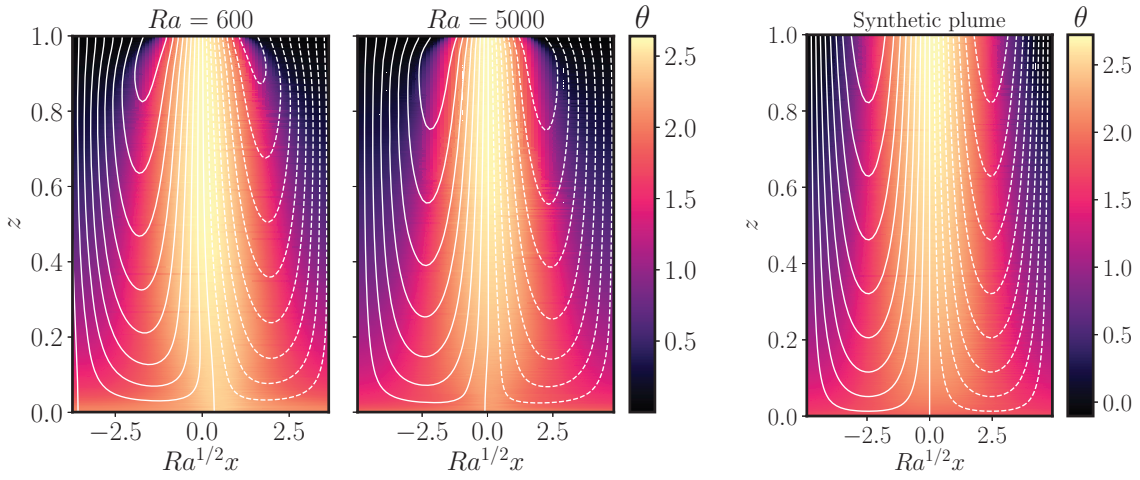

Figure 16: **Left:** single plume isolated in the regime where the flow is steady and periodic in x, with boundary condition BC 1. **Right:** synthetic field for a single plume obtained from the solution (42). The rescaled wave number $\hat{k}$ is chosen to match the $Ra = 5000$ case, and its value is around 0.64. f_0 is chosen around 1.8 to roughly match the bottom temperature profiles observed in 13. Note that although the streamlines do not seem to be vertical at the top boundary, a zoom shows that they ultimately bend to match verticality very close to the top boundary.

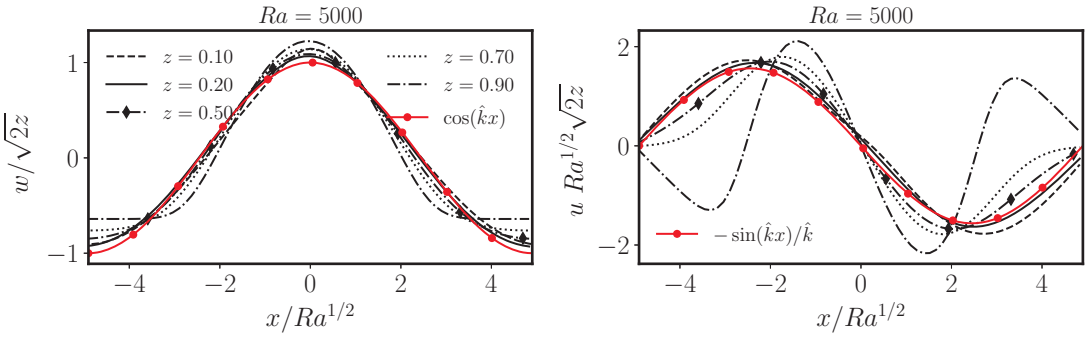

Figure 17: Horizontal profiles at different heights z of the scaled vertical (**left**) and horizontal (**right**) velocity across a plume. The amplitudes are normalised accordingly to the non-linear solution (42). The expected structure is shown in red and the only fitting parameter is the rescaled wave number $\hat{k} \simeq 0.64$. The Rayleigh number is $Ra = 5000$ and the top boundary condition is BC 2.

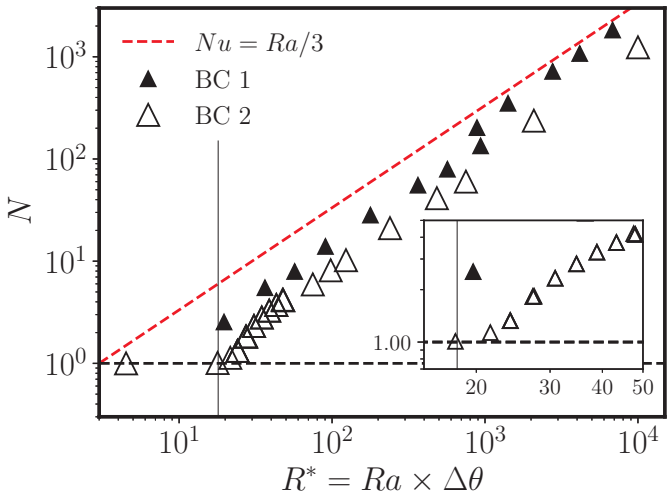

Figure 18: Plot of the Nusselt number N defined in (45) as a function of the diagnostic Rayleigh number $R^* = Ra \times \Delta\theta$ for both boundary conditions BC 1 and BC 2 and an aspect ration of $L = 4$. The transition around $R^* = 10^3$ corresponds to the emergence of a steady state in the saturation of the instability —see snapshots of the flow in figures 8 and 9. The line $N = 1$ materialises purely diffusive heat transfer, and the vertical line marks the theoretical onset of convective instability. The insert shows the same data close to the threshold of the instability.

amplitude of both the horizontal and vertical velocities, and hence of temperature fluctuations.

4.3 Quantifying heat transport across the porous layer

Earlier in this proceeding, we have shown that heat is carried away by convection. This results into a well-mixed interior with a temperature that remains $\mathcal{O}(1)$ whereas it would be $\mathcal{O}(Ra)$ if advection was not efficient. Nevertheless, we would like to quantify this transport efficiency and to compare it to the more classical setup of Rayleigh-Bénard convection.

In the case of Rayleigh-Bénard convection, be it in an unconfined fluid or a porous medium, advective heat transport efficiency is characterised by the Nusselt number which quantifies the enhancement of the heat flux compared to a purely diffusive case. In the case of internal heating, as the system has reached a statistically steady state, the flux crossing the top boundary must match the heat produced in the layer. Quantifying heat transport efficiency therefore requires using a more general definition of the Nusselt number. On solution is to generalise the definition of the Nusselt number considering that it compares the volume and time average of the total heat flux —including advection and diffusion— to the diffusive heat transport [10]. Calling N this number, its definition reads:

$$N \equiv \frac{\langle w\theta - Ra^{-1}\partial_z\theta \rangle}{-Ra^{-1}\langle \partial_z\theta \rangle} = 1 + Ra\frac{\langle w\theta \rangle}{\Delta\theta} \ , \tag{43}$$

where $\Delta\theta = \langle \partial_z\theta \rangle = \overline{\theta}(0) - \overline{\theta}(1) > 0$.

In order to compare the present setup to Rayleigh-Bénard convection in porous media, we must use an effective Rayleigh R^* for which the temperature scale is based on the temperature difference across the layer. We recall that, according to (9), the temperature and velocity scales are proportional to one another. Here, we introduce a diagnostic Rayleigh number that is based on the temperature scale $\Delta\theta \times \Delta\Theta$ instead, and therefore on a velocity scale $U' = \Delta\theta U^*$. Consequently, as $Ra = hU^*/\kappa$, the diagnostic Rayleigh number based on $\Delta\theta \times \Delta\theta$ writes:

$$R^* \equiv \Delta\theta Ra \ . \tag{44}$$

The "Rayleigh"-Nusselt law that we must use for comparison with the Rayleigh-Bénard setup is therefore a mapping between R^* and N. It is explicited from (43) as:

$$N = 1 + R^* \frac{\langle w\theta \rangle}{\Delta\theta^2} \ . \tag{45}$$

Because $\Delta\theta = \mathcal{O}(1)$, the asymptotic regime of high Ra corresponds to high values of R^*. Moreover, because $\langle w\theta \rangle = \langle z \rangle = 1/2$, the scaling between N and R^* boils down to the simple law:

$$N \propto R^* \ . \tag{46}$$

This scaling is observed in our simulations for both conditions at the top boundary — BC 1 and BC 2— as shown in figure 18. Interestingly, there is a clear enhancement of the efficiency of heat transport as steady states emerge in the non-linear saturation of the instability around $R^* = 10^3$.

The same scaling between N and R^* is also found in the classical Rayleigh-Bénard setup [25, 14, 15]. The fact that the Rayleigh-Bénard and internally heated convection both lead to the same efficiency is specific to the porous media: in unconfined fluid, it has recently been shown experimentally that the Nusselt-Rayleigh laws are different between the two setups [21] because of the important role of inertia.

4.4 Conclusion on the asymptotic regime

In the present section devoted to the study of the large Rayleigh number regime, we have shown via simulations that, as expected, the heat produced in the layer is mostly carried by the flow. This is characterised by the observed balance between vertical advection and heat production in figure 12, or by the large values of the Nusselt number which compares the total heat flux to the diffusive heat flux —see figure 18. We have also shown that the efficiency of heat transport by the flow is similar to the classical Rayleigh-Bénard setup in porous media.

Lastly, we have exhibited a low order solution to the non-linear problem (14) that captures the velocity amplitude in the bulk of the layer, and that also reveals that the scaling between the plume size and the Rayleigh number is set by a balance between horizontal diffusion and vertical advection of the mean thermal energy.

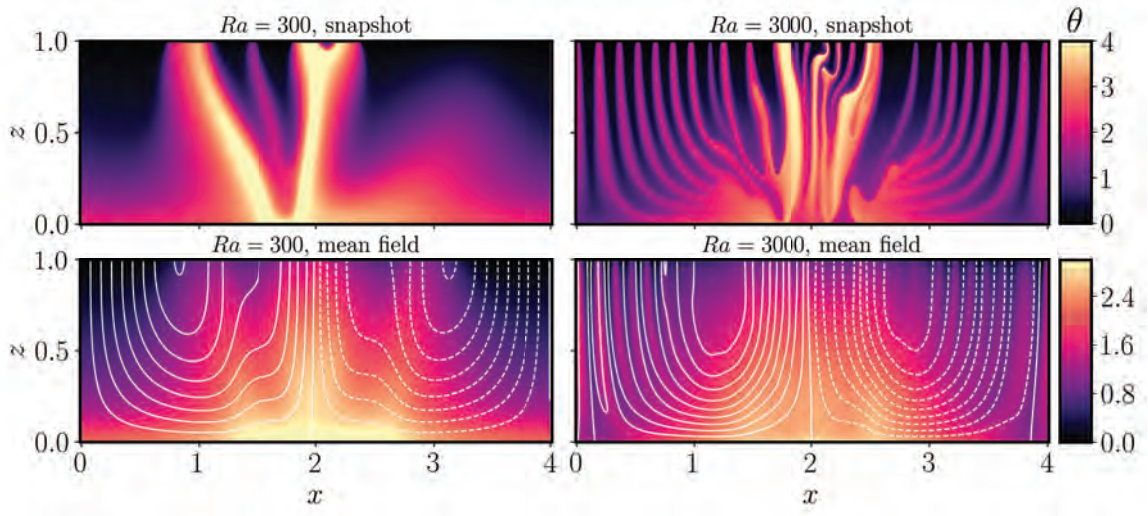

Figure 19: Snapshot of the temperature field for the heterogeneous heating case (**top**) and the mean temperature and mean flow streamlines averaged of the the saturated phase of the instability (**bottom**).

5 Accounting for Tidal Heating: Spatial Modulation of Heating

5.1 Large scale modulation of heating

We explore in this section the change in the transport brought by large-scale modulation of the internal heating. This is important for the case of Enceladus in which heterogeneity of tidal heating has been shown to play a role in focusing the heat flux where heating is the most intense [5]. We consider here a domain with aspect ratio $L = 4$ for which q takes the following form:

$$q(x) = 1 - \Delta q \cos\left(\frac{2\pi}{L}x\right) \tag{47}$$

which is such that the mean heat production is unchanged compared the homogeneous case. In addition, the maximum heat production is located at the centre of the domain. In the following, we only illustrate heat modulation with $\Delta q = 0.5$ in the case of the boundary condition BC 1. $\Delta q = 0.5$ is a good proxy for tidal heating which bears latitudinal and longitudinal variations up to a factor 2 between minima and maxima.

5.2 Large scale flow and pulsatility

The first striking feature emerging from heterogeneous heating is the attraction of the plumes towards the centre where internal heating is the strongest. Although plumes may exist in the whole interior of the domain, they merge towards the centre, which results in a higher temperature region with larger heat flux anomaly, as illustrated in figure 19. Note that despite the plume merging in the centre, the upwelling zones remain narrow and their number is increased with Ra.

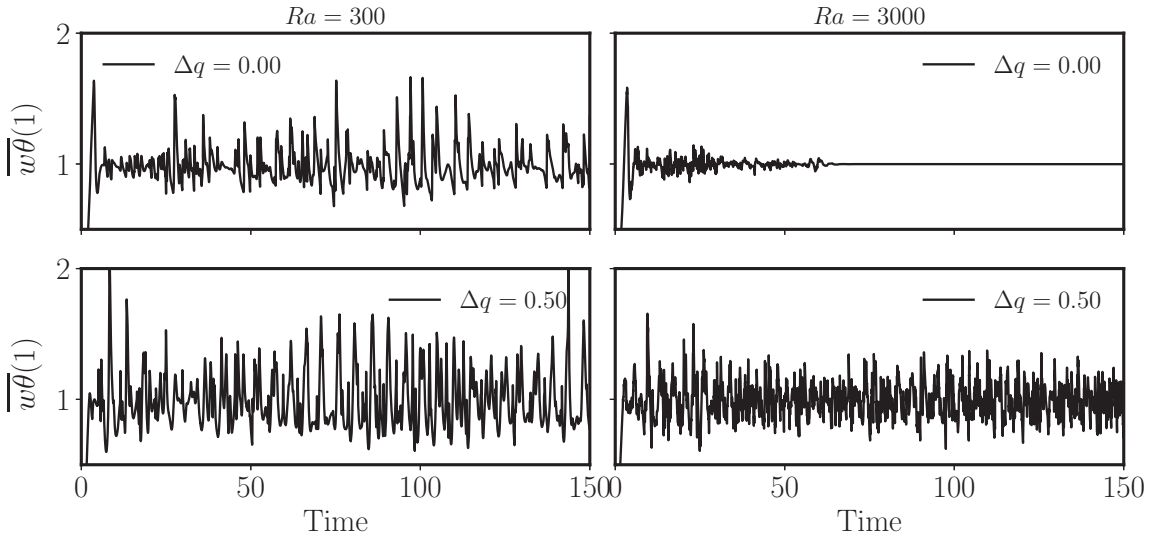

Figure 20: Horizontally averaged advective heat flux at the top boundary at $Ra = 300$ (**left**) and $Ra = 3000$ (**right**), with comparison between homogeneous (**top**) and heterogeneous (**bottom**).

Plume merging towards the centre is driven by a large scale mean flow that is also shown in figure 19. Note though that fine structures may still be traced in the mean flow, especially at $Ra = 3000$ where the side plumes persist over a long time. Although we attempted to describe this mean flow in a way very similar to the plume solution found in the previous section, a simple solution remained elusive. This is because time-dependent fluctuations play a collective role in establishing the mean flow and transporting heat, and they remain difficult to handle without any proper closure method.

Sweeping and merging of plumes also leads to pulsatility in the advected heat flux, as shown in figure 20. At intermediate Rayleigh number ($Ra = 300$), whereas the flux was intermittent for homogeneous heating, it exhibits a quasi-periodic behaviour for a modulated heating. The typical period is of order one, *i.e.* it takes place over a convective time scale, and corresponds to the time needed for plume formation, advection and merging. The effects of heterogeneous heating are even more striking at high Ra: the steady state observed in the homogeneous case is replaced by quick oscillations of the heat flux. They correspond to the many plumes observed in the centre of the domain hitting the top boundary non synchronously —see figure 19.

5.3 Similarities with the homogeneous heating case

Despite the existence of a mean flow and the pulsatile behaviour, convection with heterogeneous internal heating bears many similarities with the homogeneous case. As already noticed earlier, small scale plumes are still present in the flow, and their typical width remains proportional to $Ra^{-1/2}$ —see figure 21— but with increased variability. This means that the balance between horizontal diffusion and vertical advection is still at play to determine the single plume dynamics.

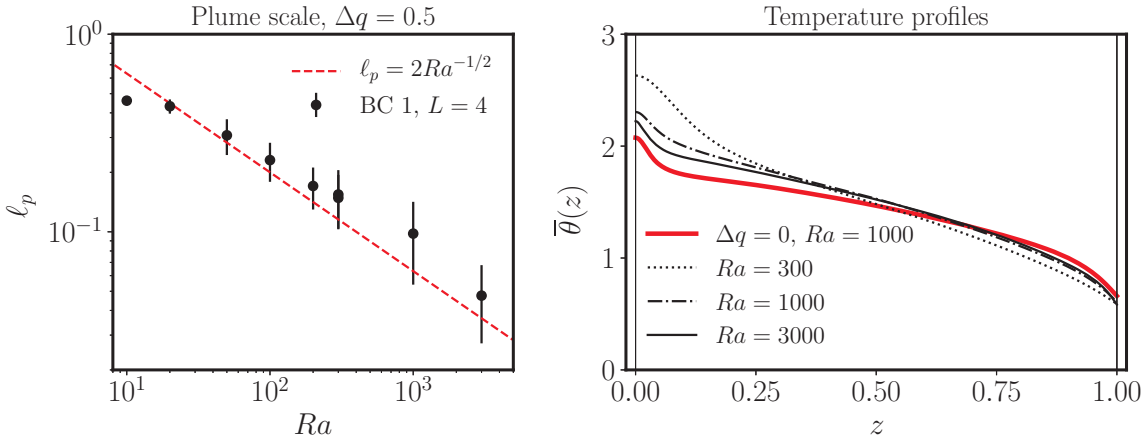

Figure 21: **Left:** typical plume size in the heterogeneous heating case, and comparison with a law $\ell_p \propto Ra^{-1/2}$. The error bars are determined in the same way as in figure 11. **Right:** mean temperature profile for the heterogeneous heating at several Rayleigh numbers; the red line corresponds to the temperature profile in the homogeneous case in the high Ra regime.

Moreover, even if lateral variations of the mean temperature are obvious in figure 19, the horizontally averaged temperature follows a trend that is very close to the homogeneous case, as it is shown in 21.

5.4 Changing Δq

The effect of the amplitude of heating modulation Δq has also been considered. As expected, increasing Δq leads to a narrower confinement of the upwelling plumes and larger heat flux anomalies at the center of the domain. It also gives rise to transtion from intermitent behaviour to quasi-periodic, even at large valeus of Ra.

6 Porous Convection with Internal Heating Inside Enceladus

6.1 Physical properties of Enceladus' core

This last part comes as a conclusion on this ideal study of porous convection with internal heating and aims at re-framing our results in the context of Enceladus core.

To characterise convection inside Enceladus' core, and to compare our results to existing literature, we use the same physical parameters as in [5]. A set of fixed physical constants are given in table 1. We reproduce the process used in [5] and do not precisely specify the permeability k and internal heat production $Q_V$values. Instead, we consider that k may range from 10^{-15} m^2 to 10^{-12} m^2 and that the tidal heating is between 10 GW[2] and 40 GW. We therefore draw a map of the behaviour of the system keeping the parameters of table 1 constant and varying both k and Q_V.

[2]This lower bound is inferred from the flux at the south pole of Enceladus

Core radius (h)	186 km
Kinematic viscosity (ν)	1×10^{-6} m^2.s^{-2}
Thermal diffusivity (κ)	1×10^{-6} m^2.s^{-2}
Water thermal expansion (α)	1.2×10^{-3}
Heat capacity (c_p)	4×10^{3} J.K^{-1}.kg^{-1}
Gravity (g)	0.1 m.s^{-2}

Table 1: A summary of the physical parameters used to transpose our idealised study to the case of Enceladus' core. They are adapted from [5] —see in particular the Supplementary Material.

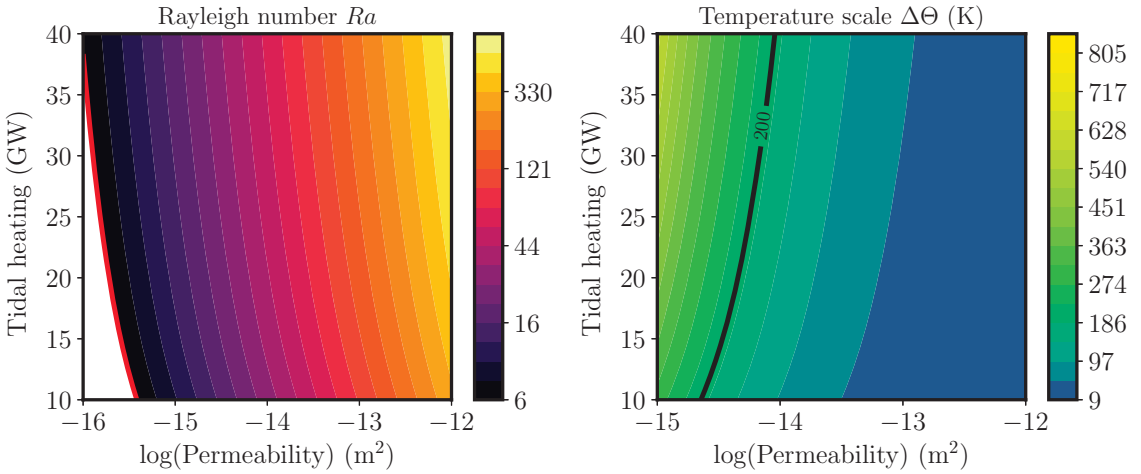

Figure 22: **Left:** the Rayleigh number as a function of the permeability and the tidal heating. The red line materialises the onset of convection for the homogeneous heating case. **Right:** typical dimensional temperature scale $\Delta\Theta$ (in Kelvin) —see (48)— inside the porous core of Enceladus. The white line gives an idea of the liquid-vapour transition that arises around 500 K at the pressure reached at the core-ocean boundary.

6.2 The Rayleigh number inside Enceladus

As explained in the second section of this proceeding, the overall behaviour of the system depends only on one dimensionless parameter, the Rayleigh number defined in (12). The map of the possible Rayleigh numbers inside the core of Enceladus is given in figure 22. In the range of values of k considered in [5], the system is always unstable to convection. Nevertheless, Ra does not reach very high values and peaks around 500.

6.3 Typical velocity and temperature inside the core of Enceladus

In this paragraph, we are interested in quantifying typical temperature and velocity —or Darcy flux— inside the porous medium. Using the scalings introduced in paragraph 2.3, we write the temperature scale $\Delta\Theta$ as a function of Ra:

$$\Delta\Theta \;=\; \frac{\kappa\nu}{k\alpha g h} Ra \tag{48}$$

This scale is shown in figure 22. We find that depending on the parameters, the expected temperature difference between the porous core and the ocean $\Delta\Theta$ ranges from a few tens of degrees to a few hundred. For a difference of 200 K, the temperature inside the porous medium reaches 500 K, which is the temperature at which liquid water turns into vapour at the pressure found at the bottom of Enceladus ocean. Beyond this temperature, our model is certainly not adapted to describe the flow inside the core.

The velocity scale is given by a diffusive velocity κ/h augmented by a factor Ra, that is:

$$U^* = \frac{\kappa}{h} Ra \ . \tag{49}$$

The diffusive velocity scale amounts to 0.1 mm.yr^{-1}; because Ra does not exceed 500, the Darcy flux remains below 5 cm.yr^{-1}.

Consequently, the convective time scale τ is:

$$\tau = \frac{h}{U^*} = \frac{h^2}{\kappa} Ra \simeq 1\text{Gy} \times Ra \ . \tag{50}$$

The typical variability timescale, for instance for the flux at the top boundary —see figure 20— is thus at least 2 million years. It is a very slowly evolving system; as a consequence, the presently observed symmetry breaking between the south pole and the north pole of Enceladus, where tidal heating is the same [5], might be a consequence of pulsatile behaviour happening over a timescale that is too long to be appreciated.

6.4 Hydrothermal velocity at the bottom of Enceladus

To evaluate the typical velocity of the buoyant hot water coming out of the core at the bottom of the ocean we must first evaluate the buoyancy flux. A first difficulty arises when we seek to transpose our two dimensional simulations into three dimension: does the source of buoyancy take the form of a point or of a line? Simulations carried out in [5, 22, 27] suggest that upwellings in the porous medium take the form of elongated sheets. We will therefore assume that the upwellings we have characterised in the porous layer here drive line sources of buoyancy, giving rise to a two dimensional buoyant plume. The two dimensional buoyancy flux B_{2d} has dimensions $[B_{2d}] = L^3 \cdot T^{-3}$, a typical hydrothermal velocity U_h is therefore given by $U_h = B_{2d}^{1/3}$. Note that a refined calculation adapting the model of Morton *et al.* [23, 30] to the case of 2d plumes in unstratified ambient leads to a similar result: the velocity inside the turbulent plume is constant and proportional to $B_{2d}^{1/3}$.

The buoyancy flux is given by [30]:

$$B_{2d} \ = \ \int_{\text{upwelling}} \alpha g \ (\Theta W)|_{z=h} \tag{51}$$

where the 1d integral is computed over an upwelling zone of typical extent $\ell_p \propto Ra^{-1/2}$. As Θ and W are proportional to Ra, B_{2d} scales like $Ra^{3/2}$, or more explicitly:

$$B_{2d} \simeq \frac{\kappa^2 \nu}{kh} \ Ra^{3/2} \ \ (w\theta)|_{z=h} \ . \tag{52}$$

Focusing of the heat flux in narrow upwelling zones leads to enhanced values of $(w\theta)|_{z=h}$, as shown in figure 23. In the case of heterogeneous heating, focusing increases by a factor 10

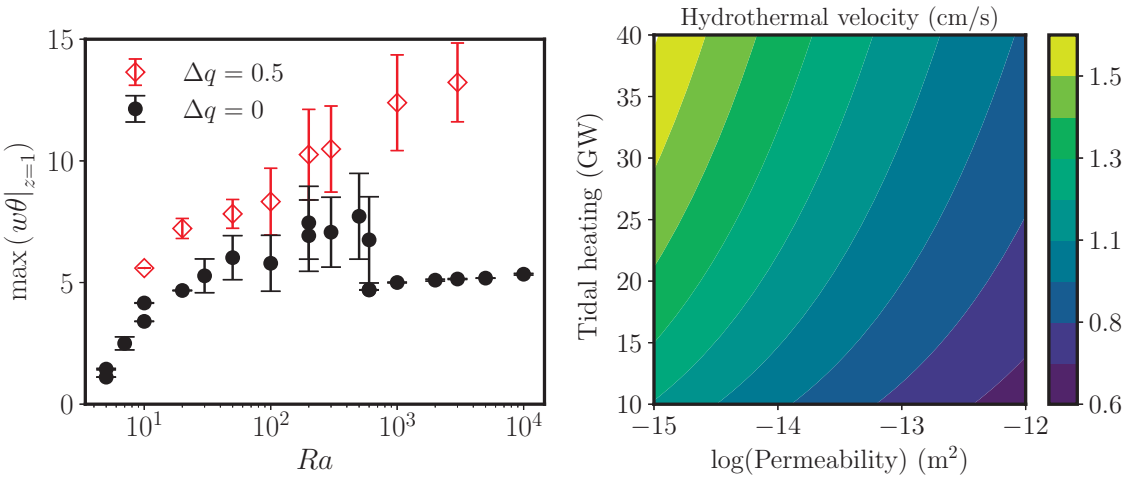

Figure 23: **Left:** maximum value of the non-dimensional advective heat flux at the top of the porous layer determined from the simulations. The error bar accounts for the standard deviation of the maximum value over the course of a simulation. Both homogeneous ($\Delta q = 0$) and heterogeneous ($\Delta q = 0.5$) are considered. **Right:** typical hydrothermal velocity obtained from the buoyancy flux at the bottom of the ocean as a function of permeability and tidal heating.

the heat flux at the bottom of the ocean. Finally, the typical hydrothermal velocity is found to be about 1 cm/s, no matter what the permeability or the tidal heating are. This value is coherent with the typical velocity found in [5] with different scaling arguments relying on the power anomaly advected to the ocean floor.

7 Conclusions and Future Works

We have carried out in this project an analysis of convection driven by internal heating in a porous layer with an open top boundary. This ideal system has been designed as a model for the core of Enceladus, following the work of Choblet *et al.* [5]. We reproduce observations that were already made in [5], such as the focusing of heat flux in narrow areas, that we have described theoretically and numerically. The model used here has also helped to highlight the underpinning of heat transport in an internally heated layer. In particular, we have shown that the plume structure is governed by a balance between the vertical advection of thermal energy with horizontal diffusion. In addition, the heat transport efficiency, which has been characterised via a generalised Nusselt number, is the same as for the classical Rayleigh-Bénard convection in porous media [25, 14, 15]. Lastly, despite the idealisation of our model, rescaling it to the core of Enceladus gives an estimate of hydrothermal activity that are coherent with those carried out in [5].

A first theoretical extension of this work would be to derive an upper bound for the heat transport in the porous medium. We have found that the transition to steady state at high Rayleigh number is associated with enhancement of the transport observed in figure 18. We don't know *a priori* whether the observed steady solutions are optimal and it would be

interesting, using the method introduced in [25], to derive the most efficient flow to carry heat away.

In addition, there is a need to clarify the behaviour of the system at the boundary and the coupling between the porous layer and the above ocean. We have stated in the second section that the two possible thermal boundary conditions used here —imposed temperature of free temperature in the upwellings— are the end-members of the system. The imposed temperature condition represents a very slow porous layer compared to the above ocean. In this configuration, the water coming out of the core is at the same temperature as the ocean and is neutrally buoyant; there is then no hydrothermal activity in the sense of what we know at the bottom of the Earth's ocean. Nevertheless, it is associated with a diffusive heat flux anomaly on the subsurface ocean's floor which is likely to drive convection and mixing in the ocean. The observed chemical signature of contact with silicate rocks at high temperature could very well happen below the thin thermal boundary layer at the top of the core. In short, it is difficult to produce a statement on the thermal structure of the subsurface ocean without a careful study of the coupled system with possibly two very different typical evolution timescales for each medium.

8 Acknowledgments

I would like to thank Ducan Hewitt for supervising this work and providing support and insight throughout the project. I am also grateful to David Goluskin for a long afternoon talk that helped me gain understanding of internally heated convection. I would also like to thank Neil Balmforth for taking two hours to review and improve my final presentation. Lastly, I am grateful to the co-directors, Neil Balmforth and Colm Caulfield, the staff and the fellows for this wonderful summer of research and fun.

References

[1] A. Bagchi and F. A. Kulacki, *Natural Convection in Superposed Fluid-Porous Layers*, SpringerBriefs in Applied Sciences and Technology, Springer New York, New York, NY, 2014.

[2] C. Beckermann, S. Ramadhyani, and R. Viskanta, *Natural Convection Flow and Heat Transfer Between a Fluid Layer and a Porous Layer Inside a Rectangular Enclosure*, Journal of Heat Transfer, 109 (1987), p. 363.

[3] R. J. Buretta and A. S. Berman, *Convective Heat Transfer in a Liquid Saturated Porous Layer*, Journal of Applied Mechanics, 43 (1976), pp. 249–253.

[4] M. Carr and B. Straughan, *Penetrative convection in a fluid overlying a porous layer*, Advances in Water Resources, 26 (2003), pp. 263–276.

[5] G. Choblet, G. Tobie, C. Sotin, M. Bhounkov, O. adek, F. Postberg, and O. Souek, *Powering prolonged hydrothermal activity inside Enceladus*, Nature Astronomy, (2017), p. 1.

[6] L. Cserepes and L. Lenkey, *Forms of hydrothermal and hydraulic flow in a homogeneous unconfined aquifer*, Geophysical Journal International, 158 (2004), pp. 785–797.

[7] Eric Jones, *SciPy: Open source scientific tools for Python*, 2001.

[8] F. J. Fontaine and W. S. D. Wilcock, *Two-dimensional numerical models of open-top hydrothermal convection at high Rayleigh and Nusselt numbers: Implications for mid-ocean ridge hydrothermal circulation*, Geochemistry, Geophysics, Geosystems, 8 (2007), pp. 1–17.

[9] D. Goluskin, *Zonal flow driven by convection and convection driven by internal heating*, PhD thesis, 2013.

[10] ——, *A Family of Convective Models*, in Internally Heated Convection and Rayleigh-Bnard Convection, SpringerBriefs in Applied Sciences and Technology, Springer, Cham, 2016, pp. 1–26.

[11] ——, *Internally Heated Convection Experiments and Simulations*, in Internally Heated Convection and Rayleigh-Bnard Convection, SpringerBriefs in Applied Sciences and Technology, Springer, Cham, 2016, pp. 49–64.

[12] ——, *Stabilities and Bounds*, in Internally Heated Convection and Rayleigh-Bnard Convection, SpringerBriefs in Applied Sciences and Technology, Springer, Cham, 2016, pp. 27–48.

[13] H. C. Hardee and R. H. Nilson, *Natural Convection in Porous Media with Heat Generation*, Nuclear Science and Engineering, 63 (1977), pp. 119–132.

[14] D. R. Hewitt, J. A. Neufeld, and J. R. Lister, *Ultimate Regime of High Rayleigh Number Convection in a Porous Medium*, Physical Review Letters, 108 (2012).

[15] ——, *High Rayleigh number convection in a three-dimensional porous medium*, Journal of Fluid Mechanics, 748 (2014), pp. 879–895.

[16] A. A. Hill and B. Straughan, *Global stability for thermal convection in a fluid overlying a highly porous material*, Proceedings of the Royal Society A: Mathematical, Physical and Engineering Sciences, 465 (2009), pp. 207–217.

[17] H.-W. Hsu, F. Postberg, Y. Sekine, T. Shibuya, S. Kempf, M. Hornyi, A. Juhsz, N. Altobelli, K. Suzuki, Y. Masaki, T. Kuwatani, S. Tachibana, S.-i. Sirono, G. Moragas-Klostermeyer, and R. Srama, *Ongoing hydrothermal activities within Enceladus*, Nature, 519 (2015), pp. 207–210.

[18] J. Kierzenka and L. F. Shampine, *A BVP Solver Based on Residual Control and the Maltab PSE*, ACM Trans. Math. Softw., 27 (2001), pp. 299–316.

[19] F. A. Kulacki and R. Ramchandani, *Hydrodynamic instability in a porous layer saturated with a heat generating fluid*, Wrme- und Stoffbertragung, 8 (1975), pp. 179–185.

[20] M. Le Bars and M. G. Worster, *Interfacial conditions between a pure fluid and a porous medium: implications for binary alloy solidification*, Journal of Fluid Mechanics, 550 (2006), p. 149.

[21] S. Lepot, S. Aumatre, and B. Gallet, *Radiative heating achieves the ultimate regime of thermal convection*, Proceedings of the National Academy of Sciences, 115 (2018), pp. 8937–8941.

[22] M. Monnereau and F. Dubuffet, *Is Io's Mantle Really Molten?*, Icarus, 158 (2002), pp. 450–459.

[23] B. R. Morton, G. I. Taylor, and J. S. Turner, *Turbulent gravitational convection from maintained and instantaneous sources*, Proc. R. Soc. Lond. A, 234 (1956), pp. 1–23.

[24] D. A. Nield and A. V. Kuznetsov, *Onset of Convection with Internal Heating in a Weakly Heterogeneous Porous Medium*, Transport in Porous Media, 98 (2013), pp. 543–552.

[25] J. Otero, L. A. Dontcheva, H. Johnston, R. A. Worthing, A. Kurganov, G. Petrova, and C. R. Doering, *High-Rayleigh-number convection in a fluid-saturated porous layer*, Journal of Fluid Mechanics, 500 (2004), pp. 263–281.

[26] C. C. Porco, P. Helfenstein, P. C. Thomas, A. P. Ingersoll, J. Wisdom, R. West, G. Neukum, T. Denk, R. Wagner, T. Roatsch, S. Kieffer, E. Turtle, A. McEwen, T. V. Johnson, J. Rathbun, J. Veverka, D. Wilson, J. Perry, J. Spitale, A. Brahic, J. A. Burns, A. D. DelGenio, L. Dones, C. D. Murray, and S. Squyres, *Cassini Observes the Active South Pole of Enceladus*, Science, 311 (2006), pp. 1393–1401.

[27] M. Rabinowicz, J. Boulgues, and P. Genthon, *Two and threedimensional modeling of hydrothermal convection in the sedimented Middle Valley segment, Juan de Fuca Ridge*, Journal of Geophysical Research: Solid Earth, 103 (1998), pp. 24045–24065.

[28] J. H. Roberts, *The fluffy core of Enceladus*, Icarus, 258 (2015), pp. 54–66.

[29] P. C. Thomas, R. Tajeddine, M. S. Tiscareno, J. A. Burns, J. Joseph, T. J. Loredo, P. Helfenstein, and C. Porco, *Enceladuss measured physical libration requires a global subsurface ocean*, Icarus, 264 (2016), pp. 37–47.

[30] A. W. Woods, *Turbulent Plumes in Nature*, Annual Review of Fluid Mechanics, 42 (2010), pp. 391–412.